A TDDFT Investigation of Excited States of the Photosystem II Reaction Centre

by

Maeve Anne Kavanagh

A Thesis submitted for the degree of Doctor of Philosophy

to

The Department of Chemistry, Imperial College London

17th June 2021

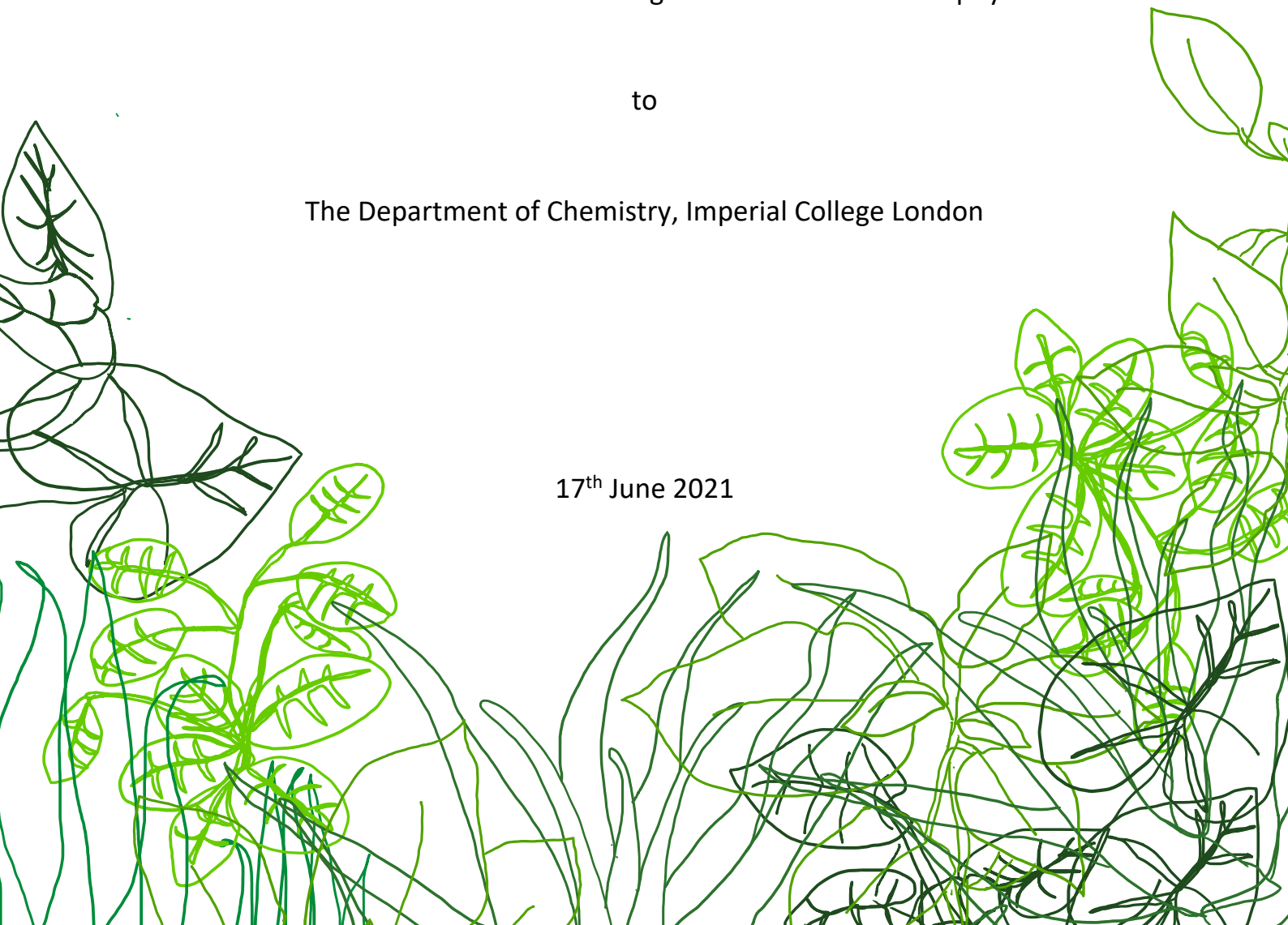




Table of Contents

Statement of Originality **2**

Copyright Declaration **3**

Acknowledgements **5**

Abstract **6**

Introduction *8*

Photosynthesis **9**

Excitons, Energy Transfer and Electron Transfer in Photosynthesis 10

Photosystem II **12**

Excitation and Charge Separation in the Reaction Centre **13**

Site Directed Mutagenesis **15**

Site One – D2-197 16

Site Two – D1-198 18

Site Three – D1-179 20

Site Four – D1-130 20

Theoretical Models of the PS II RC **22**

The Multimer Model and Related Work 22

Quantum Mechanical Models of the Reaction Centre 22

Research Aims of this Thesis **24**

An Important Note on the Scope of this Thesis 24

Methods *26*

Theoretical Background **27**

Background to Electronic Structure Computation 27

Choice of Basis Set 32

Semi-Empirical Approximations to HF – Austin Model 1 33

Density Functional Theory 34

Time Dependence 39

Building Models **46**

Running Excited State Calculations 48

Analysing Excited State Results 48

Analysing individual states 49

Chapter One: Wild Type Photosystem II Reaction Centre Models with Time Dependent-Density Functional Theory..... 50

Results & Discussion 51

Model 1 - ωB97X-D/6-31G**: The Simplest Model 55

Model Comparison (Models 1-4, ωB97X-D/6-31G**)..... 77

Method Comparison (Models 1-4, ωB97X-D/6-31G** and CAM-B3LYP/6-31G**) 86

Model 4 - ωB97X-D/6-31G**: Benchmark Results..... 91

Conclusion 99

Chapter Two: Site Directed Mutation of the P_{D2} Ligand, D2-197 101

Results & Discussion 102

Excitation Energies and Oscillator Strengths..... 104

Excited State Profiles – Cofactor Excitations..... 106

Excited State Profiles – Transition Classes 112

P Chlorophyll Transitions..... 115

Soret Region 121

Conclusion 127

Chapter Three: Site-Directed Mutation of the P_{D1} Ligand, D1-198..... 129

Results & Discussion 130

Excitation Energies and Oscillator Strengths..... 132

Excited State Profiles – Cofactor Excitations..... 134

Active Branch Transitions..... 137

P Chlorophyll Transitions..... 141

Soret Region and Charge Transfer States..... 144

Soret Region - Absorption Difference Spectral Shifts..... 147

Conclusions..... 150

Chapter Four: Site-Directed Mutation in the Chl_{D1} and Phe_{D1} regions 151

Results & Discussion 152

Experimental Findings..... 153

Excitation Energies and Oscillator Strengths..... 155

Excited State Profiles – Cofactor Excitations..... 157

Excited State Profiles – Transition Classes 161

Conclusion 169

Chapter Five: Extended Wild Type Models *171*

Results & Discussion **172**

Model 2A (ωB97X-D/ 6-31G**) 172

Model 5 (CAM-B3LYP/6-31G**) 176

Conclusion **185**

Chapter Six: Final Conclusions & Further Work *186*

Summary of Research and Conclusions 186

Further Work 188

Bibliography *190*

Appendix One – Python Code Repository *196*

General Imports and Variables 196

Utilities Functions 197

Processing Mulliken Population Analysis Output 198

Processing Information from Gaussian Output 201

Plotting Simulated Absorption Spectra 203

Labelling MOs and Transitions Using Mulliken Population Analysis 205

Appendix Two – Investigating the Effect of Water Molecules on Model 1 Results *208*

Appendix Three – A Comparison of Two Methods of Transition Classification *218*

Appendix Four – Supplementary Figures *224*

Appendix Five – Rights and Permissions *280*

List of Figures

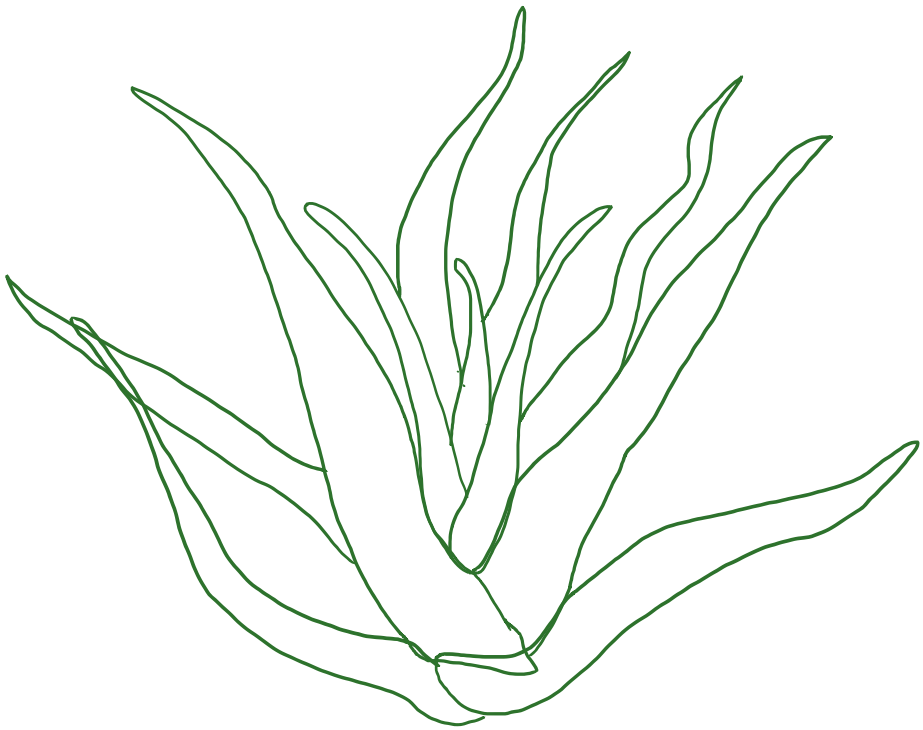
Figure	*Description*	*Page*
1	A simple cartoon thylakoid membrane	*9*
2	Three possible interactions between neighbouring pigments	*11*
3	The layout of the pigments in the PS II RC	*12*
4	The wild type reaction centre of T. vulcanus	*15*
5	The position of D1-130 (Gln) as in WT T. vulcanus	*20*
M.1	Flow chart showing model preparation, calculation and analysis procedure	*46*
M.2	Chlorophyll Chl_{D1} with truncated and full phytol chain	*47*
1.1	Diagram of model 1-4 structures	*54*
1.2	MOs which contribute to ES 1 for Model 1	*57*
1.3	Model 1 ωB97X-D/6-31G** excited states 1-12	*61*
1.4	Model 1 ωB97X-D/6-31G** excited states 13-22	*62*
1.5	The direction of electron density movement during transitions	*63*
1.6	MO diagrams showing dominant transitions for Model 1	*64*
1.7	Contributions from each transition class to ES 1-12 for Model 1	*68*
1.8	Contributions from each transition class to ES 13-22 for Model 1	*69*
1.9	Showing the profile of the first three ES for model 1 all methods	*72*
1.10	ES 3 and ES 5 dominant transitions for Model 1 (CAM-B3LYP/6-31G**)	*74*
1.11	ES 3 and ES 5 dominant transitions for Model 1 (CAM-B3LYP/6-31+G**)	*75*
1.12	Dominant transitions for ES 3 and ES 5 for Model 1	*75*
1.13	Showing the profile of the first three ES for models 1-4	*80*
1.14	Showing the profile of ES 3-6 for models 1-4	*81*
1.15	Showing the contributions from active branch transitions for models 1-4	*82*
1.16	Showing the contributions from P chlorophyll transitions for models 1-4	*83*
1.17	Showing the contributions from inactive branch transitions for models 1-4	*83*
1.18	CT states in the Soret region for Models 1-4 by DCT analysis	*85*
1.19	Model 2 CAM-B3LYP/6-31G** excited states 1-6	*87*
1.20	Contributions from transition classes to ES 1-6 for model 3	*88*
1.21	Model 4 ωB97X-D/6-31G** excited states 1-12	*92*
1.22	Model 4 ωB97X-D/6-31G** excited states 13-22	*93*
1.23	MO diagrams for dominant transitions of model 4	*95*
1.24	Contributions from each transition class for model 4	*96*
1.25	Calculated absorption spectrum for model 4	*98*
2.1	Closeup of the P chlorophylls and mutated D2-197 residue for three mutants	*102*
2.2	Showing the profile of ES 4-6 for WT Model 4 , H197A, H197N and H197Q	*106*
2.3	MO diagrams for transitions contributing to ES 4 for H197A	*108*
2.4	MOs contributing to ES 5 and 6 for H197N	*109*
2.5	P chlorophyll excitations in the Q_X region for WT Model 4, H197A, H197N and H197Q	*110*
2.6	Phe excitations in the Qx region for WT Model 4, H197A, H197N and H197Q	*111*
2.7	Transition classes in the Q_Y branch for WT and H197A, H197N and H197Q models	*112*

2.8 H197N up active transition *112*
2.9 MO diagrams exemplifying the down inactive transition classes for H197A *113*
2.10 Down inactive transition for H197Q *114*
2.11 P chlorophyll contribution to ES 1-6 *115*
2.12 H197A P_{D1} to P_{D2} transitions *116*
2.13 P chlorophyll transitions for H197N *118*
2.14 MO diagrams showing P chlorophyll transitions for H197Q *119*
2.15 P^+-P mutant difference spectra for D2-His197 mutants *121*
2.16 P_{D1} and P_{D2} absorption bands for WT Model 4, H197A, H197N and H197Q *122*
2.17 MOs for the two highest contributing transitions to H197A ES 16 *123*
2.18 MOs for the two highest contributing transitions to H197N ES 16 *124*
2.19 MOs for the highest contributing transition for H197Q ES 21 *124*
2.20 MOs for the highest contributing transition to H197Q ES 22 *125*
2.21 MOs for the highest contributing transition for H197A ES 20 *125*
2.22 MOs for the highest contributing transition for H197N ES 21 *126*
3.1 Closeup of the P chlorophylls *130*
3.2 Phe excitations in the Q_Y region for WT model 4, H198A, H198N and H198Q *134*
3.3 P chlorophyll excitations in the Q_Y region for WT model 4, H198A, H198N and H198Q *134*
3.4 Chl_{D1} and Chl_{D2} excitations in the Q_Y region for WT model 4, H198A, H198N and H198Q *135*
3.5 P_{D1} and Chl_{D1} excitations in the Q_X region for WT model 4, H198A, H198N and H198Q *136*
3.6 P_{D2} and Chl_{D2} excitations in the Q_X region for WT model 4, H198A, H198N and H198Q *136*
3.7 Active branch transition contributions to ES 1-6 for WT model 4, H198A, H198N and H198Q *137*
3.8 MOs making up the highest contributing transitions for ES 1 for H198A *138*
3.9A MOs making up the highest contributing transition for ES 1 for H198A *139*
3.9B MOs making up the highest contributing transition for ES 5 for H198A *140*
3.10 P chlorophyll transition contributions to ES 1-6 for WT model 4, H198A, H198N and H198Q *141*
3.11 MOs making up the highest contributing transition to ES 3 and 4 for H198A *142*
3.12 MOs making up the highest contributing transition to ES 3 and 4 for H198Q *143*
3.13 Excitation out of P_{D1} contributions in the Soret region for WT model 4, H198A, H198N and H198Q *144*
3.14 P_{D2} to P_{D1} and up inactive transition contributions in the Soret region for WT model 4, H198A, H198N and H198Q *146*
3.15 P^+-P mutant difference spectra for D1-His198 mutants *148*
3.16 Gaussian broadened P_{D1} absorption bands in the Soret region at two different resolutions *148*
3.17 Gaussian broadened P_{D2} absorption bands in the Soret region at two different resolutions *149*
4.1 Closeup of the Chl_{D1} chlorophyll and residue at position D1-179 *152*
4.2 Closeup of Phe_{D1} and D1-130 residue *152*
4.3 Phe_{D1} Q_x band mutant shifts *153*

4.4	Chl_{D1} Q_Y band mutant shifts	*154*
4.5	Contribution from Phe occupied orbitals to ES 1-3 for WT model 4, T179E, T179H, Q130E and Q130L	*157*
4.6	Contribution from P chlorophyll occupied orbitals to ES 1-6 for WT model 4, T179E, T179H, Q130E and Q130L	*158*
4.7	Contribution from Chl_{D1} and Chl_{D2} occupied orbitals to ES 1-6 for WT model 4, T179E, T179H, Q130E and Q130L	*158*
4.8	Contribution from Phe_{D1} and Chl_{D1} occupied orbitals to ES 7-12 for WT model 4, T179E, T179H, Q130E and Q130L	*159*
4.9	Active branch transition contributions to ES 1-6 for WT model 4, T179E, T179H, Q130E and Q130L	*161*
4.10	MOs making up the highest contributing transition for ES 1 for T179E, T179H, Q130E and Q130L	*163*
4.11	MOs making up the highest contributing transition for ES 5 for T179E, T179H, Q130E and Q130L	*164*
4.12	P chlorophyll transition contributions to ES 1-6 for WT model 4, T179E, T179H, Q130E and Q130L	*165*
4.13	P chlorophyll transitions for T179E and T179H	*166*
4.14	P chlorophyll transitions for Q130E and Q130L	*167*
5.1	Structure of model 2A	*172*
5.2	Excited states 1-6 for model 2 and 1-8 for model 2A	*173*
5.3	Contributions from each transition class to model 2 and model 2A	*174*
5.4	Local $Chlz_{D1}$ excitation contributing to ES 4 for model 2A	*175*
5.5	Local $Chlz_{D2}$ excitation contributing to ES 4 for model 2A	*175*
5.6	Structure of model 5	*176*
5.7	Structure of model 5 viewed from below	*176*
5.8	Phe excitation contributions to ES 1-6 for model 4 and 5	*178*
5.9	P chlorophyll excitation contributions to ES 1-6 for models 4 and 5	*179*
5.10	Chl_{D1} and Chl_{D2} excitation contributions to ES 1-6 for models 4 and 5	*180*
5.11	Active branch transition contributions to ES 1-6 for models 4 and 5	*180*
5.12	P chlorophyll transition contributions to ES 1-6 for models 4 and 5	*181*
5.13	Inactive branch transition contributions to ES 1-6 for models 4 and 5	*182*
5.14	MO diagrams showing dominant transitions contributing to ES 1-6 for model 5 (CAM-B3LYP/6-31G**)	*183*

List of Tables

Table	*Description*	*Page*
1.1	Summary of the four models discussed in chapter 1	*51*
1.2	Table of which residues were included in model 3 (and model 4)	*53*
1.3	Energies and Oscillator Strengths for model 1	*55*
1.4	TD results for state 1, Model 1	*56*
1.5	MultiWfn output for MOs contributing to state 1 for model 1	*56*
1.6	Transitions contributing to state 1 for model 1	*59*
1.7	D_{CT} vectors-nearest atom data for Model 1	*70*
1.8	Energies and Oscillator Strengths for Model 1 Qy region, all methods comparison.	*71*
1.9	Energies and Oscillator strengths for ES 1-22 of Models 1-4	*78*
1.10	CT states in the Soret region for model 1-4	*85*
1.11	Excitation energies and oscillator strengths for model 4 (CAM-B3LYP/6-31G**)	*89*
2.1	Excitation energies and oscillator strengths for WT Model 4, His-197-Ala (H197A), His-197-Asn (H197N) and His-197-Gln (H197Q)	*104*
2.2	Cofactor occupancy for MOs in ES 4 transitions for H197A	*108*
2.3	Cofactor occupancy for MOs in ES 5 and ES 6 transitions for H197N	*109*
2.4	Cofactor occupancy for inactive branch orbitals of H197A and WT Model 4	*114*
2.5	P chlorophyll occupancy of P chlorophyll MOs of H197A and WT Model 4	*116*
2.6	Occupancy of P chlorophyll MOs for H197Q	*118*
2.7	Occupancy of ChlD1 MOs for H197Q and WT Model 4	*120*
2.8	ES data for all ES used to plot the simulated P absorption bands in the Soret region for WT model 4, H197A, H197N and H197Q	*122*
2.9	MO occupancies for highest contributing transitions to H197A ES 20 and H197N ES 21	*126*
3.1	Excitation energies and oscillator strengths for WT model 4 and three mutant RC models	*132*
3.2	Active branch MOs for H198A	*138*
3.3	Dominant transitions to ES 1 for H198N and WT model 4	*139*
3.4	Dominant transitions to ES 5 for H198A (top two rows) and WT model 4	*140*
3.5	P chlorophyll MOs for H198A	*142*
3.6	P chlorophyll MOs for WT model 4	*142*
3.7	P chlorophyll MOs H198Q	*143*
3.8	CT states in the Soret region for WT model 4, H198A, H198N and H198Q	*145*
4.1	Excitation energies and oscillator strengths for WT model 4, T179E and T179H	*155*
4.2	Excitation energies and oscillator strengths for WT model 4, Q130E and Q130L	*156*
4.3	Active branch orbital occupancy for WT model 4, T179E, T179H, Q130E and Q130L	*161*
4.4	P chlorophylls orbital occupancy for WT model 4, T179E, T179H, Q130E and Q130L	*165*
5.1	Excitation energies and oscillator strengths for Model 2 and Model 2A	*172*
5.2	List of residues included in models 4 and 5	*177*
5.3	Excitation energies and oscillator strengths for Model 4 and Model 5	*178*
5.4	MO Occupancy for ChlD1 and PheD1 MOs of Model 5 (CAM-B3LYP/6-31G**)	*181*
5.5	MO Occupancy for ChlD1 and PheD1 MOs of Model 4 (CAM-B3LYP/6-31G**)	*181*
5.6	MO Occupancy for P chlorophyll MOs of Model 5 (CAM-B3LYP/6-31G**)	*182*
5.7	MO Occupancy for P chlorophyll MOs of Model 4 (CAM-B3LYP/6-31G**)	*182*



Statement of Originality

I declare that thesis is an original work composed solely by me and that all of the research presented in this thesis has been carried out by me, Maeve Kavanagh, alone.

I declare that this work has not been submitted previously for any other degree or professional qualification.

Parts of this work appear in the jointly authored research article ‘A TDDFT investigation of the Photosystem II reaction center: Insights into the precursors to charge separation‘ published in PNAS August 2020 to which my contribution was carrying out all calculations and analysis presented and writing the manuscript, the contribution of joint authors on this paper included reading and editing the manuscript and carrying out preliminary calculations and analysis which are not presented in that work or in this thesis.

Copyright Declaration

The copyright of this thesis rests with the author. Unless otherwise indicated, its contents are licensed under a Creative Commons Attribution-Non Commercial 4.0 International Licence (CC BY-NC).

Under this licence, you may copy and redistribute the material in any medium or format. You may also create and distribute modified versions of the work. This is on the condition that: you credit the author and do not use it, or any derivative works, for a commercial purpose.

When reusing or sharing this work, ensure you make the licence terms clear to others by naming the licence and linking to the licence text. Where a work has been adapted, you should indicate that the work has been changed and describe those changes.

Please seek permission from the copyright holder for uses of this work that are not included in this licence or permitted under UK Copyright Law.

To Sheila, Alan and William, there are no words. Thank you for everything.

To the memories of Maureen and Carys, every girl needs strong women like you in her life. Thank you for inspiring strength in me.

To Aisha, Amandine, Andrew, Ben, Chiara, Chris, Dani, Francesca, Gayatri, Isobel, Joanne, Juan, Karl, Laura, Leonie, Loreley, Luke, Maciej, Matt, Mica, Nadia, Nathalie, Neil, Sarah, Shukai and Tom. I owe the completion of this work to your encouragement, friendship and support.



Acknowledgements

To the Gould group past and present and to the rest of Lab 109, thank you for having the time to talk when I needed and for making our work space such a positive place to be. Particular thanks go to Francesca Vianello and Shukai Wang who were a huge help when I was learning python for the first time. Also thank you to Qi Yuan, Dimitrios Toroz and Tristan Mackenzie for their immense knowledge of Gaussian and for their patience.

I would like to thank each of my supervisors Ian Gould and Laura Barter for their guidance throughout the PhD. I greatly appreciated our meetings which led to many thoughtful discussions, these were vital to keeping the work on track or helping to identify interesting new directions. Most of all thank you for your enthusiasm and energy over the last four years, your confidence in me and commitment to this project have been incredibly motivating for me.

Finally, thank you to the Engineering and Physical Sciences Research Council for funding this research.

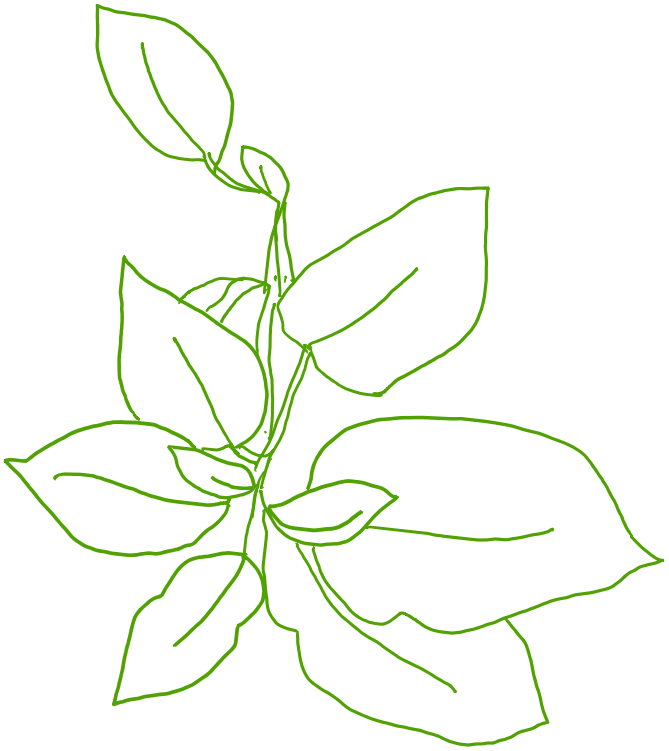
Abstract

A deeper understanding of the mechanisms involved in natural photosynthesis could inspire new artificial photosynthetic systems and bio-engineered organisms. Study of photosystem II, a pigment-protein complex responsible for the first step of solar energy conversion in oxygenic photosynthesis, is therefore driven by the need for clean energy and robust crops.

Following excitation of the reaction centre of photosystem II, electron transfer proceeds selectively up one branch (the D1 branch) of the pseudo-C_2-symmetric reaction centre producing a highly oxidative charge separated state, capable of abstracting electrons from substrate water. The structural reasons for the D1 branch preference are unclear, and remain difficult to probe due to the complexity of the system and its spectral features. Finding these will necessarily rely on detailed modelling, the challenge of which can finally be met with sufficient computational resource using Density Functional Theory.

Results of Time Dependent Density Functional Theory calculations of excited states of the Photosystem II reaction centre are presented. It was found that pigment phytol chains and surrounding amino acid residues must be explicitly included in any model in order for the D1 branch preference to be reproduced. Building on this insight, results of calculations on mutant models of the same size are presented. A qualitative agreement with experimental shifts in simulated absorption difference spectra is achieved for seven out of ten mutant reaction centre models. Including further regions of the reaction centre was found to exaggerate the D1 branch preference further but overall larger models were in agreement with the benchmark model results.

This work takes steps towards a working model of the reaction centre that could be used to investigate the individual structural features which lead to the D1 branch preference and as a predictive tool for the action of specific mutations.



Introduction

Research into Photosystem II (PS II) has spanned many decades and has several, globally impactful motivations. The pressing need for cleaner, more efficient solar technologies of our own,[1,2] whether through artificial photosynthesis[3] or semi-artificial systems,[4] drives a desire to better understand how photosynthesizing organisms have evolved to capture and harness energy from the sun. Furthermore, the study of PS II advances us towards new bio-engineered solutions to tackle global hunger:[5] understanding the effects of an altered climate and atmosphere on crop growth will be key to planning climate change adaptation as it relates to agriculture.[6,7] In 2020, where a global temperature increase of 1.5° is already locked-in,[8] this work is vitally important.

The Sun's energy, chemically stored through photosynthesis, is the source of all organic fuel including fossil fuels.[9] Since solar energy and biomass will form the majority of a renewable energies mix as we continue to move away from coal, gas and oil as our main fuel sources,[10] finding ways to mimic photosynthesis and to increase energy-crop yield is vital to our energy needs. Cheap and efficient solar fuel production would allow mitigation of further climate change and halt the depletion of fossil fuel reserves. Many design features (*e.g.* proton-coupled electron transfer[11] and coherence[12]) taken from the study of PS II have already been implemented into the development of new bio-inspired materials.

As the pinnacle of crop growth enhancement via traditional farming practice appears to have been reached,[5] it seems inevitable that we will soon turn to genetic enhancement more widely in order to feed our growing population.[13] Organisms with enhanced photosynthetic rates or better adaptation to changing atmospheric or light conditions would be highly desirable. PS II is also a key target for herbicidal inhibition, which would benefit crop yield by reducing competition from robust weeds.[14]

Photosynthesis

The process by which many species are able to convert solar energy into stored chemical energy is called photosynthesis. Oxygenic photosynthesis specifically, in plants, algae and cyanobacteria, takes in substrate water and carbon dioxide to produce stored carbohydrates (generically CH_2O) and by-product oxygen. These so-called photoautotrophs use light as their energy source and CO_2 as their sole source of carbon.[15] A simple reaction scheme for oxygenic photosynthesis is written below (scheme 1):

Scheme 1: $CO_2 + H_2O \rightarrow (CH_2O) + O_2$

Two photon absorption events are required to complete the overall process described by scheme 1, requiring photons to be taken up by two different photosystems.[16] The first step in oxygenic photosynthesis is carried out by PS II, see scheme 2.[9]

Scheme 2: $2H_2O \rightarrow 4e^- + 4H^+ + O_2$

The electrons are transported to photosystem I (PS I) where reduction of nicotinamide adenine dinucleotide phosphate ($NADP^+$) takes place, whilst the protons generated are used to drive adenosine triphosphate (ATP) production.[16] The two photosystems PS I and PS II are embedded in the thylakoid membrane, a system of membranes found in cyanobacteria, or within the chloroplasts of photosynthesising eukaryotes.[15] The complexes which carry out the light dependent reactions in photosynthesis are organised in sequence as shown in Figure 1. Outside the membrane the final synthesis steps take place including CO_2 fixation.[15]

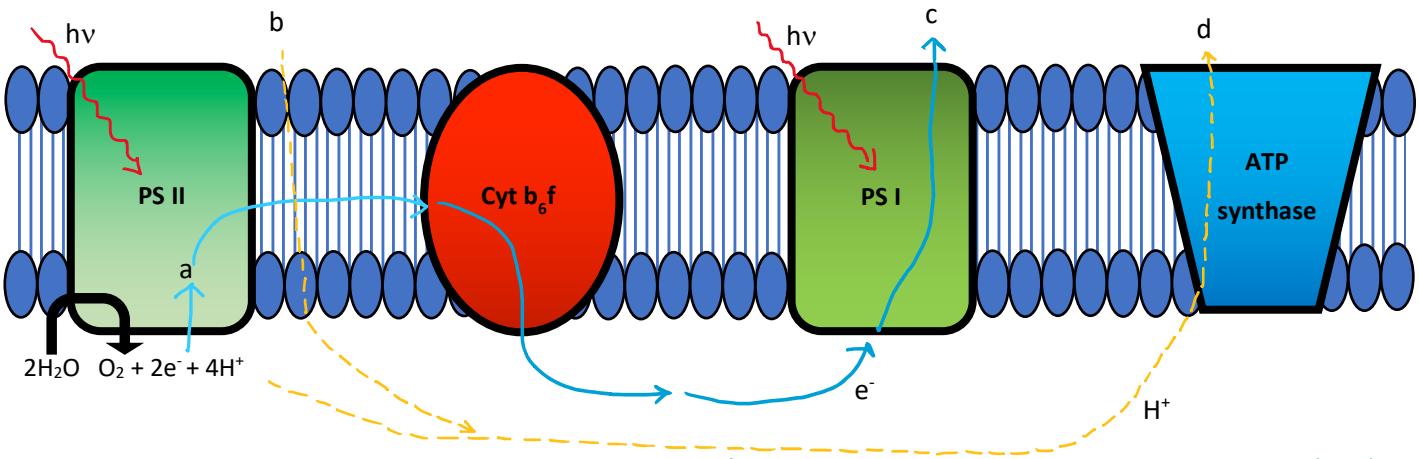


Figure 1 : A simple cartoon showing the organisation of the thylakoid membrane including photosystem II (PS II), cytochrome b_6 f (Cyt b_6 f), photosystem I (PS I) and ATP synthase, adapted from Blankenship 2014.[15] Red wavy arrows showing incident photons, blue arrows showing electron transport and yellow dashed arrows showing photon transport. a) reduction of plastoquinone to plastoquinol, b) transmembrane proton gradient, c) $NADP^+$ reduction and carbon fixation and d) ATP synthesis powered by protonmotive force.

Excitons, Energy Transfer and Electron Transfer in Photosynthesis

Before discussing the behaviour of the PS II in detail, it is worth briefly describing the light harvesting stage of photosynthesis, which employs chlorophylls, the same pigment molecules found in photosynthetic reaction centres. Light harvesting antennae are networks of densely-packed pigment molecules primed to absorb incoming energy from the sun and transport it efficiently to the reaction centre.[15] The specific protein environments of each pigment in an antenna complex means that the pigments are tuned to absorb photons of a specific wavelength. Through this specification, peripheral absorbing pigments can absorb high energy photons whilst those closer to the reaction centre absorb at lower energies. This arrangement allows each pigment to transfer excitation energy to their nearest neighbours, ensuring efficient energy absorption at every step, allowing energy to be transferred over a long distance. Both close and long range interactions between absorbing pigments are important, due to conformational motion of the pigments and protein environment creating pockets of order and disorder within light harvesting complexes.

To describe short range interactions, we must consider the formation of excitons. The theory of excitons was developed in reference to close-packed, ordered systems (*e.g.* solid state crystals) where molecules are strongly coupled.[17] In photosynthetic complexes (reaction centres and light harvesting antennae) short distances between pigments leading to overlapping molecular orbitals give rise to excitonic interactions. Excitons in photosynthesis are thus described as shared excitation over two or more pigment molecules.[18] Formally, an exciton can be described as a linear combination of the excited states of the participating pigment molecules. Similar to molecular orbital theory, we might expect to see an absorption splitting associated with the formation of an exciton (as shown in Figure 2, middle panel), although in practice this may be impossible to identify for a disordered bulk protein sample.[18]

The mechanism of excitation energy transfer between weakly-coupled pigments was proposed by Förster,[19] in which an excited (donor) pigment may transfer energy to a neighbouring (acceptor) pigment due to dipole coupling between the donor and acceptor.[19] Unlike excitonic interactions, Förster energy transfer mechanisms are inherently non-coherent (they do not rely on formation of superpositions of excited states). A Förster-like energy transfer is assumed for carrying energetic equivalents over long ranges where momentary coherences may easily be destroyed by energetic fluctuations over time[18] (*e.g.* incident photon energy from peripheral antenna complexes towards the PS II RC). The use of exciton theory and Förster theory are not entirely mutually exclusive. Generalized Förster theory recognised that the donors and acceptors may be groups of strongly-coupled pigments, thus regarding the delocalised states (excitons) themselves as donors and acceptors.[20]

Entirely different from the Förster mechanism – in which the excited electrons of each pigment or local group of pigments remain bound to their respective nuclei – is the mechanism of electron transfer. Electron transfer events take place in the RC, leading to a charge separated state. The term charge transfer (CT) is used synonymously with electron transfer in this thesis and throughout the literature. A CT state can be thought of as the product of a charge transfer interaction.[21] Furthermore, an exciton-CT state is the term given to a mixing between excitonic and CT interactions, the product of which will be a bound, delocalised excited state (ES), which has undergone a fraction of inter-pigment electron transfer from ground to excited state. The cartoon below (Figure 2) summarises the mechanisms of energy and charge transfer which are relevant to this thesis.

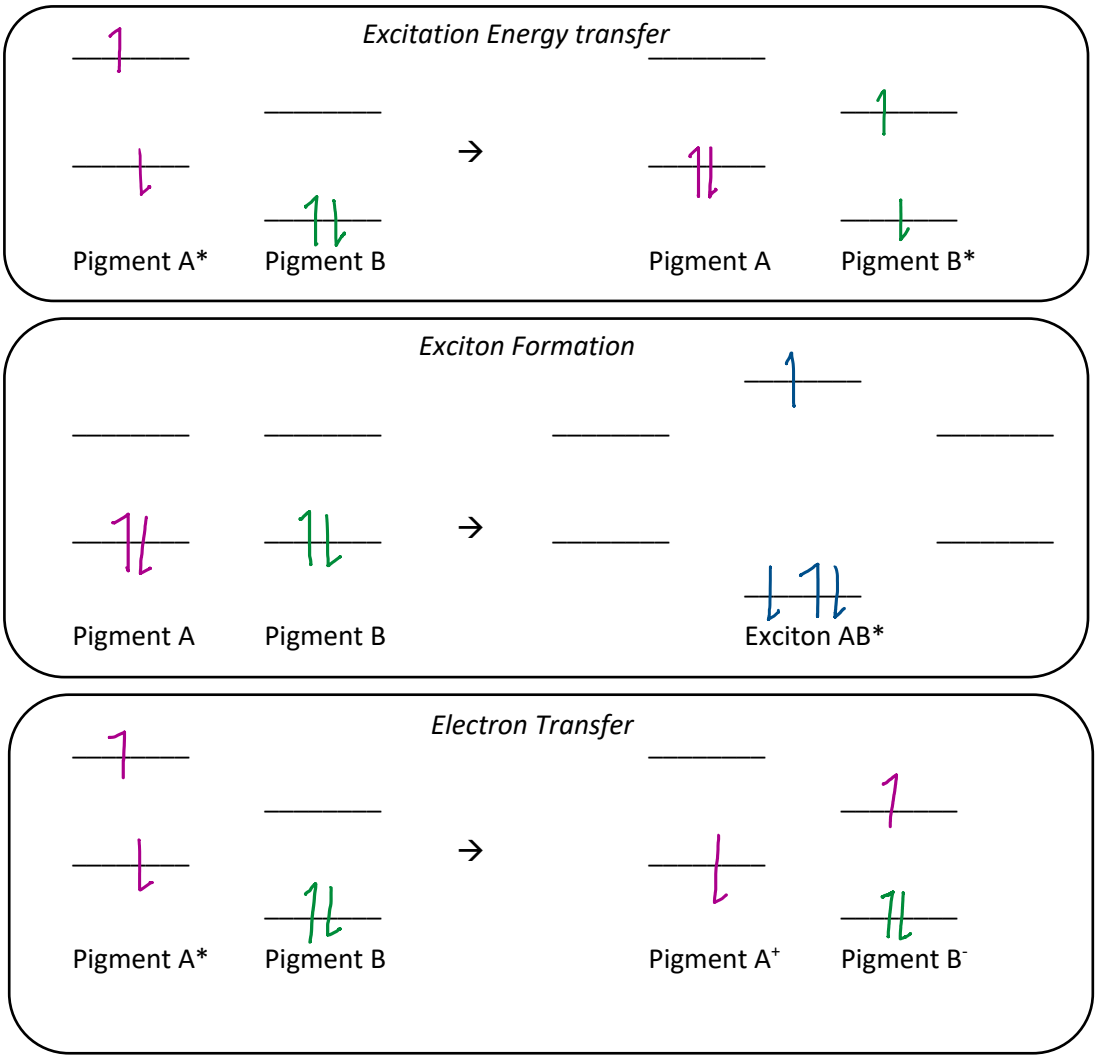


Figure 2 : A cartoon depicting three possible interactions between neighbouring pigments: Top – excitation energy transfer, which, when pigments A and B are sufficiently weakly coupled to each other, is assumed to go via the Förster mechanism.[19] Middle – formation of an exciton;[17] a delocalised excited state, which may implicate two or more closely coupled pigments. Bottom – electron transfer (synonymous with charge transfer) in which an electron is transferred from an excited donor pigment A to a neighbouring acceptor B.

Photosystem II

PS II is the complex responsible for the first step in oxygenic photosynthesis (see scheme 2). One PS II monomer contains 20 protein sub-units[22] (PS II may function as a monomer or dimer[23] within the thylakoid membrane), and many light absorbing *chlorophyll a* molecules and other pigments bound non-covalently within the protein matrix.[22] In plants and algae, peripheral light harvesting complex II (LHC II) and core CP43 and CP47 complexes (not pictured in Figure 1) surround PS II, functioning as light harvesting antennae.[15] Although PS II evolved ~2.45 billion years ago, its structure is still conserved today in all oxygenic photosynthesising organisms.[24] Evidently, the structure of PS II is biologically optimized to perform its function.

The reaction centre (RC) in the heart of the PS II complex is the site of light-catalysed water splitting, and the focal point of this thesis. Two protein chains (D1 and D2) bind the pigments in the RC, which are arranged in two branches with pseudo C2 symmetry[22] (see Figure 3).

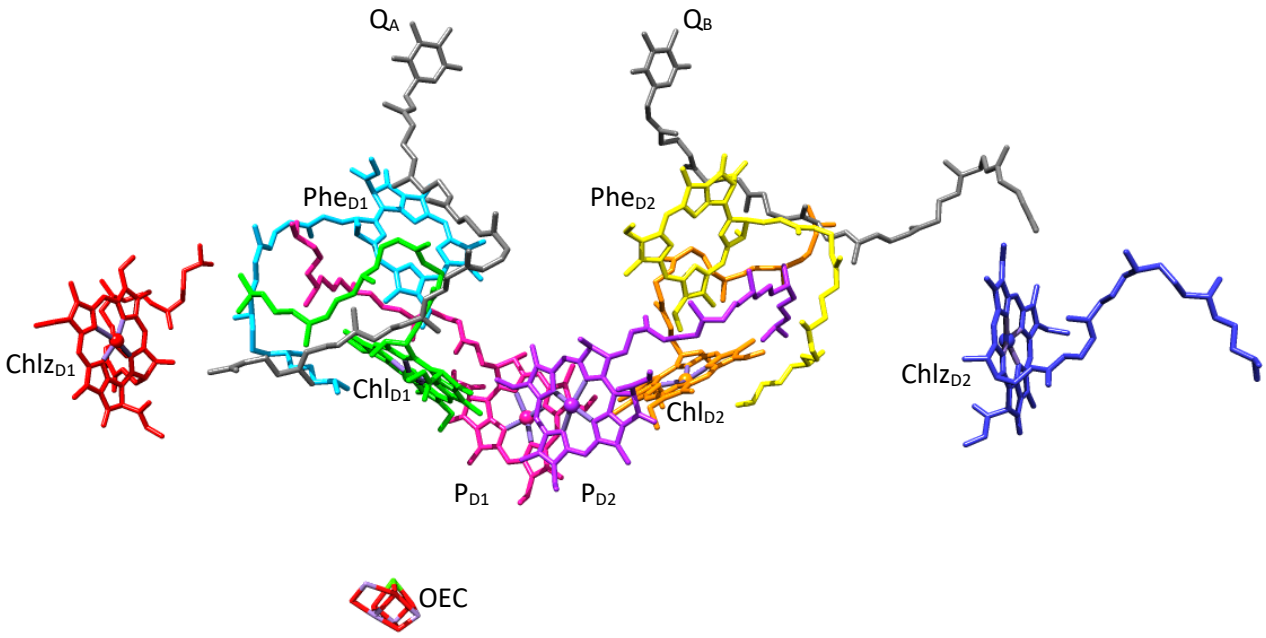


Figure 3 : The layout of the pigments in the PS II RC from the crystal structure of *T. vulcanus* (Umena, 2011). Pigments are arranged in two pseudo-symmetrical branches with the pigments comprising the branch on the left hand side bound by protein chain D1 and the right hand side pigments bound by chain D2. Found in each branch from bottom to top are a P chlorophyll (P_{D1}, pink and P_{D2}, purple), an accessory chlorophyll (Chl_{D1}, green and Chl_{D2}, orange), a peripheral chlorophyll ($Chlz_{D1}$, red and $Chlz_{D2}$, dark blue), a pheophytin (Phe_{D1}, light blue and Phe_{D2} yellow) and a plastoquinone (Q_A and Q_B both in grey).

There are six core pigments: four *chlorophyll a* and two *pheophytin*, in the RC. The two closest *chlorophyll a* to the oxygen evolving complex (OEC) are labelled P_{D1} and P_{D2}, with subscripts corresponding to the protein chain by which they are bound. The next closest pigments are Chl_{D1} and Chl_{D2}, followed by the two pheophytin Phe_{D1}

and Phe_{D2}. Two *plastoquinone* (PQ) molecules, Q_A (D1 branch – tightly bound) and Q_B (D2 branch – weakly bound) follow the pheophytin at the end of each branch, and on the periphery two further *chlorophyll a* $Chlz_{D1}$ and $Chlz_{D2}$ are found.[22]

Complexes containing the RC can be isolated with some difficulty from preparations of PS II in order to obtain an absorption spectrum. In this work, features of the low temperature UV-vis absorption spectrum of the D1-D2-cyt b559 complex[25] (the smallest charge separating complex that can be isolated from PSII) are compared to calculated absorption spectra of RC-only models. It should be noted that the D1/D2 Cyt b559 RC contains 6 Chl and 2 Phe, and thus contains two peripheral chlorophyll molecules, which are not included in every models discussed in this thesis. Therefore, it is striking that the models studied in this thesis are able to reproduce the main features: each having three distinct peaks in the region from 700 to 400 nm with similar relative peak heights. The spectrum from ref.[25] is reproduced with permission in chapter one alongside the simulated absorption spectrum for model 4 for ease of comparison.

Excitation and Charge Separation in the Reaction Centre

During photosynthesis, energy captured by absorption of a single photon is channelled through the PS II complex towards the RC, there producing a delocalised excited state.[26] Following excitation of the RC, a series of charge transfer (CT) steps are initiated in which electrons are transported up the D1 branch pigments from $P_{D1} \rightarrow Chl_{D1} \rightarrow Phe_{D1}$. This charge separation (CS) results in the primary radical pair species $P^+Phe_{D1}^-$, which has oxidative power unparalleled in nature (~+1.1V). Catalysed by the OEC, substrate water is oxidised, producing an electron which regenerates the cationic side of the RC for another photosynthetic cycle. At the other end, the electron on Phe_{D1}^- transfers to Q_B via Q_A. After two successive photons have been absorbed, Q_B becomes doubly reduced and is protonated, producing plastoquinol (see Figure 1, label a), which leaves the photosystem carrying two reductive equivalents over to PS I.[27] Q_B is replaced and the RC is ready to go through another cycle of photon absorption and H_2O reduction. After four successive cycles, O_2 is produced at the site of the OEC and released to the atmosphere.[28,29] Scheme 3 below outlines the total redox reaction after four photons have been absorbed:

$$\text{Scheme 3 : } 2H_2O + 2PQ + 4H^+ \rightarrow O_2 + 4H^+ + 2PQH_2$$

Several aspects of this general scheme have been under debate in the literature for the past few decades: Firstly, what is the nature of the initial RC excited state (RC*) and the intermediates generated following the CT steps towards primary radical pair $P^+Phe_{D1}^-$? Secondly, how and why does the RC select for CT to travel up the D1 branch and not D2 (although it is nearly symmetrical to D1)? The former of these already has a definitive

answer at the time of writing and will be discussed in further detail below. However, the answers to the final question are still unclear, seeking ways to address this question forms the motivation behind this thesis.

The search for the initial excited state, RC* was hampered by the early assumption that PS II structure was closely linked to that of the purple bacterial (PB) RC. The PB RC does indeed have a similar structure to the PS II RC, one major difference being the distance between the two bottom-most chlorophylls P_{D1} and P_{D2} is greater in PS II than the distance between PB analogues P_A and P_B.[30] Early models of the PS II RC therefore overestimated the coupling between P_{D1} and P_{D2}[31] (for lack of a better resolution crystal structure to advise otherwise), which would wrongly predict a strongly coupled $P_{D1}P_{D2}$ dimer to generate a low energy trap (as found for the P_AP_B dimer in PB RC). The Multimer model showed that when a similar coupling between all RC pigments was considered, modelling led to a more accurate fit of the PS II spectrum.[32] This has subsequently been confirmed by the publication of finer resolution crystal structures,[22] from which the pigment couplings can be better approximated. It therefore came to light that the true excited state was delocalised over two or more of the RC pigments (an excitonic state). Our current understanding, the culmination of a wealth of work by both modellers and experimental researchers, is that RC* is a pair of exciton-charge-transfer states ($Chl_{D1}^{\delta+}$ $Phe_{D1}^{\delta-}$)* and ($P_{D2}^{\delta+}$ $P_{D1}^{\delta-}$)*.[33]

Proceeding from RC*, it was suggested that two competing CT pathways are available (scheme 4 and scheme 5 below)[34–36]:

Scheme 4 : $(Chl_{D1}^{\delta+}\ Phe_{D1}^{\delta-})^* \rightarrow Chl_{D1}^{+}\ Phe_{D1}^{-} \rightarrow P^{+}\ Phe_{D1}^{-}$

Scheme 5 : $(P_{D2}^{\delta+}\ P_{D1}^{\delta-})^* \rightarrow P_{D2}^{+}\ P_{D1}^{-} \rightarrow P^{+}\ Chl_{D1}^{-} \rightarrow P^{+}\ Phe_{D1}^{-}$

Both schemes 4 and 5 result in primary radical pair P_{D1}^{+} Phe_{D1}^{-}. The conformation of the RC pigments may force CT to go down one of these routes over the other.[36] It has also been shown that PS II relies on coupling of vibrational modes between the intermediate states,[21] which allows switching between the two pathways.[37] Mutagenesis studies identified a shared hole on P_{D1} and P_{D2} as the identity of P^+ in $P^+Phe_{D1}^-$, with the cationic charge held by each chlorophyll in the approximate ratio of ~80% : 20%.[38–41†]

† It is important to note that throughout the literature the P^+ species where the cation is localised is often referred to as P_{680}^+ which is a reflection of the main absorption maximum for the core RC at 680 nm. This convention will be used throughout this thesis in order to faithfully report experimental findings in the literature, when encountering this term the reader should bear in mind that P_{680}^+ is known to be a cationic state localised ~80% on P_{D1} and ~20% on P_{D2}.

Site Directed Mutagenesis

Due to the spectral overlap arising to many RC pigments absorbing in the same region, site-directed mutagenesis (the specific mutation of a single residue) has been a necessary tool leading to the elucidation of RC*, the CT pathway(s) and their intermediates. Below is a discussion of four sites of mutation (see Figure 4).

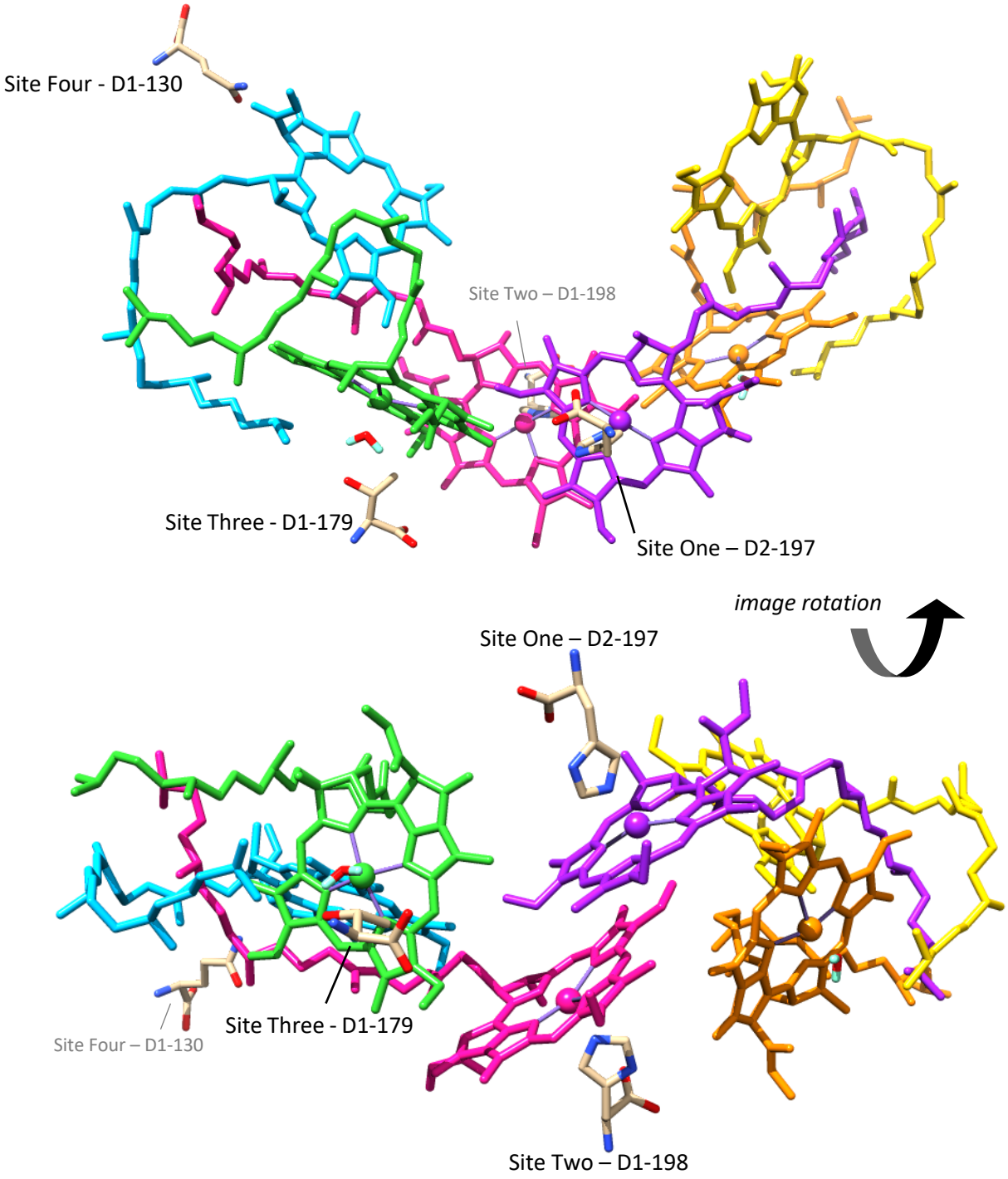


Figure 4 : The wild type reaction centre of T. *vulcanus*[22] viewed face on (TOP) and from underneath showing cofactors P_{D1} (pink), P_{D2} (purple), Chl_{D1} (green), Chl_{D2} (orange), Phe_{D1} (light blue) and Phe_{D2} (yellow) with four labelled residues (coloured according to heteroatoms) the sites of mutation investigated in this thesis: D2-197, D1-198 (both His in wild type [WT]), D1-179 (Thr in WT) and D1-130 (Gln in WT).

Site One – D2-197

Over thirty years ago, the residue D2-His-197 was targeted as the subject of a site-directed mutagenesis study.[42] The significance of the residue at D2-197 was recognized at an early stage, although not immediately for the right reasons. As the histidine at position D2-197 is the ligand to the P_{D2} chlorophyll, it was once thought to be crucial to the dynamics of the $P_{D1}P_{D2}$ dimer – believed to be the PS II equivalent to the bacterial photosynthetic reaction center 'special pair' (P_AP_B).[42] As the elucidation of the key energetic and structural differences between the bacterial and oxygenic photosynthetic reaction centres became apparent,[22,32] the notion of a 'special pair' in PS II had to be corrected. However, D2-197 has not lost its significance, as it was discovered that the P_{D2} chlorophyll shares the electron hole in the P_{680}^+ cation of the primary radical pair species.[40,43,44] Furthermore, as already discussed, P_{D2} may be implicated in delocalized excited states of the RC which are precursors to charge separation.[32,34]

Unfortunately the earliest experiments, mutation from histidine to tyrosine[42] or leucine[38] resulted in a loss of the reaction center. This proved that, unlike in the case of the purple bacterial reaction center,[45] the replacement of one of the central P chlorophylls with a pheophytin is structurally impossible in PS II. However, the authors reported successful photoautotrophic growth of *Synechocystis* cells constructed with the mutation of D2-His-197 to alanine, asparagine and glutamine.[38] In the case of alanine and asparagine this suggests the insertion of a water ligand to coordinate the P_{D2} metal center, preventing a pheophytin from binding here. Mutation of D2-197 to alanine increased the rate of recombination of the radical pair in cells by a factor of 3.3[38], this can be explained by the new water ligand stabilising P_{D2} to the cationic charge.[38] Furthermore, in the Soret‡ region all three mutations resulted in a displacement of the P_{D1} chlorophyll absorption band at ~433 nm (identified from a bleaching band in the P^+-P difference spectra) to the red by 0.5-1.5 nm with H197A the most red-shifted. The authors explain this small shift as P^+ being more evenly shared over the two P chlorophylls for the mutants, and P_{D2} absorbance being blue-shifted by the mutation compared to the WT (with P_{D1} absorbing at shorter wavelengths than P_{D2}). [38]

Steady-state light-induced Fourier Transform infrared difference spectra of the WT, alanine and glutamine mutants (H197A and H197Q) showed faster rates of energy transfer from the antenna complexes to the RC for both H197A (rate increases between 1.4 and 1.8 from WT to H197A) and H197Q (rate increases in ¾ of tests between 1.04 and 1.17 from WT to H197Q).[46] These results were consistent with both mutations lowering the reduction potential of P_{680}^+/P_{680}.[38] The overall rate of electron transfer is not affected, as later

‡ Chlorophyll absorption spectra give three distinct bands which are typically labelled, from low to high energy, the Q_Y, the Q_X and the Soret bands.

steps leading to the primary radical pair species $P^{+}Phe_{D1}^{-}$ are slower for these mutant RCs than for the WT.[46] IR bands pertaining to Chl vibrational modes are perturbed by mutation to H197A, which indicates a redistribution of charge on P_{680}^{+}.[46] The authors estimate that a $2cm^{-1}$ shift in the absorption at ~$1700cm^{-1}$ for H197A relative to WT is representative of increased delocalization of the electron hole in P_{680}^{+} over P_{D2}.[46]

A secondary significance postulated, again based at first on the comparison to the structure of the purple bacterial reaction center, is the linking of the D2-197 residue, via a H-bonded water network, to the Chl_{D1} cofactor.[46] The link to Chl_{D1}[46] via a water channel was later confirmed by the crystal structure,[22] and again provides a strong motivation to study the effect of mutations at this site.

Analysis of the Stark spectra of the D2-197 mutants[33] also showed that mutation at D2-197 to Ala, Asn and Gln affects a $P_{D1}P_{D2}$ exciton state. The authors report a 075-1.75 nm blue shift in the stark spectrum minimum (at 673 nm for the WT) for mutants H197A, H197N and H197Q due to the interaction between Chl_{D1} and D2-197, noting that histidine has a stabilizing effect on the Chl_{D1} containing exciton states. Both H197A and H197N show reduced mixing of exciton state $P_{D1}P_{D2}Chl_{D1}$ with $P_{D2}^{+}P_{D1}^{-}$ CT states compared to the WT, therefore reducing the contribution of this particular pathway to charge separation in these mutants. All three studies[33, 38,46] consistently report that mutating D2-197 to alanine produces the greatest effect, whilst mutation to glutamine results in RCs most similar to the WT.

Site Two – D1-198

The residue at D1-198, arguably of greater import than D2-197 as the ligand to the active branch central P chlorophyll P_{D1}, has been involved in many site-directed mutagenesis studies[33,38,47,48] and theoretical models.[40,49,50]

Merry et al.[47] found that D1-198 can be mutated to alanine, a residue with no side chain to coordinate the P_{D1} chlorophyll, and still a *chlorophyll a* molecule will bind at this site. This means there is likely a water molecule coordinating the Mg atom of P_{D1} in this mutant, much like the H197A mutant discussed in the previous chapter. The presence of a water molecule in the alanine mutant (H198A) is later confirmed by calculating redox potentials of P_{D1} and P_{D2} in models of H198A with and without the water molecule,[40] with water being necessary to reproduce experimental changes in the redox potentials of the $P_{D1}P_{D2}$ pair. Mutation of D1-198 to a glutamine (H198Q), [33, 38,47,48] asparagine (H198N) [33, 38,47] and cysteine [38] is also accomplished without loss of photosynthetic activity. Whilst *Synechocystis PCC 6803* is the species studied in the majority of the literature,[33, 38,47] H198A and H198Q mutants of *Thermosynechococcus Elongatus* (*T. Elongatus*) were also successfully made and studied.[48]

The consensus of the experimental works cited in this introduction is that two separate effects are observed on mutation of the residue at D1-198. The first, discovered in 1998,[47] is a tuning of the free energy of the radical pair state $P_{680}^{+}Phe_{D1}^{-}$ in which the cationic charge of P_{680}^{+} is shared between P_{D1} and P_{D2}. Subsequent work achieves good agreement[38] to excellent quantitative agreement[48] with the finding that mutation to H198A increases the quantum yield of radical pairs to 94% relative to the WT (60-75%), whilst the H198Q mutation decreases quantum yield of radical pairs to 46%. [47] Energetically, this means that the P_{680}^{+} cation is more stable for H198A than in the WT, whereas the cation is less stable for H198Q. The increased energy gap between $P_{680}Phe_{D1}$ and $P_{680}^{+}Phe_{D1}^{-}$ for H198A results in a slower measured rate of electron transfer from Y_Z to P_{D1},[38] thereby reducing the driving force for electron abstraction from water via the OEC for this mutant (oxygen evolution for H198A is 50-70% of the WT rate) [38]. The effect on the reduction potential of redox couple P_{680}^{+}/P_{680} is investigated by measuring charge recombination rates which are ~18x higher than WT for H198A and similar to WT for H198Q.[38] All of these results confirm that the H198A mutant produces a more stable radical pair state than the WT, one possible explanation for this would be a stabilisation of the positive charge onto the new water ligand to the P_{D1} chlorophyll.[40] Whilst the timescales for electron transfer events to form P_{680}^{+} mean this analysis is outside of the scope of this thesis, this method may allow us to intuit how mutation affects the stabilisation of a positive charge on P_{D1} based on the identities of the vertical excited states.

Diner et *al.*[38] report a second effect, visible in the Soret region of the spectrum, with no apparent correlation to the first. They explore a bleaching band in the P^+ - P absorption difference spectrum of the WT and its shifts produced by mutation of D1-198. The authors report that mutation to H198Q blue-shifts by 3 nm the P^+-P bleaching band, found at 433 nm for WT. A smaller blue shift is reported for H198N and still smaller for H198A (~2 and ~1.5 nm respectively), leading to the conclusion that the effect of mutation decreases from H198Q to H198N to H198A. Furthermore, in the lower energy region of the spectrum, the pattern a of 3 nm blue shift is observed for a bleaching band at 672.5 nm, a sideband between 665 and 672, but not the bleaching band at 682-3 nm. The same shift was later observed in H198Q mutants of *T. Elongatus*[48], which has an identical structure to *T. vulcanus*[22] and therefore is better approximated by the models in this thesis. This work[38] was instrumental in identifying the site of the cationic charge ($P_{D1}P_{D2}$ expected to be ~80% localised on P_{D1}), and showed that there must be P_{D1} absorption at 672.5 nm (at 80 K) and 433 nm (ambient temperatures).

Stark spectroscopy on WT and D1-198 mutants of the PS II RC revealed a further effect of mutation, finding that in all cases (H198A, H198N and H198Q) mutation reduced the extent of mixing of CT states with exciton states.[33] Shifts in stark bands reveal the presence of excitonic interactions in both mutants and WT RCs, including exciton $P_{D1}P_{D2}Chl_{D1}$ (ordered by decreasing contribution) with a minimum in the WT stark spectrum at 673.25 nm. The blue shift in this band for H198Q is 3.25 nm, 2.75 nm for H198N and 2.25 nm for H198A (from supplementary table S2 in ref. [33]), reflective of the shifts of P^+-P absorption difference bands for the same mutants in the Soret region. [38] The authors[33] conclude that the degree of mixing of exciton and CT states determines the efficiency of charge separation (CS), although this appears from previous evidence to have a complex relationship to the energetics of radical pair formation. If more mixing of CT states led to more efficient CS, H198A - with the highest quantum yield of radical pairs[47] - would be expected to exhibit a higher degree of mixing of CT states. Clearly these mutants would benefit from some further study, with an aim to unify the cause of the many observations made in experimental work so far.

Beyond the scope of this work but nonetheless an interesting contribution to this discussion is the effect of the axial ligand on the degree of puckering of the P_{D1} porphyrin ring. Although there is no mention of the addition of a water molecule to ligate P_{D1} in this work, [50] modelling found that the distortion of P_{D1}, mostly described by a 'doming' shape in the crystal structure was reduced by replacement of D1-198 with an alanine. The finding with heme-proteins has been that more distorted porphyrins are easier to oxidise and harder to reduce,[51] suggesting that P_{D1} with the porphyrin ring in a more dome-like conformation would be more stable to loss of an electron than a more planar conformation. This observation appears counter to the higher radical pair yield observed for H198A in *Synechosystis*,[47] but it remains to be seen what the effect of a water ligand would be on the puckering of P_{D1} in the H198A mutant. However, the effect of ring distortion on the redox

behaviour of *chlorophyll a* is small compared to the effect of the electrostatic environment, suggesting that the static models presented in this thesis will still provide ample insight into the effects of mutation.

Site Three – D1-179

The third site of mutation that was explored in this thesis was the threonine residue D1-179 in the vicinity of the Chl_{D1} accessory chlorophyll on the active branch. Its mutation to a histidine (T179H) and glutamic acid (T179E) results in the new mutant residue replacing a water molecule as the axial ligand to the Chl_{D1}.[52]

Changes in the absorption spectra of D1-179 mutants relative to the WT were observed in the low energy Q_Y band of the spectrum, instead of the Soret region as in the case of the D1-198 and D1-197 mutants (discussed above). The spectral changes due to mutation could be probed by triplet-minus-singlet absorption difference spectra, since Chl_{D1} is the site of a triplet state occurring due to recombination of the radical pair state $P_{680}^{+}Phe_{D1}^{-}$.[52] It was found that the main bleaching band in the triplet-minus-singlet absorption difference spectra of the mutants (occurring at 673 nm for the WT) was shifted 2 nm to the red for T179H and 1 nm to the blue for the mutant T179E.[52] An electrochromic band shift in the $P_{680}^{+}Q_A^{-}$ minus $P_{680}Q_A$ spectrum is similarly displaced by both mutants.[52] These shifts are attributed to the polarizability of histidine stabilising excitation on nearby pigment Chl_{D1} for the T179H mutant and conversely the anionic charge on glutamic acid destabilising Chl_{D1} site energy for mutant T179E.[52] The authors also reported a broadening of the Chl_{D1} Q_y absorption band which they attribute to increased disorder in the vicinity of the mutation.[52] Similarly, broadening of the Soret Chl_{D1} absorption is reported for the T179H mutant at low temperatures.[53]

Site Four – D1-130

Finally, the effect of two mutations at site D1-130, was chosen to be studied and is presented in Chapter four of this thesis. The residue site is near to the Phe_{D1} active branch pheophytin in the RC, and different residues will hydrogen bond (H-bond) with different strengths to the porphyrin C=O group shown in Figure 5 and lead to changes in the Q_X region of the spectrum.[54–59]

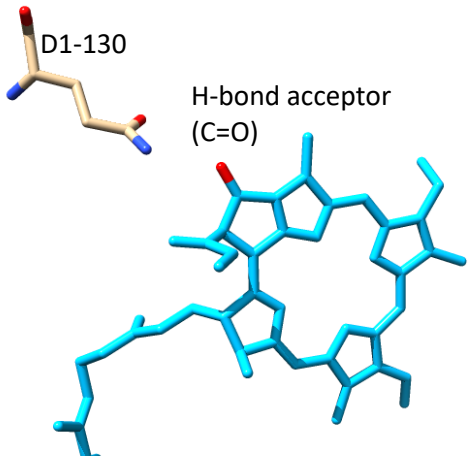


Figure 5 – The position of D1-130 (Gln) as in WT T. *vulcanus*[22] relative to Phe_{D1} (blue) hydrogen bond acceptor (labelled, red)

Cyanobacterium *Thermosynechococcus elongatus* hosts a glutamate residue (E) at position D1-130 in the high-light expression of the gene coding for D1-subunit which is a glutamine (Q) residue in low light.[56] The overall effect is thought to be in order to reduce the production of destructive singlet oxygen in high-light conditions and therefore protect PS II from photodegradation.[56] For T. *vulcanus* (the species for which the highest resolution crystal structure[22] has been elucidated) D1-130 is a glutamine residue (Q). Mutation of Q130 containing WT RCs to glutamic acid (Q130E) resulted in an increased energy gap between $Phe_{D1}^{-}Q_A$ and $Phe_{D1}Q_A^{-}$ leading to lower singlet oxygen yield[56] and increased radical-pair quantum yield compared to the WT.[54] In the Q_x region of the spectrum, a band at 541.5 nm for D1-Q130 RCs was blue shifted by ~2.5 nm for D1-E130 containing RCs.[54]

Mutation of D1-130 from Q to leucine (Q130L) however, was shown to have decreased quantum yield of the radical-pair state compared to WT,[54] increased singlet oxygen production and therefore increased risk of photodamage.[56] It may be assumed that increased singlet oxygen production could be due to a decreased energy gap between $Phe_{D1}^{-}Q_A$ and $Phe_{D1}Q_A^{-}$ for this mutant, as indicated by spectral shifts in the opposite direction to Q130E (Phe_{D1} Q_x absorption max at 541.5 nm is shown to red-shift to 540 nm for Q130L).[54] This effect can be rationalised by considering the interaction between the Phe_{D1} (see Figure 5) and the mutant D1-130 residue in WT (Q130), Q130E and Q130L, the interaction is strongest (H-bonding) between C=O and the carboxylate group, weaker (although still a H-bonding interaction) between the Phe_{D1} and the amine group in WT (Q130) and weakest (no H-bond donor) between leucine and Phe_{D1} in the Q130L mutant.

Theoretical Models of the PS II RC

Modelling photosystem II (PS II) has been a goal of the scientific community for many decades. Without the aid of clear spectroscopic insight due to large spectral overlap of the RC pigments' absorption bands, much of what we know about the function of the complex has been drawn from theoretical models. Early models of the PS II reaction centre (RC) were made without reference to the specific atomic positions of the core pigments and based on the assumption that the bacterial photosynthetic RC bore a strong resemblance to the PS II RC. Subsequently, more specific and accurate models have been constructed – based on the crystal structure at high resolution.[22]

The Multimer Model and Related Work

As discussed above, it was the Multimer model[32] that first showed there was no 'special pair' of highly coupled chlorophylls in the PS II RC as could be found in the PB RC. A full 3 years later, the crystal structure[60] of the RC was resolved to suggest a Mg-Mg spatial separation between the P chlorophylls (~10 Å) in the PS II RC that was much greater than that of the bacterial special pair. Subsequent higher resolution crystal structures were published and we now know the distance is closer to 8 Å.[22]

Descendants of the Multimer model[61,62] were built, taking as input the pigment site energies and coupling constants of neighbouring pigments derived from the improved crystal structures[63,64] or fitting to experimental data[62]. They were able to achieve improved fitting to spectroscopic features and electron and energy transfer dynamics than the original Multimer model. The simple nature of the multimer excited state (ES) representation (the ES manifold is treated as localised singlet excited states coupled via a dipole-dipole approximation) meant that energetic disorder in the form of inhomogeneous broadening of cofactor excitation energies[61] and coherence[65] could be effectively modelled in this way.

Redfield relaxation theory[65,66] and later Modified Redfield theory[34,35,67–69] has been used to reproduce spectral line shapes with increasing accuracy and accomplish simultaneous fitting to absorption, linear dichroism, circular dichroism and fluorescence spectra[34]. We can thank these models for demonstrating advantageous mixing of charge transfer (CT) and exciton states[33], vibronic coupling between states[21] and elucidating the exciton-charge transfer states which are precursors for charge separation (CS)[33].

Quantum Mechanical Models of the Reaction Centre

Despite the need for multimeric calculations on the RC, shown by the Multimer model and others[26, 32, 34,61], examples of atomic models can be found in the literature which treat only one or two pigments at a time[41,70–

[73]. Other tactics to mitigate the great computational cost of modelling the whole complex have been to employ hybrid methods[40,41,73,74] or to use simpler, idealized models of the pigments[74,75]. In tandem with these, geometry optimization[40,70,74] and Molecular Dynamics[73,76,77] have been employed to find relaxed conformations of the crystal structure atomic positions. Other models have largely retained crystal structure geometries[75,78].

The first example of a multimeric QM model that included the six RC chromophores (without phytol chains) came in 2011[75]. In this work the authors were restricted to the configuration interaction singles (CIS) method, a lower level of theory than time dependent density functional theory (TDDFT) – the chosen method in this thesis. Before now, the largest TDDFT model of the RC built to date comprised ~300 atoms.[74] The model in question includes six chromophores and two quinones.[74] As well as cutting the phytol chains out of the QM region, the side chains of the pigment molecules are excluded.[74] In this thesis and in associated published work[79] are presented the results of the largest excited state calculation on the PS II RC (1299 atoms) including six whole pigments and 23 amino acid residues.

Research Aims of this Thesis

The aims of this thesis were to construct models of the PS II RC, which demonstrated sufficient agreement with experimental behaviour, in the hope that the structural features leading to the D1 branch preference could be pinpointed. In order to accomplish this, first it was necessary to identify the region of the RC which needed to be included in a model in order to obtain a life-like system. This is covered in chapter one and chapter five. A method for building, probing and analysing the models built needed to be verified. Some different methods are compared in chapter one and the calculation and analysis procedure is also outlined in the first chapter. In order to verify results from models built, mutant RC models were also built and are discussed in chapters two through to four. Comparison between mutant RC model results and wild-type (WT) RC models provided a framework for validating the models and methods chosen.

In light of the delocalised nature of the excited states leading to CS, a comprehensive QM model including all RC pigments at the same level of theory was chosen as the best approach to modelling the RC. Given the restrictive size of this system, a single conformation of the RC pigments was all that could be explored in the time allowed to complete this work. Choosing to use a fixed geometry for the vast majority of heavy atoms in the system made it possible to compare models of different sizes, with different site-directed mutations and to observe the effect of using different methods on the results. In light of this, geometry optimisation of the pigments, leading to an arbitrary relaxed point on a high-dimensional potential energy surface, was decided not to be used. The crystal structure[22] geometry was chosen as the starting point for all models discussed in this thesis.

An Important Note on the Scope of this Thesis

This thesis presents results of TDDFT calculations on models which comprise different regions of the PS II RC. As such, the scope of this work is restricted to finding vertical excited states of the RC before any relaxation of the system has been allowed to take place (that is, under the Born-Oppenheimer approximation). In the following chapters the goal is to identify the excited states which are precursors to CS, which may comprise exciton states and/or states with a degree of CT character. CS itself will not be observable using the chosen method of TDDFT.



Methods

This section contains details of all methods used for the work in this thesis. First there will be a brief introduction to the theory behind each computational method used, followed by a description of the process employed to build models of the PS II RC, evaluate their excited states and assess the results of excited state calculations.

Theoretical Background

What follows will be a short overview of the relevant theory behind Density Functional Theory (DFT), the ground state basis for Time Dependent Density Functional Theory (TDDFT), as well as some details of other related methods in quantum chemistry including a description of the basis sets that were used. Following this will be a summary of the theory behind modelling excited states using TDDFT and the form of the two functionals used in this work, ωB97X-D and CAM-B3LYP. Finally, an outline of the theory behind some alternative methods that were employed in this work such as quantifying orbital occupancy through Mulliken charges and the D_{CT} charge transfer metric is presented. The aim here is not to cover the derivations to any great depth (which can be found in many of the textbooks and theoretical works cited here), but to give the reader enough context with which to view the results presented in the later chapters.

Background to Electronic Structure Computation

The Time-independent Schrödinger equation states that, given a wavefunction Ψ, the energy of a system may be found as the eigenvalue *E* in the equation:[80]

$$\hat{H}\Psi = E\Psi \tag{1}$$

$\hat{H}$ is the Hamiltonian operator, which for a single particle of mass *m* in three-dimensions has the form:[80]

$$\hat{H} = -\frac{\hbar^2}{2m}\nabla^2 + V \tag{2}$$

The Hamiltonian operator consists of a kinetic energy term which invokes the Laplacian differential operator ∇^2:[81]

$$\nabla^2 = \frac{\partial^2}{\partial \mathrm{x}^2} + \frac{\partial^2}{\partial \mathrm{y}^2} + \frac{\partial^2}{\partial \mathrm{z}^2} \tag{3}$$

and a potential energy term *V* which depends on the position (*x, y, z*) of the particle in space (see below).

For calculation of the energy of a system comprising more than one particle we need to include terms for attraction and repulsion of the different particles in the system. In the specific case of an atomic system, where the particles in question are nuclei (*N*) and electrons (*e*), the contributions to the total energy are nuclear kinetic energy T_N , electronic kinetic energy T_e, nuclear-nuclear repulsion V_{NN}, nuclear-electron attraction V_{Ne} and electron-electron repulsion V_{ee}:[81]

$$E = T_N + T_e + V_{NN} + V_{Ne} + V_{ee} \quad (4)$$

The Hamiltonian operator for an atomic system must therefore include terms to evaluate all of these contributions to the total energy.

The Born-Oppenheimer Approximation

The Born-Oppenheimer approximation states that, as the mass of an electron is ~2000 x smaller than the nucleus of an atom (and therefore electron motion is fast compared to nuclear motion), the nuclei in chemical system may be treated as fixed relative to the electrons.[82] The nuclear kinetic energy term therefore need not be included, leaving only an electronic kinetic energy contribution to the total energy.

The potential energy terms each take the form of Coulomb's law[81] and are summed over all relevant particles. The nuclear-nuclear repulsion term for two nuclei A and B (with charges Z_A and Z_B, at a distance of R_{AB} from each other) is written:[81]

$$\hat{V}_{NN} = \frac{e^2}{4\pi\epsilon_0}\frac{Z_A Z_B}{R_{AB}} \quad (5)$$

The remaining terms make up the electronic Hamiltonian, $\hat{H}_{el}$ consisting of both kinetic and potential energy parts, which for a diatomic molecule with fixed nuclei *A* and *B* and electrons *i* will be:[81§]

$$\hat{H}_{\mathrm{el}} = -\frac{\hbar^2}{2\mathrm{m_e}}\sum_i \nabla_i^2 + \frac{\mathrm{e}^2}{4\pi\epsilon_0}\left(-\sum_{\mathrm{i}}\frac{Z_A}{r_{Ai}} - \sum_{\mathrm{i}}\frac{Z_B}{r_{Bi}} + \frac{1}{2}\sum_{\mathrm{i}}\sum_{j\neq i}\frac{1}{r_{ij}}\right) \quad (6)$$

The final term relies on the positions of both electrons *i* and *j* simultaneously and cannot be solved analytically. Therefore, in all but a small number of known cases where there are fewer than two electrons in the system, the Schrödinger equation cannot be solved exactly and the total energy must be approximated.

§ Invoking atomic units ($m_e = 4\pi\epsilon_0 = \hbar = \mathrm{e} = 1$) means that equation 6 can be written as simply $\hat{H}_{\mathrm{el}} = -\frac{1}{2}\sum_i \nabla_i^2 - \sum_{\mathrm{i}}\frac{Z_A}{r_{Ai}} - \sum_{\mathrm{i}}\frac{Z_B}{r_{Bi}} + \frac{1}{2}\sum_{\mathrm{i}}\sum_{j\neq i}\frac{1}{r_{ij}}$, **atomic units are used throughout the remainder of this chapter.**

Dirac Notation

Dirac formalised the notation of complex vectors representing quantum states (eigenfunctions of the Hamiltonian for a given system) as bras $\langle i|$ and kets $|j\rangle$.[83] In one dimension the ket is defined as $|j\rangle = \Psi_j{}^*(x)$ and the bra is the complex conjugate of the corresponding ket $\langle i| = \Psi_i{}^*(x)$ (practically we can consider kets as column vectors and bras as row vectors made up of elements which are complex conjugates of the elements in the corresponding ket vector).[83]

Overlap integrals in one dimensional Dirac notation are then written as $\langle i|j\rangle = \int_{-\infty}^{\infty} \Psi_i{}^*(x)\Psi_j(x)dx$ and will evaluate to scalars.[83]

Finally, the matrix elements H_{ij} of operator $\widehat{H}$ are defined as $\langle i|\widehat{H}|j\rangle = \int_{-\infty}^{\infty} \Psi_i{}^*(x)\widehat{H}\Psi_j(x)dx$.[83]

Hartree-Fock Theory

Hartree's first approximation was to exclude the electron-electron repulsion term entirely and treat the electrons as non-interacting, so that all the terms in the electronic Hamiltonian are separable.[84] In this case the total electronic wavefunction Ψ, which depends on the positions of all electrons r_i, can be written as the product of all one electron wavefunctions (or *orbitals)* ψ as so:[85]

$$\Psi(r_1, r_2, r_3, \dots\ r_N) = \psi_1(r_1)\psi_2(r_2)\psi_3(r_3)\dots\psi_N(r_N) \tag{7}$$

The expression above is known as a *Hartree Product*.

The Hartree product was adapted by Slater and Fock in order to ensure that exchange of any two electrons in the system would result in a change in the overall sign of the wavefunction. First, a spin coordinate was added to the three spatial coordinates r_i to give spin coordinates x_i which populate spin orbitals χ_i. Second, the product was rewritten as a Slater determinant, in which columns are spin orbitals and rows are electron coordinates.[86]

$$\Psi(x_1, x_2, x_3, \dots\ x_i) = \frac{1}{\sqrt{N!}}\begin{vmatrix} \chi_1(x_1) & \chi_2(x_1)\dots & \chi_N(x_1) \\ \vdots & \ddots & \vdots \\ \chi_1(x_N) & \chi_2(x_N)\dots & \chi_N(x_N) \end{vmatrix} \tag{8}$$

It was then necessary to rewrite the electronic Hamiltonian in light of this new wavefunction expression. The resultant Fock operator[87] is described below.

The Fock Operator

The analogue to the Schrödinger equation is known as the Hartree-Fock (HF) equation:[85]

$$\hat{F}\Psi = E_{elec}^{HF}\Psi \tag{9}$$

Here we seek to find the HF energy E_{HF}. The HF equation is solvable for all systems as the electron-electron cloud repulsion depends only on the position of one electron and the average repulsion it feels from all other electrons in the system.[85]

$$\hat{F}(\chi_i) = \hat{h}(\chi_i) + \sum_{j>i}^{n}[\hat{J}_j(\chi_i) - \hat{K}_j(\chi_i)] \tag{10}$$

For which we define our three operators $\hat{h}$ (the one electron hamiltonian) $\hat{J}$ (the Coulomb operator) and $\hat{K}$ (the exchange operator), as having non-zero matrix elements:[85]

$$h_i = \left\langle \chi_i(x_1) \middle| -\frac{1}{2}\nabla_i^2 - \sum_a^{N_{nuclei}} \frac{Z_a}{|R_a - r_i|} \middle| \chi_i(x_1) \right\rangle \tag{11}$$

$$J_{ij} = \left\langle \chi_i(x_1)\chi_j(x_2) \middle| \frac{1}{|r_i - r_j|} \middle| \chi_i(x_1)\chi_j(x_2) \right\rangle \tag{12}$$

$$K_{ij} = \left\langle \chi_i(x_1)\chi_j(x_2) \middle| \frac{1}{|r_i - r_j|} \middle| \chi_j(x_1)\chi_i(x_2) \right\rangle \tag{13}$$

For a set of n orthogonal spin orbitals $\{\chi_i\}$. It can be seen from equations 12 and 13 that whilst the Coulomb operator the two electrons x_1 and x_2 are in the same orbitals on both sides of the integral, the exchange operator involves switching the two electrons between the orbitals.

This gives the total contribution to the HF energy as:[85]

$$E_{HF} = \sum_{i=1}^{n} h_i + \sum_{i=1}^{n}\sum_{j=1}^{n}(J_{ij} - K_{ij}) + V_{NN} \tag{14}$$

In HF theory, each electron feels the repulsion of all other electrons as though it is travelling in a fixed electron cloud, meaning that there is an error in E_{HF} due to electron correlation.

Approximating Wavefunctions as a Linear Combination of Basis Functions

An exact wavefunction Ψ can be approximated (we will denote approximate wavefunctions using Greek letter Φ) as a linear combination of basis functions $|\Phi\rangle = \sum_{i=1}^{N} a_i |\phi_i\rangle$ where $\{|\phi_i\rangle\}$ is the basis set (set of basis functions).[88]hod The coefficients $\{a_i\}$ are parameters which can be varied using the Raleigh-Ritz procedure,[89] outlined below, to better approximate the true wavefunction.

The Variational Principle & The Secular Equation

To solve for the eigenfunctions and eigenvalues of the Schrödinger and HF equations it is convenient to start from a guess wavefunction for a given system and evaluate the energy of this guess wavefunction. The variational principle states that whatever guess energy this gives, the result may never be lower than the true ground state energy of your system.[81]

Taking the guess wavefunction Φ, the expectation value for the energy can be evaluated like so (where *H* is the Hamiltonian operator from equation 2 and E_0 is the *actual* ground state energy of your system):[88]

$$\frac{\langle \Phi | \widehat{H} | \Phi \rangle}{\langle \Phi | \Phi \rangle} \geq E_0 \tag{15}$$

This inequality facilitates optimising the guess wavefunction to find the lowest possible energy and therefore get as close as possible to the real wavefunction. For example, if your guess wavefunction Φ was chosen as a linear combination of *N* primitive functions ϕ_i with coefficients a_i, the a_i could be optimised until the best guess (giving the lowest *E* value) Φ was found.

Optimising the wavefunction to find the eigenfunction that give the lowest energy involves solving *N* linear equations to find *N* variables a_i for basis functions ϕ_i:[88]

$$\frac{\sum_{ij} a_i^* a_j}{\sum_{ij} a_i^* a_j} \frac{\langle \Phi | \widehat{H} | \Phi \rangle}{\langle \Phi | \Phi \rangle} = E \tag{16}$$

For which we seek $\frac{\partial E}{\partial a_k} = 0 \; \forall \; k$. To facilitate this, we define two matrices, the Hamiltonian matrix and the overlap matrix: Equivalent to the integral $\langle \phi_i | \widehat{H} | \phi_j \rangle$ is the ith, jth matrix element of Hamiltonian matrix H_{ij}. Similarly, equivalent to the overlap integral of the ith and jth primitive functions $\langle \phi_i | \phi_j \rangle$ is an overlap matrix element S_{ij}.

Now there are N *secular equations* (one for each value i) to solve:

$$\sum_{i=1}^{N} a_i \left(H_{ki} - ES_{ki}\right) = 0 \; \forall \; k \tag{17}$$

Which will have solutions if:

$$det|H_{ki} - ES_{ki}| = 0 \tag{18}$$

Equation 18 is the *secular determinant* which has N possible solutions *E* (the allowed energies) which can be used to find solutions a_i to secular equations 18. The equivalent set of equations for a HF calculation would be found by substituting the Hamiltonian matrix for the Fock matrix using the Fock operator.

Self-Consistent Field Procedure

The density or field of electrons in the molecule can be guessed to begin the procedure of solving a HF calculation for a given molecular system and set of basis functions (basis set). Using the variational principle we can iterate through a number of steps, solving for the coefficients of the basis functions to generate a new guess for the density of the system. Once the new guess density (output from the most recent iteration) is sufficiently close to the input guess density (subject to some convergence criteria which may be specified for a given calculation) we can say that self-consistency has been reached. Operating in this way to find the optimal orbitals to describe a given system is known as the Self Consistent Field procedure or SCF.[88]

Choice of Basis Set

Linear combinations of gaussian functions allow us to approximate the solutions to the Schrödinger equations for the hydrogenic atom (*i.e.* atomic orbitals). We call the resultant functions gaussian type orbitals (GTO). GTOs are non-physical, having a flat gradient at the nucleus, but may nonetheless be chosen based on the calculation speed they can afford.[81]

6-31G**, the chosen basis set for the majority of this thesis, comes from 6-31G, a split-valence basis based on these GTOs.[90] 'Split-valence' in this specific case means it takes six GTOs to describe core electron orbitals, three basis functions for the inner valence electron orbitals and one for the outer valence orbitals. Specifically the core and inner valence orbitals are made up of a fixed linear combination (constant coefficients) of primitive Gaussian Type Orbitals resulting in one 'contracted' Gaussian Type Orbital (CGTO) each. Because this method reduces the number of parameters which can be optimised, contracted basis sets such as 6-31G have

limited variability and therefore result in higher energies according to the variational principle than similar non-contracted basis sets. However, as these basis set families result in functions which can accurately represent orbital shapes and afford great savings in computational cost they have been widely adopted within computational chemistry.[81]

The ** in 6-31G** denote polarization functions. d-functions (6 degenerate functions) are added to each non-hydrogen atom and p-functions (3 degenerate) are added to hydrogen atoms.[91] In the first chapter some results are presented using 6-31+G**, with the + signalling that this basis includes diffuse gaussian functions on heavy (non-hydrogen) atoms, and is therefore useful in computing Rydberg and charge transfer states as they facilitate description of MOs with electron density far away from the nucleus.[91–97]

Semi-Empirical Approximations to HF – Austin Model 1

Semi-empirical theory seeks to reduce the cost of HF in several ways, beginning by restricting to 1st and 2nd row atoms and considering only a minimal valence basis (one basis function per electronic subshell: 1s, 2s, $2p_x$ *etc.*). Overlap integrals tend to be simplified to $S_{ij} = \delta_{ij}$. And electron repulsion integrals are only calculated if the two basis functions specifying the two electrons are the same, *i.e.* $(\mu\nu|\lambda\sigma) = \delta_{\mu\nu}\delta_{\lambda\sigma}(\mu\mu|\lambda\lambda)$. Empirical values are then used for electron-electron repulsion for electrons on the same atom γ_{AA} (taken as the difference between the atomic ionisation energy and electron affinity) to simplify the electron repulsion portion even further).[98]

$$\gamma_{AA} = IP_A - EA_A \tag{19}$$

For electrons on different atoms the electron repulsion takes the form of coulombs law:

$$\gamma_{AB} = \frac{\gamma_{AA} + \gamma_{BB}}{2 + r_{AB}(\gamma_{AA} + \gamma_{BB})} \tag{20}$$

This scheme is known as complete neglect of differential overlap (CNDO). Intermediate neglect of differential overlap (INDO) improved on CNDO by specifying new electron-electron repulsions between electrons on the same atom, *i.e.* repulsion between two s electrons on the same atom is no longer equivalent to repulsion between an s and a p electron on the same atom.[98] An advancement on this is to neglect only electron-electron repulsion between electrons on different atoms, in a scheme known as neglect of diatomic differential overlap (NDDO). NDDO specifies that when the basis functions for the first electron are on the same atom and the basis functions for the second electron are on the same atom the electron-electron repulsion will not go to 0.

Austin Model 1 (AM1) is a semi empirical method which has its roots in the NDDO approximation.[98] Over the years, the electron repulsion terms for each element in the main group have been parameterised using atomic spectroscopic data, and further fitting to experimental values of additional parameters has also been undertaken. AM1 was used for optimisation of hydrogen positions and mutant residue side chains throughout this thesis.

Density Functional Theory

A great shift in the popularity of quantum mechanical calculations was sparked by the discovery that the density, and not just the wavefunction, could be used to determine observable properties of a system. This was Hohenberg and Kohn's first theorem[99] which promised to reduce the complexity of intractable many body quantum mechanical calculations from 4*N* coordinates for an *N* electron system to just 3 spatial coordinates as the wavefunction no longer needed to be used.

The second Hohenberg and Kohn theorem[99] states that the exact ground state density of a system in a particular external potential can be found by minimisation of an energy functional (function of a function) acting on the density ρ. This meant that the variational principle could be used to find solutions to a new eigenvalue equation involving the density instead of the wavefunction.

Once it had been shown that the ground state density of a system contained all of the same information that could be obtained from the wavefunction, density functional theory (DFT) was born. The challenge is now to find the functionals that exactly map the density to observable properties of a system, for example its energy. So far, only approximate functionals have been developed, so in practice DFT is not an exact method.[88]

Kohn-Sham Orbital Approximation

Replacing the usual elements of the Hamiltonian operator for use with a density instead of a wavefunction was eventually achieved by Kohn and Sham in 1965[100] using the assumption that the ground state density of a system of interacting particles could be approximated by the ground state density of reference system of non-interacting particles (a Kohn-Sham system).

We can obtain the density of a system of *N* electrons by squaring the wavefunction, integrating over all but one coordinate and normalising to the number of electrons in the system:

$$\rho(r) = N \int \Psi^*(r^1, r^2 \dots r^n)\Psi(r^1, r^2 \dots r^n) dr_2 \dots r_n \quad (21)$$

In this way $\rho(r)$ describes the probability of finding any electron at a point r.[98]

The functional to relate the density to the energy can be written as a sum of its constituent functionals:

$$E_{DFT}[\rho] = T_S[\rho] + E_{ne}[\rho] + J[\rho] + E_{xc}[\rho] \quad (22)$$

Where T_S is the kinetic energy calculated from a Slater determinant of one electron orbitals (a non-interacting system):

$$T_S = \sum_i^{N_{electrons}} \langle \phi_i \left| -\frac{1}{2}\nabla^2 \right| \phi_i \rangle \quad (23)$$

(Note that as the electrons are actually interacting so you need a correction to get the real kinetic energy which is included in the exchange correlation term E_{xc}.) E_{ne} is the nuclear-electronic attractive potential energy:

$$E_{ne} = - \sum_i^{N_{electrons}} \langle \phi_i | \sum_k^{nuclei} \frac{Z_k}{|r_i - r_k|} | \phi_i \rangle \quad (24)$$

The Coulomb electron-electron repulsive potential energy J is:

$$J = \sum_i^{N_{electrons}} \langle \phi_i \left| \frac{1}{2} \int \frac{\rho(r')}{|r_i - r'|} dr' \right| \phi_i \rangle \quad (25)$$

(Note that SCF needs to be used to solve for new densities iteratively.) And finally the exchange correlation term E_{xc} which will correct for all deviation from the exact energies due to the use of non-interacting, one electron orbitals.

Exchange Correlation Functional

The exchange correlation element of Kohn Sham (KS) DFT may be split into two elements, the exchange energy and the correlation energy. DFT exchange should reflect the energy change upon exchange of any two electrons:[98]

$$|\phi_1(1)\phi_2(2)\rangle \rightarrow |\phi_2(1)\phi_1(2)\rangle \quad (26)$$

The correlation energy is defined as the difference between the exact energy and the HF energy, meaning that an xc functional should contain correction for the kinetic energy (see eq. 26 above) and for self-interaction energy.

Choosing the form of the exchange correlation functional dictates the precise DFT method used. All xc functionals that have been developed so far are approximate.

Local Spin-Density Approximation

An early approximate xc functional was the Local Spin-Density Approximation (LSDA) or Local Density Approximation (LDA) for closed systems. LSDA assumes the density locally is the same as that of a uniform electron gas, *i.e.* the density varies slowly. The exchange and correlation parts of the LSDA depend only on the density at a given position. In molecular systems LSDA underestimates exchange energy and overestimates correlation energy, therefore predicting bond strengths to be around 100 kJ/mol greater than experiment.[88]

Generalised Gradient Approximation

To improve on the poor energy calculated by the LDA approach a correction was introduced, in the form of the Generalised Gradient Approximation (GGA). In GGA the LDA exchange functional has an added dependence on the normalised gradient of the density, as well as the density itself.[101] Early GGA exchange functional B88 is expressed below:[102]

$$E_x^{B88} = E_x^{LDA} + \Delta E_x^{B88} \quad (27)$$

$$\Delta E_x^{B88} = -\beta\rho^{\frac{1}{3}}\frac{x^2}{1 + 6\beta x sinh^{-1}x} \quad (28)$$

$$x = \frac{|\nabla\rho|}{\rho^{\frac{4}{3}}} \quad (29)$$

It has one adjustable parameter β which in the functional's standard usage is taken to be 0.2743. B88 exchange may be used in conjunction with a correlation functional, for example the four-parameter Lee, Yang and Parr (LYP) correlation functional.[103]

Hybrid DFT functionals

Newer methods attempt to better model a fully interacting system using a set of non-interacting Kohn Sham orbitals. Hybrid functionals are constructed based on the reasoning that for a fully non interacting system HF theory predicts the exact exchange energy correctly, so we can include the full HF exchange as a part of the total exchange. In light of this hybrid functionals improve on traditional DFT by adding the HF exchange to some fraction (α in the equation below) of the difference between DFT exchange correlation and HF exchange (*i.e.* the improvement given by opting to use DFT instead of HF).[88]

$$E_{xc}^{Hybrid} = E_x^{HF} + \alpha(E_{xc}^{DFT} - E_x^{HF}) \tag{30}$$

Hybrid functional usage scales like HF (N^4) but afford far greater accuracy than HF calculations. B3LYP[104] is an early hybrid functional which uses B88 exchange and the LYP correlation functional as well as HF exchange, notably it has 3 parameters *a*, *b* and *c* which are optimized to give best performance, in Gaussian 16 they take the default values 0.20, 0.72 and 0.81:[104]

$$E_{xc}^{B3LYP} = (1-a)E_x^{LSDA} + aE_x^{HF} + b\Delta E_x^{B88} + (1-c)E_c^{LSDA} + cE_c^{LYP} \tag{31}$$

B3LYP is the most widely used functional to date.[88]

Long-Range Corrected Hybrid Functionals

The two functionals used in this work (CAM-B3LYP[105] and ωB97X-D[106,107]) are hybrid, and are long-range corrected, meaning they use a different scheme to treat long and short range interactions. CAM-B3LYP is the long-range corrected version of the B3LYP functional. The short range exchange is given by 0.19 x E_x^{HF} and 0.81 x E_x^{B88}, and the long range exchange by 0.65 x E_x^{HF} and 0.35 x E_x^{B88}. The interelectronic distance r is partitioned into long range and short range components according to:

$$\frac{1}{r_{12}} = \frac{1 - [\alpha + \beta \cdot \mathrm{erf}\ (\mu r_{12})]}{r_{12}} + \frac{\alpha + \beta \cdot \mathrm{erf}(\mu r_{12})}{r_{12}} \tag{32}$$

Where the first term is the short range interaction and the second term is the long range interaction. There is one optimizable parameter μ which is generally set to 0.33.[105] CAM-B3LYP uses the error function to manage the transition between the long and short-range schemes:

$$\mathrm{erf}(z) = \frac{2}{\sqrt{\pi}} \int_0^z e^{-t^2} dt \tag{33}$$

Dispersion Correction

ωB97X-D is related to the long-range corrected hybrid functional ωB97X (adopting the B97[108] correlation and exchange components) which uses 100% HF exchange for long range electron-electron interactions and an exchange functional for short range interactions.[107] Parameter ω controls the partitioning of interelectronic distance r, whilst parameter X corresponds to the fraction of short-range HF exchange (22% in the functional's standard form).[107]

The lack of long range correlation posed an issue for non-covalent electron interactions neglecting London dispersion forces of attraction between uncharged molecules when using ωB97X.[106] To correct for this the ωB97X functional was subsequently optimised to include empirical dispersion effects[106] via the DFT-D[109] (dispersion) scheme, for which:[106]

$$E_{DFT-D} = E_{KS-DFT} + E_{dispersion} \tag{34}$$

where:

$$E_{dispersion} = -\sum_{i=1}^{N_{atoms}-1} \sum_{j=i+1}^{N_{atoms}} \frac{C_6^{ij}}{R_{ij}^6} f_{damp}(R_{ij}) \tag{35}$$

For which C_6^{ij} is an empirically derived, atom-dependent parameter for atom pair i and j with interatomic distance R_{ij}, C_6^{ij}/R_{ij}^6 corresponds to dipole-induced dipole interactions, and:

$$f_{damp}(R_{ij}) = \frac{1}{1 + a\left(\frac{R_{ij}}{R_r}\right)^{-12}} \tag{36}$$

Which includes a single parameter a to adjust the dispersion potential. The resultant dispersion corrected functional was called ωB97X-D. ωB97X-D out-performed other dispersion corrected functionals in all testing, including improvements in calculation of charge transfer states.[106]

Time Dependence

When examining the excited states of a system we are interested in the evolution of the wavefunction over time. The time-dependent Schrödinger equation is the partial derivative of the wavefunction with respect to time, t:[110]

$$i\frac{\partial\Psi(\mathrm{t})}{\partial t} = H(t)\Psi(t) \tag{37}$$

Where the initial state corresponds to the time dependent wavefunction at time 0: $\Psi(t_0) = \Psi_0$.
The action integral, $\mathcal{A}$ has stationary points which are solutions to the time-independent Schrödinger equation:[110]

$$\mathcal{A} = \int_{t_{initial}}^{t_{final}} dt \left\langle \Psi(t) \middle| i\frac{\partial}{\partial t} - \hat{H}(t) \middle| \Psi(t) \right\rangle \tag{38}$$

A Brief Note on Perturbation Theory

From perturbation theory, when the Hamiltonian evolves within a radiation field as:[81]

$$\hat{H} = \hat{H}^0 + \hat{H}^1(t) \tag{39}$$

Which takes the known Hamiltonian of a reference system $\hat{H}^0$ and a new Hamiltonian $\hat{H}^1(t)$ which is due to the perturbation from the external potential. After time evolution we can express the new perturbed wavefunction Ψ as a linear combination of the complete set of H^0 eigenstates Φ_k:[81]

$$\Psi = \sum_k c_k e^{-\left(\frac{iE_k t}{\hbar}\right)} \Phi_k \tag{40}$$

Coefficients c_k when taken as a square modulus $|c_k|^2$ gives the probability that Ψ will collapse to a given stationary state k. In fact, c_k evolve in time such that $c_k \to \infty$ for a transition between the ground state and state k when ν is equal to the difference in energies ω between the ground state and a given excited state, and when the transition dipole moment $\langle \Phi_{excited} | r | \Phi_{ground} \rangle$ is large.[88]

Time Dependent-Density Functional Theory

Application of DFT as derived by Hohenberg and Kohn to solve for excited states was not possible, as the use of the variational principle meant that only one root (corresponding to the ground state) could be found. Instead, Runge and Gross proved that for a given system; the two time-dependent densities that arise due to the action of two different** external potentials on that system must not be the same as each other. That is to say that the density maps to an external potential exactly.[110]

Linear Response of the Density

With the proof of a direct mapping between external applied potential and density, the time dependent density of a system of interacting particles may be written as a functional of the external potential,[111]

$$\rho(r,t) = \rho[V_{ext}](r,t) \tag{41}$$

and vice-versa:

$$V_{ext}(r,t) = V_{ext}[\rho](r,t) \tag{42}$$

From perturbation theory, expanding $\rho[V_{ext}]$ with respect to $V_{ext}(r,t)$ gives:

$$\rho(r,t) - \rho_0(r) = \rho_1(r,t) + \rho_2(r,t) + \rho_3(r,t) + \cdots \tag{43}$$

If we are only concerned with the linear response of the density to the external potential, we may take only the first term.

The Time Dependent-Density Functional Theory Equations

The linear response of the density $\rho(\boldsymbol{r})$ of an interacting system to perturbation by an external potential v_{ext} may be written in the form (known as the Lehmann representation): [112]

$$\chi(\boldsymbol{r},\boldsymbol{r}',\omega) = \sum_I \left[\frac{\langle\Psi_0|\rho(\boldsymbol{r})|\,\Psi_I\rangle\langle\Psi_I|\rho(\boldsymbol{r}')|\,\Psi_0\rangle}{\omega - \Omega_I + i0^+} - \frac{\langle\Psi_0|\rho(\boldsymbol{r}')|\,\Psi_I\rangle\langle\Psi_I|\rho(\boldsymbol{r})|\,\Psi_0\rangle}{\omega + \Omega_I + i0^+} \right] \tag{44}$$

for incoming frequency ω, having poles at excitation energies $\Omega_I = E_I - E_0$ for excited states Ψ_I.

To avoid having to calculate the above, we first re-write the density-response function for a Kohn Sham system of non-interacting orbitals $\varphi_j{}^{(0)}$ with energies ε_j, for which $\rho(r,t) = \rho[v_{ext}](r,t)$ as: [112]

** 'Different' external potentials must not be relatable by a purely time-dependent function: $V_{ext} \neq V'_{ext} + f(t)$

$$\chi_{KS}(\boldsymbol{r},\boldsymbol{r}',\omega) = \lim_{\eta\to 0^+}\sum_{k,j}\left(f_k - f_j\right)\delta_{\sigma_k\sigma_j}\left[\frac{\varphi_k^{(0)*}(\boldsymbol{r})\varphi_j^{(0)}(\boldsymbol{r})\varphi_j^{(0)*}(\boldsymbol{r}')\varphi_k^{(0)}(\boldsymbol{r}')}{\omega - \left(\varepsilon_j - \varepsilon_k\right) + i\eta}\right] \quad (45)$$

for which f_k denotes fermi occupation (+1 for occupied and -1 for unoccupied) and σ_k is the spin orientation of orbital k. Then we find that the exact linear density response of an interacting system can be written: [112]

$$\rho_1(\boldsymbol{r},t) = \int_0^\infty dt' \int d^3r'\ \chi_{KS}(\boldsymbol{r}t,\boldsymbol{r}'t')\delta v_{KS}(\boldsymbol{r}',t') \quad (46)$$

which describes the linear density response of a non-interacting system to perturbation $\delta v_{KS}(\boldsymbol{r},t)$:

$$\delta v_{KS}(\boldsymbol{r},t) = \delta v_{ext}(\boldsymbol{r},t) + \int d^3r' \frac{\rho_1(\boldsymbol{r}',t)}{|\boldsymbol{r}-\boldsymbol{r}'|} + \int d^3t' \int d^3r' f_{xc}\left[\rho_{GS}\right](\boldsymbol{r}t,\boldsymbol{r}'t')\rho_1(\boldsymbol{r}',t') \quad (47)$$

in terms of the initial ground state density ρ_{GS}.

Combining equation 46 and 47 gives the Dyson-like equation:

$$\begin{aligned}\chi[n_{GS}](\boldsymbol{r}t,\boldsymbol{r}'t') &= \chi_{KS}[\rho_{GS}](\boldsymbol{r}t,\boldsymbol{r}'t') \\ &+ \int dt_1 \int d^3r_1 \int dt_2 \int d^3r_2 \chi_{KS}[\rho_{GS}]\,(\boldsymbol{r}t,\boldsymbol{r}_1t_1) \\ &\times \left[\frac{\delta(t_1-t_2)}{|\boldsymbol{r}_1-\boldsymbol{r}_2|} + f_{xc}[\rho_{GS}](\boldsymbol{r}_1t_1,\boldsymbol{r}_2t_2)\right]\chi[\rho_{GS}](\boldsymbol{r}_2t_2,\boldsymbol{r}'t')\end{aligned} \quad (48)$$

Relating this to the KS orbitals for closed shell singlet systems and applying the single-pole approximation: [112]

$$\Omega = \omega_q + 2\Re\mathfrak{e}\int d^3r \int d^3r'\ \Phi_q^*(r) f_{Hxc}\left(r,r',\omega_q\right)\Phi_q(r') \quad (49)$$

where q is a double index indicating transitions $q = (i,a)$, having transition frequency:

$$\omega_q = \varepsilon_a - \varepsilon_i, \quad (50)$$

with transition q having transition density:

$$\Phi_q(\boldsymbol{r}) = \varphi_i^*(\boldsymbol{r})\varphi_a(\boldsymbol{r}) \tag{51}$$

and defining the Hartree-xc-kernel:

$$f_{Hxc}(r, r', \omega) = \frac{1}{|r - r'|} + f_{xc}(r, r', \omega). \tag{52}$$

The small-matrix approximation, which arises from keeping the backward transitions (from virtual to occupied orbitals), is also applied: [112]

$$\Omega^2 = \omega_q^2 + 4\omega_q \int d^3r \int d^3r' \, \Phi_q(r) f_{Hxc}(r, r', \Omega) \Phi_q(r') \tag{53}$$

We can now define: [112]

$$\zeta_q(\omega) = \int d^3r' \int d^3r'' \Phi_q^*(r') f_{Hxc}(r', r'', \omega) \xi(r'', \omega) \tag{54}$$

and use this to write an eigenvalue equation:

$$\sum_q \frac{M_{qq\prime}}{\omega - \omega_{q\prime} + i0^+} \zeta_{q\prime}(\omega) = \lambda(\omega)\zeta_q(\omega) \tag{55}$$

finding eigenvalues $\lambda(\omega)$ such that $\lambda(\Omega) = 1$, with Matrix elements:

$$M_{qq'}(\omega) = \alpha_{q'} \int d^3r' \int d^3r'' \Phi_q^*(r) f_{Hxc}(r, r', \omega) \Phi_{q'}(r') \tag{56}$$

where α_q is the difference in occupation of the two orbitals in transition q,

$$\alpha_q = f_i - f_a \tag{57}$$

i.e. $\alpha_q = +2$ for a forward transition (occupied to unoccupied), 0 for a transition between orbitals of the same occupancy and -2 for a backward transition.

Finally we can rewrite the eigenvalue equation as:

$$\sum_{q'}\left[M_{qq'}(\Omega)+\omega_q\delta_{qq'}\right]\beta_{q'}=\Omega\beta_q \tag{58}$$

in which $\beta_q = \zeta_q(\Omega)/(\Omega-\omega_q)$. [112]

In practice we solve Casida's equations to find the true frequencies (for the interacting system) Ω_I:

$$RF_I = \Omega_I^2 F_I \tag{59}$$

$$R_{qq'}=\omega_q^2\delta_{qq'}+4\sqrt{\omega_q\omega_{q'}}\int d^3r\int d^3r'\,\Phi_q^*(r)f_{Hxc}(r,r',\Omega_I)\Phi_{q'}(r') \tag{60}$$

for eigenvectors F_I.

We can also find the oscillator strengths f_I:

$$f_I=\frac{2}{3}\left(\left|x\mathbb{S}^{-\frac{1}{2}}F_I\right|^2+\left|y\mathbb{S}^{-\frac{1}{2}}F_I\right|^2+\left|z\mathbb{S}^{-\frac{1}{2}}F_I\right|^2\right)/|F_I|^2 \tag{61}$$

using:

$$\mathbb{S}_{ij,kl}=\frac{\delta_{i,k}\delta_{j,l}}{\alpha_q\omega_q}>0 \tag{62}$$

for transition $q=(k,l)$. [112]

TDDFT tends to be more accurate than comparable methods such as configuration interaction singles (CIS), especially when hybrid functionals with long range correction or correction for dispersion interactions are used.[88] On the other hand TDDFT can afford valuable savings in time compared with more exact methods of excited state calculation such as equation of motion coupled cluster methods.[113] For the purposes of this thesis where the system in question was very large (up to 1299 atoms in chapter 1) TDDFT was the only reasonable choice considering the trade-off between accuracy and time.

Mulliken Population Analysis

When doing quantum chemical computation for sizeable systems one tends to encounter huge matrices and diffuse molecular orbital surfaces which can be difficult to interpret analytically. Mulliken population analysis[114] is a useful tool that can convert each molecular orbital into a measure of the electronic population of each atom in the system.

The density matrix, describing charge distribution for a given state, derives from the construction of molecular orbitals as a linear combination of atomic orbital basis functions, and is defined for a closed shell system (all MOs doubly occupied) for basis functions δ,γ describing molecular orbitals j:[98]

$$D_{\gamma\delta} = 2 \sum_{j}^{occupied\ MOs} {c_{\gamma j}}^{*} c_{\delta j} \tag{63}$$

Where $c_{\delta j}$ is the coefficient of basis function δ in the expression describing molecular orbital j. The total number of electrons in a system N can be found by integrating over all space for all occupied orbitals which simplifies to the product of the density matrix and the overlap matrix:[98]

$$N = \sum_{\gamma\delta} D_{\gamma\delta} S_{\gamma\delta} \tag{64}$$

From which the electron population of atom A can be found if all basis functions are disregarded unless they centre on atom A, and a partial charge (Mulliken charge) can be assigned to the atom based on the difference between its nuclear charge and resultant electronic charge:[114]

$$q_A = Z_A - \sum_{\gamma \in A} \sum_{\delta} D_{\gamma\delta} S_{\gamma\delta} \tag{65}$$

Provided the basis set used to describe different densities is kept consistent, Mulliken population analysis can be a quick and easy way to compare electron density distributions quantitatively and has been useful throughout this thesis. This method is not without its flaws, particularly where diffuse basis functions are used as electron density far away from a given nucleus may still be attributed to that atom.[98] In light of this, care has been taken in this thesis to use Mulliken population analysis in conjunction with other methods to represent the density (such as visualising molecular orbital surfaces and evaluating the D_{CT} metric – see below).

Density Difference Calculations

Finally, classifying a transition between occupied and virtual MOs or even linear combinations of MO pairs (as is the case for almost all calculated excited states discussed in this thesis) as a charge transfer transition risks becoming a subjective exercise. One method to combat this that has been used in this thesis involves seeking the difference of the densities of ground and excited states as so:[115]

$$\Delta\rho = \rho_{ES} - \rho_{GS} \tag{66}$$

From this point the centre of electron density increase r^+ can be determined by integration over all space of all the positive regions of $\Delta\rho$ and the centre of depletion r^- is found by integration over all negative regions.[116] This allows a vector to be plotted onto the model in question which represents the movement of charge from one region of space to another associated with a particular excitation. The length of the vector is given by the metric D_{CT}:[116]

$$D_{CT} = |r^+ - r^-| \tag{67}$$

Evaluation of the D_{CT} metric is a useful way to visualise CT and to compare the extent of CT for different excitations of the system.

Building Models

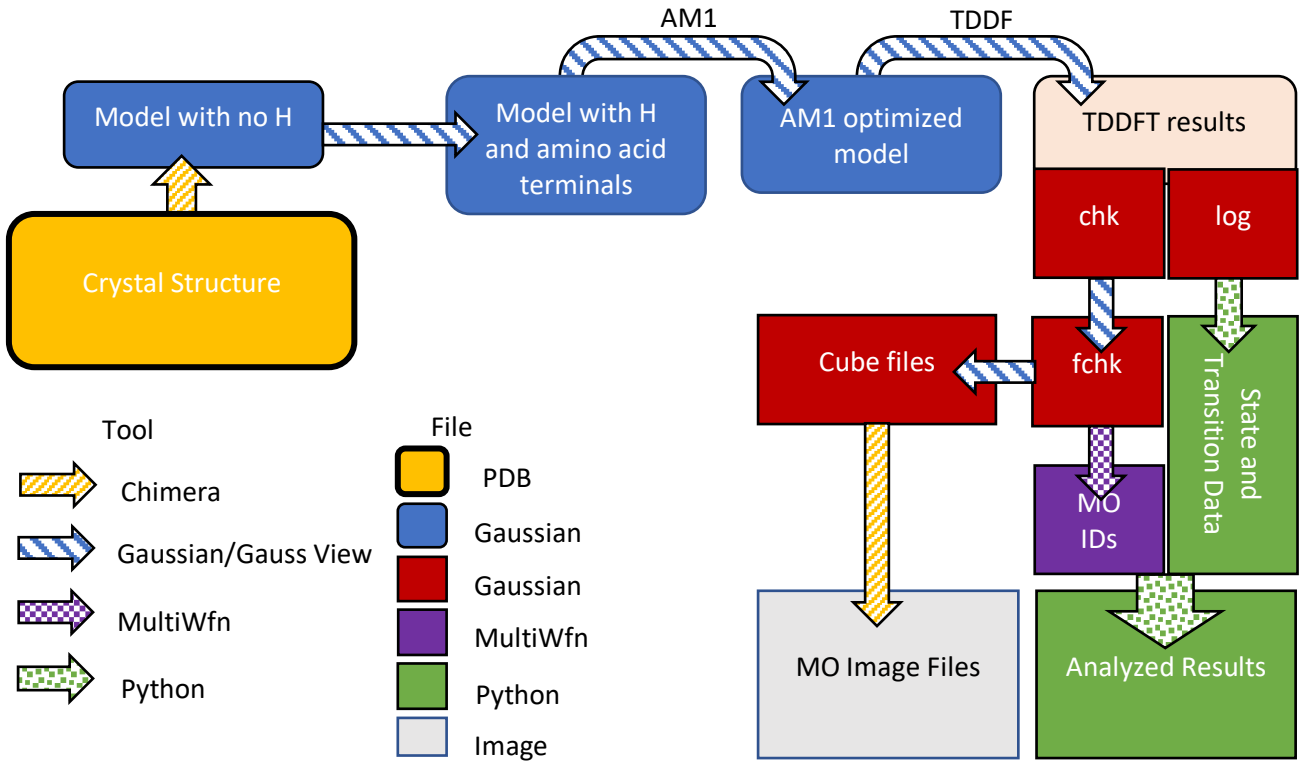


Figure M.1 : Flow chart showing model preparation, calculation and analysis procedure

The schematic in Figure M.1 outlines the model preparation, calculation and analysis pipeline that was developed for work on the models in chapter 1 and was used throughout work described in this thesis.

Models were built from the crystal structure 3ARC[22] which includes the whole PS II dimer without hydrogen atoms. Using Chimera,[117] from the crystal structure protein data bank (pdb) file, a single monomer of the PSII dimer was identified. Models were consistently taken from the monomer in 3ARC with the letter codes for the protein chains capitalised. For all models the six core RC chromophores were selected: P_{D1}, P_{D2}, Chl_{D1}, Chl_{D2}, Phe_{D1} and Phe_{D2}. Each model structure is presented in the relevant results and discussion section in the proceding chapters.

After isolating the desired atoms for a new model, a new pdb file was created so that the structure could be viewed and edited in Gaussview.[118] In some models the chromophore phytol chains were truncated up to the methyl group on C7 (see Figure M.2). This was achieved manually in Gaussview.[118]

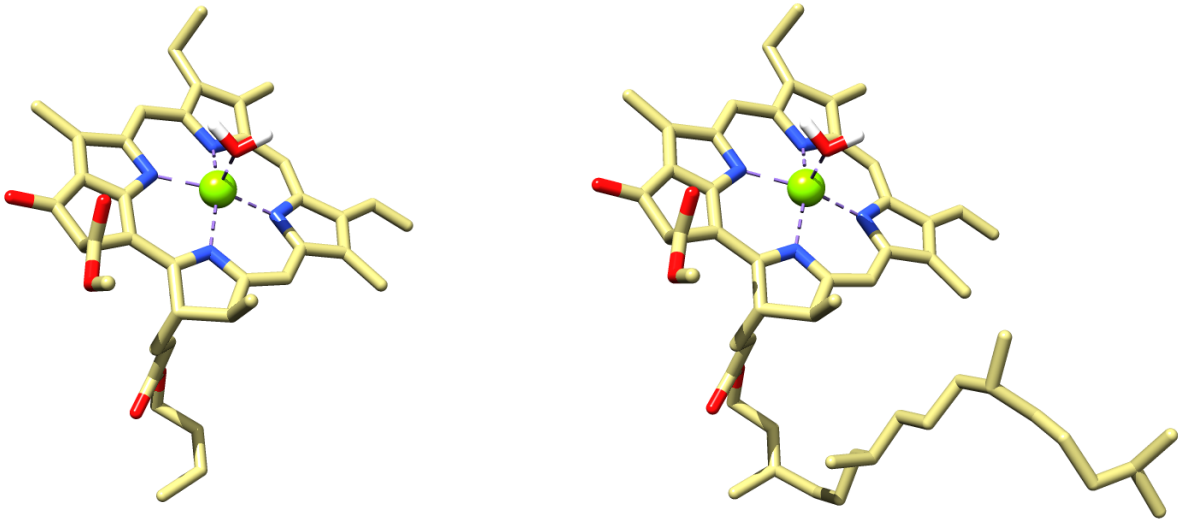


Figure M.2 : Left – Chlorophyll Chl_{D1} from Umena et al.[22] with truncated phytol chain. Right – Chlorophyll Chl_{D1} from Umena et al.[22] with full phytol chain.

In all models hydrogen atoms were added using GaussView.[118] The automatic tool in GaussView for this was found to confuse the valency on the porphyrin rings, therefore it was necessary with every new model structure to do a manual check of each chromophore to ensure that hydrogen atoms were, and were only, present where they needed to be. All hydrogen atom positions were then optimized using AM1 semi empirical theory[119–124] in Gaussian[125] with heavy atom (non-hydrogen) positions frozen.

For models which included amino acid residues the neutral terminals -NH_2 and -COOH were added manually in GaussView[118]. Carboxylic acid terminal groups had the COOH dihedral angle manually set to 0° prior to AM1 hydrogen optimisation.

For models which included mutated residues, the side group of the residue was mutated to the relevant amino acid in GaussView. In some cases water molecules were added (in the case of mutants D2-197-Ala, D2-197-Asn, D1-198-Ala and D1-198-Asn) to the structure and in others (D1-179-Glu and D1-179-His) water molecules were removed from the model to accommodate for the new mutated residue. Where the mutation involved replacement of a chlorophyll axial ligand[††] with a new group, the starting position of the new ligating atom was always chosen as the exact position of the old ligating atom (*e.g.* new water molecules were positioned with the O in place of the coordinating N of the histidine prior to optimisation). The nuclear positions of all

[††] Chlorophyll molecules in all models presented in this thesis have axial ligands.

new atoms were then unfrozen during the AM1 optimisation step. Beyond the mutated side chain all heavy atoms were unchanged and their nuclear positions were frozen during optimisation.

Once the AM1 optimisation had reached convergence the model was ready for the excited state calculation. All models discussed in this thesis had a neutral charge and singlet multiplicity.

Running Excited State Calculations

Models prepared by the method discussed above had between six and 22 excited states calculated using time dependent density functional theory (TDDFT) in Gaussian[125]. Two different long-range corrected, hybrid functionals were used over the course of the PhD: CAM-B3LYP[105] and ωB97X-D[106,107] for comparative purposes.

Basis set 6-31G**[91–97] was employed for the most part across all models. Certain models had their excited states calculated again with the diffuse function added (6-31+G**).[91–97]

Analysing Excited State Results

In the interest of utmost clarity, a full illustrated example of the analysis method is included in the first chapter (subsection on model 1 results and discussion). A description of the methods and program details are given below.

Gaussian log files contained excited state energies, oscillator strengths (f values) and the identities of the transitions (occupied and virtual molecular orbital labels) and their contributions to each excited state. This information was parsed from the log file using my own python code. A calculated absorption spectrum was produced using gaussian functions to broaden the peaks of each excited state and then taking the whole spectrum as the sum of these, this was accomplished in python.

Gaussian checkpoint files from excited state calculations were used to generate formatted checkpoint files (fchk) which in turn could be used to generate cube files for each of the molecular orbitals involved in the calculated excited states.

Cube files could be opened in Chimera[117] and molecular orbitals viewed as surfaces overlaid on the model structure. To automatically generate images of the molecular orbital surfaces a python script was written which would feed Chimera commands. This ensured that the angle at which the model was viewed did not change from MO to MO and that the isosurface value and colour settings were the same for all MOs for all

models. The isosurface value for viewing MOs in chimera was chosen to be +/- 0.002 and all MO images printed in this thesis were created with this isosurface value unless otherwise specified.

Multiwfn[126] was used to print out the atomic contributions to each molecular orbital from Mulliken population analysis[114]. A program in python code was written to parse these values from the Multiwfn output file for each MO.

Each atom was then assigned to the cofactor or residue that it belongs to in the model structure. From here the sum of contributions from all atoms in a single cofactor or residue could be found, resulting in a reduced table with cofactor contributions to each MO. In this way I was able to quantitatively compare MOs with each other for the same model and classify transitions contributing to the excited states within the same model's results or even across models. The MO surfaces (cube files generated from formatted checkpoint files - see above) were an illustration of this quantitative measure and were used in the development of this method to check that the assignments of a particular MO to a particular cofactor's contribution were correct.

Analysing individual states

Using the table of cofactor contributions to each MO (produced from MultiWfn analysis, see above) it was possible to determine the cofactor on which each excitation took place. Charge transfer (CT) transitions were identifiable also, as these had their occupied and virtual orbitals located on different cofactors.

The direction of charge movement during transitions was also analysed based on the movement of electron density during a single transition from occupied to virtual MOs. This was done simply by subtracting the contribution from each cofactor to the occupied MO from its contribution to the virtual MO and choosing the cofactors which had lost and gained the most electron density during the transition. The resulting transition descriptor (*e.g.* 'P_{D1} to Chl_{D1}' or 'Phe_{D2} to P_{D2}') was assigned to a transition class. An alternative method for classifying these transitions was developed during the final year, please see appendix three for a discussion of this.

The D_{CT} index[116] was evaluated for each state calculated for all models in Gaussian[125] using keyword 'pop=DCT'. The nearest atoms to the positions of the resultant vectors, representing the direction of CT, were identified using python (see appendix one).

Chapter One: Wild Type Photosystem II Reaction Centre Models with Time Dependent-Density Functional Theory

Validation of Model and Method Choice

Chapter Overview

Results from four models of the Photosystem II reaction centre (RC) are presented. Each model is evaluated using Time-Dependent Density-Functional Theory (TDDFT), and its excited state profile is analysed. The largest model investigated, which comprises the six core RC pigments with their full phytol chains as well as a significant portion (23 amino acids) of the surrounding protein environment, displays the strongest preference for charge transfer to proceed along the active branch as well as a robustness to the different methods used. The model in question is the largest model of the RC to be investigated using TDDFT to date, and repeat calculations are presented for each model with two functionals (ωB97XD and CAM-B3LYP). The effect of two basis sets (6-31G** and 6-31+G*) is shown on a smaller model for comparison. These results inform future modellers of the importance of both the phytol chains and the amino acids in the vicinity of the RC.

The work presented in this chapter informed the development of procedures for building models, running calculations and conducting analysis which underpin all results presented in this chapter. Furthermore, the results presented in this chapter are used as a comparison for mutant RCs investigated in chapters 2 to 4 of this thesis, and as a benchmark for extended RC models (in chapter 5).

Looking at the mutant-WT comparison in the next chapter, further justification for the improved performance of the largest model over all smaller models can be made. However, a great deal of insight can be taken from examining the differences between the four WT models as well as the action of the different methods on these model calculations.

Results & Discussion

The first research problem tackled was to determine which structural features need to be included in an effective model of the PS II RC. An effective model is one which closely mimics the behaviour of the PS II RC and reproduces experimental findings. In this chapter it will be shown that the pigment phytol chains and surrounding amino acids have the combined effect of directing charge up the active branch preferentially. To illustrate this, results of four models are presented, showing the inclusion of neither, one or both of these parts of the RC environment. The main conclusion of this chapter is that both phytol chains and surrounding amino acids must be included in models of the RC so that the preference for charge to travel up the active branch is reproduced. In later chapters it will also be shown that this model can reproduce experimentally observed band shifts for mutant RCs only when both the phytol chains and amino acids are included.

Investigation of smaller models in this chapter enables repeat calculations with different methods (two functionals and two basis sets). The results of four calculations on the smallest model are presented below. Two functionals were employed to investigate larger models, and overall the largest model is shown to be the most robust with the most similarity between calculations with different functionals.

Table 1.1 : Summary of the four models discussed in this chapter

Model	Amino Acids	Phytol Chains
1	2	Truncated
2	2	Full
3	23	Truncated
4	23	Full

Table 1.1 outlines the elements that were included in each model 1-4. The simplest model built included only the six chromophores with truncated phytol chains and ligands to the four chlorophylls (two water ligands for the two accessory chlorophylls and two histidine residues for the two P chlorophylls). This will be called model 1. Using functional ωB97X-D and basis set 6-31G** the first 22 excited states of model 1 were calculated. This model comprised 582 atoms, employing 6086 basis functions for the 6-31G** basis. Calculation times were around three days to calculate six states on eight cores for 6-31G** calculations. It took an additional four days to calculate 22 states for 6-31G** on eight cpus. Full results for model 1 will be presented, as well as a walk-through of the analysis procedure for this model. The same analysis was carried out for all calculations presented in this work.

Building on model 1, seeking to identify the influence of the pigment phytol chains on the excited state profile of the reaction centre, a new model was built which included them explicitly, model 2. Model 2 included the six chromophores with their full phytol chains included as well as two histidine residues ligating the P

chlorophylls and two water molecules ligating the accessory Chl_{D1} and Chl_{D2} chlorophylls. Full results from calculations on this model are presented in the appendix (see appendix four – model 2 results) and comparison of results across models will be made below.

Model 2 consisted of 870 atoms, employing 8486 basis functions for calculation with the 6-31G** basis set. This model was evaluated with CAM-B3LYP functional and 6-31G** basis set for 6 excited states and to 22 excited states for ωB97X-D with the same basis set. The initial calculation with CAM/6-31G** took 2.5 days on 20 cores to calculate 6 ES. It was recalculated for the ωB97X-D functional for these 6 states, and then took 6.5 days to increase to 22 ES for ωB97X-D/6-31G** on 20 cores.

Next, the effect of including the protein environment on the excited state profile of the reaction centre was investigated with model 3. Model 3 was built, including the six chromophores with truncated phytol chains, the histidine ligands to chlorophylls P_{D1} and P_{D2} and the water ligands to chlorophylls Chl_{D1} and Chl_{D2} as in model 1. Additionally model 3 included 19 amino acid residues which were found within a 6 angstrom radius of the centres of the six porphyrin rings and 2 amino acids which were known sites of mutation (Gln 129 and Gln 130). A list of the residues included in model 3 are presented in table 1.2.

The 23 residues included in model 3 (and model 4) all lay within 6 Å of the centres of the six porphyrin rings of the RC pigments. Two glutamine residues (D1-130 and D2-129) which lie ~ 8 Å away from the centres of the two pheophytins were also included. The glutamines were chosen as they have been the subject of mutagenesis studies. Model 3 comprised 1011 atoms in total, as such calculation with 6-31G** requires 10,233 basis functions. Calculation times were ~4.5 days to find the first six excited states on 20 cores, and an additional ~2 weeks to find the remaining 16 states.

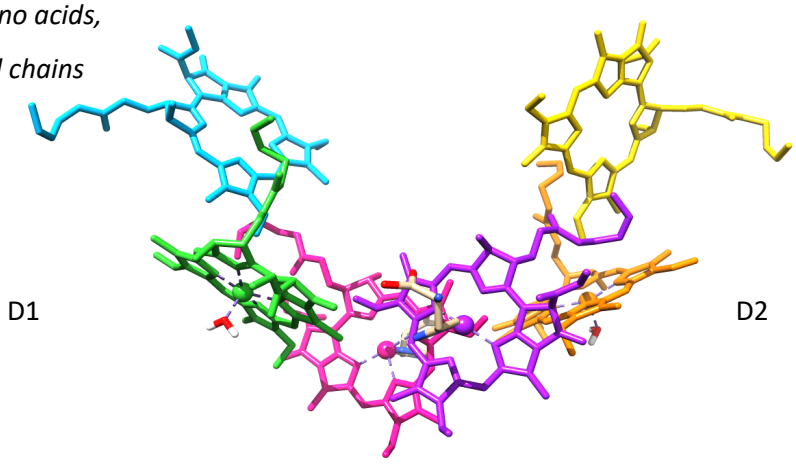
Table 1.2 : Table of which residues were included in model 3 (and model 4)

D1 chain	D2 chain
D1-Gln-130	D2-Gln-129
D1-Tyr-147	D2-Phe-146
D1-Pro-150	D2-Pro-149
D1-Met-172	
D1-Thr-179	D2-Ile-178
D1-Met-183	D2-Leu-182
D1-Ile-192	D2-Trp-191
D1-Leu-193	D2-Thr-192
D1-His-198	D2-His-197
D1-Val-202	D2-Val-201
D1-Phe-206	D2-Leu-205
D1-Met-214	D2-Ile-213

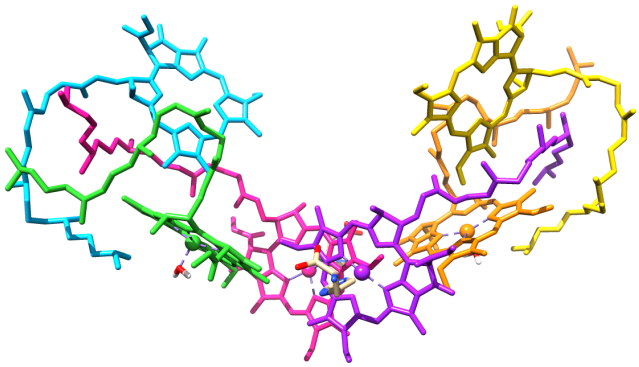
To investigate the combined effect of including the phytol chains and the surrounding protein environment a fourth model was built. Model 4 included the six chromophores with full phytol chains and histidine and water ligands to the four chlorophylls as in model 2, with a total of 23 amino acids as in model 3 (see table 1.2). The fourth model is also the largest studied so far, it comprises 1299 atoms. Calculation with 6-31G** required 12,633 basis functions, note that for this contracted basis set this amounts to 22,092 primitive gaussian functions. The size of the gaussian output checkpoint file for this calculation is 121GB. Calculating the first 6 excited states took 11.5 days, extending to 16 states took ~19.5 days and the last 6 states took ~23 days to calculate (all calculations run using 20 cpus). This means that in total, from model building and optimisation to final results output, calculating 22 ES for this model involved around two months of computational time.

The structures of all four models discussed in this chapter are presented in Figure 1.1.

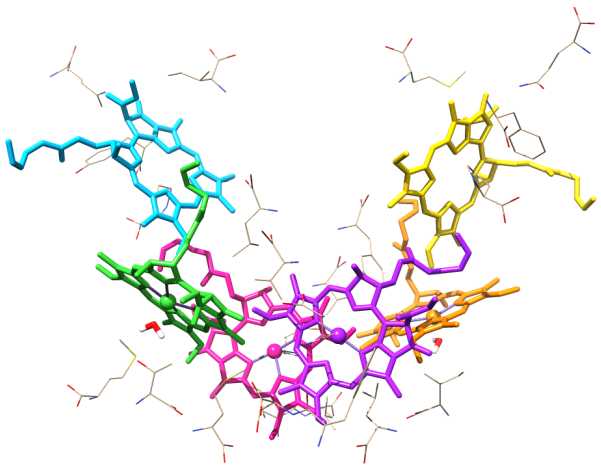
Model 1 – *2 amino acids, truncated phytol chains*



Model 2 – *full phytol chains*



Model 3 – *23 amino acids*



Model 4 – *23 amino acids, full phytol chains*

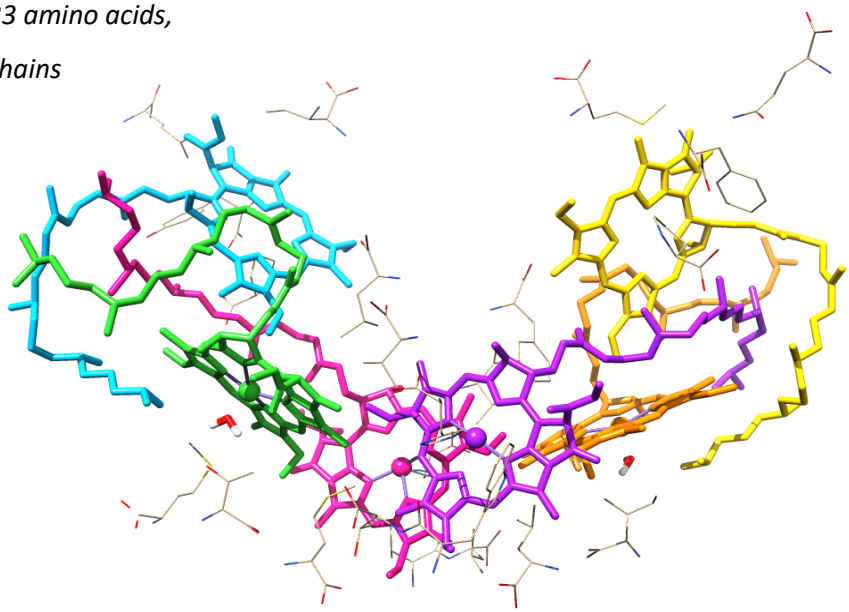


Figure 1.1 : Models 1 (top), 2 (middle left), 3 (middle right) and 4 (bottom) from PS II:[22] Including six chromophores with (hydrogen atoms not depicted) [from left to right Phe_{D1} (blue), Chl_{D1} (green), P_{D1} (pink), P_{D2} (purple), Chl_{D2} (orange) and Phe_{D2} (yellow)], two water molecules (red oxygen atoms, white hydrogen atoms) coordinating the Chl_{D1} and Chl_{D2} chlorophylls and up to 23 amino acid residues (wire structure: tan carbon atoms, red oxygen atoms, yellow sulphur atoms and blue nitrogen atoms, hydrogen atoms not shown) as listed in table 1.2.

Model 1 - ωB97X-D/6-31G**: The Simplest Model

The results for model 1 (including two amino acids and truncated phytol chains) are presented in full below. See table 1.3 for the excitation energies and oscillator strengths of model 1:

Table 1.3 : Energies and Oscillator Strengths for model 1 (ωB97X-D/ 6-31G**)

State	Absorption Band*	Energy (nm)	Oscillator Strength
1	Qy (679 and 671 nm)	673.74	0.3895
2		668.90	0.4010
3		667.17	0.1259
4		655.77	0.0792
5		651.55	0.3688
6		645.97	0.1525
7	Qx (542 nm)	570.99	0.0603
8		566.15	0.0663
9		563.35	0.0500
10		559.28	0.0229
11		556.25	0.1384
12		555.23	0.0623
13	Soret (~432 and 416nm)	442.34	0.1095
14		429.72	0.0071
15		422.06	0.0047
16		417.87	0.0828
17		406.76	0.0010
18		402.78	0.0062
19		401.13	0.3973
20		397.18	0.1957
21		396.64	0.0640
22		393.73	0.2271

* Experimental 10 K absorption spectrum for D1-D2-Cyt b-559 complex band peaks from[25] are given in brackets

This calculation gives three distinct bands, labelled in table 1.3 as the Qy, Qx and Soret regions of the spectrum. There are six excitations in the Qy and Qx regions and 10 in the Soret region. Each excited state (ES) is described by a linear combination of transitions which are discussed below.

Illustrated Analysis Method

Table 1.4 : TD results for state 1 (excitation energy 673.74 nm and oscillator strength 0.3895), Model 1 (ωB97X-D/ 6-31G**)

Occupied MO	Virtual MO	contribution	Normalised contribution (%)
1136	1148	-0.28	15.48
1136	1154	-0.23	10.15
1141	1147	0.11	2.27
1142	1148	0.49	48.74
1142	1154	-0.17	5.88
1144	1149	0.17	5.47
1144	1150	-0.12	2.72

Table 1.4 gives the numbered MOs for the ES 1 for model 1 (ωB97X-D/ 6-31G**). The contribution column tells us the coefficient for each MO pair. The operation to normalise the contribution, derived from the time dependent density functional theory equations (see methods section), is as follows:[98]

$$Contribution^2 \times 200 = Normalised\ Contribution$$

As such, the normalised contribution corresponds to the percentage of the ES that is described by that transition.

MultiWfn[126] can be used to quantify the occupancy of the MOs for each atom using Mulliken population analysis,[114] and summing over the atoms in each cofactor gives the occupancy for each MO for all the cofactors. See the result of this analysis for model 1 ES 1 in table 1.5 below:

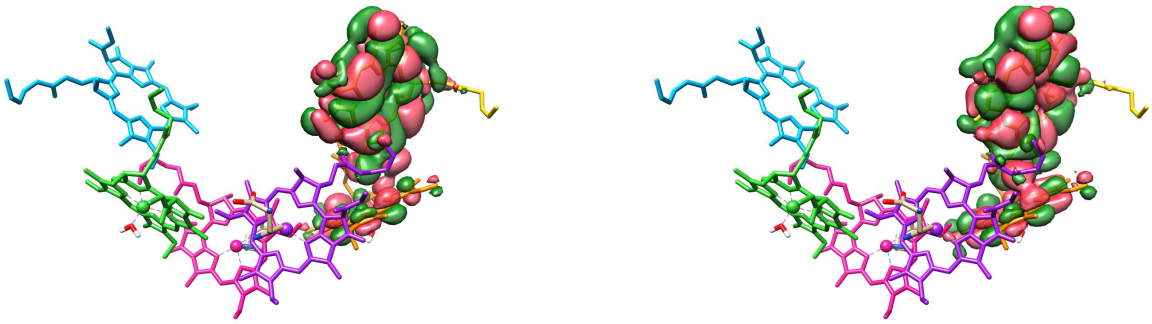
Table 1.5 : MultiWfn output for MOs contributing to state 1 for model 1 (ωB97X-D/ 6-31G**)

MO	MO Type	Phe_{D2}	Chl_{D2}	P_{D2}	P_{D1}	Chl_{D1}	Phe_{D1}
1136	Occupied	98.53%	1.32%	0.08%	0.00%	0.00%	0.00%
1141		0.00%	0.00%	0.12%	0.28%	0.61%	98.98%
1142		99.77%	0.09%	0.08%	0.00%	0.00%	0.00%
1144		0.00%	0.04%	9.28%	90.29%	0.06%	0.00%
1147	Virtual	0.00%	0.00%	0.02%	0.21%	8.62%	91.14%
1148		97.74%	2.02%	0.13%	0.00%	0.00%	0.00%
1149		0.00%	0.08%	33.67%	66.05%	0.12%	0.00%
1150		0.00%	0.07%	66.93%	32.79%	0.08%	0.00%
1154		99.47%	0.20%	0.22%	0.00%	0.00%	0.00%

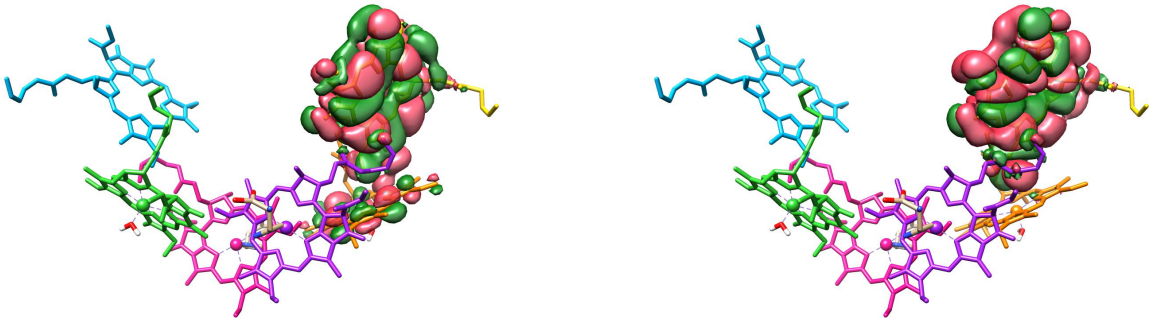
The cofactor with the highest occupancy for each MO is highlighted in colour in the table above (yellow for Phe_{D2}, purple for P_{D2}, pink for P_{D1} and blue for Phe_{D1}). From the table it can be seen that ES 1 is contributed to by Phe_{D2}, Phe_{D1} and P chlorophyll excitations into Phe_{D2}, Phe_{D1}, P_{D1} and P_{D2} virtual MOs.

To illustrate the ES, the Gaussian Cubegen utility allows each of the MOs in the table to be visualised, as shown in Figure 1.2.

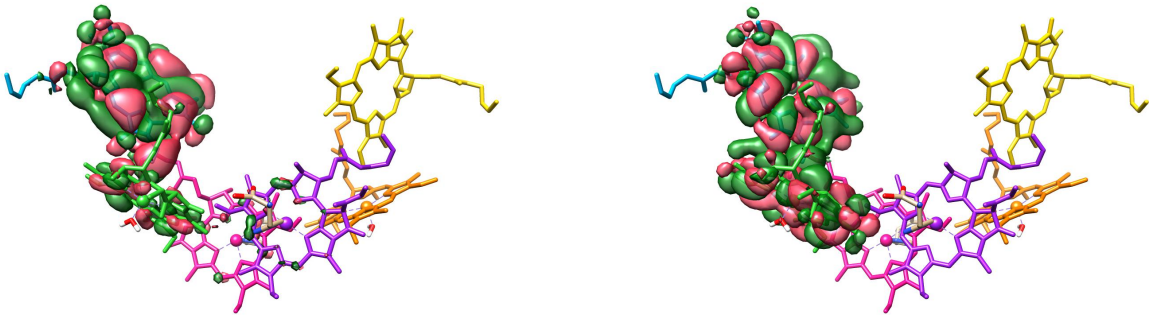
1136 → 1148: 15.48%



1136 → 1154: 10.15%



1141 → 1147: 2.27%



1142 → 1148: 48.74%

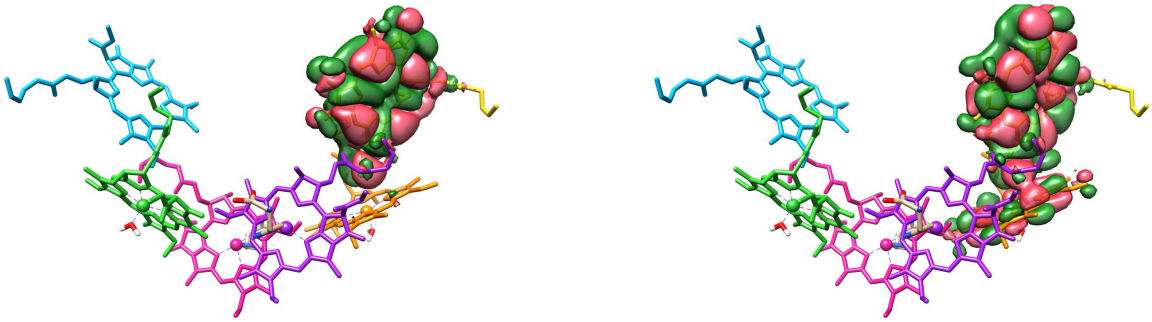
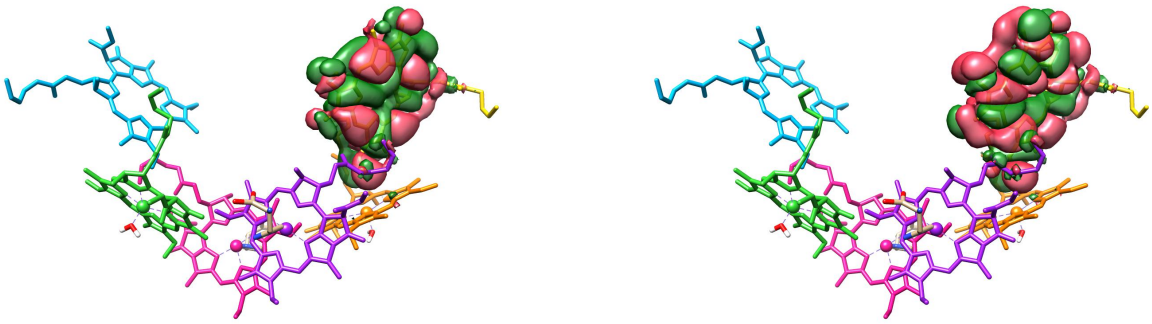
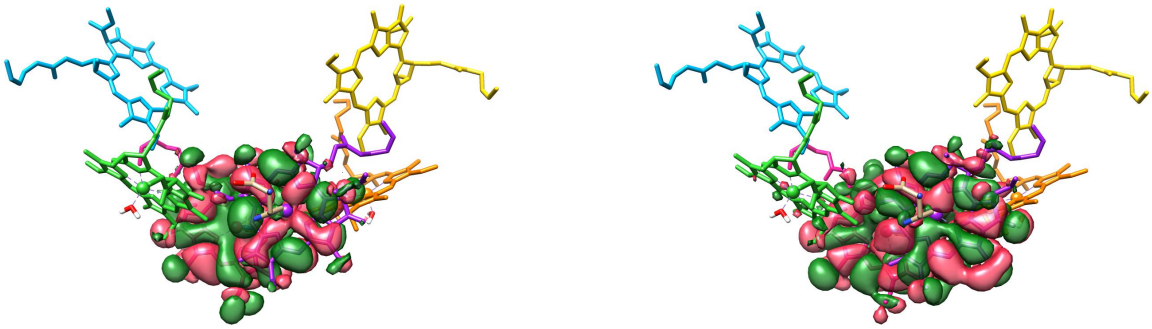


Figure 1.2 : MOs which contribute to ES 1 for Model 1 (ωB97X-D/6-31G**): left column – occupied orbitals, right column – virtual orbitals (page 1)

1142 → 1154: 5.88%



1144 → 1149: 5.47%



1144 → 1150: 2.72%

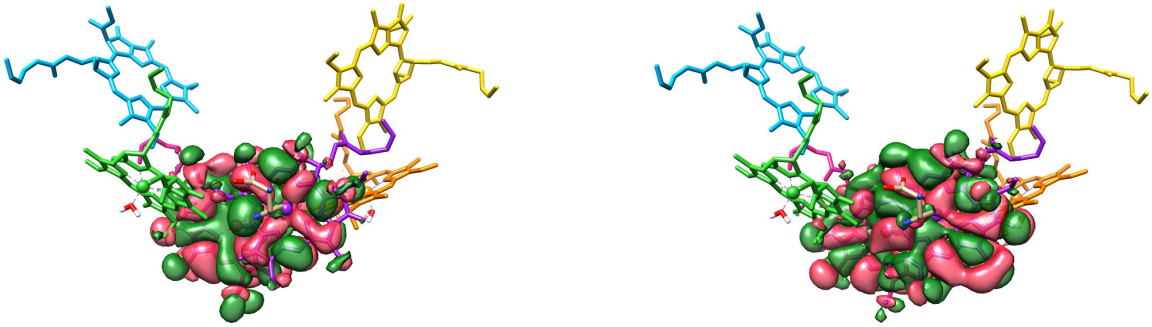


Figure 1.2 : MOs which contribute to ES 1 for Model 1 (ωB97X-D/6-31G**): left column – occupied orbitals, right column – virtual orbitals (page 2)

Combining the two tables above (1.4 and 1.5) gives the contribution from each excitation to the first ES. Selecting only the dominant cofactor gives us a quick way to evaluate the nature of the state. Using this method, it can be seen that ES 1 for model 1 (ωB97X-D/ 6-31G**) is made up of contributions from Phe_{D2}, Phe_{D1} and P_{D1}/P_{D2} excitations (table 1.6). Furthermore, the sum of Phe_{D2} local excitation contributions is 80% (adding together all contributions for Phe_{D2} excitations – those highlighted in yellow in Table 1.6).

Table 1.6 : Transitions contributing to state 1 for model 1 (ωB97X-D/ 6-31G**) with each MO assigned to one cofactor (the cofactor with maximum occupancy). Rows which are described by Phe_{D2} excitations are highlighted yellow.

Occupied MO	Cofactor	Virtual MO	Cofactor	Contribution % to state 1
1136	Phe D2	1148	Phe D2	15%
1136	Phe D2	1154	Phe D2	10%
1141	Phe D1	1147	Phe D1	2%
1142	Phe D2	1148	Phe D2	49%
1142	Phe D2	1154	Phe D2	6%
1144	P D1	1149	P D1	5%
1144	P D1	1150	P D2	3%

This is not a complete picture, for a couple of reasons: first of all, the transitions themselves are only printed in the TD output if they have a contribution above a threshold value. Printing more transitions is possible and would lead to a higher proportion of the state being represented (the sum of contributions getting closer to 100%), but this requires printing huge lists of transitions with contributions below 1%.

Secondly, the choice to represent each MO by one cofactor (which has maximum occupancy) fails to acknowledge that each MO has some degree of delocalisation over other cofactors. This was addressed by choosing to analyse the states using a second representation; the transitions between cofactors, as discussed later. By using these two methods, the nature of the results are captured in a way that allows effective comparison. With these limitations in mind, the broad picture of the excitation profile can be seen when plotting the percentage contribution from each cofactor to each state.

Excitation Profile

Figure 1.3 shows that the six excited states in the Qy band (ES 1-6) can be attributed to excitations of the six cofactors for model 1 ωB-97X-D/6-31G**. States with high (> 0.3) oscillator strength (or 'bright' states) for this model in the Qy region are ES 1, 2 and 5. ES 1 and 2 are similar in oscillator strength and near-degenerate in energy (see table 1.3). Both were attributed to pheophytin excitations with Phe_{D2} (ES 1) and Phe_{D1} (ES 2). The ordering of the Phe transitions tells us that Phe_{D2} excites at a lower energy than Phe_{D1} and the relative oscillator strengths shows that Phe_{D1} excitation is more likely than Phe_{D2} excitation. ES 5 is attributed to Chl_{D1} excitation.

Lower oscillator strength states or 'dark' states in the Qy region are ES 3, 4 and 6. State 3 is dominated by P_{D1} excitation and it can be seen that this includes some charge transfer from P_{D1} into P_{D2} as the P_{D2} contribution increases for the virtual orbitals. Finally, ES 4 and 6 are attributed to a combination of P_{D2} and Chl_{D2} excitations. Note that mixing of other cofactor excitations in each state can be seen in Figure 1.3 (below).

All ESs in the Qx region (ES 7-12) have a very low oscillator strength (< 0.15). In this region mixed P_{D1} and P_{D2} excitation in states 7 and 9 and mixed Chl_{D1} and Phe_{D1} excitations in ES 10 and 11 is seen. ES 8 is attributed to Phe_{D2} excitation and ES 12 is Chl_{D2} excitation.

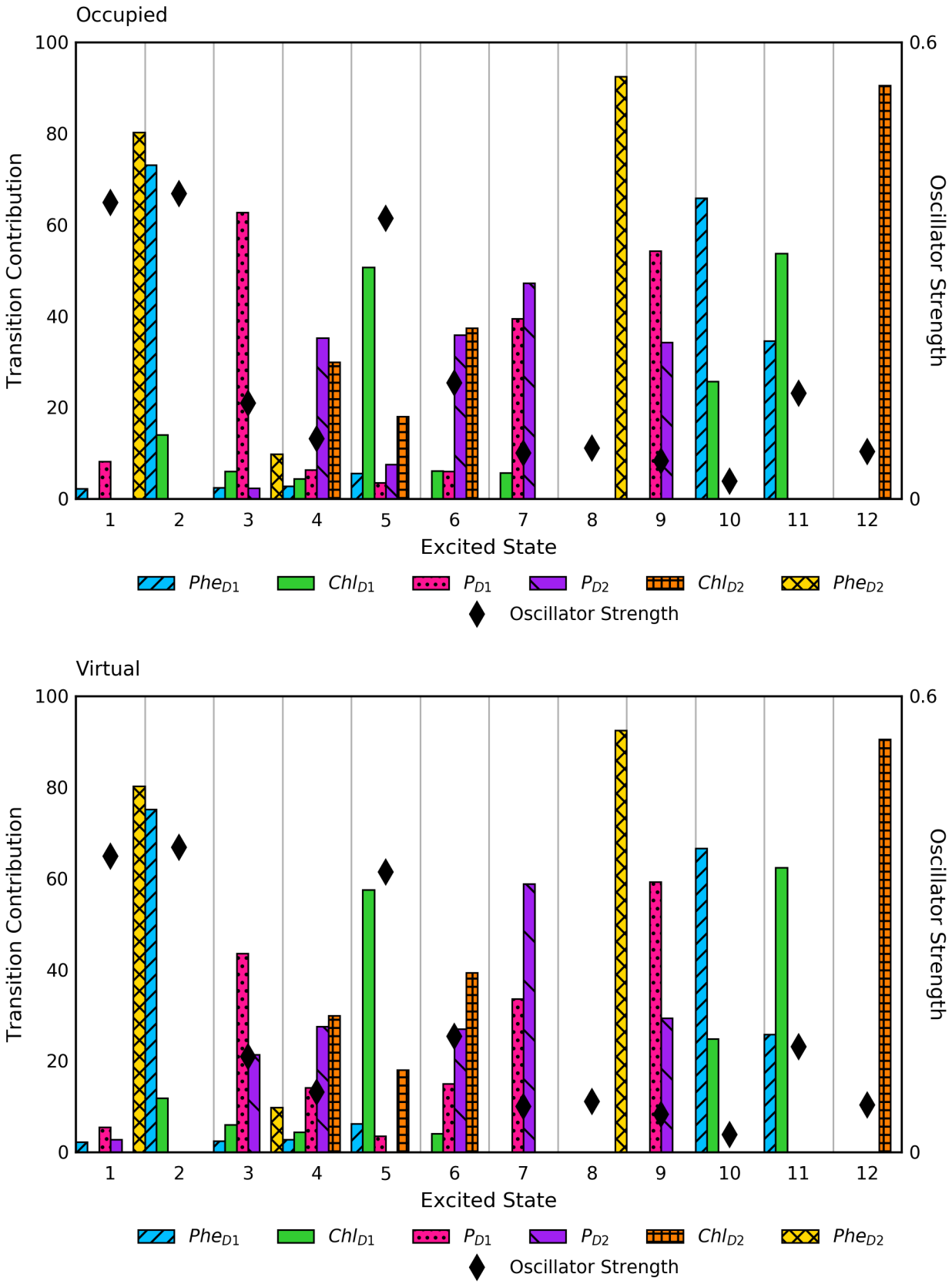


Figure 1.3 : Model 1 ωB97X-D/6-31G** excited states 1-12, (bar chart, left y axis) % of state contributed to by each cofactor (occupied orbital occupancy analysis with MultiWfn from Mulliken method) and (black diamonds, right y axis) oscillator strength of each state. Cofactors coloured as in all figures in this thesis. TOP – occupied orbitals, BOTTOM – virtual orbitals.

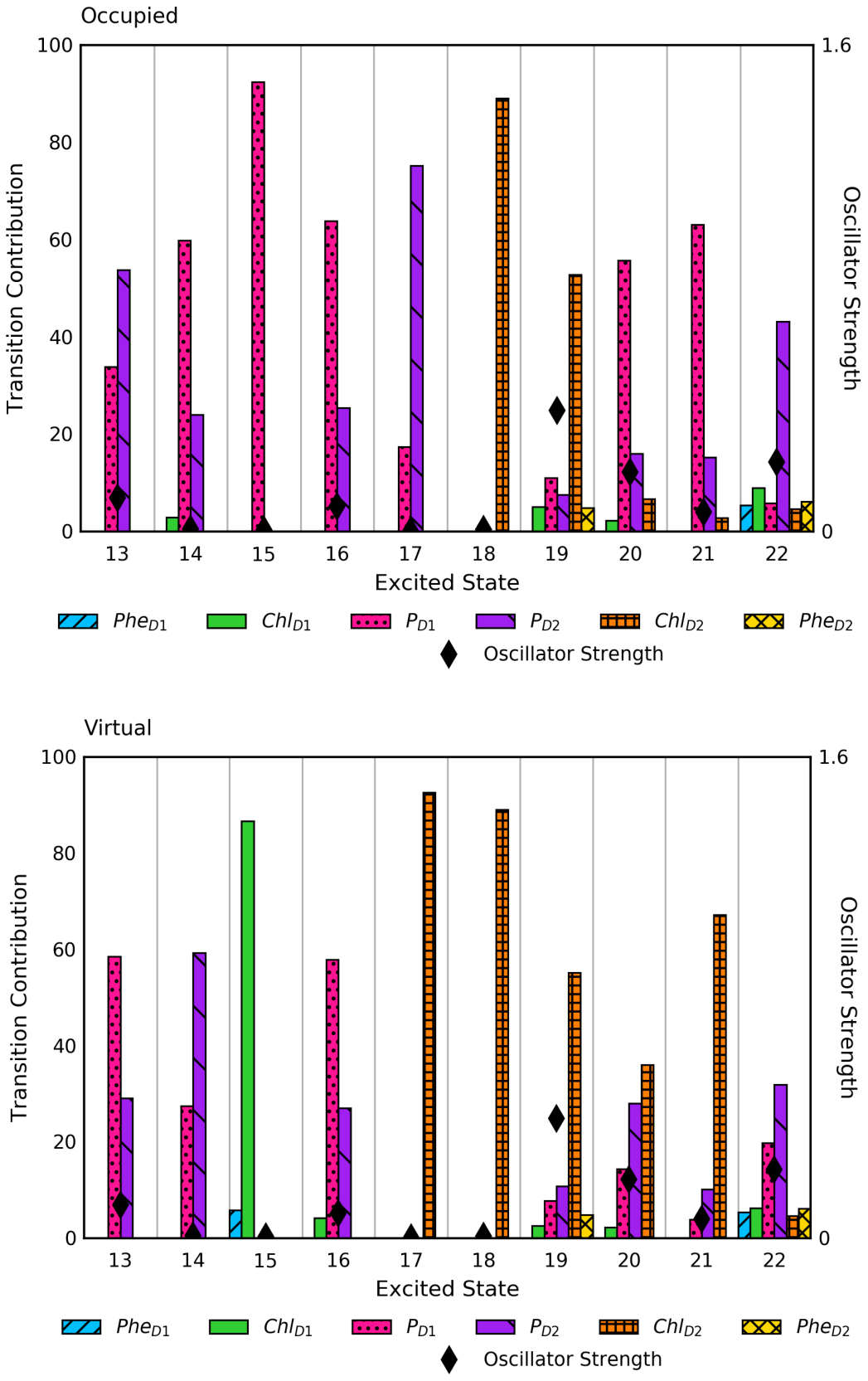


Figure 1.4 : Model 1 ωB97X-D/6-31G** excited states 13-22, (bar chart, left y axis) % of state contributed to by each cofactor (occupied orbital occupancy analysis with MultiWfn from Mulliken method) and (black diamonds, right y axis) oscillator strength of each state. Cofactors coloured as in all figures in this thesis. TOP – occupied orbitals, BOTTOM – virtual orbitals.

Looking at the occupied molecular orbitals contributing to each state in the Soret region (ES 13-22, shown in Figure 1.4), three states excite out of P_{D2} orbitals, five states excite out of P_{D1} orbitals and two states excite out of Chl_{D2} orbitals. In this region there is some charge transfer (CT) character. Notably P_{D2} to P_{D1} in ES 13, P_{D1} to P_{D2} in ES 14, P_{D1} to Chl_{D1} transition in ES 15, P_{D2} to Chl_{D2} transition in ES 17 and P_{D1} to Chl_{D2} transition in ES 20 and 21.

The majority of states in the Soret region are very dark (< 0.15), excepting the one bright state ES 19 (f = 0.3973) which is attributed to Chl_{D2} excitation. ES 20 and 22 have some oscillator strength with calculated values of 0.1957 and 0.2271 respectively, see table 1.3.

Transition Classes

Another way to view these results is to identify which class of transitions each MO pair falls into. For example, if a transition with an occupied MO on cofactor A has a virtual orbital on cofactor B we would say this transition has CT character from A to B. Similarly if a transition has both its occupied and virtual orbitals on cofactor C but an increased occupancy on cofactor D in the virtual orbital compared to the occupied, we would say this transition has CT character from C to D. This classification is summarised in Figure 1.5. An algorithm was written to capture all of these rules which is detailed in appendix three. The degree of CT can also be analysed by a vector comparison method, this is discussed further in appendix three.

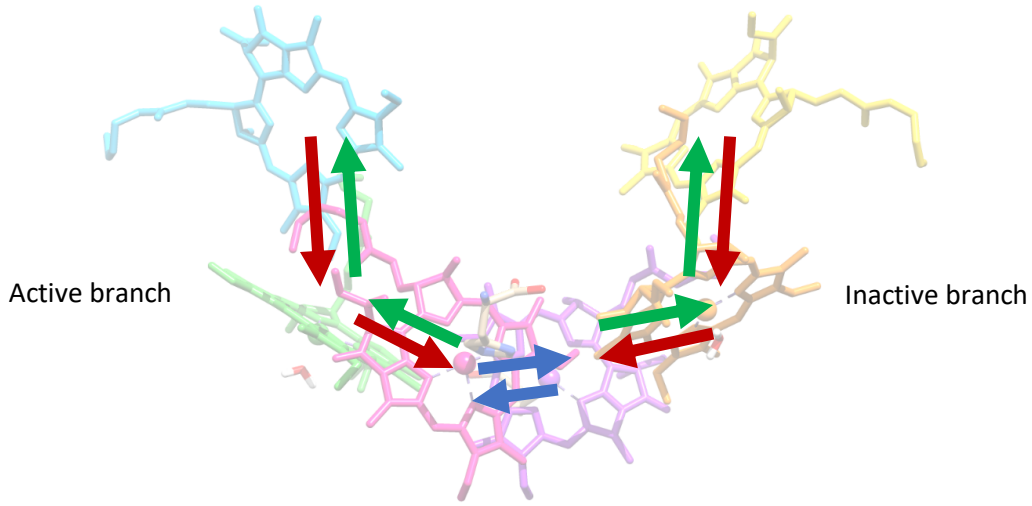


Figure 1.5 : The direction of electron density movement during transitions can either be down the active/inactive branch (red arrows), up the active/inactive branch (green arrows) or between the P chlorophylls (blue arrows)

Examining the transitions which contribute to each state, the highest contributing MO pair (the MO pair describing the dominant transition for each state) is printed in Figures 1.6a-f.

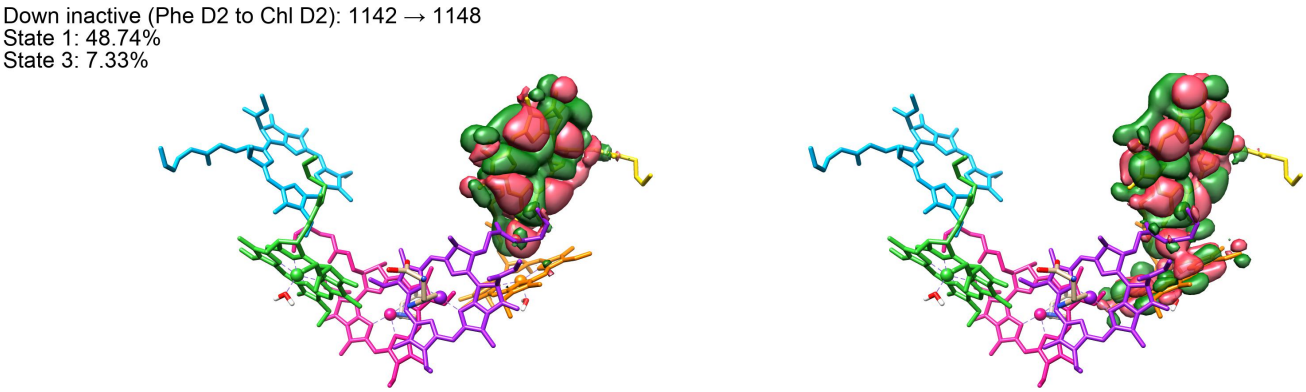


Figure 1.6a : MO diagrams for Down Inactive (Phe D2 to Chl D2) transition which contributes 48.74% to ES 1 and 7.33% to ES 2 for Model 1 ωB97X-D/6-31G**.

This transition shows electron density moving from the Phe_{D2} down the inactive branch to Chl_{D2}. Transitions of this type are broadly labelled 'down inactive' to denote the direction of electron density movement during the transition. Also in this class would be a transition with movement from Phe_{D2} towards the P chlorophylls or from Chl_{D2} towards the P chlorophylls.

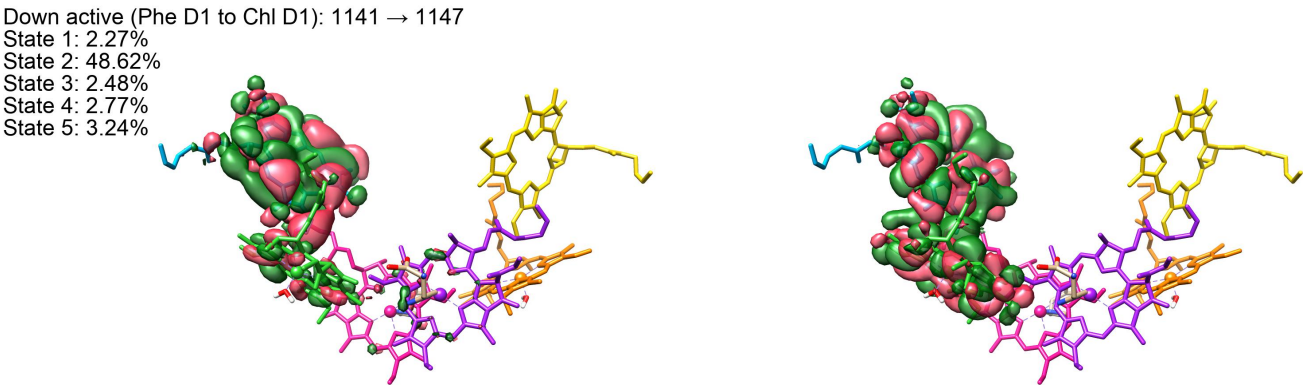


Figure 1.6b : MO diagrams for Down Active (Phe D1 to Chl D1) transition which contributes 48.62% to ES 2 and 2.27% to ES 1, 2.48% to ES 3, 2.77% to ES 4 and 3.24% to ES 5 for Model 1 ωB97X-D/6-31G**.

This transition shows movement from the Phe_{D1}, travelling down the active branch towards the Chl_{D1} and is therefore labelled 'down active'. Also transitions from Phe_{D1} or Chl_{D1} towards the P chlorophylls are labelled as 'down active'.

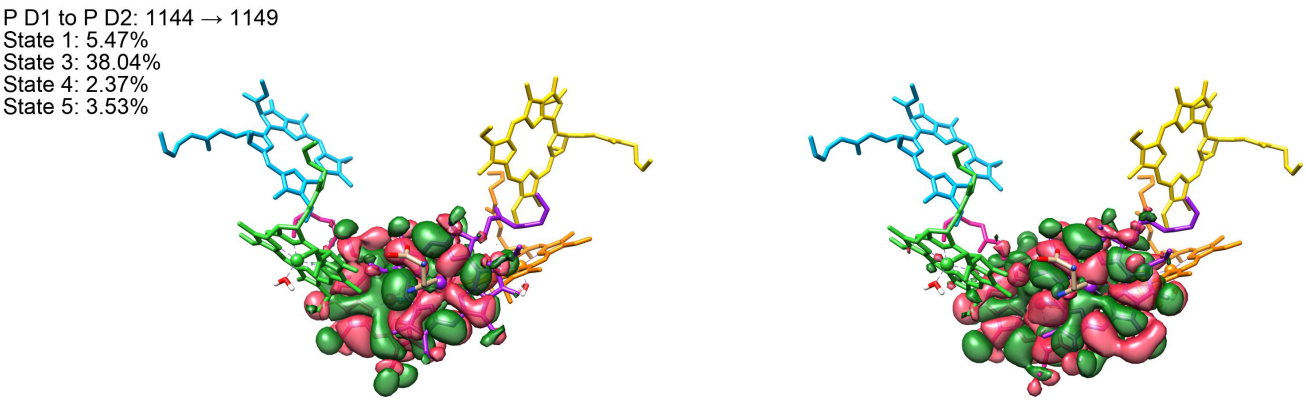


Figure 1.6c : MO diagrams for P D1 to P D2 transition which contributes 38.04% to ES 3 and 5.47% to ES 1, 2.37% to ES 4 and 3.53% to ES 5 for Model 1 ωB97X-D/6-31G**.

This transition, depicting movement between the two P chlorophylls, is labelled 'P_{D1} to P_{D2}'.

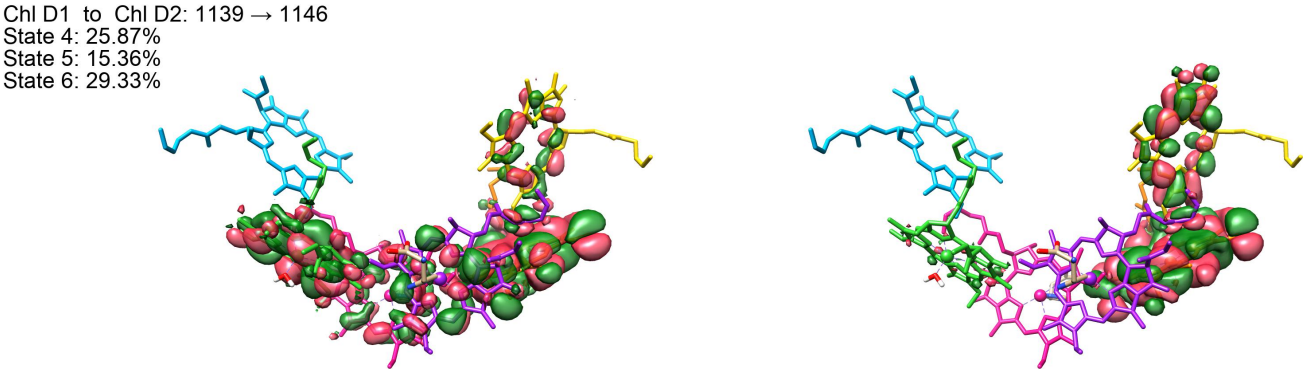


Figure 1.6d : MO diagrams for Chl D1 to Chl D2 transition which contributes 25.87% to ES 4, 15.36% to ES 5 and 29.33% to ES 6 for Model 1 ωB97X-D/6-31G**.

From an occupied orbital delocalised over Chl_{D1}, Chl_{D2} and the two P chlorophylls electron density moves up the inactive branch towards the Chl_{D2} and Phe_{D2} cofactors. The algorithm (see appendix three) defines the transition by selecting the cofactors which see the largest change in occupancy from occupied to virtual. For this MO pair the transition is from Chl_{D1} to Chl_{D2}. This is not in a common class of transitions, but could be thought of as the inactive branch analogue to the 'up active' transition below as electron density travels up the inactive branch. Please see appendix three for discussion of an alternative algorithm to classify the transition classes.

It is worth noting that as the transition above contributes less than 30% to state 4, the second highest contributing transition is 1143 to 1150 23.57% which is depicted in state 6, in Figure 1.6g.

Up active (P D2 to Chl D1): 1138 → 1145
State 2: 6.05%
State 3: 6.01%
State 4: 4.38%
State 5: 38.94%
State 6: 4.04%

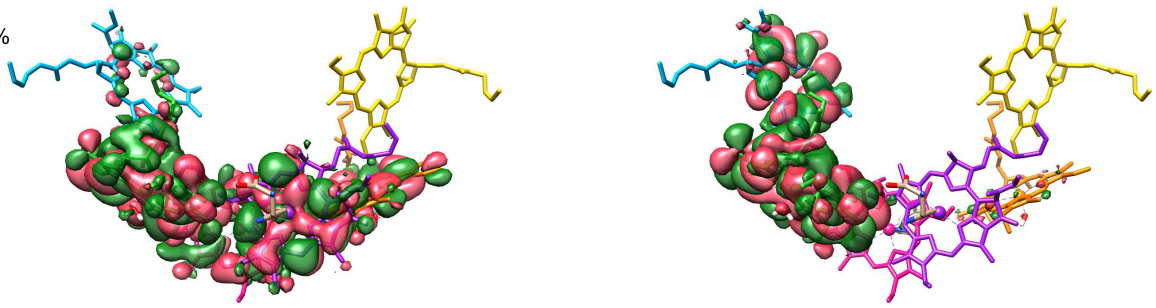


Figure 1.6e : MO diagrams for Up Active (P D2 to Phe D1) transition which contributes 38.94% to ES 5, 6.05% to ES 2, 6.01% to ES 3, 4.38% to ES 4 and 4.04% to ES 6 for Model 1 ωB97X-D/6-31G**.

This transition is classed as 'up active' as electron density moves from a delocalised state away from the P chlorophylls and towards the Chl_{D1} and Phe_{D1} cofactors. The algorithm identifies P D2 as the cofactor which loses the most occupancy, and Chl_{D1} as the cofactor which gains the most during this transition.

P D2 to P D1: 1143 → 1150
State 4: 23.56%
State 6: 20.78%

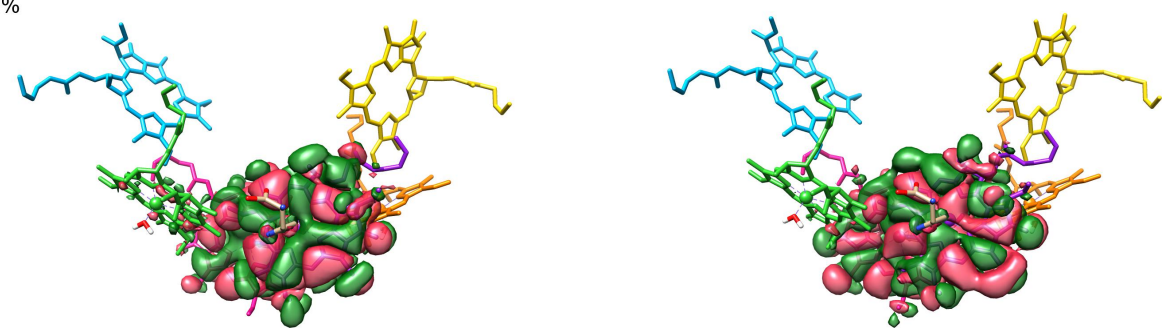


Figure 1.6f : MO diagrams for P D2 to P D1 transition which contributes 23.56% to ES 4 and 20.78% to ES 6 for Model 1 ωB97X-D/6-31G**.

State 6 has its major contribution from the transition in Figure 1.6d. The next largest contribution is from the transition shown above, this transition shows movement between the two P chlorophylls, it is labelled 'P_{D2} to P_{D1}'.

Up inactive (Chl D2 to Phe D2): 1136 → 1154
State 1: 10.15%

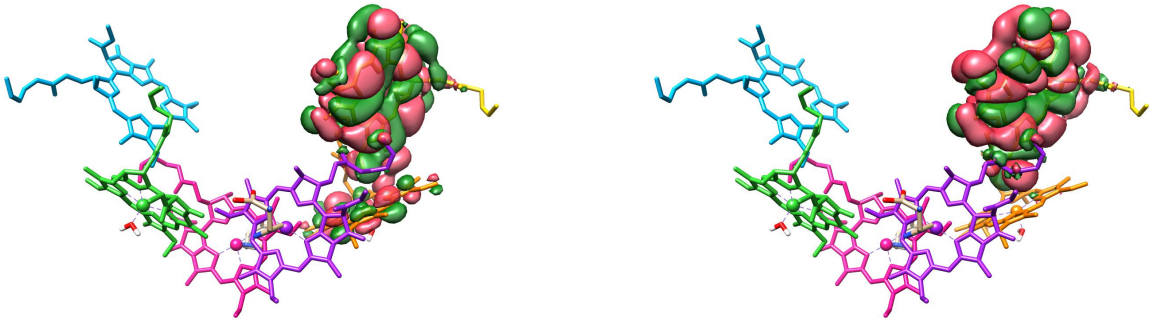


Figure 1.6g : MO diagrams for Up Inactive (Chl D2 to Phe D2) transition which contributes 10.15% to ES 1 for Model 1 ωB97X-D/6-31G**.

For the sake of completeness this MO pair which is described by the algorithm as 'up inactive' is shown above. It has a small contribution to the sixth ES.

A new representation for the results for Model 1 is presented in figures 1.7 and 1.8; depicting the contribution from all of these transitions to each state. Together with the picture in figures 1.3 and 1.4 we now have a way to compare results across models and methods. Where transitions do not fit into the categories described above they are included in the figures separately, and named as a transition from the highest occupancy cofactor for the occupied MO to the highest occupancy cofactor for the virtual MO (*e.g.* "Chl_{D1} to Chl_{D2}" in Figure 1.7).

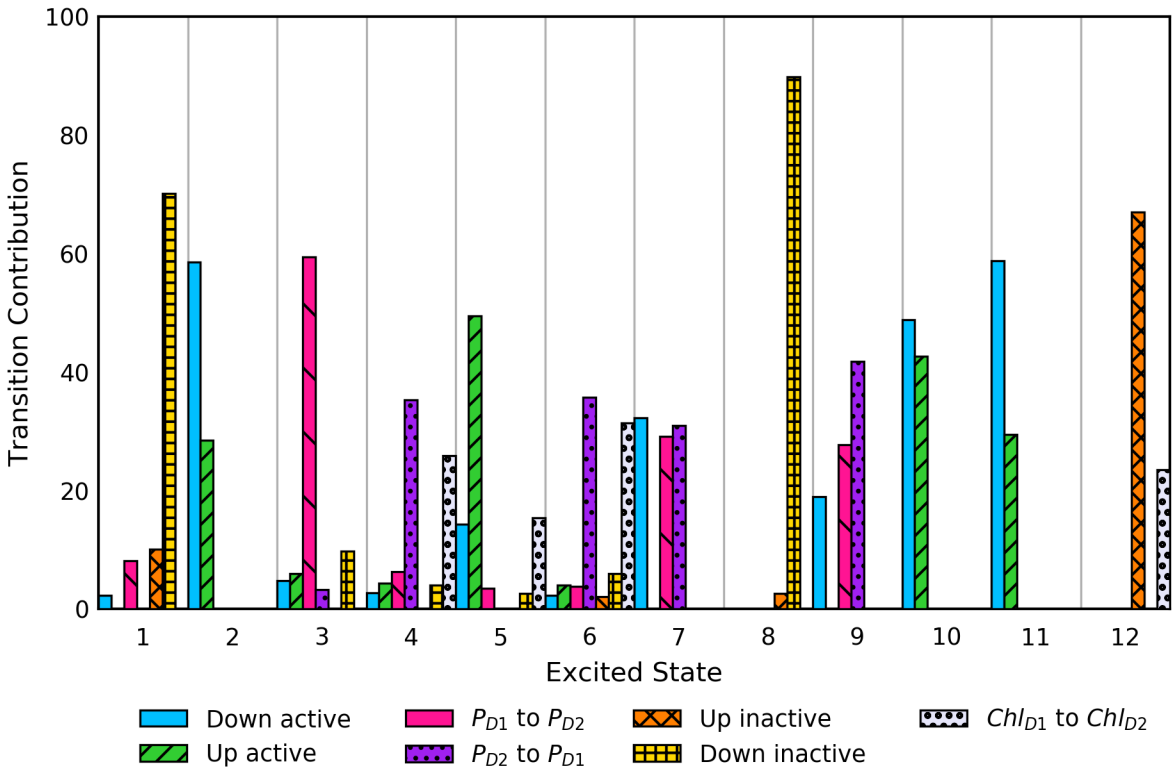


Figure 1.7 : Contributions from each transition class to ES 1-6 (Qy region) and 7-12 (Qx region) for model 1 (ωB97X-D/ 6-31G**)

For ES 1-6 (Qy region), Figure 1.7, for model 1 (ωB97X-D/ 6-31G**) the transition classes in the bright states are down inactive (ES 1, f = 0.3895), down active (ES 2, f = 0.4010) and up active (ES 5, f = 0.3688). The darker states are contributed to by the P excitations and the Chl_{D1} to Chl_{D2} transition.

In the Qx region for this model, brightest state ES 11 (f = 0.1384) has its highest contribution from down active transitions.

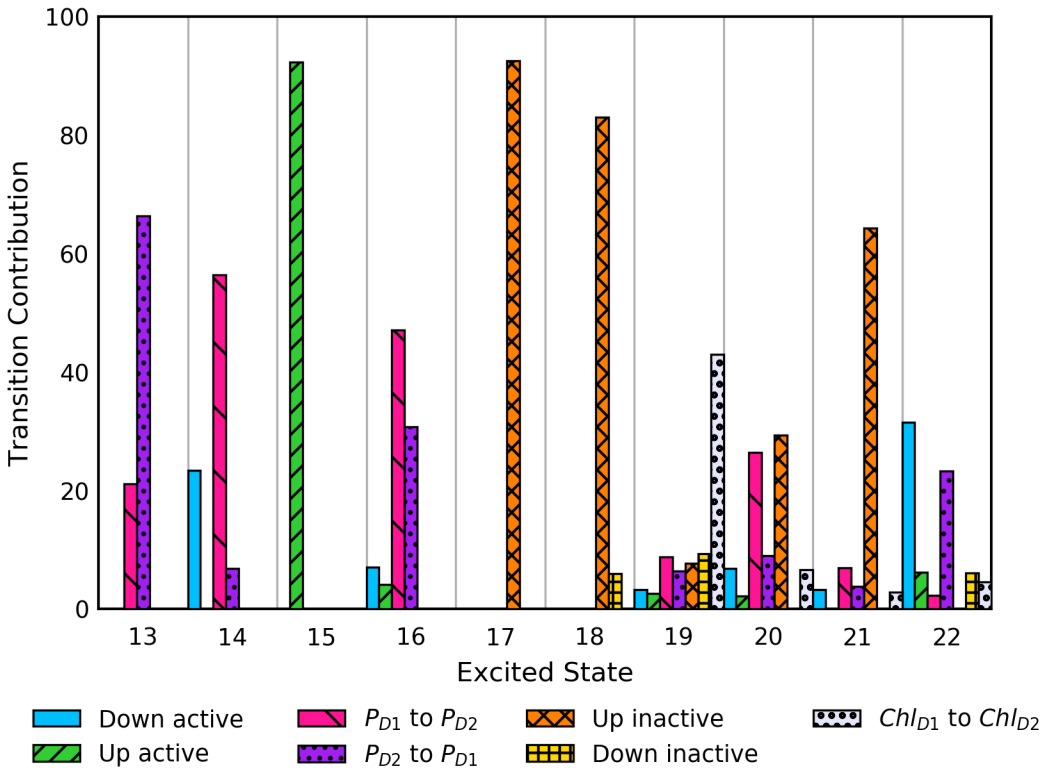


Figure 1.8 : Contributions from each transition class to ES 13-22 for model 1 (ωB97X-D/ 6-31G**)

Figure 1.8 depicts the contribution from transitions to ES in the Soret region for model 1 (ωB97X-D/ 6-31G**). Most ES in the Soret region have oscillator strengths below 0.15 for this model. The brightest state in the Soret region ES 19 (f = 0.3973) is highly mixed and has its highest contribution from Chl_{D1} to Chl_{D2} transition. ES 20 and 22 have oscillator strengths 0.1957 and 0.2271 and are very mixed with contributions from up inactive and P_{D1} to P_{D2} transitions for ES 20 and P_{D2} to P_{D1} and down active to ES 22.

Charge Transfer Character

So far the discussion in this chapter has focussed on movement of charge within a single transition, however ESs are made up of linear combinations of these. The metric D_{CT}[116] can be used to analyse the CT character of a whole ES, which can be thought of as the weighted sum of the transition directions.

In Gaussian, running D_{CT} analysis results in a printout of vectors depicting the movement of charge during an excitation. The length of the vector corresponds to the extent of CT. Below is a table of the D_{CT} vector data for model 1 (ωB97X-D/ 6-31G**), where the nearest atom to each tail and head of the vectors has been identified.

It can be seen from table 1.7 that the overall CT character for ES 1-12 is negligible, as the CT vector head and tail are both found nearest to atoms from the same cofactor, and often the same atom. However, for higher energy ES (those within the Soret region) CT is observed, for example between the P chlorophylls (ES 13, 14,

16 and 22), down the active branch from Chl_{D1} to P_{D1} (ES 15) and down the inactive branch from Chl_{D2} to P chlorophylls (ES 17 and 21). ES 15 has the second lowest oscillator strength in the region (f = 0.0047) whilst ES 17 has the lowest (f = 0.0010). ES 21 has oscillator strength of 0.0640. Bright state ES 19 does not have overall CT character, nor do dark states ES 18 and 20.

Table 1.7 : D_{CT} vectors-nearest atom data for model 1 (ωB97X-D/ 6-31G**) – rows for CT states are coloured by transition class, following the colour convention in Figure 1.7 and 1.8.

ES	Tail Atom	Tail Elem	Tail Cofactor	Head Atom	Head Elem	Head Cofactor
1	295	C	Phe D2	317	C	Phe D2
2	206	C	Phe D1	228	C	Phe D1
3	45	N	P D1	45	N	P D1
4	52	C	P D1	52	C	P D1
5	534	H	P D2	534	H	P D2
6	94	H	P D1	94	H	P D1
7	473	N	P D2	500	N	P D2
8	297	N	Phe D2	355	H	Phe D2
9	34	N	P D1	29	Mg	P D1
10	220	C	Phe D1	223	C	Phe D1
11	270	H	Phe D1	271	H	Phe D1
12	121	N	Chl D2	148	N	Chl D2
13	468	Mg	P D2	45	N	P D1
14	29	Mg	P D1	468	Mg	P D2
15	29	Mg	P D1	412	N	Chl D1
16	488	C	P D2	53	N	P D1
17	468	Mg	P D2	148	N	Chl D2
18	155	O	Chl D2	151	C	Chl D2
19	149	C	Chl D2	120	C	Chl D2
20	45	N	P D1	94	H	P D1
21	45	N	P D1	149	C	Chl D2
22	470	C	P D2	46	C	P D1

Method Comparison for Model 1

Four methods were used to investigate the first six excited states of model 1, employing two basis sets 6-31G** and 6-31+G** each with two functionals CAM-B3LYP and ωB97X-D. The results from different methods (functionals CAM-B3LYP and basis sets 6-31G** and 6-31+G**) on model 1 for states 1-6 are presented below:

7,350 basis functions were employed for the 6-31+G** basis. Calculation times were around three days to calculate six states on eight cores for 6-31G** calculations. It took around one week to calculate 6 states on 20 processors for 6-31+G** calculations. Table 1.8 lists the energies and oscillator strengths for results of calculating ES 1-6 of model 1 using the four methods.

Table 1.8 : Energies and Oscillator Strengths for model 1 (CAM-B3LYP/6-31G**, CAM-B3LYP/6-31+G**, ωB97X-D/6-31G** and ωB97X-D/6-31+G**) Qy region.

	Energy (nm)				Oscillator Strength			
	6-31G**		6-31+G**		6-31G**		6-31+G**	
State	CAM	ωB	CAM	ωB	CAM	ωB	CAM	ωB
1	657.67	673.74	669.60	684.33	0.4463	0.3895	0.3751	0.4350
2	654.06	668.90	665.48	680.06	0.0563	0.4010	0.1808	0.1199
3	652.39	667.17	663.14	678.72	0.5234	0.1259	0.5433	0.4169
4	643.95	655.77	656.37	667.88	0.0533	0.0792	0.0303	0.0535
5	638.58	651.55	650.35	663.12	0.3514	0.3688	0.3530	0.3750
6	634.50	645.97	646.09	657.15	0.1505	0.1525	0.1484	0.1573

Considering table 1.8, overall there is a similar profile for the four methods (the two functionals ωB97X-D and CAM-B3LYP combined with the two basis sets 6-31G** and 6-31+G**) for model 1. Consistent across all four methods, there are three high (> 0.3) oscillator strength states and three darker states. ES 1 and 5 are also consistently bright states (ES 1 f > 0.37 and ES 5 f > 0.35) whilst ES 4 and 6 are consistently dark states (ES 4 f < 0.8 and ES 6 f < 0.16). For all four methods states 1-3 lie close in energy, the main variation in the methods can be seen in these three states.

Looking at the MO identities (full data presented in appendix four – model 1 results) ES 1-3 are attributed to two Phe excitations and a P_{D1} excitation. For all methods ES 4 and 6 are contributed to by Chl_{D2} and P_{D2} excitations and ES 5 is always dominated by Chl_{D1} excitation.

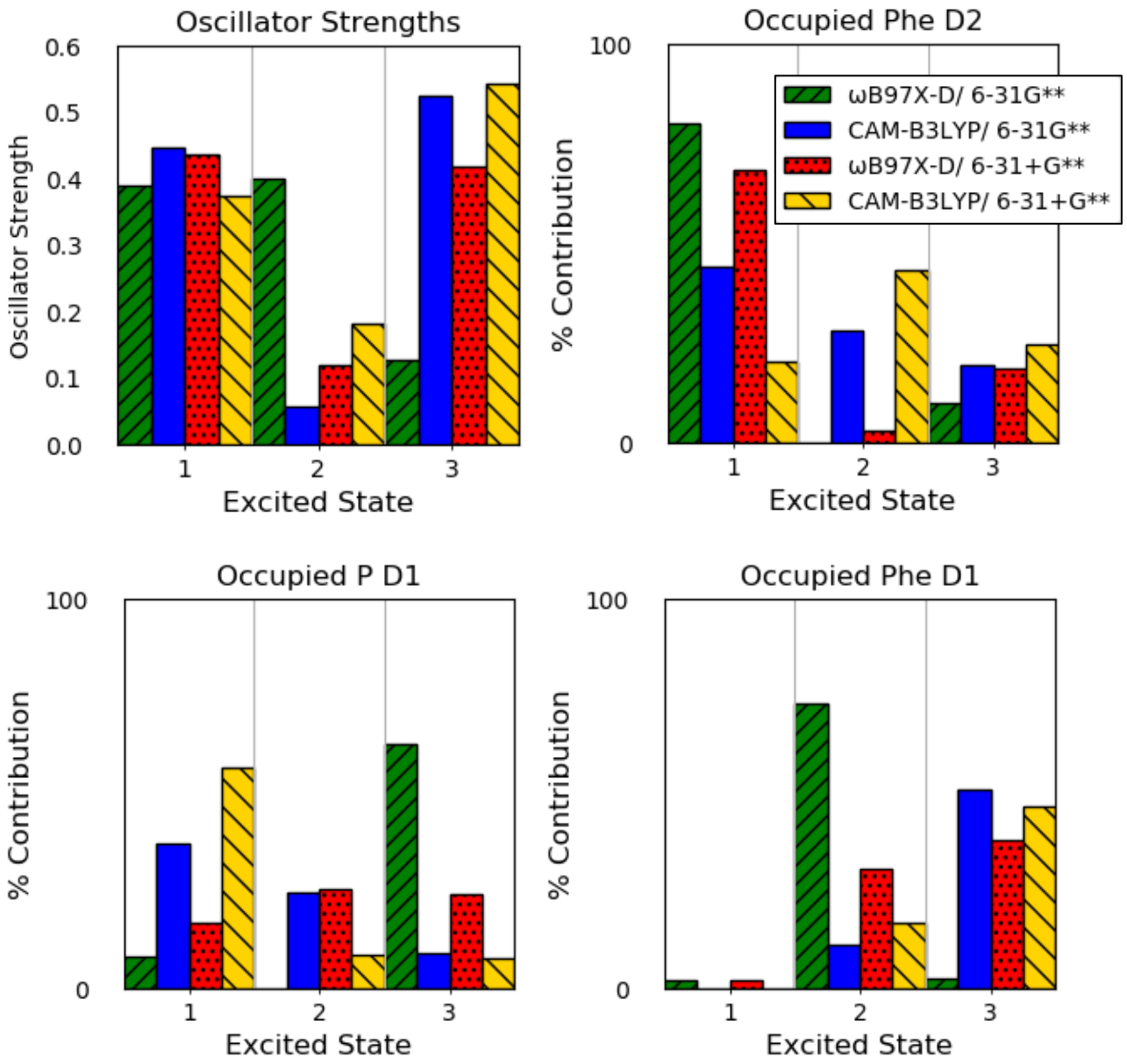


Figure 1.9 : Showing the profile of the first three ES for model 1 all methods. TOP LEFT – Oscillator strengths, TOP RIGHT Phe_{D2} occupied orbital contribution, BOTTOM LEFT P_{D1} contribution and BOTTOM RIGHT Phe_{D1} contribution.

For Figure 1.9, P_{D1} excitation energy, relative to the Phe excitation energies, is dependent on the method used. P D1 excitation has a greater contribution to lower energy states for CAM calculations than for ωB and a greater contribution to high energy excited states for 6-31G** than for 6-31+G** calculations.

ES 1 always has a high oscillator strength (see Figure 1.9). This state is dominated by Phe_{D2} excitation for the two ωB97X-D calculations, so it can be postulated that Phe_{D2} excitation will contribute to high energy oscillator strength states. In fact the CAM-B3LYP calculations each have mixed contributions from P_{D1} and Phe_{D2}

excitation for ES 1, but the higher Phe_{D2} contribution (CAM-B3LYP/6-31G**) gives a higher oscillator strength, supporting this assumption.

ES 3 has a high oscillator strength for three of the four methods (top left figure). As the height of the bars for ES 2 and 3 follow a similar pattern for oscillator strength (top left) and Phe_{D1} excitation (bottom right) we can say that Phe_{D1} excitation also contributes to high energy oscillator strength states. This leaves P_{D1}, which clearly dominates ES 1 for CAM-B3LYP/6-31+G** and ES 3 for ωB97X-D/6-31G**. However, the top two figures show that the higher the contribution of Phe_{D2} excitation for the CAM-B3LYP calculations, the greater the oscillator strength for that ES, which leads to the conclusion that pure P_{D1} excitation would have a low oscillator strength state regardless of the method used.

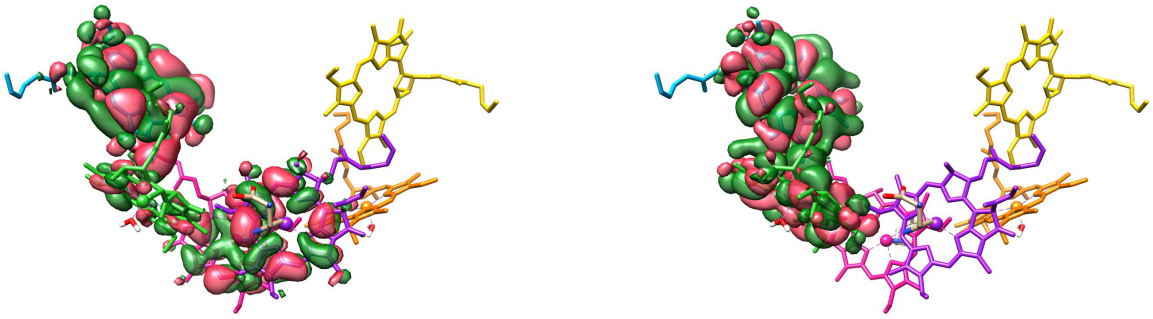
CAM-B3LYP MO Comparison

Overall the major P_{D1} to P_{D2} and P_{D2} to P_{D1} transitions for both CAM-B3LYP calculations involve very similar MOs, but for some phase change.

Transition down the inactive branch contributes highly to ES 1 and 2 for both basis sets, the constituent MOs for the highest contributing transition are similar for both bases and involve the same orbitals (see appendix four – model 1 results for the full set of MO pictures).

The MOs contributing to ES 3 and 5 for model 1 (CAM-B3LYP/6-31G**) and model 1 (CAM-B3LYP/6-31G**) are shown in Figures 1.10 and 1.11. In ES 3 the dominant transition for 6-31G** falls into the up active transition class, whereas for 6-31+G** the Phe_{D1} transition fits the down active class. MO 1140 for 6-31G** is delocalised over the P chlorophylls whereas for 6-31+G** this orbital is more localised on the Phe_{D1}, meaning that for the smaller basis set the transition from 1140 – 1147 represents the ‘up active’ transition class and the down active transition class for the larger basis. The highest contributing up active transition for 6-31+G** is comparable to the Chl_{D2} to Chl_{D1} transition for 6-31G**, both form the highest contribution to ES 5.

Up active (P D1 to Chl D1): 1140 → 1147
State 2: 11.40%
State 3: 33.94%
State 4: 4.74%
State 5: 4.87%



Chl D2 to Chl D1: 1139 → 1146
State 2: 6.08%
State 5: 23.72%
State 6: 2.54%

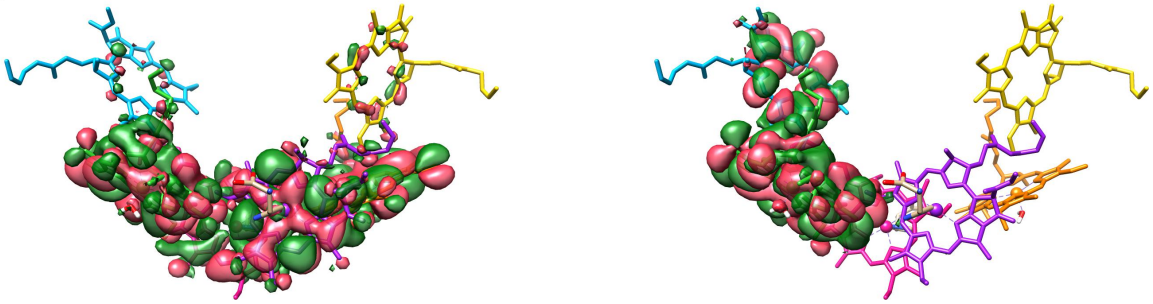
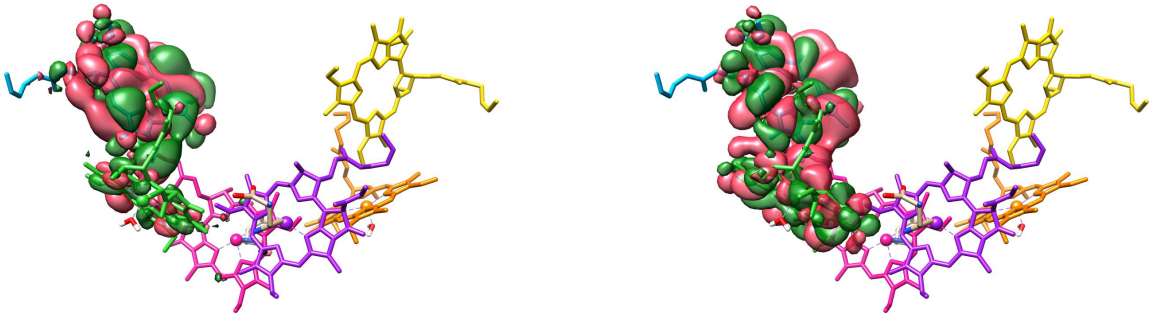


Figure 1.10 : ES 3 and ES 5 dominant transitions for Model 1 (CAM-B3LYP/6-31G**)

ES 4 and 6 have high contributions from Chl_{D1} to Chl_{D2} for CAM-B3LYP/6-31G**, this transition is very similar to the up inactive MO pair which contributes highly to the same states for 6-31+G** (these MO pictures are included in appendix four – model 1 results).

Down active (Phe D1 to Chl D1): 1140 → 1147
State 2: 14.59%
State 3: 32.02%
State 4: 7.46%
State 5: 7.35%



Up active (P D2 to Chl D1): 1137 → 1145
State 1: 2.69%
State 2: 6.20%
State 5: 24.61%
State 6: 2.85%

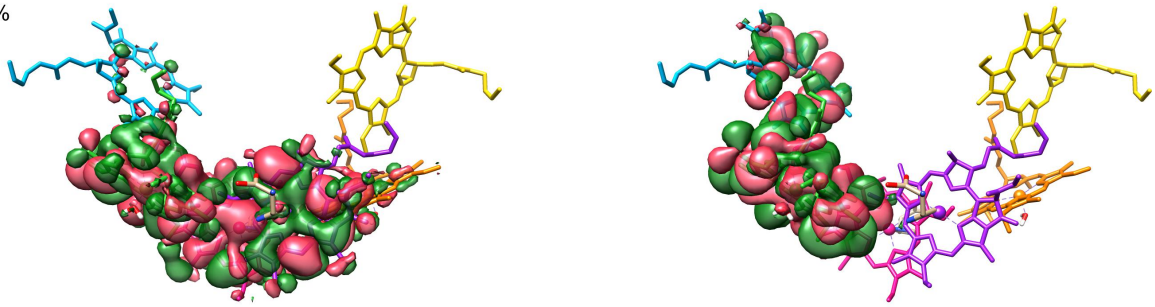
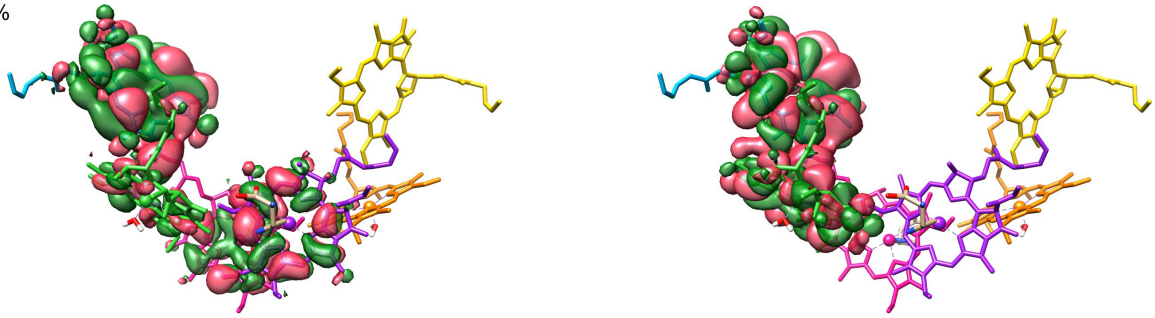


Figure 1.11 : ES 3 and ES 5 dominant transitions for Model 1 (CAM-B3LYP/6-31+G**)

Up active (P D1 to Chl D1): 1140 → 1147
State 1: 2.04%
State 2: 21.22%
State 3: 26.95%
State 4: 3.27%
State 5: 4.32%



Up active (P D2 to Chl D1): 1138 → 1145
State 2: 12.68%
State 4: 2.65%
State 5: 37.03%
State 6: 3.87%

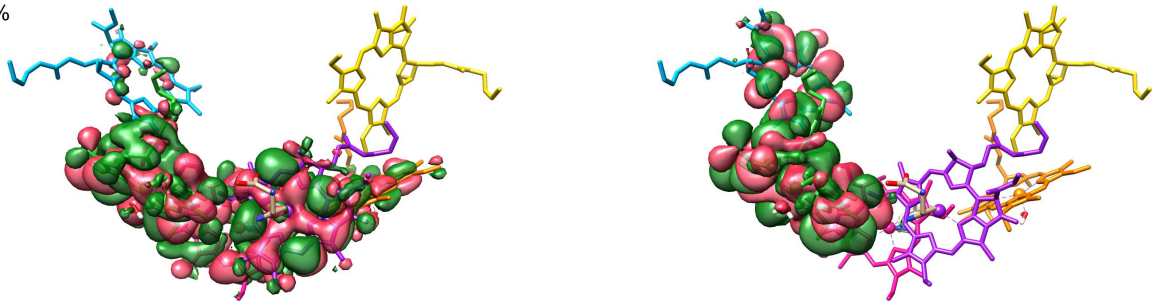


Figure 1.12 : Dominant transitions for ES 3 and ES 5 for Model 1 (ωB97X-D/6-31+G**)

The MOs contributing to ES 3 and 5 for model 1 (ωB97X-D /6-31G**) are shown in Figure 1.12. ES 2 and 3 for ωB97X-D/6-31+G** have high contributions from Phe_{D1} excitation which falls into the transition class up active, whilst for ωB97X-D/6-31G** ES 2 is mostly down active (Figure 1.6). The MOs contributing to the dominant transition in ES 3 for CAM-B3LYP/6-31G** (Figure 1.10) are the same as the ωB97X-D/6-31+G** MOs for ES 2 and 3 (Figure 1.12), whilst CAM-B3LYP/6-31+G** MOs 1140 to 1147 (Figure 1.11) describe the same transition as ωB97X-D/6-31G** ES 2 (Figure 1.6). ES 5 and has high contributions from transitions where electron density travels up the active branch (or Chl_{D2} to Chl_{D1} transition in the case of CAM-B3LYP/6-31G**). The dominant ES 5 transition looks similar for all methods and involves the same MOs for both ωB97X-D calculations. Although with CAM-B3LYP the occupied orbital is more delocalised on D2 branch cofactors for 6-31G** and less so for 6-31+G**. Up inactive for ωB97X-D/6-31+G** bears a strong resemblance to Chl_{D1} to Chl_{D2} for ωB97X-D/6-31G**, the MOs for this transition are included in appendix four – model 1 results. P chlorophyll transitions are very similar for all four models.

Model Comparison (Models 1-4, ωB97X-D/6-31G**)

This next section focuses on all four RC models. Using the analysis method described above and the chosen method of ωB97X-D/6-31G**, the effect of including phytol chains and surrounding amino acids in RC models can be examined and compared.

For all four models there are three distinct bands within the 22 ES calculated, the states are distributed over these bands as in model 1 (ES 1-6 Q_Y, ES 7-12 Q_X and the rest in the Soret region). Three high oscillator strength states are seen in the Qy band for each of models 1-4, for calculations with ωB97X-D these are invariably ES 1, ES 2 and ES 5. For this functional the three bright states correspond to Phe excitations (ES 1-2) and Chl_{D1} excitation (ES 5) (see figures 1.13 and 1.14). The brightest state in the Q_y band is consistently ES 2 for all but model 2 (ES 5 is the brightest state with f = 0.5015), suggesting that including the phytol chains raises the oscillator strength of ES 5. For model 3, the oscillator strength of the Phe_{D1} excitation (ES 2) is raised when more amino acids are added to the model (in comparison to model 1 which has 2 amino acids), increasing the gap in oscillator strength between Phe_{D2} and Phe_{D1} excitation. As could be expected, ES 2 and 5 have similar oscillator strengths for model 4, this can be explained by the combination of effects of the phytol chains (see model 2 results) and the amino acids (see model 3).

Table 1.9 : Energies (left, colour gradient for each model within each band showing degeneracies and intervals in excitation energies) and Oscillator strengths (right, green shading for brighter states and purple shading for darker states across the whole spectrum) for ES 1-22 of Models 1-4 (ωB97X-D/6-31G**)

State	Band* ↓	Energy (nm)				Oscillator Strength			
	AAs: Phytol:	Model 1 2 Trunc'	Model 2 2 **Full**	Model 3 23 Trunc'	Model 4 23 **Full**	Model 1 2 Trunc'	Model 2 2 **Full**	Model 3 23 Trunc'	Model 4 23 **Full**
1	Qy (679, 671)	673.74	677.29	684.92	692.46	0.3895	0.3075	0.4114	0.3746
2		668.9	670.53	681.07	687.23	0.401	0.4045	0.5523	0.4202
3		667.17	669.01	673.9	675.93	0.1259	0.0977	0.0733	0.0915
4		655.77	657.06	667.67	665.76	0.0792	0.0603	0.1158	0.1809
5		651.55	654.72	657.23	660.4	0.3688	0.5015	0.3809	0.4078
6		645.97	646.4	654.59	655.24	0.1525	0.1468	0.0847	0.1396
7	Q_X (542)	570.99	572.88	583.28	584.79	0.0603	0.0688	0.0656	0.0663
8		566.15	569.13	575.54	579.51	0.0663	0.0585	0.0796	0.0825
9		563.35	564.27	570.86	576.34	0.05	0.0561	0.0545	0.0668
10		559.28	562.26	567.57	571.17	0.0229	0.0306	0.0371	0.0383
11		556.25	559.69	564.05	565.19	0.1384	0.0891	0.1306	0.1015
12		555.23	556.92	559.71	560.76	0.0623	0.1074	0.067	0.0715
13	Soret (~432 ~416)	442.34	440.74	442.88	443.03	0.1095	0.1045	0.0728	0.0757
14		429.72	432.94	435.25	432.99	0.0071	0.0001	0.0175	0.0329
15		422.06	431.37	425.34	426.15	0.0047	0.0105	0.1684	0.1421
16		417.87	418.72	411.55	410.44	0.0828	0.1027	0.0008	0.0008
17		406.76	411.42	406.44	404.14	0.001	0.0003	0.2816	0.4472
18		402.78	399.83	404.36	401.23	0.0062	0.3993	0.0126	0.0377
19		401.13	399.23	404.01	400.68	0.3973	0.0906	0.1872	0.0787
20		397.18	399.04	400.24	399.46	0.1957	0.0119	0.0022	0.1436
21		396.64	396.51	398.18	398.55	0.064	0.1682	0.2467	0.3109
22		393.73	394.07	397.6	396	0.2271	0.3778	0.0651	0.0051

* Experimental 10 K absorption spectrum for D1-D2-Cyt b-559 complex band peaks from[25] are given in brackets

Table 1.9 lists the energies and oscillator strengths calculated for ES 1-22 for models 1-4 (ωB97X-D/6-31G**). The highest oscillator strength state in the Q_X region is ES 11 (f=0.1015) for models 1, 3 and 4 and ES 12 for

model 2. As in model 1, ES 11 is attributed to Chl_{D1} excitation for models 3 and 4 and ES 12 for model 2 is also attributed to Chl_{D1} excitation (see Figure 1.21 for model 4 and appendix four- sections on results for models 2 and 3).

Models 2 and 4 have two states in the Soret region (ES 17 and 21 for model 4 and ES 18 and 22 for model 2) with higher oscillator strengths (>0.3). For model 2 and model 4 the bright states correspond to two mixed states (see figures 1.22 for model 4 and in appendix four - model 2 results). Of the highest oscillator strength states in the Soret region for model 3 ES 17 (f = 0.2816) is P_{D1} to P_{D2} CT, and ES 19 (f = 0.1872) and ES 21 (f = 0.2467) are both mixed with high contribution from Chl_{D2} and Phe_{D2} for ES 21 (see appendix four). As such there is no bright state attributed to Chl_{D2} excitation in the Soret region for models 2-4 as there is for model 1 (ES 19).

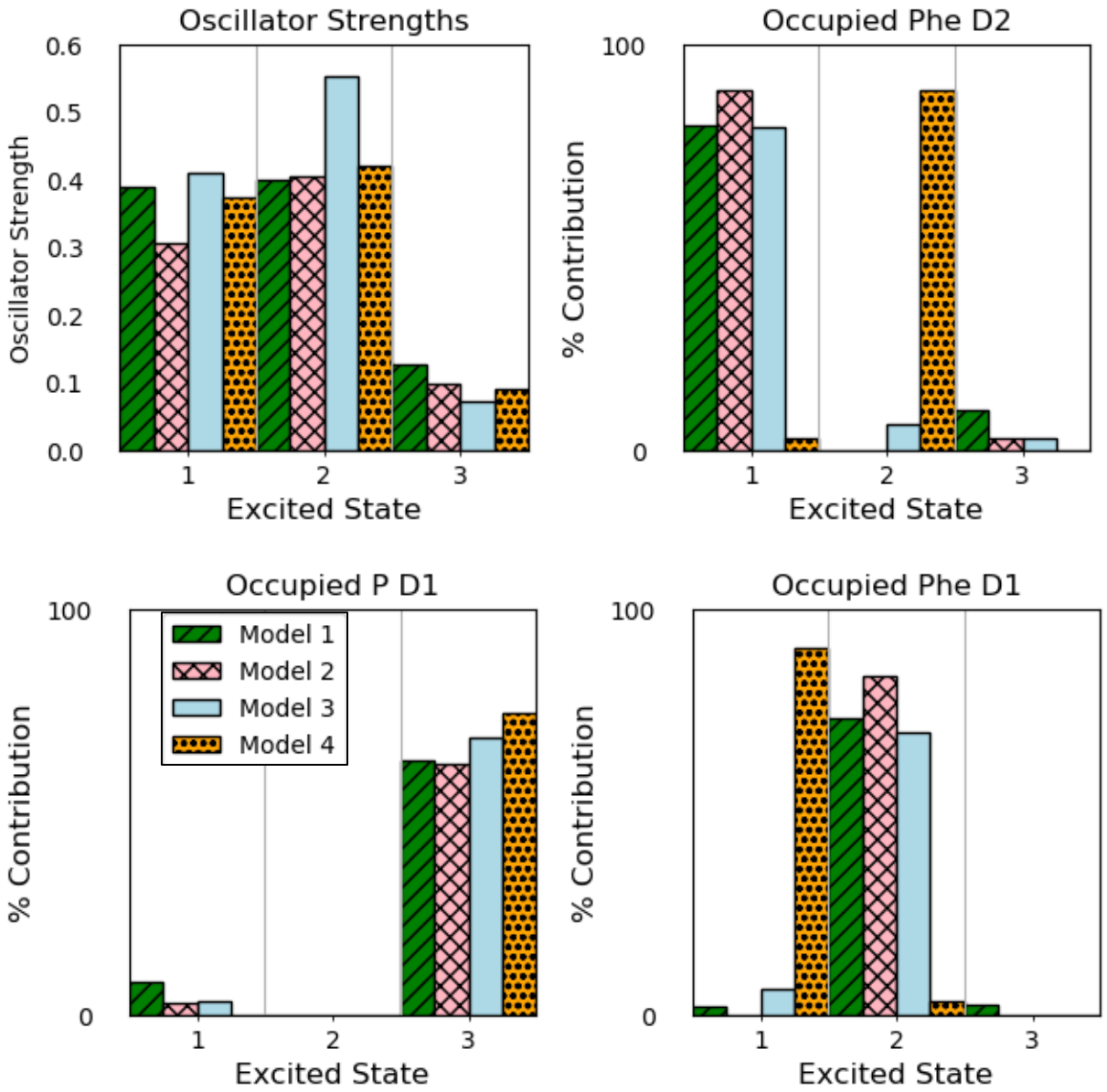


Figure 1.13 : Showing the profile of the first three ES for models 1-4 (ωB97X-D/6-31G**). TOP LEFT – Oscillator strengths, TOP RIGHT Phe_{D2} occupied orbital contribution, BOTTOM LEFT P_{D1} contribution and BOTTOM RIGHT Phe_{D1} contribution.

A striking difference between models 1-3 and model 4 is the reordering of the ES attributed to Phe excitations (see Figure 1.13). Model 4 is the only model for which Phe_{D1} excitation is the lowest energy ES. Thus, the combined effect of the phytol chains and the amino acids is lowering Phe_{D1} cofactor site energy to drive CT up the active branch. It is important to note that this is in agreement with previous assignment of Chl_{D1} as having the lowest energy excited state,[77] as ES 1 for model 4 involves occupied MOs with delocalisation over Chl_{D1} and Phe_{D1}. P_{D1} excitation dominates in ES 3 for all models.

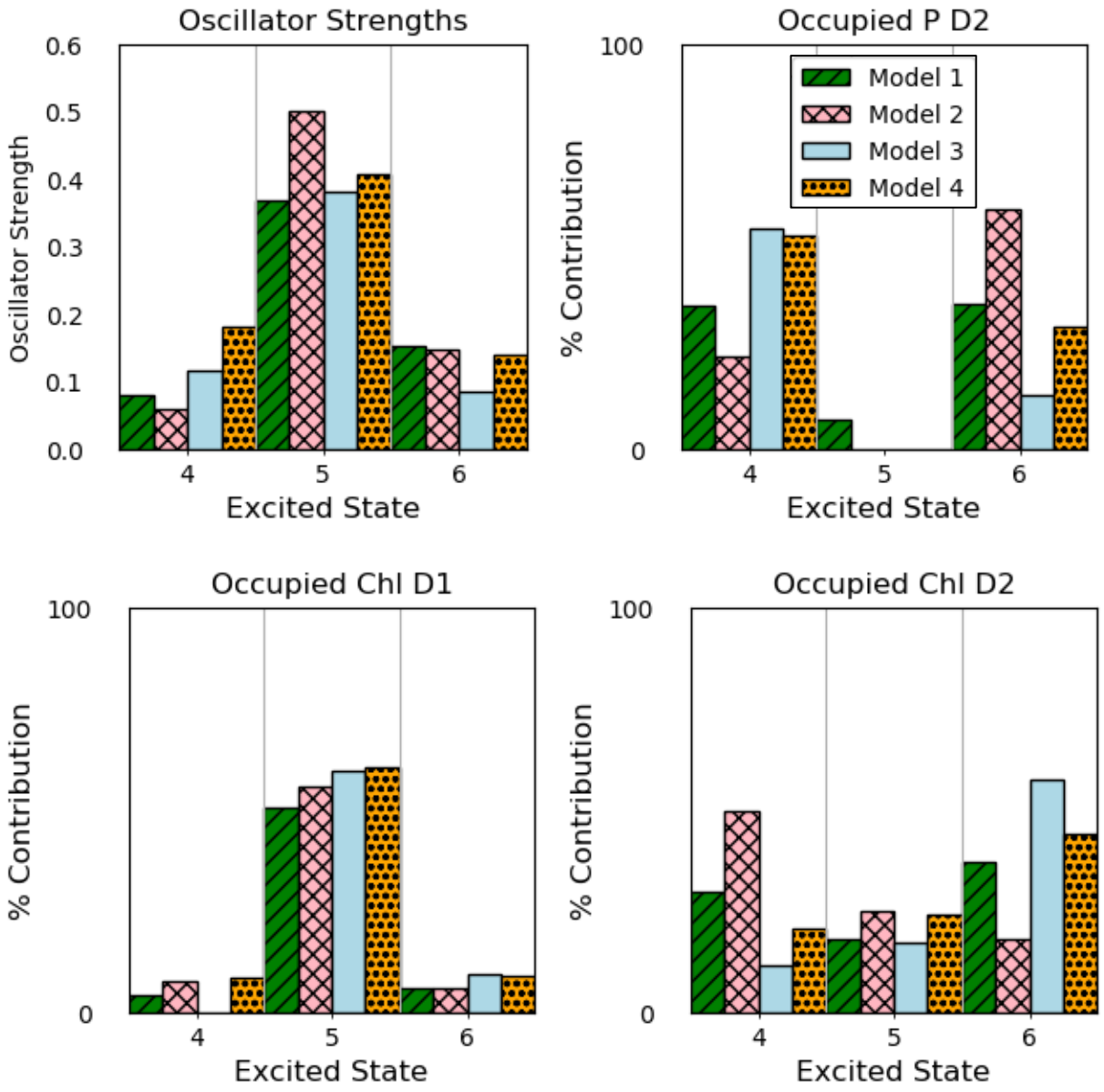


Figure 1.14 : Showing the profile of ES 3-6 for models 1-4 (ωB97X-D/6-31G**). TOP LEFT – Oscillator strengths, TOP RIGHT P_{D2} occupied orbital contribution, BOTTOM LEFT Chl_{D1} contribution and BOTTOM RIGHT Chl_{D2} contribution.

From Figure 1.14, ES 5 is always dominated by Chl_{D1} excitation. ES 4-6 are all contributed to by Chl_{D2} excitation, for model 2 Chl_{D2} contributes most highly to ES 4 and the least to ES 6, meaning this transition is low in E for this model. Relative to models 3 and 4 for which Chl_{D2} excitation contribution contributes more to ES 6 than ES 4. In summary, it has been shown that adding the amino acids increases the energy of the Chl_{D2} excitation and that adding the phytol chains decreases it. P_{D2} excitation experiences the opposite effect of Chl_{D2} excitation, increasing in lower energy states for models 3 and 4 (on addition of the amino acids) and increasing in higher energy states for model 2 (on addition of the phytol chains).

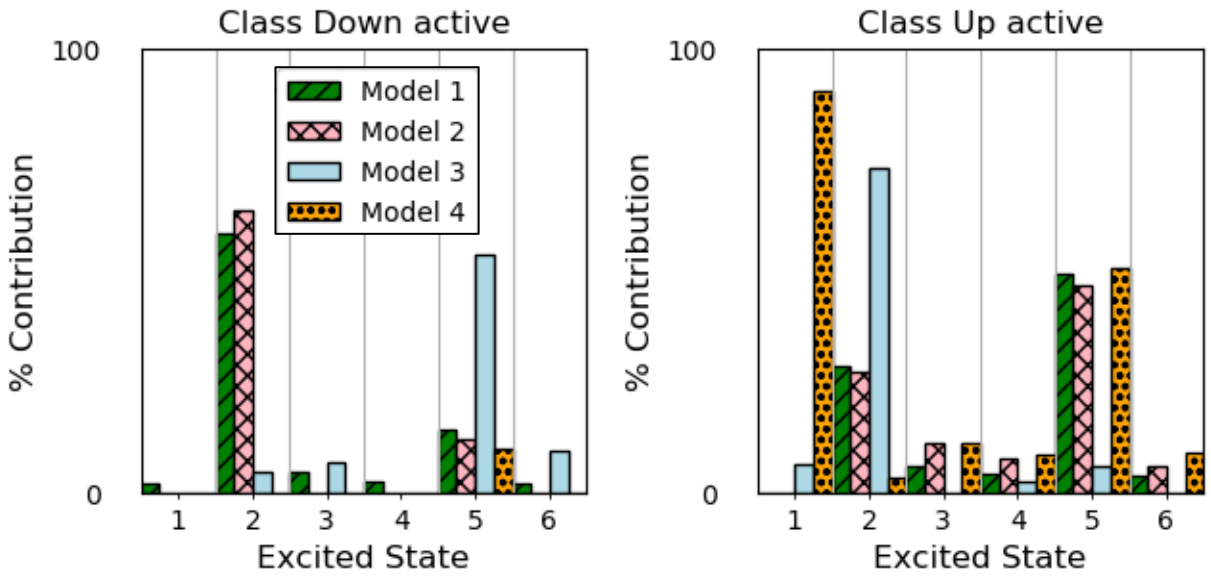


Figure 1.15 : Showing the contributions from active branch transitions for models 1-4 (ωB97X-D/6-31G**) ES 1-6. LEFT – Down active branch transitions, RIGHT - Up active branch transitions.

Figure 1.15 shows contribution from active branch transitions for models 1-4. Whilst transition down the active branch appears to dominate in one ES for each of models 1-3, model 4 has no states dominated by this transition class in the Q_Y band, Figure 1.15. Instead, model 4 has two ES (1 and 5) which are dominated by transition up the active branch, leading to successful photosynthesis. The effect of adding the amino acids in model 3 seems to reverse the direction of the transition in the active branch states 2 and 5. But only the combined effect of the phytol chains and the amino acids (model 4) produces a preference for active branch transitions to head in the direction of successful photosynthesis. Also of note, the configuration of the MOs which contribute to two high oscillator strength states (ES 1 and ES 5) for model 4 are consistent with the exciton-charge-transfer excited state ($Chl_{D1}{}^{\delta+}$ $Phe_{D1}{}^{\delta-}$)* which has been identified as one of two precursor states to charge separation.[33]

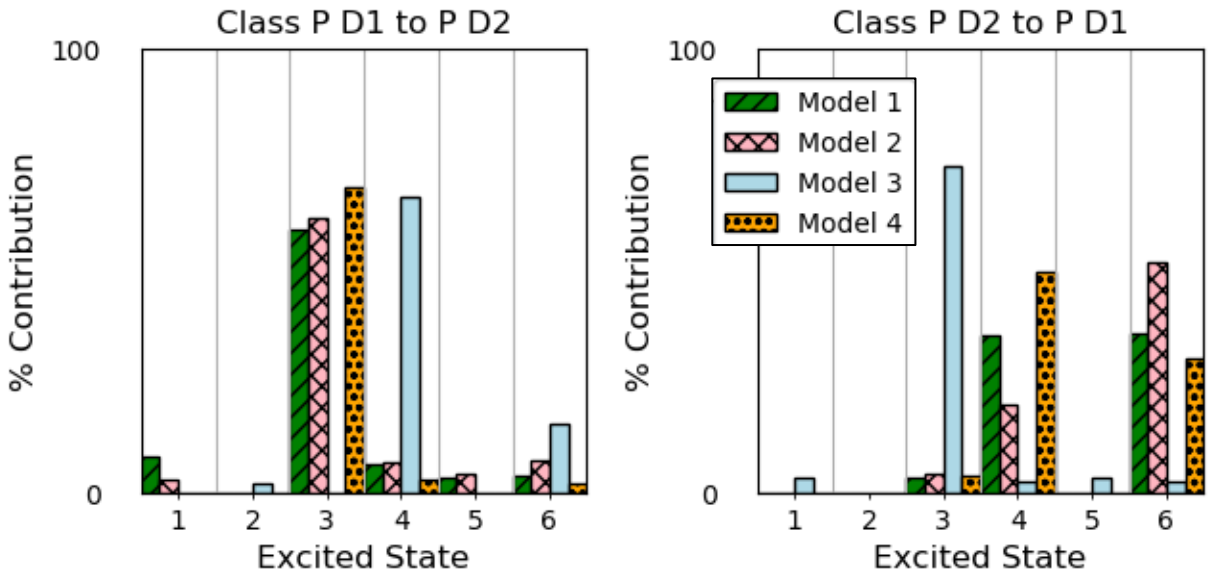


Figure 1.16 : Showing the contributions from P chlorophyll transitions for models 1-4 (ωB97X-D/6-31G**) ES 1-6. LEFT – P_{D1} to P_{D2}, RIGHT – P_{D2} to P_{D1}.

As with the active branch transitions (Figure 1.15), in Figure 1.16 it can be seen that model 3 has a tendency to reverse the direction of transitions between the P chlorophylls. With ES 4 described by a P_{D1} to P_{D2} transition although it is centred on a P_{D2} localised orbital. Interestingly, the nature of these transitions correspond with the second possible precursor state to CS which is identified as originating in the P chlorophyll pair.[26,36]

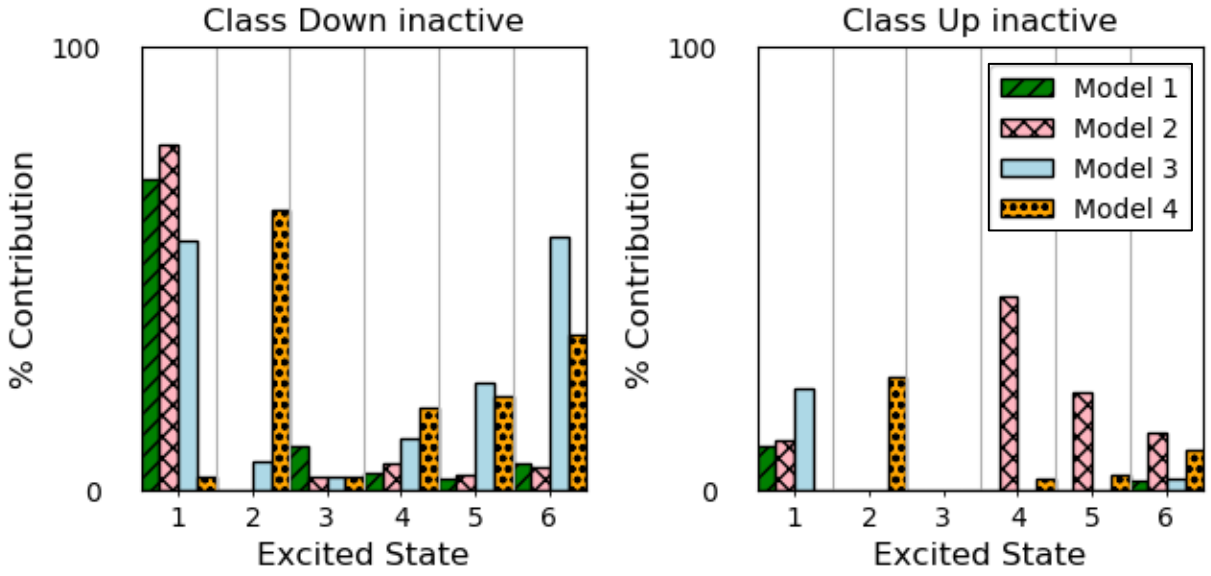


Figure 1.17 : Showing the contributions from inactive branch transitions for models 1-4 (ωB97X-D/6-31G**) ES 1-6. LEFT – Down inactive branch transitions, RIGHT - Up inactive branch transitions.

Inactive branch transition contributions for all models are shown in Figure 1.17. Transitions up the inactive branch are already unfavourable for smaller models with transition down the active branch contributing more to Phe_{D2} excitation dominant state (ES 1 for models 1-3 and ES 2 for model 4). Chl_{D2} excitation is described by a transition up the inactive branch (model 2) and down the inactive branch for larger models which include the amino acids (models 3 and 4).

MOs for models 1 and 2 are very similar (see the MO pictures for models 2 and 3 in appendix four), the up inactive transition which dominates ES 4 for model 2 is reminiscent of the Chl_{D1} to Chl_{D2} transition which contributes to ES 4, 5 and 6 for model 1 (see Figure 1.6d). Similarly, models 3 and 4 have comparable MOs. The P_{D2} to P_{D1} transition which dominates in ES 4 for model 3 involves MOs which are delocalised over Chl_{D1} whereas the analogous transition for model 4 involves MOs which are delocalised over P_{D1} and P_{D2}. The transition up the active branch, and involves an occupied and a virtual MO centred on Chl_{D1}, which dominates in ES 5 for model 4 has no analogue for model 3.

A number of CT states are found in the Soret region for each model as shown in Figure 1.18. Each model has at least one P_{D1} to P_{D2} CT state, a P_{D2} to P_{D1} CT state and an up inactive CT state. Models 1, 2 and 4 all have up active CT states. Models 2 and 4 have bright states (model 4 ES 17 (f = 0.4472) and 21 (f = 0.3109) and model 2 ES 18 and 22 (f = 0.3993 and 0.3778)) attributed to P chlorophyll CT. For model 1 the brightest CT state is ES 22 (f=0.2271) and all CT states for model 3 have f<0.1. Model 2 has two states attributed to CT up the active branch compared with one for model 1, it could be that this is due to a lowering in energy of CT states that lie above ES 22 for model 1. This result confirms that including the phytol chains in the model leads to a stronger preference for CT to travel up the active branch. Similarly, model 4 has one state attributed to CT up the active branch whereas model 3 has none.

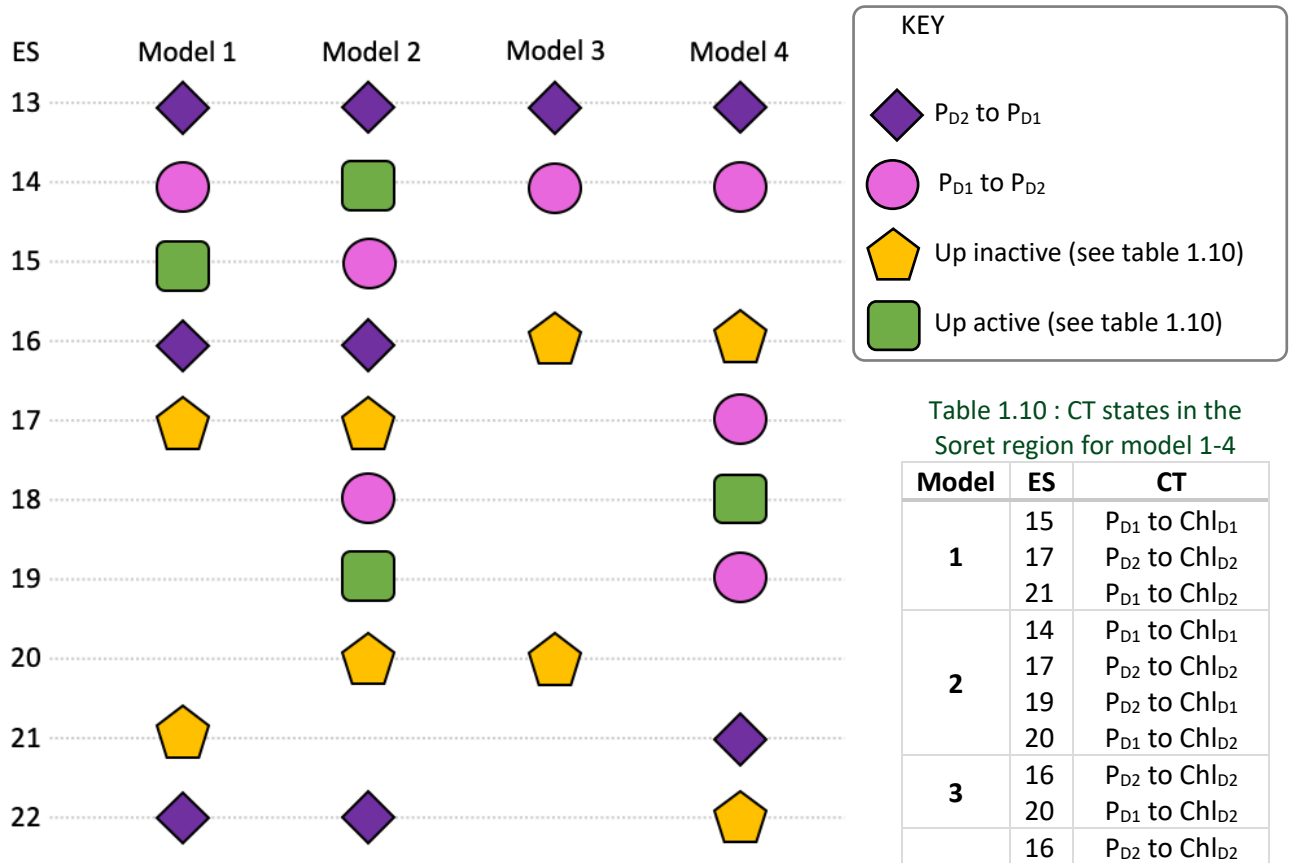


Figure 1.18 : CT states in the Soret region for Models 1-4 by D_{CT} analysis

Table 1.10 : CT states in the Soret region for model 1-4

Model	ES	CT
1	15	P_{D1} to Chl_{D1}
	17	P_{D2} to Chl_{D2}
	21	P_{D1} to Chl_{D2}
2	14	P_{D1} to Chl_{D1}
	17	P_{D2} to Chl_{D2}
	19	P_{D2} to Chl_{D1}
	20	P_{D1} to Chl_{D2}
3	16	P_{D2} to Chl_{D2}
	20	P_{D1} to Chl_{D2}
4	16	P_{D2} to Chl_{D2}
	18	P_{D1} to Chl_{D1}
	22	P_{D1} to Chl_{D2}

In Figure 1.18, a summary of CT states predicted by analysis of the D_{CT} metric is shown. Overall it can be seen that model 4 (with the full phytol chains, and 23 amino acids explicitly included) displays the strongest preference for transitions to direct charge up the active branch. Transitions up the inactive branch are also unfavourable for model 4, and transitions down the active branch contribute even less. There must be significant structural reasons for the D1 branch cofactors to form the favoured charge transfer pathway, it seems that these early results have uncovered two important factors; the phytol chains of the pigments and the nearest amino acid residues are both contributing to directing charge up the active D1 branch.

Method Comparison (Models 1-4, ωB97X-D/6-31G** and CAM-b3LYP/6-31G**)

Calculations on models 1-4 were all repeated with the CAM-b3LYP functional for up to 16 excited states (model 4). Full results for CAM-b3LYP for models 2-4 are presented in appendix four. The majority of features of the excitation profile are the same for calculations with both functionals on each model, however some key differences are discussed below. Overall, model 4 overwhelmingly shows the best agreement between the two functionals used out of the four models tested.

The ordering of cofactor excitations was changed when calculating excited states with CAM-B3LYP vs. ωB97X-D for models 1 (see discussion above) and model 2 (see Figure 1.19) with P_{D1} excitation dominating in the first ES for model 1 (CAM-B3LYP) and the second for model 2 (CAM-B3LYP). Both of these results suggest that CAM-B3LYP predicts a lower site energy for P_{D1} than ωB97X-D (for which P_{D1} excitation dominates in ES 3 for models 1-4, see Figure 1.13).

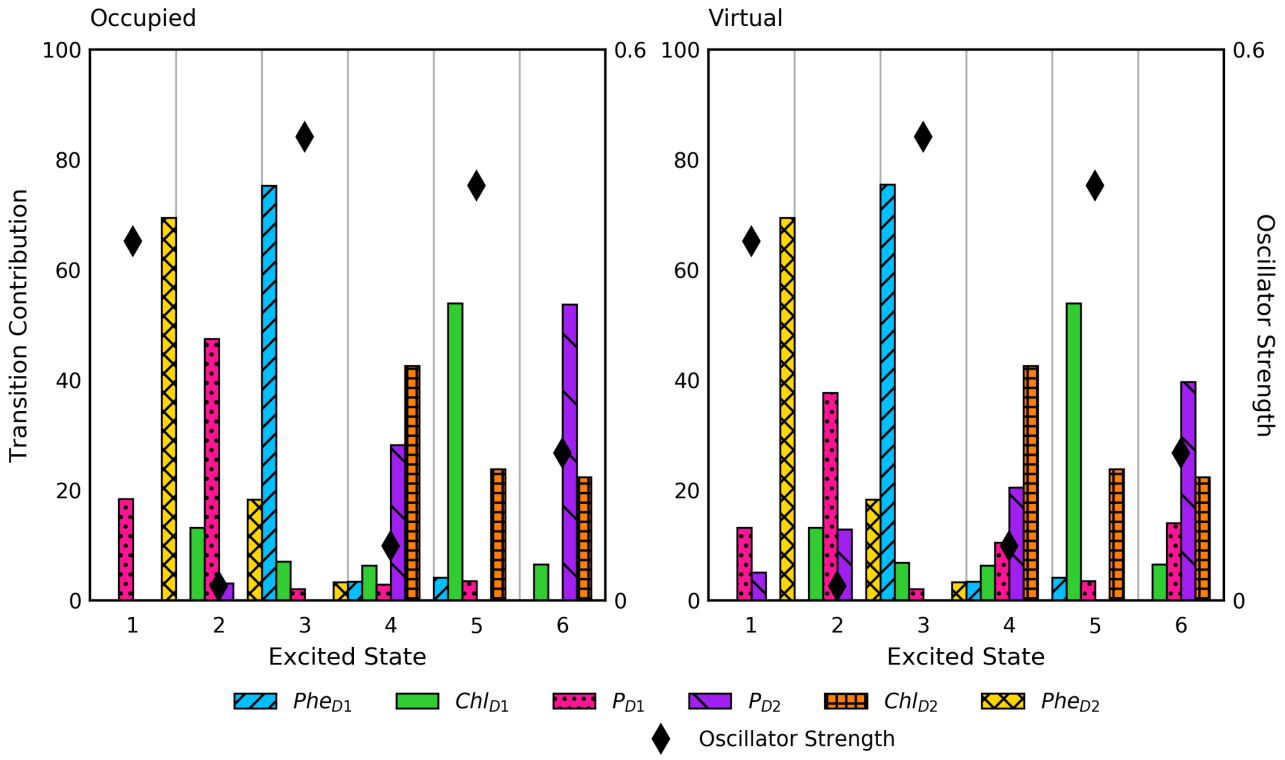


Figure 1.19 : Model 2 CAM-B3LYP/6-31G** excited states 1-6, (bar chart, left y axis) % of state contributed to by each cofactor (occupied orbital occupancy analysis with MultiWfn from Mulliken method) and (black diamonds, right y axis) oscillator strength of each state. Cofactors coloured as in all figures in this thesis. TOP – occupied orbitals, BOTTOM – virtual orbitals.

For model 3 (Figure 1.20), although the cofactor excitations appear in the same order for both functionals, the active branch transitions in the Q_X region go in opposite directions for the CAM-B3LYP and ωB97X-D calculations. The Phe_{D1} excitation in ES 2 is classed as a down active transition for CAM-B3LYP (see Figure 1.20) and an up active transition for ωB97X-D (see Figure 1.15). Meanwhile, ES 5 is assigned to an up active Chl_{D1} transition for CAM-B3LYP (Figure 1.20) and a down active transition for ωB97X-D (Figure 1.15).

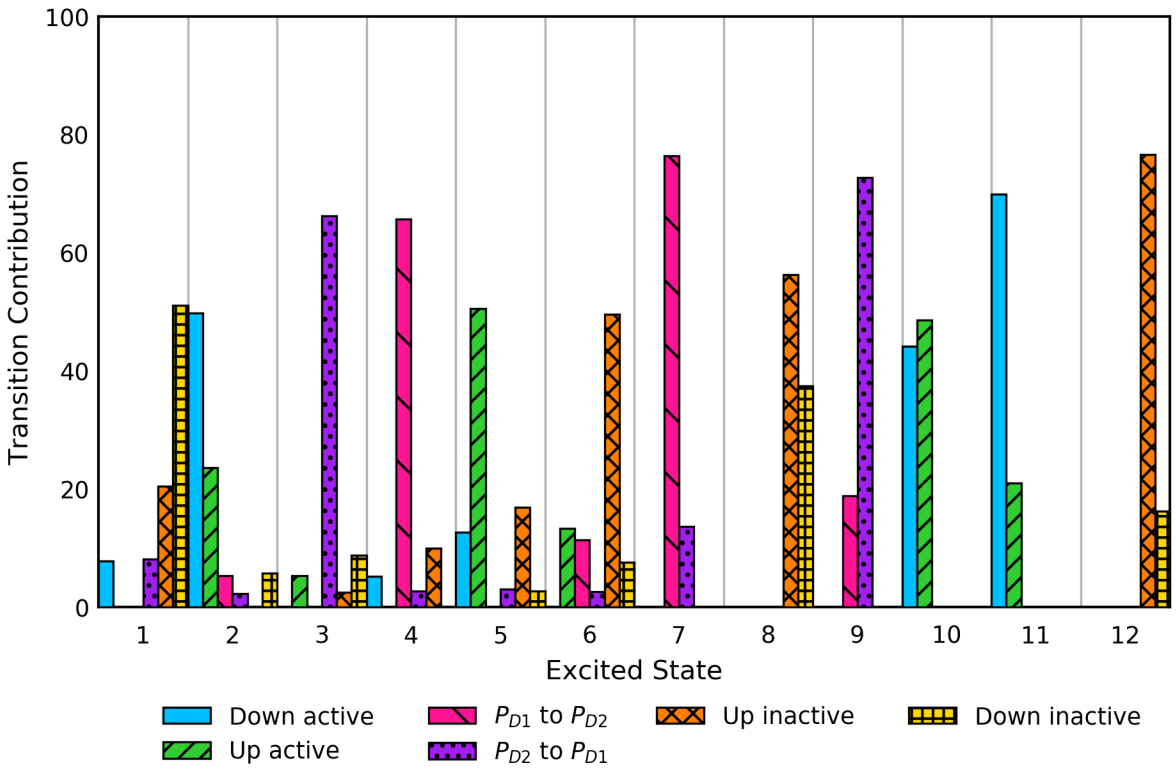


Figure 1.20 : Contributions from each transition class to ES 1-6 for model 3 (CAM-B3LYP/ 6-31G**).

Table 1.11 lists the excitation energies and oscillator strengths for model 4 (CAM-B3LYP/6-31G**).

Table 1.11 : Excitation energies and oscillator strengths for model 4 CAM-B3LYP/6-31G**

State	Absorption Band	Energy (nm)	Oscillator Strength
1	Q_Y	675.05	0.4194
2		669.89	0.4629
3		663.44	0.0683
4		653.84	0.1888
5		647.57	0.3882
6		643.13	0.1601
7	Q_X	585.21	0.0621
8		576.59	0.0787
9		573.08	0.0694
10		572.29	0.0276
11		563.96	0.1009
12		559.03	0.0706
13	Soret	481.02	0.0003
14		479.56	0.0099
15		473.7	0.0214
16		469.1	0.0001

For model 4, CAM-B3LYP gives a lower oscillator strength for ES 5 than for ES 1, table 1.11, whereas the relative oscillator strengths of these states were the other way around for ωB97X-D (ES 1 f=0.3746 and ES 2 f=0.4078). ES 11 has the highest oscillator strength in the Q_X region for model 4 with both ωB97X-D and CAM-B3LYP. All four states in the Soret region that were calculated for this model with CAM-B3LYP are low oscillator strength states. The excitations contributing to ES 1-12 for model 4 are very similar for each functional. In the Soret band ES 13 is P_{D2} to Chl_{D2} CT and ES 16 is P_{D1} to Chl_{D2} CT for model 4 with CAM-B3LYP. Comparing to ωB97X-D, the CAM-B3LYP ES 13 has the same identity as ES 16 for ωB97X-D and ES 16 for CAM-B3LYP has the same identity as the ωB97X-D ES 22. All have near zero oscillator strength. The contribution from the transition classes for model 4 ES 1-12 are very similar for both functionals.

Having confirmed that model 4, including both 23 amino acids and full phytol chains, is the best model produced so far, it will be used as a benchmark for further results from mutant and other WT models. The

choice of functional going forwards was arbitrary as model 4 results were similar with both ωB97X-D and CAM-B3LYP. Basis set 6-31G** was chosen based on the time constraints of the PhD and similarity in the results for 6-31G** and 6-31+G** for model 1. Full results for model 4 (ωB97X-D/6-31G**) are produced below for comparison in later chapters.

Model 4 - ωB97X-D/6-31G**: Benchmark Results

The results for model 4 (ωB97X-D/6-31G**) are presented below for reference in later chapters. The majority of discussion of these is included above.

Figures 1.21 and 1.22 present the full results for ES 1-22 for model 4 (ωB97X-D/6-31G**). In the Q_X region ES 8 is attributed to pure Phe_{D1} excitation, in previous models Phe_{D1} excitation appeared in higher energy states ES 10 (models 1-3) and was mixed with Chl_{D1} excitation in ES 11 (models 1 and 3) or 12 (model 2). Clearly a reduction in the site energy of Phe_{D1} is an effect of the combined inclusion of phytol chains and amino acids in this model. ES 11 is therefore attributed to pure Chl_{D1} excitation for model 4, similar to models 1 and 3. ES 20 is dominated by Phe_{D1} excitation, which has not been seen for any other model so far, reinforcing the hypothesis that Phe_{D1} excitation has decreased in energy for this model.

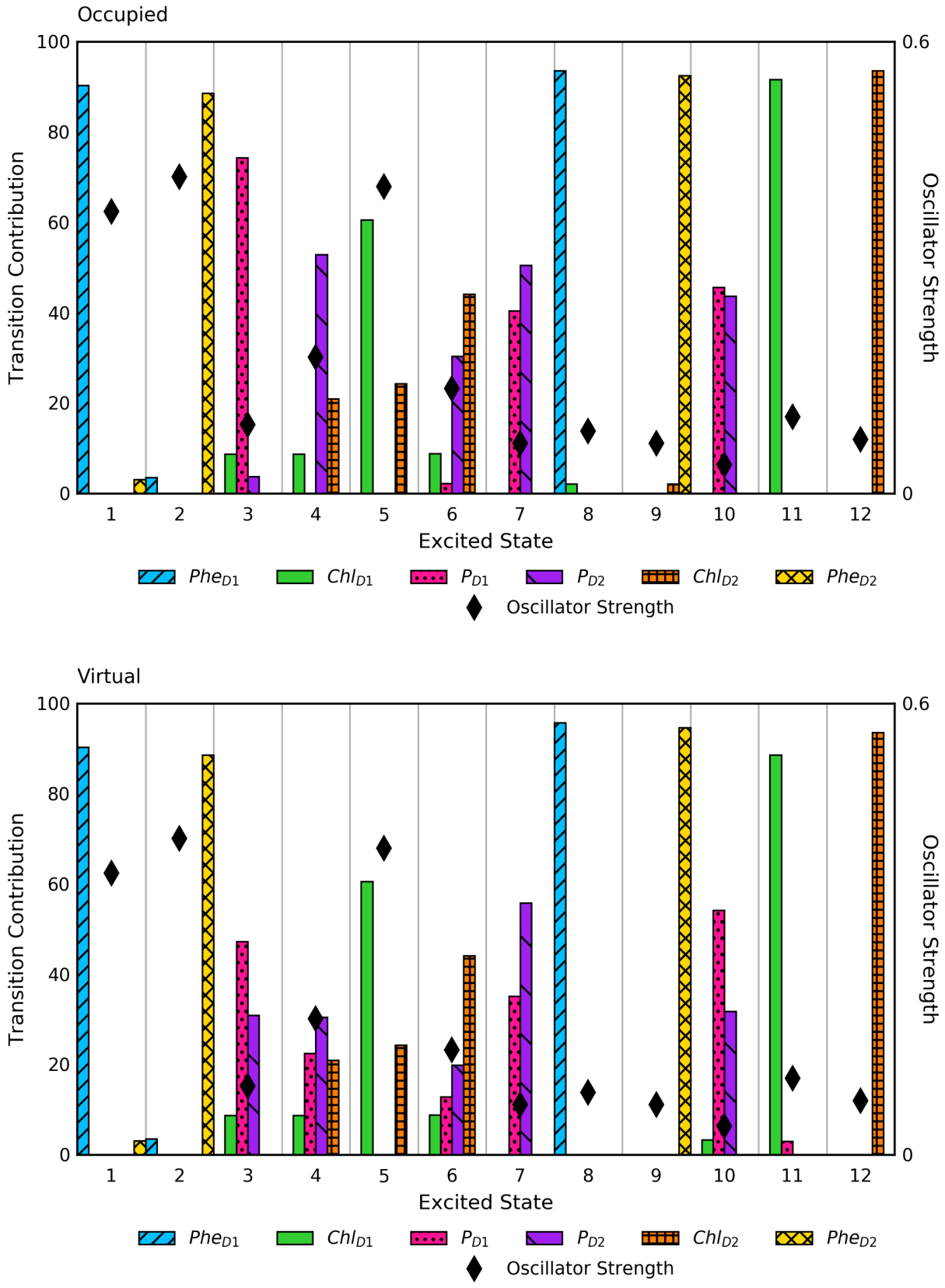


Figure 1.21 : Model 4 ωB97X-D/6-31G** excited states 1-12, (bar chart, left y axis) % of state contributed to by each cofactor (occupied orbital occupancy analysis with MultiWfn from Mulliken method) and (black diamonds, right y axis) oscillator strength of each state. Cofactors coloured as in all figures in this thesis. TOP – occupied orbitals, BOTTOM – virtual orbitals.

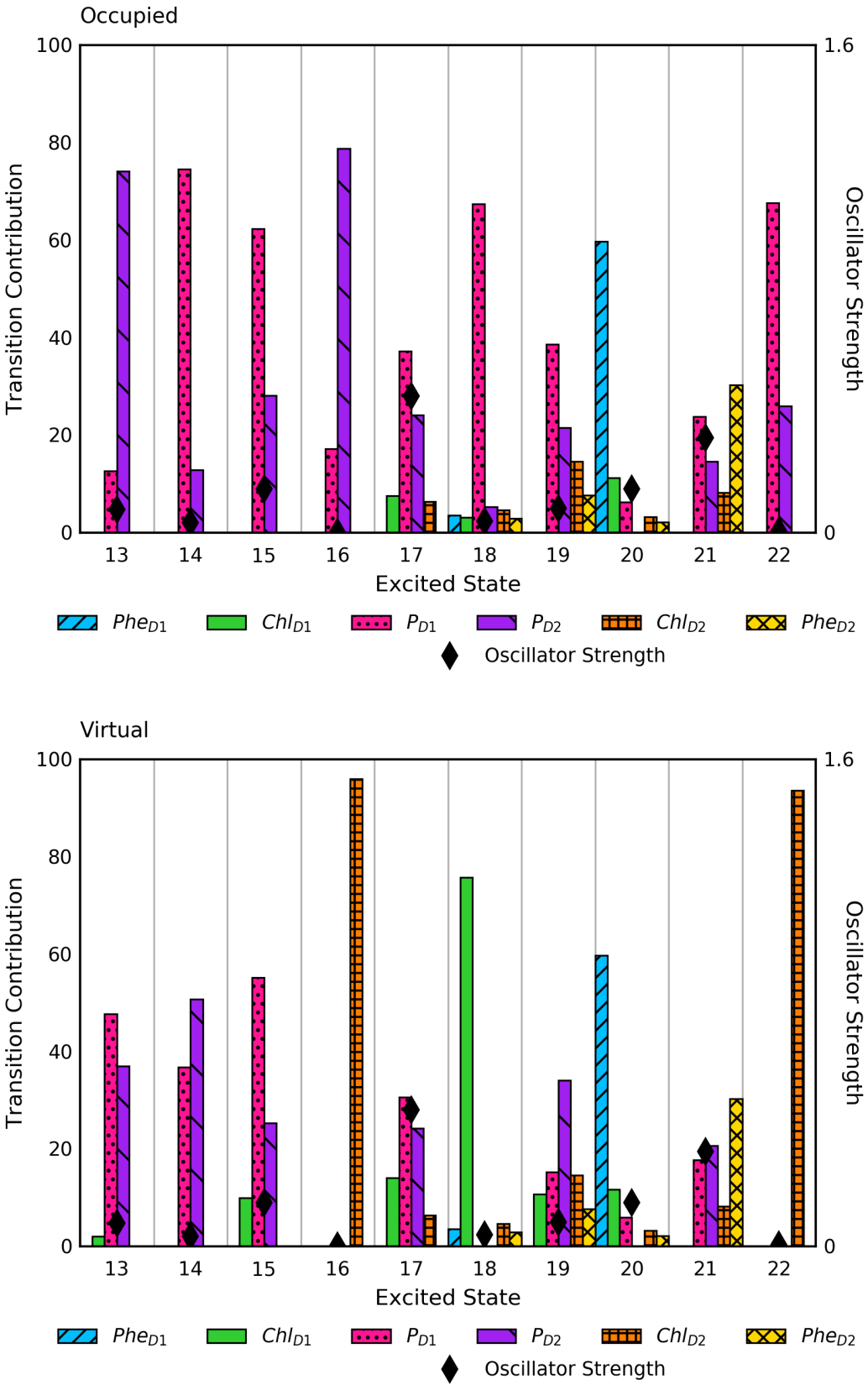
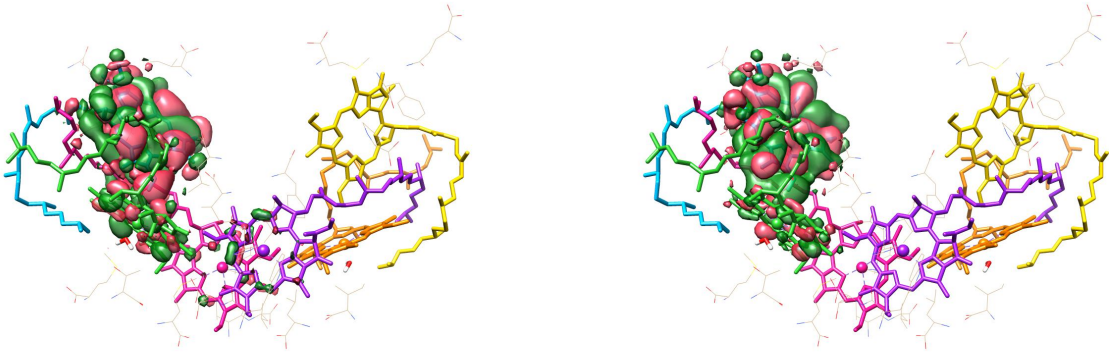
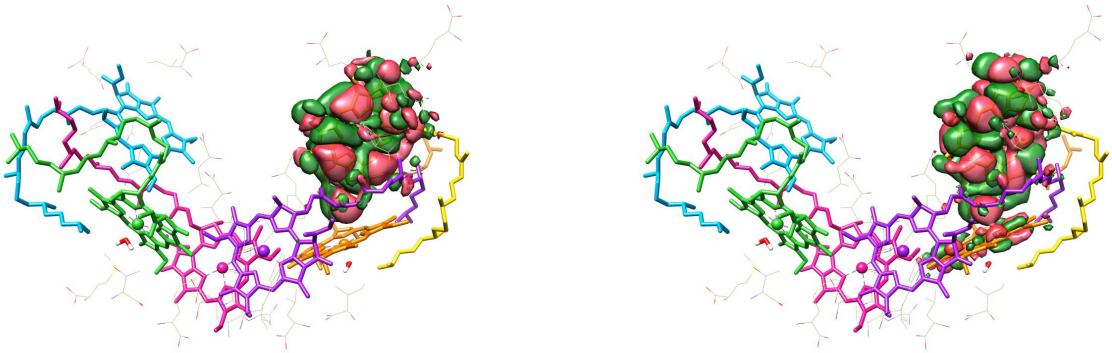


Figure 1.22 : Model 4 ωB97X-D/6-31G** excited states 13-22, (bar chart, left y axis) % of state contributed to by each cofactor (occupied orbital occupancy analysis with MultiWfn from Mulliken method) and (black diamonds, right y axis) oscillator strength of each state. Cofactors coloured as in all figures in this thesis. TOP – occupied orbitals, BOTTOM – virtual orbitals.

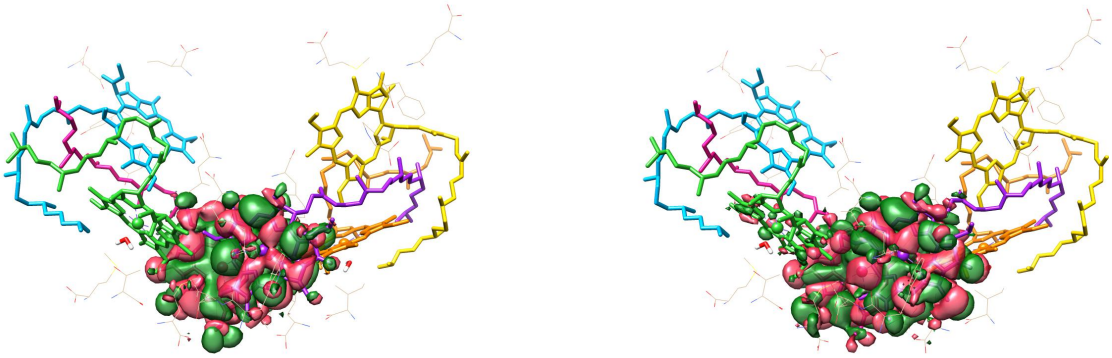
Up active (Chl D1 to Phe D1): 2308 → 2313
State 1: 64.87%
State 2: 3.55%



Down inactive (Phe D2 to Chl D2): 2310 → 2316
State 1: 3.07%
State 2: 57.63%



P D1 to P D2: 2312 → 2317
State 3: 38.03%



P D2 to P D1: 2311 → 2318
State 4: 22.62%
State 6: 14.92%

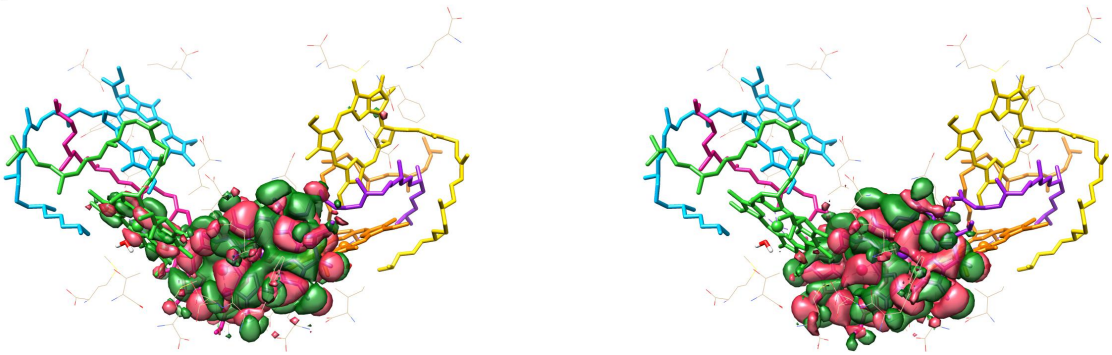
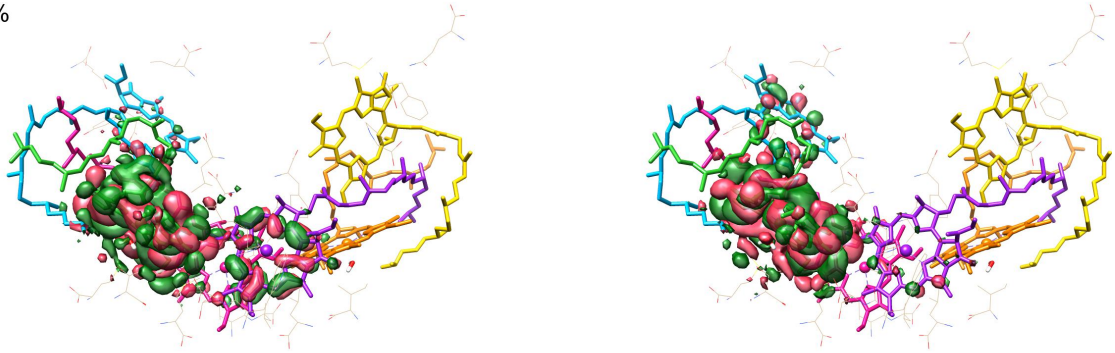
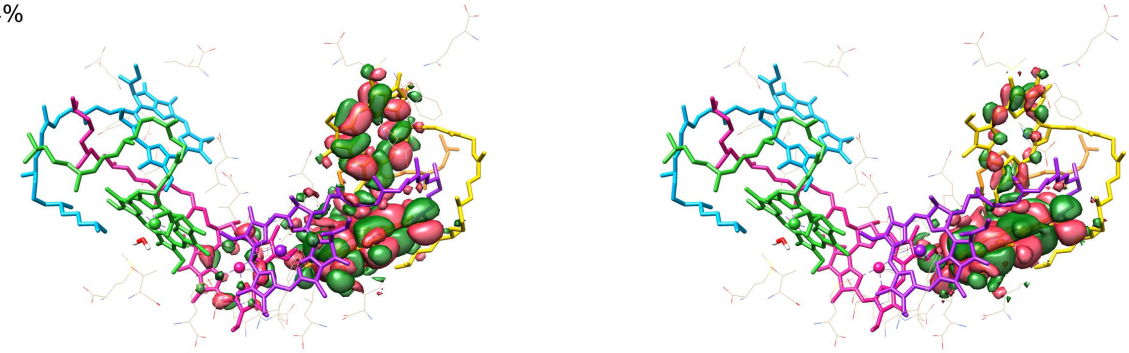


Figure 1.23 : MO diagrams exemplifying all transition classes for model 4 ωB97X-D/6-31G** including dominant transitions contributing to ES 1-6, LEFT COLUMN - Occupied MO, RIGHT COLUMN – Virtual MO (PAGE 1).

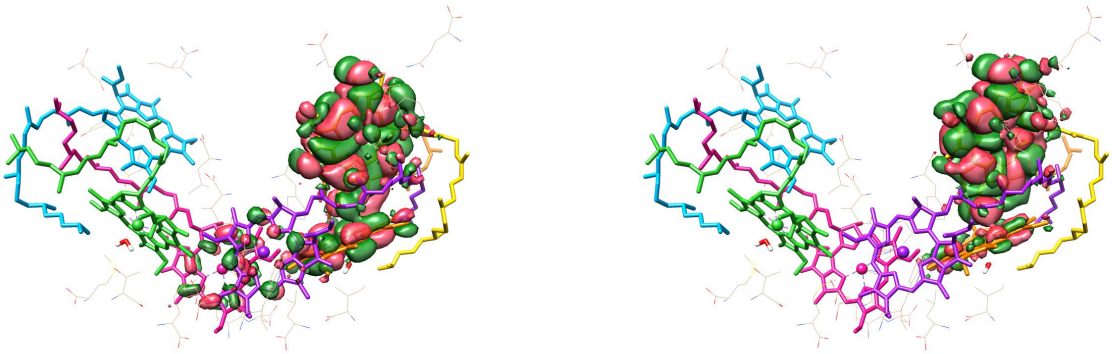
Up active (P D2 to Phe D1): 2309 → 2315
State 3: 8.71%
State 4: 8.74%
State 5: 50.65%
State 6: 8.87%



Down inactive (Phe D2 to Chl D2): 2306 → 2314
State 4: 18.44%
State 5: 20.98%
State 6: 35.04%



Up inactive (Chl D2 to Phe D2): 2304 → 2316
State 2: 15.83%



Down active (Chl D1 to P D1): 2303 → 2321
State 5: 6.25%

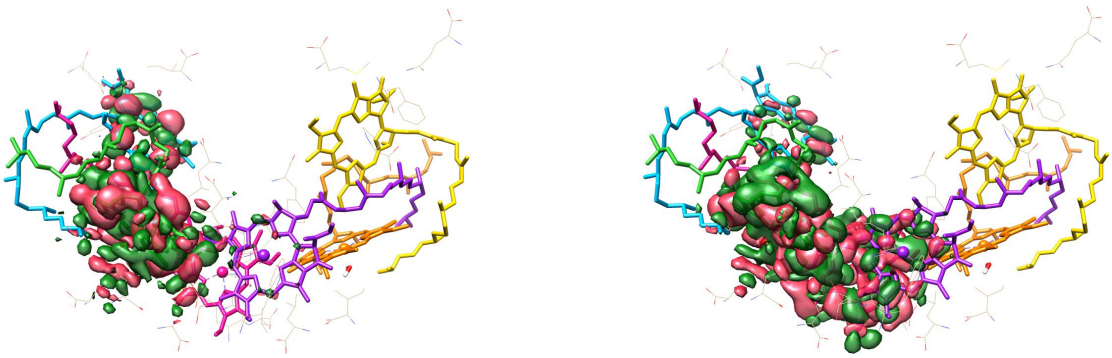


Figure 1.23 : MO diagrams exemplifying all transition classes for model 4 ωB97X-D/6-31G** including dominant transitions contributing to ES 1-6, LEFT COLUMN - Occupied MO, RIGHT COLUMN – Virtual MO (PAGE 2)

The MOs describing the highest contributing transition to each ES in the Q_Y band for model 4 (ωB97X-D/6-31G**) are shown in Figure 1.23 for reference in later chapters.

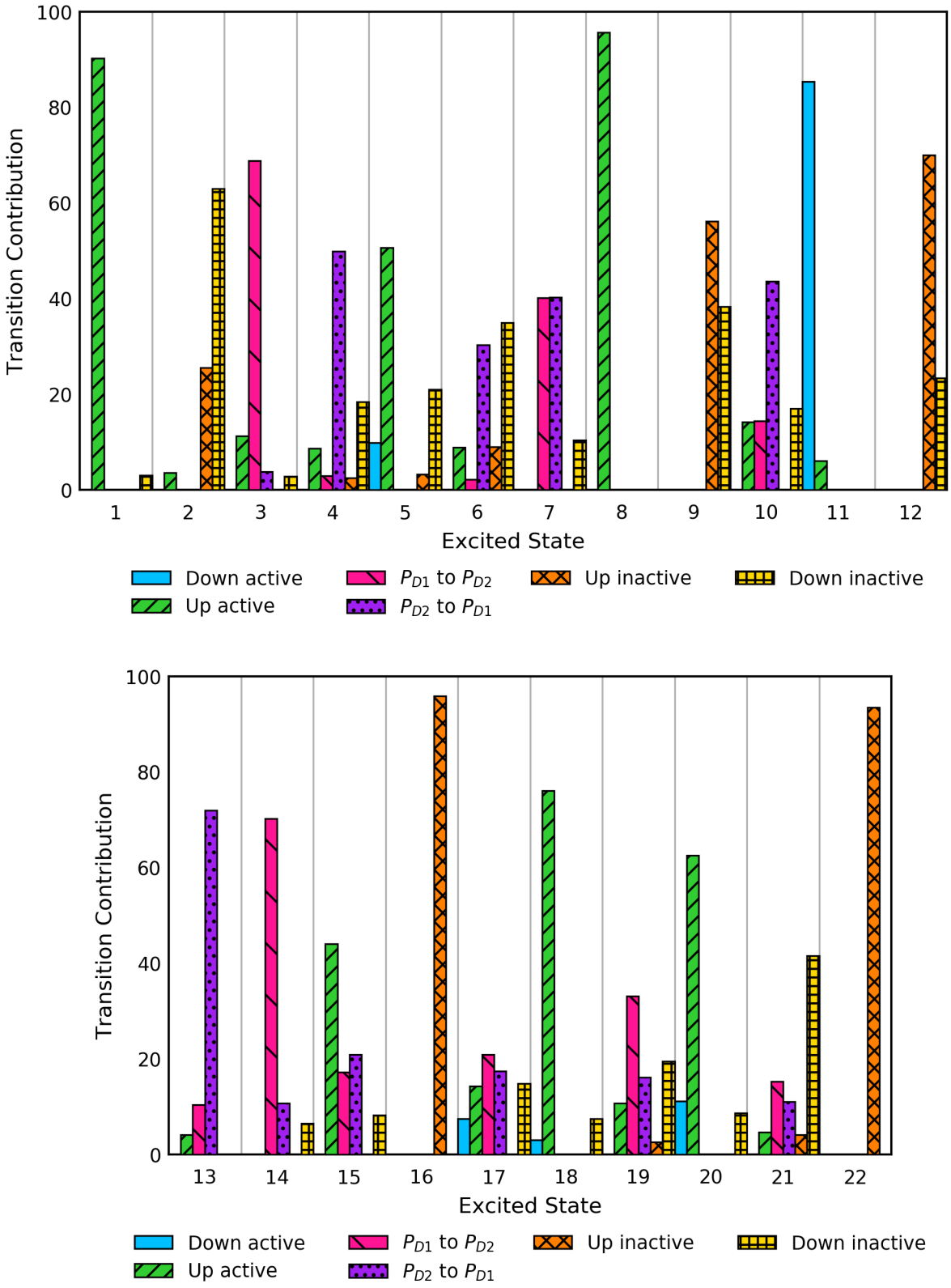


Figure 1.24 : Contributions from each transition class for model 4 (ωB97X-D/ 6-31G**), TOP : ES 1-12 (Qy and Qx regions), BOTTOM : ES 13-22 (Soret region).

Contributions from the six transition types are shown in Figure 1.24 for ES 1-22 for model 4 (ωB97X-D/6-31G**). Strikingly, both active branch transitions in the Q_Y region are classed as transition up the active branch for model 4. ES 1, centred on Phe_{D1} is similar to ES 2 for model 3 and ES 5 to the same state for models 1-2 both with up active Chl_{D1} excitations. Contrastingly there are no states dominated by transition up the inactive branch in the Q_Y region (ES 1-6) for model 4. Looking at this low energy region of the spectrum it can be concluded that both the phytol chains and the amino acids are contributing to driving CT up the active branch preferentially.

In the Q_X region that the Phe_{D1} it can be seen that state 8 is also classed as transition up the active branch, and that there are significant contributions from up active transitions to three states in the Soret region. One state in the whole 22 ES manifold is dominated by transition down the active branch.

The oscillator strength is related to the likelihood of a given transition and is therefore analogous to intensity for an experimental absorption spectrum. Plotting the results of TDDFT calculations (ES energy vs oscillator strength) for a single point energy calculation is the equivalent of seeing the spectrum of one RC unit. This is far from the observable UV spectrum in which a bulk sample is measured, where different orientations of the pigments lead to broad bands. A more realistic UV absorption spectrum can be derived from these results using gaussian functions to broaden each ES. The sum of all the single ES gaussian functions is the calculated absorption spectrum which is the black line in Figure 1.25 B below:

The Q_Y region for model 4 has two clear peaks owing to the similar relative intensities of ES 1, 2 and 5. This is the best reproduction of the shape of the low temperature absorption spectrum of the D1-D2-Cytochrome b559 complex (see figure 1.25 A for absorption spectrum data) [25] in this region of the spectrum for all models so far (see simulated absorption spectra for models 1-3 in appendix four). The height of the peak in the Soret region is above that of the whole Q_Y band, as it is in the experimental absorption spectrum (see figure 1.25 A).

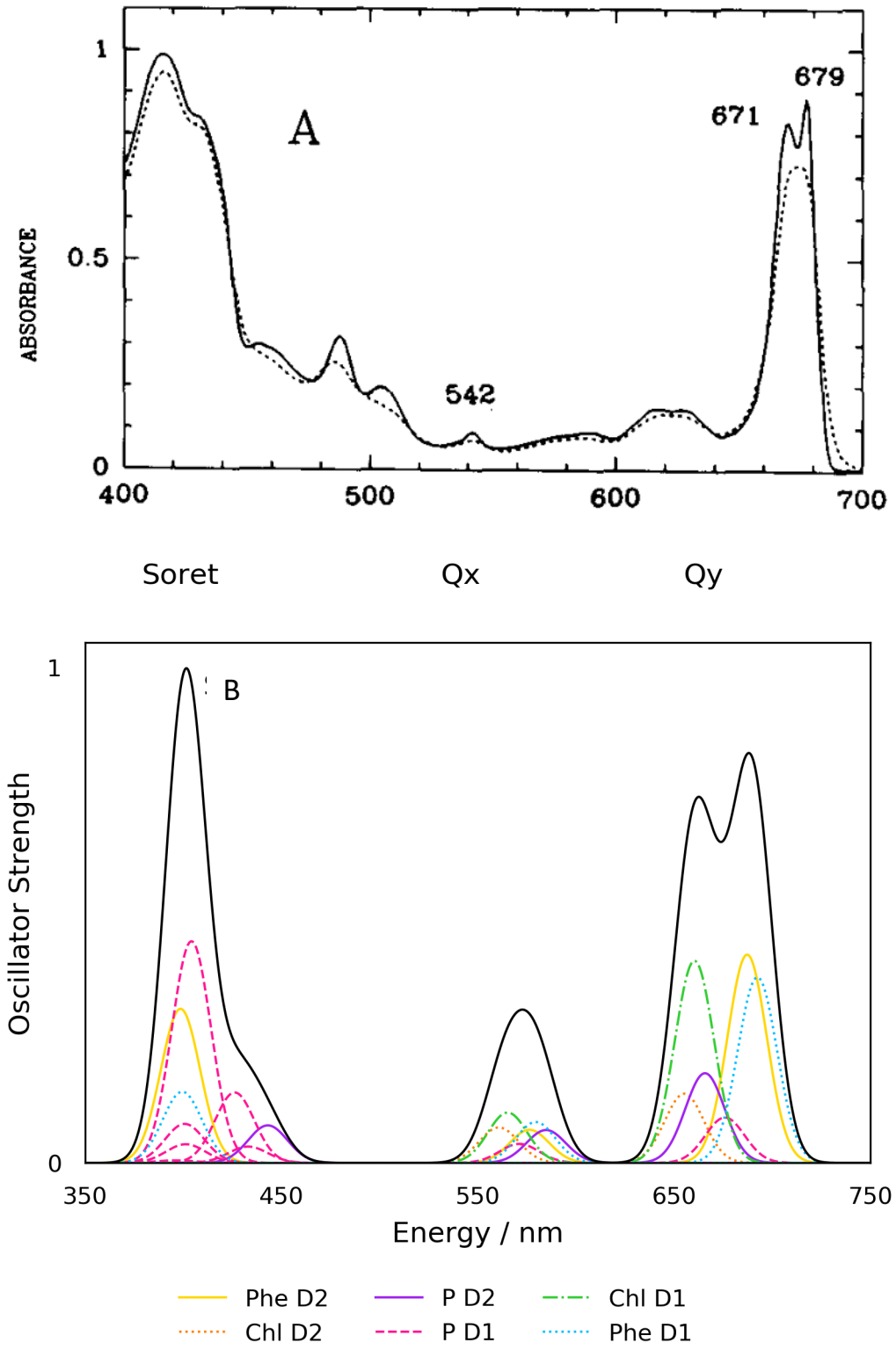


Figure 1.25 : A (top)- Absorption spectra at 10 K (solid line) and 230 K (dashed line) of D1D2 cytochrome b-559 complex reproduced with permission from[25], B (bottom) - Calculated absorption spectrum for model 4 (ωB97X-D/ 6-31G**), black line – full spectrum from sum of single ES broadened by gaussian functions, coloured lines – single ES broadened by gaussian functions coloured by occupied orbital cofactor: Phe_{D2} (yellow), Chl_{D2} (orange), P_{D2} (purple), P_{D1} (pink), Chl_{D1} (green) and Phe_{D1} (blue).

Conclusion

In this chapter the results of excited state calculations on comprehensive models of the PSII RC are presented. The models discussed in this chapter included all six chromophores in a super-molecular, all-QM model of the RC. This allowed for any combination of exciton or charge-transfer interaction among the six core chromophores to be modelled – using the robust method of TDDFT. Larger models further included full phytol chains of the six chromophores, and/or up to 23 whole amino acid residues from the surrounding protein structure, within the QM region and at the same level of theory. At 1,299 atoms, this work constitutes the largest QM model of the PSII reaction centre to date.

In general, the 6-31+G** predicts a lower energy of P_{D1} excitation for model 1 than 6-31G**. However, similar oscillator strengths and MO transitions are predicted by both basis sets. Of the two basis sets that were employed, the computational cost of the larger one (6-31+G**) cannot be justified for larger models. Therefore, with this comparison between 6-31G** and 6-31+G** for model 1 in mind, the 6-31G** basis set will be adopted for the majority of calculations going forwards. Two functionals ωB97X-D and CAM-B3LYP show good agreement for model 4, which is satisfying proof that the features of this model are producing results robust to small changes in the method. Choosing between these two functionals is arbitrary, so in later chapters an effort was made to repeat calculations with both methods. For ease of comparison the ωB97X-D functional was the first choice for new model calculations.

So far, the conclusions that can be drawn from the models built are not straightforward to link to experimental data. The justification for choosing model 4 over the three preceding models also considered the outcome of mutant model results which will be discussed in the next chapter. However, this chapter has examined in detail the differences in the excitation profiles of the four models, and come to the conclusion that model 4 is the minimum system that must be included as it successfully reproduces the D1 branch preference.

It has been shown that the amino acid residues in the vicinity of the RC pigments in combination with the phytol chains are responsible for driving CT up the active branch to result in successful photosynthesis. Active branch excitations are favoured when both the phytol chains and the surrounding amino acids are included. First, when including the phytol chains for model 2, the relative oscillator strength of ES 5 is increased compared to model 1 for which the phytol chains were truncated. Noteably, ES 5 pertains to a Chl_{D1} excitation with transitions showing movement up the active branch. Next, on including the amino acids, the transition character of ES 2 and ES 5 are swapped compared to model 1, meaning that ES 2 is now the state with the most ‘up active’ transition character. The relative oscillator strength of this state is increased for model 2.

Finally, the combined effect of the phytol chains and amino acids has been demonstrated in model 4, for which both ES 1 and ES 5 are dominated by transitions moving up the active branch. Furthermore, the energy of the D1 branch Phe excitation (ES 2 for all other models) drops below that of the D2 branch Phe excitation for model 4. Furthermore, for the largest model there is a good agreement with experimental low T absorption spectrum of D1-D2-cyt b559 complex.

This chapter has provided a working model of the RC, some insight into the effects of different methods and the effect of inclusion of the phytol chains and surrounding protein environment on the results of TDDFT calculations on the PS II RC. The following chapters explore further validation for the choice of model 4 as the best model presented in this thesis so far. This will be achieved by recreating some experimental results on mutant RCs and expanding the region of PS II included in further models to show that model 4 is both accurate and cost-effective. The predictive capability of model 4 will become clear as models with different single residue mutations are explored (chapters 2 and 3). Then in chapter five, the results of including more of the protein environment and some additional nearby pigment molecules in RC models are discussed, aiming to identify the smallest model at which convergence of the results is reached.

Chapter Two: Site Directed Mutation of the P_{D2} Ligand, D2-197

The Mutant Reaction Centre Adopts An Alternative Excitonic Pathway

Chapter Overview

This chapter includes results of three mutant models of the PS II RC. Building on the findings of the previous chapter, the size of the system under investigation is fixed and all models include full phytol chains, 23 amino acids and at least two water molecules. Using the same methodology as described in chapter 1, in this chapter the effects of site-directed mutations at the site D2-197, which in the WT is the ligand to central pigment P_{D2}, will be investigated. To obtain geometries for mutant RC models, the side chain of the mutated residue was altered manually, using the atom ligating the chlorophyll metal centre as a guide. Where water molecules were introduced (in the case of mutation to Ala and Asn) the water O atom was initially placed where the ligating histidine N had been in the WT. In the case of mutation to Gln the carbonyl O of the residue side chain was initially placed at the histidine N position. AM1 was then used to optimise positions of all new atoms, leaving the carbon backbone fixed in position so that results could be compared to WT models from the same crystal structure.

Based on the method and results produced in chapter 1, it is now possible to examine the effects of the mutation of D2-197 within the model RC. Attention will be paid to the extent of delocalisation of P chlorophyll MOs, already postulated to be increased for ala and asn mutants.[46] Shifts in the simulated absorption spectrum relative to WT results from model 4 can be observed and compared with the experimental findings.[33] Whilst it is difficult to observe the secondary effects on Chl_{D1} without optimization steps to account for changes in the H-bonding water network, this method will provide new insight into the degree of mixing of exciton and CT states and how this changes with respect to the shapes of the MOs and excitation profiles. Effects on the excitation profile due to any perturbation of the P_{D2} ring[46] will also not be observed by the chosen method but may be of interest as further work on these models.

Results & Discussion

In order to validate the method used and models built so far, it is vital show comparison between these results and experimental data. The next step therefore was to build models of mutant RCs which have been made and studied extensively. This chapter will show how the mutant-WT absorption difference spectrum can be simulated from these results, and that a good agreement is achieved for two of the three mutants discussed in this chapter. This chapter contains results of calculations on mutant models where the residue at D2-His-197 was mutated to alanine (H197A), asparagine (H197N) and glutamine (H197Q). The positions of the three mutant residues are depicted in Figure 2.1. Of the three, it is found that glutamine has the least impact on the excitation profile of the RC. Surprisingly, the results presented in this chapter point to a possible alternative excitonic pathway for CT in mutant RCs between P_{D2} and Chl_{D1} for H197A and H197N.

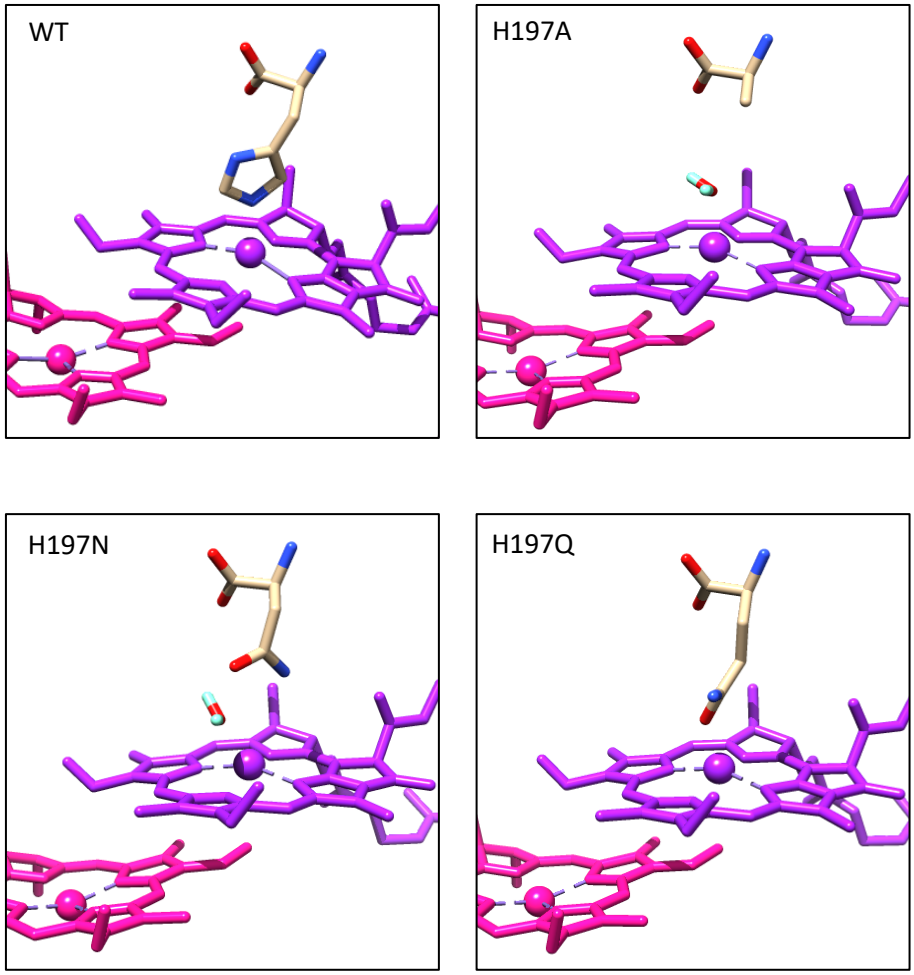


Figure 2.1 : Closeup of the P chlorophylls (P_{D1} – pink, P_{D2} – purple) and mutated D2-197 residue from histidine (WT, top left) to alanine (H197A, top right), asparagine (H197N, bottom left) and glutamine (H197Q, bottom right). Mutation to alanine and asparagine left space for a water molecule to coordinate the P_{D2} chlorophyll which is also shown.

For the H197A and H197N mutants, space for a water molecule remained on mutating the 197 residue, so this was included in the structure (see Figure 2.1 for the position of the mutant residue and water molecule). For mutation to H197Q however, no space remained for a water molecule to be inserted, and the glutamine O instead coordinates the P_{D2} metal centre. All results presented in this chapter are from calculations with ωB97x-D and 6-31G** and all models comprise six pigments (P_{D1}, P_{D2}, Chl_{D1}, Chl_{D2}, Phe_{D1} and Phe_{D2}) with their full phytol chains, two water molecules ligating Chl_{D1} and Chl_{D2} and a total of 23 amino acids (see table 1.2 from chapter one). It is therefore relevant to compare the results of the three mutant models presented in this chapter with WT model 4 (ωB97x-D/6-31G**) from the previous chapter.

Excitation Energies and Oscillator Strengths

Table 2.1 : Excitation energies and oscillator strengths for WT model 4 and three mutant RC models, His-197-Ala (H197A), His-197-Asn (H197N) and His-197-Gln (H197Q)†

State	Absorption Band	Energy (nm)				Oscillator Strength			
		WT	H197A	H197N	H197Q	WT	H197A	H197N	H197Q
1	Q_Y	692.46	692.27	692.2	692.26	0.3746	0.3703	0.366	0.3666
2		687.23	687.16	687.11	687.21	0.4202	0.4181	0.4181	0.4186
3		675.93	675.49	675.31	675.29	0.0915	0.0949	0.1124	0.1051
4		665.76	665.27	662.68	663.76	0.1809	0.1796	0.137	0.1386
5		660.4	660.04	659.49	659.49	0.4078	0.4057	0.4181	0.4403
6		655.24	654.69	651.64	653.41	0.1396	0.1405	0.1679	0.1496
7	Q_X	584.79	579.36	579.36	580.13	0.0663	0.0725	0.0793	0.0661
8		579.51	577.93	576.71	579.28	0.0825	0.1128	0.0996	0.0938
9		576.34	576.24	573.81	576.37	0.0668	0.0296	0.0351	0.0557
10		571.17	570.92	570.82	571.2	0.0383	0.0376	0.0448	0.0386
11		565.19	564.75	563.62	563.31	0.1015	0.1021	0.1021	0.1014
12		560.76	561.09	560.97	560.9	0.0715	0.0713	0.0695	0.0691
13	Soret	443.03	446.14	447.01	443.05	0.0757	0.0162	0.0151	0.0859
14		432.99	431.1	431.02	432.24	0.0329	0.0495	0.0958	0.0467
15		426.15	423.59	423.66	425.48	0.1421	0.2646	0.2121	0.1205
16		410.44	411.07	412.23	411.33	0.0008	0.141	0.1373	0.0006
17		404.14	401.18	401.19	403.51	0.4472	0.1081	0.0913	0.4787
18		401.23	399.56	400.54	400.07	0.0377	0.2612	0.0098	0.0656
19		400.68	398.81	399.48	399.56	0.0787	0.0095	0.2868	0.2248
20		399.46	395.24	396.03	398.4	0.1436	1.5715	0.1871	0.0069
21		398.55	393.79	394.83	397.46	0.3109	0.2008	1.5915	0.3539
22		396	393.1	393.6	394.41	0.0051	0.0361	0.1709	0.5739

†All four models contain 23 amino acids, full phytol chains and two water molecules coordinating Chl_{D1} and Chl_{D2}, H197A and H197N also include a water molecule coordinating P_{D2} in place of the mutated His residue N. Results calculated with ωB97x-D and 6-31G**. Oscillator strengths > 1 not included in colouring by value, cell shading as in table 1.9 in chapter 1: Energies (left, colour gradient for each model within each band showing degeneracies and intervals in excitation energies), Oscillator strengths (right, green shading for brighter states and purple shading for darker states across the whole spectrum, yellow for states with f>1).

The excitation energies and oscillators strengths for ES 1-22 are presented in table 2.1 for the WT model 4 and three mutant models, H197A, H197N and H197Q. From table 2.1 it can be seen that the excitation energies of the three mutants are similar to the WT for ES 1-3. The presence of three bright states in the Q_Y region (ES 1, 2 and 5) is also consistent for WT and all three mutants. The excitation energy of ES 4 for H197Q and H197N

is upshifted by ~2-3 nm and ES 6 by ~2-3.5 nm for the same two mutants. Overall, H197A excitation energies are most similar to the WT in the Q_Y region out of the three mutants tested and H197N deviate the most.
In the Q_x region the H198Q mutant gives results that are most similar to the WT. ES 7 for all three mutants is between ~4.5 and 5.5 nm higher in energy than the WT ES 7, bringing the excitation energy for ES 7 above that of WT ES 8 (580 nm) for H197A and H197N. Excitation at new wavelengths 578 (H197A ES 8) and 574 nm (H197N ES 9) appears for the mutants, as the reader will see below this is due to the shifting energy of P_{D2} excitation (585 nm, ES 7 for WT) upon mutation of the residue His-197.

Due to there being a fixed number of ES calculated for each model, a different region of the spectrum is explored depending on the model. In the Soret region H197A and H197N excite to higher wavelengths than previously seen for the WT, resulting in two states with oscillator strength > 1 (H197A ES 20 and H197N ES 21). Whilst no such oscillator strength is seen for the WT ES 1-22, similar results have been seen for conjugated polymers.[127,128] It could be that a state with similar oscillator strength lies higher in energy than ES 22 for the WT, but the expense of calculating further ES was too great and therefore beyond the scope of this work. Below 396 nm (the excitation energy for WT ES 22) there are no ES for H197A and H197N with f > 0.3. The WT and H197Q models each have bright states ES 17 and 21 with f > 0.3, however H197Q also has additional bright state ES 22 at 394 nm. Generally, H197Q give the most similar result to the WT in the Soret and in the Q_X region.

Excited State Profiles – Cofactor Excitations

ES 1-3 are invariably attributed to two Phe excitations and P_{D1} excitation across all three mutants, in agreement with the WT results (full results for the three D2-197 mutants can be found in appendix four, for ease of reading, some relevant examples will be presented in this chapter). However, the contribution of different cofactor excitations to ES 4-6 is seen to change on mutating the residue at D2-197, as shown below in Figure 2.2.

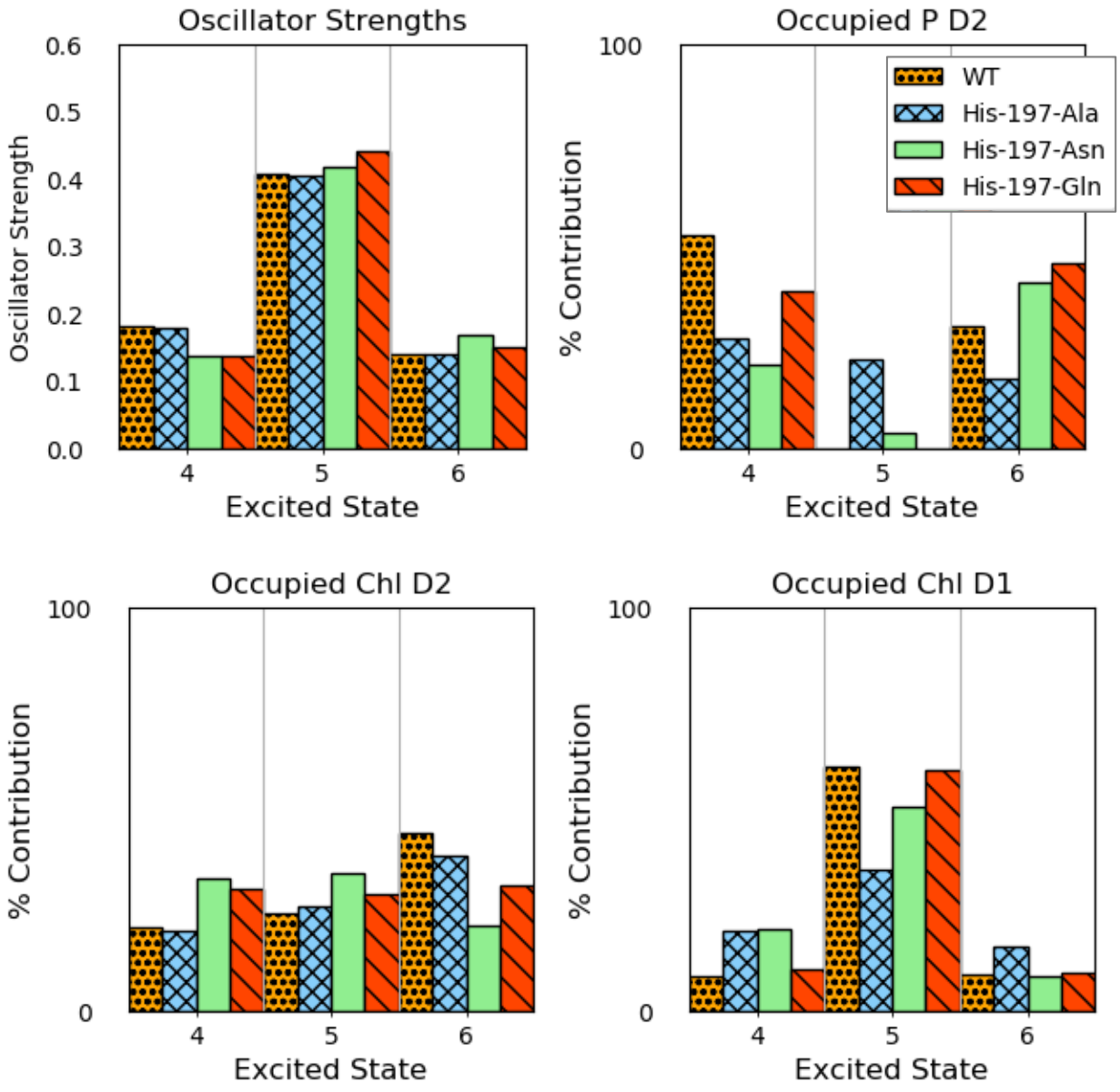


Figure 2.2 : Showing the profile of ES 4-6 for WT model 4 and three mutants, H197A, H197N and H197Q all calculated with ωB97x-D/6-31G**. TOP LEFT – oscillator strengths, TOP RIGHT - P_{D2} occupied orbital contribution, BOTTOM LEFT Chl_{D2} occupied orbital contribution and BOTTOM RIGHT Chl_{D1} contribution.

From Figure 2.2 it can be seen that mutating the D2-197 residue to glutamine results in the least change to the WT excitation profile compared with the alanine and asparagine mutants. ES 6 has a higher contribution from P_{D2} excitation for the mutant than the WT making this the dominant excitation for this state (Chl_{D2} dominates ES 6 for WT). Otherwise, the Q_Y region is extremely similar for WT and H197Q (see Figure 1.21 and appendix four – H197Q results).

In contrast with WT model 4 (for which ES 4 is 52.8% P_{D2} excitation and 8.7% Chl_{D1} and ES 5 is 60.5% Chl_{D1} excitation with no contribution from P_{D2} excitation) there are both P_{D2} and Chl_{D1} excitations contributing similar amounts to ES 4 and 5 for the H197A mutant (ES 4 is 27.3% P_{D2} excitation and 20.0% Chl_{D1} excitation whilst ES 5 is 35.1% Chl_{D1} excitation and 22.0% P_{D2} excitation). It could therefore be postulated that P_{D2} excitation is shifted to higher energies for this mutant, making it near-degenerate with Chl_{D1} excitation. Additionally, ES 4 for H197A is contributed to by previously unseen transitions, so making this comparison with the WT results does not give the full picture. The major contributing transitions for H197A ES 4 are depicted below in Figure 2.3:

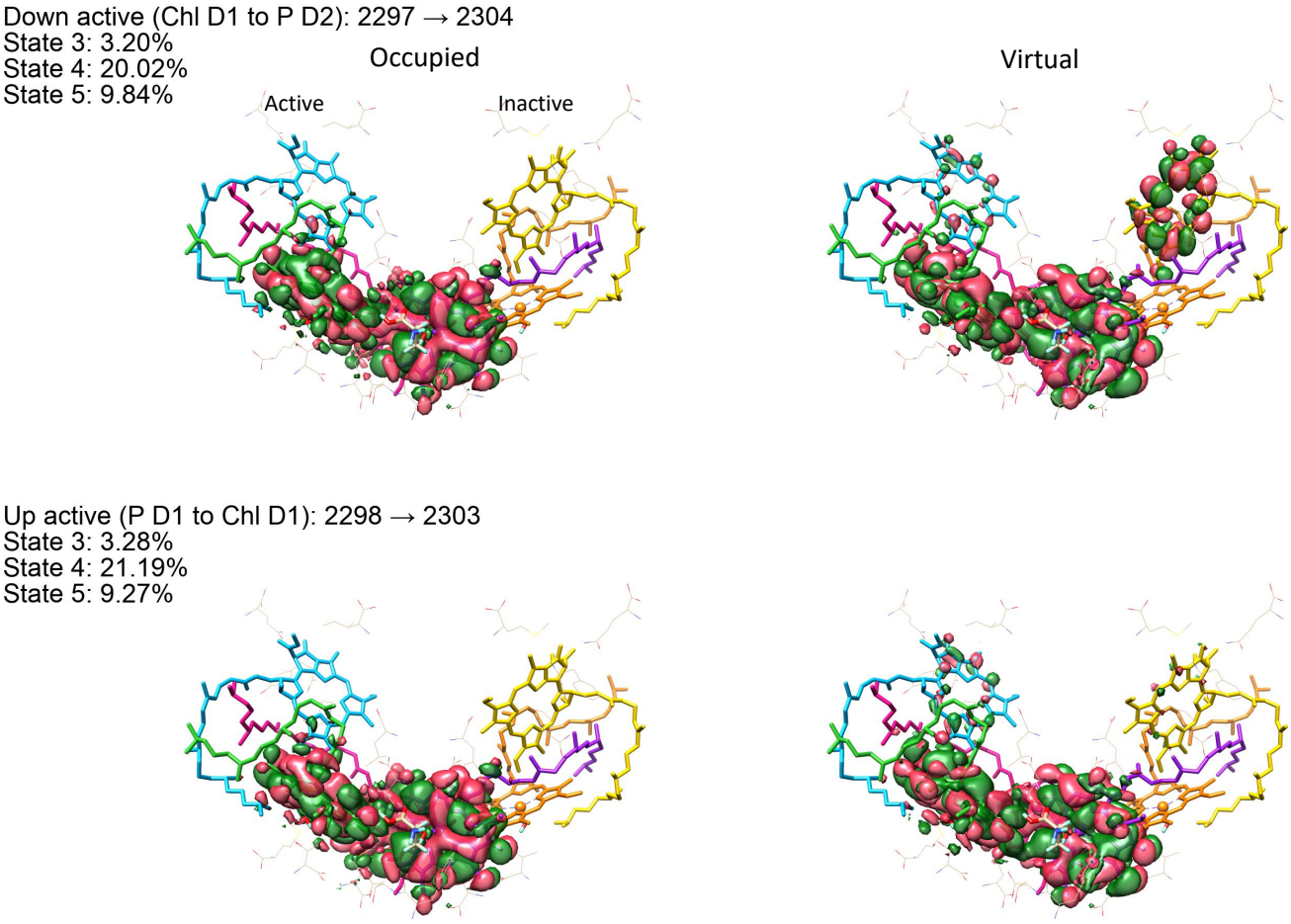


Figure 2.3 : MO diagrams for transitions contributing to ES 4 for H197A ωB97X-D/6-31G**, LEFT COLUMN - Occupied MO, RIGHT COLUMN – Virtual MO.

The orbitals involved in the transitions depicted above have cofactor occupancy detailed in table 2.2 below. Considering the delocalisation of the orbitals in Figure 2.3, it appears that mutating D2-197 to alanine has opened up a pathway between P_{D2} and Chl_{D1} which was not accessed by the WT.

Table 2.2 : Cofactor occupancy for MOs making up ES 4 transitions for H197A (ωB97X-D/6-31G**)

MO	Chl_{D1} occupancy	P_{D1} occupancy	P_{D2} occupancy
2297	56.6%	7.9%	34.9%
2298	42.4%	13.8%	43.2%
2304	43.6%	0.9%	52.3%
2303	53.8%	1.4%	43.4%

From Figure 2.2 it is shown that the contribution of P_{D2} excitation is highest in ES 6 for the H197N mutant, for WT excitation out of P_{D2} occupied orbitals contributes 52.9% to ES 4 and 30.4% to ES 6. Again, MOs of the transitions contributing in this region for H197N show a high degree of delocalisation over Chl_{D1} and P_{D2} that was not present for the WT (see Figure 2.4):

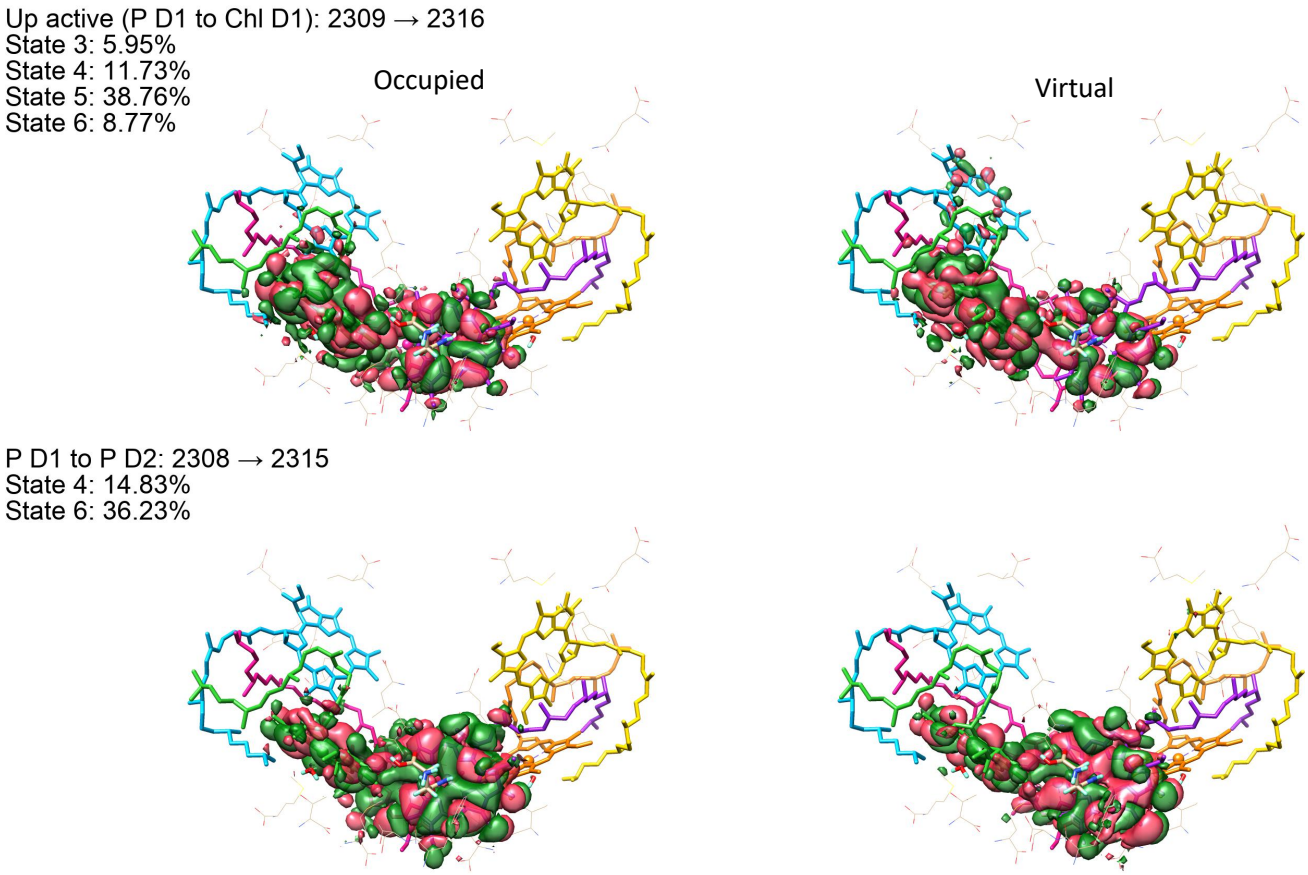


Figure 2.4 : MOs contributing to ES 5 and 6 for H197N ωB97X-D/6-31G**, LEFT COLUMN - Occupied MO, RIGHT COLUMN – Virtual MO.

Table 2.3 shows the cofactor occupancy, calculated from Mulliken population analysis[114], for the MOs depicted in Figure 2.4.

Table 2.3 : Cofactor occupancy for MOs making up ES 5 and ES 6 transitions for H197N ωB97X-D/6-31G**

MO (H197N)	Chl_{D1} occupancy	P_{D1} occupancy	P_{D2} occupancy
2308	11.1%	21.0%	67.2%
2309	87.9%	3.9%	7.6%
2315	6.8%	2.2%	89.9%
2316	91.4%	0.4%	7.1%

From table 2.3 it is clear that P_{D2} orbitals 2308 and 2315 have a higher degree of delocalisation into Chl_{D1} for H197N than WT analogues MO 2311 and 2318 (see table 2.5 below in discussion of P chlorophyll transitions). However, for H197A there were four MOs with high contributions to Q_Y states for which electron density was

almost evenly shared over Chl_{D1} and P_{D2} (see table 2.1) which do not exist for H197N. In this respect the H197N mutant transitions are more similar to the WT than the H197A mutant.

Comparing table 2.3 to the results for H197A above (table 2.2 and Figure 2.3), for which P_{D2} excitation has a high contribution to ES 4 and ES 5 (Figure 2.2), it appears that excitation out of P_{D2} occupied orbitals is pushed even further to higher energy states by mutating to H197N. This reasoning is supported by the appearance of a P_{D2} dominated state ES 9, higher in energy than both Q_X band Phe excitations for the H197N mutant, whereas for the WT ES 7 is a P_{D2} dominated state and for H197A ES 8 is P_{D2} dominated (see Figures 2.5 and 2.6 below).

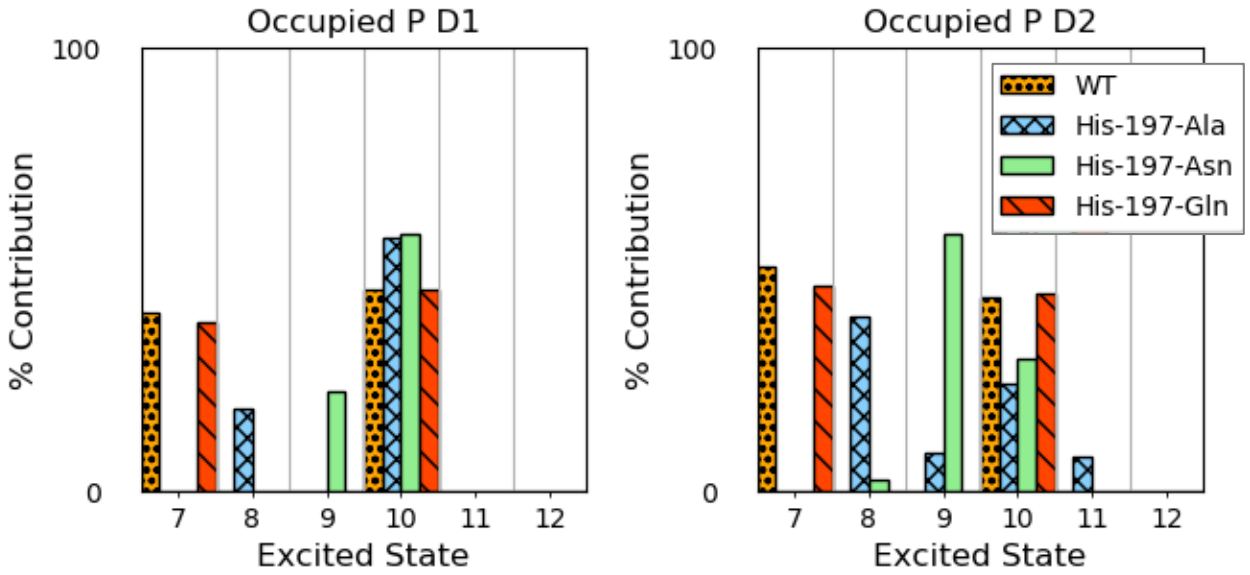


Figure 2.5 : P chlorophyll excitations in the Q_X region for WT model 4 and three mutants H197A, H197N and H197Q all calculated ωB97X-D/6-31G**

In the Q_x region a reordering of states takes place for H197A and H197N relative to the WT. P chlorophyll excitations P_{D2} and to a lesser extent P_{D1} which dominated in ES 7 for the WT are shifted to higher energy ES 8 for H197A and ES 9 for H197N (Figure 2.5). Whilst the ordering of states is the same for WT and H197Q, note that the excitation energy of ES 7 is upshifted by just under 5 nm for the H197Q mutant relative to the WT (table 2.1).

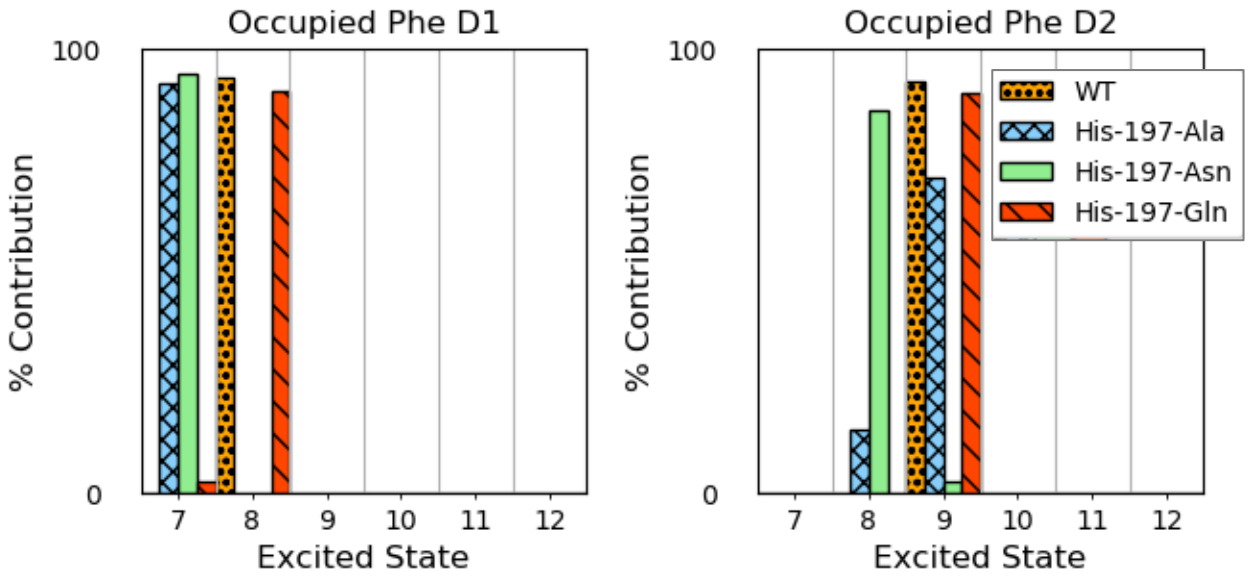


Figure 2.6 : Phe excitations in the Q_x region for WT model 4 and three mutants H197A, H197N and H197Q all calculated ωB97X-D/6-31G**

Figure 2.6 shows that the identity of H197A and H197N ES 7 is the same as that of H197Q and WT ES 8, and that H197N ES 8 has the same identity as ES 9 for the WT and other two mutants.

Excited State Profiles – Transition Classes

As for the WT, transitions travelling up the inactive branch or down the active branch were rare for the three D2 branch mutants. For all mutants ES 1 is dominated by transitions where charge travels up the active branch and ES 2 is dominated by transition down the inactive branch, see Figure 2.7.

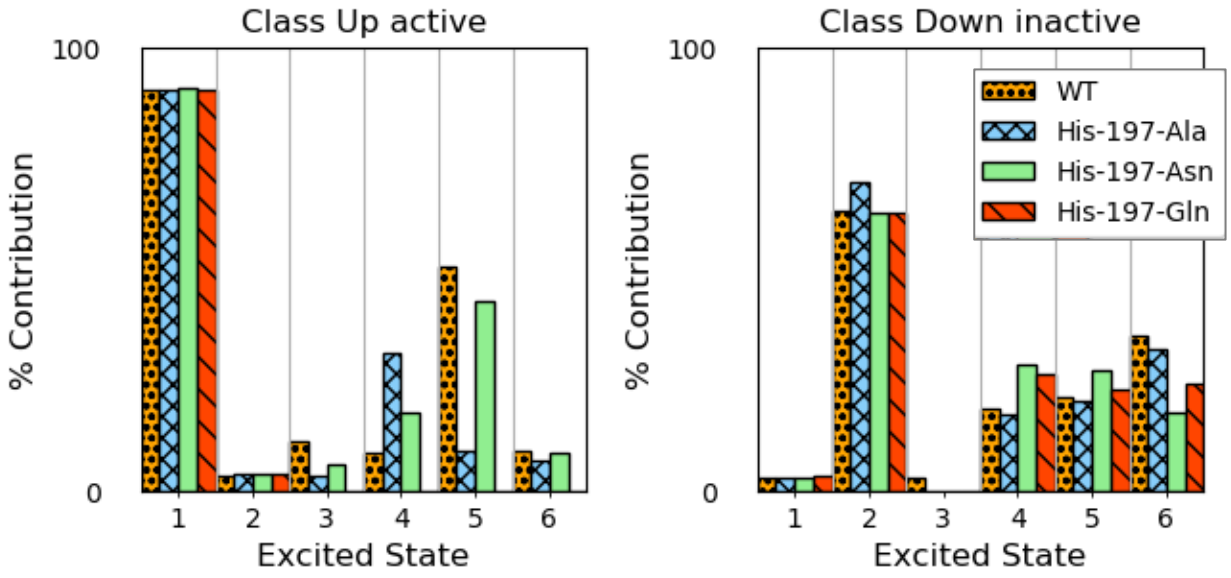


Figure 2.7 : Transition classes in the Q_Y branch for WT and H197A, H197N and H197Q models (ωB97X-D/6-31G**)

ES 5, dominated by transition up the active branch for WT, is instead attributed to a mix of transition types for the H197A mutant. Instead, ES 4 has considerable contribution from transitions up the active branch for H197A (see Figure 2.3 for an example transition).

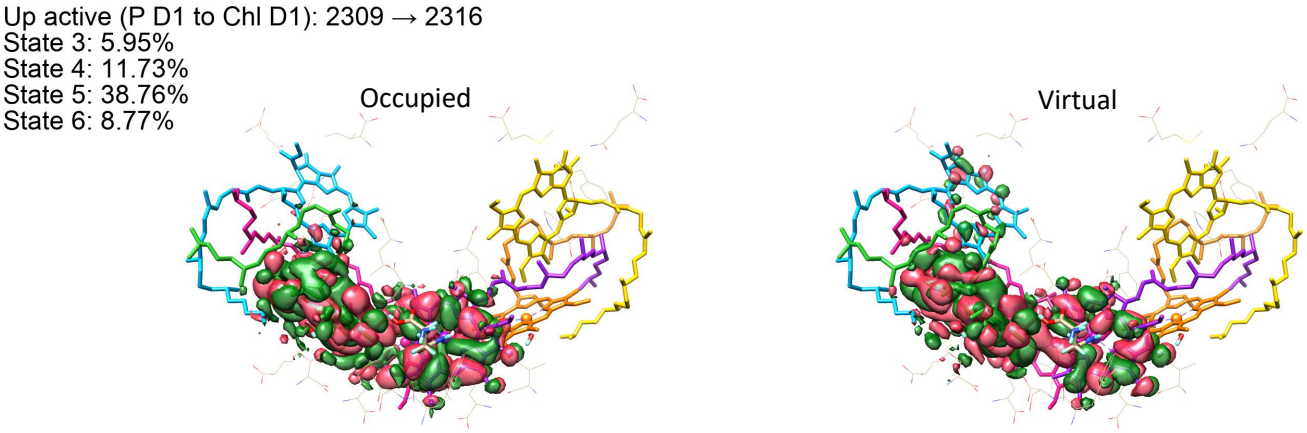


Figure 2.8 : H197N (ωB97X-D/6-31G**) up active transition

Like H197A, the up active transition for H197N (pictured in Figure 2.8) features extensive delocalisation onto the P chlorophylls. See Figure 1.23 to compare the MO pictures for the WT with Figures 2.3 and 2.8. This figure

also shows that coupling between P_{D2} and Chl_{D1} has increased for mutants H197A and H197N relative to the WT, leading to more delocalisation of MOs over the two cofactors.

From Figure 2.7, H197Q appears to be missing a second state attributed to transfer up the active branch, the reader will see in the next section that this is not the case, and that a P chlorophyll transition having significant up active branch character is dominating ES 5 for this mutant.

Meanwhile, on the inactive branch occupied MOs are more delocalised for H197A than their analogues for the WT. For example, occupied MO 2295 characterises the down inactive type transition which contributes to ES 4-6 (see Figure 2.9).

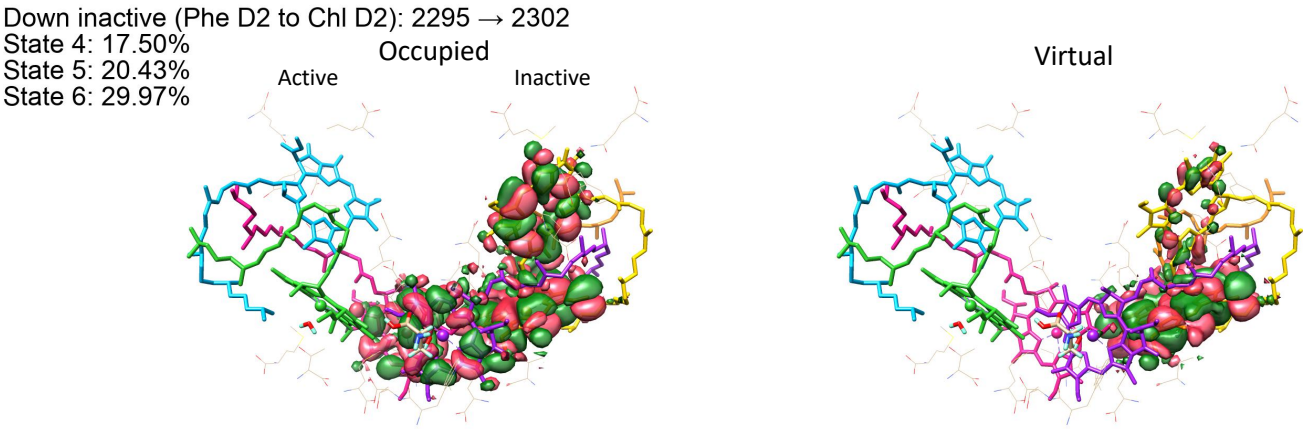


Figure 2.9 : MO diagrams exemplifying the down inactive transition classes for H197A ωB97X-D/6-31G**, LEFT - Occupied MO, RIGHT – Virtual MO

H197A 2295 has ~10x higher occupancy of the P chlorophylls than its analogue for the WT MO 2306 (see table 2.4). In contrast the inactive branch MOs for H197N and H197Q are localised to a similar degree than those for the WT (see table 2.4 for orbital occupancies and Figure 2.10 for H197Q MO diagrams).

Table 2.4 : Cofactor occupancy for inactive branch orbitals of H197A and WT (model 4) both with ωB97X-D/6-31G**

MO (H197A)	P_{D1} Occupancy	P_{D2} Occupancy	Chl_{D2} Occupancy	Phe_{D2} Occupancy
2295	3.1%	3.1%	86.9%	6.6%
2302	0.0%	0.2%	98.7%	0.7%
MO (H197N)				
2305	0.1%	0.3%	94.0%	5.4%
2313	0.0%	0.2%	98.7%	0.7%
MO (H197Q)				
2304	0.4%	0.4%	94.8%	4.1%
2312	0.0%	0.2%	98.6%	0.8%
MO (WT)				
2306	0.4%	0.3%	95.4%	3.6%
2314	0.0%	0.2%	98.6%	0.8%

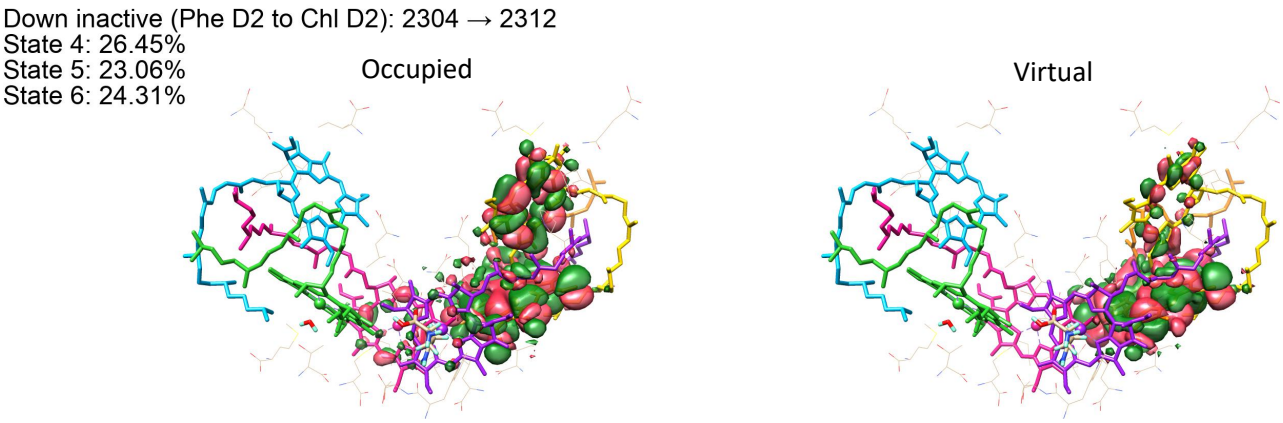


Figure 2.10 : Down inactive transition for H197Q ωB97X-D/6-31G**, LEFT - Occupied MO, RIGHT – Virtual MO

P Chlorophyll Transitions

Also of interest are the P chlorophyll transition MOs. Whilst H197A and WT have the same identity for ES 3 and 4 (see Figure 2.11), H197A and H197N have the reverse P chlorophyll transition to the WT contributing in ES 3-6.

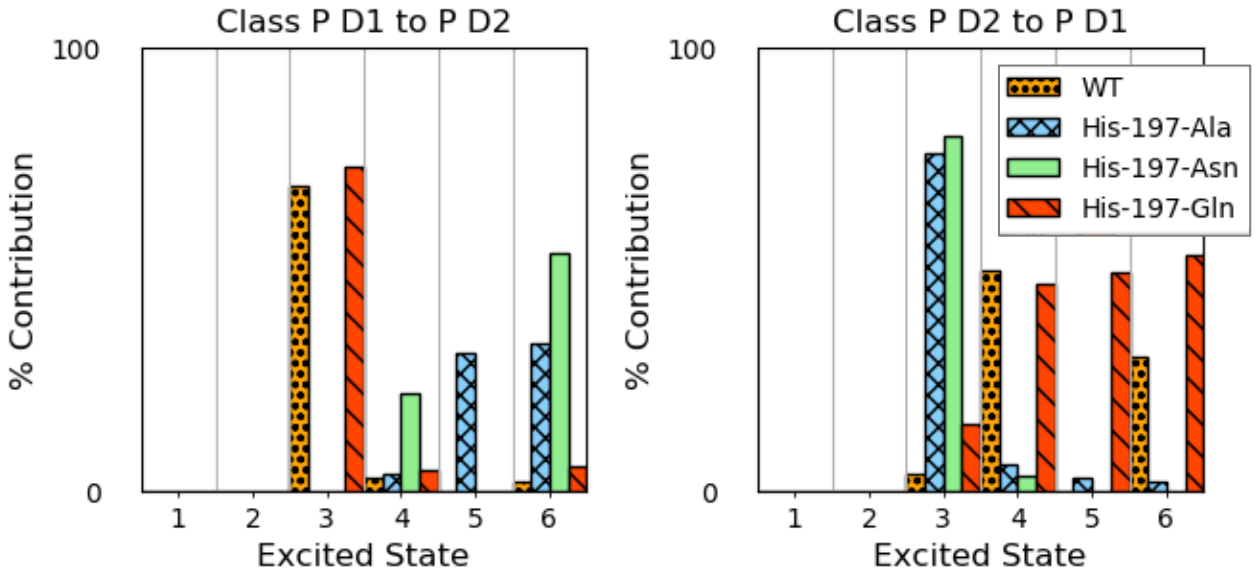


Figure 2.11 : P chlorophyll contribution to ES 1-6

For H197A ES 3 is now P_{D2} to P_{D1} transition (whereas for WT it was P_{D1} to P_{D2}), see Figure 2.11. The MO pictures in Figure 2.6 along with the cofactor occupancies in table 2.5 show that the transition contributing here has hardly any transfer of electron density between the P chlorophylls, and is instead a highly localised P_{D1} excitation. Comparatively, the WT MOs making up the P_{D1} to P_{D2} transition are 2312 and 2317 (see table 2.5), both having their highest occupancy on P_{D1} and exciting into a virtual orbital which is shared almost equally between the two P chlorophylls.

Table 2.5 : P chlorophyll occupancy of P chlorophyll transition orbitals of H197A and WT (model 4) both with ωB97X-D/6-31G**

MO (H197A)	Chl_{D1}	P_{D1} occupancy	P_{D2} occupancy
2300	0.1%	92.6%	6.3%
2306	0.2%	96.2%	2.6%
MO (H197N)			
2308	11.1%	21.0%	67.2%
2311	0.1%	93.0%	5.9%
2315	6.8%	2.2%	89.9%
2317	0.3%	95.9%	2.8%
MO (WT)			
2311	0.5%	12.0%	86.6%
2312	0.1%	87.7%	11.2%
2317	0.3%	56.1%	42.5%
2318	0.1%	42.2%	56.7%

From table 2.5, it seems that the strong coupling between P_{D1} and P_{D2} for the WT, which led to shared MOs and transitions involving a significant transfer of electron density between these two cofactors, is not as prominent for the H197A mutant. The MOs describing P chlorophyll transitions for H197A can be seen in Figure 2.12.

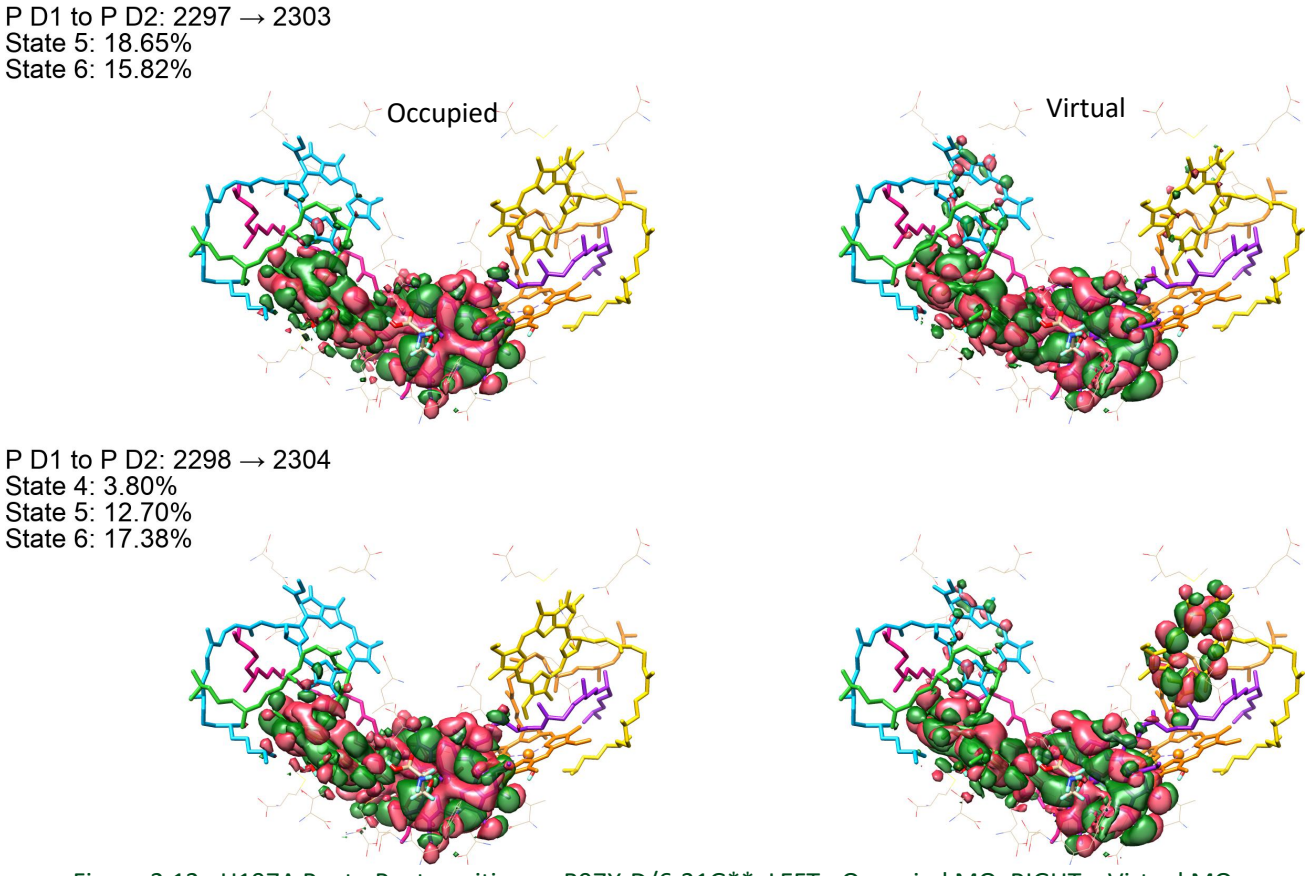


Figure 2.12 : H197A P_{D1} to P_{D2} transitions ωB97X-D/6-31G**, LEFT - Occupied MO, RIGHT – Virtual MO

High oscillator strength state ES 5 (f=0.4057 for H197A), which for WT was predominantly a transition up the active branch from Chl_{D1} to Phe_{D1}, for H197A is contributed to by P_{D1} to P_{D2} type transitions which involve MOs with their highest occupancy on P_{D2} and Chl_{D1} (see table 2.1 and discussion above). In contrast, the WT P_{D2} to P_{D1} transition MOs are 2311 which is localised on P_{D2} and 2318 which is each shared by the two P chlorophylls (table 2.5). This has interesting implications for the action of this mutant as ES 5 is a potential precursor for CS, both due to the high occupancy of Chl_{D1} and the high oscillator strength of this state. Instead of coupling between P_{D1} and P_{D2} as in the WT, a strong coupling between P_{D2} and Chl_{D1} is observed. Potentially this means that there are alternative electron transfer pathways, involving novel excitonic states, available for H197A.

Like H197A, ES 3 is dominated by the transition class P_{D2} to P_{D1} for the H197N mutant. Transition from P_{D1} to P_{D2} instead appears in ES 5 and 6 for H197N (see MOs in Figure 2.13). From table 2.5 it is clear that orbitals 2308 and 2315 have a higher degree of delocalisation into Chl_{D1} for H197N than WT analogues MO 2311 and 2318. However, for H197A there were four MOs with high contributions to Q_Y states for which electron density was almost evenly shared over Chl_{D1} and P_{D2} (see table 2.2) which do not exist for H197N. In this respect the H197N mutant is more similar to the WT than the H197A mutant. Similar to H197A, table 2.6 shows that P_{D1} MOs are highly localised, in contrast to the WT MOs which are delocalised across P_{D2} (see table 2.4). This result is similar to H197A.

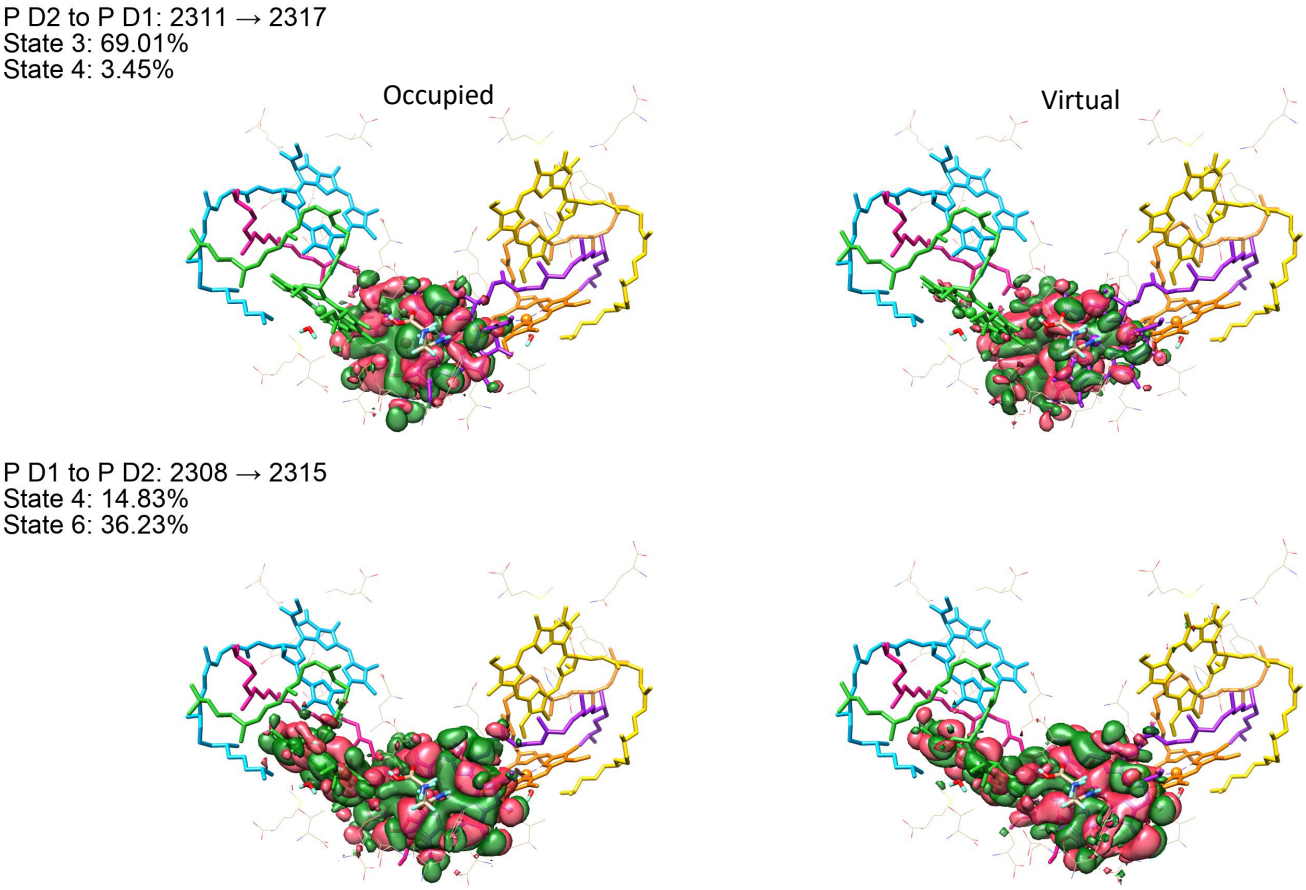


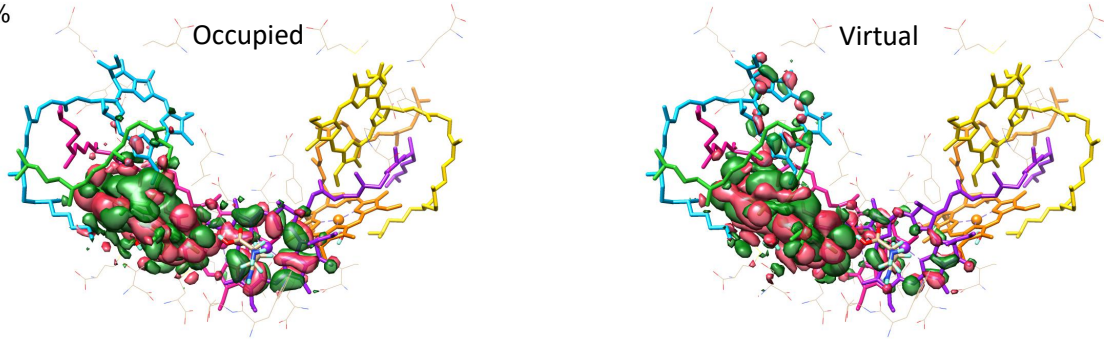
Figure 2.13 : P chlorophyll transitions for H197N ωB97X-D/6-31G**, LEFT - Occupied MO, RIGHT – Virtual MO

Unlike the other mutants discussed, ES 3 and 4 have the same identity for H197Q as for the WT (see Figure 2.11). For H197Q there are four MOs which make up the four dominant P chlorophyll transitions. These are pictured below in Figure 2.14. The occupancies for these MOs are given in table 2.6. Clearly the effect of mutating His-197 to Gln is much subtler than the previous mutants H197A and H197N, as the P transitions bare a strong resemblance to the WT P transitions. In comparison with the WT analogue 2311, occupied P_{D2} MO 2309 has very slightly higher Chl_{D1} occupancy (1.4% vs 0.5% for WT MO 2311) and compared to its WT analogue 2312, occupied P_{D1} MO 2310 is marginally more localised on P_{D1} (88.4% vs 87.7% in the WT). The virtual MOs 2315 and 2316 are a little more evenly shared over the two P chlorophylls for H197Q than their WT analogues 2317 and 2318 (The virtual H197Q P chlorophyll MOs are split ~51:47 whereas the WT analogues are split ~56:42).

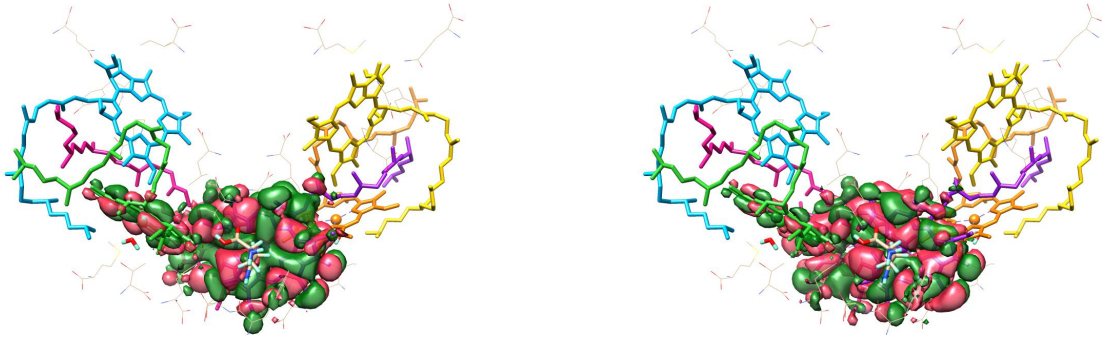
Table 2.6 : Occupancy of P chlorophyll MOs for H197Q (ωB97X-D/ 6-31G**).

MO (H197Q)	Chl_{D1}	P_{D1} occupancy	P_{D2} occupancy
2309	1.4%	12.0%	85.9%
2310	0.1%	88.4%	10.6%
2315	0.7%	50.8%	47.4%
2316	0.1%	47.3%	51.5%

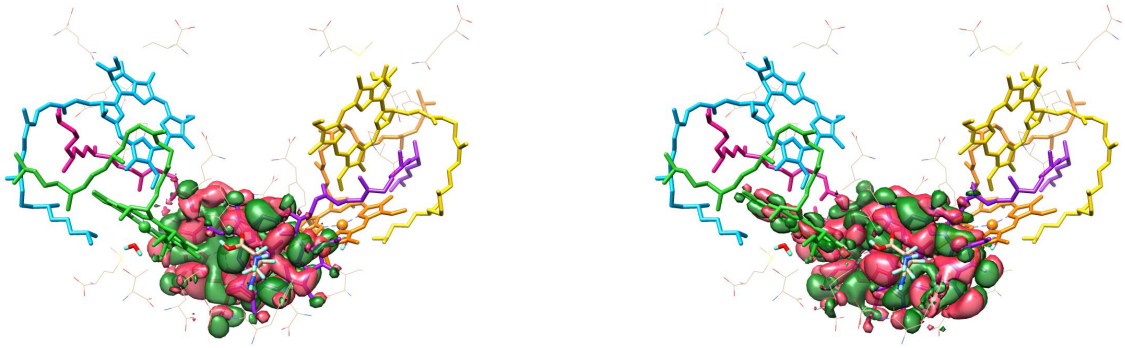
P D2 to P D1: 2307 → 2314
State 3: 7.23%
State 4: 10.16%
State 5: 49.26%
State 6: 9.58%



P D2 to P D1: 2309 → 2315
State 4: 16.76%
State 6: 19.96%



P D2 to P D1: 2309 → 2316
State 4: 16.36%
State 6: 17.70%



P D1 to P D2: 2310 → 2316
State 3: 33.01%

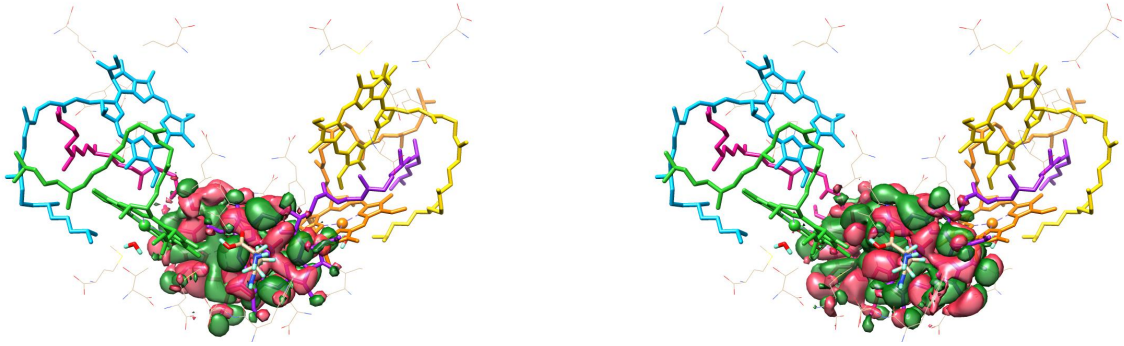


Figure 2.14 : MO diagrams showing P chlorophyll transitions for H197Q ωB97X-D/6-31G**, LEFT COLUMN - Occupied MO, RIGHT COLUMN – Virtual MO

H197Q ES 5 is labelled as P_{D2} to P_{D1} by the transition algorithm (see appendix three for a discussion of this). But on inspection of the MOs involved (table 2.7) it is seen that the MO pair with the highest contribution to this state (2307 and 2314) are very localised on Chl_{D1}. Comparing to WT analogues MO 2309 and 2315 (transition which contributes 50.65% to ES 5 for WT model 4 [ωB97X-D/ 6-31G**], see table 2.7) reveals there is a lot of similarity here. Whilst transition from WT 2309 to 2315 constitutes a loss of electron density on Chl_{D1}, H197Q 2307 to 2314 constitutes an increase in Chl_{D1} electron density. In the table the highest increase and decrease are shaded green and red, showing how the transition algorithm has come to label them P_{D2} to P_{D1} (H197Q 2307 to 2314) and P_{D2} to Phe_{D1} ('up active') (WT 2309 and 2315).

Table 2.7 : Occupancy of Chl_{D1} MOs for H197Q and WT model 4 (ωB97X-D/ 6-31G**) with change in occupancy during transition from occupied to virtual orbitals.

MO (H197Q)	Phe_{D1}	Chl_{D1}	P_{D1} occupancy	P_{D2} occupancy
2307	0.3%	97.4%	0.2%	1.7%
2314	0.6%	97.6%	0.6%	0.6%
Change in occupancy %	+0.3	+0.2	+0.4	-1.1
MO (WT)				
2309	0.4%	98.0%	0.4%	0.9%
2315	0.8%	97.8%	0.5%	0.4%
Change in occupancy %	+0.4	-0.2	+0.1	-0.5

Soret Region

The WT P^+-P difference spectrum features a prominent bleach at ~433 nm in the Soret region. Diner et al.[38] reported shifts to the red for H197A, H197N and H197Q mutants of this band (see Figure 2.15)., deduced to be due to the effect of the mutation on the absorption of P_{D1} (and to a lesser extent P_{D2}).

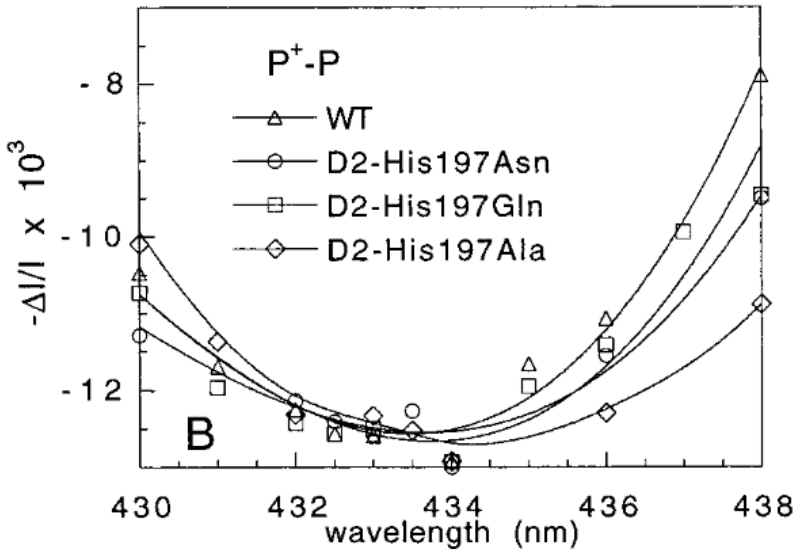


Figure 2.15 : P^+-P difference spectra measured 1 μs after a saturating actinic flash on PSII core complexes of WT and strains containing mutations H197N (D2-His197Asn), H197Q (D2-His197Gln, and H197A (D2-His197Ala). The Reprinted with permission from Diner, B. A., Schlodder, E., Nixon, P. J., Coleman, W. J., Rappaport, F., Lavergne, J., Vermaas, W. F. J. & Chisholm, D. A. Site-directed mutations at D1-His198 and D2-His197 of photosystem II in Synechocystis PCC 6803: Sites of primary charge separation and cation and triplet stabilization. *Biochemistry* **40**, 9265–9281 (2001).[38] Copyright (2001) American Chemical Society.

To model this, the ES which are dominated by P chlorophyll absorption were selected (see table 2.8), based on the output of the MultiWfn analysis, and their excitation energies and oscillator strengths were broadened with gaussian functions. The sum of all gaussian broadened P chlorophyll states is plotted in Figure 2.16 for WT and three D2-197 mutants.

We see from Figure 2.16 that the P_{D1} band is the most red-shifted for H197A, closely followed by H197N. H197Q however, is slightly blue-shifted compared to the WT. This data can be directly compared to the P^+-P difference spectra,[38] with which is found to be in qualitative agreement for H197A and H197N. The result for H197Q appears to disagree with the experimental data (Diner et al. report a shift of ~0.5 nm to the red for H197Q, see Figure 2.15).[38] The P_{D2} band is blue shifted for H197N and H197A and not shifted at all relative to the WT for H197Q, this analysis is included because 20% of the P^+ cation is thought to be shared by P_{D2}. It could be that the blue shift of the H197Q P_{D1} band is decreased by the contribution from P_{D2} absorption at lower energies.

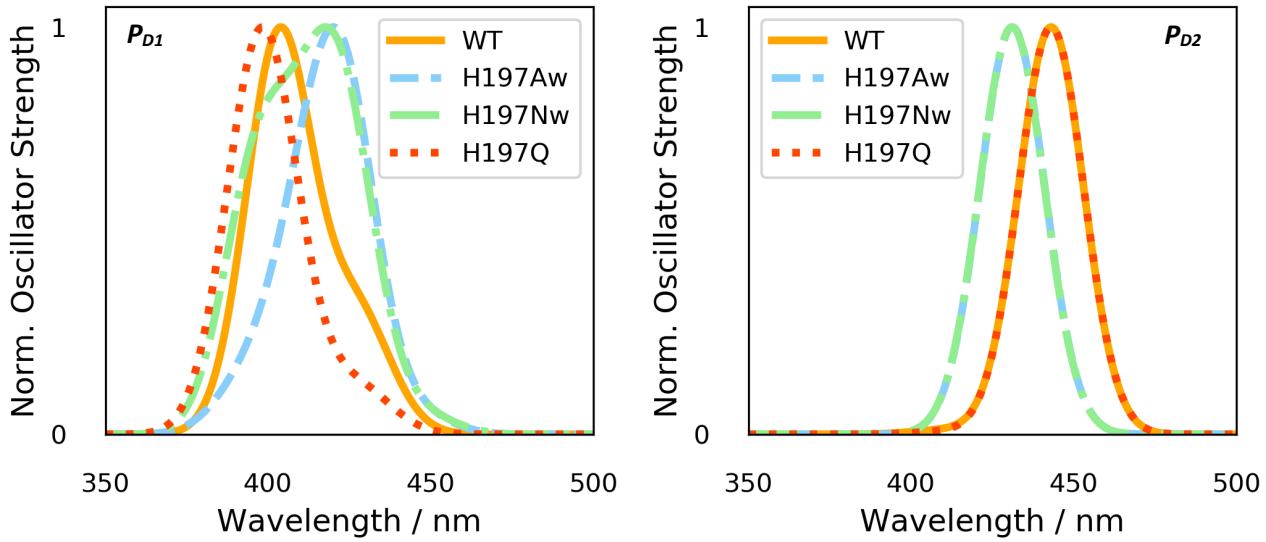


Figure 2.16 : P_{D1} (LEFT) and P_{D2} (RIGHT) absorption bands for WT (Orange line) and mutants H197A (blue dashed line), H197N (green dotted line) and H197Q (red dash-dot line) in the Soret region. Highest oscillator strengths normalised to 1. All calculations were performed using ωB97X-D/ 6-31G**

Table 2.8 : ES data for all ES used to plot the simulated P absorption bands (Figure 2.16) in the Soret region for WT model 4, H197A, H197N and H197Q (ωB97X-D/ 6-31G**)†

Model	P_{D1} dominated states (P_{D1} % contribution)	P_{D2} dominated states (% contribution)
WT	ES 14: 433 nm, f = 0.0329 (74.6%) ES 15: 426 nm, f = 0.1421 (62.3%) ES 17: 404 nm, f = 0.4472 (37.2%) ES 18: 401 nm, f = 0.0377 (67.4%) ES 19: 401 nm, f = 0.0787 (38.6%) ES 22: 396 nm, f = 0.0051 (67.6%)	ES 13 ES 14
H197A	ES 13: 446 nm, f = 0.0162 (60.4%) ES 15: 424 nm, f = 0.2646 (69.6%) ES 16: 411 nm, f = 0.1410 (64.0%) ES 19: 399 nm, f=0.0095 (32.8%) ES 22: 393 nm, f = 0.0361 (85.9%)	ES 14: 431 nm, f=0.0495 (45.3%)
H197N	ES 13: 447 nm, f = 0.0151 (67.0%) ES 15: 424 nm, f = 0.2121 (67.9%) ES 16: 412 nm, f = 0.1373 (69.6%) ES 18: 401 nm, f = 0.0098 (39.2%) ES 20: 396 nm, f = 0.1871 (51.2%)	ES 14
H197Q	ES 14: 432 nm, f = 0.0467 (76.0%) ES 15: 425 nm, f = 0.1205 (63.4%) ES 17: 404 nm, f = 0.4787 (28.0%) ES 18: 400 nm, f = 0.0656 (21.9%) ES 20: 398 nm, f = 0.0069 (69.2%) ES 21: 397 nm, f = 0.3539 (34.7%) ES 22: 394 nm, f = 0.5739 (53.3%)	ES 13 ES 16

†Mutant ES data coloured blue if blue shifted relative to a similar (close in E) WT ES, red if red shifted relative to a similar WT ES, black if not shifted relative to a similar WT ES and grey if no WT analogue exists.

In table 2.8, the ES data that is used to plot the above gaussian curves to simulate the P absorption band is shown. A colour scheme has been included to try to understand which ES are giving rise to the shifts in the P_{D1} absorption band in an effort to understand why there is a poor match with the experimental shift for H197Q. ES which are coloured red are red-shifted compared to a WT ES of a similar energy, data which is coloured blue is blue shifted relative to a similar WT ES, black ES are not shifted compared to the WT and grey ES are for ES which do not have WT analogues.

ES 14 and 15 for the WT are compared to H197A and H197N ES 13 and 15, and WT ES 19 and 22 are compared to H197A ES 19 and 22 and H197N ES 18 and 20 respectively. It can be seen from table 2.8 that, as most of these four states are blue shifted or not shifted at all relative to WT excitation energies, the red shift in the P absorption band arises due to the appearance of a new P_{D1} excitation at 411-412 nm for the two mutants. The MOs for the highest contributing transitions to ES 16 for H197A and H197N are depicted below in Figures 2.17 and 2.18. In both cases (Figures 2.17 and 2.18) P_{D1} to Chl_{D1} charge transfer can be seen, meaning that H197A and H197N ES 16 are comparable to ES 18 for the WT (see Figures 1.18 and 1.22 for evidence of a P_{D1} to Chl_{D1} CT state at ES 18 for WT model 4). In this case, the reason for the overall red shift in the P_{D1} absorption band is due to a 10-11 nm shift in energy of the P_{D1} to Chl_{D1} CT state in both H197A and H197N mutants.

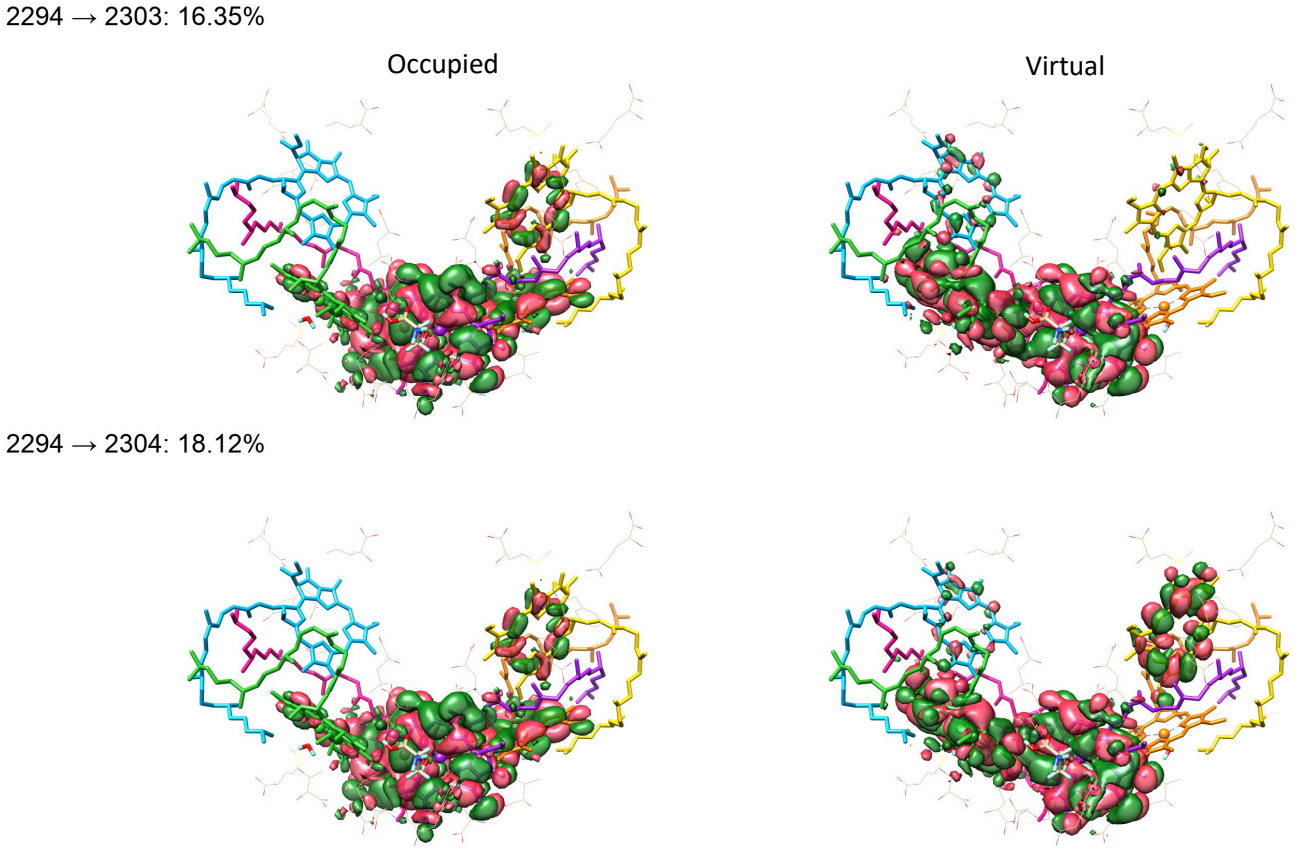
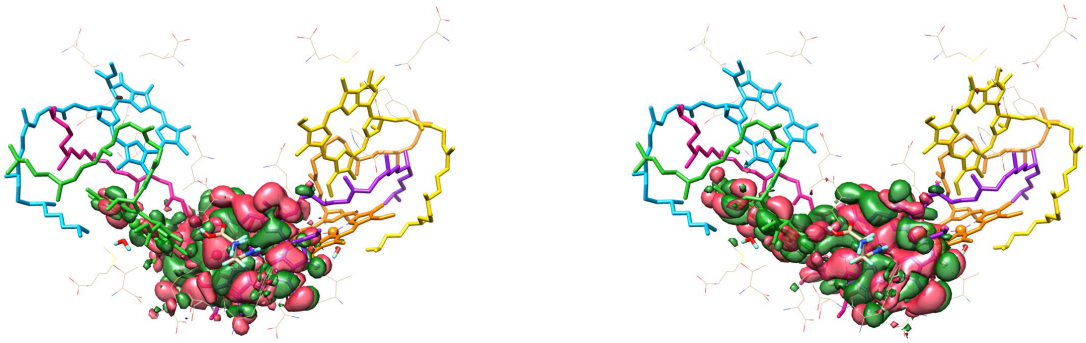


Figure 2.17 : MOs for the two highest contributing transitions to H197A ES 16 ωB97X-D/6-31G**, LEFT - Occupied MO, RIGHT – Virtual MO

2306 → 2315: 31.38%



2311 → 2315: 15.90%

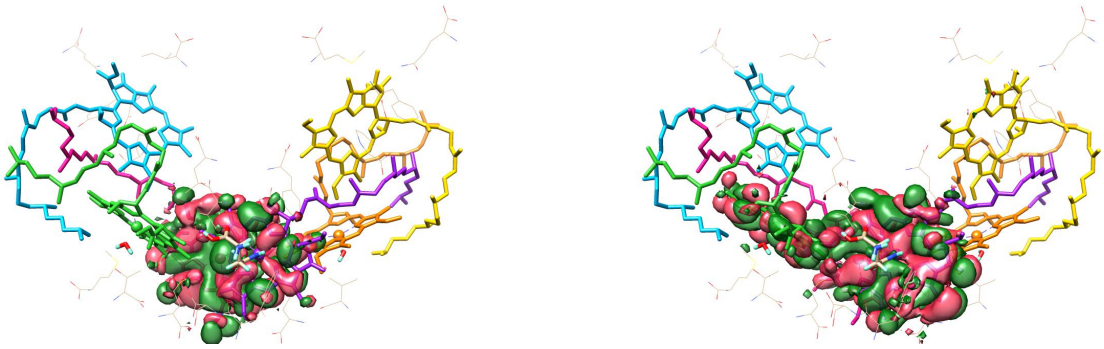


Figure 2.18: MOs for the two highest contributing transitions to H197N ES 16 ωB97X-D/6-31G**, LEFT - Occupied MO, RIGHT – Virtual MO

For H197Q however, two high oscillator strength states at high energies (ES 21 and 22) are large contributors to the blue shift in the simulated P_{D1} absorption band for H197Q, these two states do not have WT analogues. This could mean that more P_{D1} excitations lie at higher energies for the WT which have not been calculated yet. Further work would be needed to model this. The MOs for the highest contributing transitions to H197Q ES 21 and 22 are depicted below.

2303 → 2316: 17.20%

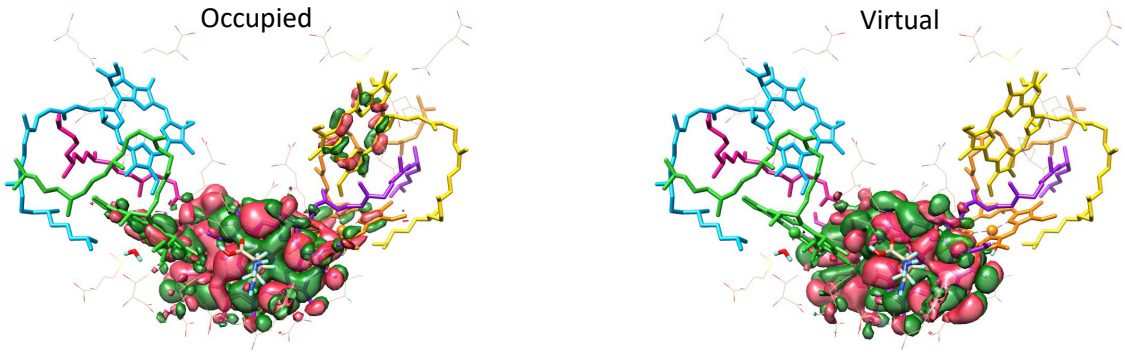


Figure 2.19: MOs for the highest contributing transition for H197Q ES 21 ωB97X-D/6-31G**, LEFT - Occupied MO, RIGHT – Virtual MO

2310 → 2314: 47.80%

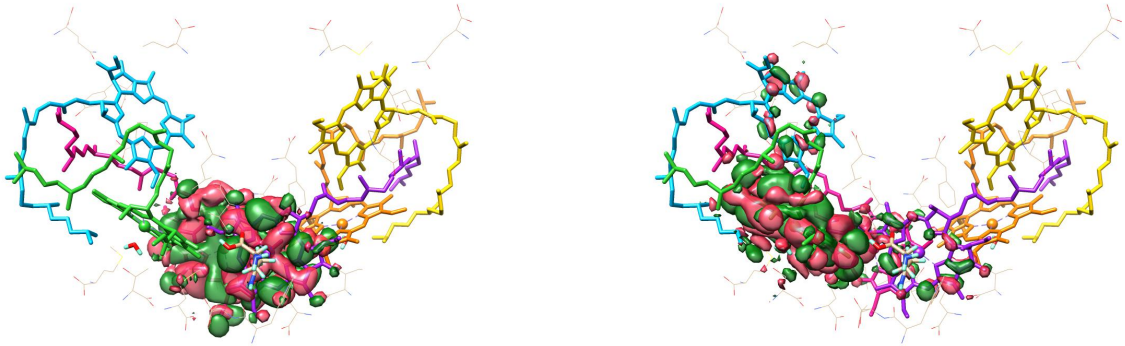


Figure 2.20 : MOs for the highest contributing transition to H197Q ES 22 ωB97X-D/6-31G**, LEFT - Occupied MO, RIGHT – Virtual MO

Contributing to the highest oscillator strength state in the Soret band for H197A (ES 20, f=1.6) MO 2297 (Figure 2.3 and Figure 2.21) and 2298 (shown in Figure 2.3) both excite into MO 2310 (Figure 2.21) with contributions of 13.9% and 8.9% to ES 20 respectively. The oscillator strength of >1 for this state indicates strong coupling in a Frenkel exciton type model for the two cofactors Chl_{D1} and P_{D2}.

2297 → 2310: 13.94%

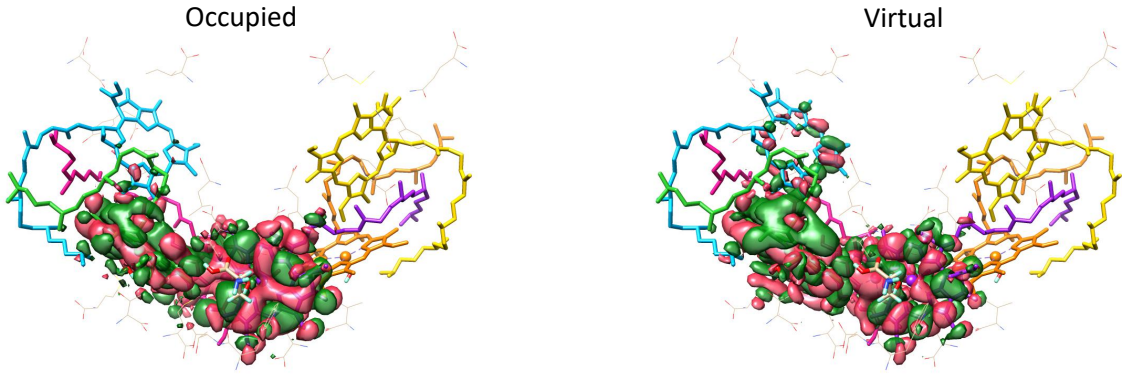


Figure 2.21 : MOs for the highest contributing transition for H197A ES 20 ωB97X-D/6-31G**, LEFT - Occupied MO, RIGHT – Virtual MO

The major contribution to H197N ES 21 (f=1.5) is from local Chl_{D1} excitation, 26.7% contribution is from transition from 2309 to 2322 (Figure 2.22) which have cofactor occupancies shown in table 2.9. Whilst there is some charge transfer for H197N ES 21 between P_{D2} and Chl_{D1}, again H197A shows a higher degree of coupling between Chl_{D1} and P_{D2}.

2309 → 2322: 26.67%

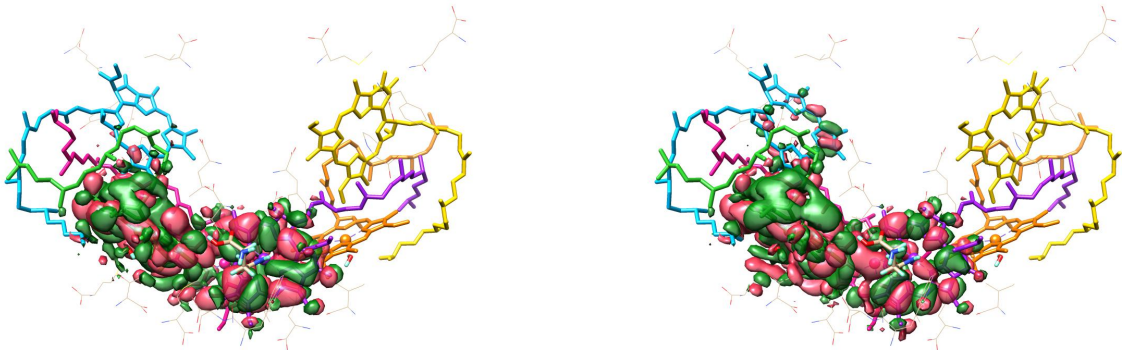


Figure 2.22 : MOs for the highest contributing transition for H197N ES 21 ωB97X-D/6-31G**, LEFT - Occupied MO, RIGHT – Virtual MO

Table 2.9 : MO occupancies for highest contributing transitions to H197A ES 20 and H197N ES 21

MO (H197A)	Phe_{D1}	Chl_{D1}	P_{D1}	P_{D2}
2297	0.2%	56.6%	7.9%	34.9%
2298	0.2%	42.4%	13.8%	43.2%
2310	0.8%	83.9%	1.8%	12.7%
MO (H197N)				
2309	0.3%	87.9%	3.9%	7.6%
2322	0.7%	90.7%	0.9%	6.9%

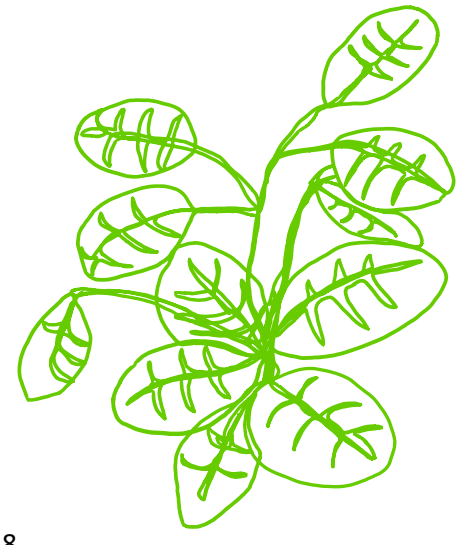
Conclusion

Several effects are seen on mutation of the residue at D2-197 to ala, asn and gln. All mutations are universally observed to raise the energy of P_{D2} excitation, the most prominent effect is seen for H197N, followed by H197A and H197Q. It follows that, as the energy of P_{D2} excitation is closest to that of Chl_{D1} for H197A, this leads to a strong coupling between the two cofactors which reveals itself as highly delocalised P_{D2}/Chl_{D1} MOs for this mutant. Some delocalisation over Chl_{D1} for all three mutants is observed for the P_{D2} excitations, as well as a reduction in the coupling between P_{D1} and P_{D2} (more localised P_{D1} orbitals for the mutants than for the WT). Interestingly this result points to a possible new excitonic interaction which could mean there is an alternative CS path available to H197A, and to a lesser extent H197N.

Increased delocalisation of inactive branch MOs is seen for H197A, although the extent of delocalisation is still small compared to the delocalisation that is seen over Chl_{D1}/P_{D2} (Chl_{D2} orbitals lie >80% on Chl_{D2} compared to Chl_{D1} orbitals which are <60% on Chl_{D1}). H197N and H197Q have inactive branch transitions which are localised to a similar extent as for the WT.

P chlorophyll transitions appear in the reverse order for H197A and H197N than they do for H197Q and the WT. P_{D2} to P_{D1} is the major contributing transition class for ES 3 for H197A and H197N and featured MOs which are very local to P_{D1} (>90%), in contrast the WT P_{D2} to P_{D1} transition dominating in ES 4 excited from an occupied MO which lay 80% on P_{D2} into a virtual MO where electron density was evenly shared between the two P chlorophylls. P_{D1} to P_{D2} transitions contribute to ES 4-6 for H197A and H197N and feature MOs delocalised over P_{D2} and Chl_{D1}.

Overall, whilst there is a good agreement between experimental P_{D1} band shifts for H197A and H197N and not H197Q, although H197Q being the least changed from WT is consistent with experimental findings[33, 38,46]. Further work may be needed to confirm the full effect of the mutation on the higher energy region of the spectrum.



Chapter Three: Site-Directed Mutation of the P_{D1} Ligand, D1-198

Qualifying Model Results with Direct Comparison to Experiment

Chapter Overview

Following on from mutant models studied in chapter two, and building on the insight from varying the model sizes and methods in the first chapter, three further mutant RC models are examined. The residue at site D1-198 is a histidine in the WT and ligates the P_{D1} core RC pigment. Its mutation to alanine, asparagine and glutamine are explored, providing the active branch analogues to all results presented in chapter 2.

Results & Discussion

This chapter contains results of calculations on mutant models where the residue at D1-His-198 was mutated. The three models discussed, with histidine 198 mutated to alanine (H198A), asparagine (H198N) and glutamine (H198Q), are depicted in Figure 3.1.

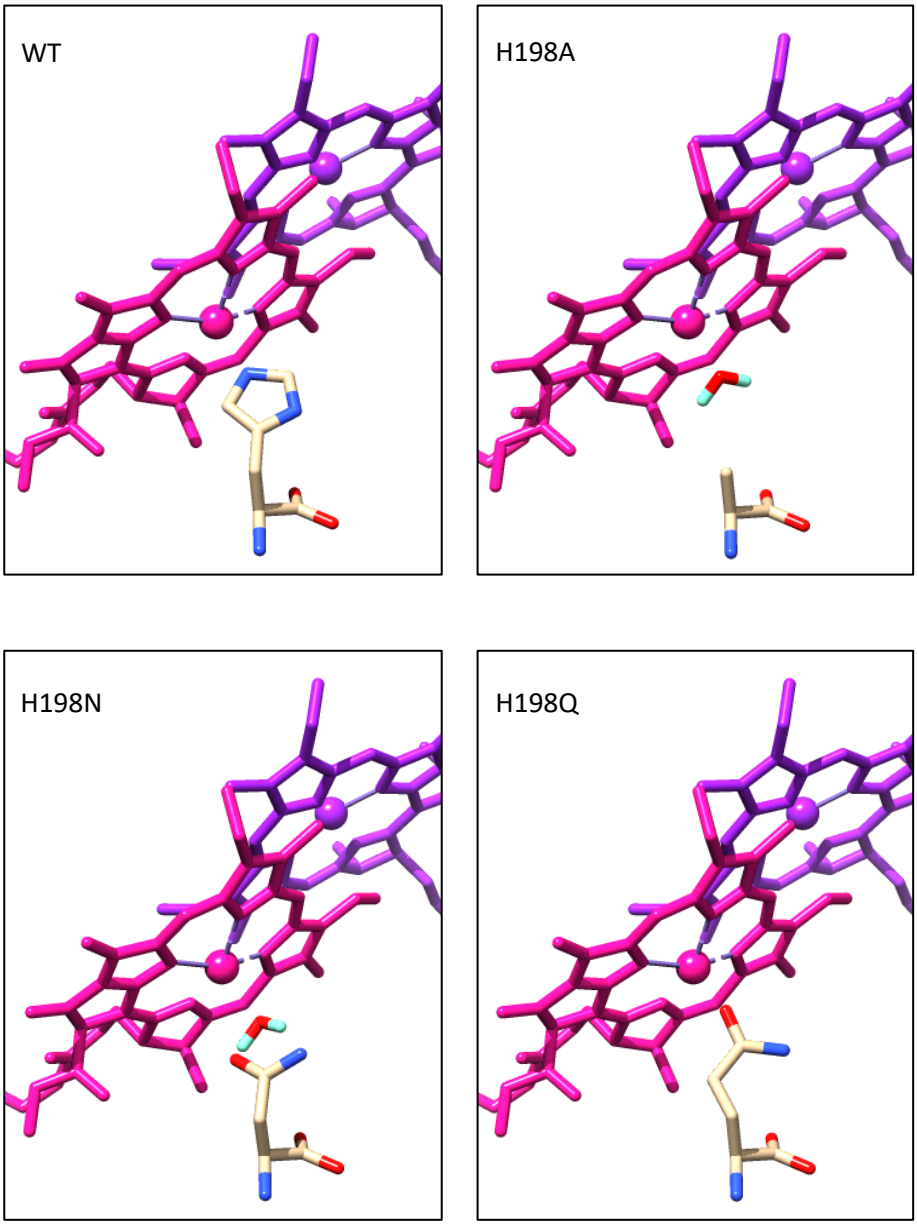


Figure 3.1 : Closeup of the P chlorophylls (P_{D1} – pink, P_{D2} – purple) for WT (top left) and mutated D1-198 residue from histidine to alanine (H198A, top right), asparagine (H198N, bottom left) and glutamine (H198Q, bottom right). Mutation to alanine and asparagine left space for a water molecule to coordinate the P_{D2} chlorophyll which is also shown.

As in the previous chapter, H198A and H198N had a water molecule included to coordinate the P_{D1} metal centre whilst the H198Q mutant did not. All results presented in this chapter are from calculations with ωB97x-

D and 6-31G** and all models comprise six pigments (P_{D1}, P_{D2}, Chl_{D1}, Chl_{D2}, Phe_{D1} and Phe_{D2}) with their full phytol chains, two water molecules ligating Chl_{D1} and Chl_{D2} and a total of 23 amino acids (see table 1.2 from chapter one). Comparisons can therefore be drawn between the results of calculations on these mutant models and the WT model 4 results presented in chapter 1.

Excitation Energies and Oscillator Strengths

Table 3.1 : Excitation energies and oscillator strengths for WT model 4 and three mutant RC models, His-198-Ala (H198A), His-198-Asn (H198N) and His-198-Gln (H198Q)†

State	Absorption Band	Energy (nm)				Oscillator Strength			
		WT	H198A	H198N	H198Q	WT	H198A	H198N	H198Q
1	Q_Y	692.46	692.27	692.36	692.27	0.3746	0.3681	0.3731	0.3742
2		687.23	687.13	687.03	687.16	0.4202	0.4074	0.4094	0.4191
3		675.93	671.81	672.89	674.91	0.0915	0.0499	0.0574	0.0881
4		665.76	665.33	665.17	665.78	0.1809	0.2393	0.2513	0.1994
5		660.4	659.91	660.23	660.37	0.4078	0.4322	0.3771	0.4104
6		655.24	654.85	654.72	655.13	0.1396	0.1167	0.1491	0.1353
7	Q_X	584.79	584.35	585.12	585.12	0.0663	0.0676	0.0665	0.067
8		579.51	579.21	579.37	579.28	0.0825	0.0815	0.0811	0.0811
9		576.34	576.51	576.04	576.46	0.0668	0.0651	0.0678	0.0659
10		571.17	565.51	571.51	566.62	0.0383	0.1046	0.0355	0.0475
11		565.19	561.12	565.23	565.33	0.1015	0.0299	0.101	0.0931
12		560.76	559.59	559.65	560.93	0.0715	0.0768	0.0711	0.0747
13	Soret	443.03	456.51	442.61	442.04	0.0757	0.0635	0.0796	0.0739
14		432.99	430.1	434.89	434.09	0.0329	0.0743	0.0357	0.0267
15		426.15	416.84	426.69	424.77	0.1421	0.0724	0.1447	0.1428
16		410.44	405	408.95	412.62	0.0008	0.1661	0.0012	0.0005
17		404.14	401.35	404.37	404.27	0.4472	0.1063	0.3468	0.2759
18		401.23	399.43	402.59	402.67	0.0377	0.2949	0.0813	0.1167
19		400.68	397.3	400.78	400.62	0.0787	0.0026	0.0772	0.0616
20		399.46	395.68	399.58	399.55	0.1436	1.2044	0.2327	0.2134
21		398.55	393.8	397.68	399.04	0.3109	0.9659	0.4369	0.0301
22		396	392.44	395.14	397.6	0.0051	0.1773	0.0098	0.4373

†All four models contain 23 amino acids, full phytol chains and two water molecules coordinating Chl_{D1} and Chl_{D2}, H198A and H198N also include a water molecule coordinating P_{D1} in place of the mutated His residue N. Results calculated with ωB97x-D and 6-31G**. Oscillator strengths for H198A ES 20 and 21 not included in colouring by value (yellow cells), cell shading as in table 1.9 in chapter 1 and table 2.1 in chapter 2: Energies (left, colour gradient for each model within each band showing degeneracies and intervals in excitation energies), Oscillator strengths (right, green shading for brighter states and purple shading for darker states across the whole spectrum, yellow for states where f>1).

In the Q_Y region the mutation to H198A increases the oscillator strength of ES 4 and 5 relative to the WT values, whilst lowering the oscillator strength of ES 2 and 3. The highest oscillator strength state for H198A is therefore ES 5, whilst for WT it was ES 2. The mutation to H198N also raises the oscillator strength of ES 4 relative to the

other states in the Q_Y region, however the WT ordering of brightest to darkest state is retained in this region of the spectrum for this mutant.

A rise in the excitation energy of ES 3 is seen for all three mutants relative to the WT. H198A is the most affected for which ES 3 is 4 nm higher in energy than WT ES 3, followed by H198N (3 nm) and H198Q (1 nm). Note that the lower oscillator strength of this state may mean that a shift in its energy is not detectable by spectroscopy.

In the Q_X region of the spectrum the excitation at ES 10 in the WT (571 nm, f=0.038) appears to have been pushed up in energy for H198A by ~10nm, with H198A ES 11 (561 nm, f=0.0299) the most similar oscillator strength. ES 11 in the WT (565 nm, f= 0.1015) bears most resemblance to H198A ES 10 (566 nm, f=0.1046). ES 10 is also upshifted in energy from 571nm in the WT to 567nm for H198Q.

Finally, in the Soret band, H198A has two highly bright states, ES 20 (f=1.2044) and ES 21 (f=0.9659). Both of which have ~2-3x greater oscillator strength than the brightest states for the WT in this region (ES 17 : f=0.4472 and ES 21: f=0.3109).

For H198N, ES 14 and 18 are 1.9 and 1.4 nm lower in energy than these states in the WT whilst ES 16 appears 1.5 nm higher. Bright Soret band states ES 17 and 21 have altered oscillator strengths for H198N compared to the WT, with ES 21 being the brightest state in this region for the H198N, whilst ES 17 is the brightest for the WT.

In the Soret region there is evidence to suggest that ES 21 and 22 have swapped for H198Q in relation to the WT (see Figure 3.13 and discussion below), otherwise the ordering of states appears to be the same as the WT. ES 17 has a lower oscillator strength for the H198Q mutant than for the WT and ES 20 has a higher oscillator strength for the mutant than the WT. ES 22 has the highest oscillator strength in the H198Q Soret region, above that of its WT counterpart ES 21. The excitation energies of ES 13 and 15 have shifted up for the H198Q mutant by ~1 nm and ~1.4 nm each. Whereas ES 14, 16 and 18 are all lower than their WT counterparts, by 1.1, 2.2 and 1.4 nm respectively.

Overall the WT and H198Q appear to give the most similar excitation profiles, whilst H198A is the most altered compared to the WT.

Excited State Profiles – Cofactor Excitations

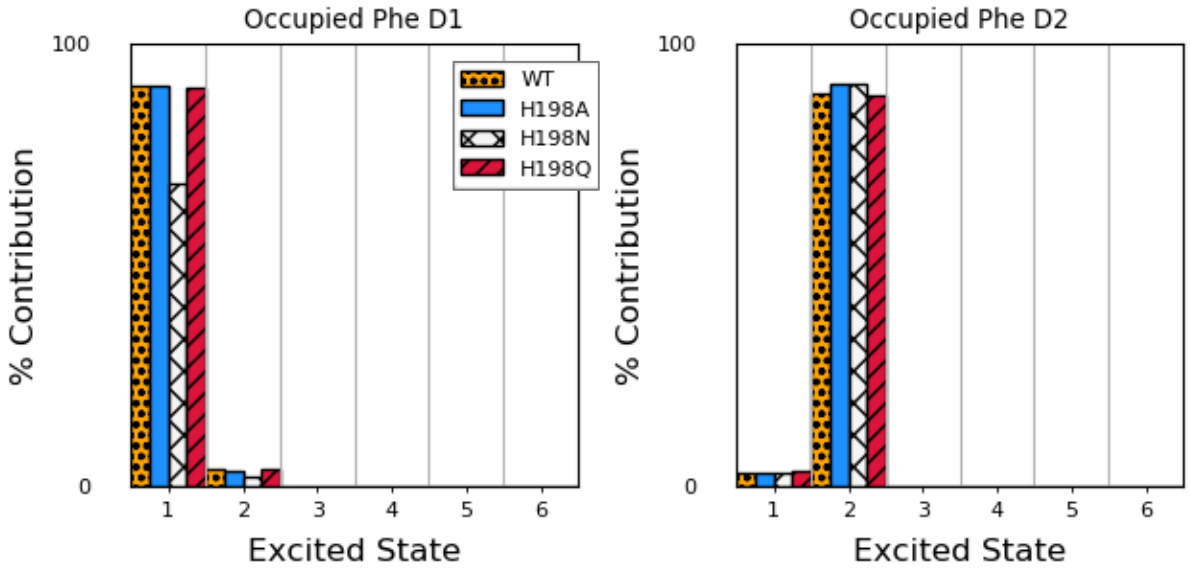


Figure 3.2 : Phe excitations in the Q_Y region for WT model 4 and three mutants H198A, H198N and H198Q all calculated ωB97X-D/6-31G**

For the WT and all three mutants Phe_{D1} and Phe_{D2} excitation dominate in the first and second ES (Figure 3.2). Differences between the WT and mutant excited state profiles can be seen for P chlorophyll excitations (figures 3.3 and 3.5).

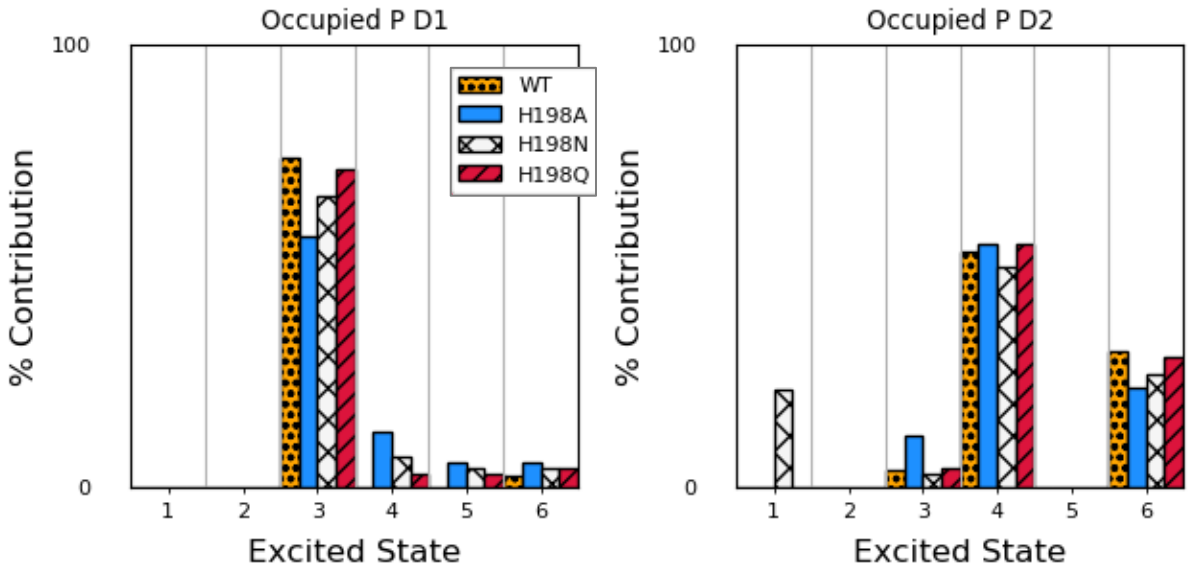


Figure 3.3 : P chlorophyll excitations in the Q_Y region for WT model 4 and three mutants H198A, H198N and H198Q all calculated ωB97X-D/6-31G**

From Figure 3.3 it can be seen that ES 3 is attributed to P_{D1} excitation for the WT and all three mutants. The increase in the excitation energy of ES 3 for all mutants may suggest that mutating D1-His-198 to Ala, Asn and Gln has increased the energy of P_{D1} excitation. Furthermore, ES 3 has reduced oscillator strength compared to

the WT (see table 3.1), meaning that the likelihood of this transition is decreased on mutation. In addition, the contribution to ES 3 from P_{D1} excitation is lower for the mutants than the WT (P_{D1} contribution to ES 3 is lowest for H198A and highest for H198Q), and contribution from Chl_{D1} excitation is higher than the WT (Chl_{D1} contribution to ES 3 is highest for H198A and lowest for H198Q, see Figure 3.4 below). More mixing of Chl_{D1} excitation into ES 3 for the three mutants could therefore be contributing to the higher excitation energy and lower oscillator strength of ES 3.

Conversely, the higher relative oscillator strength for ES 4 suggests that P_{D2} excitation has become more favourable for this mutant. H198N ES 4 has the most increased oscillator strength compared to the WT ES 4, for this mutant we also see mixing of P_{D2} excitation into ES 1 suggesting a lower energy for P_{D2} excitation for H198N. H198A ES 3 also has an increased contribution from P_{D2} excitation to the WT, suggesting that P_{D2} excitation is lower in energy for this mutant as well.

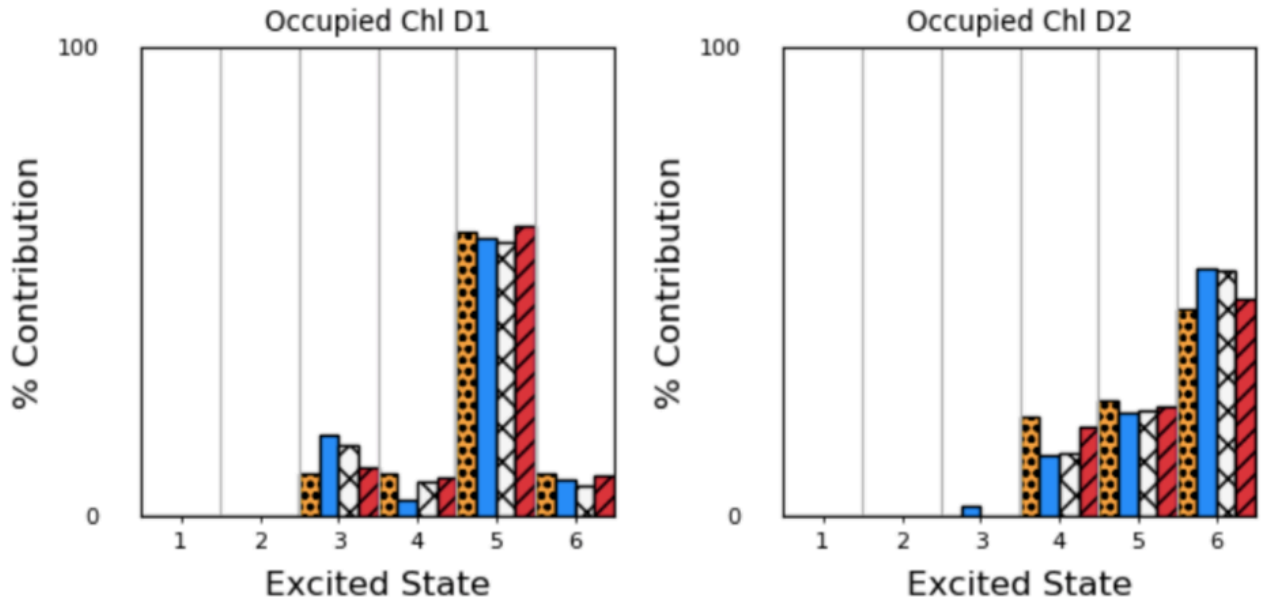


Figure 3.4 : Chl_{D1} and Chl_{D2} excitations in the Q_Y region for WT model 4 and three mutants H198A, H198N and H198Q all calculated ωB97X-D/6-31G**

Chl_{D1} excitation dominates in the fifth and Chl_{D2} excitation contributes increasing amounts to ES 4-6, dominating the sixth ES for the WT and all three mutants (see Figure 3.4). Figure 3.4 further demonstrates that mutant H198Q is the most similar to the WT out of the three mutants discussed in this chapter.

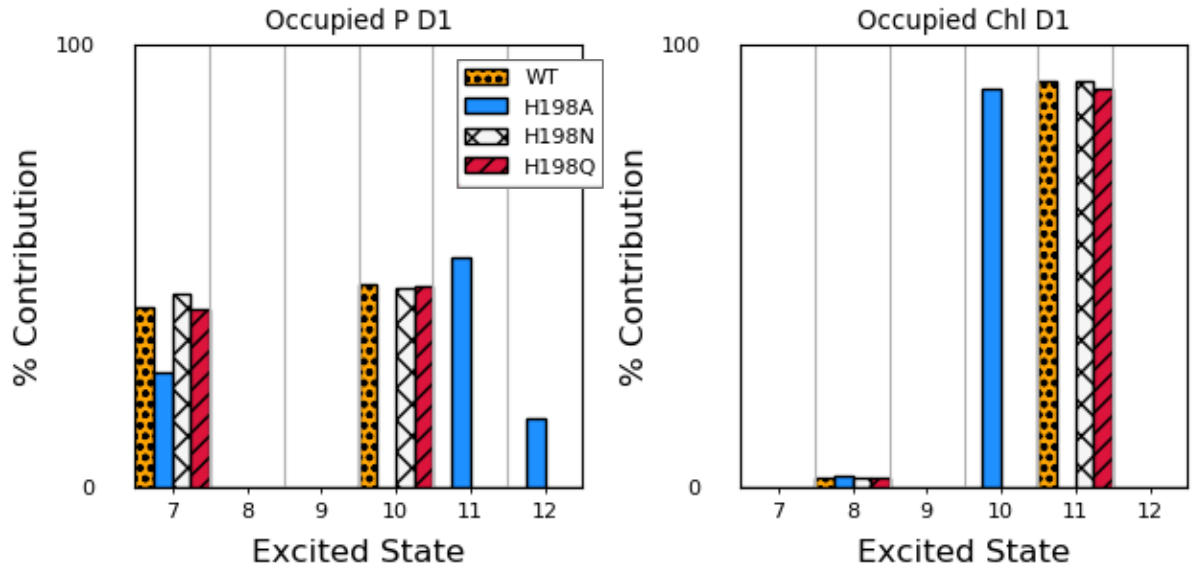


Figure 3.5 : P_{D1} and Chl_{D1} excitations in the Q_X region for WT model 4 and three mutants H198A, H198N and H198Q all calculated ωB97X-D/6-31G**

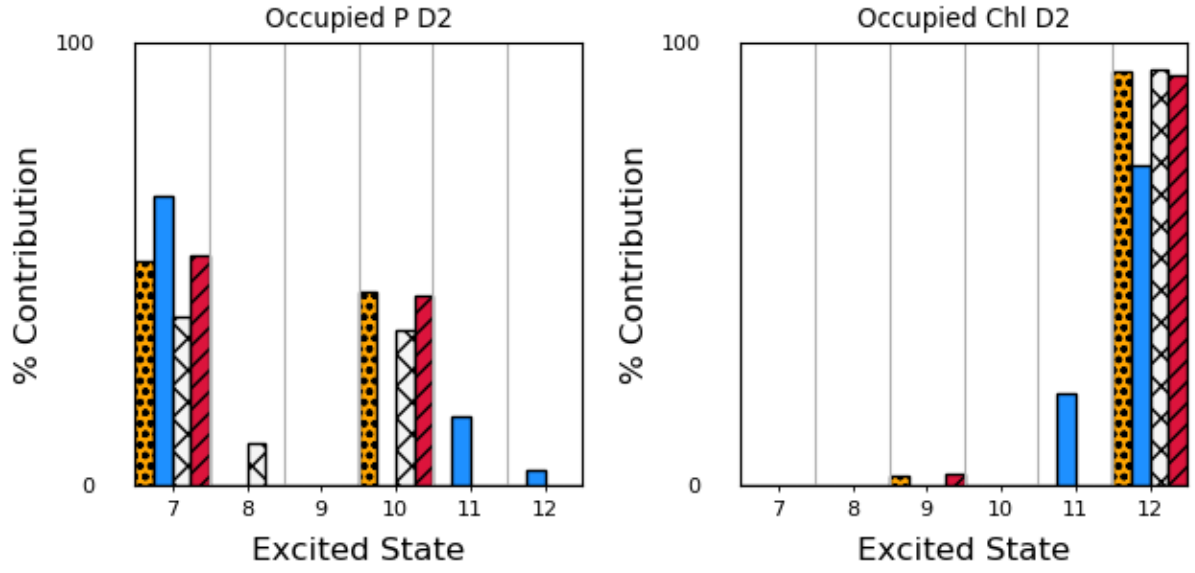


Figure 3.6 : P_{D2} and Chl_{D2} excitations in the Q_X region for WT model 4 and three mutants H198A, H198N and H198Q all calculated ωB97X-D/6-31G**

As suspected from table 3.1, we can see from Figure 3.5 that the H198A ES 10 is attributed to Chl_{D1} excitation, most similar to WT ES, whilst H198A ES 11 and 12 have mixed contributions from P_{D1}, P_{D2} and Chl_{D2} excitations (see figures 3.5 and 3.6). This is consistent with this mutation increasing the energy of P_{D1} excitation as seen in the Q_Y region. Similarly, ES 10 has ~4.5 nm higher excitation energy for H198Q than the WT and has a high contribution from P_{D1} excitation.

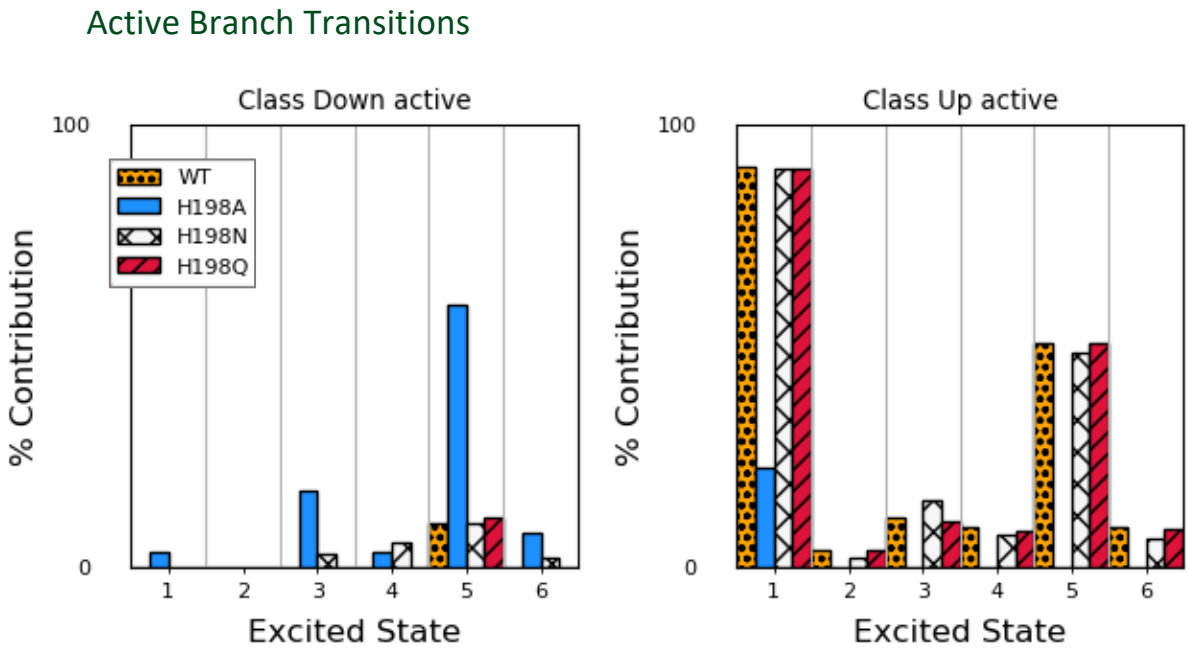


Figure 3.7 : Active branch transition contributions to ES 1-6 for WT model 4 and three mutants H198A, H198N and H198Q all calculated ωB97X-D/6-31G**

Looking at Figure 3.7, the H198A mutant is the only model for which the transitions contributing to the Q_Y states have significantly changed relative to the WT of the three mutants studied. Where for WT, H198N and H198Q the first ES is dominated by an up active transition, the H198A mutant has only very low contribution to ES 1 from this transition class. Also, in ES 5 the H198A mutant is dominated by transitions down the active branch, a transition class that is not seen to dominate for any ES in this region for WT, H198N or H198Q. In short, the H198A mutation appears to have destroyed the preference for CT to travel up the active branch that was seen so clearly for the WT model 4 result.

Considering the MOs that contribute to ES 1 for H198A (see Figure 3.8) it can be seen that this state is dominated by a very local Phe_{D1} excitation.

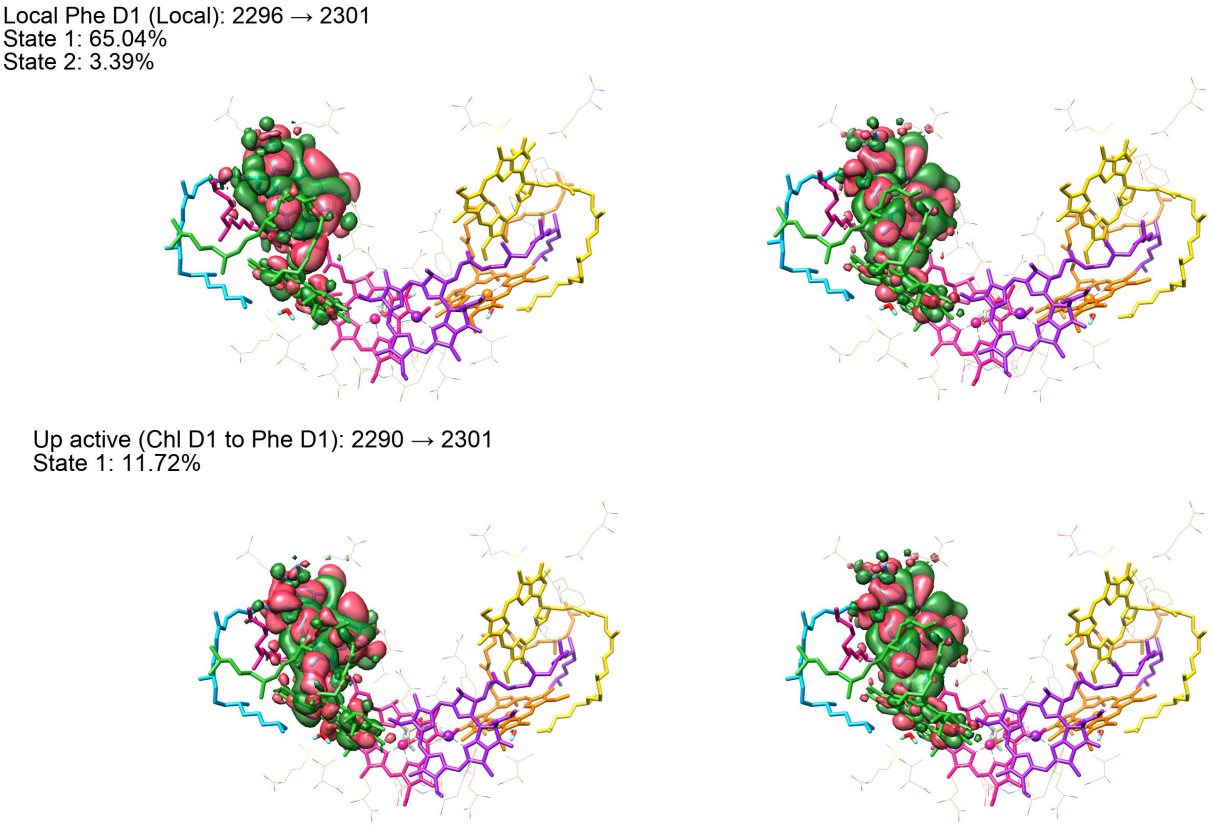


Figure 3.8 : MOs making up the highest contributing transitions for ES 1 for H198A, LEFT COLUMN - Occupied MO, RIGHT COLUMN – Virtual MO

In fact all cofactors experience a decrease in electron density when going from MO 2296 to 2301 (see table 3.2).

Table 3.2 : Active branch MOs for H198A (ωB97X-D/6-31G**)

MO	Phe_{D1}	Chl_{D1}	P_{D1}	P_{D2}
2296	98.31035	0.91466	0.41547	0.00164
2301	98.19927	0.8468	0.37014	0.00155

Therefore we can say with confidence that this excitation is a local Phe_{D1} excitation, and that it does not fall into any of our six CT categories ('up active', 'down active' *etc.*). In contrast, for the WT the dominant transition for ES 1 was 'up active' with clear movement from Chl_{D1} into Phe_{D1}. The dominant WT ES 1 transition is therefore similar to the transition from 2290 to 2301 (bottom panel in Figure 3.8) which constitutes 11% of ES 1 for H198A. Evidence from Stark spectroscopy on H198A and related mutants has shown that mixing of CT and exciton states is reduced for mutant RCs compared to the WT.[33] Certainly, the CT character of H198A ES 1 is negligible compared with the WT ES 1, which could be characterised as a $Chl_{D1}Phe_{D1}$ exciton with $Chl_{D1}^{+}Phe_{D1}^{-}$ CT character.

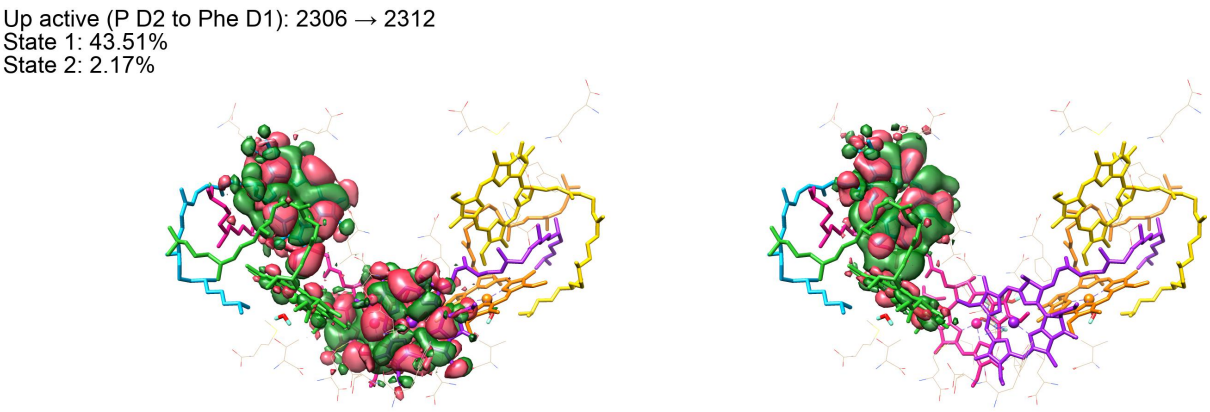


Figure 3.9A : MOs making up the highest contributing transition for ES 1 for H198A, LEFT COLUMN - Occupied MO, RIGHT COLUMN – Virtual MO

The MO diagrams for H198N look very similar to the WT results, except for the dominant transition in ES 1 (Figure 3.9A). Whilst the virtual MO 2312 bares a strong resemblance to WT MO 2313, the occupied MO 2306 looks unlike any MO we have seen before as there is a high degree of delocalisation over the P chlorophylls and the Phe_{D1}.

Table 3.3 : Dominant transitions to ES 1 for H198N and WT model 4 (both with ωB97X-D/6-31G**).

MO Type	MO	Phe_{D1}	Chl_{D1}	P_{D1}	P_{D2}
Occupied	H198N 2306	65.59159	0.5006	14.524	18.75726
	WT 2308	97.9282	1.0246	0.5327	0.15294
Virtual	H198N 2312	98.32906	0.7156	0.37129	0.00124
	WT 2313	98.32761	0.71777	0.37037	0.00125

ES 5 for H198A is attributed to the 'down active' transition class, with movement from Chl_{D1} to P_{D1} (MO diagrams in Figure 3.9B and cofactor occupancy in table 3.3). For the WT the dominant transition contributing to ES 5 was 'up active': P_{D2} to Phe_{D1} from MO 2309 to 2315 (see table 3.3).

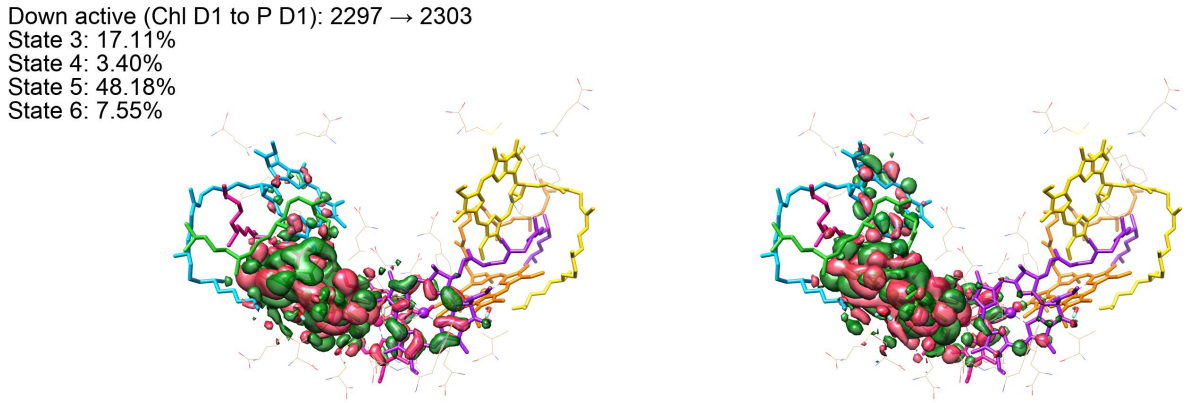


Figure 3.9B: MOs making up the highest contributing transition for ES 5 for H198A, LEFT COLUMN - Occupied MO, RIGHT COLUMN – Virtual MO

Table 3.4 : Dominant transitions to ES 5 for H198A (top two rows) and WT model 4 (both with ωB97X-D/6-31G**).

MO	Phe_{D1}	Chl_{D1}	P_{D1}	P_{D2}
2297	0.43634	98.14808	0.41784	0.71202
2303	0.91463	96.77327	1.34983	0.41029
WT 2309	0.3854	98.03817	0.35943	0.92839
WT 2315	0.79503	97.84238	0.46082	0.35186

WT model 4 and the H198A mutant have similar transitions contributing to ES 5 (see table 3.4), both centred on the Chl_{D1}, both increasing on P_{D1} and Phe_{D1} and decreasing on Chl_{D1} and P_{D2}. However, the significant difference is that the P_{D1} increase is greater than Phe_{D1} increase for the H198A mutant, meaning the overall movement during the transition is down the active branch instead of up. This gives us some insight into the subtle changes in the energies of the cofactors which lead to the active branch pathway being overall less favourable for the H198A mutant than the WT. If we consider mixing of CT states $P_{D2}^{+}P_{D1}^{-}$ and $Chl_{D1}^{+}Phe_{D1}^{-}$ with exciton states as illuminated by Stark spectroscopy experiments [33] to be producing these ES it may be argued that a different proportion of these two CT states gives rise to two different transition classes to WT and H198A.

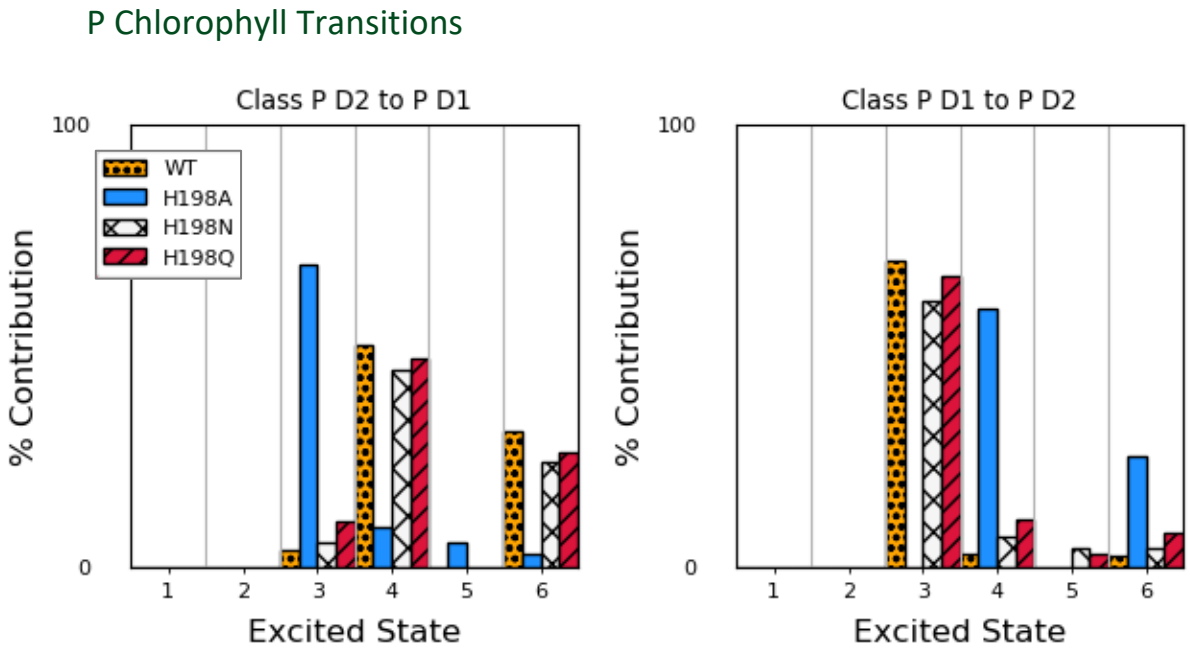


Figure 3.10 : P chlorophyll transition contributions to ES 1-6 for WT model 4 and three mutants H198A, H198N and H198Q all calculated ωB97X-D/6-31G**

From Figure 3.10 it can be seen that the P chlorophyll transitions appear in the reverse order for H198A as for the WT, with P_{D1} to P_{D2} dominating in ES 4 and P_{D2} to P_{D1} dominating in ES 3. From Figure 3.3 however we see that ES 3 is centred on P_{D1} and ES 4 on P_{D2}, which is the same result as for the WT. This could be explained by a reordering of CT state energies: $P_{D1}^{+}P_{D2}^{-}$ has increased in energy, whilst $P_{D2}^{+}P_{D1}^{-}$ has decreased. An interesting observation, considering the experimental observation that there is reduced mixing of exciton and CT states for this mutant, as a change in the CT state energies would affect mixing between states.

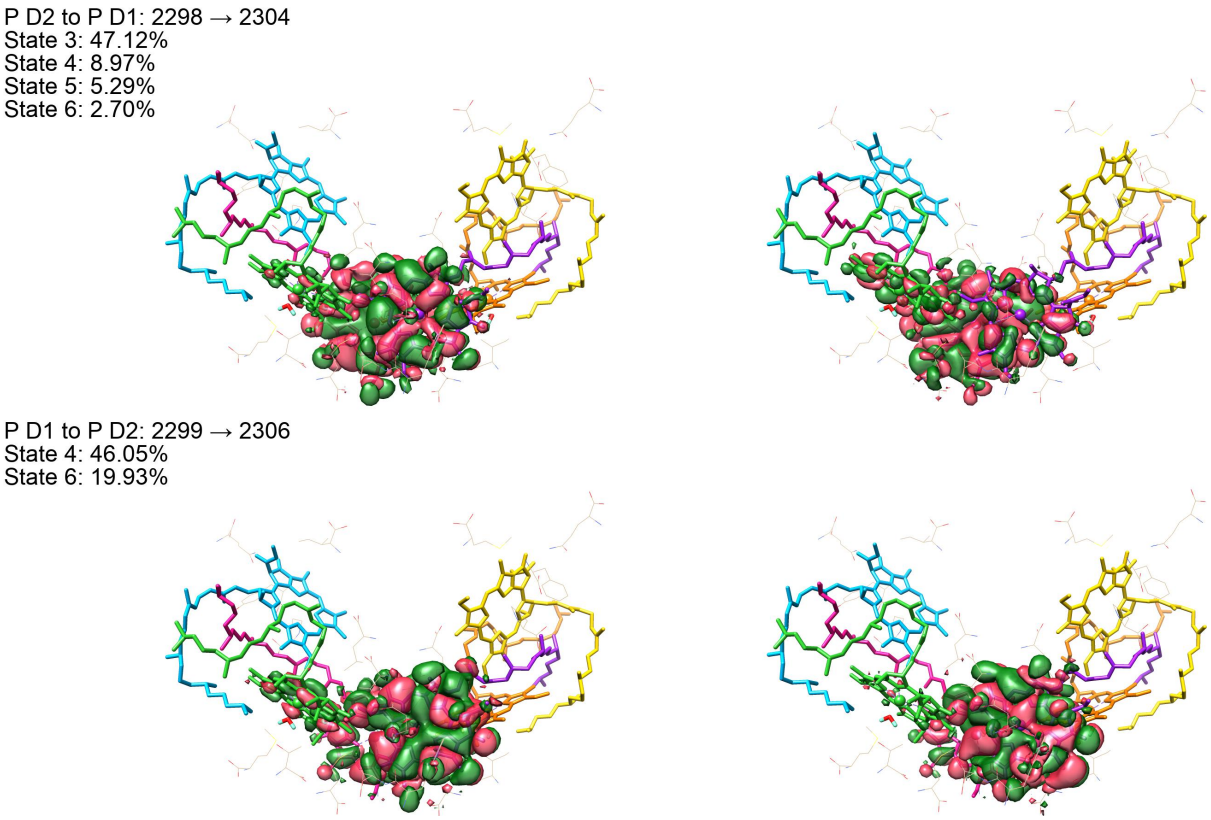


Figure 3.11 : MOs making up the highest contributing transition to ES 3 and 4 for H198A, LEFT COLUMN - Occupied MO, RIGHT COLUMN – Virtual MO

The second observation that can be made from looking at ES 3 and 4 for H198A is that there is less CT character (movement overall between cofactors from occupied to virtual orbitals) for the mutant than for the WT (see table 3.5, 23% movement between P chlorophylls for 2298 – 2304 (ES 3) and ~6% for 2299 to 2306 (ES 4) P_{D1} to P_{D2} compared to WT ~30% for both states, see table 3.6). This finding would tend to support the experimentally observed reduced mixing between CT states and exciton states for this mutant.

Table 3.5 : P chlorophyll MOs for H198A

MO type	MO	P_{D1} Occupancy	P_{D2} Occupancy
Occupied	2298	72.9%	25.8%
	2299	7.5%	91.3%
Virtual	2304	95.9%	1.9%
	2306	1.7%	97.0%

Table 3.6 : P chlorophyll MOs for WT model 4

MO type	MO	P_{D1} Occupancy	P_{D2} Occupancy
Occupied	WT 2311	12.0%	86.6%
	WT 2312	87.7%	11.2%
Virtual	WT 2317	56.1%	42.5%
	WT 2318	42.2%	56.7%

There is less CT mixing for H198Q P chlorophyll transitions also, characterised by a lower overall transfer of electron density between the P chlorophylls in transitions dominating ES 3 and 4 (see Figure 3.12 and table 3.7), compared with the WT (table 3.6). From tables 3.6 and 3.7, it can be seen that ~14-16% of the total MO density is transferred between the P chlorophylls in ES 3 (2310 to 2316) and ES 4 (2309 to 2315) for H198Q. This observation is in keeping with experimental findings.[33]

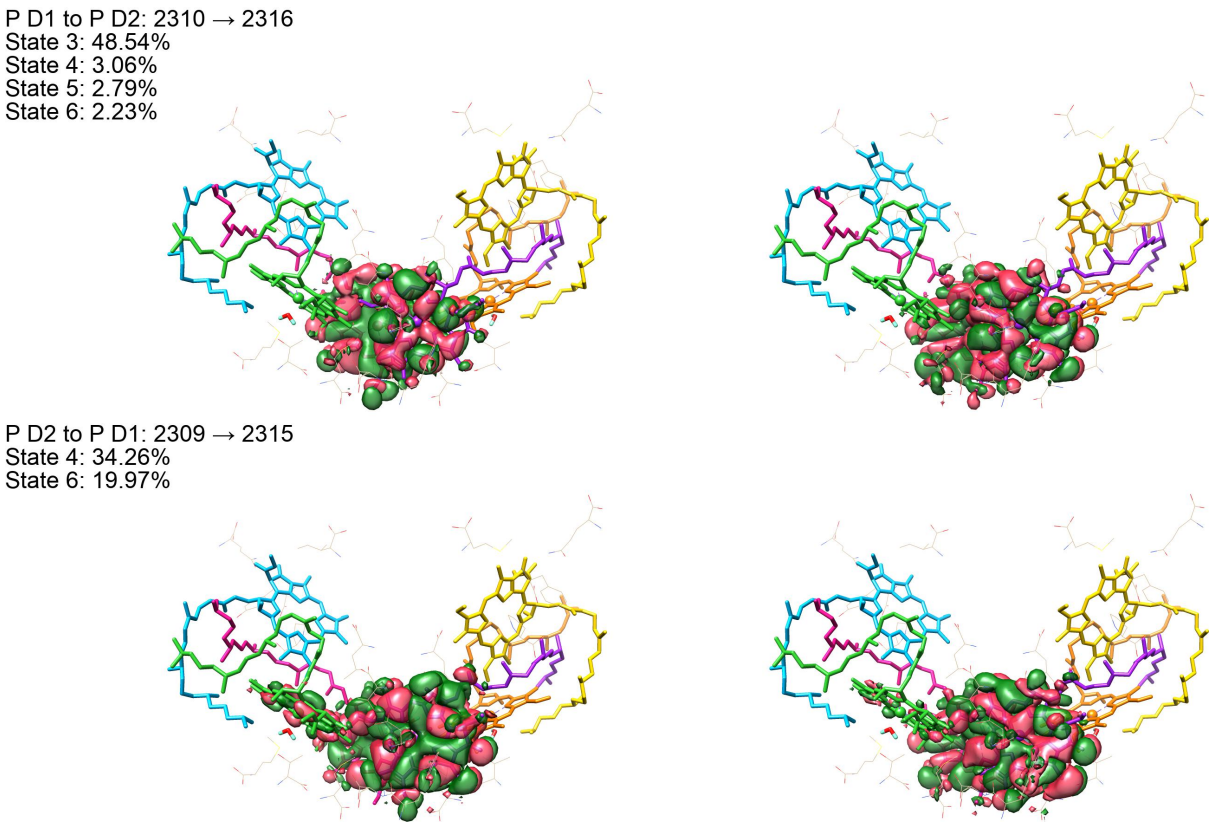


Figure 3.12 : MOs making up the highest contributing transition to ES 3 and 4 for H198Q, LEFT COLUMN - Occupied MO, RIGHT COLUMN – Virtual MO

Table 3.7 : P chlorophyll MOs H198Q

MO type	MO	P_{D1} Occupancy	P_{D2} Occupancy
Occupied	2309	12.0%	86.8%
	2310	88.3%	10.6%
Virtual	2315	26.0%	72.6%
	2316	72.2%	26.7%

Soret Region and Charge Transfer States

Examining the Soret region is more complex than the Q_Y and Q_x bands, but uncovers some supporting evidence for conclusions made earlier in this chapter.

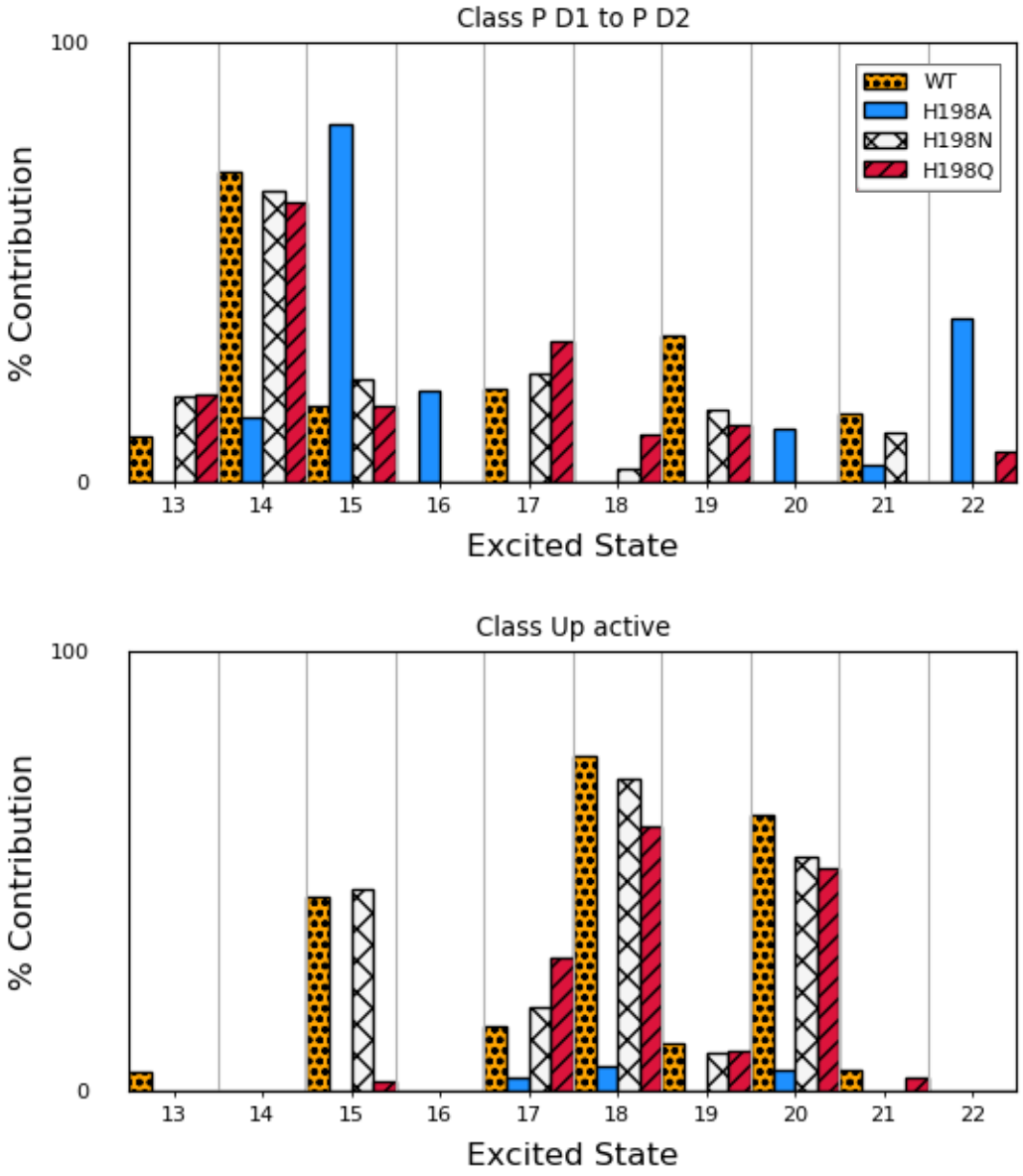


Figure 3.13 : Excitation out of P_{D1} (P_{D1} to P_{D2} and up active transitions) contributions in the Soret region for WT model 4 and three mutants H198A, H198N and H198Q all calculated ωB97X-D/6-31G**

For H198A, no states in the Soret region are dominated by transition up the active branch, as can be seen in Figure 3.13. Overall, for the WT the up active transition dominated in ES 1, 5, 8, 15, 18 and 20, but for H198A only ES 8 has a dominant contribution from this transition (see appendix four). In contrast, down active transitions contribute highly to ES 18 and dominate ES 5, 10, 17 and 20 for H198A. Note also from table 3.1 that the highest oscillator strength states in each band are ES 5, 10 and 20 respectively, all of which are attributed to transitions down the active branch. This evidence further suggests that the mutation to H198A

has destroyed the preference for CT to travel up the active branch. CT states in the Soret region for WT, H198A, H198N and H198Q are listed in table 3.8.

Table 3.8 : CT states in the Soret region for WT model 4 and three mutants H198A, H198N and H198Q all calculated ωB97X-D/6-31G**[†]

ES	WT[‡]	H198A[‡]	H198N	H198Q
13	$P_{D2} \rightarrow P_{D1}$	$P_{D2} \rightarrow P_{D1}$	$P_{D2} \rightarrow P_{D1}$	$P_{D2} \rightarrow P_{D1}$
14	$P_{D1} \rightarrow P_{D2}$	$P_{D2} \rightarrow P_{D1}$	$P_{D1} \rightarrow P_{D2}$	$P_{D1} \rightarrow P_{D2}$
15		$P_{D1} \rightarrow P_{D2}$	$P_{D1} \rightarrow P_{D2}$	
16	$P_{D2} \rightarrow Chl_{D2}$	$P_{D2} \rightarrow P_{D1}$	$P_{D2} \rightarrow Chl_{D2}$	$P_{D2} \rightarrow Chl_{D2}$
17	$P_{D1} \rightarrow P_{D2}$		$P_{D1} \rightarrow P_{D2}$	
18	$P_{D1} \rightarrow Chl_{D1}$		$P_{D1} \rightarrow Chl_{D1}$	$P_{D1} \rightarrow Chl_{D1}$
19	$P_{D1} \rightarrow P_{D2}$	$P_{D2} \rightarrow Chl_{D2}$		
20				
21	$P_{D2} \rightarrow P_{D1}$			$P_{D1} \rightarrow Chl_{D2}$
22	$P_{D1} \rightarrow Chl_{D2}$		$P_{D1} \rightarrow Chl_{D2}$	

[†]"CT states" are defined by dominant transition from one cofactor to another

[‡]confirmed with D_{CT} metric analysis, see Figure 1.18 for WT results and appendix four for H198A results.

Figure 3.13 also shows that mutating to H198N has lowered the energy of CT out of P_{D1}, because the identity of the states with >1nm lower excitation energy than the WT are attributed to P_{D1} to P_{D2} and P_{D1} to Chl_{D1} CT states (ES 14 and 18 for both H198N and WT). In contrast CT out of P_{D2} towards Chl_{D2} has increased in energy (ES 16 for both H198N and WT).

From table 3.1 it was seen that ES 13 and 14 are closer in energy for H198Q than for the WT, and there is a greater mixing of the P chlorophyll transitions in these two states for the mutant than for the WT (see top panel in both figures 3.13 and 3.14). Otherwise there is a high degree of similarity between WT and H198Q in the Soret region as there was in the lower energy regions of the spectrum.

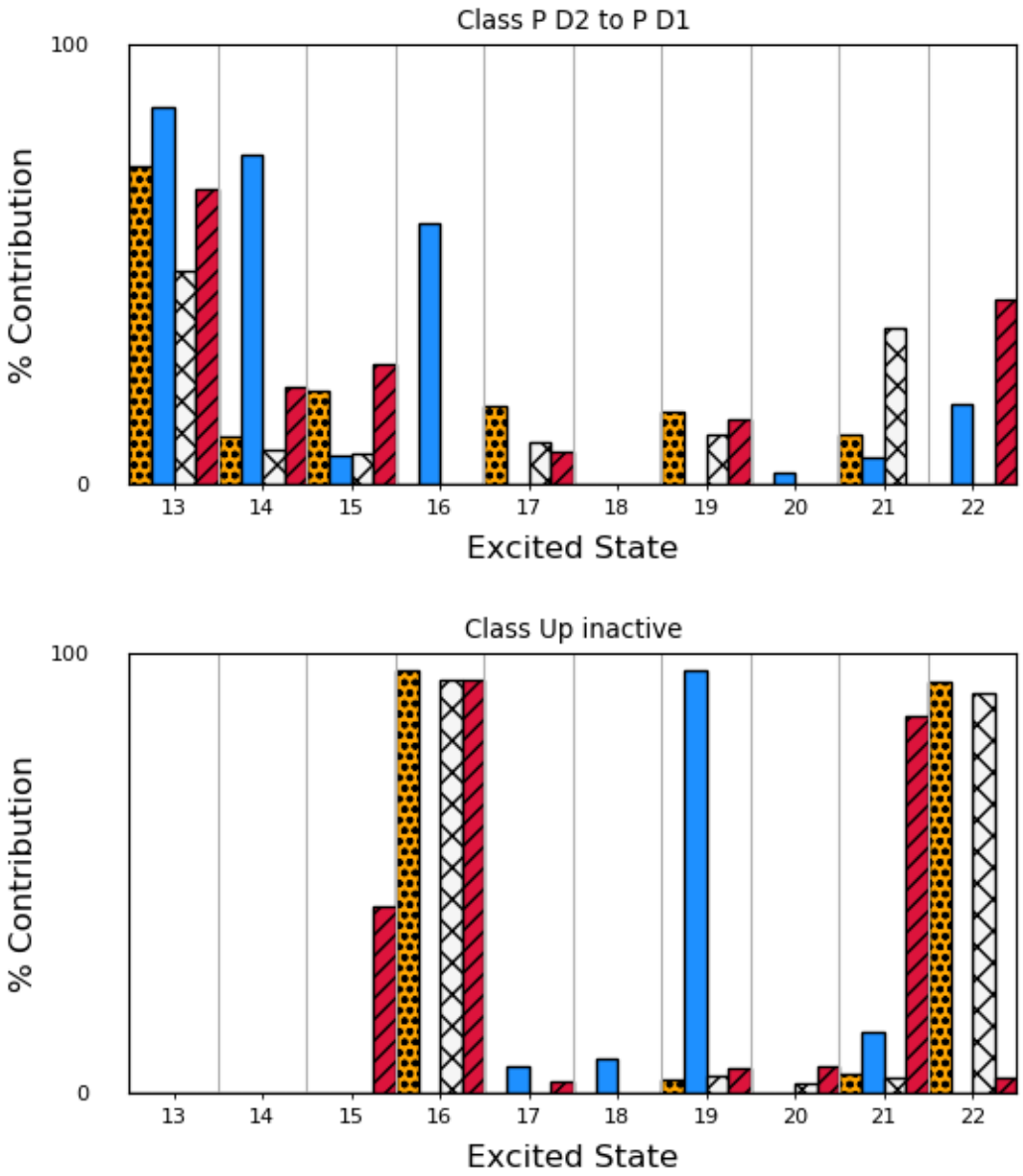


Figure 3.14 : P_{D2} to P_{D1} and up inactive transition contributions in the Soret region for WT model 4 and three mutants H198A, H198N and H198Q all calculated ωB97X-D/6-31G**

Soret Region - Absorption Difference Spectral Shifts

Taking the ES which are dominated by excitation out of P_{D1} occupied orbitals, it was possible to simulate the bleaching band in the P^+-P difference spectra (experimental spectrum shown in Figure 3.15) for the WT model 4 and the three D1-198 mutants. Experimental spectra show a shift higher in energy for all three mutants, which the simulated spectra have all reproduced (see Figure 3.16). However, the shift in the experimental spectra is greatest for H198Q and the least pronounced for H198A, whereas the models presented in this chapter have H198A shifted the farthest to the blue and H198N and H198Q each blue shifted less than H198A (see Figure 3.16). Assuming the H198A model to be the incorrect one, with over-estimated shift of the P_{D1} band, it could be said that the H198N and H198Q models were still a good match with experiment. There are several possible reasons why H198A may not match experimental P_{D1} band shifts.

Firstly, the effect of the alanine mutant on the planarity of the porphyrin ring[50] may be significant enough to red-shift the site energy of the P_{D1} in the H198A mutant. Further work is needed to explore this effect in the presence of the water ligand. Secondly, as discussed in the previous chapter, it is possible that in calculating only the lowest 22 excited states is not enough to see the full effect of band shifts in the Soret region. It could be that more excited states have to be calculated in order to see this effect. There may be more states close in energy to ES 22 which involve excitation of P_{D1}, unfortunately the size of these models is limiting as to the number of states that can be calculated within reasonable computational time. Finally, considering also how the mutation to H198A affects the P_{D2} band (see Figure 3.17 below), it appears that the dominant P bands are split for the alanine mutant, and not for the asparagine and glutamine or WT RCs. Considering the failure of DFT to predict higher energy excitation energies (*e.g.* Rydberg states) without diffuse functions, this could account for the discrepancy between the model results and the experimental result. Could it be that the reduction of CT-exciton mixing[33] in the alanine mutant leads to a purer exciton state for $P_{D1}P_{D2}$ (see discussion above also for evidence of this) and that at a higher level of theory the correct overall shift would be seen for H198A (less pronounced than H198N and H198Q)?

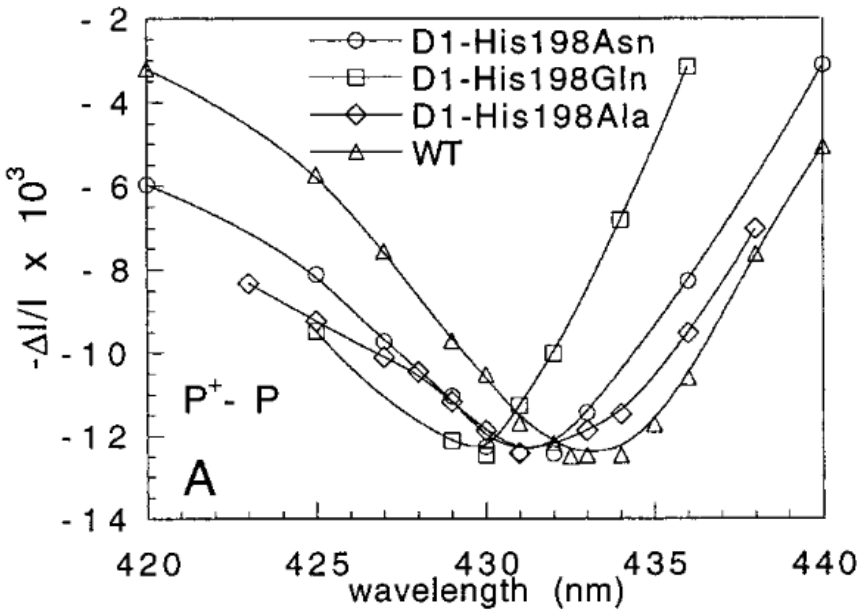


Figure 3.15 : P^+-P difference spectra measured 1 μs after a saturating actinic flash on PSII core complexes of WT and strains containing mutations H198N (D1-His198Asn), H198Q (D1-His198Gln, and H198A (D1-His198Ala). The Reprinted with permission from Diner, B. A., Schlodder, E., Nixon, P. J., Coleman, W. J., Rappaport, F., Lavergne, J., Vermaas, W. F. J. & Chisholm, D. A. Site-directed mutations at D1-His198 and D2-His197 of photosystem II in Synechocystis PCC 6803: Sites of primary charge separation and cation and triplet stabilization. *Biochemistry* **40**, 9265–9281 (2001).[38] Copyright (2001) American Chemical Society.

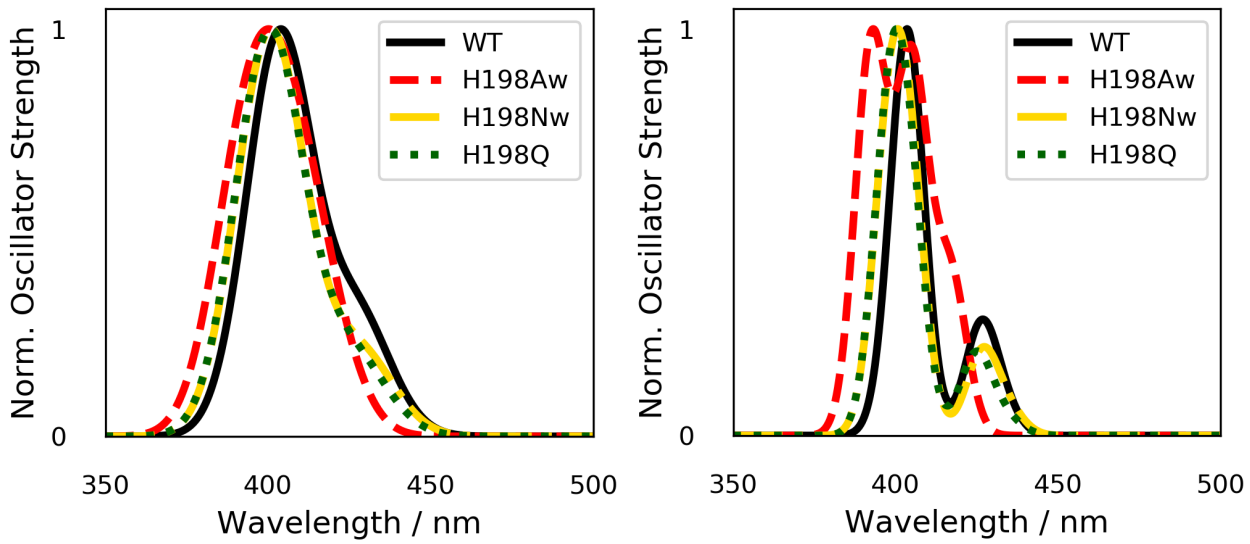


Figure 3.16 : Gaussian broadened P_{D1} absorption bands in the Soret region at two different resolutions (LEFT) c = 0.1[††], (RIGHT) c = 0.2. Only ES where P_{D1} occupied orbitals are dominant have been plotted.

[††] c is a variable in the gaussian function used to broaden the single ES peaks that determines the width of the curves produced – see python code for the generation of these simulated absorption spectra in appendix one.

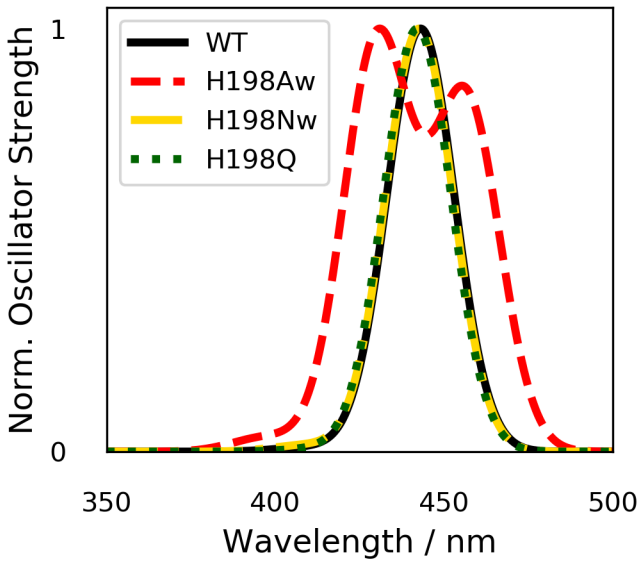


Figure 3.17 : Gaussian broadened P_{D2} absorption bands in the Soret region at two different resolutions (c = 0.1), only ES where P_{D2} occupied orbitals are dominant have been plotted.

Conclusions

Exploring three further mutant RCs, focussing on the ligand to P_{D1} as the site of mutants, finds that H198Q is very similar to WT whilst H198A is significantly different overall. There is a rise in the energy of ES 3 on mutation which is attributed to P_{D1} excitation for all three mutants, the difference between WT ES 3 excitation energy and mutant ES 3 excitation energy is greatest for H198A and smallest for H198Q. Increased mixing of Chl_{D1} excitation into ES 3 is also seen compared with the WT, likely due to the higher energy for this ES bringing it closer to the Chl_{D1} site energy. Again, H198A has the most mixing of Chl_{D1} excitation into ES 3 and H198Q the least.

Considering the nature of transitions contributing to the ES for the three mutants, transition from P_{D1} to P_{D2} (dominant in ES 3 for WT, H198N and H198Q) does not dominate ES 3 for H198A, appearing instead in ES 4. This result suggests that this mutant is destabilised to transfer away from P_{D1}.

Crucially, H198A does not display the D1 branch preference that was seen very clearly for the WT (dominant transitions in both ES 1 and ES 5 describe movement of electron density up the active branch). Instead, H198A Phe_{D1} excitation is extremely local with no movement towards any of the six cofactors calculated, movement down the active branch also contributes the dominant portion of ES 5 for H198A. H198N and H198Q however retain the WT preference and have high contribution from transitions up the active branch.

Similar to the H197A and H197N result, two higher oscillators strength states (ES 20, f=1.2 and ES 21, f=0.97) are found at higher energies for the H198A mutant, beyond the region of the spectrum previously explored for the WT. As a result of this, when comparing the P band shifts in the Soret region with the experimentally observed P^+-P absorption difference spectra for these mutants, H198A shifts too far to the higher energy end of the spectrum, beyond H198N and H198Q. It is encouraging however, that comparing H197A and H198A P_{D1} shifts gives a qualitative agreement with experimental results, and that all three mutants discussed in this chapter display band shifts to the blue.

In the next chapter, a final set of mutant models was made using the same methods, this time focussing on the pigments in the region of Chl_{D1} and Phe_{D1} on the active branch.

Chapter Four: Site-Directed Mutation in the Chl_{D1} and Phe_{D1} regions

Chapter Overview

This chapter focuses on results of four mutant RC models, two where the site of mutation was a threonine residue (D1-179) in the vicinity of the Chl_{D1} cofactor, and two where the site of mutation is a glutamine (D1-130) nearest to the Phe_{D1}. In the case of mutating D1-179 from threonine, the mutated residues histidine and glutamic acid replace the water molecule ligating the Chl_{D1} metal centre. The same method was used for the models in this chapter as in the previous two chapters on mutants of P_{D1} and P_{D2} residues.

Whilst no Soret band P absorption analysis is included in this chapter, there are comparisons that can be made between results from the D1-179 and D1-130 mutant RC models and absorption difference spectra in the Q_Y and Q_X regions. In both T179E and Q130E models a glutamic acid residue was chosen to be used instead of the charged glutamate residue, introducing a single charge to the models at this stage would make it difficult to compare mutant RC models to the existing data for WT model 4 which included all neutral residues.

A good agreement is found between the results of the T179H model and the experimental shift in Chl_{D1} absorption, the Phe_{D1} excitation is shifted to higher energies for Q130L experimentally and in the model results for this mutant. The model results also support the experimental finding that mutation to Q130L would increase singlet O_2 production due to more favourable recombination of $Phe_{D1}Q_A^-$ to $Phe_{D1}{}^-Q_A$. However, T179E and Q130E model results do not agree with experimental shifts in Q_Y and Q_X bands. One reason for this could be because of the neutral acid form chosen for mutated residues in the models, however significant further work including benchmarking of WT models including charged residues would be needed before it was possible to confirm this. Interestingly, the model results show that P chlorophyll coupling is significantly reduced for all four models, including D1-130 mutants where the site of mutation is far from the P chlorophylls. This work serves as a further reminder that RC models which divide the RC into its constituent cofactors cannot be expected to accurately describe the excited states of this complex system.

Results & Discussion

The two D1-179 mutant models were T179E (mutating D1-179 to a glutamic acid residue) and T179H (mutating D1-179 to a histidine). Shown in Figure 4.1 are the positions of the new residues after manual mutation and geometry optimisation of the new side chains for both D1-179 mutant models.

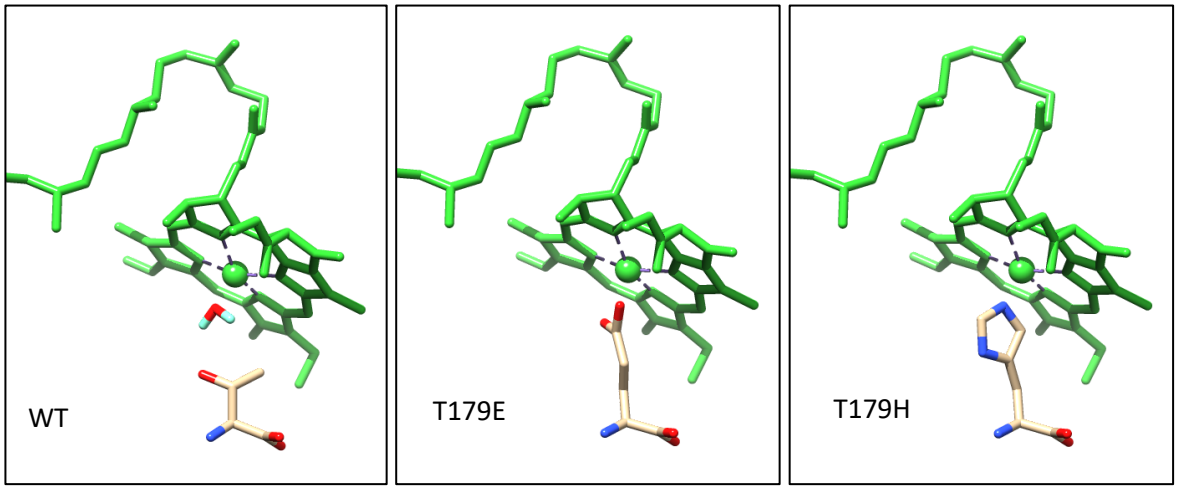


Figure 4.1 : Closeup of the Chl_{D1} chlorophyll (green) and residue at position D1-179 (wire structure: tan carbon atoms, red oxygen atoms and blue nitrogen atoms, hydrogen atoms not shown). LEFT – WT with water molecule coordinating the Chl_{D1} and Thr residue at position D1-179. MIDDLE – Thr-179-Glu mutant with D1-179 mutated to glutamic acid and acid group of the mutated residue coordinating the Chl_{D1}. RIGHT – Thr-179-His mutant with D1-179 mutated to histidine and nitrogen coordinating the Chl_{D1}.

The D1-130 residue is a glutamine in the T. vulcanus crystal structure[22] that has been used throughout this thesis (see Figure 4.2 left panel). Shown in Figure 4.2 are the positions of the two D1-130 mutant residues, glutamic acid (Q130E) and leucine (Q130L) in relation to the Phe_{D1}.

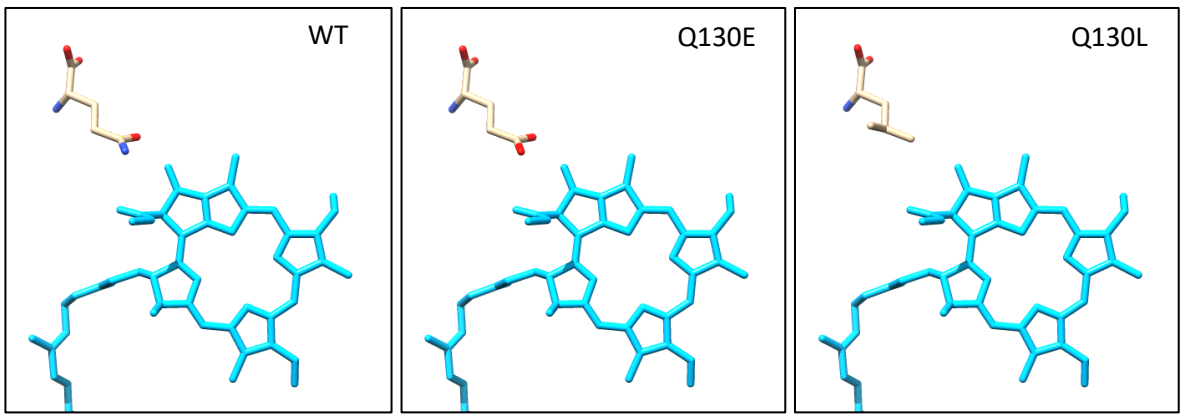


Figure 4.2 : Closeup of Phe_{D1} (blue) and D1-130 residue (tan carbon atoms, red oxygen atoms and blue nitrogen atoms). LEFT – WT with glutamine in position D1-130. MIDDLE – Gln-130-Glu mutant with glutamic acid in position D1-130. RIGHT – Gln-130-Leu mutant with leucine in position D1-130.

Experimental Findings

An electrochromic shift in the Phe_{D1} absorption once Q_A has been reduced identifies the Phe_{D1} absorption max in the Q_x region. This band is shifted 1.5 nm to the blue for the Q130L mutant relative to the WT, whereas for the Q130E mutant the same band shifts 2.5 nm to the red (see Figure 4.3).[54] Further experimental work is discussed in the introduction which showed the increased production of singlet oxygen for mutant Q130L.[55–59]

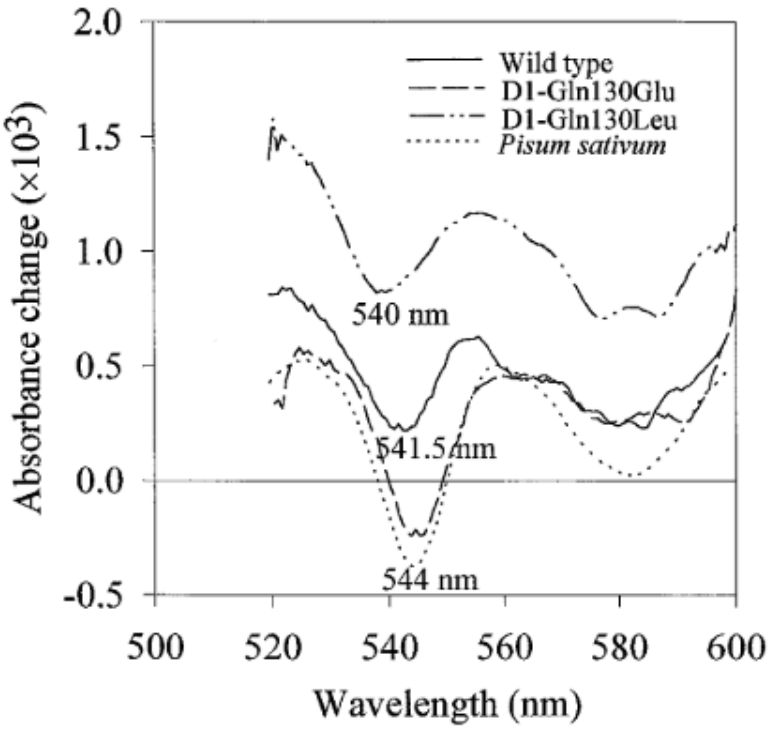


Figure 4.3 – Spectrum of the non-decaying component in the region of Phe_{D1} absorption max following selective excitation of P_{680}, for Wild Type *Synechocystis* (solid line) and mutants Q130E (D1-Gln130Glu, dashed line) and Q130L (D1-Gln130Leu, dot-dashed line). Reprinted from Giorgi, L. B., Nixon, P. J., Merry, S. a P., Joseph, D. M., Durrant, J. R., De Las Rivas, J., Barber, J., Porter, G. & Klug, D. H. Comparison of primary charge separation in the photosystem II reaction center complex isolated from wild-type and D1-130 mutants of the cyanobacterium Synechocystis PCC 6803. *J. Biol. Chem.* **271**, 2093–2101 (1996). Copyright (1996) Elsevier, Creative commons license.

For site D1-179, mutation T179H and T197E was shown to affect a bleaching band in the triplet minus singlet RC absorption spectrum in the Q_Y region (see Figure 4.4).[52] The bleach – pertaining to Chl_{D1} absorption (the site of triplet localisation) – exhibits a shift to higher energies of ~1 nm for the mutant T179E. Conversely, mutation to T179H shifts the Chl_{D1} excitation to lower energies by ~2.5 nm.

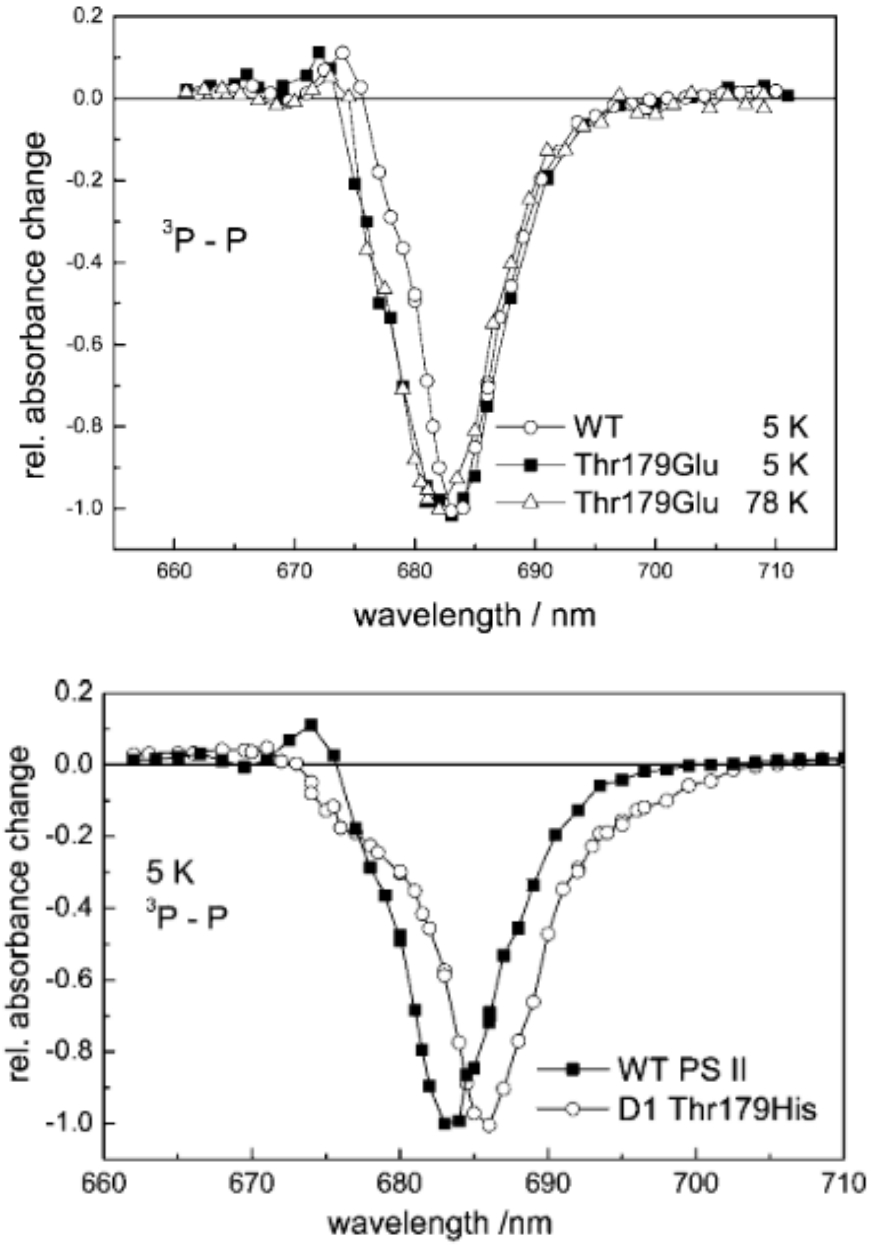


Figure 4.4 – Top - Flash-induced (^{3}P - ^{1}P) absorbance difference spectra of PS II complexes from WT *Synechocystis PCC 6803* (open circles) and T197E (D1- Thr179Glu mutant, filled squares at 5 K, open triangles at 78 K) Bottom – As above for WT *Synechocystis PCC 6803* (filled squares) and T197H (D1- Thr179His mutant, open circles measured at 5 K. Reprinted with permission from Schlodder, E., Renger, T., Raszewski, G., Coleman, W. J., Nixon, P. J., Cohen, R. O. & Diner, B. A. Site-directed mutations at D1-Thr179 of photosystem II in Synechocystis sp. PCC 6803 modify the spectroscopic properties of the accessory chlorophyll in the D1-branch of the reaction center. *Biochemistry* **47**, 3143–3154 (2008). Copyright (2008) American Chemical Society.

Excitation Energies and Oscillator Strengths

Table 4.1 : Excitation energies and oscillator strengths for WT model 4, T179E and T179H

State	Absorption Band	WT Energy (nm)	T179E Energy (nm)	T179H Energy (nm)	WT Oscillator Strength	T179E Oscillator Strength	T179H Oscillator Strength
1	Q_Y	692.46	687.86	687.89	0.3746	0.355	0.3567
2		687.23	682.17	682.25	0.4202	0.5013	0.503
3		675.93	675.64	676.6	0.0915	0.0667	0.0473
4		665.76	666.35	667.01	0.1809	0.2012	0.3552
5		660.4	661.96	664.14	0.4078	0.4024	0.1559
6		655.24	656.26	656.69	0.1396	0.117	0.2056
7	Q_X	584.79	581.43	581.45	0.0663	0.0656	0.0642
8		579.51	575.22	575.21	0.0825	0.0696	0.0684
9		576.34	570.73	571.38	0.0668	0.0527	0.048
10		571.17	566.49	570.91	0.0383	0.0483	0.0557
11		565.19	560.69	565.52	0.1015	0.1432	0.1159
12		560.76	559.85	559.84	0.0715	0.0599	0.0784
13	Soret	443.03	442.17	442.92	0.0757	0.075	0.0834
14		432.99	435.25	434.33	0.0329	0.0232	0.0163
15		426.15	424.45	424.66	0.1421	0.1621	0.1507
16		410.44	412.58	414.75	0.0008	0.0004	0.0003
17		404.14	405.49	405.13	0.4472	0.2492	0.5096
18		401.23	401.66	402.75	0.0377	0.0053	0.0022
19		400.68	401.36	401.18	0.0787	0.0129	0.1003
20		399.46	400.64	399.78	0.1436	0.1197	0.263
21		398.55	397.41	397.19	0.3109	0.5005	0.4022
22		396	395.85	395.17	0.0051	0.3364	0.0769

ES 1 excitation energy for the two D1-179 mutants is close to ES 2 excitation energy for the WT, immediately suggesting that the identity of this first ES has changed on mutation. A new excitation appears at 682 nm for both mutants at ES 2, this is the brightest state for both mutants in this region. A decrease in energy for ES 4-6 compared to the WT is also seen for both mutants, this is more pronounced for the T179H mutant than the T179E mutant. The oscillator strength of ES 5 is greatly reduced for the T179H mutant (from 0.4 in the WT to 0.16 for T179H) and instead ES 4 and 6 oscillator strengths are increased.

In the Q_X region ES 7 for the two 179 mutants is close to the WT ES 8 excitation energy. It is possible to map the mutant ES 8 and 9 to WT ES 9 and 10 given these all have similar excitation energies, however a new

excitation appears for T179H around 571 nm (either ES 9 and 10 as they are near degenerate). A new excitation at 560 nm then appears for T179E (either ES 11 or ES 12 as they are near degenerate). ES 11 also has an increased oscillator strength for both mutants (from 0.1 in the WT to 0.14 in T179E and 0.12 in T179H).

~1-4 nm lower excitation energies are seen in the Soret region for the two mutants in ES 14, 16 and 17 compared with the WT and ~1 nm higher excitation energies are seen for the two mutants for ES 15 and 21. T179H has high oscillator strength states ES 17 and 21, like the WT, and T179E has bright Soret states 21 and 22.

Table 4.2 : Excitation energies and oscillator strengths for WT model 4, Q130E and Q130L

State	Absorption Band	WT Energy (nm)	Q130E Energy (nm)	Q130L Energy (nm)	WT Oscillator Strength	Q130E Oscillator Strength	Q130L Oscillator Strength
1	Q_Y	692.46	687.79	687.63	0.3746	0.3566	0.3764
2		687.23	682.72	678.33	0.4202	0.4955	0.4821
3		675.93	676.25	676.28	0.0915	0.0832	0.1034
4		665.76	666.46	666.27	0.1809	0.1829	0.1414
5		660.4	662.2	662.13	0.4078	0.3697	0.3632
6		655.24	656.51	656.5	0.1396	0.1404	0.1416
7	Q_X	584.79	581.36	581.35	0.0663	0.0654	0.0656
8		579.51	575.42	575.42	0.0825	0.0693	0.0684
9		576.34	571.41	571.4	0.0668	0.0538	0.0483
10		571.17	568.23	566.46	0.0383	0.0246	0.0581
11		565.19	565.07	560.34	0.1015	0.144	0.1261
12		560.76	560.1	560.07	0.0715	0.077	0.0612
13	Soret	443.03	443.75	443.82	0.0757	0.0815	0.0814
14		432.99	433.63	433.54	0.0329	0.0159	0.0159
15		426.15	425.01	425.03	0.1421	0.1483	0.1474
16		410.44	413.23	413.54	0.0008	0.0004	0.0003
17		404.14	404.34	404.29	0.4472	0.4144	0.4277
18		401.23	400.91	401.05	0.0377	0.0676	0.0305
19		400.68	400.56	400.64	0.0787	0.035	0.0779
20		399.46	400.11	399.52	0.1436	0.0103	0.01
21		398.55	398.7	398.62	0.3109	0.3702	0.4545
22		396	397.42	397.05	0.0051	0.1853	0.0905

As for the T179 mutants, the Q130 mutant ES 1 both appear at similar excitation energies to WT ES 2. New excitations appear at 683 and 678 nm for Q130E and Q130L respectively in ES 2. ES 2 is again the brightest

state in the region for both Q130 mutants. A reduction in the oscillator strength of ES 5 is seen for both Q130 mutants relative to the WT. In the Q_X region, again the ES 7 excitation energy for both mutants matches WT ES 8. New excitations instead appear at 568 (ES 10) for Q130E and 560 (ES 11 and 12, degenerate) for Q130L. The oscillator strength of ES 11 rises for both Q130 mutants as well as for the T179 mutants. Little variation is seen in the Soret region for the Q130 mutants compared with the WT. ES 15 is ~1 nm higher in energy for the mutants compared with the WT and ES 16 and 22 are between ~1 and ~3 nm lower in energy for mutants than for WT. Like the WT, ES 17 and 21 are the brightest states in the Soret region for both Q130E and Q130L.

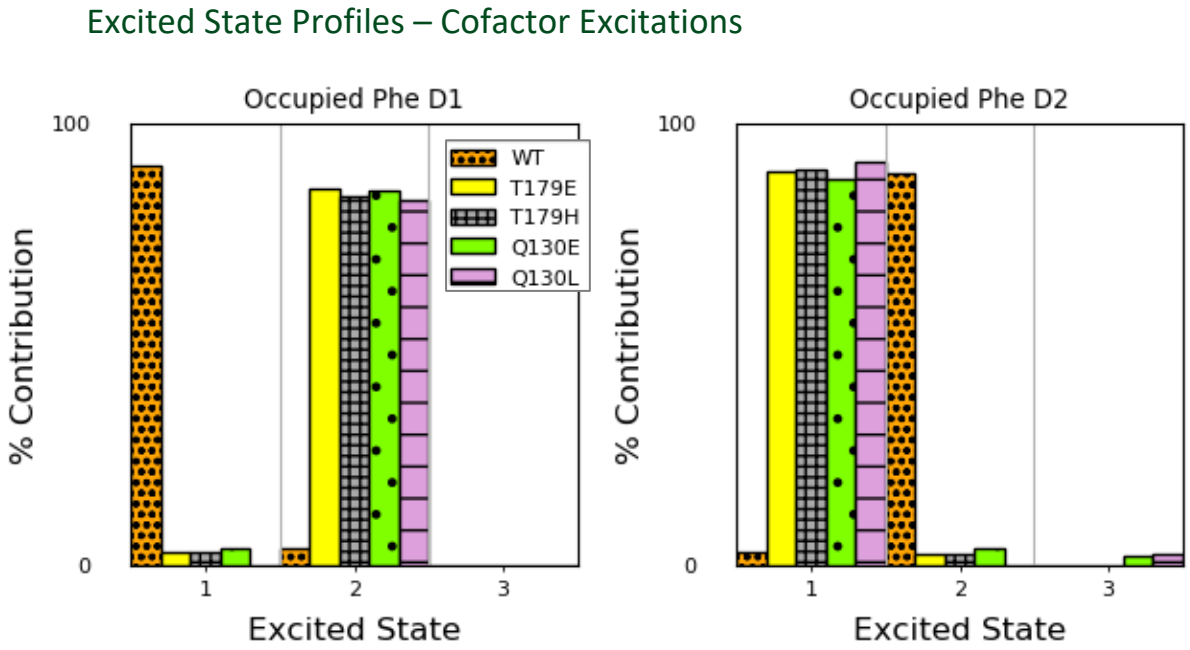


Figure 4.5 : Contribution from Phe occupied orbitals to ES 1-3 for WT model 4, T179E, T179H, Q130E and Q130L

We find that Phe_{D1} has risen in energy for all four mutants, dominating in ES 2 instead of ES 1 (WT). Looking at the excitation energies in tables 4.1 and 4.2 this is the equivalent of a ~10 nm rise in energy for Phe_{D1} excitation for T179 mutants and Q130E, and ~14 nm for Q130L compared to the WT Phe_{D1} excitation. Note also that ES 2 is the brightest state in the Q_Y region for all four mutants and that this is attributed to Phe_{D1} excitation.

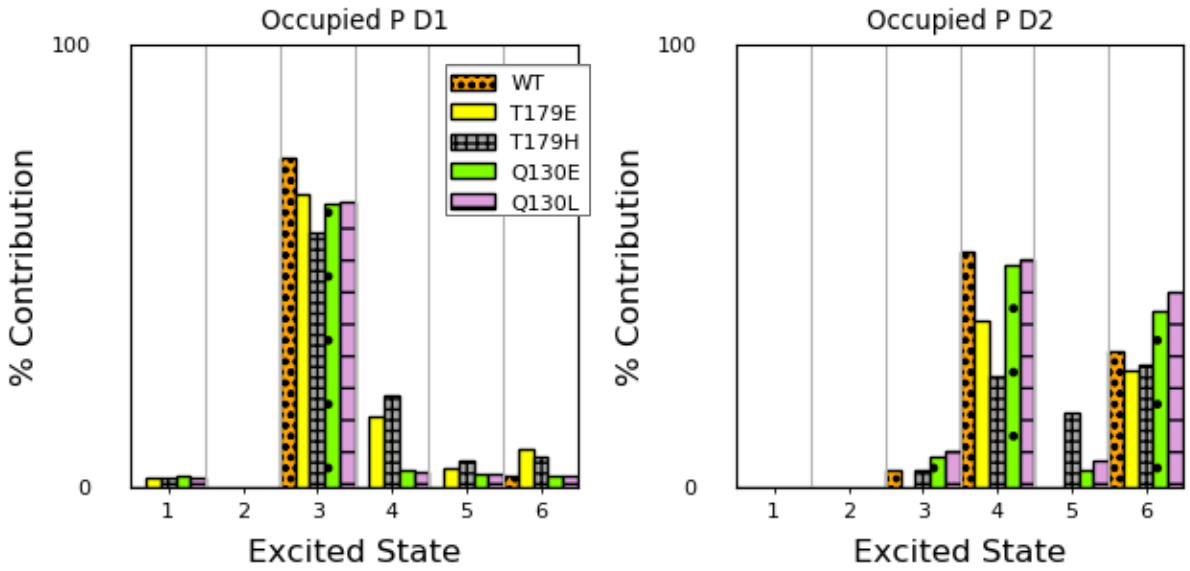


Figure 4.6 : Contribution from P chlorophyll occupied orbitals to ES 1-6 for WT model 4, T179E, T179H, Q130E and Q130L

Consistently for the WT and four mutants, P_{D1} excitation dominates the third ES and P_{D2} contributes to ES 4 and 6. The two T179 mutations appear to have raised the energy of P_{D1} excitation as contribution to higher ES is more common for these mutants than for the WT. T179H has some contribution from P_{D2} excitation to ES 5, this might explain the lower oscillator strength for ES 5 for this mutant.

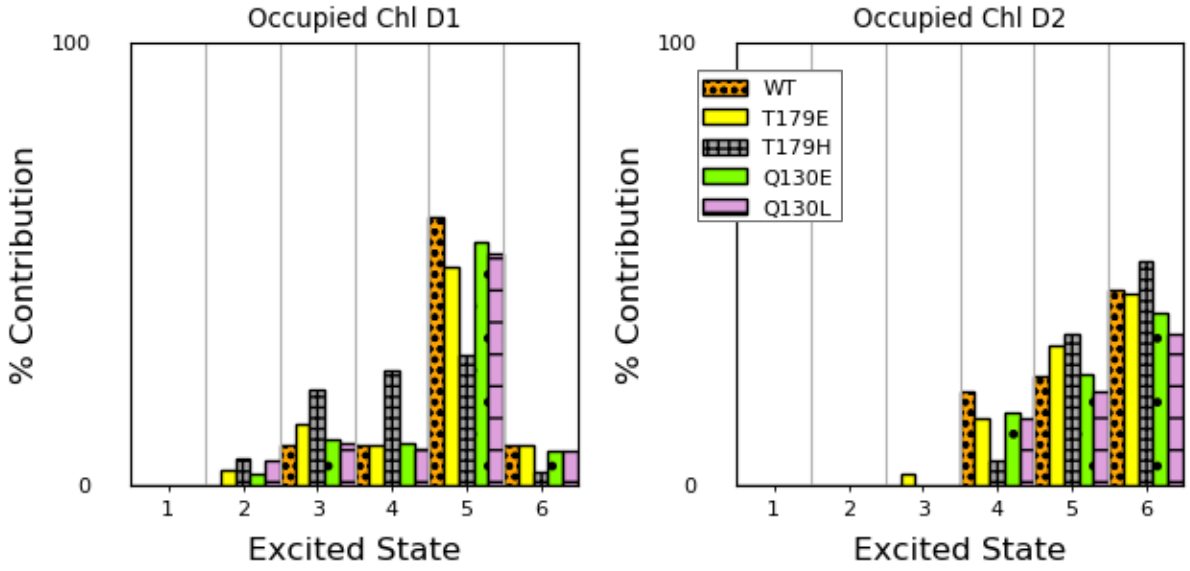


Figure 4.7 : Contribution from Chl_{D1} and Chl_{D2} occupied orbitals to ES 1-6 for WT model 4, T179E, T179H, Q130E and Q130L

For the Q130 mutants this means that there is no state in the Q_Y region that is dominated by Chl_{D2} excitation. Chl_{D2} excitation appears to have risen in energy for T179H as this cofactor excitation contributes very little to ES 4. For all four mutants Chl_{D2} excitation has increasing contributions to ES 4-6.

Chl_{D1} excitation contributes to lower E states for T179H than for the WT, coupled with the observations from table 4.1 including the lower energy of ES 4-6 compared to the WT and reduced oscillator strength of ES 5 for T179H, it appears that the results for this mutant are in good, quantitative agreement with experiment[52], for which mutation to T179H was seen to lower the energy of Chl_{D1} absorption by ~3 nm (observed as a shift in the triplet minus singlet spectrum main bleach at 673 nm) and to decrease absorption in this region of the spectrum as well.

T179E is expected to exhibit a ~1 nm up-shift in the energy of the Chl_{D1} absorption band, in keeping with experiment.[52] However the higher contribution from Chl_{D1} to lower E excited states for the mutant T179E model, together with the lower energies calculated for ES 4-6 for this mutant (see table 4.1) compared with the WT, would suggest that the model results are not in agreement with this finding. Use of a glutamic acid residue instead of a charged glutamate may be the reason for this lack of agreement between the experimental shifts in absorption difference bands and the model results in this case.

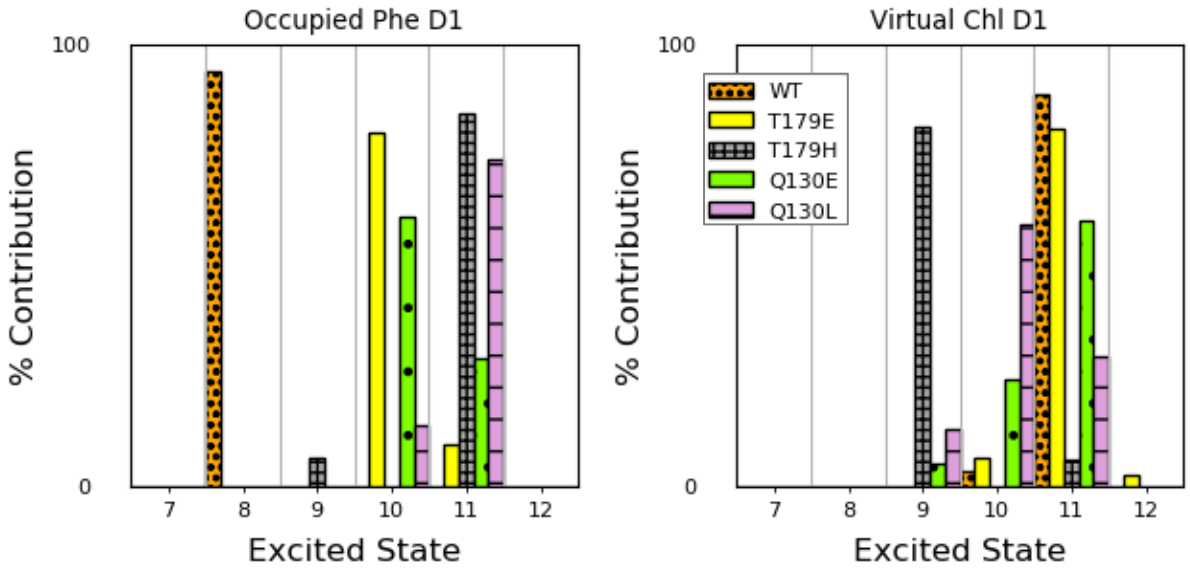


Figure 4.8 : Contribution from Phe_{D1} and Chl_{D1} occupied orbitals to ES 7-12 for WT model 4, T179E, T179H, Q130E and Q130L

In the Q_x region the increase in energy of the Phe_{D1} excitation is visible again for all four mutants. Considering the action of the Q130E mutation to red-shift a Phe_{D1} band in this region[55–59] we can say that the result for this mutant does not agree with the experimental result. Mutation to Q130L results in an increase in the Phe_{D1} Q_x absorption energy, from 541.5 to 540 nm,[54] and the two mutants Q130E and Q130L have opposite effects on the rate of singlet O_2 production due to decreasing (Q130E) and increasing (Q130L) rates of charge recombination of $Phe_{D1}Q_A^-$ to $Phe_{D1}{}^-Q_A$.[55–59]

Chl_{D1} absorption is again seen to appear at lower energies for T179H than for the WT, in agreement with experimental shifts in the triplet minus singlet spectrum main bleach[52] (see discussion above). Mutation to T179E appears to have less of an effect on the Chl_{D1} absorption in the Q_X region than mutation to T179H, as Chl_{D1} dominates the same ES (ES 11) with similar excitation energies (565.19 nm for WT and 565.07 nm for T179E) for both the WT and T179E.

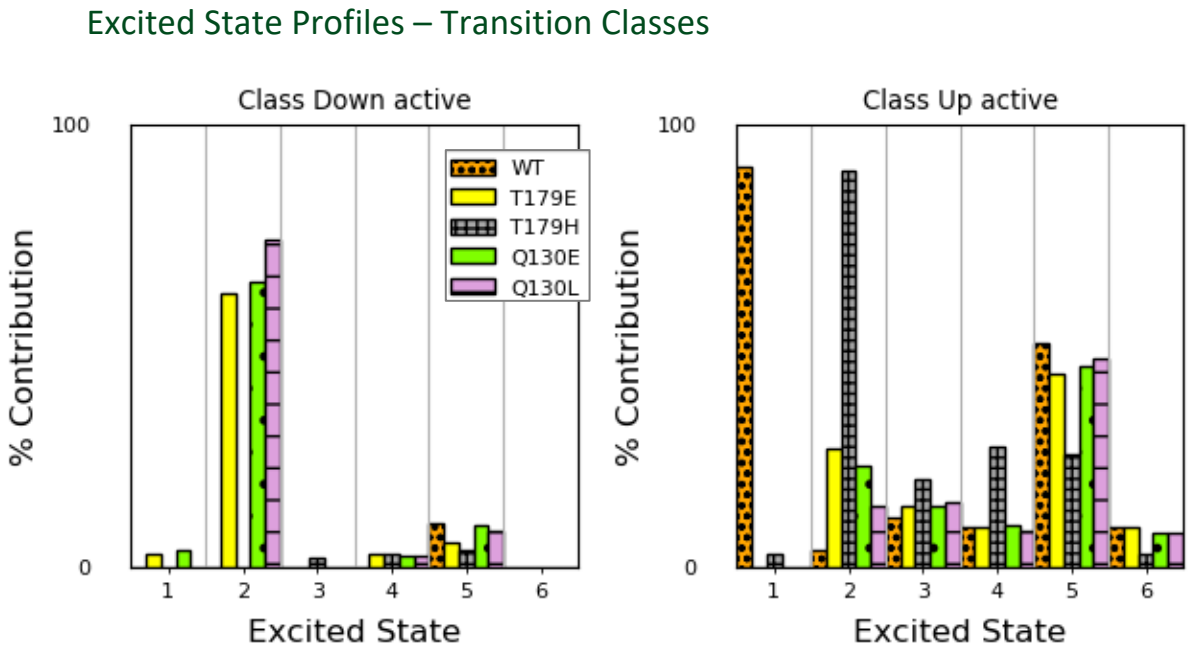


Figure 4.9 : Active branch transition contributions to ES 1-6 for WT model 4, T179E, T179H, Q130E and Q130L

The up the active branch transition in Phe_{D1} excitation dominated ES 1 for the WT appears again for the T179H mutant for ES 2 (also dominated by Phe_{D1} excitation). All other mutants, Q130E, Q130L and T179E, are dominated by a transition down the active branch for ES 2. ES 5 is dominated by up active transitions for the WT and for mutants Q130E, Q130L and T179E, however the up active transition contributes ~equally to ES 4 and 5 for T179H, indicating that this transition out of Chl_{D1} is lower in energy for this mutant than for the WT.

Table 4.3 : Active branch orbital occupancy for WT model 4, T179E, T179H, Q130E and Q130L

	ES 2 MO	Phe_{D1} occupancy	Chl_{D1} occupancy	ES 5 MO	Phe_{D1} occupancy	Chl_{D1} occupancy
WT*	2308	97.9%	1.0%	2309	0.4%	98.0%
	2313	98.3%	0.7%	2315	0.8%	97.8%
T179E	2310	97.5%	1.7%	2311	0.9%	97.4%
	2316	95.7%	3.4%	2318	3.4%	95.4%
T179H	2312	97.3%	1.8%	2314	0.3%	95.6%
	2318	97.4%	1.7%	2320	1.7%	96.9%
Q130E	2308	97.5%	1.7%	2309	1.0%	97.4%
	2314	95.0%	4.0%	2316	4.0%	94.8%
Q130L	2306	97.2%	2.0%	2305	1.6%	96.8%
	2312	62.1%	37.0%	2313	37.1%	61.9%

*WT ES 1 MOs are given in the table because WT ES 1 is attributed to Phe_{D1} excitation and ES 2 is attributed to inactive branch Phe_{D2}.

Both Phe_{D1} and Chl_{D1} excitations are local for T179E, T179H and Q130E, with both occupied orbitals and virtual orbitals having >94% occupancy for all three mutants. This is similar to the WT MOs for these two states. Q130L however involves more delocalised orbitals and more transfer between Phe_{D1} and Chl_{D1} in both ES 2 and ES 5. Looking at table 4.2 we can see that the energy of the Phe_{D1} excitation has been increased the most for the Q130L mutant relative to the WT, therefore the stronger coupling between Chl_{D1} and Phe_{D1} can be explained by the mutation bringing the two cofactors closer in energy.

Compared to the WT, all four mutants appear to have reduced likelihood of CT proceeding up the active branch. ES 5 for the mutants T179E and Q130E involves a larger shift in cofactor occupancy between the occupied and virtual orbitals, from Chl_{D1} to Phe_{D1}, but ES 2 is still contributed to by a transfer down the active branch for these two mutants. T179H is the only mutant for which ES 2 is dominated by an up active transition, although from the table above, the movement between Chl_{D1} and Phe_{D1} is 0.1%. T179H ES 5 is dominated by a transition from P_{D2} to Phe_{D1} (see Figure 4.9b), it can be seen from table 4.3 that this transition also involves ~1.3% movement from Phe_{D1} to Chl_{D1} (see appendix three for discussion of transition classification).

From tables 4.1 and 4.2, all four mutants have lower Chl_{D1} excitation energy and higher Phe_{D1} excitation energy. If Chl_{D1} and Phe_{D1} are closer in energy this can be expected to reduce the driving force for CT to travel up the active branch, which explains the results in table 4.3.

Down active (Phe D1 to Chl D1): 2310 → 2316
State 1: 2.67%
State 2: 59.66%
State 4: 2.78%

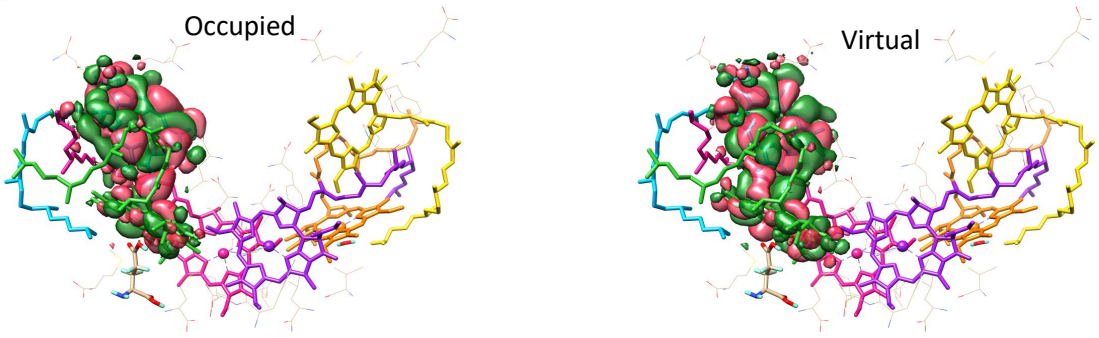


Figure 4.10a : MOs making up the highest contributing transition for ES 1 for T179E

Up active (Chl D1 to Phe D1): 2312 → 2318
State 1: 2.65%
State 2: 59.60%
State 4: 4.31%

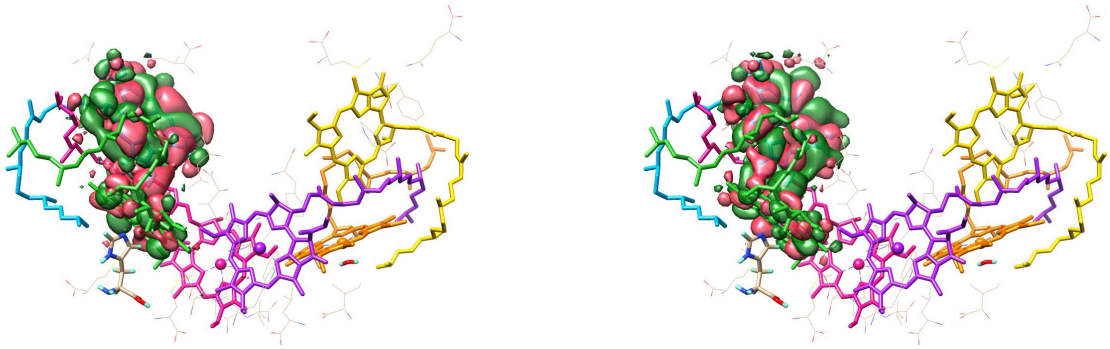


Figure 4.10b : MOs making up the highest contributing transition for ES 1 for T179H

Down active (Phe D1 to Chl D1): 2308 → 2314
State 1: 3.53%
State 2: 58.86%
State 4: 2.48%

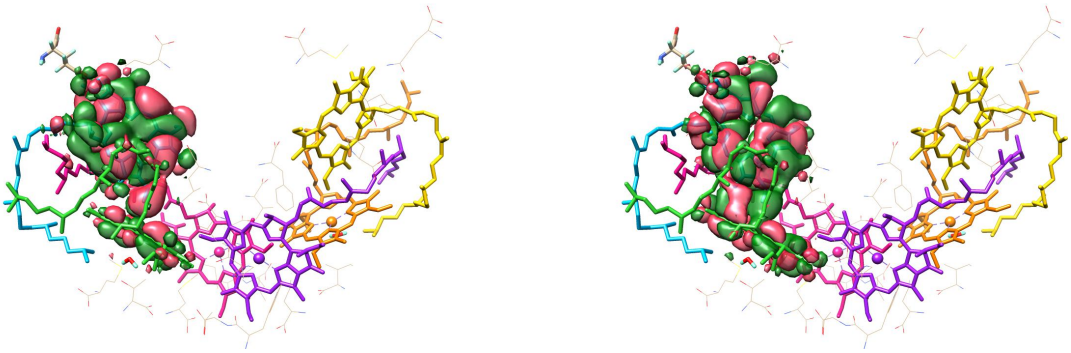


Figure 4.10c : MOs making up the highest contributing transition for ES 1 for Q130E

Down active (Phe D1 to Chl D1): 2306 → 2312
State 2: 40.86%

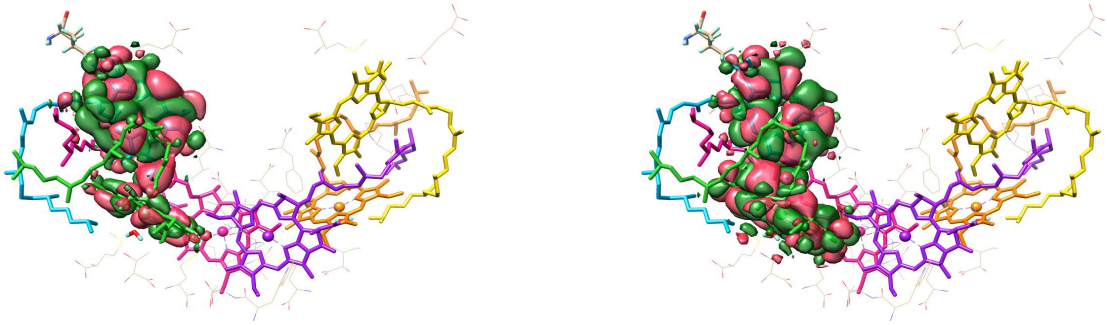


Figure 4.10d : MOs making up the highest contributing transition for ES 1 for Q130L

Up active (Chl D1 to Phe D1): 2311 → 2318
State 2: 3.42%
State 3: 13.56%
State 4: 8.75%
State 5: 43.59%
State 6: 9.02%

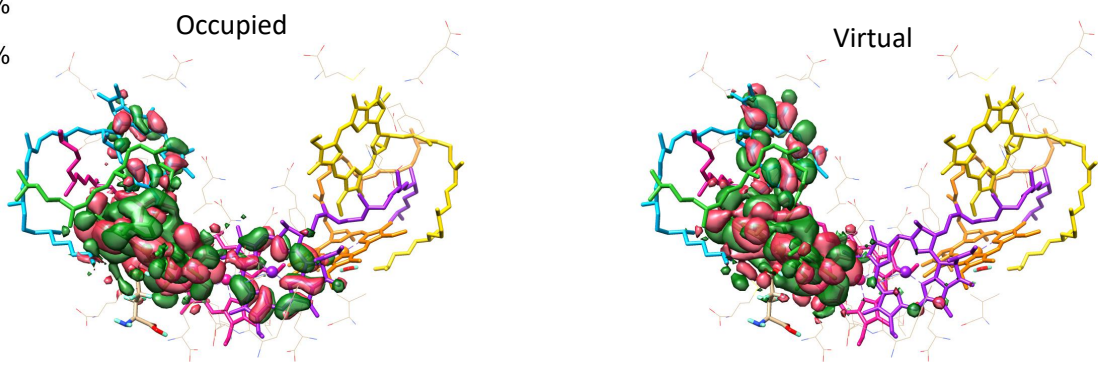


Figure 4.11a : MOs making up the highest contributing transition for ES 5 for T179E

Up active (P D2 to Phe D1): 2314 → 2320
State 2: 5.80%
State 3: 19.69%
State 4: 22.79%
State 5: 25.52%
State 6: 2.99%

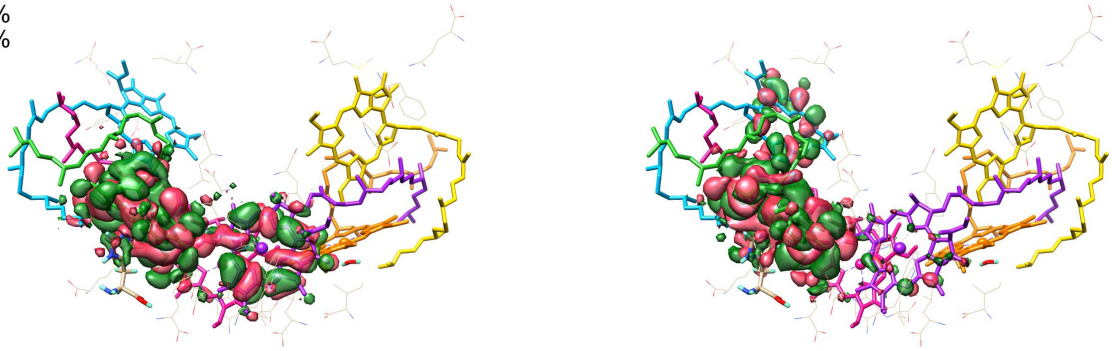


Figure 4.11b : MOs making up the highest contributing transition for ES 5 for T179H

Up active (Chl D1 to Phe D1): 2309 → 2316
State 2: 2.29%
State 3: 10.40%
State 4: 9.55%
State 5: 45.32%
State 6: 7.61%

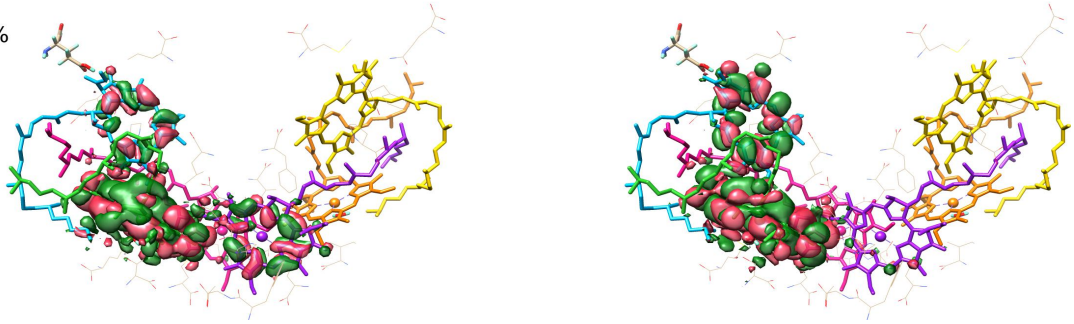


Figure 4.11c : MOs making up the highest contributing transition for ES 5 for Q130E

Up active (Chl D1 to Phe D1): 2305 → 2313
State 2: 5.42%
State 3: 5.52%
State 4: 4.24%
State 5: 27.38%
State 6: 4.73%

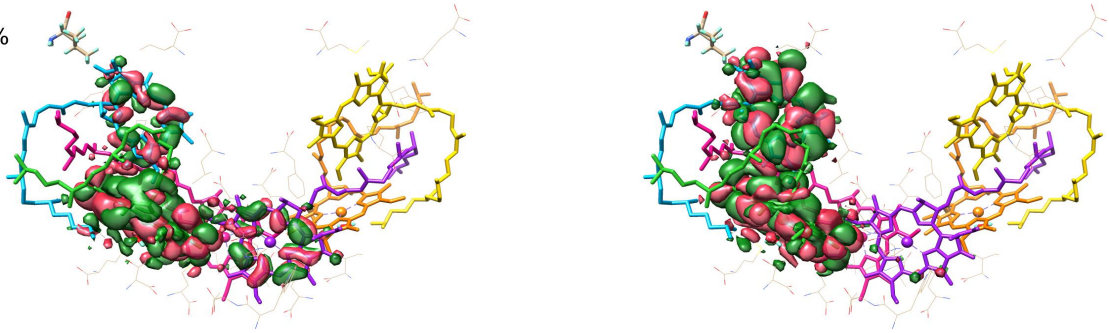


Figure 4.11d : MOs making up the highest contributing transition for ES 5 for Q130L

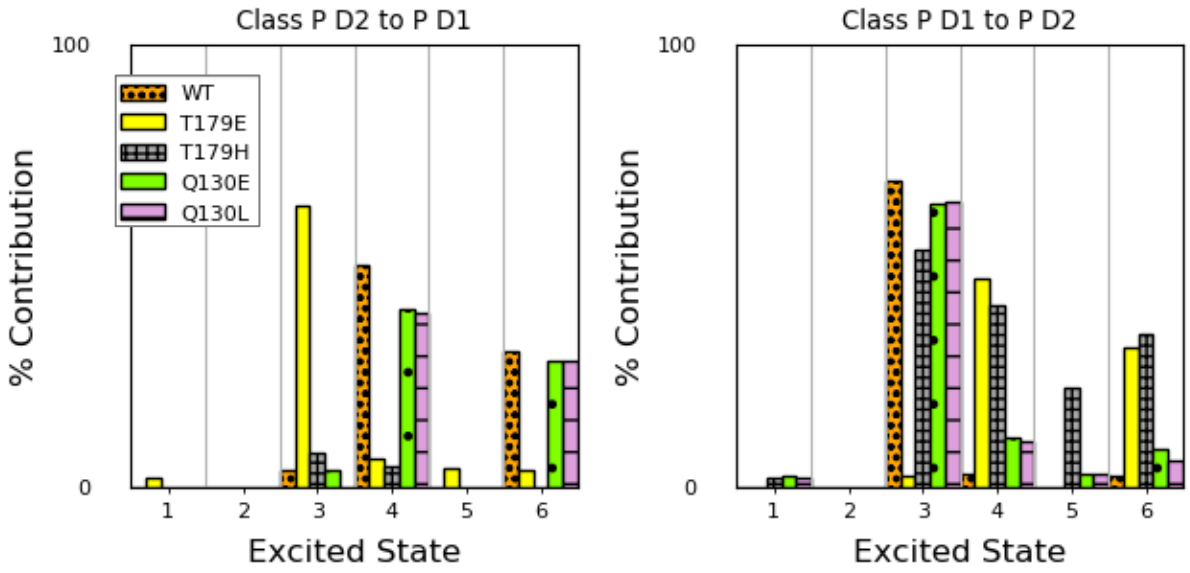


Figure 4.12 : P chlorophyll transition contributions to ES 1-6 for WT model 4, T179E, T179H, Q130E and Q130L

Table 4.4 : P chlorophylls orbital occupancy for WT model 4, T179E, T179H, Q130E and Q130L. Virtual orbital occupancies are coloured red if there has been a decrease in occupancy on that cofactor during the transition and green if there has been an increase.

	ES 3 MO*	Chl_{D1}	P_{D1}	P_{D2}	ES 4 MO*	Chl_{D1}	P_{D1}	P_{D2}
WT	2312	0.0	87.7	11.2	2311	0.5	12.0	86.6
	2317	0.3	56.1	42.5	2318	0.1	42.2	56.7
T179E	2314	0.1	90.3	8.6	2313	1.0	15.7	82.5
	2320	0.2	93.1	5.7	2319	0.2	4.9	93.7
T179H	2316	0.1	89.7	9.2	2315	3.4	14.4	81.5
	2322	0.2	88.2	10.7	2321	0.3	9.8	88.6
Q130E	2312	0.1	89.7	9.2	2311	0.7	13.4	85.1
	2318	0.1	76.4	22.5	2317	0.2	21.7	76.9
Q130L	2309	0.1	89.6	9.3	2308	0.8	13.4	85.1
	2315	0.1	74.8	24.1	2314	0.2	23.3	75.2

*Top row - occupied orbital number, bottom row - virtual orbital number

Form table 4.4 we see that T179H has two significant P_{D1} to P_{D2} transitions, one with both occupied and virtual MOs centred on P_{D1} (similar to the WT P_{D1} to P_{D2} transition) and one with both centred on P_{D2}. T179E has a similar P_{D1} to P_{D2} transition to T179H, with both MOs having high P_{D2} occupancy, however the P_{D2} to P_{D1} transition is between MOs with high P_{D1} occupancy for T179H. Both Q130 mutants P chlorophyll transitions are similar to the WT P chlorophyll transitions in that one centred on P_{D1} involves transition towards P_{D2} and the one centred on P_{D2} involves transition towards P_{D1}.

The extent of delocalisation across the two P chlorophylls and the transfer of occupancy is less for all mutants than for the WT. It is not surprising that the Q130 P transitions are more similar to WT with more movement of electron density than the T179 mutants, as the site of mutation is farther from the P chlorophylls therefore less likely to affect them. Nonetheless, the effect of these far away mutations on the nature of the P chlorophyll excitations is remarkable and points to the importance of including a wide region of the RC environment in future models of the RC.

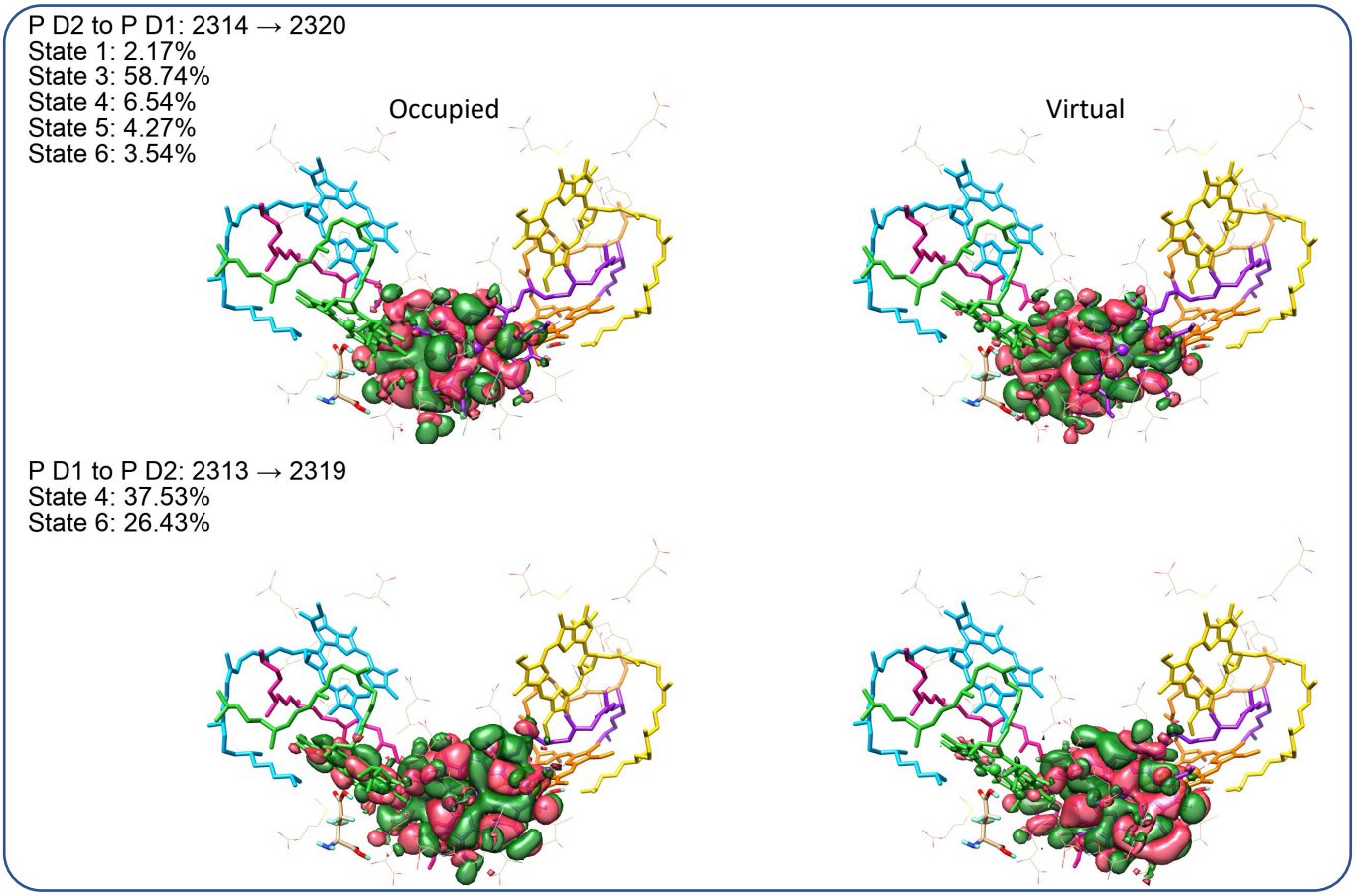


Figure 4.13a : P chlorophyll transitions for T179E

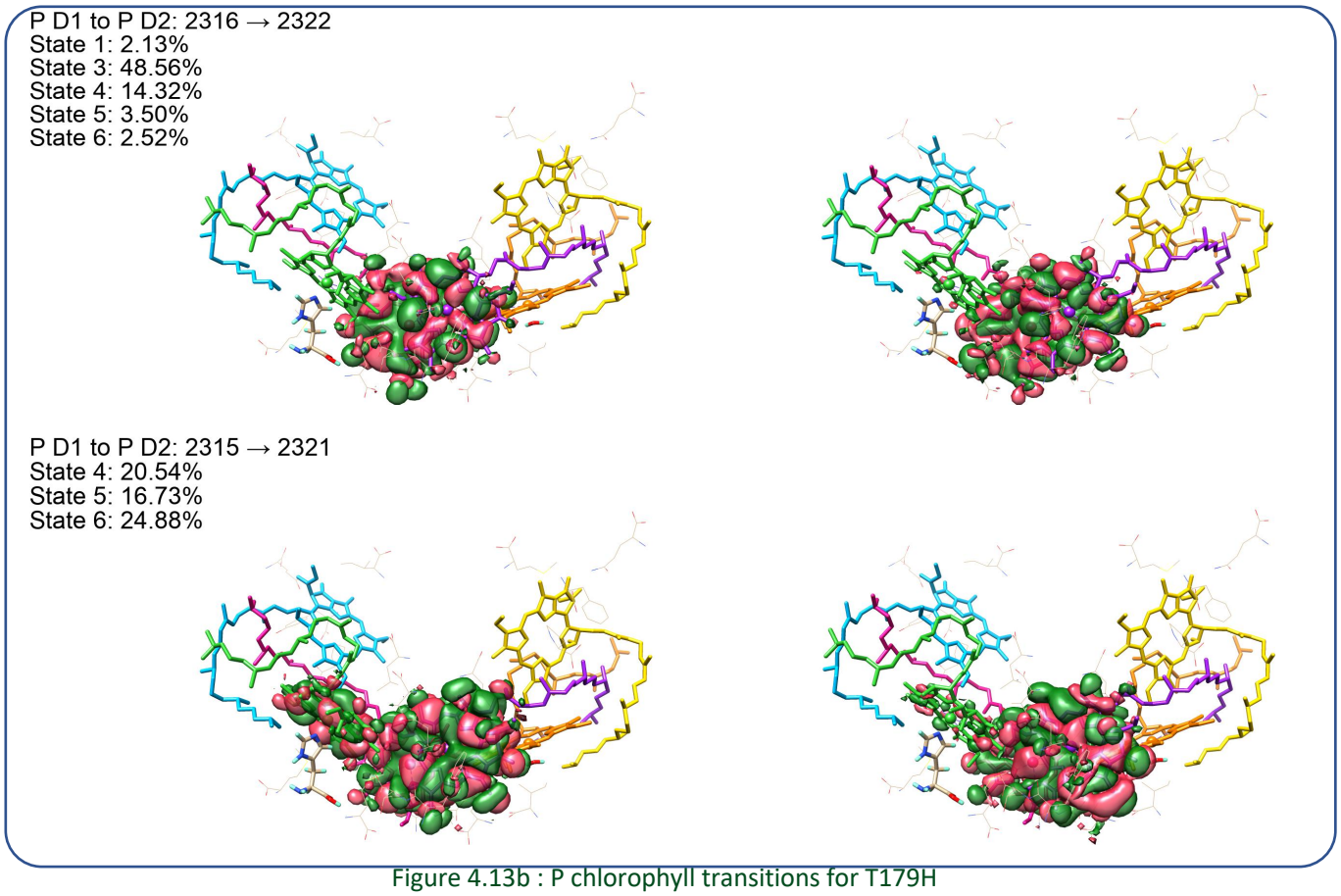


Figure 4.13b : P chlorophyll transitions for T179H

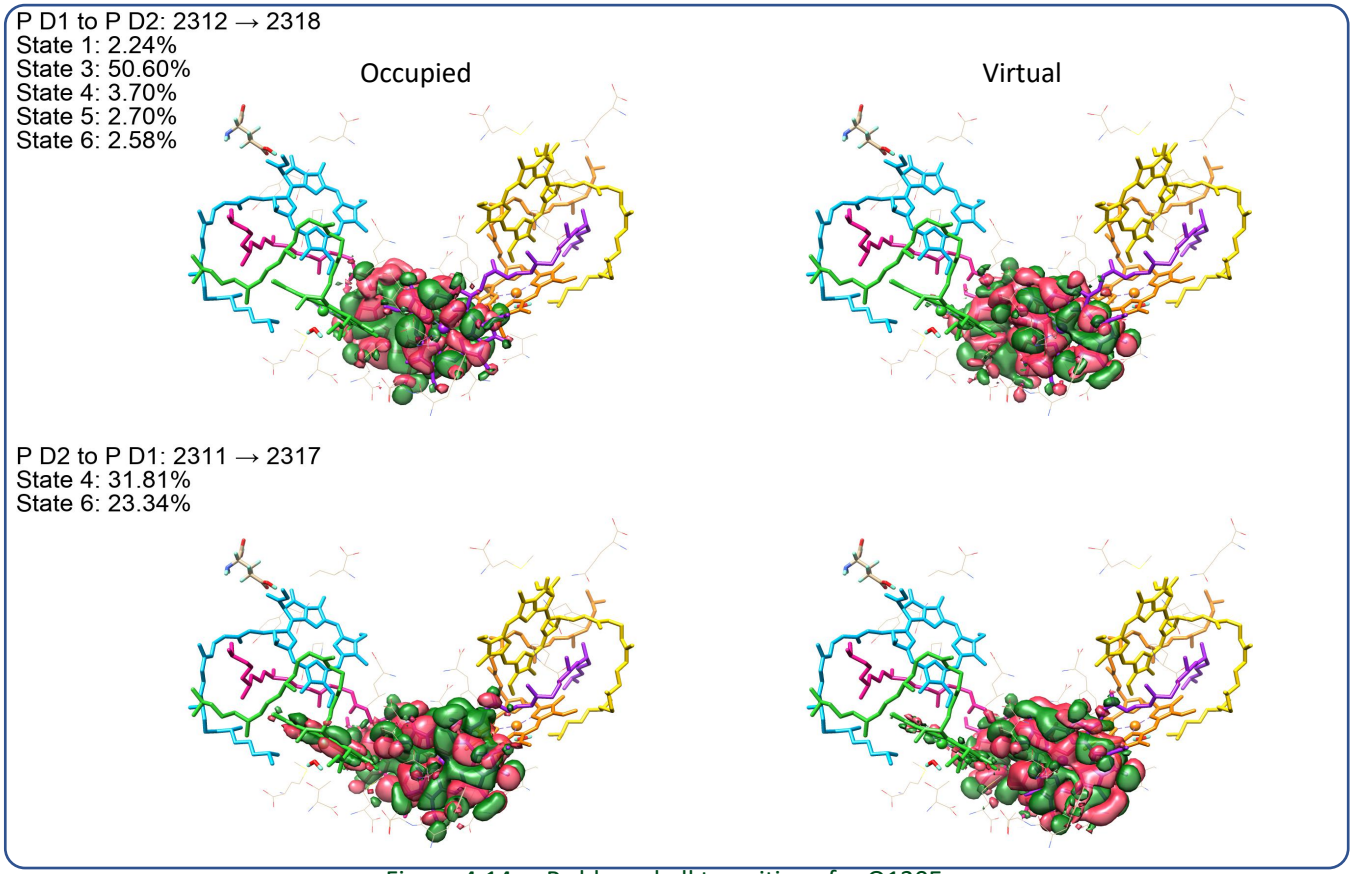


Figure 4.14a : P chlorophyll transitions for Q130E

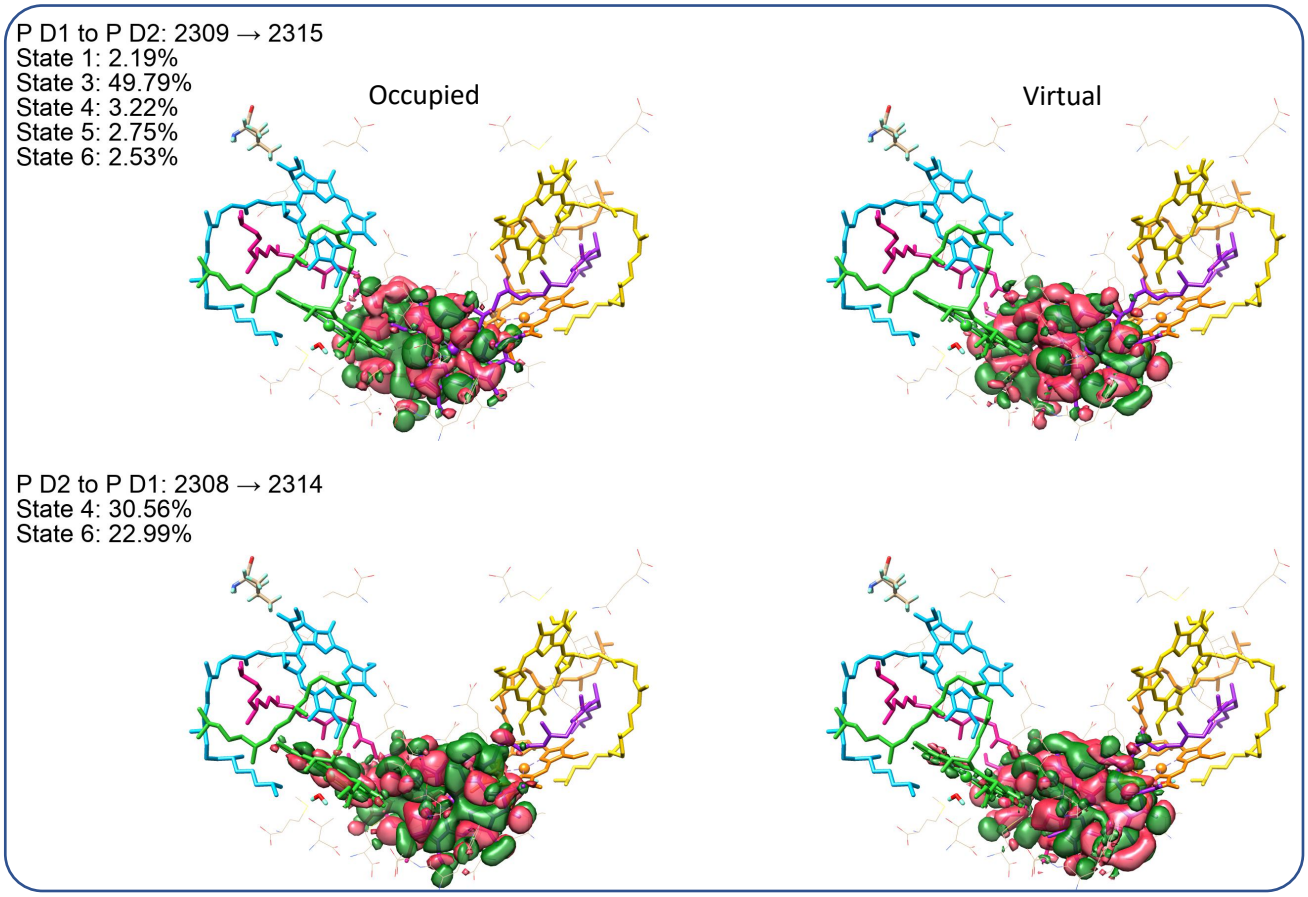


Figure 4.14b : P chlorophyll transitions for Q130L

Conclusion

In conclusion, modelling a further set of site directed mutations brings the total number of mutant RC models up to eight. Discussed in this chapter are the results of mutating two residues, D1-179 in the vicinity of Chl_{D1} and D1-130 in the vicinity of D1-130. All results have been compared with experimental shifts in absorption difference spectra and there is a good agreement for two of the four models discussed in this chapter with experimental findings.

T179H showed a lowering in energy of Chl_{D1} excitation, both through the increased contribution of Chl_{D1} excitation into lower energy ES (3-4) and through the lowering in energy of ES 4-6 compared with the WT model 4. This is in good agreement with the experimental shift in the main bleach of the triplet minus singlet absorption difference spectrum of ~3nm to the red for the T179H mutant.[52] Furthermore, a decrease in oscillator strength of the ES dominated by Chl_{D1} excitation (ES 5) is seen for the mutant T179H model, compared to the Q_Y absorption spectra in Figure 2 in ref [52] for which mutant T179H displays a lower absorption of the peak at ~672 nm this is also in agreement with spectroscopic data. As a reminder to the reader, the assignment of Chl_{D1} as the lowest energy site in the RC has not been reproduced by the model results which may be a result of the specific conformation of the pigments in the crystal structure, however molecular orbital assignment means that Chl_{D1} absorption has shifted to the red for the model compared with the WT. Mutation to T179E was seen to shift the triplet minus singlet bleaching band ~1 nm to the blue, however this result was not reproduced by the model, possibly due to the necessity of including a neutral glutamic acid residue as the mutant residue instead of a charged glutamate.

In the case of mutation of D1-130 to glutamic acid, again the shift in Phe_{D1} absorption to the blue that has been observed experimentally was not reproduced by this mutant model. Further work is needed to model the glutamate anion in place of the neutral glutamic acid residue and determine whether the model could better agree with the experimental result for the two mutants Q130E and T179E. Unfortunately this would be a great computational effort, as including a single mutated residue in a new mutant model would make it impossible to compare the mutant result to existing WT benchmark (which has no charged residues). This is potentially a very valuable avenue of further work however, and one that would lend itself well to a less-costly, hybrid model of the RC and its surrounding environment.

Finally, mutating to Q130L increased the energy of Phe_{D1} excitation, this is observed in the Q_Y region where Q130L ES 11 (560 nm) is dominated by Phe_{D1} excitation as opposed to ES 8 (WT Phe_{D1} excitation dominated state, 580 nm). This is in good agreement with the experimental shift of the Phe_{D1} absorption max for Q130L of 1.5 nm to the blue.[54]

It is striking to see that the P chlorophyll excitations are so affected by mutation of D1-179 and D1-130. Mutation to T179H disappears the P_{D1} to P_{D2} transition from the excitation profile, and all mutants have MOs which are less delocalised over P_{D1} and P_{D2} than were calculated for the WT. This result stands to show that the method used in this thesis, treating the whole RC as one large QM system, is key to uncovering the nature of the excited states of the RC and mutant RCs. Models which choose to divide the RC into its constituent cofactors may not have been capable of observing this long-range affect.

In the next and final chapter we will see the results of some extended RC models, including more surrounding amino acids and other nearby pigments.

Chapter Five: Extended Wild Type Models

Has the Minimum System Been Reached?

Chapter Overview

In the final chapter of this thesis are presented the results of larger calculations on the PS II RC than model 4, which was concluded in chapter one to be the minimum system required for accurate modelling of the D1 branch preference. In an ideal case, where model 4 is truly the minimum system required; extending the radius of the portion of the crystal structure used in a model will not greatly affect the excited state profile, therefore proving that some convergence of results relative to model size has been reached. Two models are discussed in this chapter, model 2A and model 5.

The first model results presented in this chapter will be model 2A. In the region of the RC are two further pigments, $Chlz_{D1}$ and $Chlz_{D2}$ which were included in this new model to determine the effects of these pigments on the excitation profile. Coupling from the six core chromophores to these peripheral chlorophylls, which lie outside of the main RC core (the centre of the Chlz rings lie ~20-30 Å away from the centres of the core RC pigments on the same branch), is expected to be weak. This new model will be called model 2A – due to it having the same components as model 2 from chapter one as well as two peripheral Chlzs and their histidine axial ligands.

Finally, model 5 will be discussed. The results in chapter one showed the effect of increasing the size of RC models, from just two amino acids and truncated phytol chains (model 1) up to full phytol chains and 23 amino acid residues (model 4). In this chapter extension up to a 60 amino acid model, including 2361 atoms (8318 electrons) and the plastoquinone Q_A and Q_B, is investigated. The size of this system is extremely prohibitive therefore only six ES are calculated for this 60 amino acid model (which will be called model 5).

Results & Discussion

Model 2A (ωB97X-D/ 6-31G**)

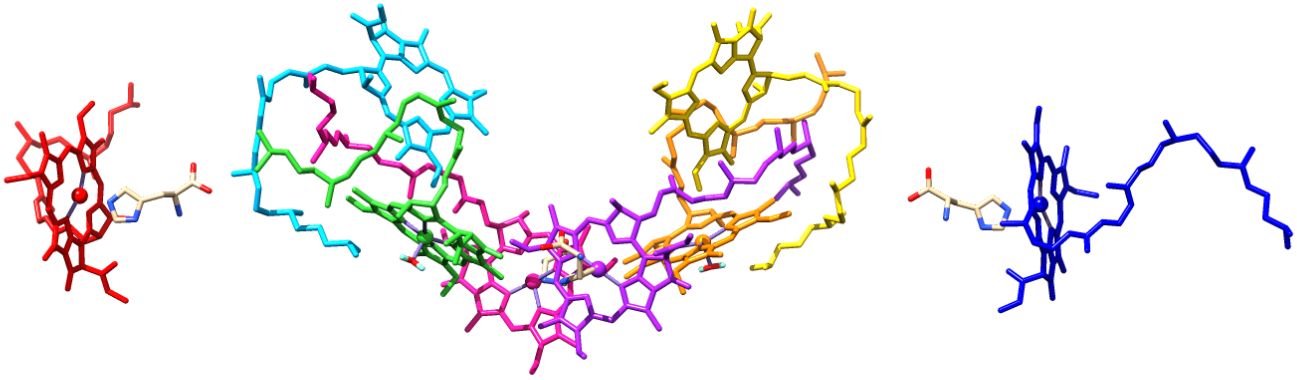


Figure 5.1 : Structure of model 2A, including P_{D1} (pink) with His ligand, P_{D2} (purple) with His ligand, Chl_{D1} (green) with water ligand, Chl_{D2} (orange) with water ligand, $Chlz_{D1}$ (red) with His ligand, $Chlz_{D2}$ (blue) with His ligand, Phe_{D1} (light blue) and Phe_{D2} (yellow).

Model 2A could be compared with the results for model 2 (see table 5.1). It is clear from table 5.1 that there are new ES in each of the chlorophyll absorption bands Q_Y and Q_X owing to the two new chlorophylls $Chlz_{D1}$ and $Chlz_{D2}$ in model 2A. In the Q_Y region, the energies and oscillator strengths of ES 1-3 are comparable for both models 2 and 2A, whilst the energies of ES 4-6 for model 2 are similar to the energies of ES 6-8 for model 2A. It can be assumed therefore, before looking at the nature of these excited states, that $Chlz_{D1}$ and $Chlz_{D2}$ have excitations in ES 4 and 5 for model 2A. The oscillator strength of ES 4 for model 2 is ~0.5x that of ES 6 for model 2A, suggesting a decrease in the likelihood of the transition occurring here on addition of $Chlz_{D1}$ and $Chlz_{D2}$ with their axial His ligands. The excitation energy of ES 7 for model 2A is the same as model 2 ES 4, whilst the oscillator strengths for these two states are similar (0.4706 and 0.5015 respectively). This suggests a decrease in the energy of the excitation here on addition of the peripheral chlorophylls.

Table 5.1 : Excitation energies and oscillator strengths for model 2 (6 chromophores, full phytol chains, 2 amino acids) and model 2A (model 2 + ChlzD1 and ChlzD2 and 2 His)

Model 2			Model 2A		
State	Energy (nm)	Oscillator Strength	State	Energy (nm)	Oscillator Strength
1	677.29	0.3075	1	676.63	0.3128
2	670.53	0.4045	2	671.26	0.3594
3	669.01	0.0977	3	669.07	0.1019
			4	662.8	0.2268
			5	659.78	0.204
4	657.06	0.0603	6	658.17	0.1387
5	654.72	0.5015	7	657.06	0.4706
6	646.4	0.1468	8	647.85	0.1401

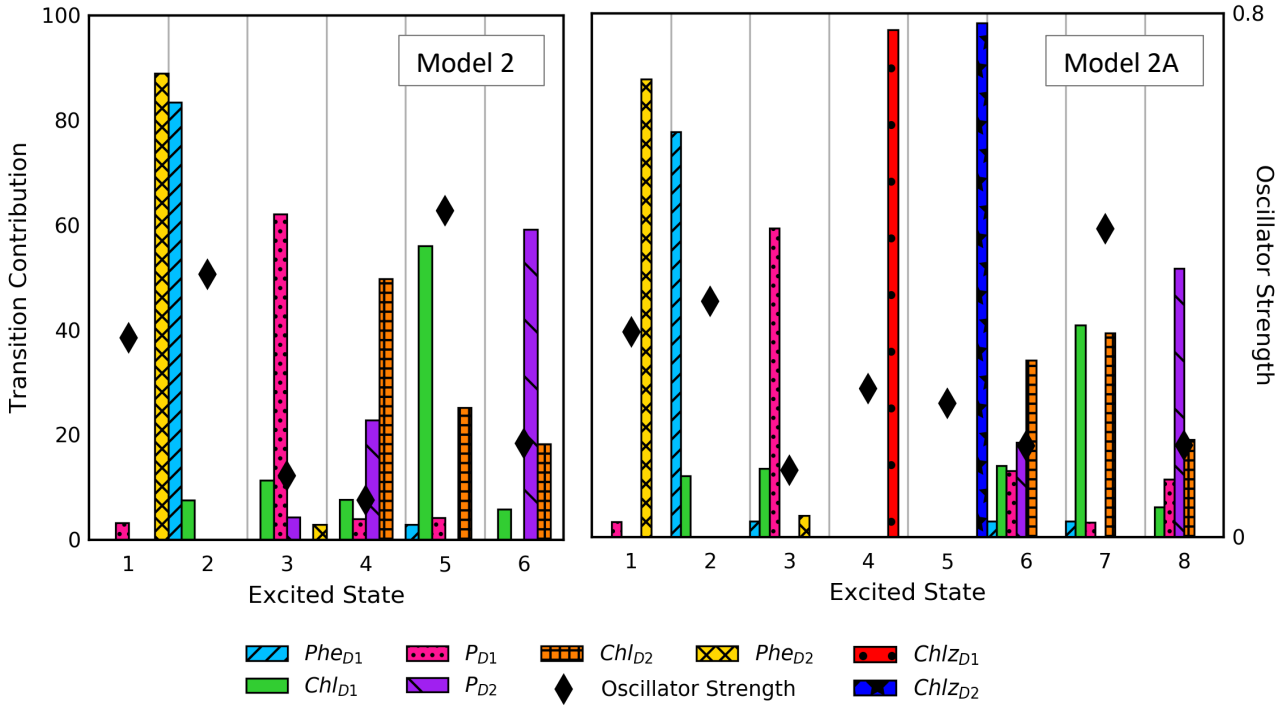


Figure 5.2 : Excited states 1-6 for model 2 (left) and excited states 1-8 for model 2A, including $Chlz_{D1}$ and $Chlz_{D2}$ (ωB97X-D/ 6-31G**) (bar chart, left y axis) % of state contributed to by each cofactor (occupied orbital occupancy analysis with MultiWfn from Mulliken method) and (black diamonds, right y axis) oscillator strength of each state. Cofactors coloured as in all figures in this thesis (see Figure 5.1).

From Figure 5.2 the contribution of excitations on each cofactor can be seen for model 2A in the Q_x region. Aside from the insertion of the two Chlz excitations at ES 4 and ES 5, the main difference between the results for this model and the results for model 2 (Figure 5.2) can be seen for the Chl_{D1} and Chl_{D2} excitations. The inclusion of the $Chlz_{D1}$ and nearby His ligand drops the energy of the Chl_{D1} excitation to near degenerate with Chl_{D2} excitation for model 2A (ES 7). From table 5.1 it can be seen that the energy of Chl_{D2} excitation (ES 4 for model 2 and ES 6 for model 2A) has also been reduced due to the effect of including the nearby $Chlz_{D2}$ and its His ligand, and that the oscillator strength for Chl_{D2} excitation is increased in model 2A relative to model 2. There are no other changes to the ordering of cofactor excitations as a result of including the Chlz cofactors in the model. The transitions in the Q_Y region are also similar for models 2 and 2A (see Figure 5.3).

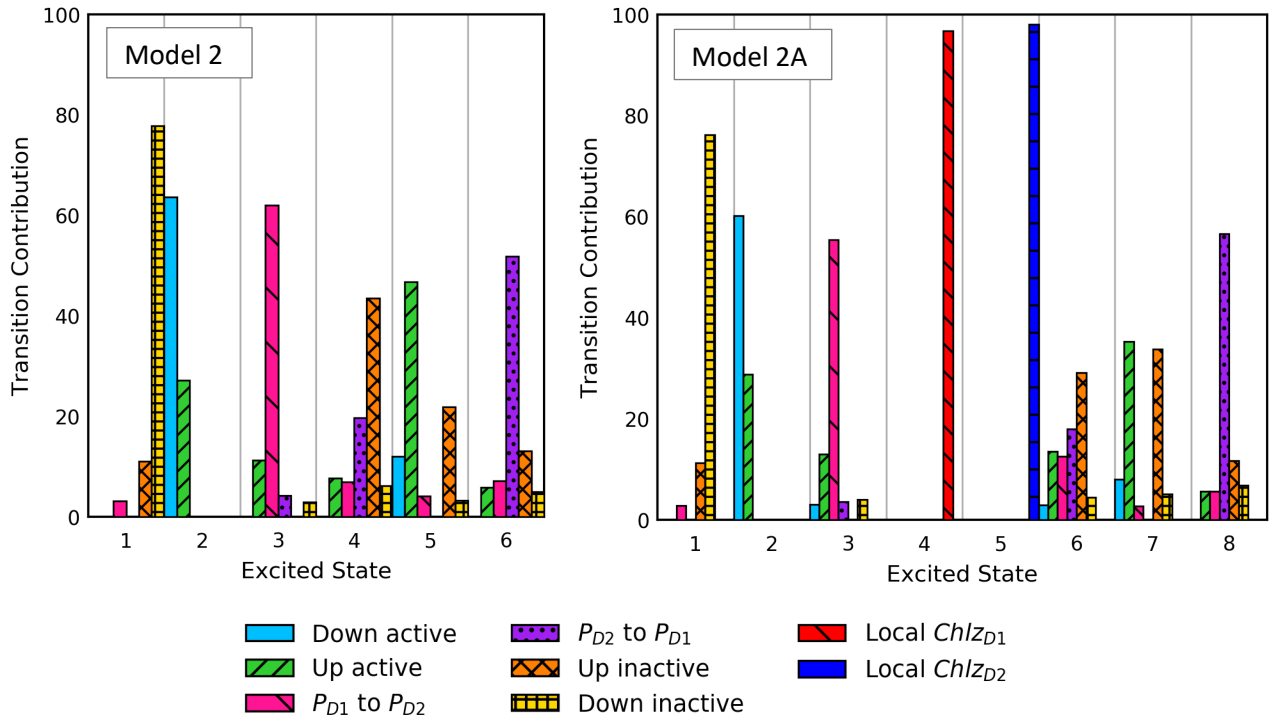


Figure 5.3 : Contributions from each transition class to model 2 (left) and model 2A, including Chlzs (right) (both at ωB97X-D/ 6-31G**)

MOs with the highest contributions to ES 4 and 5 for model 2A are presented in figures 5.4 and 5.5. Both ES 4 and ES 5 are contributed to solely by local Chlz excitations:

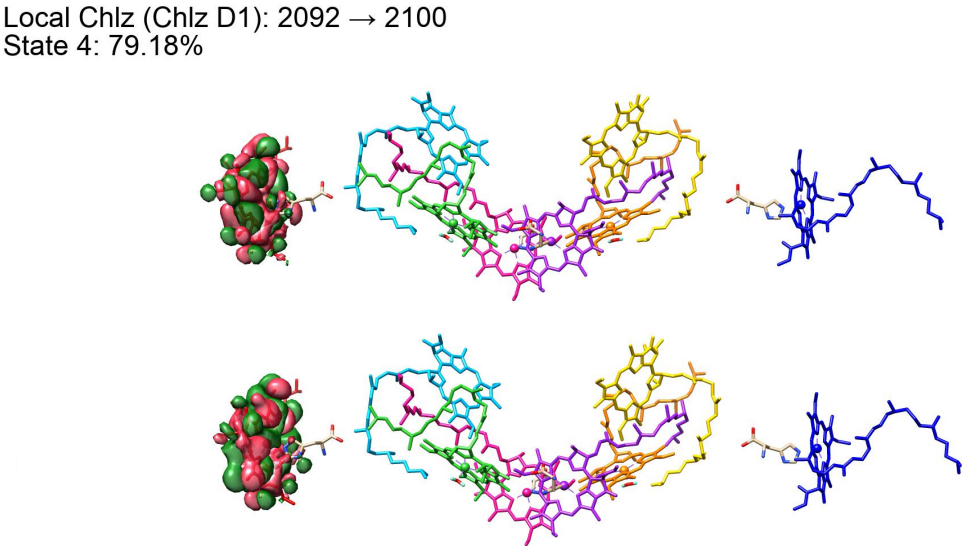


Figure 5.4 : Local $Chlz_{D1}$ excitation contributing to ES 4 for model 2A (ωB97X-D/ 6-31G**)

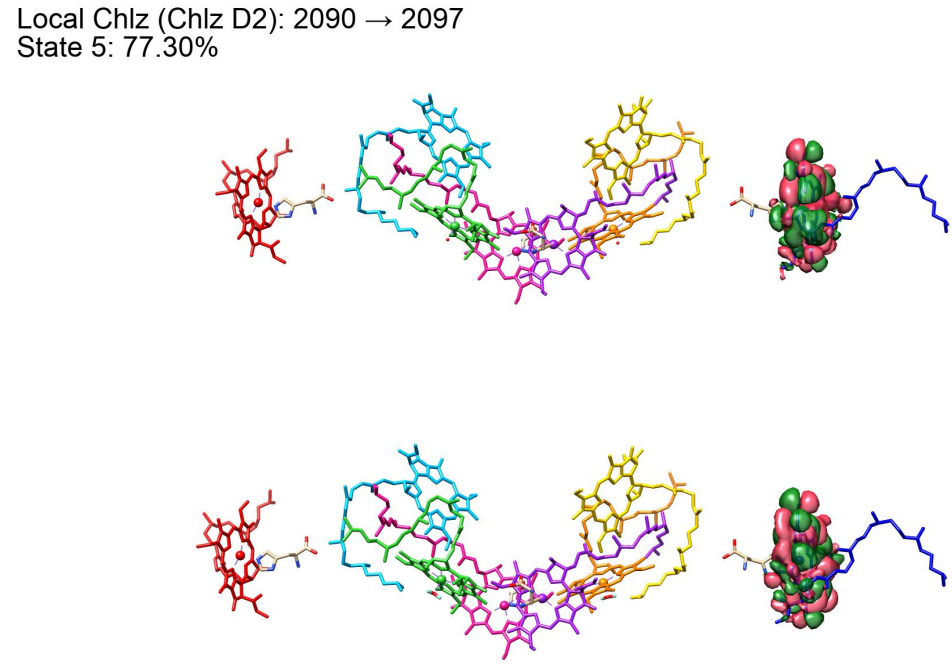


Figure 5.5 : Local $Chlz_{D2}$ excitation contributing to ES 4 for model 2A (ωB97X-D/ 6-31G**)

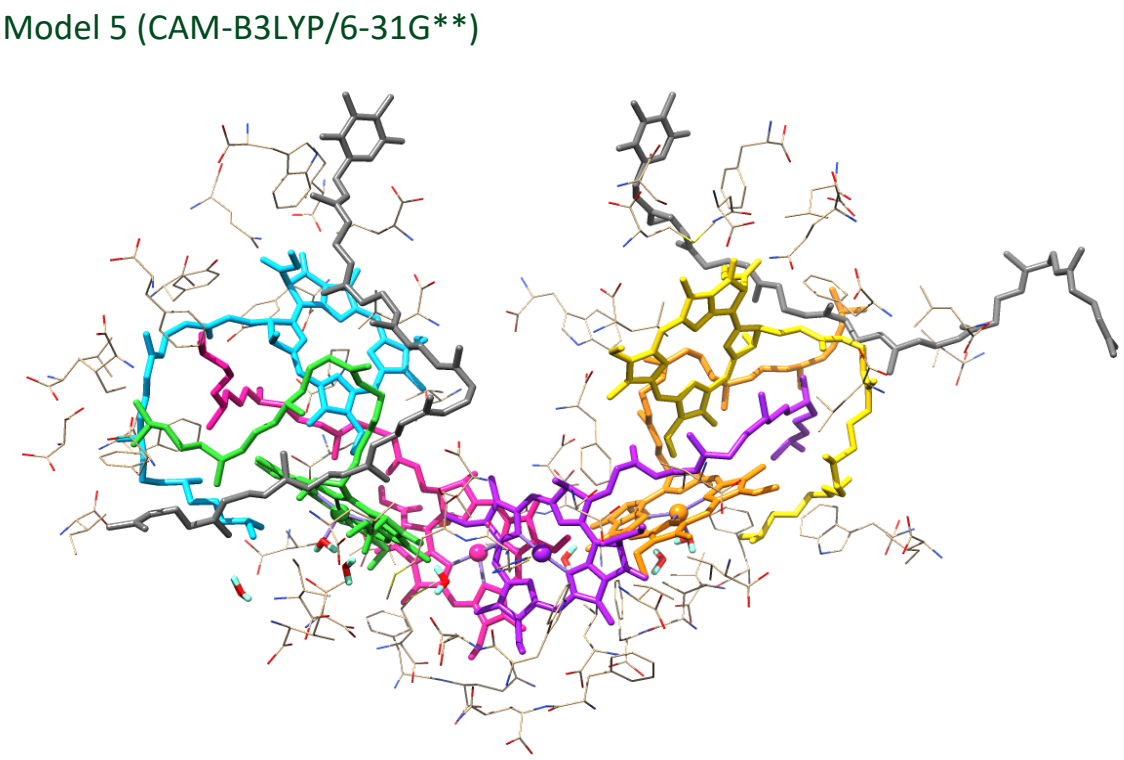


Figure 5.6 : Structure of model 5 including 60 amino acids (wire structure) P_{D1} (pink), P_{D2} (purple), Chl_{D1} (green), Chl_{D2} (orange), $Chlz_{D1}$ (red), $Chlz_{D2}$ (blue), Phe_{D1} (light blue), Phe_{D2} (yellow) and Q_A and Q_B (grey).

Model 5 includes 60 amino acids and a total of eight water molecules (see Figure 5.7) compared to model 4's 23 amino acids and two waters. The effect of including more of the nearby water molecules is explored in appendix two. Going from model 4 to model 5, the plastoquinones (Q_A and Q_B) have also been added. The effect of adding just Q_A and Q_B to model 4 has not yet been explored and is suggested to be included in further work.

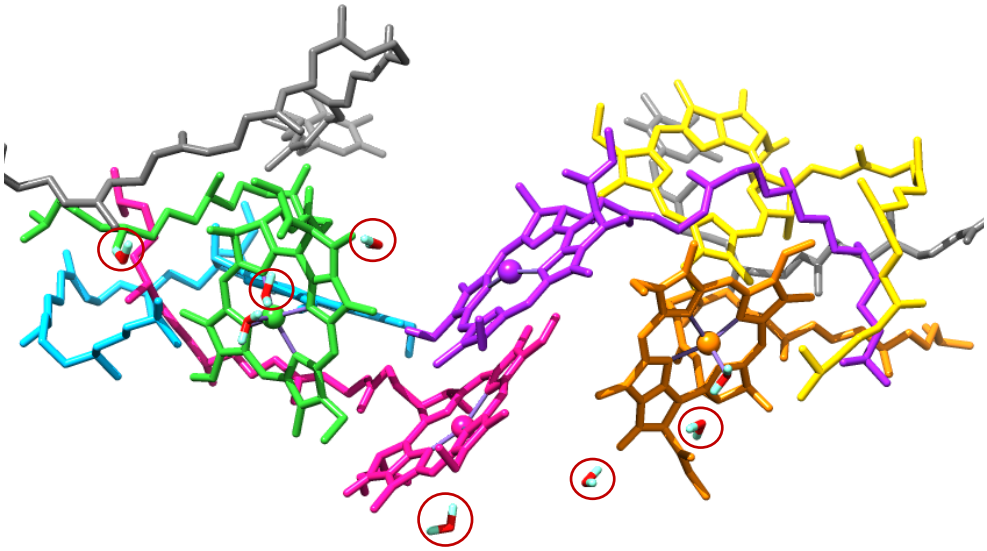


Figure 5.7 : Structure of model 5 (viewed from below) as in Figure 5.6 but without the amino acids, and with six water molecules circled in red. These waters are not included in model 4.

A list of all amino acid residues included in model 5 is presented in table 5.2. Not all residues included in model 4 are included in model 5 (see five grey cells in table 5.2), this should be borne in mind when comparing the two models' results. More similar models should be made in future work so the effects of adding and taking away residues from the model are not combined when comparing results. However, the majority of residues included in model 4 are included in model 5, making them suitable for a brief, qualitative comparison.

Table 5.2 : List of residues included in models 4 and 5: Yellow cells – residues included in model 5 but not model 4, white cells – residues included in models 4 & 5, grey italicised cells – residues included in model 4 but not model 5

D1	D2	Other chains
Leu 41	Leu 37	Leu 26 branch F
Thr 45	Trp 48	Leu 30 branch L
Ile 78	Phe 73	Phe 10 branch T
Ile 115	Ile 114	Ile 14 branch T
Phe 119	Leu 122	Phe 17 branch T
Tyr 126	Phe 125	
Gln 130	Gln 129	
Ile 143	Asn 142	
Tyr 147	*Phe 146*	
Pro 150	*Pro 149*	
Ser 153	Val 152	
Val 157	Val 156	
Met 172	Val 175	
Ile 176	Ile 178	
Thr 179	Phe 179	
Met 183	Leu 182	
Phe 186	Phe 185	
Gle 187	Gln 186	
Ile 192	Trp 191	
Leu 193	Thr 192	
His 198	His 197	
Gle 199	Met 198	
Val 202	Val 201	
Phe 206	Leu 205	
Leu 210	Leu 209	
Met 214	Ile 213	
Ser 217	Trp 253	
Phe 255	Ser 282	
Leu 258	Val 286	
Trp 278		
Val 283		
Ile 290		

Table 5.3 : Excitation energies and oscillator strengths for model 4 (23 amino acids) and model 5 (60 amino acids), CAM-B3LYP/6-31G**

State	Model 4 (ωB97X-D/6-31G**)		Model 4 (CAM-B3LYP/6-31G**)		Model 5 (CAM-B3LYP/6-31G**)	
	Energy (nm)	Energy (nm)	Energy (nm)	Oscillator Strength	Energy (nm)	Oscillator Strength
1	692.46	0.3746	675.05	0.4194	632.59	0.3284
2	687.23	0.4202	669.89	0.4629	631.09	0.5300
3	675.93	0.0915	663.44	0.0683	621.14	0.1044
4	665.76	0.1809	653.84	0.1888	617.57	0.0181
5	660.4	0.4078	647.57	0.3882	610.94	0.7855
6	655.24	0.1396	643.13	0.1601	601.85	0.0925

Looking at table 5.3, model 5 has three states calculated with higher oscillator strengths and three with lower oscillator strengths, similar to the result for the WT model 4 with both CAM-B3LYP functional and ωB97X-D for the 6-31G** basis. The oscillator strength of ES 5 (f=0.7855) makes it the brightest state in the region followed by ES 2 (f = 0.5300). Compared with model 4 there is an increased variance among the high oscillator strength states 1, 2 and 5 for model 5, this leads to the preliminary conclusion that including more of the surrounding protein environment further tunes the pigment absorption energies to maximise the population of excited states that lead to CS.

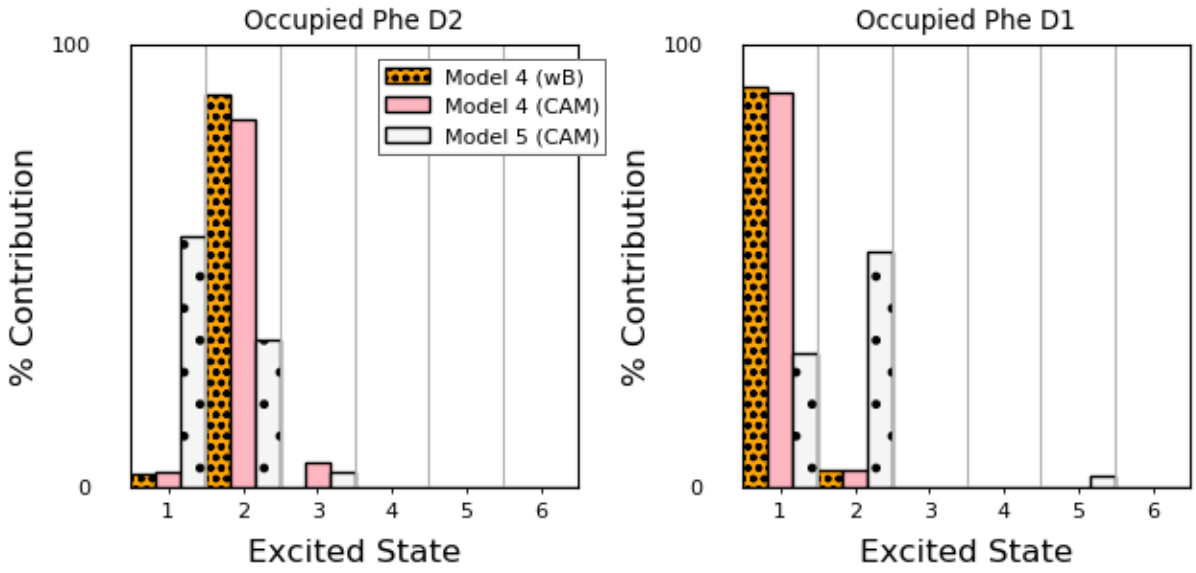


Figure 5.8 : Phe excitation contributions to ES 1-6 for model 4 and 5.

From Figure 5.8 it can be seen that the energies of the two pheophytin are close in energy for model 5, producing mixed ES 1 and 2 – with both Phe_{D1} and Phe_{D2} excitations contributing >30% to each. The state with the highest contribution from Phe_{D1} (ES 2) has the higher oscillator strength of the two states contributed to by Phe_{D1} excitation (ES 1 and ES 2). Compared to model 4, the ordering of Phe excitations has changed (see

Figure 5.8) although this is not surprising considering that smaller models 1-3 all predicted Phe_{D2} excitation to be the lowest energy ES (see chapter one).

Model 5 predicts a higher energy of P_{D1} excitation than model 4. P_{D1} excitation, which dominates ES 3 for model 4, contributes to ES 3-6 for model 5 (see Figure 5.9). P_{D2} excitation (dominant in ES 4 for model 4) is also predicted to have a higher energy by model 5, for which it dominates in ES 6 (see Figure 5.9). Figure 5.11 shows that Chl_{D2} excitation contributes to ES 3 and dominates in ES 4 for model 5, giving Chl_{D2} a lower excitation energy for model 5 than model 4. In chapter one it was shown that the nature of ES 4 and ES 6 were sensitive to the size of the model, and tended to be contributed to by P_{D2} and Chl_{D2} excitations.

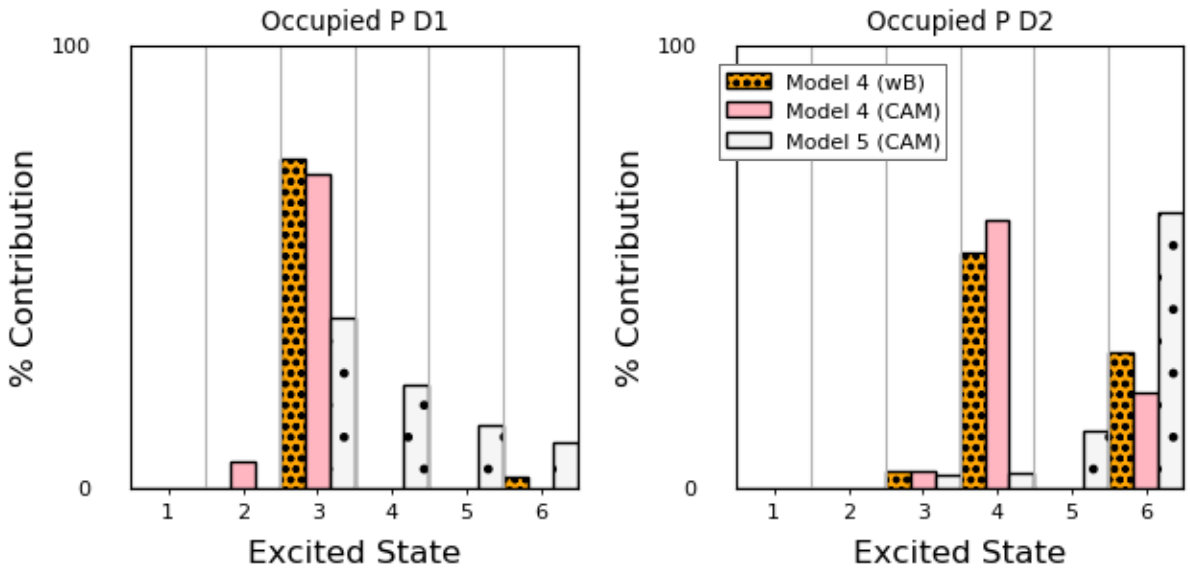


Figure 5.9 : P chlorophyll excitation contributions to ES 1-6 for models 4 and 5

Chl_{D1} excitation consistently gives the dominant contribution to ES 5 (see Figure 5.10), which is consistently a bright state in the Q_Y region (see table 5.3). ES 5 is the brightest state for model 5 (f=0.7855), whereas for model 4 the brightest state is ES 2 for both functionals. Also, the difference in oscillator strengths between ES 1, 2 and 5 is much greater for model 5 than model 4, meaning that Chl_{D1} excites with increased likelihood for model 5.

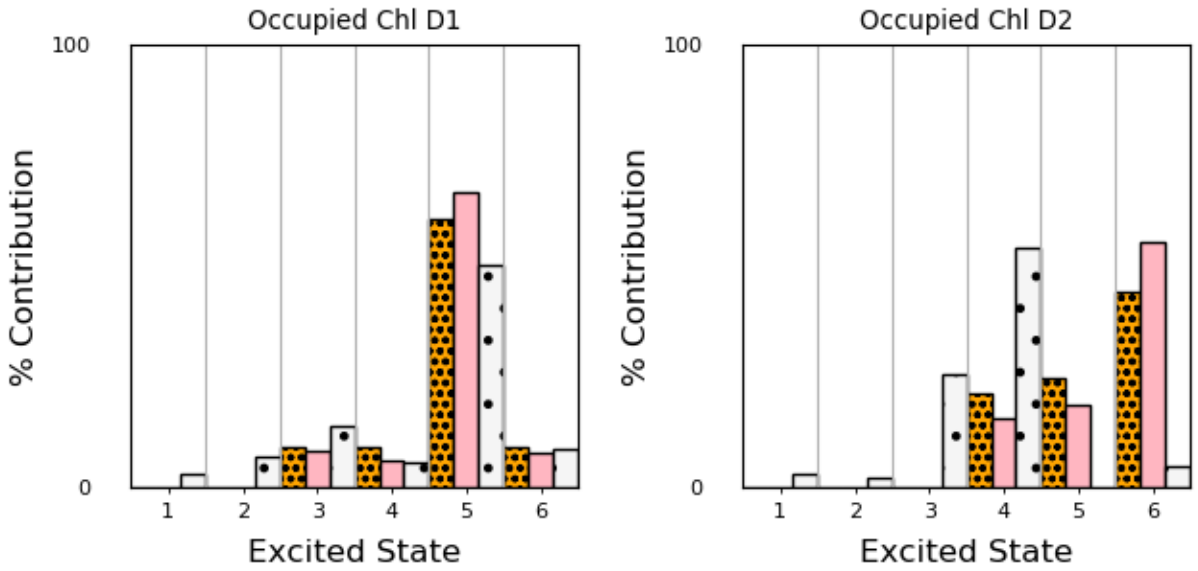


Figure 5.10 : Chl_{D1} and Chl_{D2} excitation contributions to ES 1-6 for models 4 and 5

From Figure 5.11 it can also be seen that the direction of CT during Phe_{D1} excitations is 'up active' for both model 4 and 5. In chapter one it was shown that the direction of CT for Phe_{D1} excitations was sensitive to the size of the model, it is therefore encouraging to see that models 4 and 5 are in agreement. In the right hand chart in Figure 5.11 it can be seen that transitions down the active branch only constitute a small fraction of ES 5 for models 4 and 5. Clearly, both of these models display a definite preference for CT to travel up the active branch.

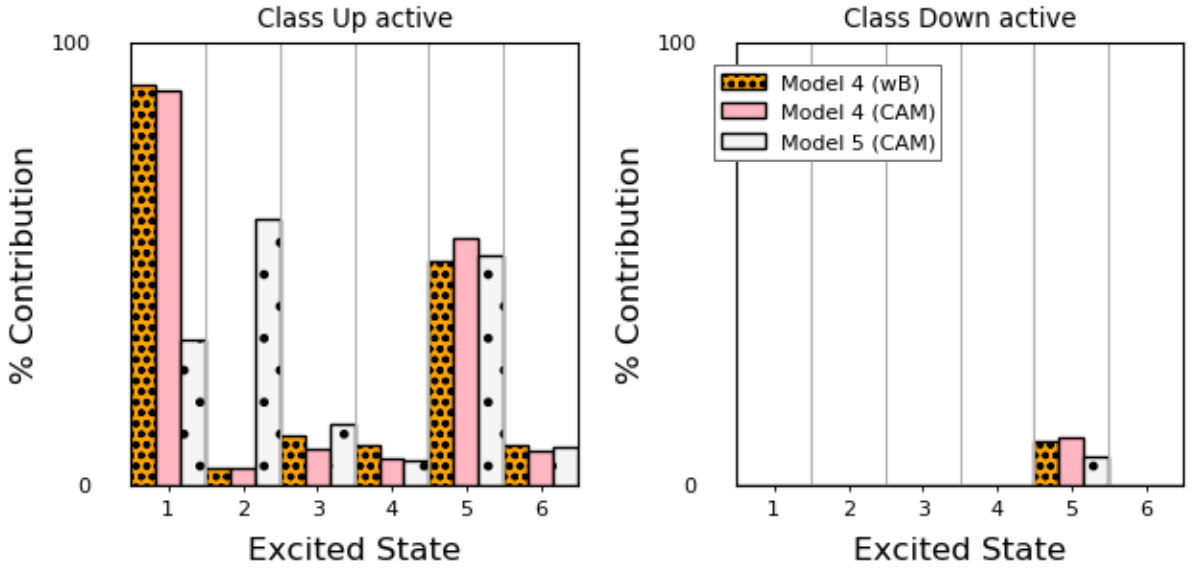


Figure 5.11 : Active branch transition contributions to ES 1-6 for models 4 and 5

Looking at the MOs which contribute to the active branch transitions for models 4 and 5 (tables 5.4 and 5.5), it can be seen that model 5 active branch transitions have more CT character than model 4. Movement during the transitions from MO 4151 → 4162 and 4155 → 4164 for model 5 constitute ~7% of electron population moving to cofactors higher up the active branch. These two transitions dominate ES 2 and ES 5, see Figure

5.14 for the depiction of these orbitals. However, table 5.5 shows that the two active branch transitions 2307 → 2313 and 2309 → 2315 describe movement of <1% of the electron population up the active branch cofactors.

Table 5.4 : MO Occupancy for Chl_{D1} and Phe_{D1} MOs of Model 5 (CAM-B3LYP/6-31G**)

Type	MO	Q_A	Phe_{D1}	Chl_{D1}	P_{D1}	P_{D2}
Occupied	4151	0.0	90.7	8.3	0.4	0.0
	4155	0	0.3	86.9	5.0	7.5
Virtual	4162	0.1	98.3	0.4	0.4	0.0
	4164	0	0.4	98.4	0.4	0.2

Table 5.5 : MO Occupancy for Chl_{D1} and Phe_{D1} MOs of Model 4 (CAM-B3LYP/6-31G**)

Type	MO	Q_A	Phe_{D1}	Chl_{D1}	P_{D1}	P_{D2}
Occupied	2307	N/A	97.3	0.9	0.8	0.6
	2309		0.4	98.0	0.4	0.9
Virtual	2313		98.3	0.7	0.4	0.0
	2315		0.8	97.8	0.5	0.4

It is likely that the addition of the Q_A to the model is in part responsible for driving charge up the active branch in model 5. Further work will need to be done to differential the effects of including the Q_A and the extra amino acid residues in model 5.

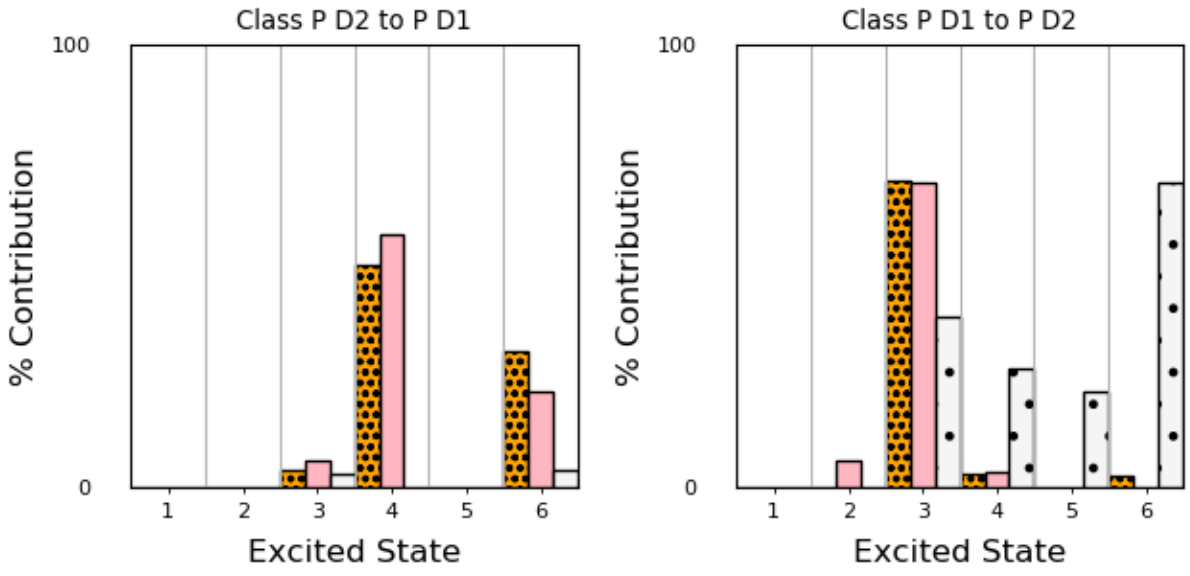


Figure 5.12 : P chlorophyll transition contributions to ES 1-6 for models 4 and 5

Transition between the P chlorophylls goes in one direction only for model 5, from P_{D1} to P_{D2} (see Figure 5.12). This is in poor agreement with the results for model 4 and the reasons behind this should be explored in further work. Taking a closer look at the MOs which describe the P chlorophyll transitions for models 4 (table 5.7) and 5 (table 5.6, Figure 5.14) it can be seen that whilst the distribution over the P chlorophylls in the

occupied MOs are similar for both models, the virtual orbitals are more evenly shared over the two P chlorophylls for model 4 (table 5.7, bottom two rows).

Table 5.6 : MO Occupancy for P chlorophyll MOs of Model 5 (CAM-B3LYP/6-31G**)

Type	MO	Chl_{D1}	P_{D1}	P_{D2}	Chl_{D2}
Occupied	4158	0.2	16.3	82.6	0.0
	4159	0.1	90.4	8.9	0.0
Virtual	4166	0.1	10.9	87.8	0.1
	4167	0.2	87.6	11.5	0.1

Table 5.7 : MO Occupancy for P chlorophyll MOs of Model 4 (CAM-B3LYP/6-31G**)

Type	MO	Chl_{D1}	P_{D1}	P_{D2}	Chl_{D2}
Occupied	2311	0.5	12.1	86.6	0.0
	2312	0.1	88.0	10.9	0.1
Virtual	2317	0.3	49.6	49.0	0.1
	2318	0.1	48.7	50.1	0.1

It is possible that model 5 results are a more accurate depiction of the precursors ES to CS than model 4 gives. The estimated charge distribution over the P chlorophylls in the P_{680}^{+} cation is ~80%:20% P_{D1} to P_{D2} which is similar to the distribution of electron density over P_{D1} and P_{D2} in the MOs 4159 and 4167 for model 5 (transition from 4159 → 4167 contributes to ES 3, 4 and 5 for model 5, see Figure 5.14). However, the identity of the exciton CT state ($P_{D2}^{\delta+}$ $P_{D1}^{\delta-}$)* implies CT in the P_{D2} to P_{D1} direction, which is only predicted for model 4.

The preference for inactive branch transitions to travel down the inactive branch is maintained for models 4 and 5 (see Figure 5.13).

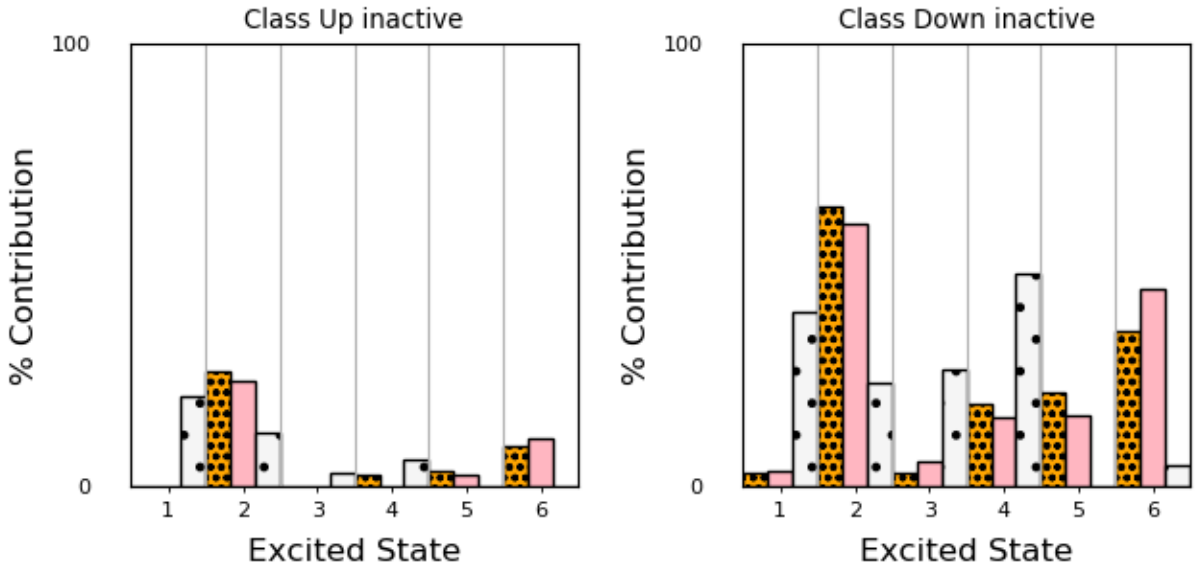
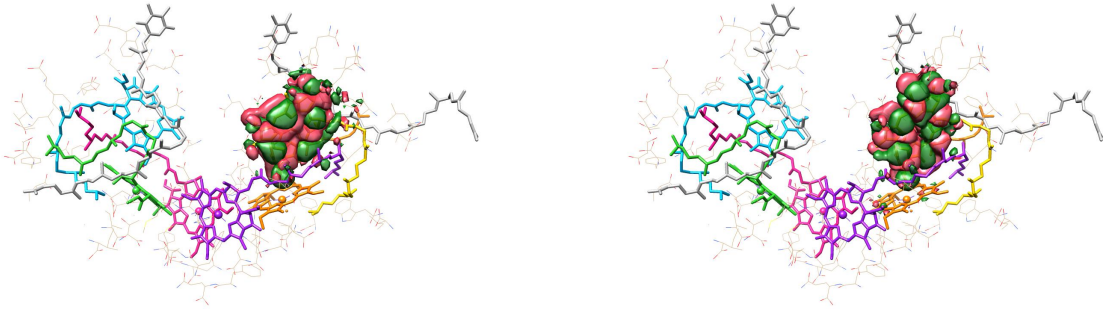
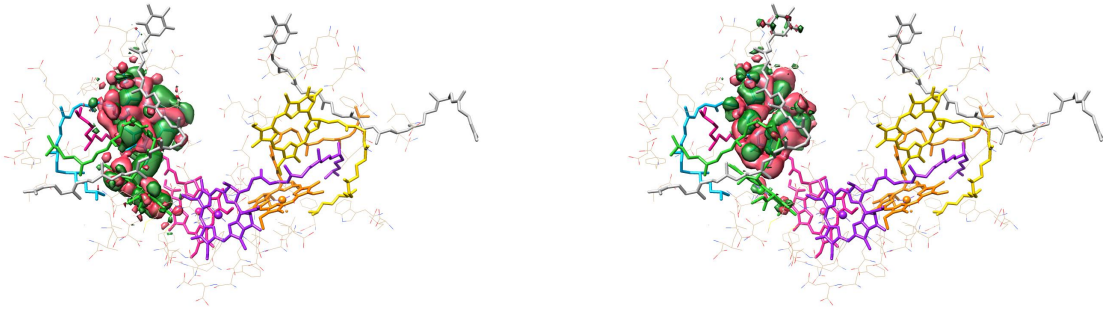


Figure 5.13 : Inactive branch transition contributions to ES 1-6 for models 4 and 5

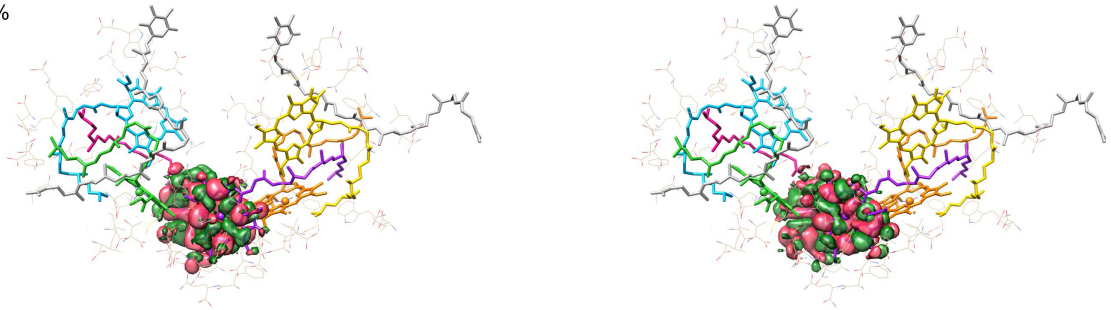
Down inactive (Phe D2 to Chl D2): 4157 → 4165
State 1: 31.42%
State 2: 18.01%
State 3: 3.38%



Up active (Chl D1 to Phe D1): 4151 → 4162
State 1: 19.96%
State 2: 32.60%
State 5: 2.40%



P D1 to P D2: 4159 → 4167
State 3: 31.98%
State 4: 21.20%
State 5: 14.31%
State 6: 2.94%



Down inactive (Phe D2 to Chl D2): 4150 → 4160
State 1: 2.71%
State 2: 2.04%
State 3: 22.72%
State 4: 47.87%
State 6: 4.75%

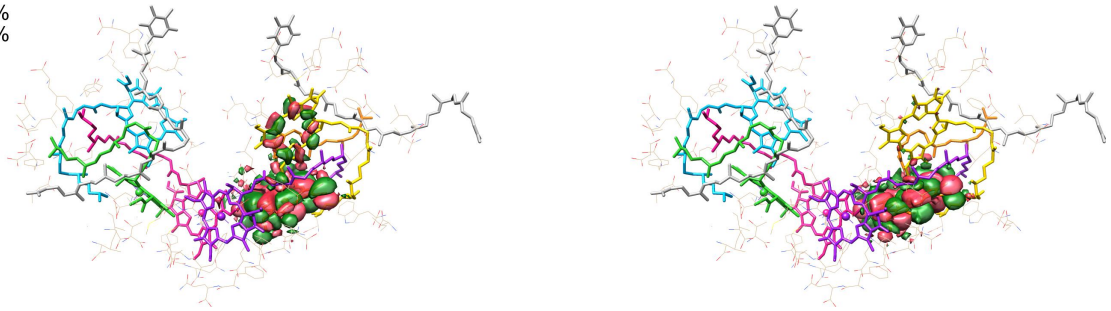


Figure 5.14 : MO diagrams showing dominant transitions contributing to ES 1-6 for model 5 CAM-B3LYP/6-31G**, LEFT COLUMN – Occupied MO, RIGHT COLUMN – Virtual MO (Page 1).

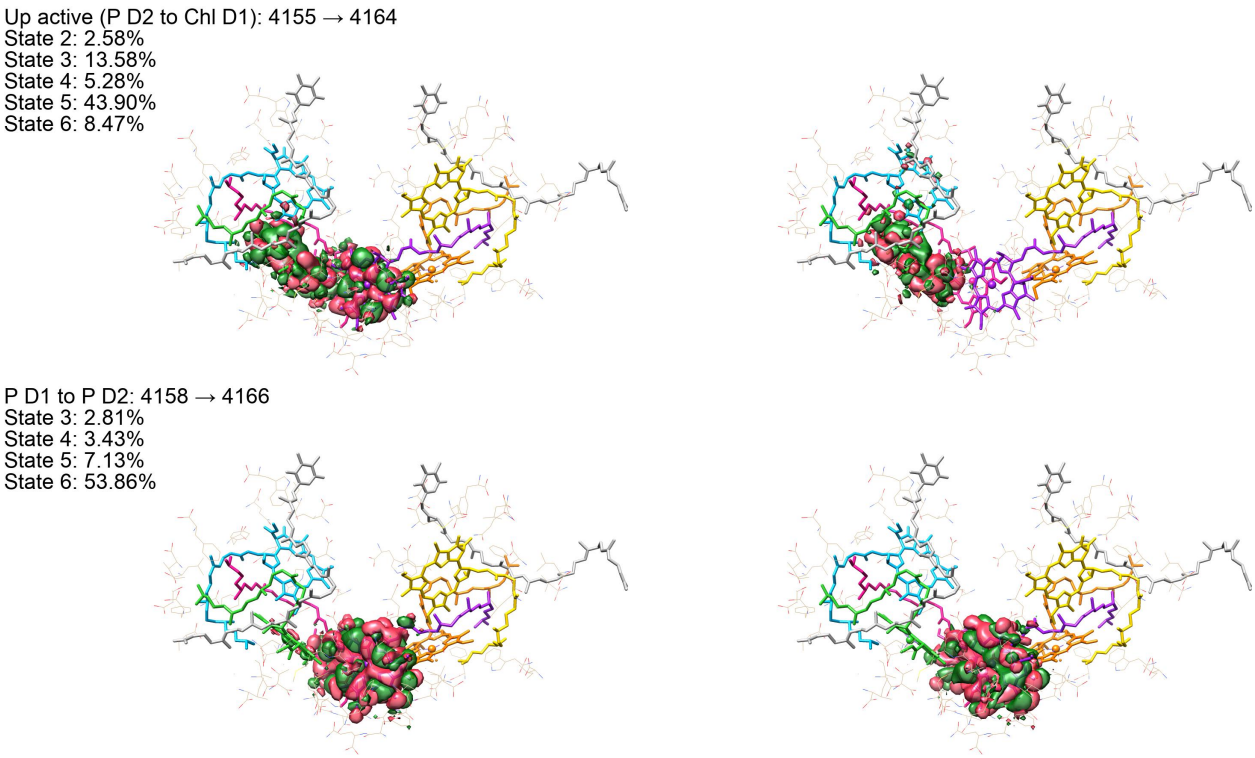


Figure 5.14 : MO diagrams showing dominant transitions contributing to ES 1-6 for model 5 CAM-B3LYP/6-31G**, LEFT COLUMN – Occupied MO, RIGHT COLUMN – Virtual MO (Page 2).

Conclusion

The results of TDDFT calculations on two WT models of the PS II RC are presented, in an attempt to observe any effects that might be missed by limiting the size of the model to that of model 4.

In the first part of this chapter the results of including the peripheral chlorophylls $Chlz_{D1}$ and $Chlz_{D2}$, in a model that was otherwise identical to model 2, was investigated. The resultant model was called model 2A. Aside from the insertion of $Chlz_{D1}$ and $Chlz_{D2}$ Q_Y excitations, there are no changes to the ordering of core RC cofactor excitation energies in the Q_Y region of the spectrum. The energy of Chl_{D1} excitation appears to have been reduced relative to model 2 due to the inclusion of the nearby $Chlz_{D1}$ and its axial His ligand. This is of interest, considering that the cofactor with the lowest excitation energy is expected to be Chl_{D1},[77] maybe providing some explanation as to why model 4 predicts Chl_{D1} absorption at higher energies than expected. The effect is small however, and Chl_{D1} excitation has the highest contribution to ES 4 for both models 2 and 2A. In light of this, earlier conclusions, that the specific conformation of the pigments in the crystal structure are primarily responsible for the higher energy of Chl_{D1} excitation in all models, still hold.

The second question posed in this chapter was 'is model 4 a sufficient benchmark model to probe the RC excited states?' Attempting to answer this involved comparison of a different, larger model of the PS II RC to the results from model 4. If the larger model 5 gave an excitation profile similar to model 4 (with the same ordering of cofactor energies, oscillator strengths and transitions) it could be concluded that model 4 was sufficient. Whilst there is a reordering of the cofactor excitations in ES 1 and 2, some features are conserved between models 4 and 5. Both models predict three high oscillator strength states (ES 1, 2 and 5) given by Phe_{D1}, Phe_{D2} and Chl_{D1} excitations. Furthermore, both Phe_{D1} and Chl_{D1} excitations describe movement of charge up the active branch for models 4 and 5 (this was not consistent between models 1-4, see chapter one). Overall, model 4 appears to be a good predictor of the direction of transitions along the two branches, but further work is needed to determine the reason for the lack of P_{D2} to P_{D1} CT predicted by model 5.

Chapter Six: Final Conclusions & Further Work

Summary of Research and Conclusions

This work focussed on the RC of PS II, where initial CS leading to solar energy storage takes place in oxygenic photosynthetic organisms. It is hoped that, with a deeper understanding of the design principles of this powerful, natural photosystem, better mimics (including artificial photosynthetic systems) and engineered organisms could be produced. The aims of this thesis, as set out in the introduction, were to build a model of the PS II RC which could be used to identify the specific features of the structure which lead to efficient charge separation up the active D1 branch. Models were built from the crystal structure of *T. vulcanus* and all non-hydrogen atoms were fixed in the crystal structure geometry. TDDFT was then used to investigate the excited states of RC models, including all six core pigments as a multimer in every model.

In the first chapter, the results of calculations on four differently-sized models of the RC are presented. It was shown that the results were sensitive to the size of the system, with the relative energies of the pigment excitations and the direction of charge movement being affected by the inclusion or exclusion of the surrounding protein or the pigment phytol chains in each model.

The largest model presented in chapter one (model 4) included full pigment phytol chains and 23 surrounding amino acids. Only model 4 predicted two high oscillator strength states with CT character travelling up the active branch. In other words, model 4 correctly predicted that the RC would direct charge up the active branch. For this reason, model 4 was chosen as the most suitable model to carry forwards to the next chapters.

Chapter two looked at the results of three mutant RC models in comparison with the WT model 4 from chapter one. The site of mutation, the ligand to P_{D2} on the inactive branch, was D2-198. Mutation to ala, asn and gln raise P_{D2} excitation energy and introduce a stronger coupling between Chl_{D1} and P_{D2} leading to exciton states involving these two cofactors. The red-shift of P^+-P absorption difference spectra for mutants H197A and H197N is reproduced by the models in this chapter, but the H197Q model displays a small shift in P_{D1} excitation to the blue. It is concluded in this chapter that modelling up to ES 22 may not be sufficient to observe the full effect of mutation on the Soret region of the mutant spectra.

In chapter three the results of calculations on D1-198 mutants are presented. The ligand to P_{D1} is mutated to ala, asn and gln, raising the energy of P_{D1} excitation and shifting the Soret region band of the same cofactor to higher energies. H198A displays the strongest deviation from WT results and suggests that this mutant lacks

the same preference for CT to travel up the active branch that is seen in the WT. Whilst each mutant displays qualitative agreement with experiment, the shift of the H198A P_{D1} band in the Soret region is farthest to the blue for the three mutants discussed in this chapter, in contrast to mutant P^{+}-P difference spectra results.

The fourth chapter looked at two further sites of mutation, D1-179 and D1-130, near the active branch pigments Chl_{D1} and Phe_{D1} respectively. This chapter included mutations to glutamic acid, modelled as a neutral residue, at both sites. Whilst mutation of D1-179 to histidine and D1-130 to leucine appeared to predict experimentally observed shifts in the excitation of Chl_{D1} and Phe_{D1}, neither site when mutated to glutamic acid achieved agreement with experiment. Therefore one conclusion from this chapter is that further work is needed to model charged glutamate residues at these sites to investigate the reason for the discrepancy between these models results and the mutant absorption spectra.

Finally, chapter five explored further regions of PS II surrounding the core RC pigments. Firstly showing that the effect of including the peripheral pigments, $Chlz_{D1}$ and $Chlz_{D2}$, on the excited states of the core RC hexamer was minimal, except for some lowering the energy of Chl_{D1} excitation to nearer degenerate with Chl_{D2}. Secondly, including a larger region of the surrounding protein (60 amino acids) and the plastoquinone Q_A and Q_B was investigated in model 5. Model 5 predicts high oscillator strength states with major contributions from Phe_{D1}, Phe_{D2} and Chl_{D1} excitation, in good agreement with results from models 1-4. Like model 4, model 5 displays a strong preference for charge movement up the active branch and charge movement down the inactive branch. It is therefore concluded in this chapter that model 4 remains a satisfactory predictor of the direction of transitions on the active and inactive branches. However, the degree of movement in active branch model 5 transitions is greater than that for model 4, meaning that the more extensive protein environment is further tuning the RC to direct charge up the active branch. One other interesting feature of model 5 is the lack of any state dominated by the P_{D1} to P_{D2} transition. It is strongly recommended that this be explored further, especially as exciton-CT state $P_{D1}^{+}P_{D2}^{-}$ has been identified as a precursor to CS.

Further Work

Two additional further work streams to that which is discussed above are described below.

A Predictive Model for Mutations

Several things are clear upon looking at the results presented as a whole. Most positively, it can be said that the crystal structure geometry and the chosen method of TDDFT do manage to produce models which predict a preference for CT travelling up the active branch (particularly when larger regions of the RC are included). Furthermore, the majority of mutant models discussed in this thesis successfully reproduce shifts in absorption difference spectra compared with the WT model. In conclusion, the models presented are valid and may be used to predict the action of specific mutations on the behaviour of the RC. The models presented in this work could therefore be used to further study the effects of mutations at different sites, which would give more insight into the specific effects of individual residues on the preference for CT to proceed along the D1 branch. A model such as this would be a powerful tool for the agricultural industry, as key targets within PS II could be identified.

Exploring Conformational Space

One major concern for future study is the fixed geometry of the pigments, based on crystal structure geometry, that was used throughout this work. It is known that Chl_{D1} is the lowest absorbing pigment in the complex, however all models in this thesis predict Phe_{D1}, Phe_{D2} or P_{D1} excitation as the major contributors to the lowest energy ES. Furthermore, this work has to rely on comparison of the excitation energies and oscillator strengths for a single point on the potential energy surface with the ensemble of disordered RCs in a living sample. Therefore, further work should aim to explore different geometries of the models used here that may be more representative of a sample of living PS II.

The two known charge separation pathways available within the RC that will lead to successful photosynthesis, are likely switched between in order to remain robust to conformational changes (Romero, 2012). Further motivation for exploring conformational space of the RC would be to understand the relationship between protein motion and the preference for one charge separation pathway over another. This will be key to engineering robust photosynthetic materials ourselves.

In order to do this it would first be necessary to reduce the cost of the method used considerably, such that a reasonable number of structural geometries could be sampled. This could be achieved using the benchmark of the models presented in this thesis, using hybrid quantum mechanics/ molecular mechanics methods to

develop a dataset of hundreds of snapshots of the RC from molecular dynamics trajectories. In this way a set of excitation energy and oscillator strength data could be produced that could be better compared with ensemble absorption data for RC complexes. This would also enable an examination of which conformational features would favour excitation at each of the RC pigments.

Bibliography

1. Barber, J. Hydrogen derived from water as a sustainable solar fuel: learning from biology. *Sustain. Energy Fuels* 927–935 (2018) doi:10.1039/C8SE00002F.
2. Montoya, J. H., Seitz, L. C., Chakthranont, P., Vojvodic, A., Jaramillo, T. F. & Nørskov, J. K. Materials for solar fuels and chemicals. *Nat. Mater.* **16**, 70–81 (2016).
3. Spitler, M. T., Modestino, M. A., Deutsch, T. G., Xiang, C. X., Durrant, J. R., Esposito, D. V., Haussener, S., Maldonado, S., Sharp, I. D., Parkinson, B. A., Ginley, D. S., Houle, F. A., Hannappel, T., Neale, N. R., Nocera, D. G. & McIntyre, P. C. Practical challenges in the development of photoelectrochemical solar fuels production. *Sustain. Energy Fuels* **4**, 985–995 (2020).
4. Zhang, J. Z. & Reisner, E. Advancing photosystem II photoelectrochemistry for semi-artificial photosynthesis. *Nat. Rev. Chem.* **4**, 6–21 (2020).
5. Batista-Silva, W., da Fonseca-Pereira, P., Martins, A. O., Zsögön, A., Nunes-Nesi, A. & Araújo, W. L. Engineering Improved Photosynthesis in the Era of Synthetic Biology. *Plant Commun.* **1**, 100032 (2020).
6. Conijn, J. G., Bindraban, P. S., Schröder, J. J. & Jongschaap, R. E. E. Can our global food system meet food demand within planetary boundaries? *Agric. Ecosyst. Environ.* **251**, 244–256 (2018).
7. Vermeulen, S. J., Campbell, B. M. & Ingram, J. S. I. Climate Change and Food Systems. *Annu. Rev. Environ. Resour.* **37**, 195–222 (2012).
8. Allen, M. ., Dube, O. ., Solecki, W., Aragón-Durand, F., Cramer, W., Humphreys, S., Kainuma, M., Kala, J., Mahowald, N., Mulugetta, Y., Perez, R., Wairiu, M. & Zickfeld, K. *Framing and Context. In: Global Warming of 1.5°C. An IPCC Special Report on the impacts of global warming of 1.5°C above pre-industrial levels and related global greenhouse gas emission pathways, in the context of strengthening the global response to the*. (2018).
9. Barber, J. Photosynthetic energy conversion: natural and artificial. *Chem. Soc. Rev.* **38**, 185–196 (2009).
10. David, C. & Mackay, J. C. *Sustainable Energy — without the hot air*. *Energy* vol. 78 (2009).
11. Odella, E., Mora, S. J., Wadsworth, B. L., Huynh, M. T., Goings, J. J., Liddell, P. A., Groy, T. L., Gervaldo, M., Sereno, L. E., Gust, D., Moore, T. A., Moore, G. F., Hammes-Schiffer, S. & Moore, A. L. Controlling Proton-Coupled Electron Transfer in Bioinspired Artificial Photosynthetic Relays. *J. Am. Chem. Soc.* **140**, 15450–15460 (2018).
12. Scholes, G. D., Fleming, G. R., Chen, L. X., Aspuru-Guzik, A., Buchleitner, A., Coker, D. F., Engel, G. S., Van Grondelle, R., Ishizaki, A., Jonas, D. M., Lundeen, J. S., McCusker, J. K., Mukamel, S., Ogilvie, J. P., Olaya-Castro, A., Ratner, M. A., Spano, F. C., Whaley, K. B. & Zhu, X. Using coherence to enhance function in chemical and biophysical systems. *Nature* **543**, 647–656 (2017).
13. Gruissem, W. Genetically modified crops : the truth unveiled. 3–4 (2015) doi:10.2527/jas.
14. Beckie, H. J. & Tardif, F. J. Herbicide cross resistance in weeds. *Crop Prot.* **35**, 15–28 (2012).
15. Blankenship, R. E. *Molecular Mechanisms of Photosynthesis, Second Edition*. (Wiley Blackwell, 2014). doi:10.1002/9780470758472.
16. Van Grondelle, R. & Novoderezhkinb, V. I. Quantum effects in photosynthesis. *Procedia Chem.* **3**, 198–210 (2011).
17. Van Grondelle, R., Van Amerongen, H. & Valkunas, L. *Photosynthetic Excitons*. (2000).
18. Fassioli, F., Dinshaw, R., Arpin, P. C. & Scholes, G. D. Photosynthetic light harvesting: excitons and coherence. *J. R. Soc. Interface* **11**, 20130901 (2014).
19. Förster, T. 10th Spiers Memorial Lecture. Transfer mechanisms of electronic excitation. *Discuss. Faraday Soc.* **27**, 7–17 (1959).
20. Beljonne, D., Curutchet, C., Scholes, G. D. & Silbey, R. J. Beyond förster resonance energy transfer in biological and nanoscale systems. *J. Phys. Chem. B* **113**, 6583–6599 (2009).
21. Romero, E., Augulis, R., Novoderezhkin, V. I., Ferretti, M., Thieme, J., Zigmantas, D. & Van Grondelle, R. Quantum coherence in photosynthesis for efficient solar-energy conversion. *Nat. Phys.* **10**, 676–682

(2014).
22. Umena, Y., Kawakami, K., Shen, J.-R. & Kamiya, N. Crystal structure of oxygen-evolving photosystem II at a resolution of 1.9 Å. *Nature* **473**, 55–60 (2011).
23. Watanabe, M., Iwai, M., Narikawa, R. & Ikeuchi, M. Is the photosystem II complex a monomer or a dimer? *Plant Cell Physiol.* **50**, 1674–1680 (2009).
24. Williamson, A., Conlan, B., Hillier, W. & Wydrzynski, T. The evolution of Photosystem II: Insights into the past and future. *Photosynth. Res.* **107**, 71–86 (2011).
25. van Kan, P. J. M., Otte, S. C. M., Kleinherenbrink, F. a. M., Nieveen, M. C., Aartsma, T. J. & van Gorkom, H. J. Time-resolved spectroscopy at 10 K of the Photosystem II reaction center; deconvolution of the red absorption band. *Biochim. Biophys. Acta - Bioenerg.* **1020**, 146–152 (1990).
26. Barter, L. M. C. & Klug, D. R. A unified picture of energy and electron transfer in primary photosynthesis. *Chem. Phys.* **319**, 308–315 (2005).
27. Barber, J. Photosystem II: its function, structure, and implications for artificial photosynthesis. *Biochem. Biokhimiia* **79**, 185–96 (2014).
28. Kok, B., Forbush, B. & McGloin, M. Cooperation Of Charges In Photosynthetic O2 Evolution–I. A Linear Four Step Mechanism. *Photochem. Photobiol.* **11**, 457–475 (1970).
29. Joliot, P., Barbieri, G. & Chabaud, R. A New Model of Photochemical Centers in System-2. *Photochem. Photobiol.* **10**, 309–329 (1969).
30. Cardona, T., Sedoud, A., Cox, N. & Rutherford, A. W. Charge separation in Photosystem II: A comparative and evolutionary overview. *Biochim. Biophys. Acta - Bioenerg.* **1817**, 26–43 (2012).
31. Rutherford, A. W. & Faller, P. The heart of photosynthesis in glorious 3D. *Trends Biochem. Sci.* **26**, 341–344 (2001).
32. Durrant, J. R., Klug, D. R., Kwa, S. L., van Grondelle, R., Porter, G. & Dekker, J. P. A multimer model for P680, the primary electron donor of photosystem II. *Proc. Natl. Acad. Sci. U. S. A.* **92**, 4798–4802 (1995).
33. Romero, E., Diner, B. A., Nixon, P. J., Coleman, W. J., Dekker, J. P. & Van Grondelle, R. Mixed exciton-charge-transfer states in photosystem II: Stark spectroscopy on site-directed mutants. *Biophys. J.* **103**, 185–194 (2012).
34. Novoderezhkin, V. I., Dekker, J. P. & van Grondelle, R. Mixing of exciton and charge-transfer states in Photosystem II reaction centers: modeling of Stark spectra with modified Redfield theory. *Biophys. J.* **93**, 1293–1311 (2007).
35. Novoderezhkin, V. I., Romero, E., Dekker, J. P. & van Grondelle, R. Multiple charge-separation pathways in photosystem II: modeling of transient absorption kinetics. *Chemphyschem* **12**, 681–688 (2011).
36. Romero, E., Van Stokkum, I. H. M., Novoderezhkin, V. I., Dekker, J. P. & Van Grondelle, R. Two different charge separation pathways in photosystem II. *Biochemistry* **49**, 4300–4307 (2010).
37. Novoderezhkin, V. I., Romero, E. & van Grondelle, R. How exciton-vibrational coherences control charge separation in the photosystem II reaction center. *Phys. Chem. Chem. Phys.* **17**, 30828–30841 (2015).
38. Diner, B. A., Schlodder, E., Nixon, P. J., Coleman, W. J., Rappaport, F., Lavergne, J., Vermaas, W. F. J. & Chisholm, D. A. Site-directed mutations at D1-His198 and D2-His197 of photosystem II in Synechocystis PCC 6803: Sites of primary charge separation and cation and triplet stabilization. *Biochemistry* **40**, 9265–9281 (2001).
39. Nagao, R., Yamaguchi, M., Nakamura, S., Ueoka-Nakanishi, H. & Noguchi, T. Genetically introduced hydrogen bond interactions reveal an asymmetric charge distribution on the radical cation of the special-pair chlorophyll P680. *J. Biol. Chem.* **292**, 7474–7486 (2017).
40. Saito, K., Shen, J. R. & Ishikita, H. Influence of the axial ligand on the cationic properties of the chlorophyll pair in photosystem II from thermosynechococcus vulcanus. *Biophys. J.* **102**, 2634–2640 (2012).
41. Saito, K., Ishida, T., Sugiura, M., Kawakami, K., Umena, Y., Kamiya, N., Shen, J. R. & Ishikita, H. Distribution of the cationic state over the chlorophyll pair of the photosystem II reaction center. *J. Am. Chem. Soc.* **133**, 14379–14388 (2011).
42. Vermaas, W. F. J., Williams, J. G. K. & Arntzen, C. J. Site-Directed Mutations of Two Histidine Residues

in the D2 Protein Inactivate and Destabilize Photosystem II in the Cyanobacterium Synechocystis 6803. *Zeitschrift für Naturforsch. C* **42**, 762–768 (1987).

43. Saito, K., Shen, J. R. & Ishikita, H. Cationic state distribution over the chlorophyll d-containing P D1/PD2 pair in photosystem II. *Biochim. Biophys. Acta - Bioenerg.* **1817**, 1191–1195 (2012).
44. Okubo, T., Tomo, T., Sugiura, M. & Noguchi, T. Perturbation of the structure of P680 and the charge distribution on its radical cation in isolated reaction center complexes of photosystem II as revealed by fourier transform infrared spectroscopy. *Biochemistry* **46**, 4390–4397 (2007).
45. Bylina, E. J. & Youvan, D. C. Directed mutations affecting spectroscopic and electron transfer properties of the primary donor in the photosynthetic reaction center. *Proc. Natl. Acad. Sci.* **85**, 7226–7230 (1988).
46. Di Donato, M., Cohen, R. O., Diner, B. a, Breton, J., van Grondelle, R. & Groot, M. L. Primary charge separation in the photosystem II core from Synechocystis: a comparison of femtosecond visible/midinfrared pump-probe spectra of wild-type and two P680 mutants. *Biophys. J.* **94**, 4783–4795 (2008).
47. Merry, S. a, Nixon, P. J., Barter, L. M., Schilstra, M., Porter, G., Barber, J., Durrant, J. R. & Klug, D. R. Modulation of quantum yield of primary radical pair formation in photosystem II by site-directed mutagenesis affecting radical cations and anions. *Biochemistry* **37**, 17439–47 (1998).
48. Sugiura, M., Ozaki, Y., Rappaport, F. & Boussac, A. Corrigendum to 'Influence of Histidine-198 of the D1 subunit on the properties of the primary electron donor, P680, of photosystem II in Thermosynechococcus elongatus'. *Biochim. Biophys. Acta - Bioenerg.* **1857**, 1943–1948 (2016).
49. Raszewski, G., Diner, B. a, Schlodder, E. & Renger, T. Spectroscopic properties of reaction center pigments in photosystem II core complexes: revision of the multimer model. *Biophys. J.* **95**, 105–119 (2008).
50. Saito, K., Umena, Y., Kawakami, K., Shen, J. R., Kamiya, N. & Ishikita, H. Deformation of chlorin rings in the photosystem II crystal structure. *Biochemistry* **51**, 4290–4299 (2012).
51. Shelnutt, J. A., Song, X. Z., Ma, J. G., Jia, S. L., Jentzen, W. & Medforth, C. J. Nonplanar porphyrins and their significance in proteins. *Chem. Soc. Rev.* **27**, 31–41 (1998).
52. Schlodder, E., Renger, T., Raszewski, G., Coleman, W. J., Nixon, P. J., Cohen, R. O. & Diner, B. A. Site-directed mutations at D1-Thr179 of photosystem II in Synechocystis sp. PCC 6803 modify the spectroscopic properties of the accessory chlorophyll in the D1-branch of the reaction center. *Biochemistry* **47**, 3143–3154 (2008).
53. Takegawa, Y., Nakamura, M., Nakamura, S., Noguchi, T., Sellés, J., Rutherford, A. W., Boussac, A. & Sugiura, M. New insights on Chl D1 function in Photosystem II from site-directed mutants of D1/T179 in Thermosynechococcus elongatus. *Biochim. Biophys. Acta - Bioenerg.* **1860**, 297–309 (2019).
54. Giorgi, L. B., Nixon, P. J., Merry, S. a P., Joseph, D. M., Durrant, J. R., De Las Rivas, J., Barber, J., Porter, G. & Klug, D. H. Comparison of primary charge separation in the photosystem II reaction center complex isolated from wild-type and D1-130 mutants of the cyanobacterium Synechocystis PCC 6803. *J. Biol. Chem.* **271**, 2093–2101 (1996).
55. Rappaport, F., Guergova-Kuras, M., Nixon, P. J., Diner, B. A. & Lavergne, J. Kinetics and pathways of charge recombination in photosystem II. *Biochemistry* **41**, 8518–8527 (2002).
56. Sugiura, M., Azami, C., Koyama, K., Rutherford, A. W., Rappaport, F. & Boussac, A. Modification of the pheophytin redox potential in Thermosynechococcus elongatus Photosystem II with PsbA3 as D1. *Biochim. Biophys. Acta - Bioenerg.* **1837**, 139–148 (2014).
57. Rehman, A. U., Cser, K., Sass, L. & Vass, I. Characterization of singlet oxygen production and its involvement in photodamage of Photosystem II in the cyanobacterium Synechocystis PCC 6803 by histidine-mediated chemical trapping. *Biochim. Biophys. Acta - Bioenerg.* **1827**, 689–698 (2013).
58. Cser, K. & Vass, I. Radiative and non-radiative charge recombination pathways in Photosystem II studied by thermoluminescence and chlorophyll fluorescence in the cyanobacterium Synechocystis 6803. *Biochim. Biophys. Acta - Bioenerg.* **1767**, 233–243 (2007).
59. Cuni, A., Xiong, L., Sayre, R., Rappaport, F. & Lavergne, J. Erratum: Modification of the pheophytin midpoint potential in photosystem II: Modulation of the quantum yield of charge separation and of charge recombination pathways (Physical Chemistry Chemical Physics (2004) 6 DOI:

10.1039/b407511k). *Phys. Chem. Chem. Phys.* **6**, 4912 (2004).
60. Rhee, K. H., Morris, E. P., Barber, J. & Kühlbrandt, W. Three-dimensional structure of the plant photosystem II reaction centre at 8 Å resolution. *Nature* **396**, 283–286 (1998).
61. Barter, L. M. C., Durrant, J. R. & Klug, D. R. A quantitative structure-function relationship for the Photosystem II reaction center: supermolecular behavior in natural photosynthesis. *Proc. Natl. Acad. Sci. U. S. A.* **100**, 946–51 (2003).
62. Raszewski, G., Saenger, W. & Renger, T. Theory of optical spectra of photosystem II reaction centers: location of the triplet state and the identity of the primary electron donor. *Biophys. J.* **88**, 986–998 (2005).
63. Biesiadka, J., Loll, B., Kern, J., Irrgang, K.-D., Zouni, A. & Saenger, W. Crystal structure of photosystem II at 3.2 Å provides new details of protein–cofactor interactions. *Acta Crystallogr. Sect. A Found. Crystallogr.* **60**, s144–s144 (2004).
64. Ferreira, K. N., Iverson, T. M., Maghlaoui, K., Barber, J. & Iwata, S. Architecture of the Photosynthetic Oxygen-Evolving Center. *Sci.* **303**, 1831–1838 (2004).
65. Leegwater, J. A., Durrant, J. R. & Klug, D. R. Exciton equilibration induced by phonons: Theory and application to PS II reaction centers. *J. Phys. Chem. B* **101**, 7205–7210 (1997).
66. Renger, T. & Marcus, R. A. Photophysical properties of PS-2 reaction centers and a discrepancy in exciton relaxation times. *J. Phys. Chem. B* **106**, 1809–1819 (2002).
67. Renger, T., Madjet, M. E. A., Schmidt Am Busch, M., Adolphs, J. & Müh, F. Structure-based modeling of energy transfer in photosynthesis. *Photosynth. Res.* **116**, 367–388 (2013).
68. Novoderezhkin, V. I., Andrizhiyevskaya, E. G., Dekker, J. P. & van Grondelle, R. Pathways and timescales of primary charge separation in the photosystem II reaction center as revealed by a simultaneous fit of time-resolved fluorescence and transient absorption. *Biophys. J.* **89**, 1464–1481 (2005).
69. Gelzinis, A., Abramavicius, D., Ogilvie, J. P. & Valkunas, L. Spectroscopic properties of photosystem II reaction center revisited. *J. Chem. Phys.* **147**, 115102 (2017).
70. Ivashin, N. & Larsson, S. Excitonic states in photosystem II reaction center. *J. Phys. Chem. B* **109**, 23051–23060 (2005).
71. Ishikita, H., Saenger, W., Biesiadka, J., Loll, B. & Knapp, E. W. How photosynthetic reaction centers control oxidation power in chlorophyll pairs P680, P700, and P870. *Proc. Natl. Acad. Sci. U. S. A.* **103**, 9855–9860 (2006).
72. Kawashima, K. & Ishikita, H. Energetic insights into two electron transfer pathways in light-driven energy-converting enzymes. *Chem. Sci.* **9**, 4083–4092 (2018).
73. Kulik, N., Kutý, M. & Řeha, D. The study of conformational changes in photosystem II during a charge separation. *J. Mol. Model.* **26**, (2020).
74. Frankcombe, T. J. Explicit calculation of the excited electronic states of the photosystem II reaction centre. *Phys. Chem. Chem. Phys.* **17**, 3295–3302 (2015).
75. Kitagawa, Y., Matsuda, K. & Hasegawa, J. Theoretical study of the excited states of the photosynthetic reaction center in photosystem II: Electronic structure, interactions, and their origin. *Biophys. Chem.* **159**, 227–236 (2011).
76. Vasil'ev, S. & Bruce, D. A protein dynamics study of photosystem II: The effects of protein conformation on reaction center function. *Biophys. J.* **90**, 3062–3073 (2006).
77. Zhang, L., Silva, D., Zhang, H., Yue, A., Yan, Y. & Huang, X. Dynamic protein conformations preferentially drive energy transfer along the active chain of the photosystem II reaction centre. *Nat. Commun.* 1–9 (2014) doi:10.1038/ncomms5170.
78. Renger, T. & Schlodder, E. Primary photophysical processes in photosystem II: Bridging the gap between crystal structure and optical spectra. *ChemPhysChem* **11**, 1141–1153 (2010).
79. Kavanagh, M. A., Karlsson, J. K. G., Colburn, J. D., Barter, L. M. C. & Gould, I. R. A TDDFT investigation of the photosystem II reaction center: Insights into the precursors to charge separation. *Proc. Natl. Acad. Sci. U. S. A.* **117**, 19705–19712 (2020).
80. Schrödinger, E. An Undulatory Theory of the Mechanics of Atoms and Molecules. *Phys. Rev.* **28**, 1049–1070 (1926).

81. Atkins, P. W. & Friedman, R. S. *Molecular quantum mechanics*. (Oxford University Press, 2011).
82. Born, M. & Oppenheimer, R. Zur Quantentheorie der Molekeln. *Ann. Phys.* **389**, 457–484 (1927).
83. Susskind, L. & Friedman, A. *Quantum Mechanics: The Theoretical Minimum*. (Penguin Books Limited, 2014).
84. Hartree, D. R. The Wave Mechanics of an Atom with a Non-Coulomb Central Field. Part I. Theory and Methods. *Math. Proc. Cambridge Philos. Soc.* **24**, 89–110 (1928).
85. Jenson, F. *Introduction to Computational Chemistry*. (John Wiley & Sons, 2007).
86. Slater, J. ~C. The Theory of Complex Spectra. *Phys. Rev.* **34**, 1293–1322 (1929).
87. Fock, V. Näherungsmethode zur Lösung des quantenmechanischen Mehrkörperproblems. *Zeitschrift für Phys.* **61**, 126–148 (1930).
88. Cramer, C. J. *Essentials of Computational Chemistry: Theories and Models*. (Wiley, 2005).
89. Ritz, W. Über eine neue Methode zur Lösung gewisser Variationsprobleme der mathematischen Physik. *J. für die reine und Angew. Math.* **1909**, 1–61.
90. Frisch, M. J., Pople, J. a. & Binkley, J. S. Self-consistent molecular orbital methods 25. Supplementary functions for Gaussian basis sets. *J. Chem. Phys.* **80**, 3265 (1984).
91. Ditchfield, R., Hehre, W. J. & Pople, J. A. Self-Consistent Molecular-Orbital Methods. IX. An Extended Gaussian-Type Basis for Molecular-Orbital Studies of Organic Molecules. *J. Chem. Phys.* **54**, 724–728 (1971).
92. Hehre, W. J., Ditchfield, R. & Pople, J. A. Self—Consistent Molecular Orbital Methods. XII. Further Extensions of Gaussian—Type Basis Sets for Use in Molecular Orbital Studies of Organic Molecules. *J. Chem. Phys.* **56**, 2257–2261 (1972).
93. Francl, M. M., Pietro, W. J., Hehre, W. J., Binkley, J. S., Gordon, M. S., DeFrees, D. J. & Pople, J. A. Self-consistent molecular orbital methods. XXIII. A polarization-type basis set for second-row elements. *J. Chem. Phys.* **77**, 3654–3665 (1982).
94. Binning Jr., R. C. & Curtiss, L. A. Compact contracted basis sets for third-row atoms: Ga–Kr. *J. Comput. Chem.* **11**, 1206–1216 (1990).
95. Blaudeau, J.-P., McGrath, M. P., Curtiss, L. A. & Radom, L. Extension of Gaussian-2 (G2) theory to molecules containing third-row atoms K and Ca. *J. Chem. Phys.* **107**, 5016–5021 (1997).
96. Rassolov, V. A., Pople, J. A., Ratner, M. A. & Windus, T. L. 6-31G* basis set for atoms K through Zn. *J. Chem. Phys.* **109**, 1223–1229 (1998).
97. Rassolov, V. A., Ratner, M. A., Pople, J. A., Redfern, P. C. & Curtiss, L. A. 6-31G* basis set for third-row atoms. *J. Comput. Chem.* **22**, 976–984 (2001).
98. Jensen, F. *Introduction to Computational Chemistry*. (Wiley, 2007).
99. Hohenberg, P. & Kohn, W. Inhomogeneous Electron Gas. *Phys. Rev.* **136**, B864--B871 (1964).
100. Kohn, W. & Sham, L. J. Self-Consistent Equations Including Exchange and Correlation Effects. *Phys. Rev.* **140**, A1133--A1138 (1965).
101. Antoniewicz, P. R. & Kleinman, L. Kohn-Sham exchange potential exact to first order in rho. *Phys. Rev. B. Condens. Matter* **31**, 6779–6781 (1985).
102. Becke, A. D. Density-functional exchange-energy approximation with correct asymptotic behavior. *Phys. Rev. A* **38**, 3098–3100 (1988).
103. Lee, C., Yang, W. & Parr, R. G. Development of the Colle-Salvetti correlation-energy formula into a functional of the electron density. *Phys. Rev. B* **37**, 785–789 (1988).
104. Becke, A. D. Density-functional thermochemistry. III. The role of exact exchange. *J. Chem. Phys.* **98**, 5648–5652 (1993).
105. Yanai, T., Tew, D. P. & Handy, N. C. A new hybrid exchange-correlation functional using the Coulomb-attenuating method (CAM-B3LYP). *Chem. Phys. Lett.* **393**, 51–57 (2004).
106. Chai, J. Da & Head-Gorden, M. Long-range corrected hybrid density functionals with improved dispersion corrections. *J. Chem. Theory Comput.* **10**, 6615–6620 (2008).
107. Chai, J. Da & Head-Gordon, M. Systematic optimization of long-range corrected hybrid density functionals. *J. Chem. Phys.* **128**, 0–15 (2008).
108. Becke, A. D. Density-functional thermochemistry. V. Systematic optimization of exchange-correlation

functionals. *J. Chem. Phys.* **107**, 8554–8560 (1997).
109. Grimme, S. Semiempirical GGA-type density functional constructed with a long-range dispersion correction. *J. Comput. Chem.* **27**, 1787–1799 (2006).
110. Runge, E. & Gross, E. K. U. Density-functional theory for time-dependent systems. *Phys. Rev. Lett.* **52**, 997–1000 (1984).
111. Gross, E. K. U., Dobson, J. F. & Petersilka, M. Density functional theory of time-dependent phenomena. *Density Funct. Theory II* **181**, 81–172 (2005).
112. Marques, M. A. L., Maitra, N. T., Nogueira, F. M. S., Gross, E. K. U. & Rubio, A. *Fundamentals of Time-Dependent Density Functional Theory*. (Springer-Verlag, 2012).
113. Caricato, M., Trucks, G. W., Frisch, M. J. & Wiberg, K. B. Oscillator strength: How does TDDFT compare to EOM-CCSD? *J. Chem. Theory Comput.* **7**, 456–466 (2011).
114. Mulliken, R. S. Electronic population analysis on LCAO-MO molecular wave functions. I. *J. Chem. Phys.* **23**, 1833–1840 (1955).
115. Adamo, C. & Jacquemin, D. The calculations of excited-state properties with time-dependent density functional theory. *Chem. Soc. Rev.* **42**, 845–856 (2013).
116. Le Bahers, T., Adamo, C. & Ciofini, I. A qualitative index of spatial extent in charge-transfer excitations. *J. Chem. Theory Comput.* **7**, 2498–2506 (2011).
117. Pettersen, E. F., Goddard, T. D., Huang, C. C., Couch, G. S., Greenblatt, D. M., Meng, E. C. & Ferrin, T. E. UCSF Chimera - A visualization system for exploratory research and analysis. *J. Comput. Chem.* **25**, 1605–1612 (2004).
118. Dennington, R., Keith, T. A. & Millam, J. M. GaussView. (2016).
119. Dewar, M. J. S. & Yuan, Y.-C. AM1 parameters for sulfur. *Inorg. Chem.* **29**, 3881–90 (1990).
120. Dewar, M. J. S., Zoebisch, E. G. & Healy, E. F. AM1: A New General Purpose Quantum Mechanical Molecular Model. *J. Am. Chem. Soc.* **107**, 3902–09 (1985).
121. Dewar, M. J. S., Jie, C. & Zoebisch, E. G. AM1 calculations for compounds containing boron. *Organometallics* **7**, 513–21 (1988).
122. Dewar, M. J. S., McKee, M. L. & Rzepa, H. S. MNDO parameters for 3rd period elements. *J. Am. Chem. Soc.* **100**, 3607–07 (1978).
123. Dewar, M. J. S. & Thiel, W. Ground-States of Molecules. 38. The MNDO Method: Approximations and Parameters. *J. Am. Chem. Soc.* **99**, 4899–907 (1977).
124. Dewar, M. J. S. & Reynolds, C. H. An improved set of MNDO parameters for sulfur. *J. Comp. Chem.* **7**, 140–43 (1986).
125. Gaussian 16, Revision B.01, M. J. Frisch, G. W. Trucks, H. B. Schlegel, G. E. Scuseria, M. A. Robb, J. R. Cheeseman, G. Scalmani, V. Barone, G. A. Petersson, H. Nakatsuji, X. Li, M. Caricato, A. V. Marenich, J. Bloino, B. G. Janesko, R. Gomperts, B. Mennucci, H. P. Hratchian, J. V. Ortiz, A. F. Izmaylov, J. L. Sonnenberg, D. Williams-Young, F. Ding, F. Lipparini, F. Egidi, J. Goings, B. Peng, A. Petrone, T. Henderson, D. Ranasinghe, V. G. Zakrzewski, J. Gao, N. Rega, G. Zheng, W. Liang, M. Hada, M. Ehara, K. Toyota, R. Fukuda, J. Hasegawa, M. Ishida, T. Nakajima, Y. Honda, O. Kitao, H. Nakai, T. Vreven, K. Throssell, J. A. Montgomery, Jr., J. E. Peralta, F. Ogliaro, M. J. Bearpark, J. J. Heyd, E. N. Brothers, K. N. Kudin, V. N. Staroverov, T. A. Keith, R. Kobayashi, J. Normand, K. Raghavachari, A. P. Rendell, J. C. Burant, S. S. Iyengar, J. Tomasi, M. Cossi, J. M. Millam, M. Klene, C. Adamo, R. Cammi, J. W. Ochterski, R. L. Martin, K. Morokuma, O. Farkas, J. B. Foresman, and D. J. Fox, Gaussian, Inc., Wallingford CT, 2016.
126. Lu, T. & Chen, F. Multiwfn : A Multifunctional Wavefunction Analyzer. (2011) doi:10.1002/jcc.22885.
127. Mewes, S. A., Mewes, J. M., Dreuw, A. & Plasser, F. Excitons in poly(para phenylene vinylene): a quantum-chemical perspective based on high-level ab initio calculations. *Phys. Chem. Chem. Phys.* **18**, 2548–2563 (2016).
128. Panda, A. N., Plasser, F., Aquino, A. J. A., Burghardt, I. & Lischka, H. Electronically excited states in poly(p-phenylenevinylene): Vertical excitations and torsional potentials from high-level Ab initio calculations. *J. Phys. Chem. A* **117**, 2181–2189 (2013).

Appendix One – *Python Code Repository*

This appendix contains the python code written by Maeve Kavanagh to analyse results produced for this thesis. Comments describing all functions are emboldened for the readers convenience.

General Imports and Variables

```
#imports
import pandas as pd
import sys
import re
import os
import numpy as np
import matplotlib
import matplotlib.pyplot as plt
import matplotlib.ticker as ticker

cofactors = ['Phe D1', 'Chl D1', 'P D1', 'P D2', 'Chl D2', 'Phe D2'] #global

all_classes = ['Down active',
               'Up active',
               'P D1 to P D2',
               'P D2 to P D1',
               'Up inactive',
               'Down inactive'] #global

all_transitions = [] #global
for x in cofactors:
   for y in cofactors:
      if x == y:
         continue
      else:
         all_transitions.append(x + ' to ' + y)
```

Utilities Functions

```
# utilities functions to find files for each calculation
def search_path(filename):
    current_path = os.getcwd()
    try:
        infile = open('%s/%s' %(current_path, filename))
        infile.close()
        return current_path + '/' # for file in this path
    except:
        return input('Type logfile file path: ')

def begin_analysis(_logfile):
    stem = _logfile[:-4]
    _mulfile = 'mulliken_' + stem + '.txt'
    _path = search_path(_logfile)
    return(_logfile, _path, _mulfile, stem)

# return list of lines between start and end flags
def sed_(file, stem, start, end):
    output = []
    copy = False
    with open(file) as file_in:
        for line in file_in:
            if re.search(start, line):
                line = line.strip()
                copy = True
                output.append(line)
            elif re.search(end, line):
                output.append(line)
                copy = False
            elif copy:
                output.append(line)
    return(output)
```

Processing Mulliken Population Analysis Output

'''
Process mulliken output from MultiWfn.
This function takes input txt file from MultiWfn, and outputs a txt file with orbital data arranged as a table.
'''

```
def grid(mul_file, path):
    stem = mul_file[9:-4]
    orbitals = []
    first_pass = -1
    df = pd.DataFrame()
    atoms = []
    elems = []
    contributions = []

    with open('%s%s' %(path,mul_file)) as m:
        for line in m:
            if re.search('Orbital:', line):
                if first_pass>=0:
                    df[orbital]=contributions
                orbital = int(line[8:13])
                orbitals.append(orbital)
                first_pass+=1
                contributions=[]
            if re.search('^ Atom  ', line):
                contributions.append(float(line.split(':')[1][:-3]))
                if first_pass<1:
                    atoms.append(int(line[6:11]))
                    el = line[12:14].strip()
                    elems.append(el)
    df[orbital]=contributions
    df['Atom']=atoms
    df['Elem']=elems
    df.to_csv('grid_%s.txt' %stem)
    return(df)
```

'''
For matching atom numbers to mulliken output from MultiWfn.
Takes a log file and outputs a csv with numbered atoms, element names and their associated cofactors.

General as long as geom=check in gaussian output log file.
'''

```
# matches main cofactor atoms to cofactor names
def match_co(logfile, stem, cartesians=False):
    full=False #full phytol chains (models 2 and 4)
    cofactor_len = 88
    if stem[0]=='f':
        full=True
        cofactor_len = 137 #atoms in full phytol chain chlorophyll
```

```
# search log file to find coordinate info
infile = open(logfile, 'r')
text_ = []
copy = False
atom = 1
cofactor = 'AA'
position = 0
count = 0
first_chlorophyll = False


def toggle(a):
    if full: # model 2, model 4 ordering
        cofactors_ = ['P D1', 'Chl D2', 'Chl D1', 'P D2', 'Phe D1', 'Phe D2']
    else: # model 1, model 3 ordering
        cofactors_ = ['P D1', 'Chl D2', 'Phe D1', 'Phe D2', 'Chl D1', 'P D2']
    return(cofactors_[a])

# get atom order
for line in infile:
    if re.search('cartesian coordinates used.', line):
        geom='cartesian'
        copy = True

    elif re.search(' Z-Matrix found in chk file.', line):
        geom='check'
        copy = True

    elif re.search('Charge =  0 Multiplicity = 1', line):
        geom='cartesian'
        copy = True

    elif re.search(' Recover connectivity data from disk', line): #for geom=check
        break

    elif copy:
        if line.split() == []:
            copy = False
            break
        elif geom=='cartesian':
            line = line.split()
        elif geom=='check':
            line = line.split(',')

        x_co, y_co, z_co = float(line[-3]), float(line[-2]), float(line[-1])

        line = line[0] # element name
        if 'M' in line: # beginning of Chlorophyll
            line = 'Mg'
            first_chlorophyll = True
            count = 0
```

```
            cofactor = toggle(position)
            position += 1
        elif count >= cofactor_len and first_chlorophyll:
            if 'C' in line: # beginning of Pheophytin
                count = 0
                line = line.strip()[0]
                try:
                    cofactor = toggle(position)
                    position += 1
                except: #amino acid COOH group comes at the end
                    cofactor = 'AA'
                    count = -1000
            if 'O' in line: # beginning of waters and amino acid terminals
                cofactor = 'AA'
                count = -1000
        else:
            line = line.strip()[0]
        if cartesians:
            text_.append([atom, line, cofactor, x_co, y_co, z_co])
        else:
            text_.append([atom, line, cofactor])
        atom += 1
        count += 1

    infile.close()

    # create dataframe
    if cartesians:
        df = pd.DataFrame(text_, columns=['Atom', 'Elem', 'Cofactor', 'x', 'y', 'z'])

    else:
        df = pd.DataFrame(text_, columns=['Atom', 'Elem', 'Cofactor'])

    df = df.set_index(['Atom'])
    df.to_csv('%s_matched_cofactors.csv' %(stem))
    return(df)
```

Processing Information from Gaussian Output

'''

Writes a file '_info.csv' which contains all excited state info from the log file.

'''

```
def get_info (log_file, stem, start, bad1, bad2, bad3, end):
    print(log_file)
    energy_nm = {}
    energy_ev = {}
    f_value = {}
    file_in = open(log_file)
    outfile = open('%s_info.csv' % (stem), 'w')
    copy = False
    headers = []
    content = []
    output = 0
    for line in file_in:
        line = line.strip()
        if re.search(start, line):
            output += 1
            line = line.replace("f=", "")
            line = line.split()
            headers.append([output, line[6], line[4], line[8]])
            info = [output, float(line[6]), float(line[4]), float(line[8])]
            copy = True
            energy_nm[output] = line[6]
            energy_ev[output] = line[4]
            f_value[output] = line[8]
        elif re.search(end, line) or re.search(bad1, line) or re.search(bad2, line) or re.search(bad3, line) or
re.match(r'^\s*$', line):
            copy = False
        elif copy:
            line = line.replace ("->", "")
            line = line.replace("<-", '-')
            line = line.split()
            line[0] = int(line[0])
            line[1] = int(line[1])
            line[2] = float(line[2])
            line.append(float(line[2])**2*200)
            add = info + line
            content.append(add)
            for item in info:
                outfile.write("%s," % item)
            for item in line:
                outfile.write("%s," % item)
            outfile.write('\n')
    file_in.close()
    outfile.close()
    with open('%s_stateInfo.csv' %stem, 'w') as outfile2:
        outfile2.write('State, Energy (nm), Oscillator Strength\n')
        for x in range(1, output+1):
```

```
        outfile2.write('%i, %s, %s\n' %(x, energy_nm[x], f_value[x]))
    return content
```

Plotting Simulated Absorption Spectra

'''A function to plot the simulated absorption spectrum from TDDFT using gaussian broadened peaks to approximate experimental spectra'''

```
c = 0.1 #This value determines the width of gaussian functions to broaden single ES

#plot spectrum
def get_spectrum (df, stem='2WT', save=True, low_range=350, high_range=750, interval=0.1):

    #get data
    df = df.groupby(['State']).mean()
    energies = df['nm'].tolist()
    f_values = df['f'].tolist()

    x = np.arange(low_range, high_range, interval)
    state = 0
    y_total = 0
    for value in energies:
        state += 1
        m_plot = (x - value)**2
        a_plot = f_values[(state - 1)]
        y_plot = a_plot * math.e ** (-m_plot/2*c**2)
        if save:
            plt.plot(x, y_plot, color=color_datapoint(cofactors[state-1], color_only=True), linestyle=':')
        y_total += y_plot

    if save:
        plt.plot(x, y_total, color='black', linestyle='-')
        plt.xlabel('Energy /nm')
        plt.ylabel('Oscillator Strength')
        plt.title('%s UVvis' % stem)
        plt.savefig('%s_UVvis_%s_%s_%s.png' % (stem, low_range, high_range, interval))

    return (y_total)

# get data to plot bands contributed to by specific cofactor excitation only
def get_cofactor_bands(df, cofactor, cut=20, dom=False):
    grouped = df.groupby(['State', 'max_x'])['norm_contr'].agg('sum').reset_index()
    piv = grouped.pivot_table(index='State', columns='max_x', values='norm_contr', fill_value=0)
    if dom:
        bools = piv[cofactor]==piv.max(axis=1)
    else:
        bools = piv[cofactor]>cut
    data = df.groupby(['State']).mean()
    return(data[bools])

# gaussian-broaden bands due to single cofactors
def cofactor_bands(df, ax, cofactor, col_, style):
    df = get_cofactor_bands(df, cofactor, dom=True)
    df = df.groupby(['State']).mean()
```

```
    energies = df['nm'].tolist()
    f_values = df['f'].tolist()

    x = np.arange(300, 800, 0.1)
    for n, value in enumerate(energies):

        m_plot = (x - value)**2
        a_plot = f_values[n]
        y_plot = a_plot * math.e ** (-m_plot/2*c**2)
        if n==0:
            ax.plot(x, y_plot, color=col_, linestyle=style, linewidth=1.5, label=find_label(cofactor))
        else:
            ax.plot(x, y_plot, color=col_, linestyle=style, linewidth=1.5)
    return

'''plots a spectrum with coloured bands for cofactor excitations and whole spectrum as sum of all excited states'''
def whole_spec(df, figname):
    fig = plt.Figure()
    fig.set_size_inches(6,4)
    ax = fig.add_subplot(111)

    #plot cofactor bands
    for n, cof in enumerate(cofactors):
        cofactor_bands(df, ax, cof, color_datapoint(cof, color_only=True), styles[n])

    #plot all states and whole thing
    x = np.arange(300, 800, 0.1)
    ys = get_spectrum(df, low_range=300, high_range=800, interval=0.1, save=False)
    plt.plot(x, ys, color='black', linestyle='-', linewidth=2)

    plt.title('')

    plt.xlim(350,750)
    plt.xticks(ax.get_xticks()[np.array([0,2,4,6,8])], [350, 450, 550, 650, 750])

    ax.set_ylabel('Oscillator Strength', labelpad=5, fontsize=12)
    ax.set_xlabel('Energy / nm', labelpad=5, fontsize=12)
    ax.tick_params(axis='both',which='both', length=0)

    ax.tick_params(axis='y',  pad=10)
    ax.tick_params(axis='both', which='major', pad=10)
    text = ax.text(0.6,-0.3, " ", transform=ax.transAxes)

    lgd = ax.legend(ncol = 3, facecolor='white', frameon=0, framealpha=1, bbox_to_anchor=(0.8, -0.2),
prop={'weight':'normal'})
    text = ax.text(0.13,0.9, 'Soret', transform=ax.transAxes, fontsize=12)
    text = ax.text(0.52,0.9, 'Qx', transform=ax.transAxes, fontsize=12)
    text = ax.text(0.76,0.9, 'Qy', transform=ax.transAxes, fontsize=12)
    fig.savefig('%s_wholeabsspec.png' %figname, dpi=300, bbox_extra_artists=(lgd, text), bbox_inches='tight')
```

Labelling MOs and Transitions Using Mulliken Population Analysis

‘’’ Determines the direction of a transition between two MOs’’’

```
def test_direction(test_set):
    test_set = np.array(test_set)
    ACTIVE=test_set.dot(up_active)
    INACTIVE=test_set.dot(up_inactive)
    Ps=test_set.dot(PD2_to_PD1)
    if min([ACTIVE,INACTIVE,Ps])<-max([ACTIVE,INACTIVE,Ps]): #negative
        return(negative_classes[[ACTIVE,INACTIVE,Ps].index(min([ACTIVE,INACTIVE,Ps]))])
    else:
        return(positive_classes[[ACTIVE,INACTIVE,Ps].index(max([ACTIVE,INACTIVE,Ps]))])
```

‘’’

Function to classify a transition as charge transfer (CT) if occupied and virtual MOs are localised on different cofactors

‘’’

```
def isCT(occ,vir):
    if occ == vir:
        return(occ)
    else:
        return('CT')
```

‘’’

This function compiles log file output (excitation energies, oscillator strengths, transition contributions, occupied and virtual MOs making up transitions) with Mulliken population analysis to identify which cofactors’ atoms occupy which MOs.
Outputs a dataframe.

‘’’

```
def prep_df(logfile):
    logfile, path, mulfile, stem = begin_analysis(_logfile=logfile)
    _matched_cofactors = match_co(logfile, stem)
    mulliken = grid(mulfile, path)
    FINAL = pd.merge(
        _matched_cofactors,
        mulliken,
        left_on=['Atom'],
        right_on=['Atom']
        )
    orbitals = mulliken.columns.to_list()
    orbitals.remove('Elem')
    orbitals.remove('Atom')
    #print(orbitals)
    nice = pd.DataFrame(index=cofactors)
    for o in orbitals:
        df = FINAL[['Cofactor', o]]
        total_contribution = df.groupby('Cofactor')[o].sum()
        nice[o]=total_contribution
    nice=nice.T
    nice.reset_index(inplace=True)
    nice['max']=nice[cofactors].idxmax(axis=1)
```

```
    info_csv = stem + '_info.csv'
    info_df = pd.read_csv(
        info_csv,
        names=['State', 'nm', 'eV', 'f', 'occ', 'vir', 'contr', 'norm_contr'],
        index_col=False
        )
    nice['Orbital']=nice['index'].astype(str).astype(int)
    nice.drop(columns='index', inplace=True)
    go = info_df.merge(nice, how='left', left_on='occ', right_on='Orbital')
    go2 = go.merge(nice, how='left', left_on='vir', right_on='Orbital')
    for cof in cofactors:
        go2[cof]=go2[cof+'_y']-go2[cof+'_x']
    go2['CT']=go2.apply(lambda x: isCT(x['max_x'], x['max_y']),axis=1)
    go2['trans']=go2.apply(lambda x: find_min(x[cofactors].values.tolist(), cofactors), axis=1)
    go2['class']=go2.apply(lambda x: classify_trans(x['trans'],x['CT']),axis=1)
    go2['vector_class']=go2.apply(lambda x: test_direction(x[cofactors]),axis=1)
    go2.drop(columns=['Orbital_x','Orbital_y'], inplace=True)

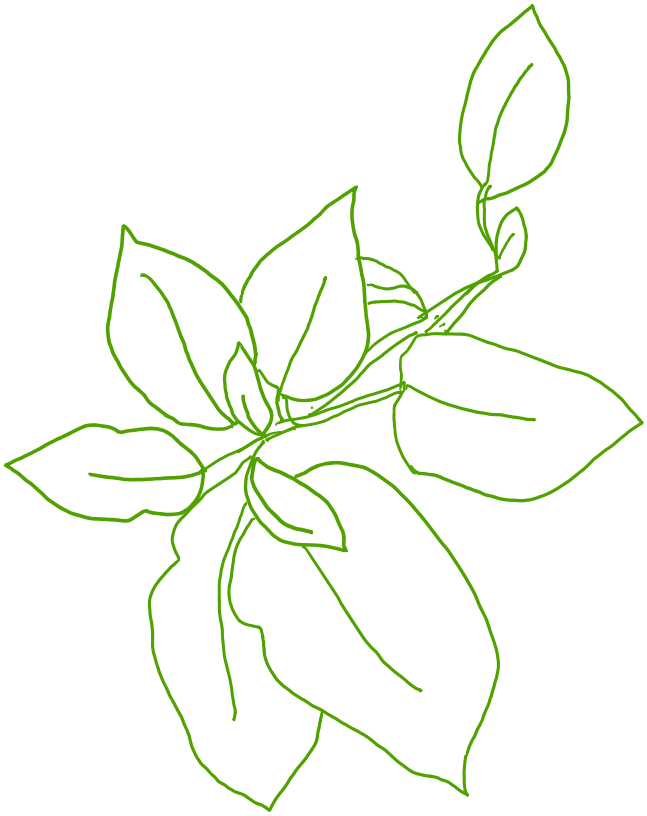
    return(go2, stem, logfile)
```

‘’’

Pivot data in data frame to assign cofactor excitation contributions to each excited state

‘’’

```
def pivots(df, feature):
    df2 = df.groupby(['State',feature])['norm_contr'].agg('sum').reset_index()
    new_pivot = df2.pivot(index='State', columns=feature, values='norm_contr')
    categories = new_pivot.columns.tolist()
    new_pivot.dropna(axis=0, how='all', inplace=True)
    new_pivot.fillna(value=0, inplace=True)
    new_pivot = new_pivot.T
    lists = new_pivot.values.tolist()
    return(new_pivot, lists, categories)
```



Appendix Two – *Investigating the Effect of Water Molecules on Model 1 Results*

This appendix contains results of six calculations on three further models of the RC which include different numbers of water molecules.

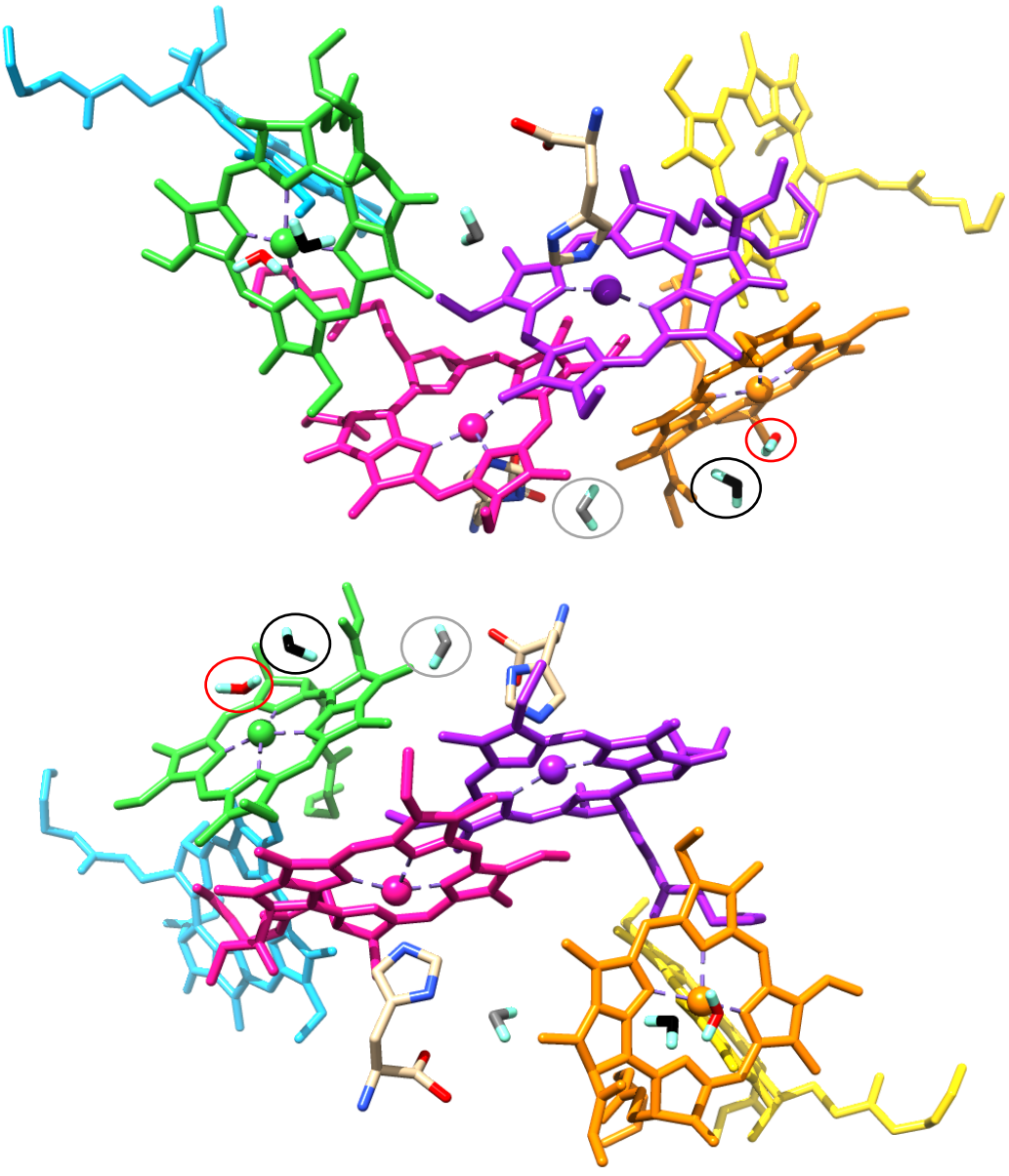


Figure A.1 – View of the six water molecules in the vicinity of the RC. The red water molecules are included in the 2, 4 and 6 water models, the black water molecules are included in the 4 and 6 water models and the grey are included only in the 6 water model. TOP – P_{D2} view with D2 waters outlined, BOTTOM – P_{D1} view with D1 waters outlined. Both Figures: Phe_{D1} blue, Chl_{D1} green, P_{D1} pink, P_{D2} purple, Chl_{D2} orange, Phe_{D2} yellow and histidine residues tan with coloured heteroatoms.

There are six water molecules in the vicinity of the RC that fall within the 6 A radius of the centre of the porphyrin rings (see Figure A.1). To investigate the effect of these, model 1 (with truncated phytol chains and two amino acids) was rebuilt with 0, 4 and 6 water molecules. A comparison of these models and model 1 (2 waters) is presented below, for the first six excited states with both ωB97X-D and CAM-B3LYP and 6-31G**.

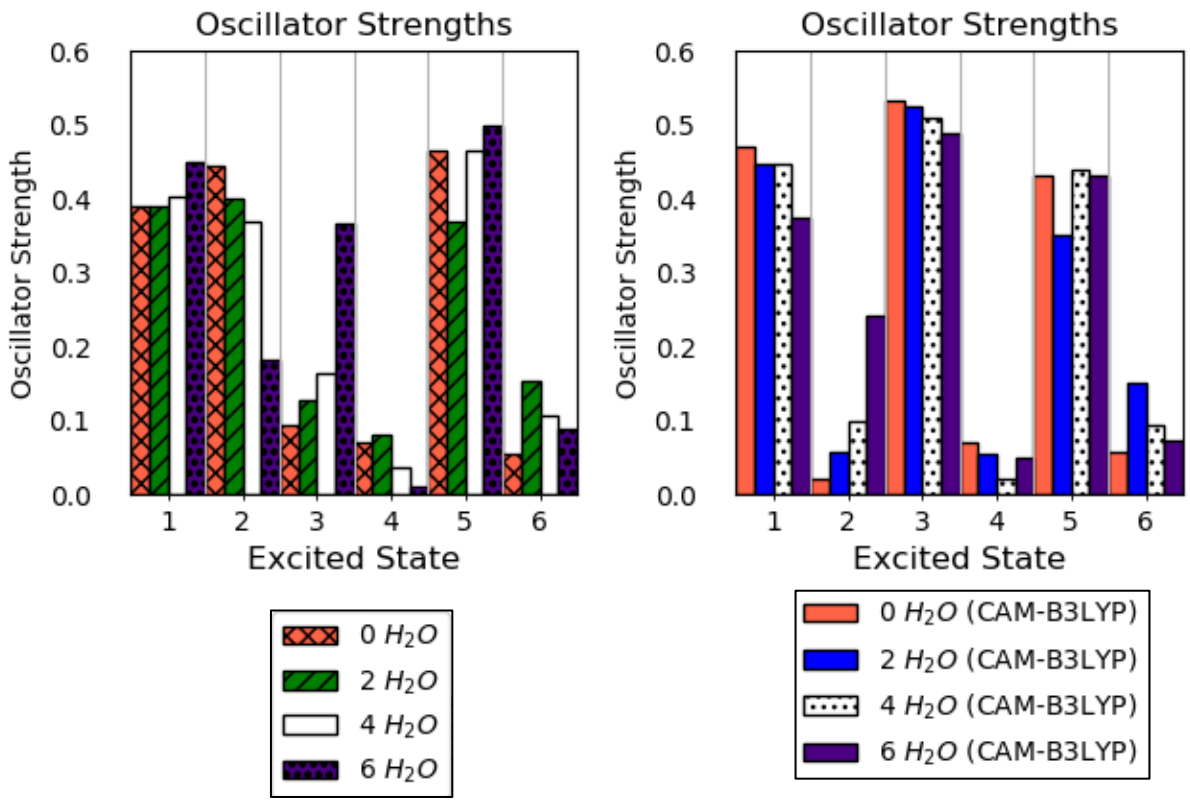


Figure A.2 : Comparing oscillator strengths of ES 1-6 for model 1 calculations with 0, 2, 4 and 6 water molecules. LEFT – ωB97X-D, RIGHT – CAM-B3LYP.

For CAM-B3LYP the oscillator strengths of states one and three decrease on adding water molecules to the models whilst the oscillator strength of state 2 is increased on adding water molecules to the models. For WB the exact opposite is observed, with the oscillator strength of 1 and 3 increasing and of 2 decreasing when adding water molecules to the models. The difference in oscillator strength profiles can be related to the difference in contributing cofactor excitations for each functional.

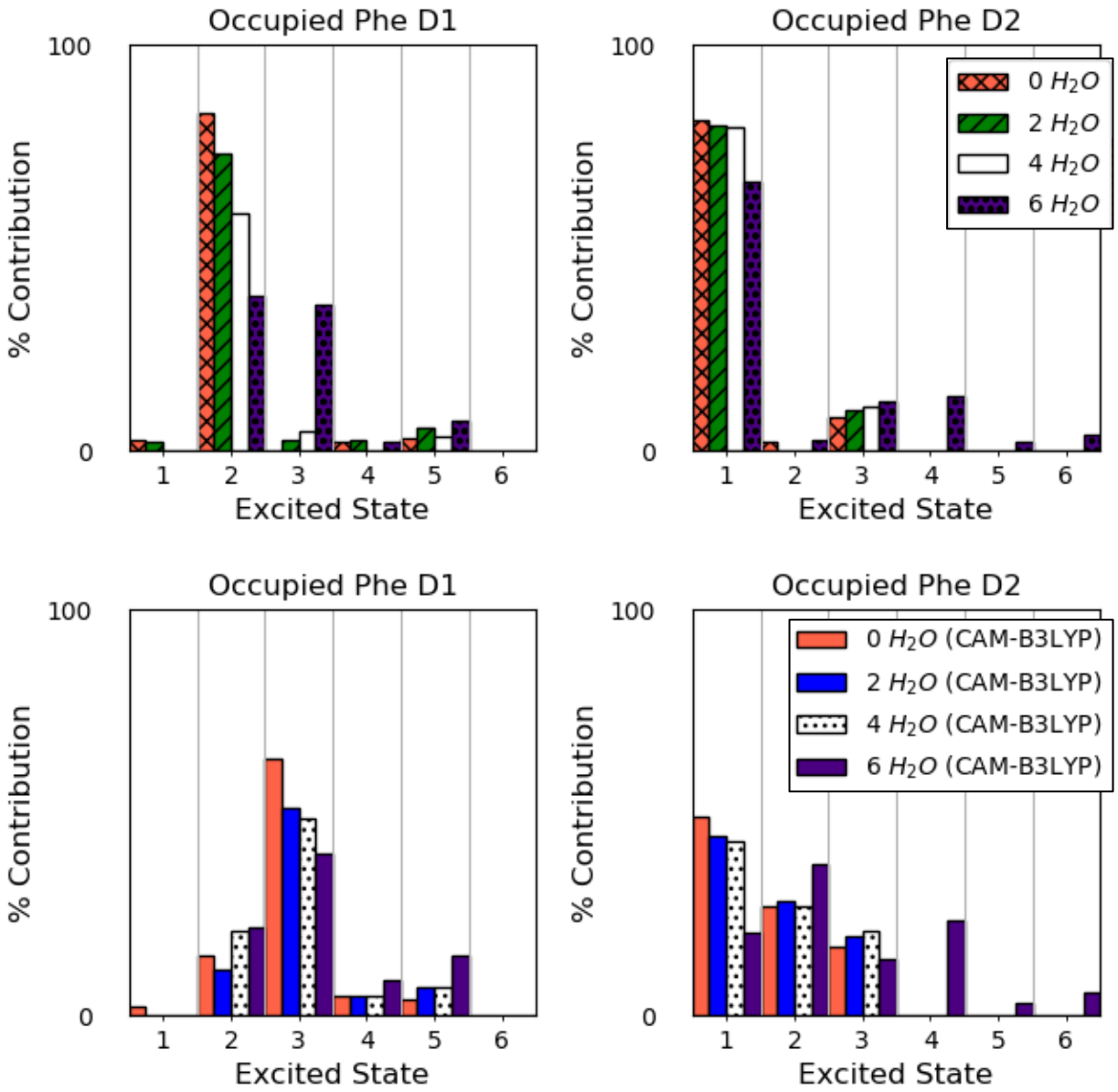


Figure A.3 : Comparing contribution from Phe occupied orbital excitations to ES 1-6 for model 1 calculations with 0, 2, 4 and 6 water molecules. LEFT – ωB97X-D, RIGHT – CAM-B3LYP.

For ωB97X-D – Phe excitations contribute less to ES 1 and 2 on the addition of further water molecules, Phe_{D1} excitation appears to be pushed up in energy by adding the waters, so that this excitation is mixed into ES 2 and 3 for the 6 water model. Similarly Phe_{D2} excitation has increasing contribution to ES 3. With CAM-B3LYP the contribution of Phe_{D1} excitation is increasing in ES 2 and decreasing in ES 3 on addition of waters. Suggesting that this excitation is pushed down in energy for this method. Whilst there is agreement between the two functionals over Phe_{D2} excitation, which is pushed to higher ES on adding further water molecules.

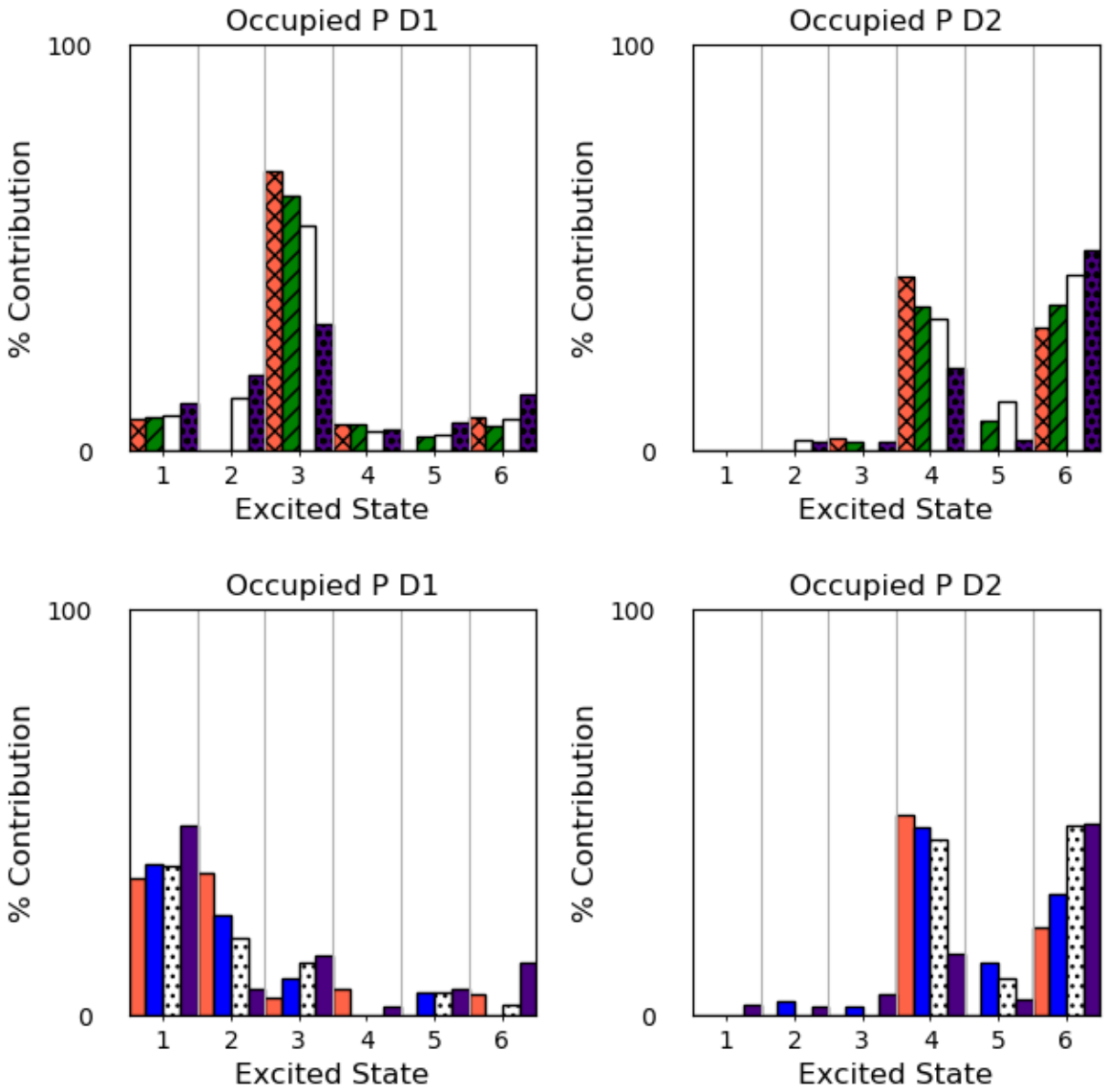


Figure A.4 : Comparing contribution from P chlorophyll occupied orbital excitations to ES 1-6 for model 1 calculations with 0, 2, 4 and 6 water molecules. LEFT – ωB97X-D, RIGHT – CAM-B3LYP.

P_{D1} excitation in increasingly mixed over all the ES for both methods when adding water molecules. For both CAM-B3LYP and ωB97X-D we see the contribution of P_{D1} excitation drop in a higher energy state, ES 3 for ωB97X-D and ES 2 for CAM-B3LYP, and increase in ES 1. P_{D2} excitation is consistently pushed higher in E on addition of further waters, increasing in ES 6 and decreasing in ES 4 for both functionals.

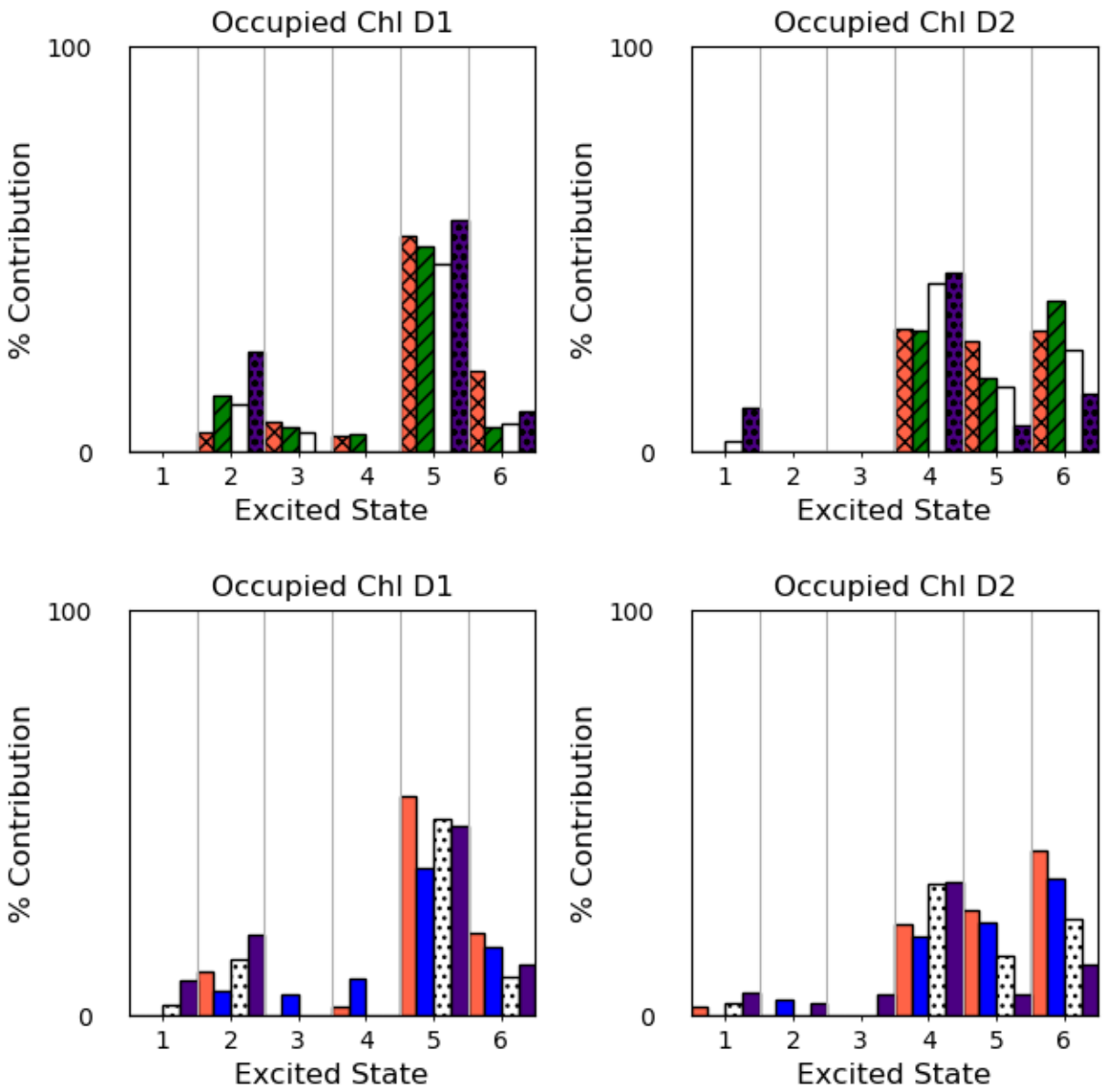


Figure A.5 : Comparing contribution from accessory chlorophyll (Chl_{D1} and Chl_{D2}) occupied orbital excitations to ES 1-6 for model 1 calculations with 0, 2, 4 and 6 water molecules. LEFT – ωB97X-D, RIGHT – CAM-B3LYP.

For Chl_{D1} excitation there is a rise in contribution to ES 2 on adding water molecules but no clear drop in ES 5 where Chl_{D1} excitation remains the dominant contribution to the state. Chl_{D2} mirrors the P_{D2} trend above, increasing in ES 4 and decreasing in ES 6.

This investigation highlights the delicate nature of the system, showing that addition or subtraction of just two water molecules can alter the order of cofactor excitations.

Full results are presented below.

Table A.1 : Excitation energies and oscillator strengths for model 1 with 0, 4 and 6 waters (ωB97X-D/6-31G**)

ES	0 waters		4 waters		6 waters	
	Energy (nm)	Oscillator Strength	Energy (nm)	Oscillator Strength	Energy (nm)	Oscillator Strength
1	673.71	0.3896	673.87	0.4024	674.57	0.449
2	668.52	0.4438	669.13	0.3675	670.44	0.1804
3	666.72	0.0939	667.28	0.1635	668.28	0.3656
4	655.25	0.0712	657.12	0.0356	660.63	0.0103
5	649.31	0.4637	652.12	0.4644	654.47	0.4987
6	645.58	0.0551	646.44	0.1055	648.04	0.0888

Table A.2 : Excitation energies and oscillator strengths for model 1 with 0, 4 and 6 waters (CAM-B3LYP/6-31G**)

ES	0 waters (CAM-B3LYP)		4 waters (CAM-B3LYP)		6 waters (CAM-B3LYP)	
	Energy (nm)	Oscillator Strength	Energy (nm)	Oscillator Strength	Energy (nm)	Oscillator Strength
1	657.48	0.4707	657.9	0.447	659.61	0.3736
2	653.52	0.0205	654.44	0.0979	655.81	0.2416
3	652.28	0.5328	652.44	0.5086	653.16	0.4877
4	643.3	0.0689	645.22	0.0217	648.91	0.0501
5	636.41	0.432	639.4	0.4384	641.87	0.4321
6	633.66	0.0562	635.25	0.0929	637.33	0.0716

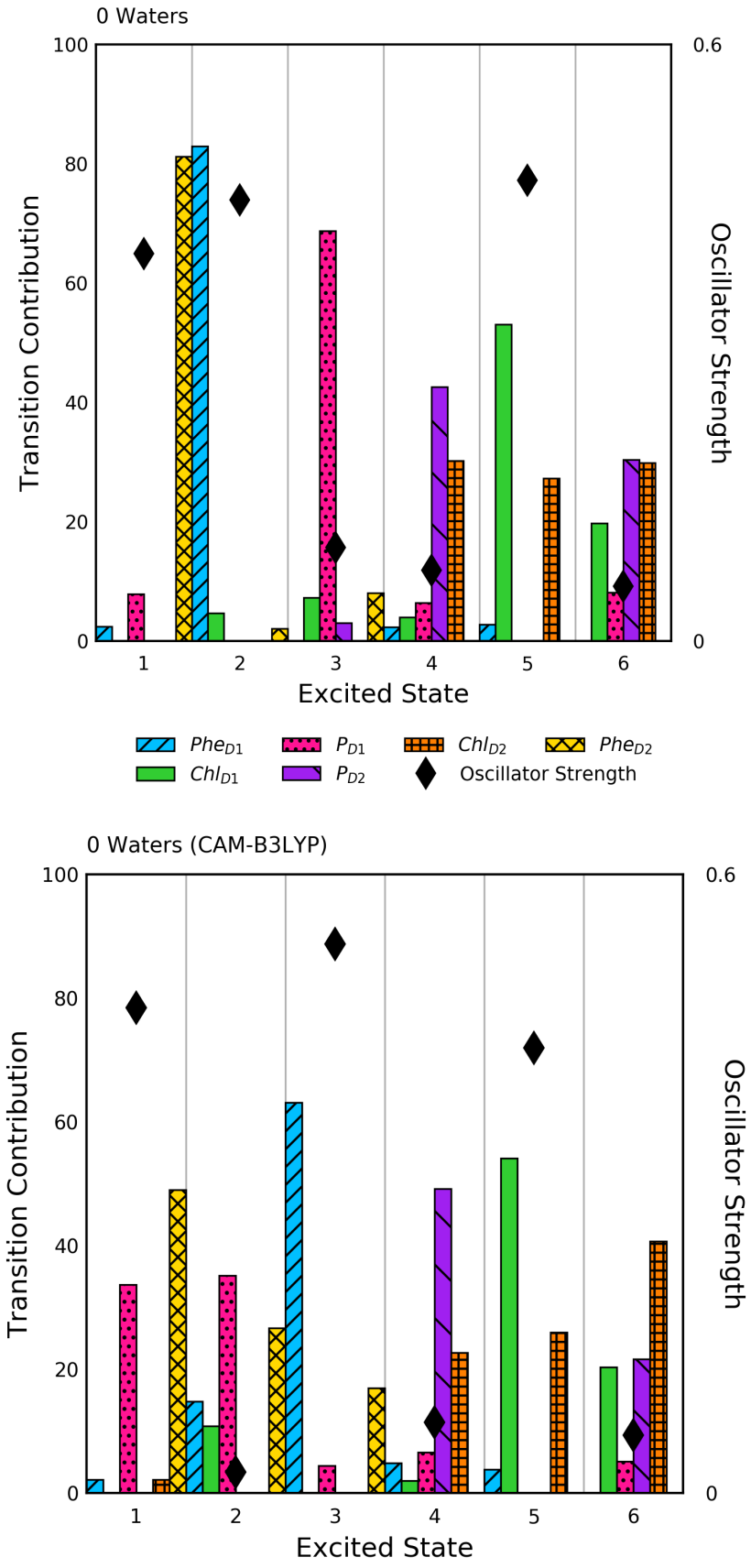


Figure A.6 : Occupied orbital contributions and oscillator strengths for model 1 (truncated phytol chain and 2 amino acids) with 0 waters, TOP – ωB97X-D, BOTTOM – CAM-B3LYP. Both with basis set 6-31G**.

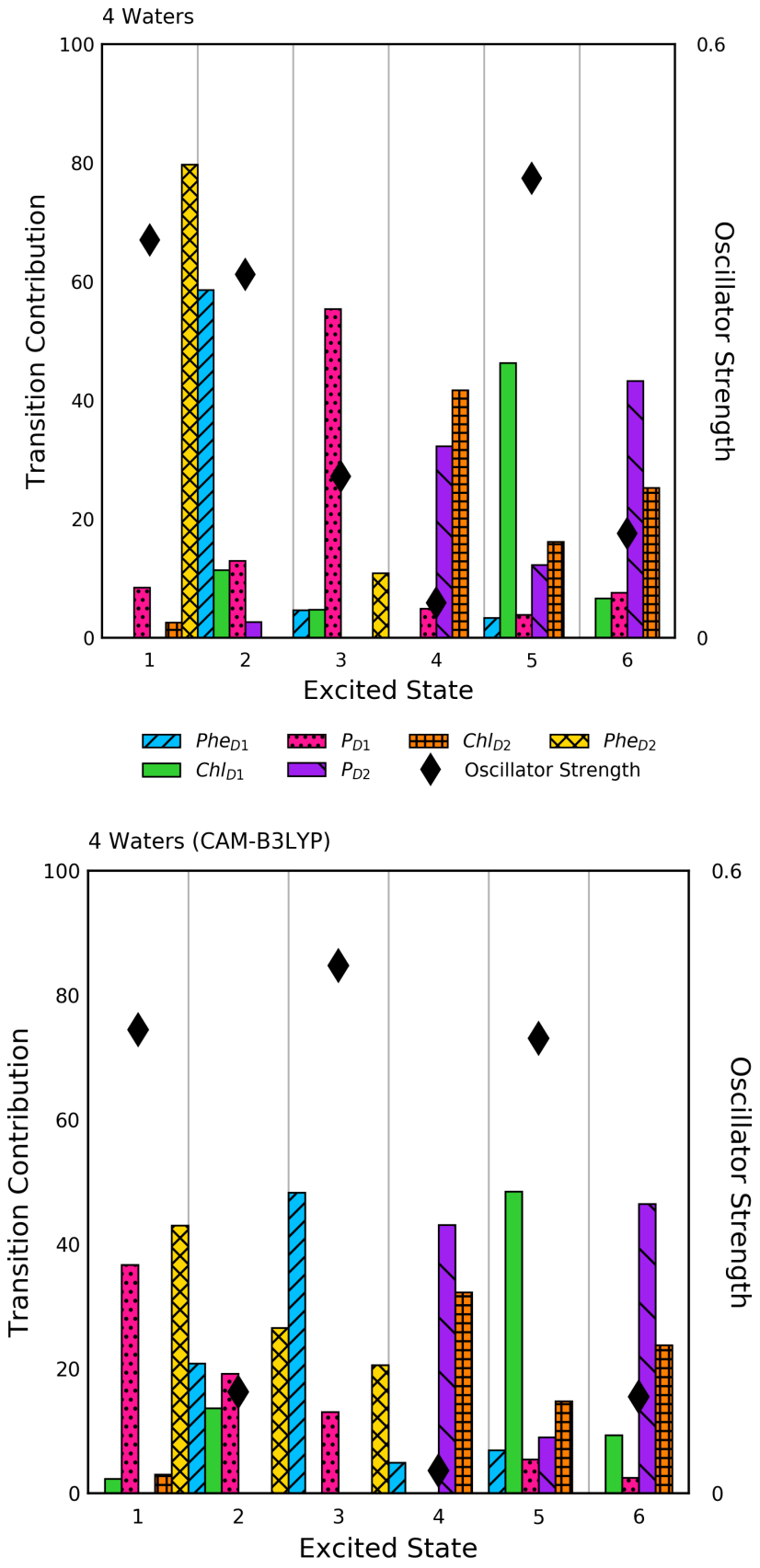


Figure A.7 : Occupied orbital contributions and oscillator strengths for model 1 (truncated phytol chain and 2 amino acids) with 4 waters, TOP – ωB97X-D, BOTTOM – CAM-B3LYP. Both with basis set 6-31G**.

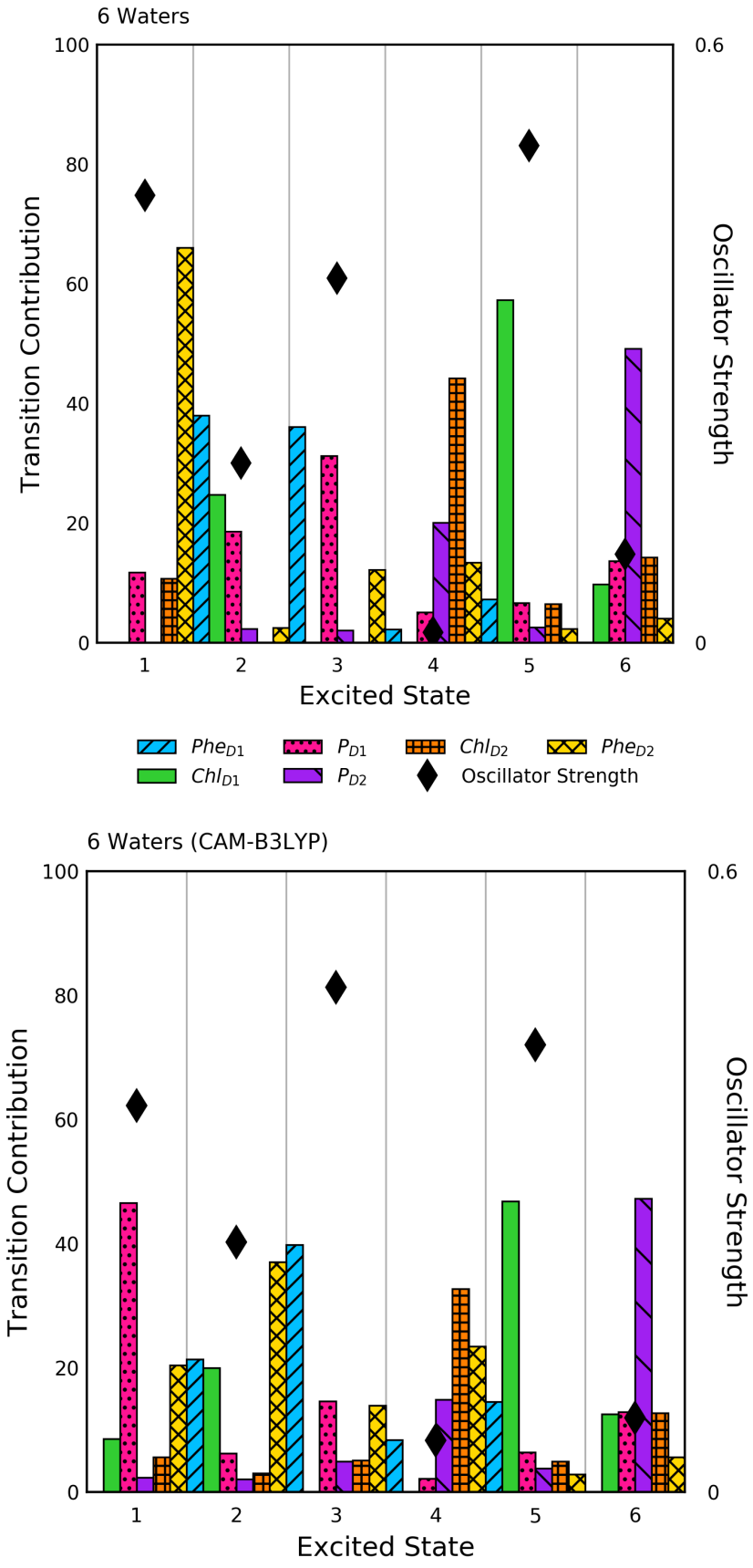
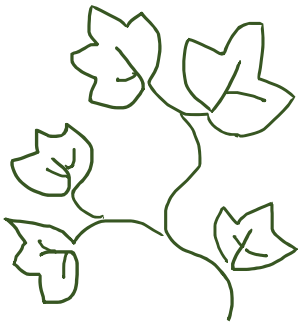


Figure A.8 : Occupied orbital contributions and oscillator strengths for model 1 (truncated phytol chain and 2 amino acids) with 6 waters, TOP – ωB97X-D, BOTTOM – CAM-B3LYP. Both with basis set 6-31G**.



Appendix Three – *A Comparison of Two Methods of Transition Classification*

This appendix contains notes on building the algorithm that classifies whether a transition is travelling 'up active', 'down active', 'P D1 to P D2' etc.

As described in the main body of this chapter, there were six possible transition types that were most commonly seen, these were: Up active, Down active, P_{D1} to P_{D2}, P_{D2} to P_{D1}, Down inactive and Up inactive (see Figure XX). To classify the transition described by an occupied and virtual MO pair, first using MultiWfn[124] the atomic contributions to each MO were found. Then, summing over all atoms in each cofactor the cofactor occupancy % for each MO was tabulated. For a pair of MOs making up a transition, the occupancy of each cofactor for the Occupied MO was subtracted from the occupancy of the same cofactor for the Virtual MO. The result was a vector describing movement towards (indicated by positive values) and away from (negative values) each cofactor during the transition, an example is given in the bottom row of this table.

Table A.3 : Vectors describing MO occupancy and transition direction

Vector Descriptor	Phe_{D2}	Chl_{D2}	P_{D2}	P_{D1}	Chl_{D1}	Phe_{D1}
Occupied MO Occupancy %	0.01178	0.32641	26.74194	70.32509	0.02087	0.00082
Virtual MO Occupancy %	0.0012	0.05747	56.68026	42.15924	0.09996	0.00006
Transition delta	-0.01058	-0.26894	29.93832	-28.1659	0.07909	-0.00076

For which:

Virtual MO occupancy % – Occupied MO occupancy % = Transition delta

Two ways to classify the transition were explored from this point onwards.

The first was to select the cofactor which has the largest negative delta and the cofactor with the largest positive delta, for the example above this would be P_{D1} (most negative) and P_{D2} (most positive). The transition would be labelled therefore as "P D1 to P D2". Then using code 1 below the transitions were classified based on the identity of these two cofactors. Rules that this algorithm obeyed were:

- Moving away from a Phe cofactor is always a transition down the branch
- Moving towards a Phe cofactor is always a transition up the branch

- Going between P chlorophylls was a separate class (neither up nor down) ‘P D1 to P D2’ or ‘P D2 to P D1’
- Moving away from P chlorophylls to anything but a P chlorophyll is always a transition up the branch

Any transition that could not be classified into one of the six transition classes by the rules stated above would be assigned to its own class, meaning that when comparing across models only like-transitions would be compared with each other.

Code 1 - Original method

```
import re

# function takes a string in the form of ‘Phe D1 to Chl D1’
# and analyses the class this transition falls into according to the identities of the cofactors
def classify_trans(trans):

   from_co=trans.split('to')[0]
   to_co=trans.split('to')[1]

   result = ''

   if re.search('Phe',from_co): # coming from Phe is always ‘down’
      result = result + 'Down'
   elif re.search('P ', from_co):
      if re.search('P ', to_co):
         return(trans) # P chlorophyll transitions are not up or down
      else:
         result = result + 'Up' # coming from P to not P is always ‘up’
   else:
      if re.search('Phe', to_co): # going to Phe is always ‘up’
         result = result + 'Up'

      if re.search('P ', to_co): # going to P is always ‘down’
         result = result + 'Down'

   if re.search('D1', to_co): # going to D1 is always ‘active’
      result = result + ' active'
   else:
      result = result + ' inactive' # going to D2 is always ‘inactive’
   if result == ' inactive':
      return from_co + " to " + to_co # catchall for results which are not classifiable
   if result == ' active':
      return from_co + " to " + to_co # catchall for results which are not classifiable
   return (result)
```

The two most common transitions that would not be classifiable by this first method were 'Chl_{D1} to Chl_{D2}' or 'Chl_{D2} to Chl_{D1}'. As this is an important transition for the smaller models 1 and 2 (see chapter 1) it was necessary to try an alternative method of classification that would group these transitions into one of the major six classes.

The second method used was to investigate the similarity (by evaluating the dot product) of each delta vector with three fixed class vectors. The class vectors were chosen to describe movement up and down the branches or between the P chlorophylls. These were:

Table A.4 : Class vectors describing typical movement during each transition type

Transition type	Phe_{D2}	Chl_{D2}	P_{D2}	P_{D1}	Chl_{D1}	Phe_{D1}
Up active	0	0	-0.2	-0.2	+0.2	+0.4
Down active	0	0	+0.2	+0.2	-0.2	-0.4
P_{D2} to P_{D1}	0	0	-0.5	+0.5	0	0
P_{D1} to P_{D2}	0	0	+0.5	-0.5	0	0
Up inactive	+0.4	+0.2	-0.2	-0.2	0	0
Down inactive	-0.4	-0.2	+0.2	+0.2	0	0

The code for implementing this second method is given below:

Code 2 - Vector method

```
import numpy as np
# A function to classify transitions according to their similarity with class vectors

# Ordering of cofactors is Phe D2, Chl D2, P D2, P D1, Chl D1, Phe D1

# class vectors
up_active = np.array([0, 0, -0.2, -0.2, 0.2, 0.4]) # up active / - down active
PD2_to_PD1 = np.array([0, 0, -0.5, +0.5, 0, 0]) # P D2 to P D1 / - P D1 to P D2
up_inactive = np.array([0.4, 0.2, -0.2, -0.2, 0, 0]) # up inactive / - down inactive

# class naming conventions
positive_classes = ['Up active', 'Up inactive', 'P D2 to P D1']
negative_classes = ['Down active', 'Down inactive', 'P D1 to P D2']

# find product with highest magnitude and classify transition as most similar class vector
def test_direction(test_set):
   ACTIVE=test_set.dot(up_active)
   INACTIVE=test_set.dot(up_inactive)
   Ps=test_set.dot(PD2_to_PD1)
   if min([ACTIVE,INACTIVE,Ps]) <- max([ACTIVE,INACTIVE,Ps]): # negative
      return (negative_classes[[ACTIVE,INACTIVE,Ps].index(min([ACTIVE,INACTIVE,Ps]))])
   else:
      return (positive_classes[[ACTIVE,INACTIVE,Ps].index(max([ACTIVE,INACTIVE,Ps]))])
```

The two methods described above were found to be in good agreement except for in certain cases which are discussed below.

This second method forces the transitions into one of the six classes e.g. Chl D1 → Chl D2 transitions are no longer unclassifiable. For example the transition below is an unclassifiable "Chl D2 to Chl D1" transition which the vector method identifies as transition up the active branch.

Model 1 (CAM-B3LYP/6-31G**) 1138 → 1146

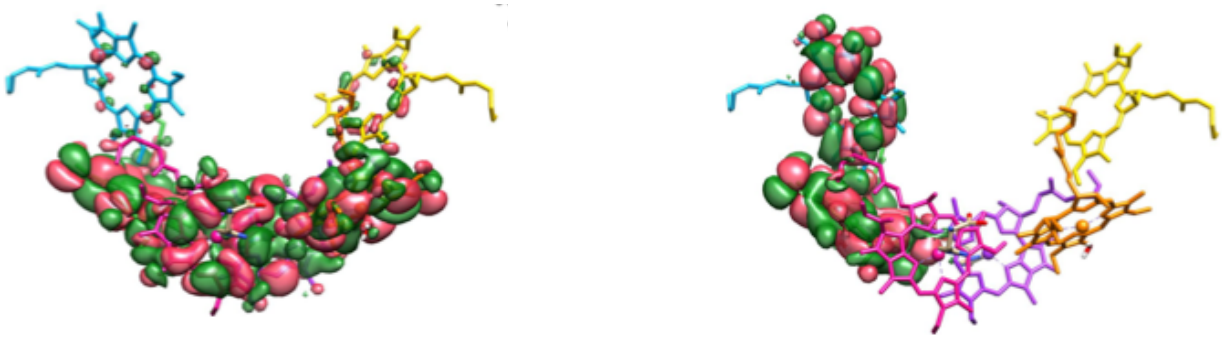


Figure A.10 : Transition from MO 1138 to 1146 for Model 1 (CAM-B3LYP/6-31G**)

The second method also revealed that some transitions are not easy to classify like the example below, both P D2 → P D1 and Chl transitions are occurring simultaneously.

Model 1 (ωB97X-D/6-31G**) 1137 → 1149

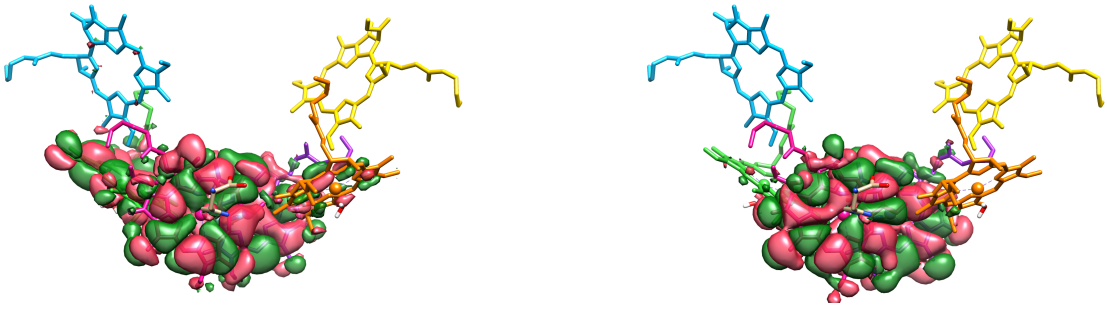


Figure A.11 : Transition from MO 1137 to 1149 for Model 1 (ωB97X-D /6-31G**)

The vector for this transition is:

Phe_{D2}	Chl_{D2}	P_{D2}	P_{D1}	Chl_{D1}	Phe_{D1}
-0.00237	-0.2565	-10.7627	27.80701	-16.4781	-0.05836

But the vectors don't always predict the most sensible transition, for example for model 4 the most significant MO pair for state 5 is a transition from P_{D2} to Phe_{D1} (shown below) which from the vector method is classified as P_{D2} to P_{D1} transition.

Model 4 (ωB97X-D/6-31G**) 2309 → 2315

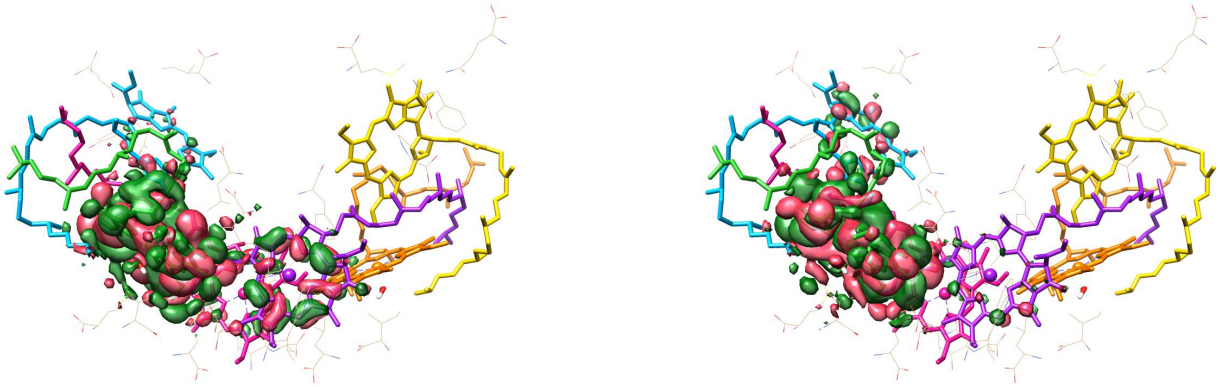
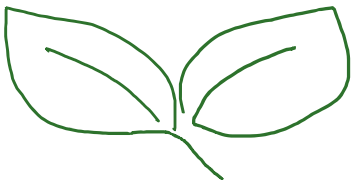


Figure A.12 : Transition from MO 2309 to 2315 for Model 4 (ωB97X-D/6-31G**)

The method using the class vectors could easily be taken further to include more types of transition described by the class vectors, in the interest of time this task is recommended as further work. With both methods having their flaws it was arbitrary to choose one over the other, the first method was chosen as it had already been implemented for many of the existing calculation results. However the ambiguity of certain transitions was made apparent when investigating the two different methods and their outcomes. This finding highlights the importance of including various metrics in the analysis of each models results, focussing not only on the transitions but also the occupied orbitals and D_{CT} results to get a clearer picture of each calculation's outcome.



Appendix Four – *Supplementary Figures*

Model 1 Results

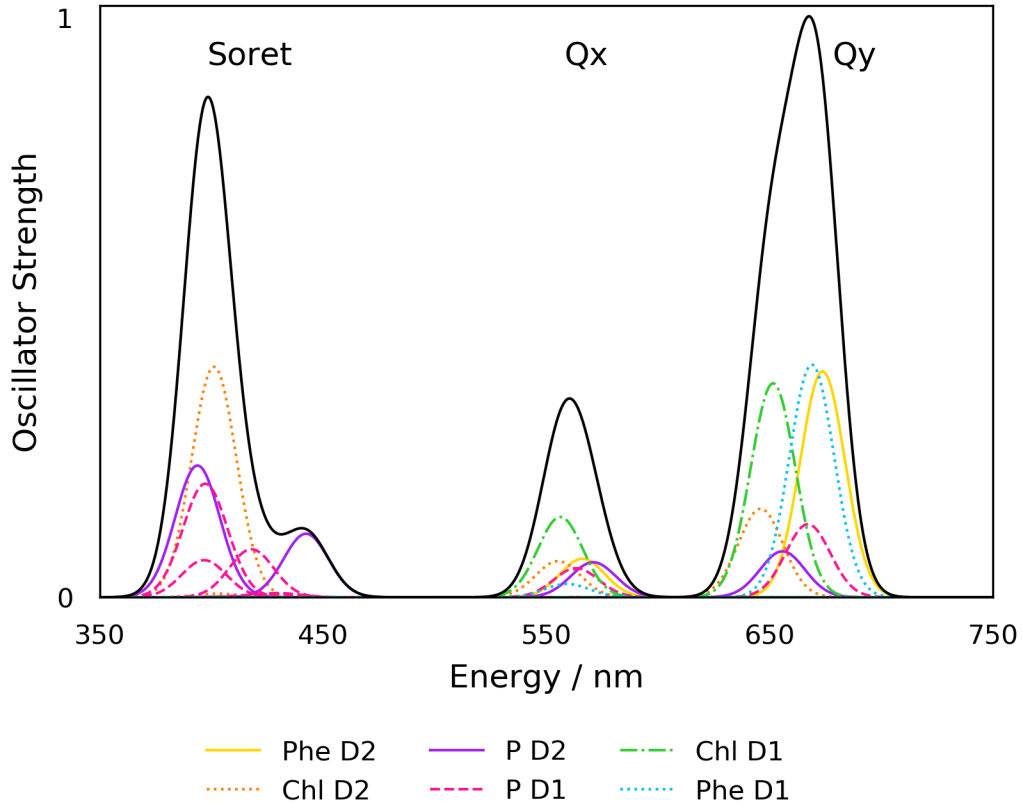


Figure A.13 : Calculated absorption spectrum for model 1 (ωB97X-D/ 6-31G**), black line – full spectrum from sum of single ES broadened by gaussian functions, coloured lines – single ES broadened by gaussian functions coloured by occupied orbital cofactor: Phe_{D2} (yellow), Chl_{D2} (orange), P_{D2} (purple), P_{D1} (pink), Chl_{D1} (green) and Phe_{D1} (blue).

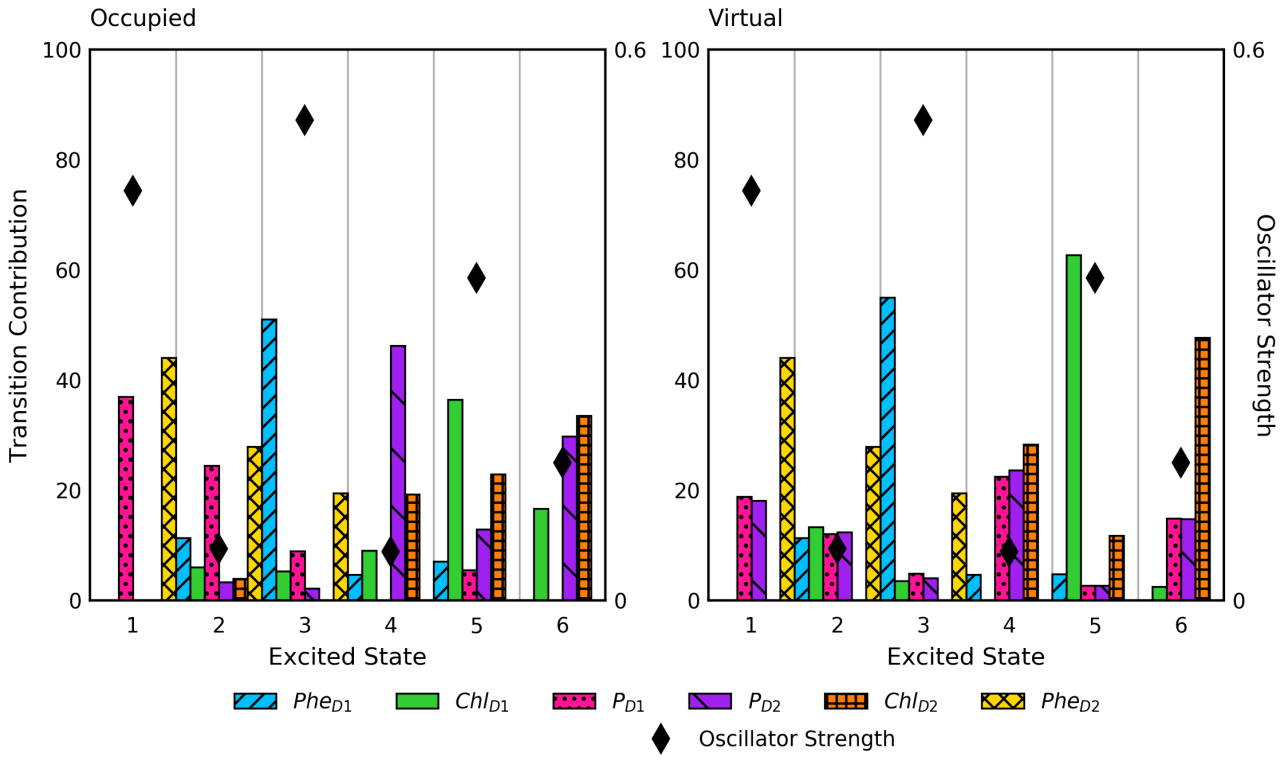


Figure A.14 : Model 1 CAM-b3LYP/6-31G** excited states 1-6, (bar chart, left y axis) % of state contributed to by each cofactor (occupied orbital occupancy analysis with MultiWfn from Mulliken method) and (black diamonds, right y axis) oscillator strength of each state. Cofactors coloured as in all Figures in this thesis. LEFT – occupied orbitals, RIGHT – virtual orbitals.

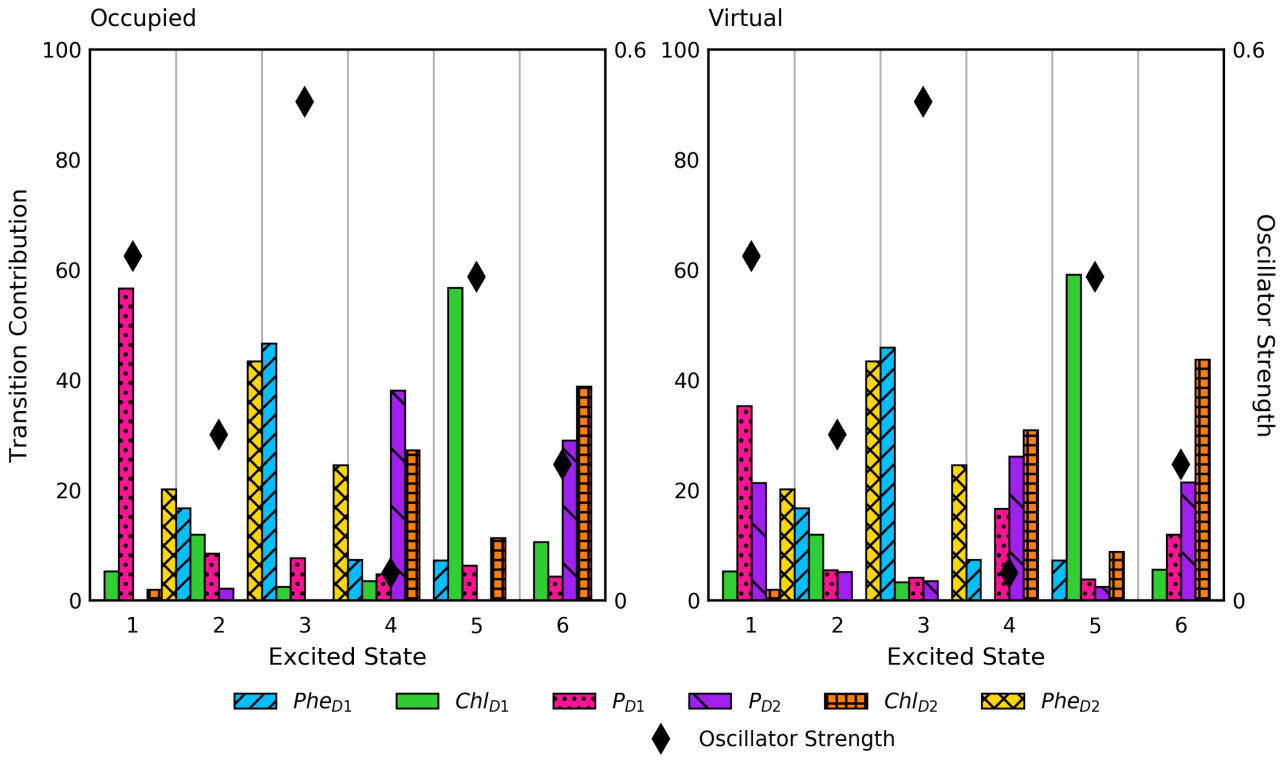


Figure A.15 : Model 1 CAM-b3LYP/6-31+G** excited states 1-6, (bar chart, left y axis) % of state contributed to by each cofactor and (black diamonds, right y axis) oscillator strength of each state. LEFT – occupied orbitals, RIGHT – virtual orbitals.

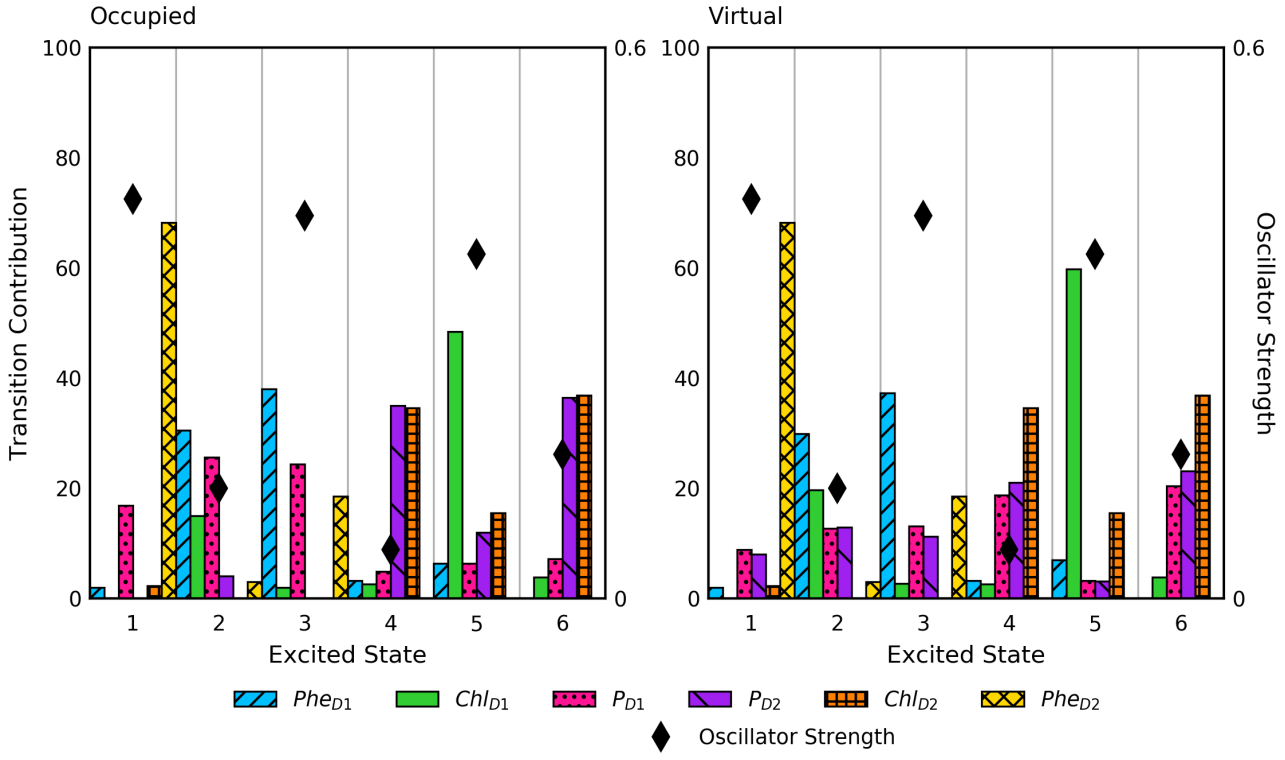
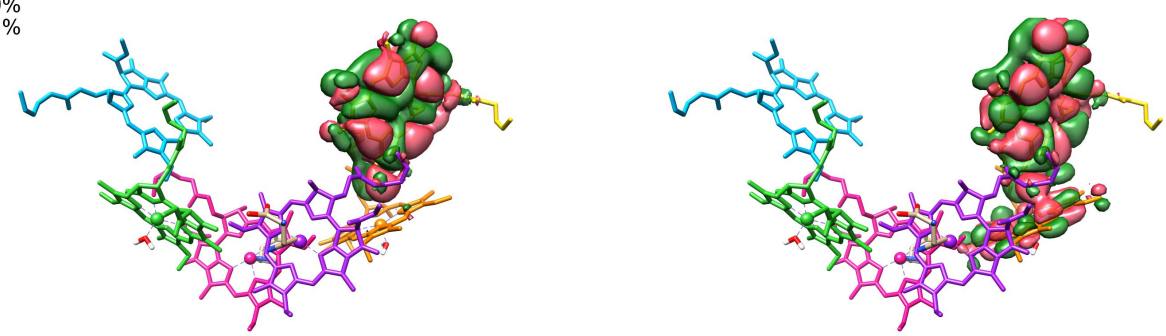
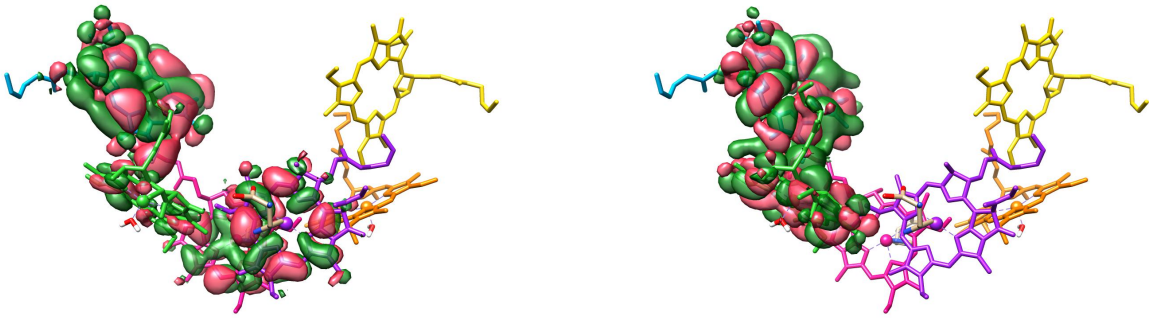


Figure A.16 : Model 1 ωB97X-D/6-31+G** excited states 1-6, (bar chart, left y axis) % of state contributed to by each cofactor and (black diamonds, right y axis) oscillator strength of each state. LEFT – occupied orbitals, RIGHT – virtual orbitals.

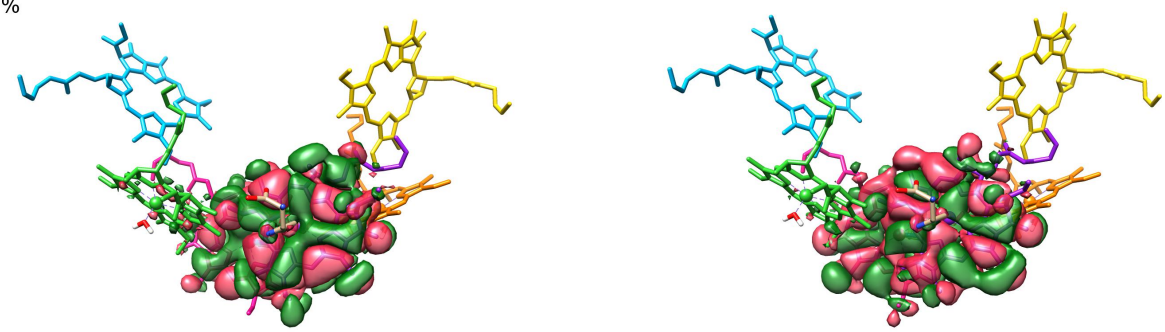
Down inactive (Phe D2 to Chl D2): 1142 → 1148
State 1: 27.02%
State 2: 16.89%
State 3: 12.51%



Up active (P D1 to Chl D1): 1140 → 1147
State 2: 11.40%
State 3: 33.94%
State 4: 4.74%
State 5: 4.87%



P D2 to P D1: 1143 → 1150
State 4: 20.58%
State 6: 12.61%



Chl D2 to Chl D1: 1139 → 1146
State 2: 6.08%
State 5: 23.72%
State 6: 2.54%

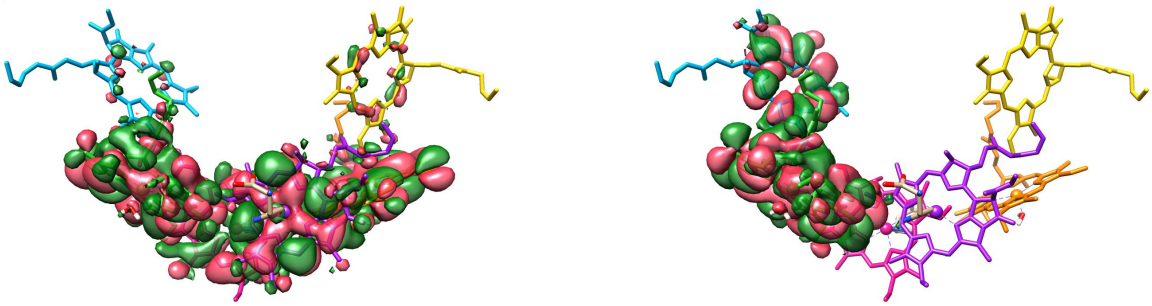
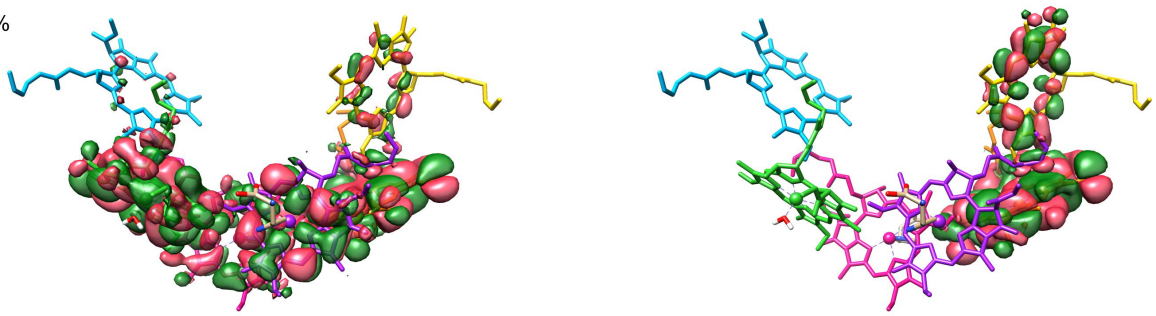
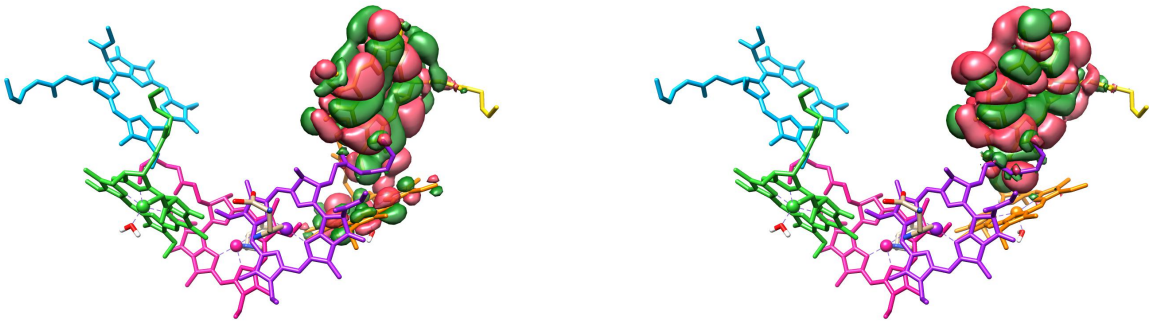


Figure A.17 : MO diagrams exemplifying all transition classes for model 1 CAM-B3LYP/6-31G** including dominant transitions contributing to ES 1-6, LEFT COLUMN - Occupied MO, RIGHT COLUMN – Virtual MO (PAGE 1).

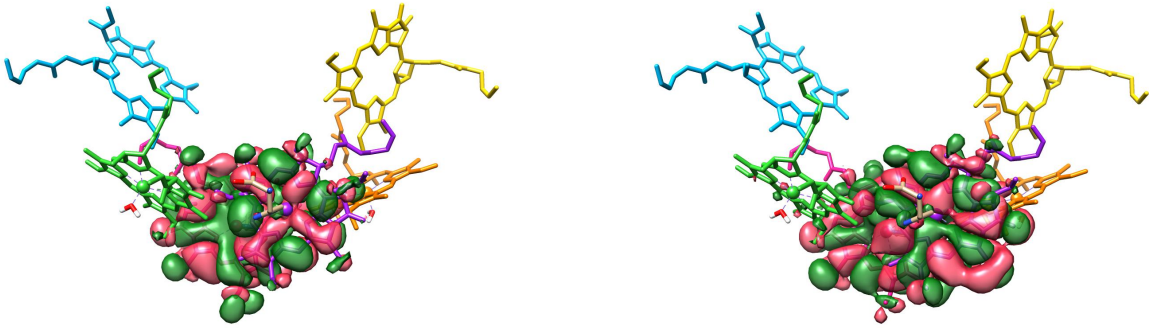
Chl D1 to Chl D2: 1138 → 1145
State 4: 15.92%
State 5: 7.84%
State 6: 24.59%



Up inactive (Chl D2 to Phe D2): 1136 → 1154
State 1: 5.18%
State 2: 3.39%
State 3: 2.64%



P D1 to P D2: 1144 → 1149
State 1: 18.93%
State 2: 12.08%
State 3: 4.90%
State 5: 2.77%



Down active (Phe D1 to Chl D1): 1134 → 1153
State 5: 6.55%

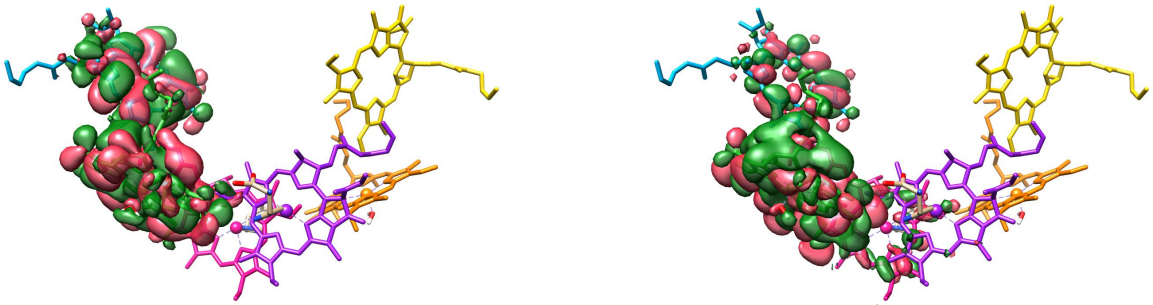
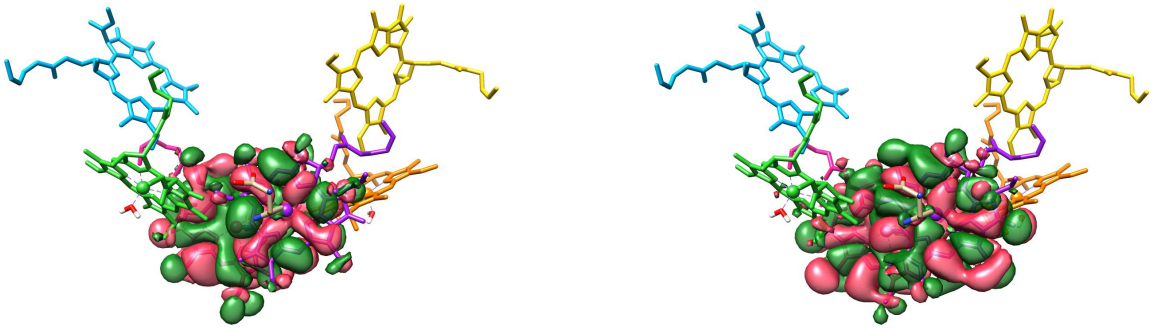
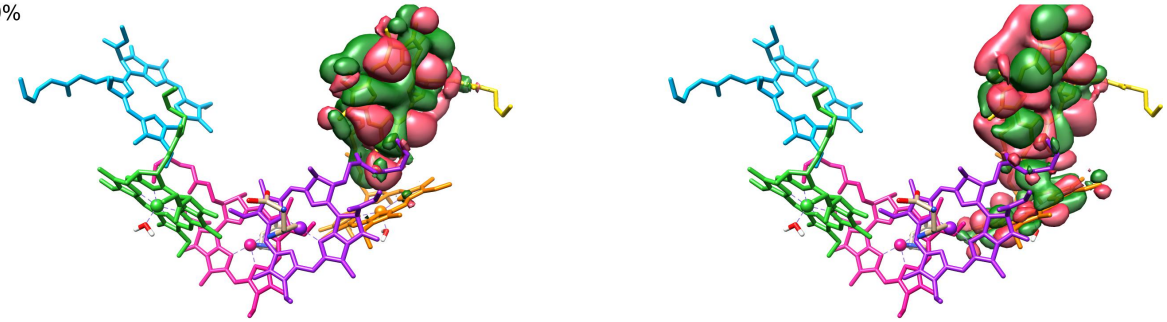


Figure A.17 : MO diagrams exemplifying all transition classes for model 1 CAM-B3LYP/6-31G** including dominant transitions contributing to ES 1-6, LEFT COLUMN - Occupied MO, RIGHT COLUMN – Virtual MO (PAGE 2).

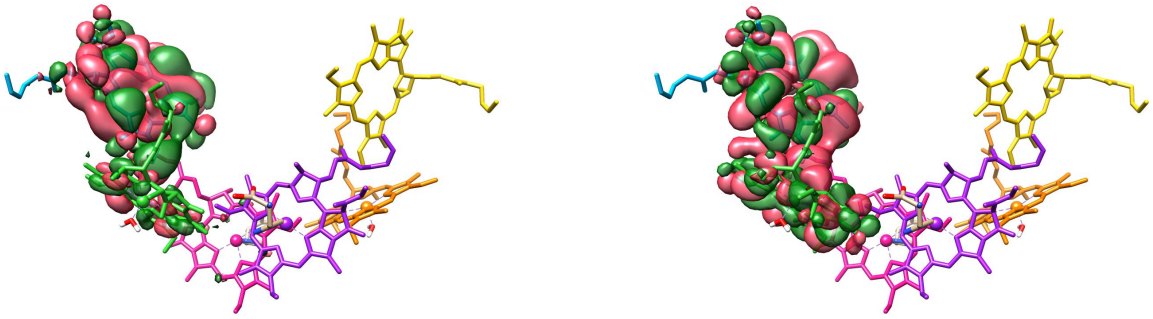
P D1 to P D2: 1144 → 1150
State 1: 32.74%
State 2: 5.54%
State 3: 4.20%
State 5: 3.88%
State 6: 2.32%



Down inactive (Phe D2 to Chl D2): 1142 → 1148
State 1: 13.81%
State 2: 27.54%
State 3: 16.29%



Down active (Phe D1 to Chl D1): 1140 → 1147
State 2: 14.59%
State 3: 32.02%
State 4: 7.46%
State 5: 7.35%



Up inactive (P D2 to Chl D2): 1139 → 1146
State 1: 2.03%
State 4: 23.77%
State 5: 8.92%
State 6: 32.54%

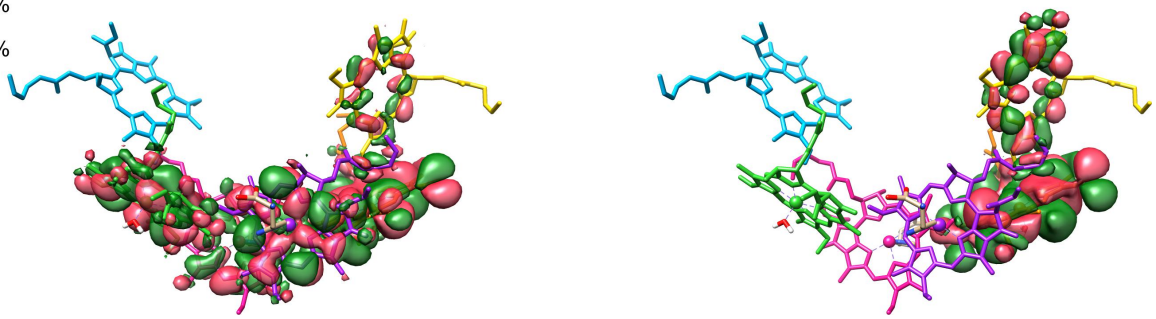
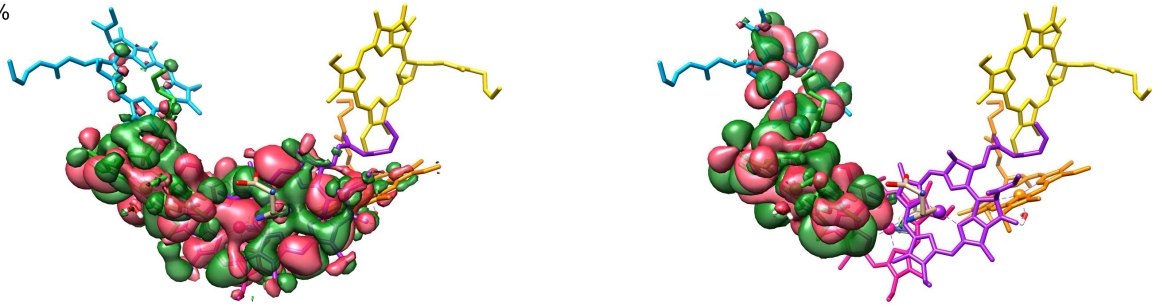


Figure A.18 : MO diagrams exemplifying all transition classes for model 1 CAM-B3LYP/6-31+G** including dominant transitions contributing to ES 1-6, LEFT COLUMN - Occupied MO, RIGHT COLUMN – Virtual MO (PAGE 1).

Up active (P D2 to Chl D1): 1137 → 1145
State 1: 2.69%
State 2: 6.20%
State 5: 24.61%
State 6: 2.85%



P D2 to P D1: 1143 → 1149
State 2: 2.21%
State 4: 23.63%
State 6: 19.38%

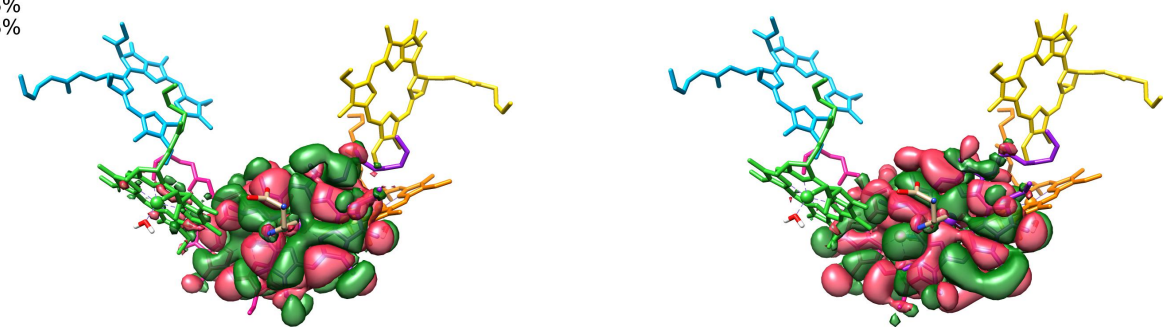
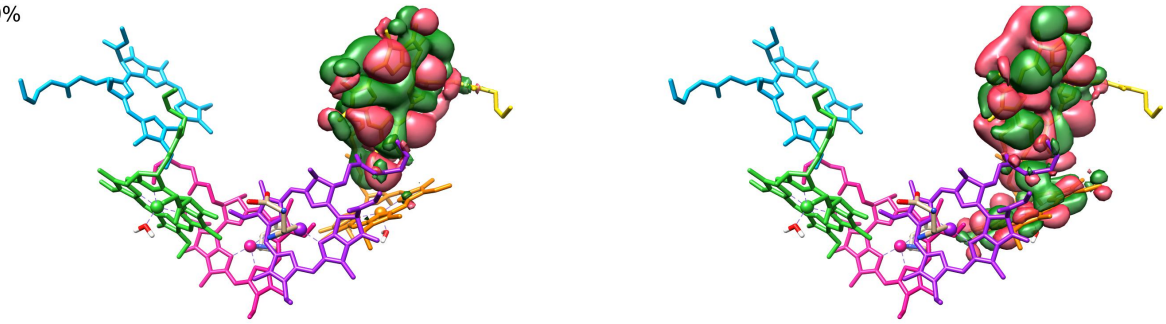
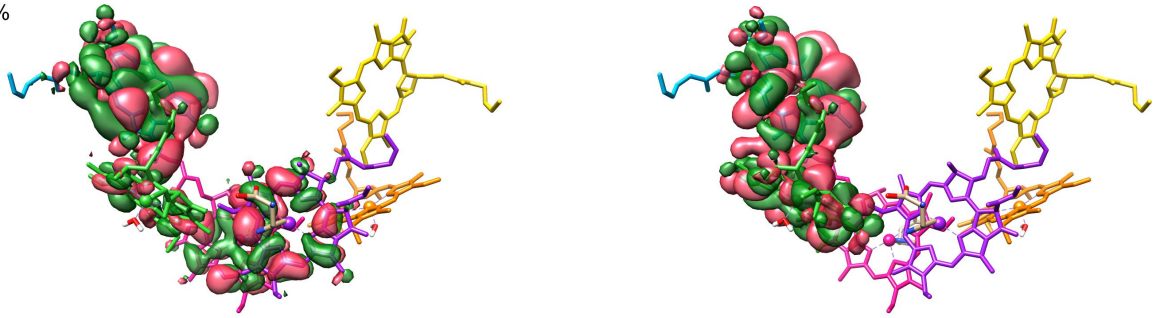


Figure A.18 : MO diagrams exemplifying all transition classes for model 1 CAM-B3LYP/6-31+G** including dominant transitions contributing to ES 1-6, LEFT COLUMN - Occupied MO, RIGHT COLUMN – Virtual MO (PAGE 2).

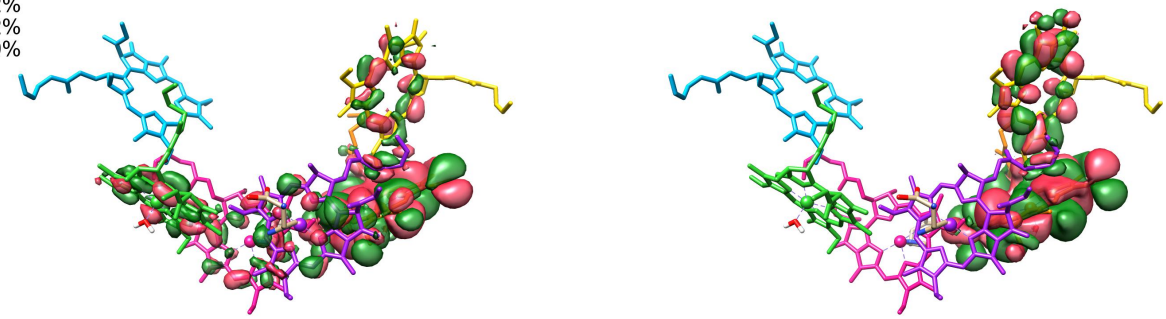
Down inactive (Phe D2 to Chl D2): 1142 → 1148
State 1: 42.61%
State 2: 3.03%
State 3: 12.19%



Up active (P D1 to Chl D1): 1140 → 1147
State 1: 2.04%
State 2: 21.22%
State 3: 26.95%
State 4: 3.27%
State 5: 4.32%



Up inactive (P D1 to Phe D2): 1139 → 1146
State 1: 2.37%
State 4: 30.22%
State 5: 13.32%
State 6: 31.09%



Up active (P D2 to Chl D1): 1138 → 1145
State 2: 12.68%
State 4: 2.65%
State 5: 37.03%
State 6: 3.87%

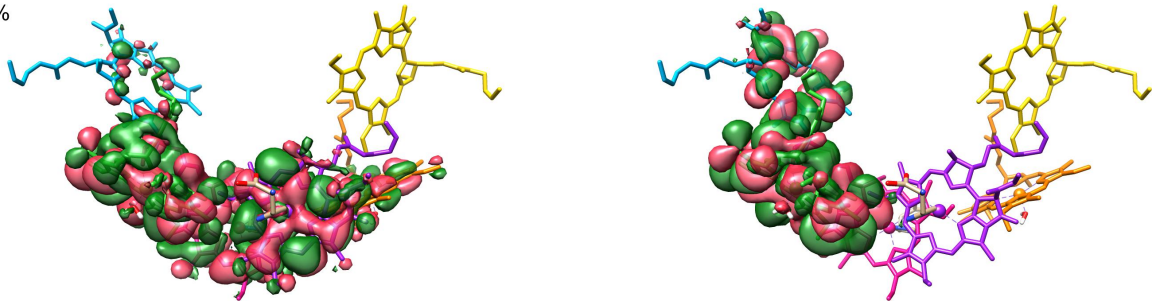
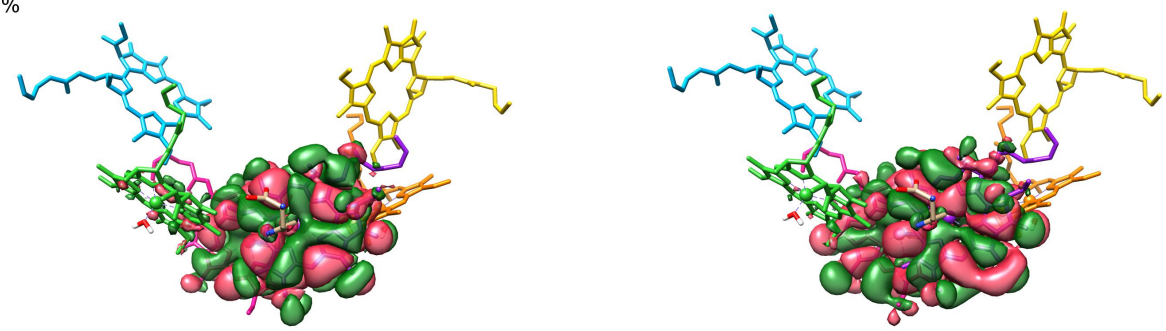
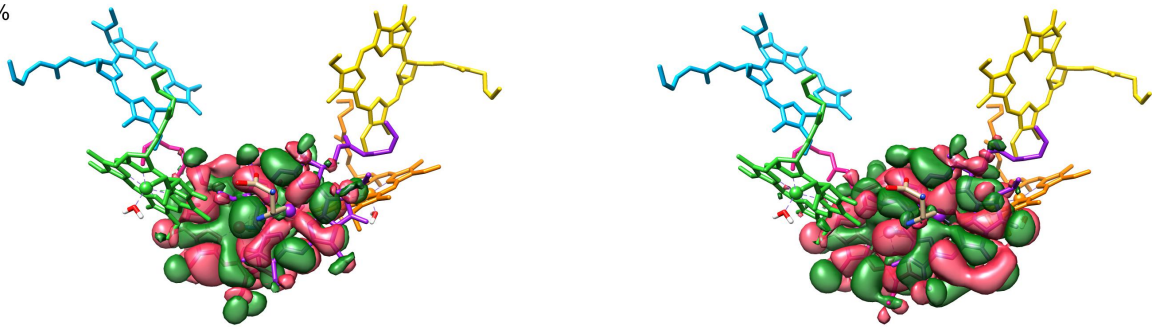


Figure A.19 : MO diagrams exemplifying all transition classes for model 1 ωB97X-D/6-31+G** including dominant transitions contributing to ES 1-6, LEFT COLUMN - Occupied MO, RIGHT COLUMN – Virtual MO (PAGE 1).

P D2 to P D1: 1143 → 1149
State 4: 16.68%
State 6: 18.35%



P D1 to P D2: 1144 → 1149
State 1: 8.90%
State 2: 12.79%
State 3: 13.15%
State 4: 2.09%
State 5: 3.27%



Down active (Phe D1 to Chl D1): 1134 → 1153
State 5: 6.71%

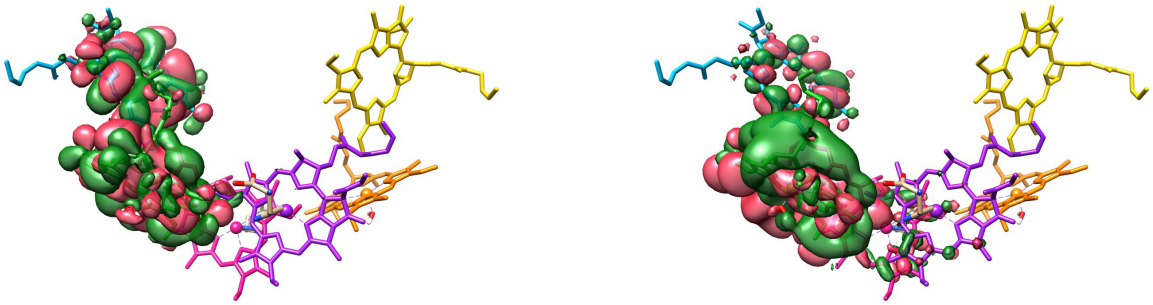


Figure A.19 : MO diagrams exemplifying all transition classes for model 1 ωB97X-D/6-31+G** including dominant transitions contributing to ES 1-6, LEFT COLUMN - Occupied MO, RIGHT COLUMN – Virtual MO (PAGE 2).

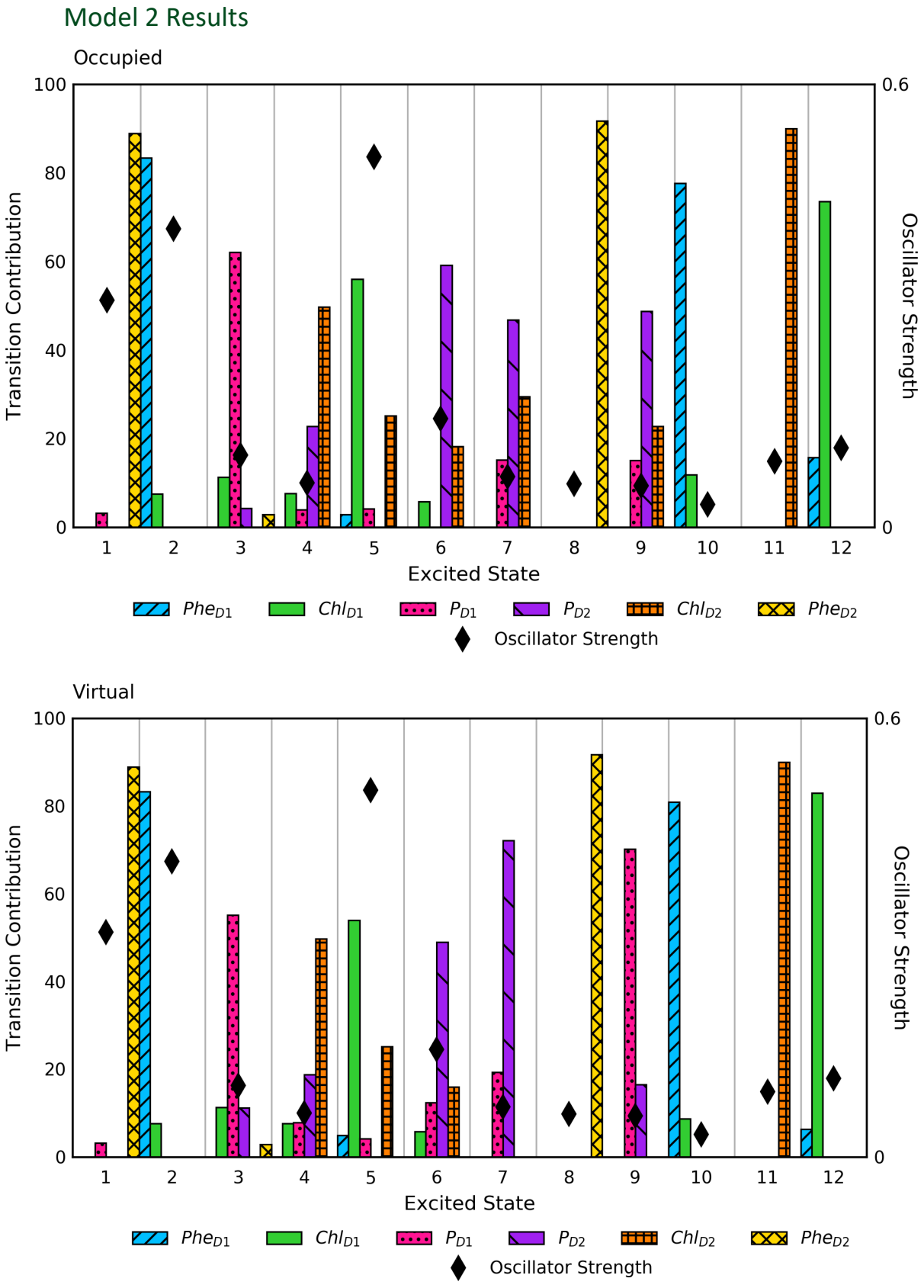


Figure A.20 : Model 2 ωB97X-D/6-31G** excited states 1-12, (bar chart, left y axis) % of state contributed to by each cofactor (occupied orbital occupancy analysis with MultiWfn from Mulliken method) and (black diamonds, right y axis) oscillator strength of each state. Cofactors coloured as in all Figures in this thesis. TOP – occupied orbitals, BOTTOM – virtual orbitals.

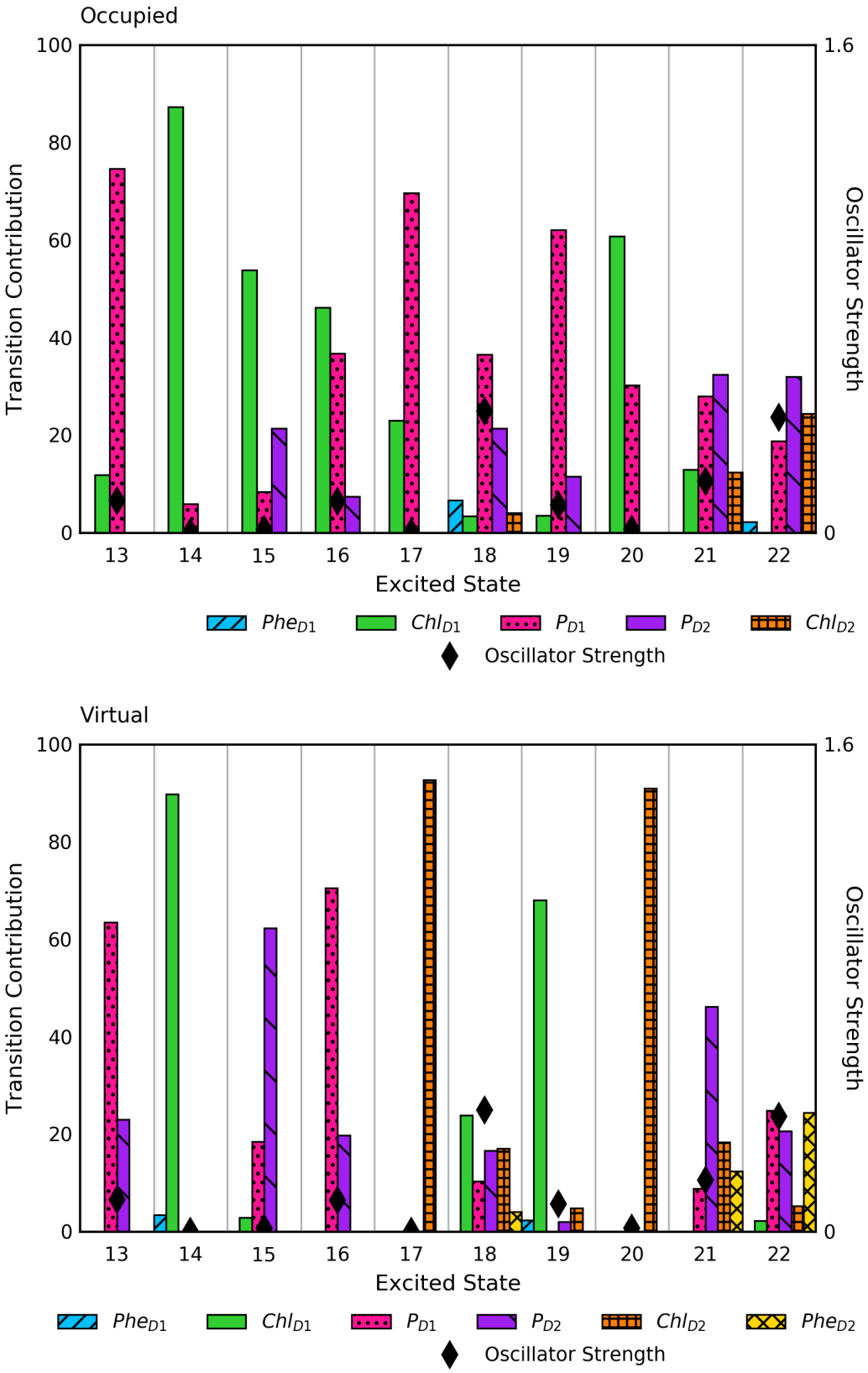
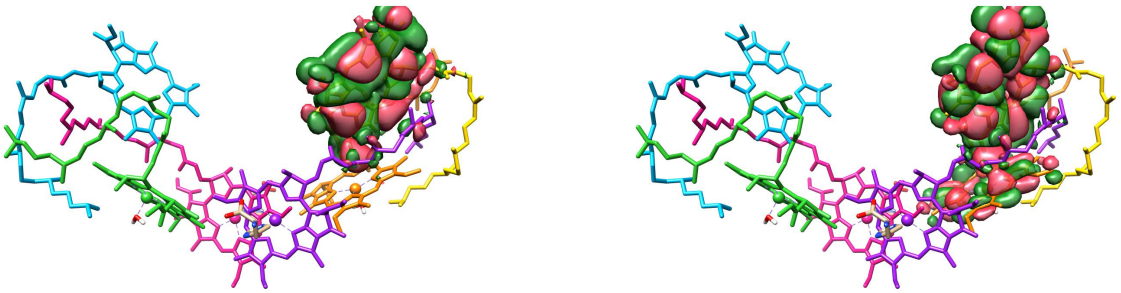
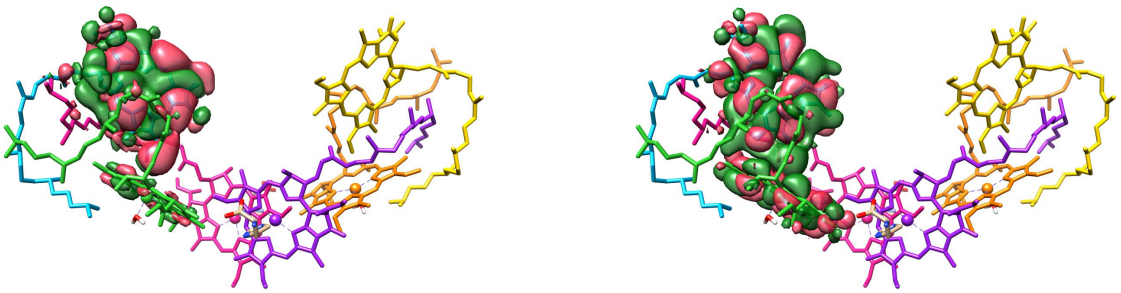


Figure A.21 : Model 2 ωB97X-D/6-31G** excited states 13-22, (bar chart, left y axis) % of state contributed to by each cofactor (occupied orbital occupancy analysis with MultiWfn from Mulliken method) and (black diamonds, right y axis) oscillator strength of each state. Cofactors coloured as in all Figures in this thesis. TOP – occupied orbitals, BOTTOM – virtual orbitals.

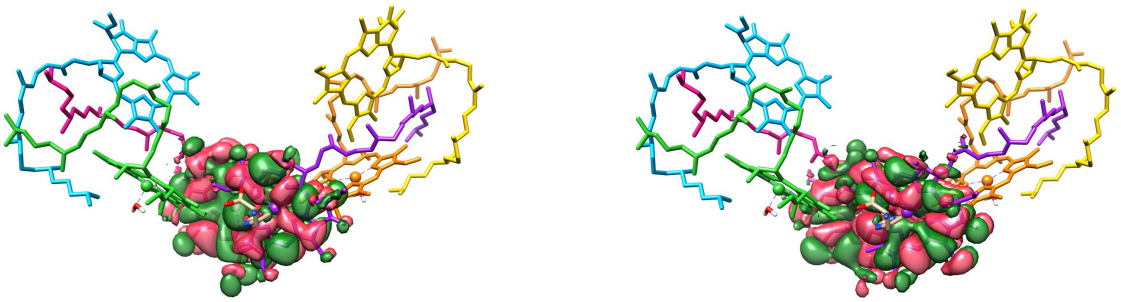
Down inactive (Phe D2 to Chl D2): 1526 → 1532
State 1: 54.21%
State 3: 2.92%



Down active (Phe D1 to Chl D1): 1524 → 1531
State 2: 55.20%
State 5: 2.83%



P D1 to P D2: 1528 → 1533
State 1: 3.20%
State 3: 50.88%
State 4: 3.91%
State 5: 4.19%



Up inactive (P D2 to Chl D2): 1523 → 1530
State 4: 21.10%
State 5: 10.16%
State 6: 6.90%

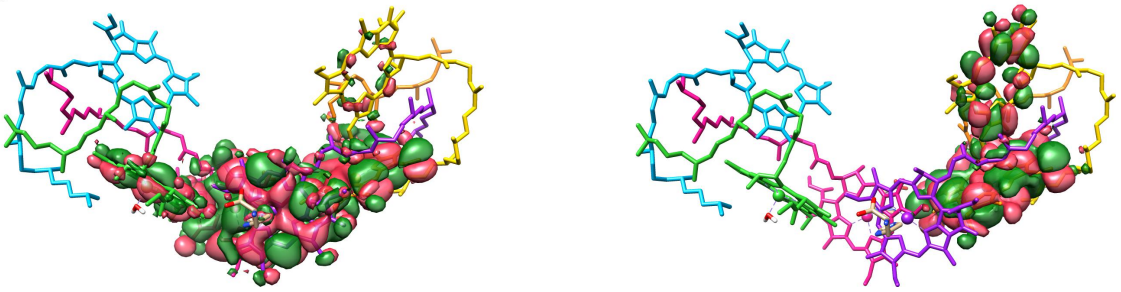
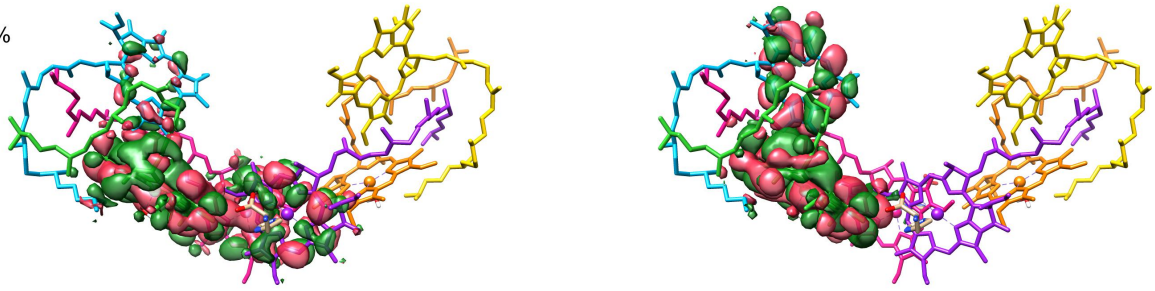


Figure A.22 : MO diagrams exemplifying all transition classes for model 2 ωB97X-D/6-31G** including dominant transitions contributing to ES 1-6, LEFT COLUMN - Occupied MO, RIGHT COLUMN – Virtual MO (PAGE 1).

Up active (P D1 to Phe D1): 1521 → 1529
State 2: 4.09%
State 3: 11.31%
State 4: 7.66%
State 5: 44.74%
State 6: 5.83%



P D2 to P D1: 1527 → 1534
State 4: 15.79%
State 6: 39.54%

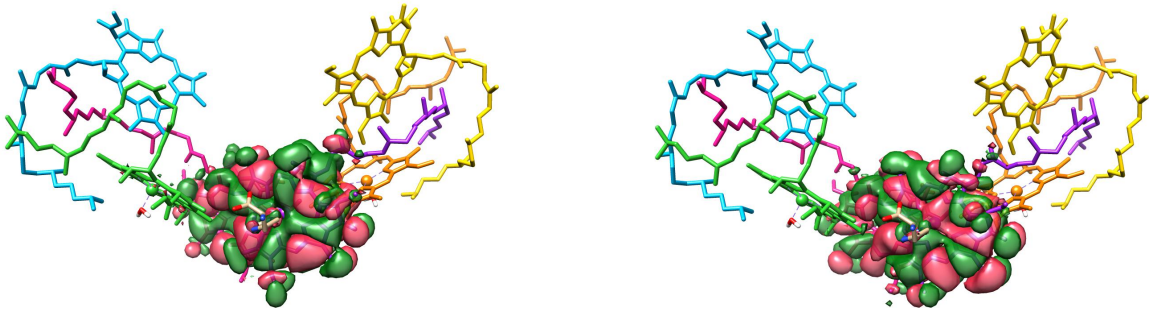


Figure A.22 : MO diagrams exemplifying all transition classes for model 2 ωB97X-D/6-31G** including dominant transitions contributing to ES 1-6, LEFT COLUMN - Occupied MO, RIGHT COLUMN – Virtual MO (PAGE 2).

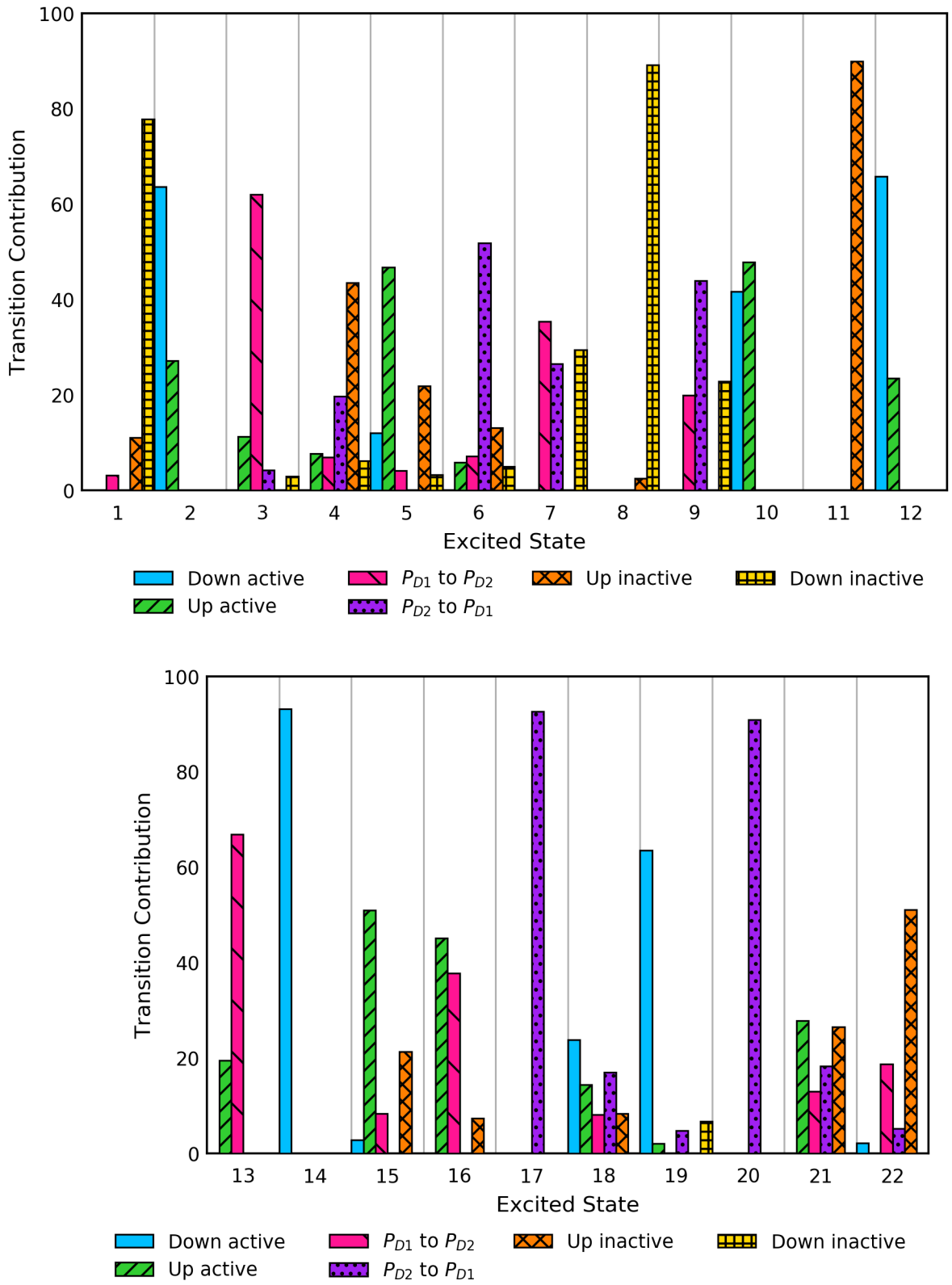


Figure A.23 : Contributions from each transition class to ES 13-22 for model 2 (ωB97X-D/ 6-31G**), TOP : ES 1-12 (Qy and Qx regions), BOTTOM : ES 13-22 (Soret region).

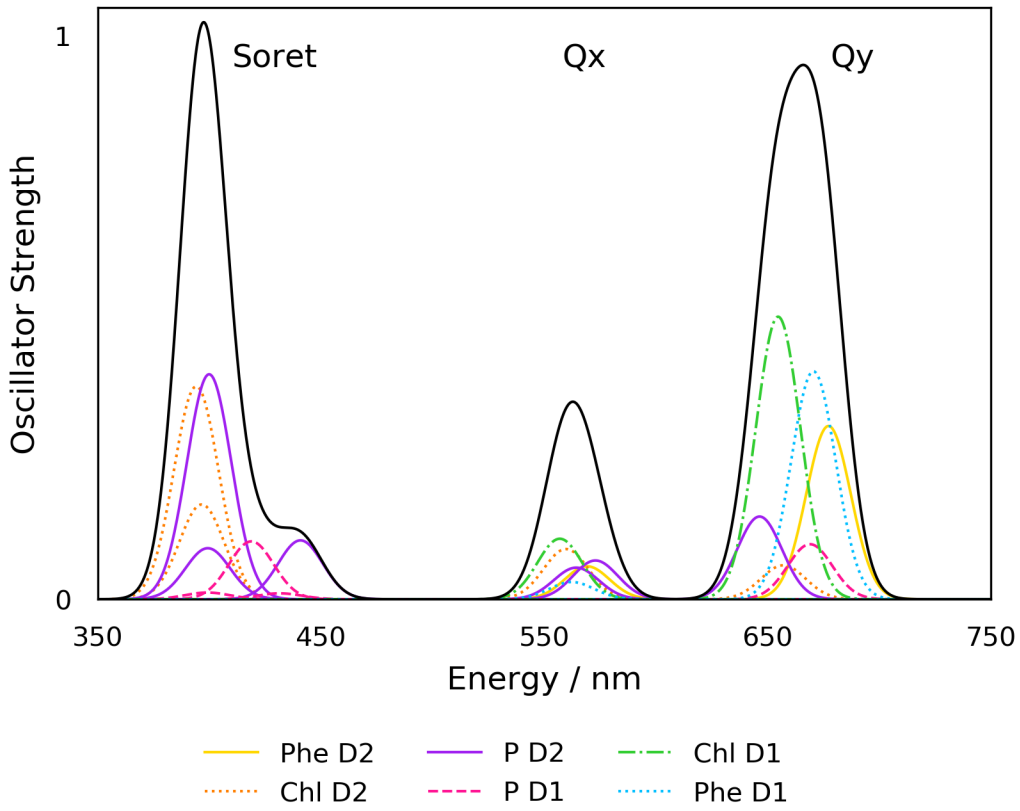


Figure A.24 : Calculated absorption spectrum for model 2 (ωB97X-D/ 6-31G**), black line – full spectrum from sum of single ES broadened by gaussian functions, coloured lines – single ES broadened by gaussian functions coloured by occupied orbital cofactor: Phe_{D2} (yellow), Chl_{D2} (orange), P_{D2} (purple), P_{D1} (pink), Chl_{D1} (green) and Phe_{D1} (blue).

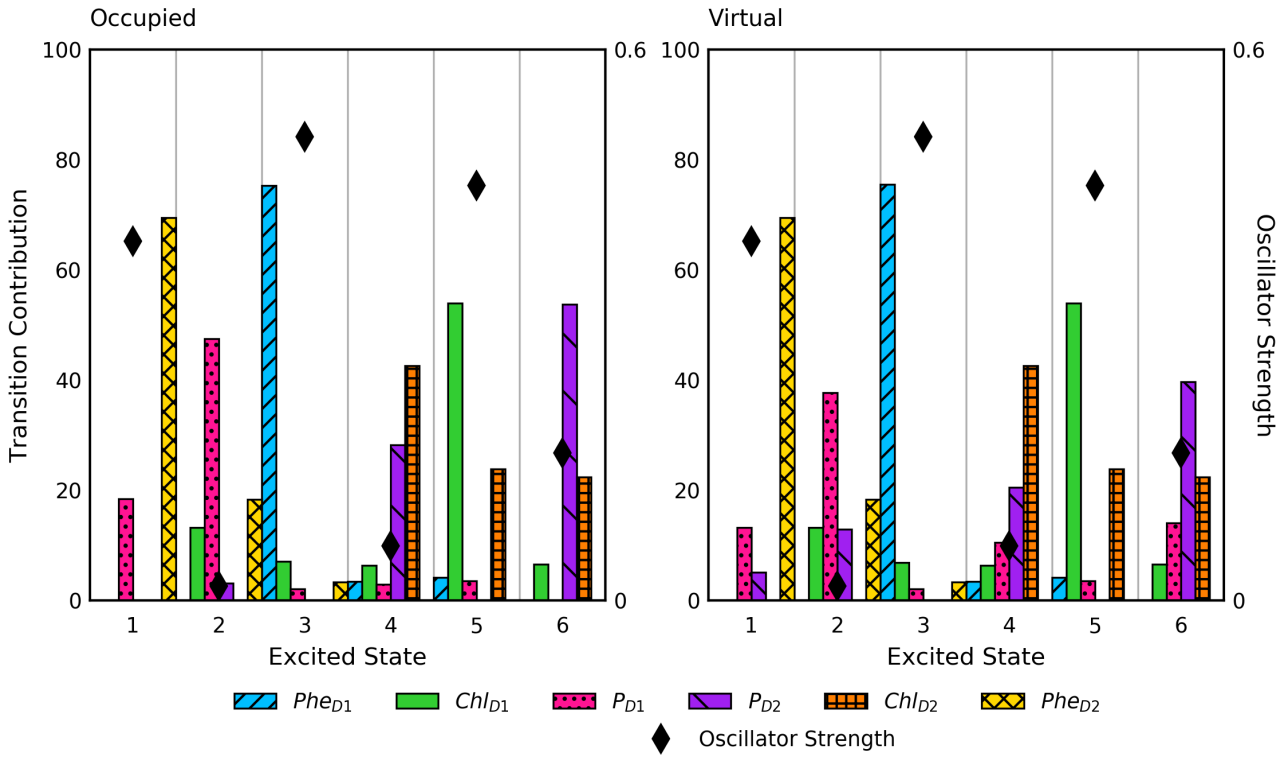


Figure A.25 : Model 2 CAM-b3LYP/6-31G** excited states 1-6, (bar chart, left y axis) % of state contributed to by each cofactor (occupied orbital occupancy analysis with MultiWfn from Mulliken method) and (black diamonds, right y axis) oscillator strength of each state. Cofactors coloured as in all Figures in this thesis. TOP – occupied orbitals, BOTTOM – virtual orbitals.

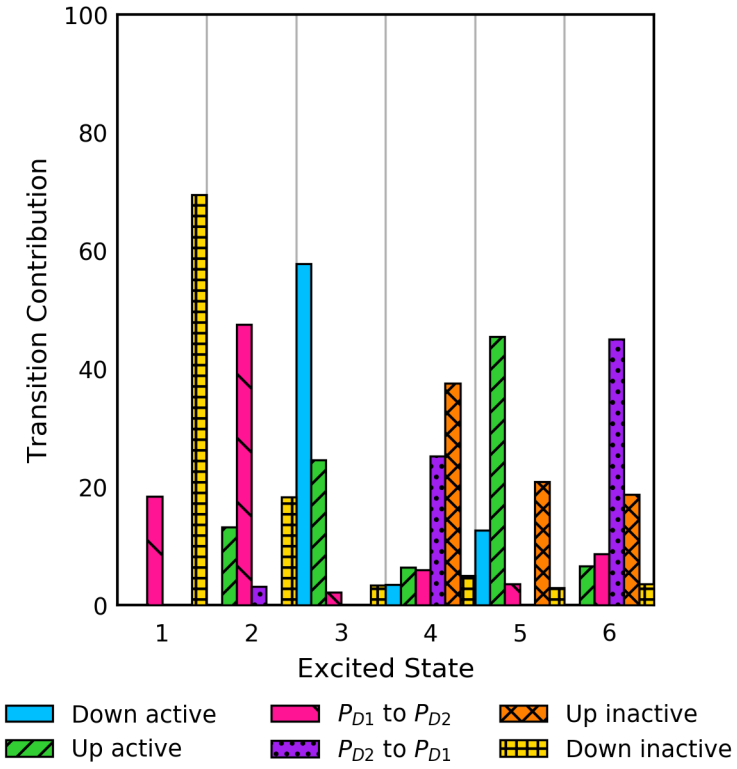


Figure A.26 : Contributions from each transition class to ES 1-6 for model 2 (CAM-b3LYP/ 6-31G**)

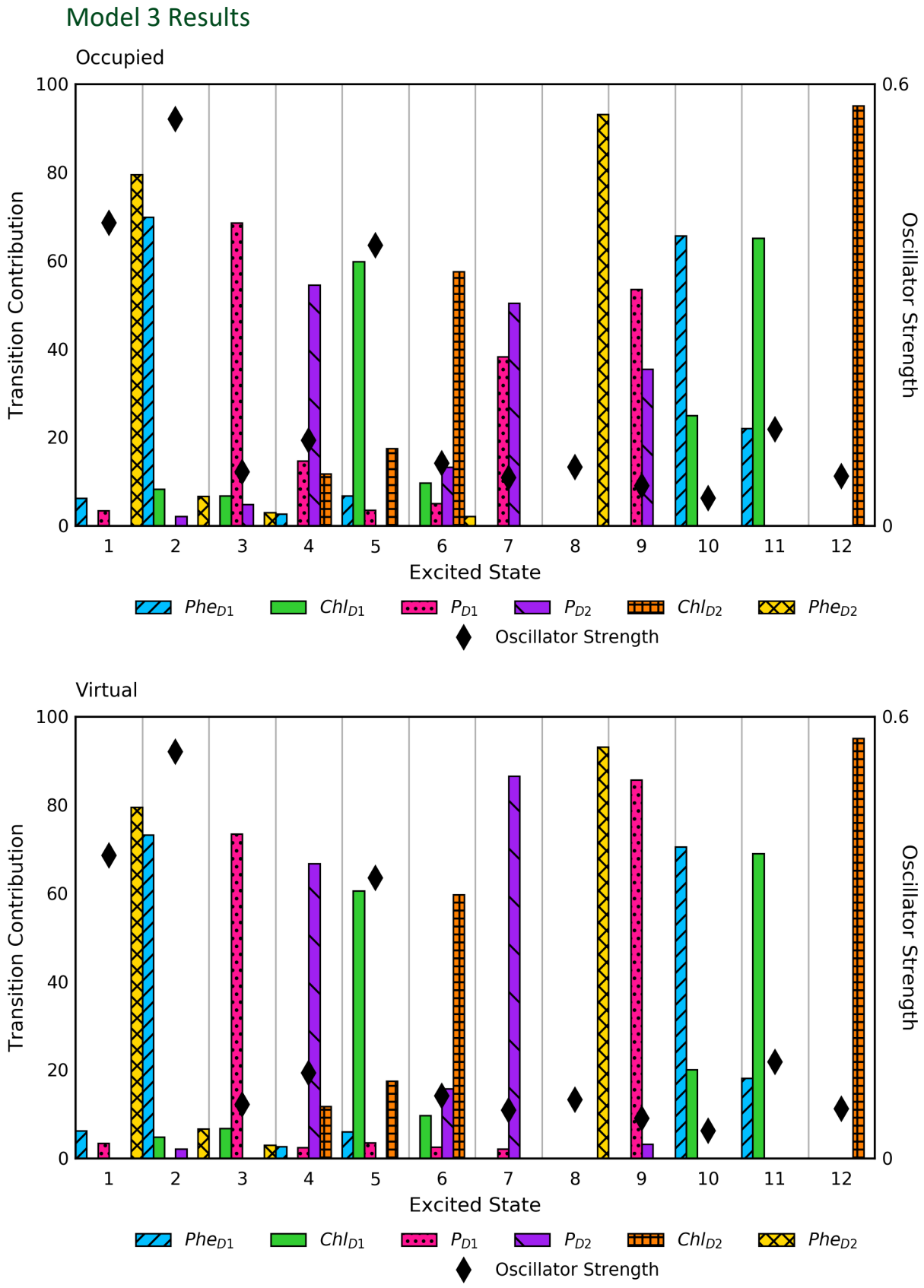


Figure A.27 – Model 3 ωB97X-D/6-31G** excited states 1-12, (bar chart, left y axis) % of state contributed to by each cofactor (occupied orbital occupancy analysis with MultiWfn from Mulliken method) and (black diamonds, right y axis) oscillator strength of each state. Cofactors coloured as in all Figures in this thesis. TOP – occupied orbitals, BOTTOM – virtual orbitals.

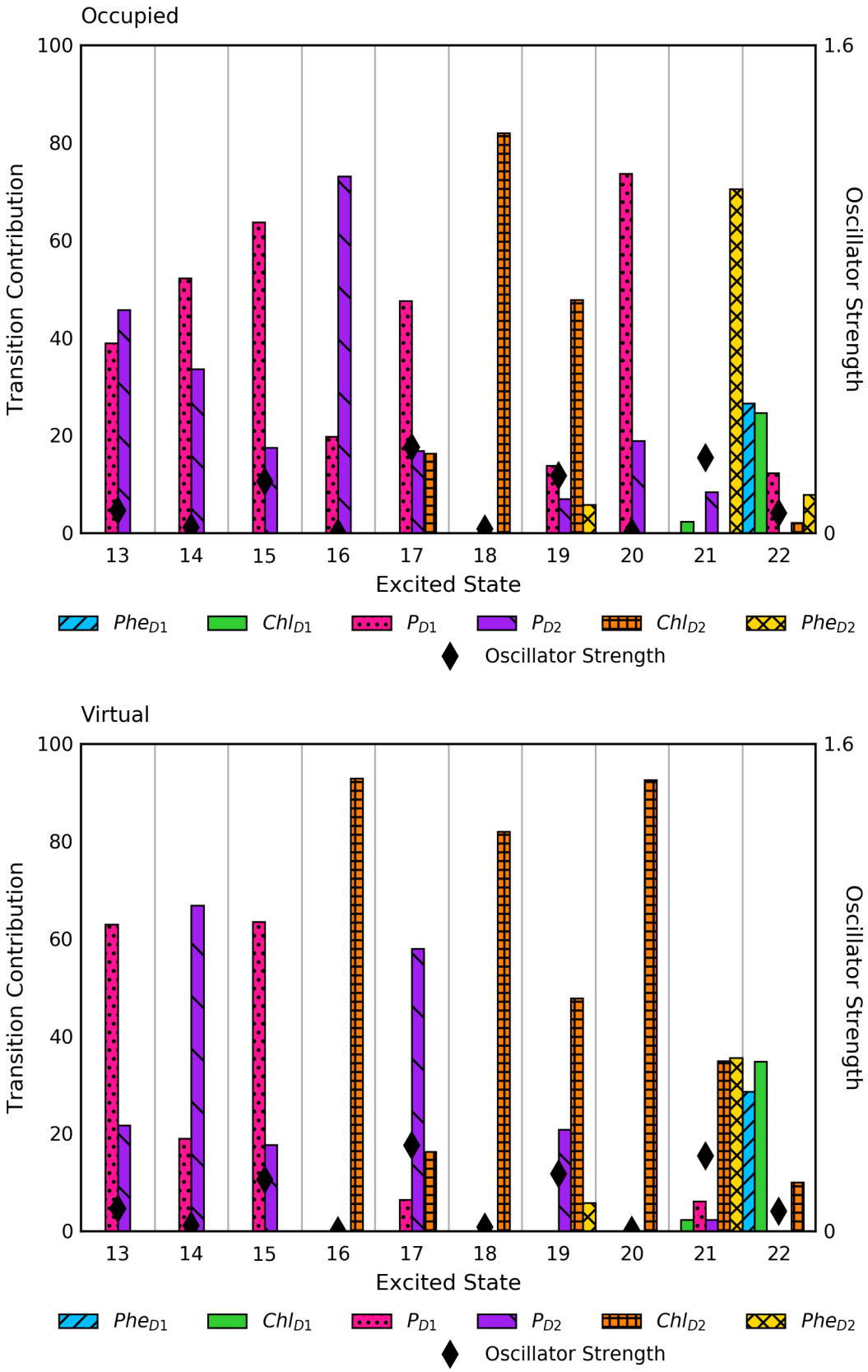
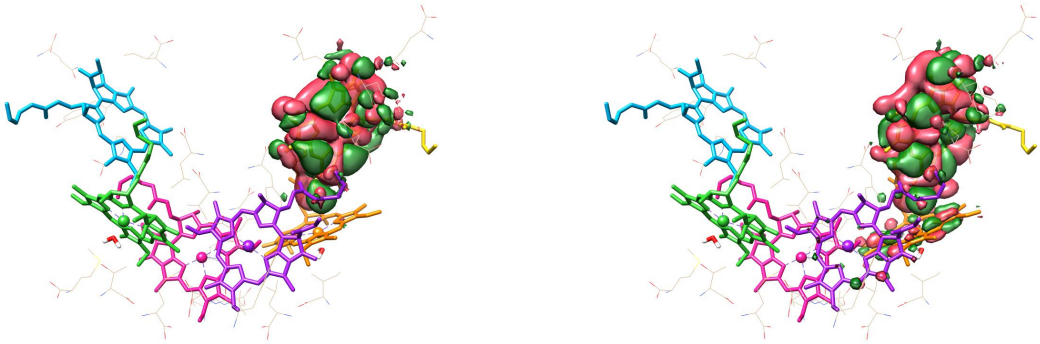
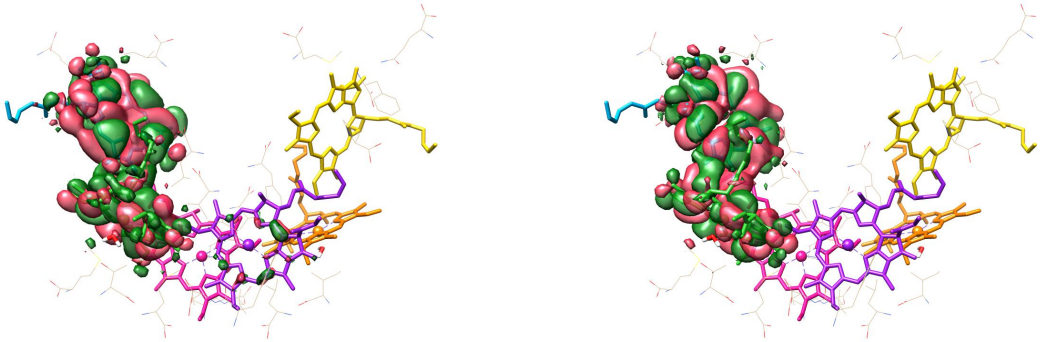


Figure A.28 : Model 3 ωB97X-D/6-31G** excited states 13-22, (bar chart, left y axis) % of state contributed to by each cofactor (occupied orbital occupancy analysis with MultiWfn from Mulliken method) and (black diamonds, right y axis) oscillator strength of each state. Cofactors coloured as in all Figures in this thesis. TOP – occupied orbitals, BOTTOM – virtual orbitals.

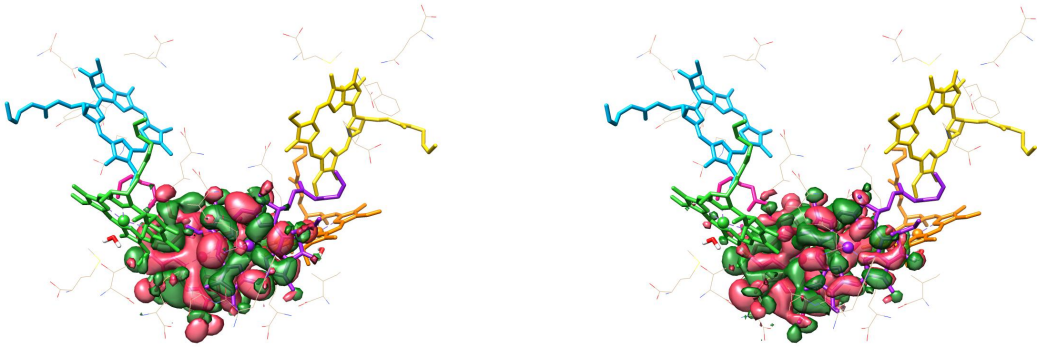
Down inactive (Phe D2 to Chl D2): 1927 → 1932
State 1: 51.89%
State 2: 6.64%
State 3: 3.02%



Up active (Chl D1 to Phe D1): 1924 → 1930
State 1: 6.28%
State 2: 45.62%
State 4: 2.67%
State 5: 3.86%



P D2 to P D1: 1928 → 1934
State 1: 3.42%
State 3: 63.48%
State 4: 2.44%
State 5: 3.56%
State 6: 2.57%



P D1 to P D2: 1926 → 1933
State 2: 2.07%
State 4: 51.36%
State 6: 13.23%

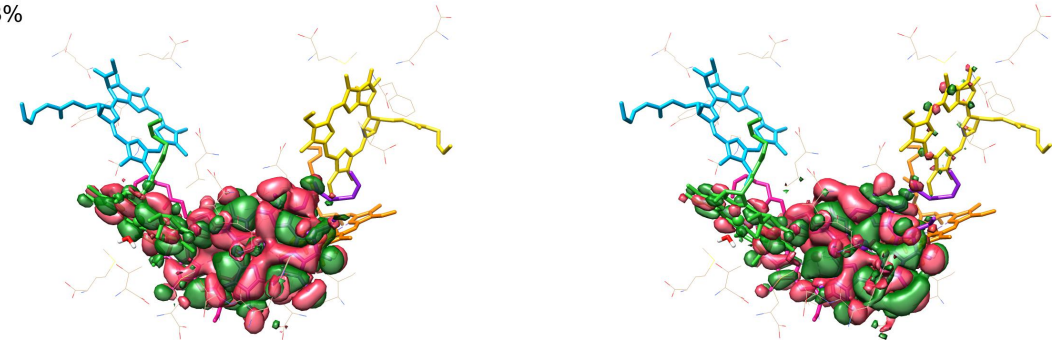
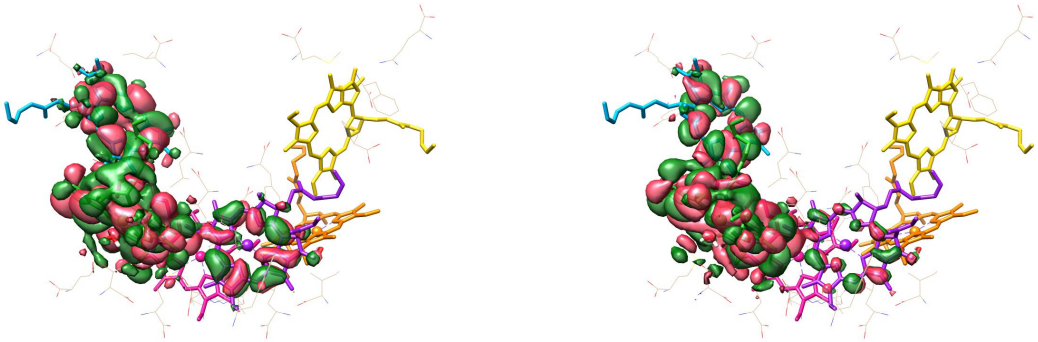
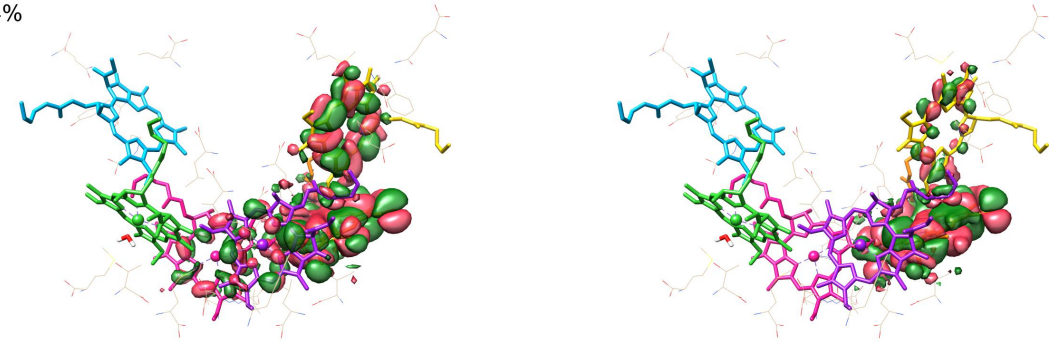


Figure A.29 : MO diagrams exemplifying all transition classes for model 3 ωB97X-D/6-31G** including dominant transitions contributing to ES 1-6, LEFT COLUMN - Occupied MO, RIGHT COLUMN – Virtual MO (PAGE 1).

Down active (Phe D1 to Chl D1): 1925 → 1931
State 3: 6.72%
State 5: 48.18%
State 6: 9.66%



Down inactive (Phe D2 to Chl D2): 1921 → 1929
State 4: 11.74%
State 5: 14.96%
State 6: 46.74%



Up inactive (Chl D2 to Phe D2): 1922 → 1932
State 1: 14.10%

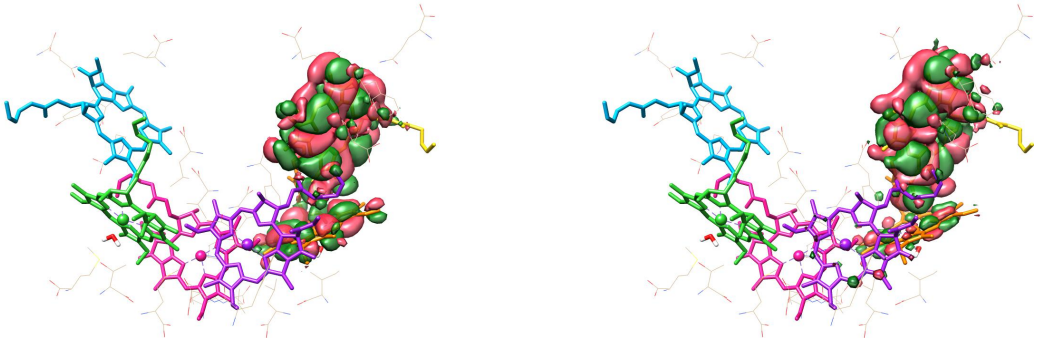


Figure A.29 : MO diagrams exemplifying all transition classes for model 3 ωB97X-D/6-31G** including dominant transitions contributing to ES 1-6, LEFT COLUMN - Occupied MO, RIGHT COLUMN – Virtual MO (PAGE 2).

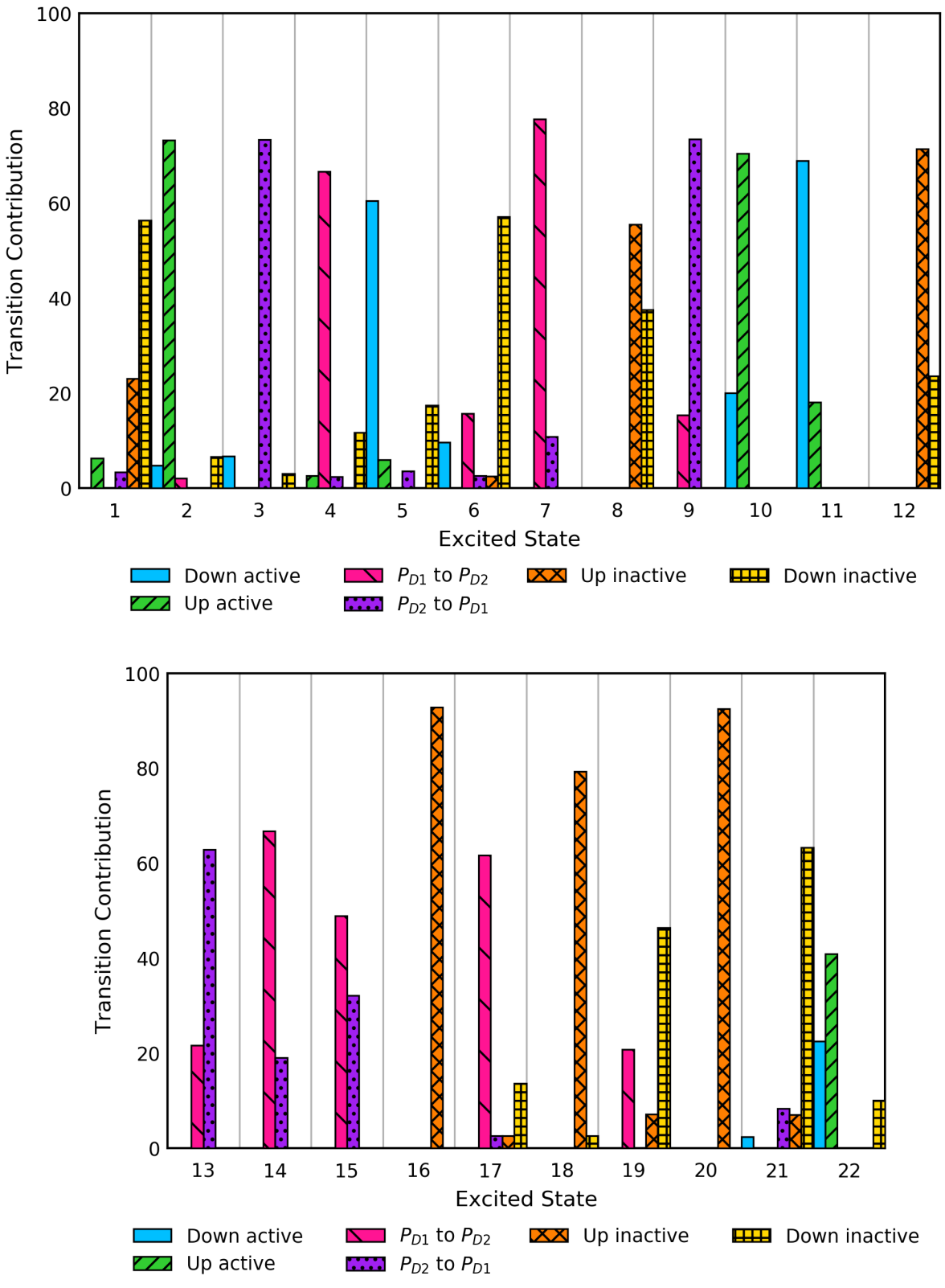


Figure A.30 : Contributions from each transition class for model 3 (ωB97X-D/ 6-31G**), TOP – ES 1-12 (Q_Y and Q_X bands), BOTTOM – ES 13-22 (Soret region).

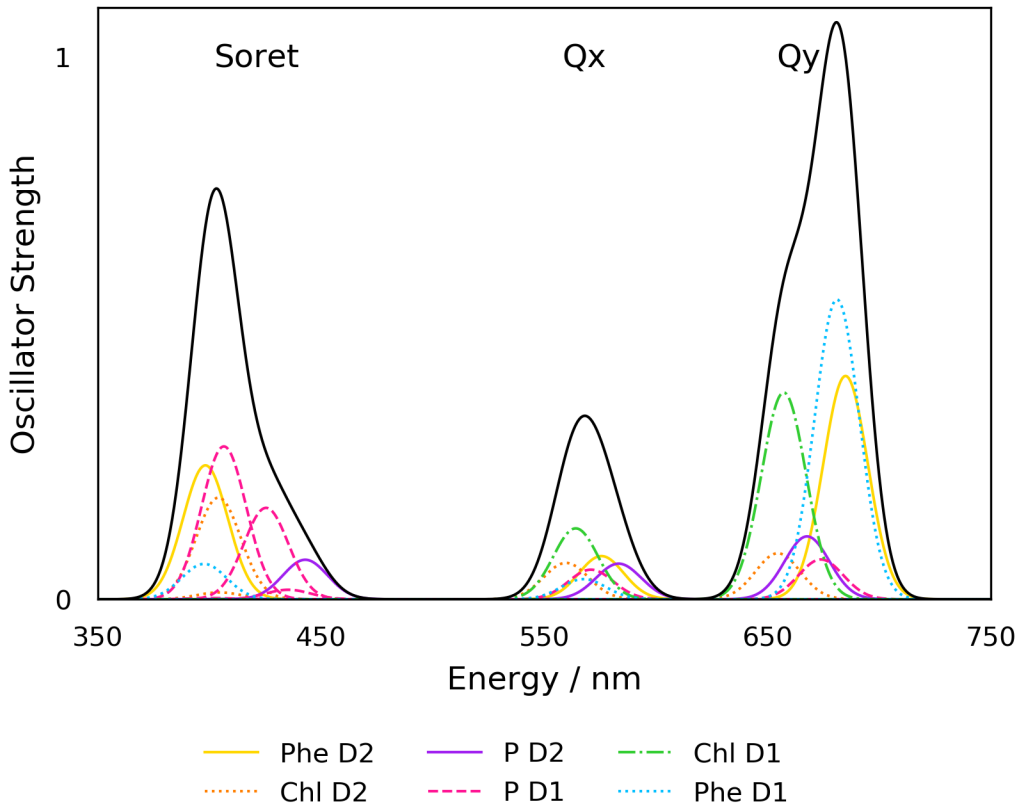


Figure A.31 : Calculated absorption spectrum for model 3 (ωB97X-D/ 6-31G**), black line – full spectrum from sum of single ES broadened by gaussian functions, coloured lines – single ES broadened by gaussian functions coloured by occupied orbital cofactor: Phe_{D2} (yellow), Chl_{D2} (orange), P_{D2} (purple), P_{D1} (pink), Chl_{D1} (green) and Phe_{D1} (blue).

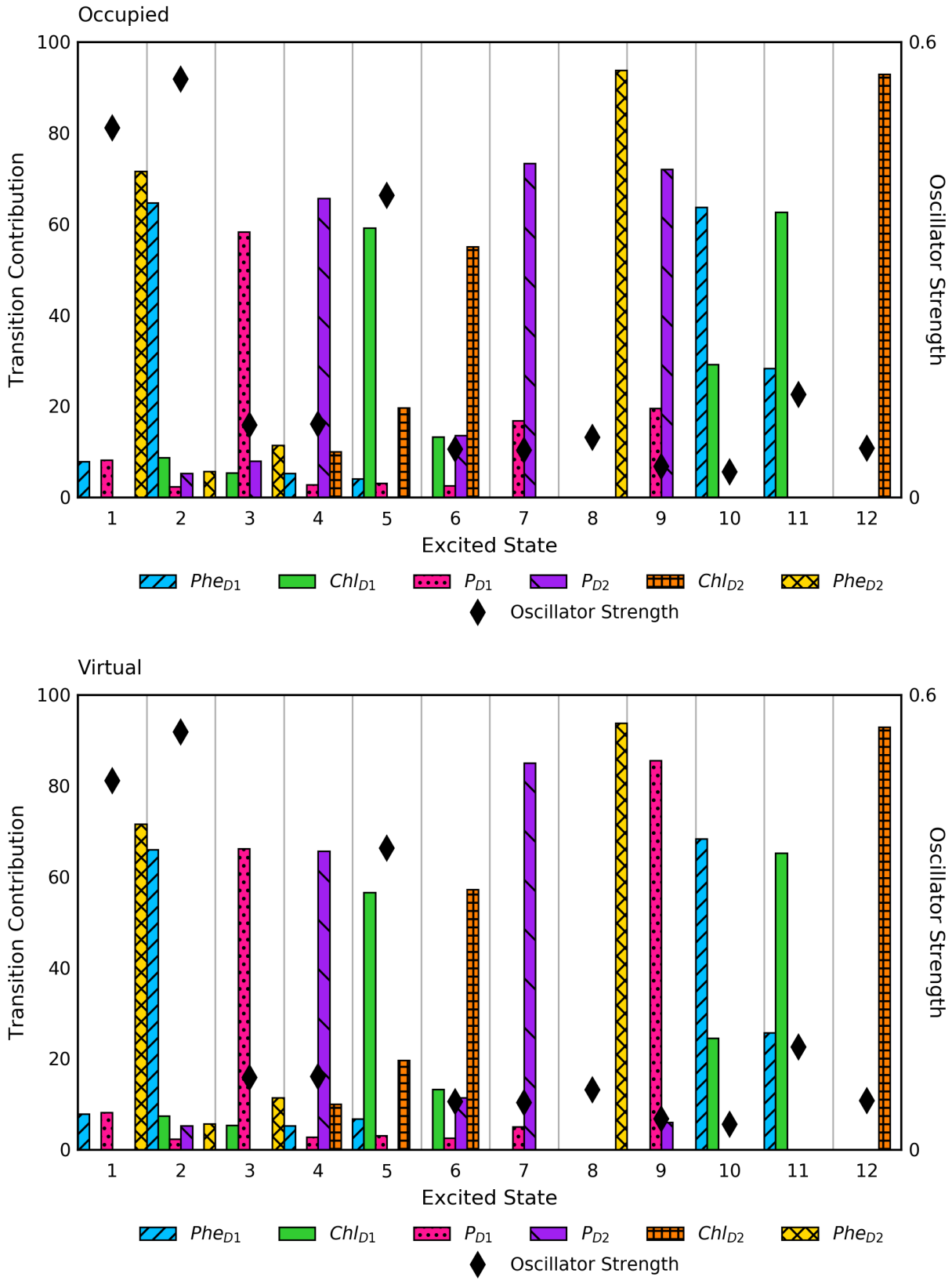


Figure A.32 : Model 3 CAM-b3LYP/6-31G** excited states 1-12, (bar chart, left y axis) % of state contributed to by each cofactor (occupied orbital occupancy analysis with MultiWfn from Mulliken method) and (black diamonds, right y axis) oscillator strength of each state. Cofactors coloured as in all Figures in this thesis. TOP – occupied orbitals, BOTTOM – virtual orbitals.

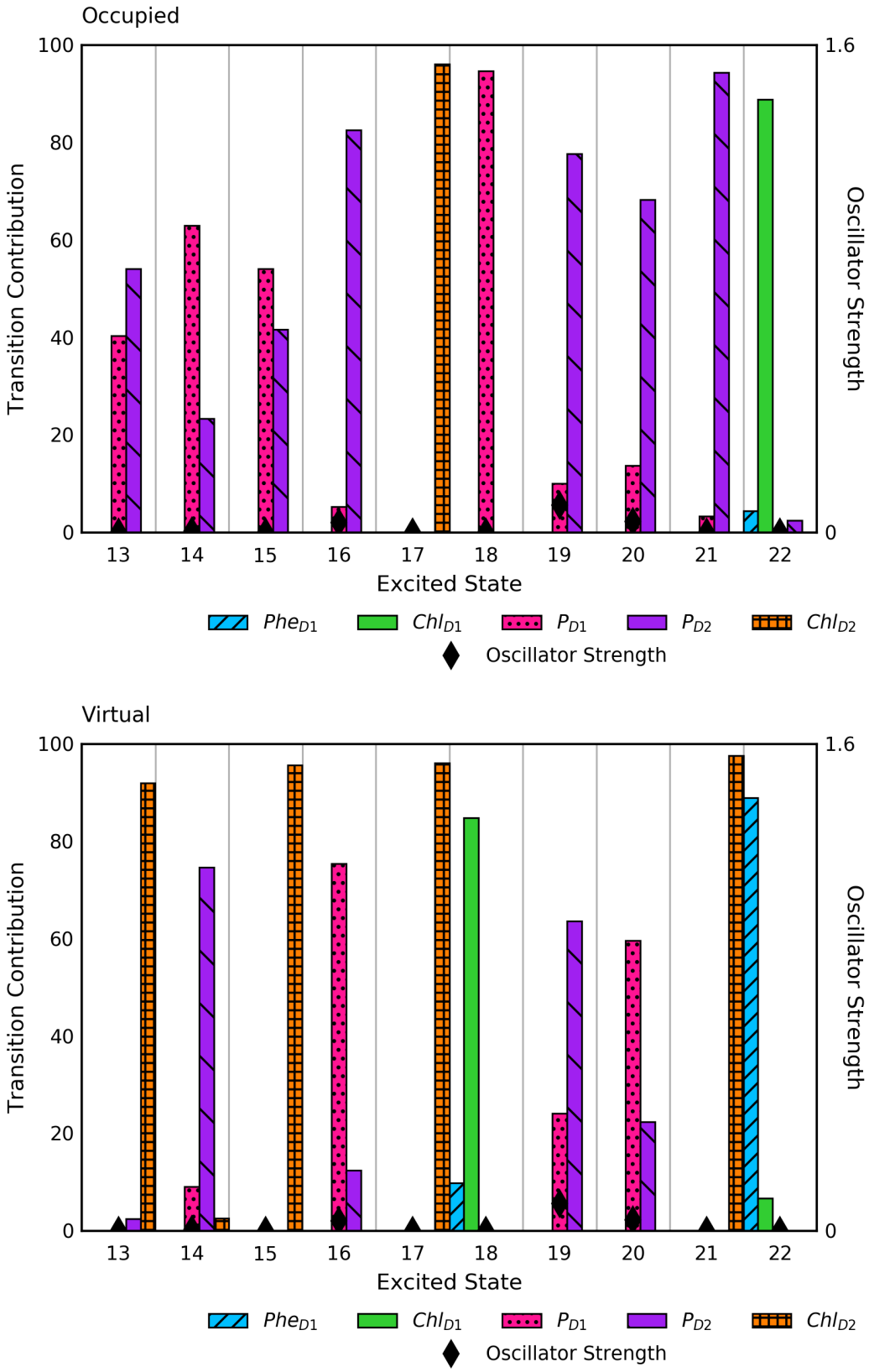


Figure A.33 : Model 3 CAM-b3LYP/6-31G** excited states 13-22, (bar chart, left y axis) % of state contributed to by each cofactor (occupied orbital occupancy analysis with MultiWfn from Mulliken method) and (black diamonds, right y axis) oscillator strength of each state. Cofactors coloured as in all Figures in this thesis. TOP – occupied orbitals, BOTTOM – virtual orbitals.

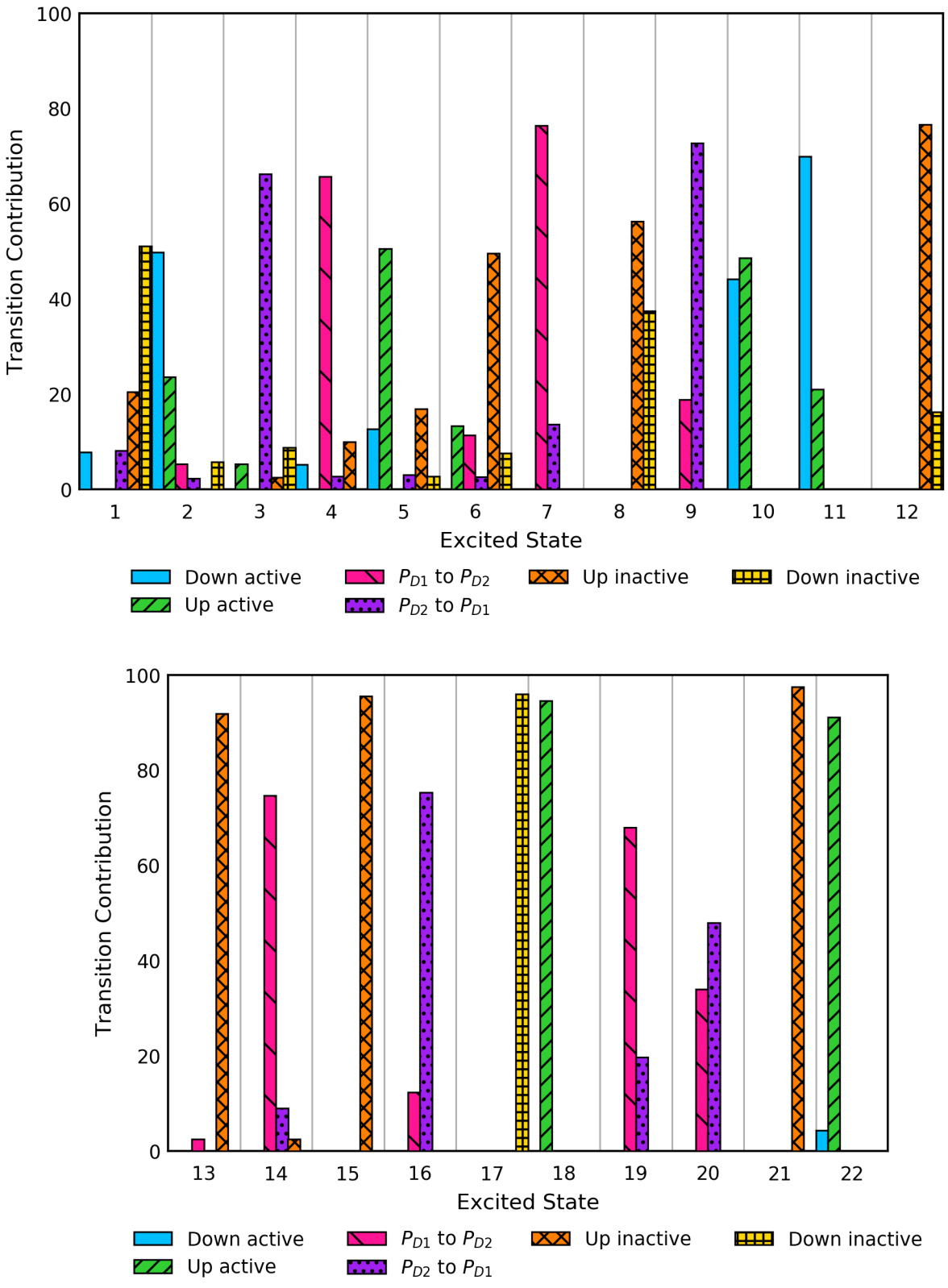


Figure A.34 : Contributions from each transition class to ES 1-6 for model 3 (CAM-b3LYP/ 6-31G**).

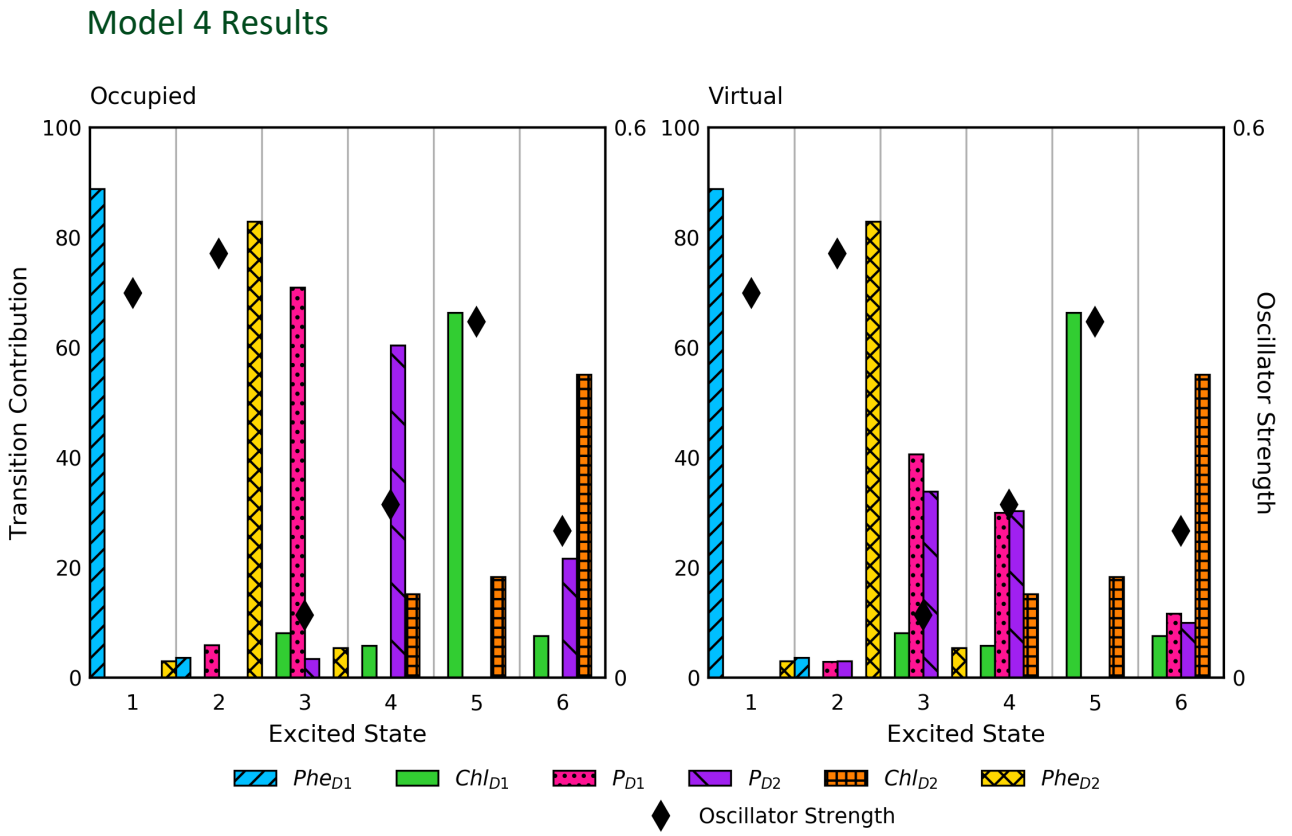


Figure A.35 : Model 4 CAM-b3LYP/6-31G** excited states 1-6, (bar chart, left y axis) % of state contributed to by each cofactor (occupied orbital occupancy analysis with MultiWfn from Mulliken method) and (black diamonds, right y axis) oscillator strength of each state. Cofactors coloured as in all Figures in this thesis. TOP – occupied orbitals, BOTTOM – virtual orbitals.

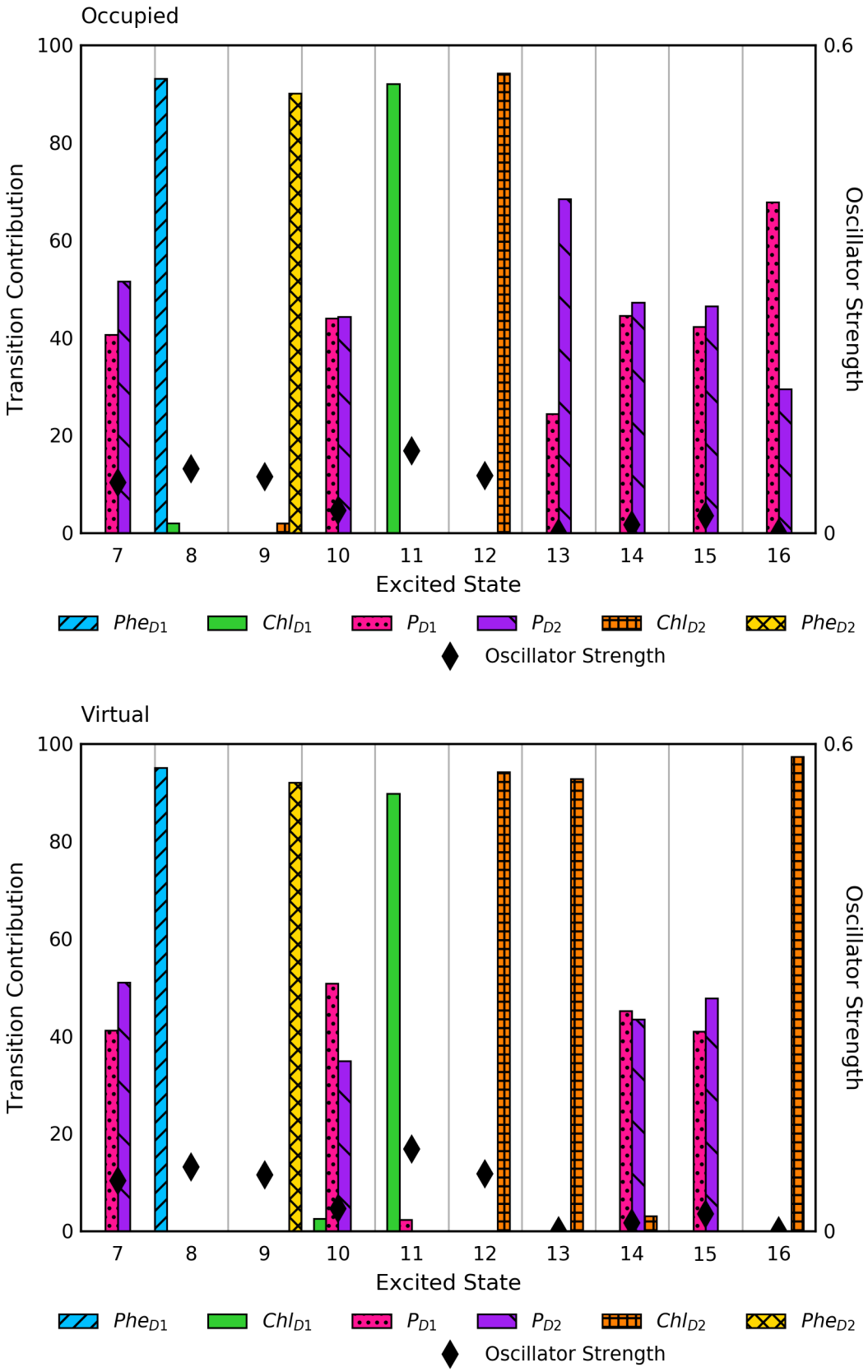


Figure A.36 : Model X CAM-b3LYP/6-31G** excited states 7-16, (bar chart, left y axis) % of state contributed to by each cofactor (occupied orbital occupancy analysis with MultiWfn from Mulliken method) and (black diamonds, right y axis) oscillator strength of each state. Cofactors coloured as in all Figures in this thesis. TOP – occupied orbitals, BOTTOM – virtual orbitals.

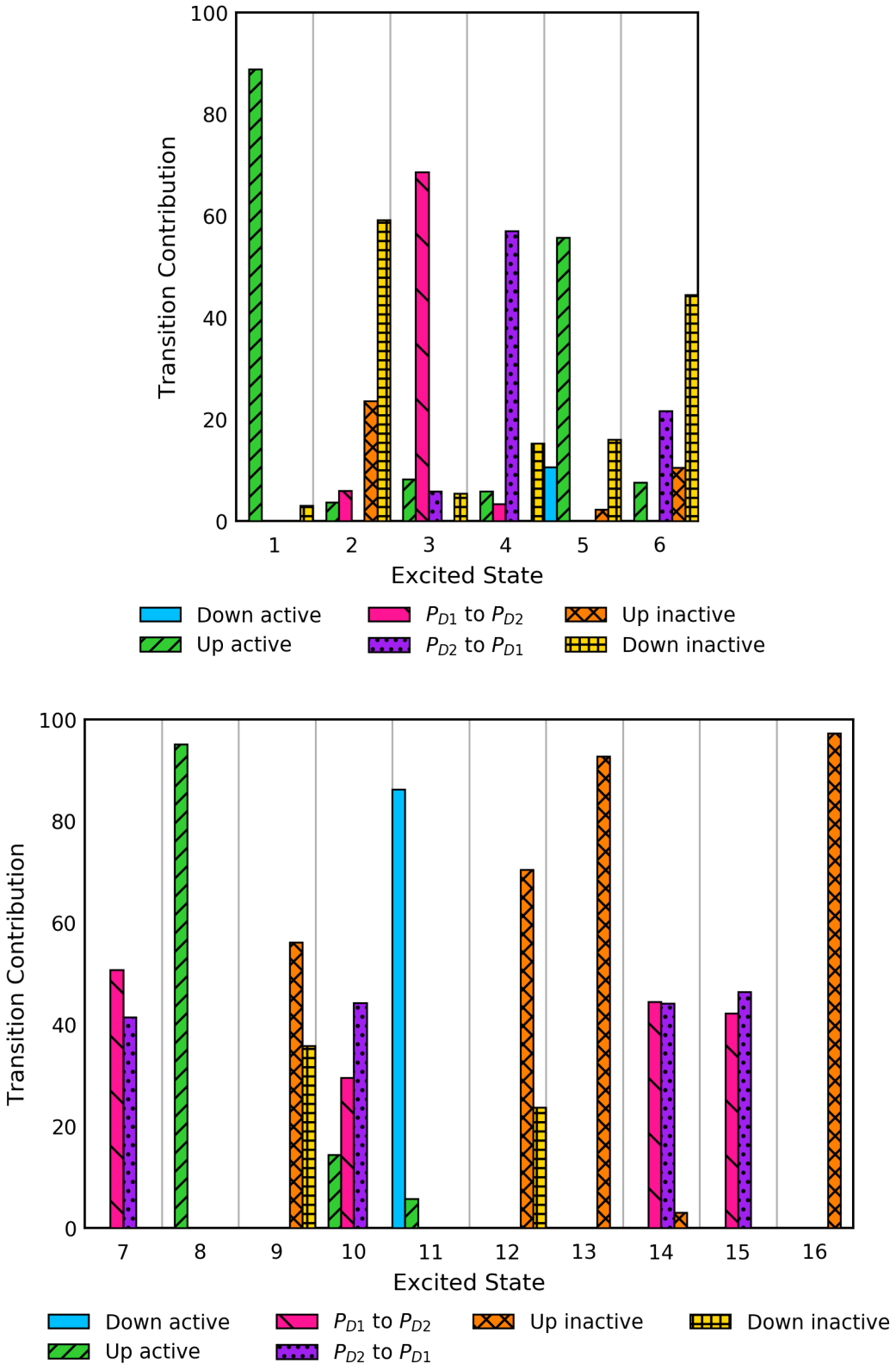


Figure A.37 : Contributions from each transition class to ES 1-6 for model 4 (CAM-b3LYP/ 6-31G**), TOP – ES 1-8, BOTTOM – ES 9-16.

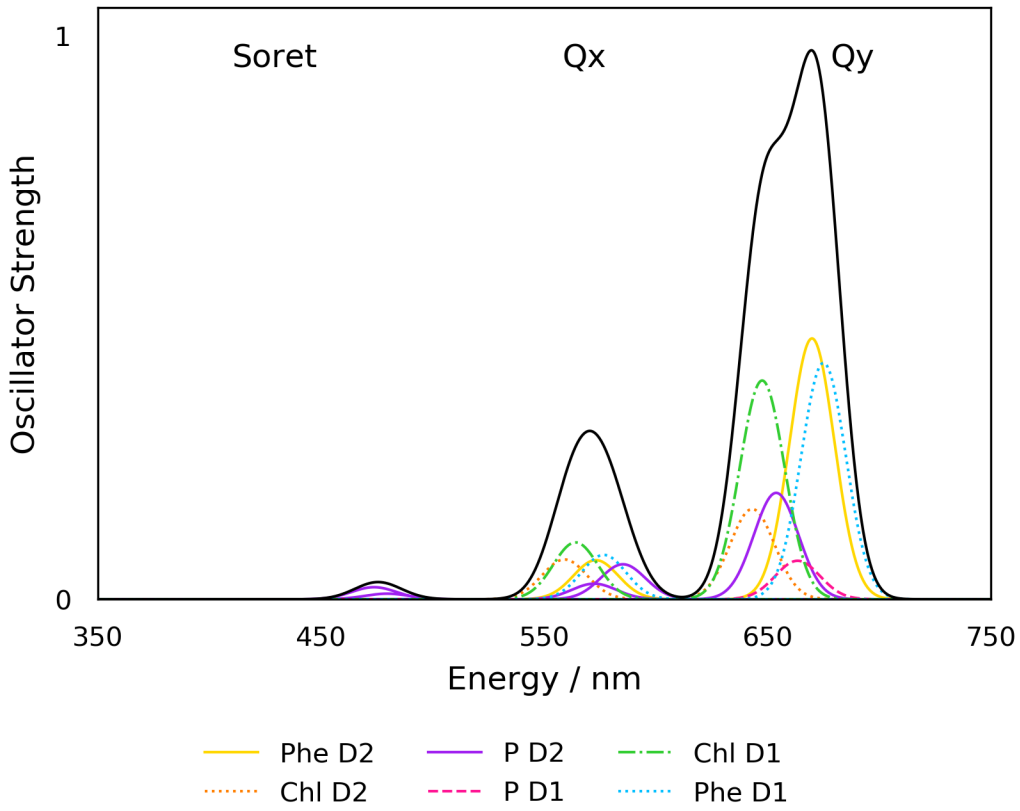


Figure A.38 : Calculated absorption spectrum for model 4 (CAM-b3LYP/ 6-31G**) ES 1-16, black line – full spectrum from sum of single ES broadened by gaussian functions, coloured lines – single ES broadened by gaussian functions coloured by occupied orbital cofactor: Phe_{D2} (yellow), Chl_{D2} (orange), P_{D2} (purple), P_{D1} (pink), Chl_{D1} (green) and Phe_{D1} (blue).

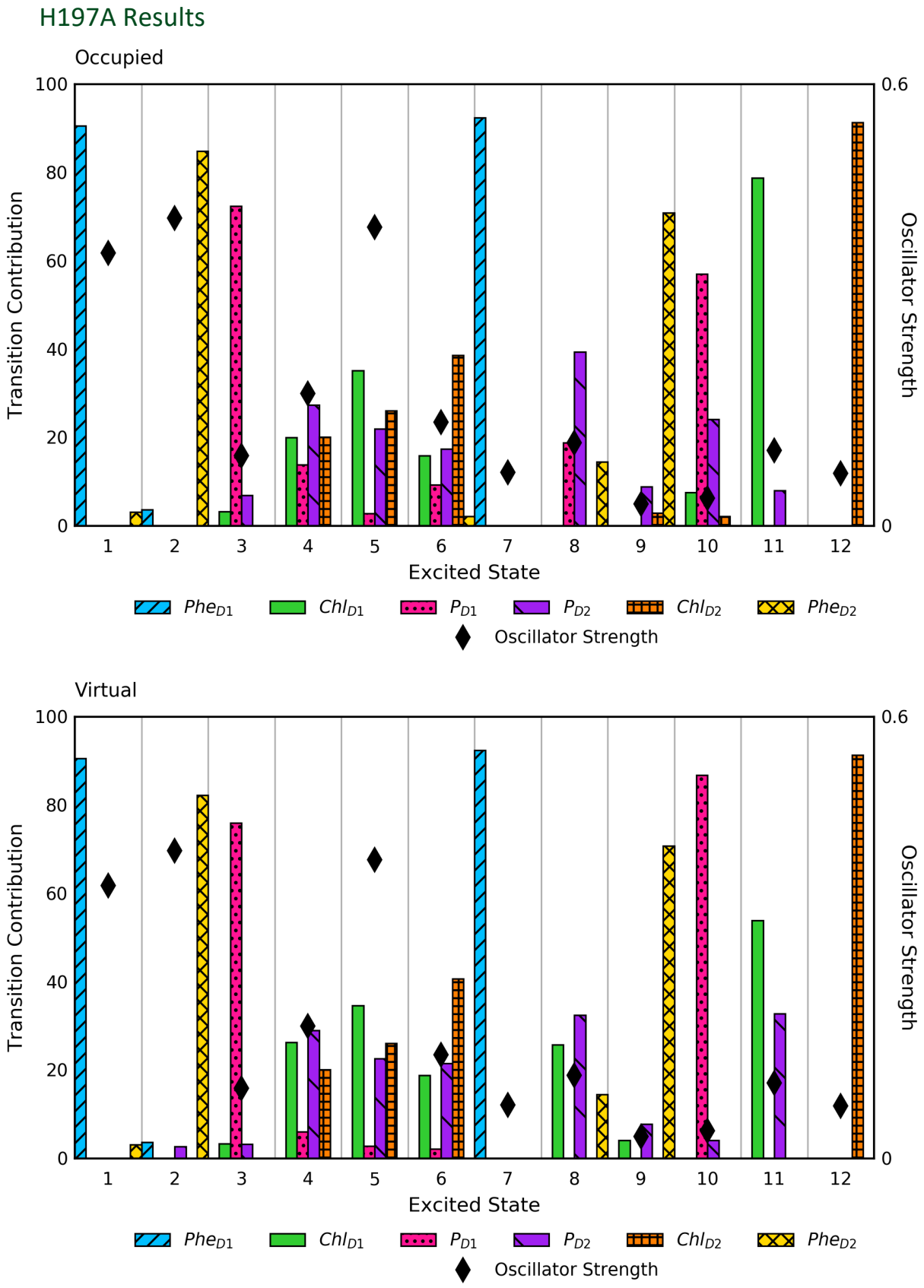


Figure A.39 : H197A with mutant water (ωB97X-D/6-31G**) excited states 1-12, (bar chart, left y axis) % of state contributed to by each cofactor (occupied orbital occupancy analysis with MultiWfn from Mulliken method) and (black diamonds, right y axis) oscillator strength of each state. Cofactors coloured as in all Figures in this thesis. TOP – occupied orbitals, BOTTOM – virtual orbitals.

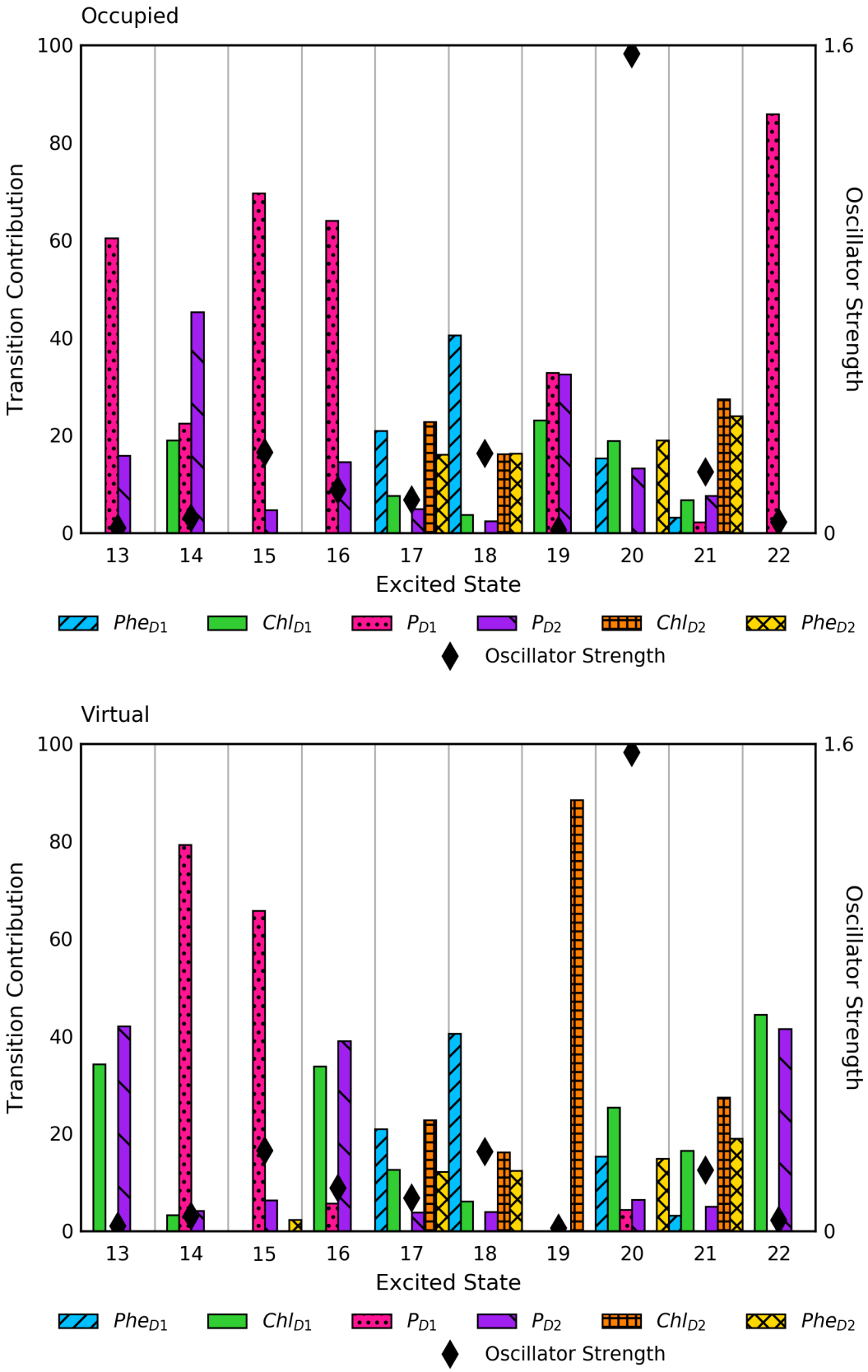
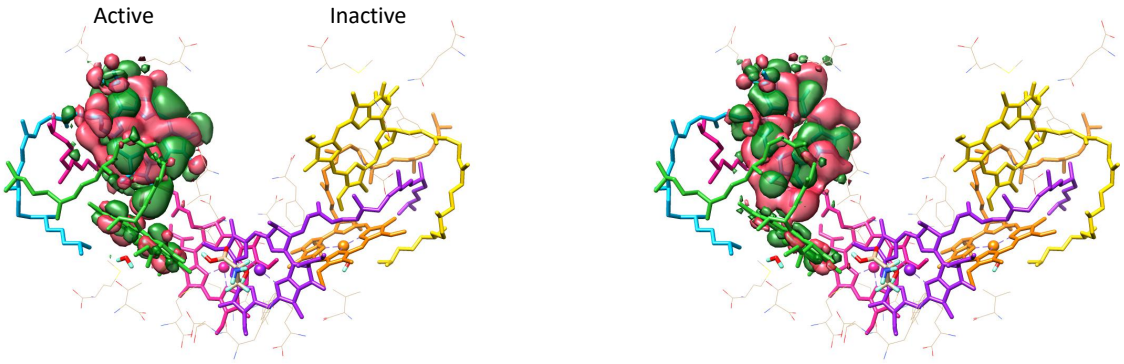
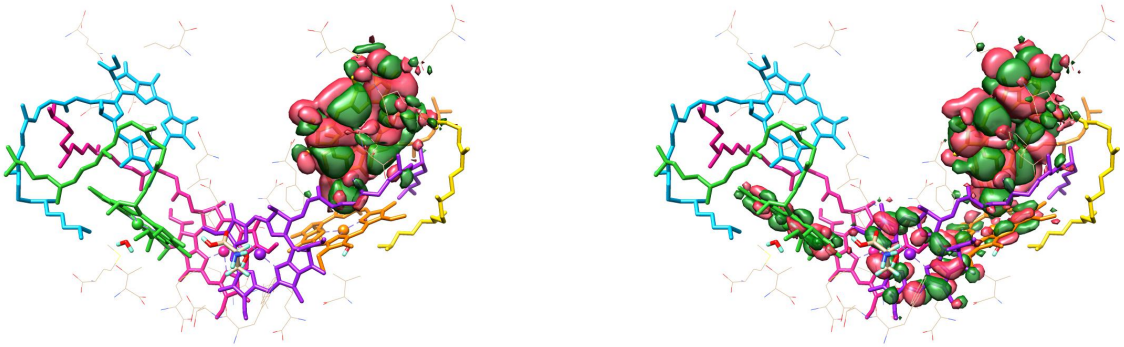


Figure A.40 : H197A with mutant water (ωB97X-D/6-31G**) excited states 13-22, (bar chart, left y axis) % of state contributed to by each cofactor (occupied orbital occupancy analysis with MultiWfn from Mulliken method) and (black diamonds, right y axis) oscillator strength of each state. Cofactors coloured as in all Figures in this thesis. TOP – occupied orbitals, BOTTOM – virtual orbitals.

Up active (Chl D1 to Phe D1): 2296 → 2301
State 1: 64.99%
State 2: 3.68%



Down inactive (Phe D2 to P D2): 2299 → 2305
State 1: 3.09%
State 2: 56.19%



P D2 to P D1: 2300 → 2306
State 3: 67.89%
State 4: 3.67%
State 5: 2.81%
State 6: 2.15%

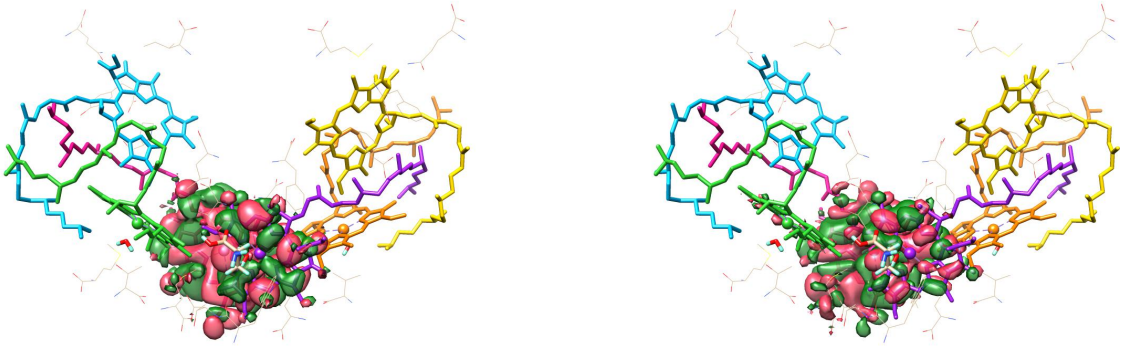
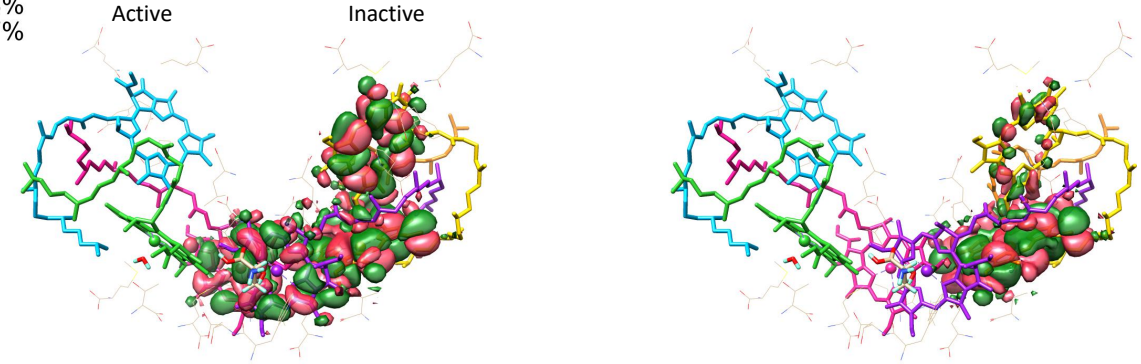


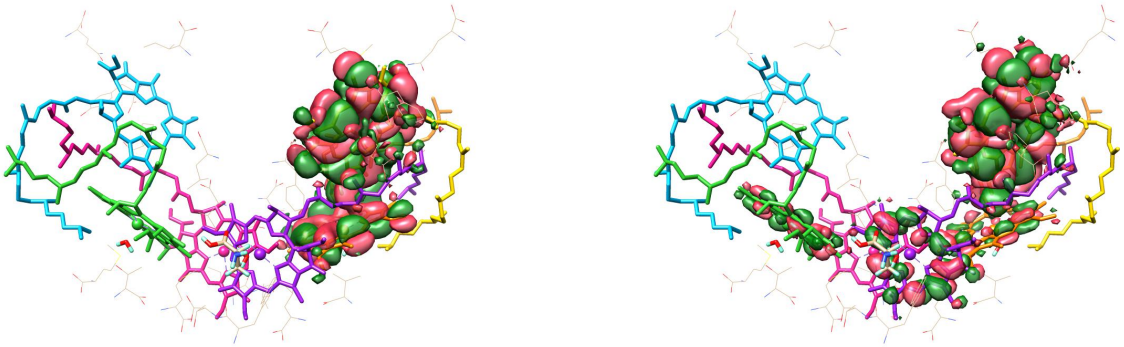
Figure A.41 : MO diagrams exemplifying all transition classes for H197A ωB97X-D/6-31G** including dominant transitions contributing to ES 1-3 and 5-6, LEFT COLUMN - Occupied MO, RIGHT COLUMN – Virtual MO (Page 1)

Down inactive (Phe D2 to Chl D2): 2295 → 2302
State 4: 17.50%
State 5: 20.43%
State 6: 29.97%

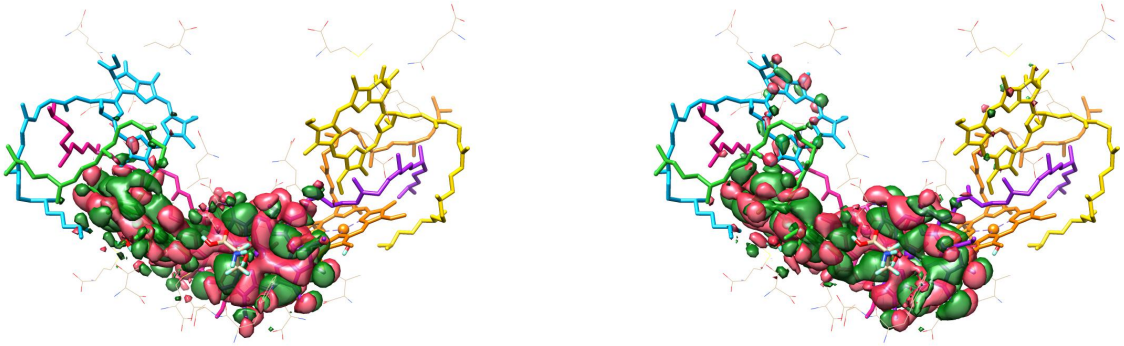
Active Inactive



Up inactive (Chl D2 to Phe D2): 2293 → 2305
State 2: 15.21%



P D1 to P D2: 2297 → 2303
State 5: 18.65%
State 6: 15.82%



P D1 to P D2: 2298 → 2304
State 4: 3.80%
State 5: 12.70%
State 6: 17.38%

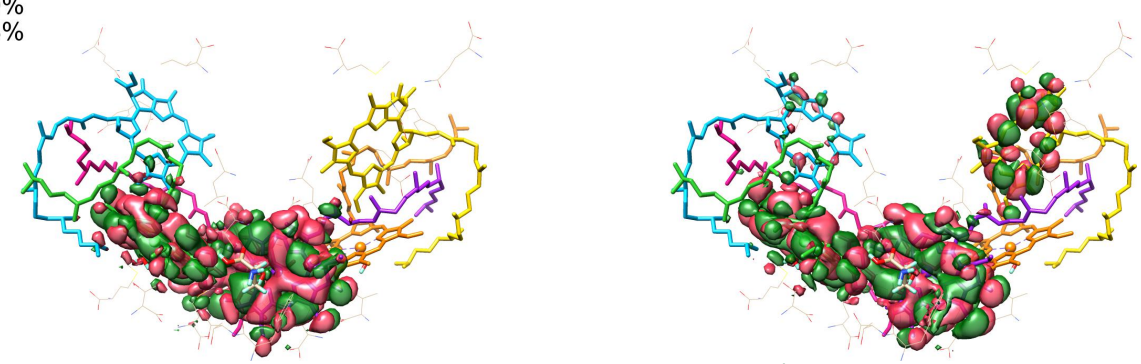


Figure A.41 : MO diagrams exemplifying all transition classes for H197A ωB97X-D/6-31G** including dominant transitions contributing to ES 1-3 and 5-6, LEFT COLUMN - Occupied MO, RIGHT COLUMN – Virtual MO (Page 2)

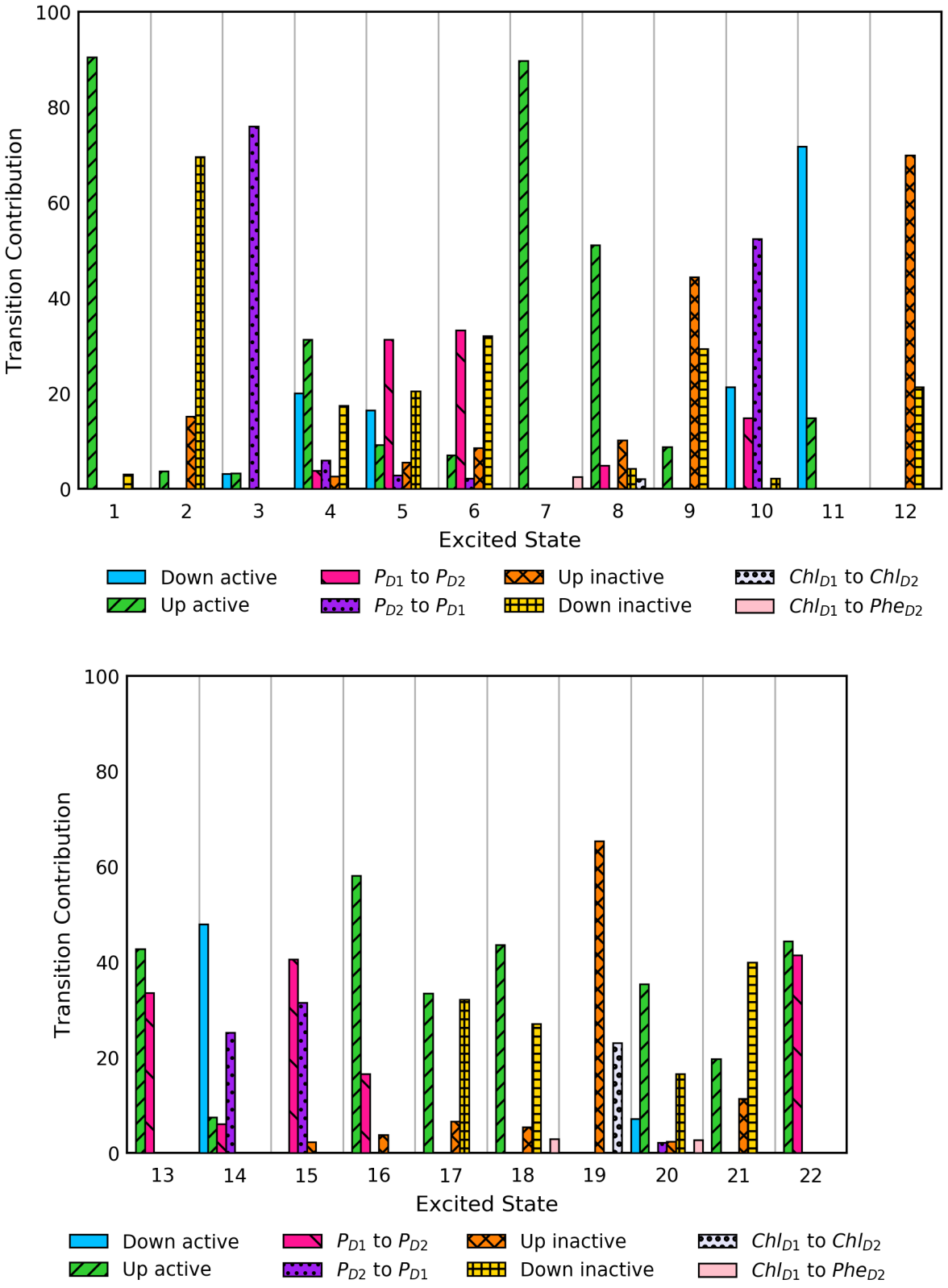


Figure A.42 : Contributions from each transition class for H197A (ωB97X-D/ 6-31G**), TOP : ES 1-12 (Qy and Qx regions), BOTTOM : ES 13-22 (Soret region)

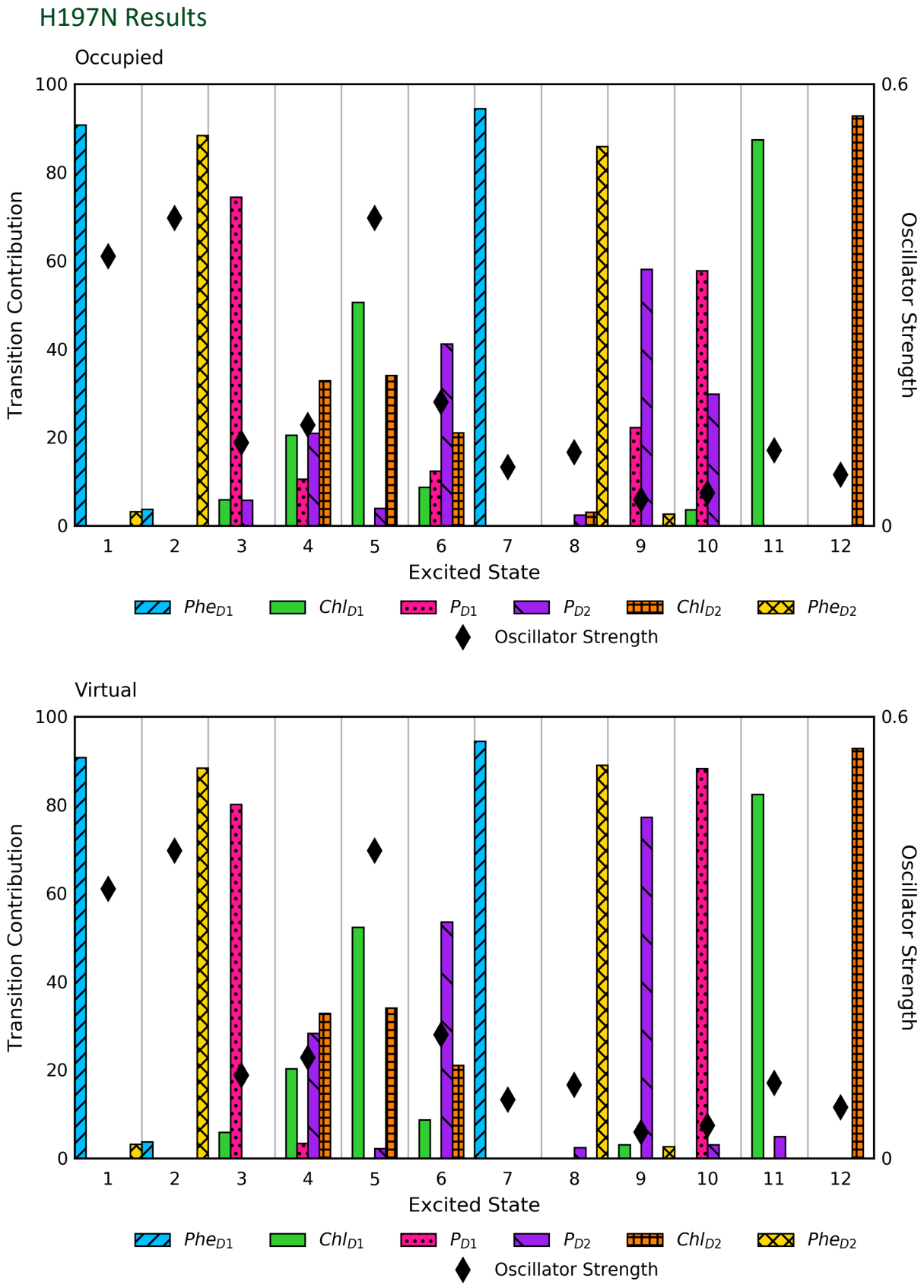


Figure A.43 : H197N with mutant water (ωB97X-D/6-31G**) excited states 1-12, (bar chart, left y axis) % of state contributed to by each cofactor (occupied orbital occupancy analysis with MultiWfn from Mulliken method) and (black diamonds, right y axis) oscillator strength of each state. Cofactors coloured as in all Figures in this thesis. TOP – occupied orbitals, BOTTOM – virtual orbitals.

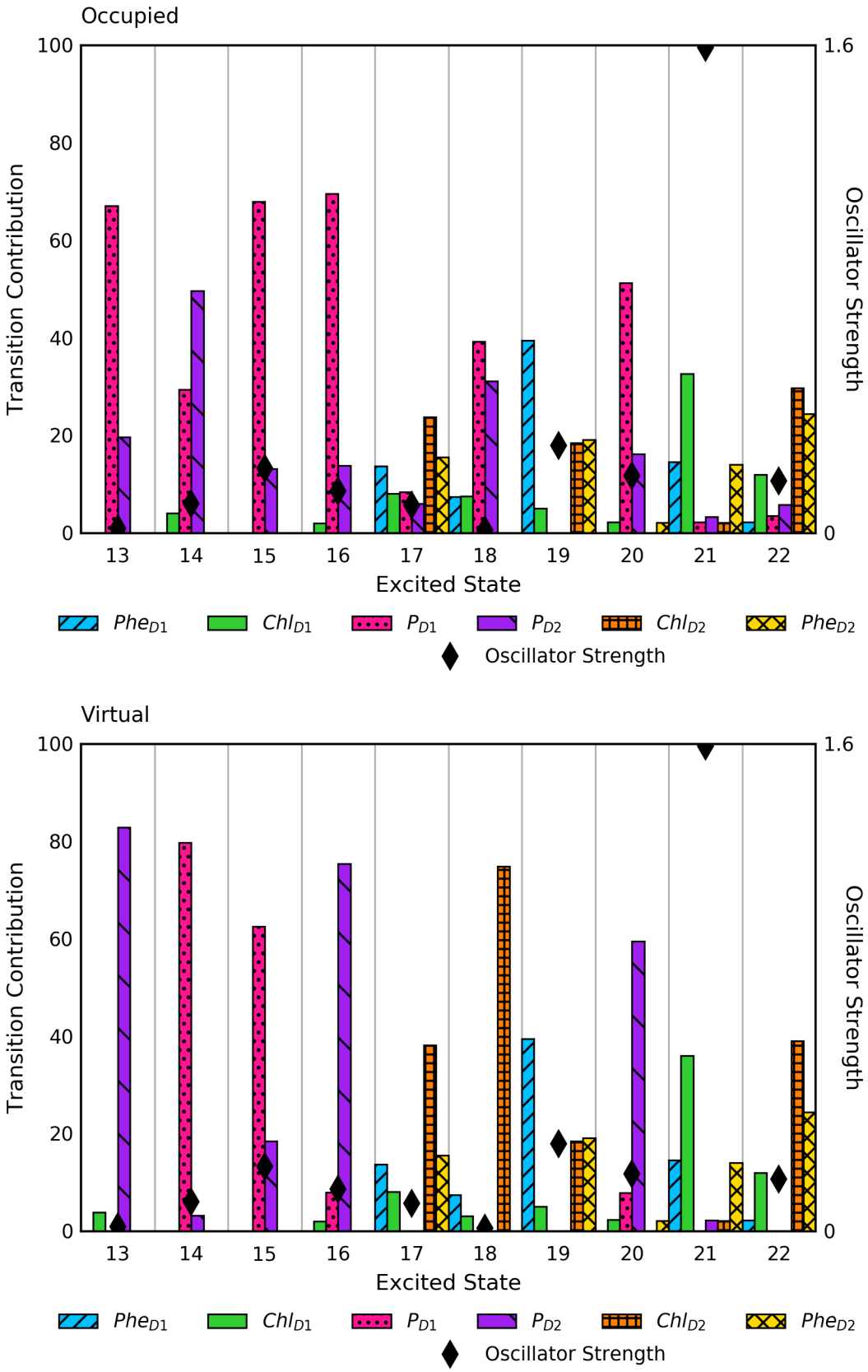
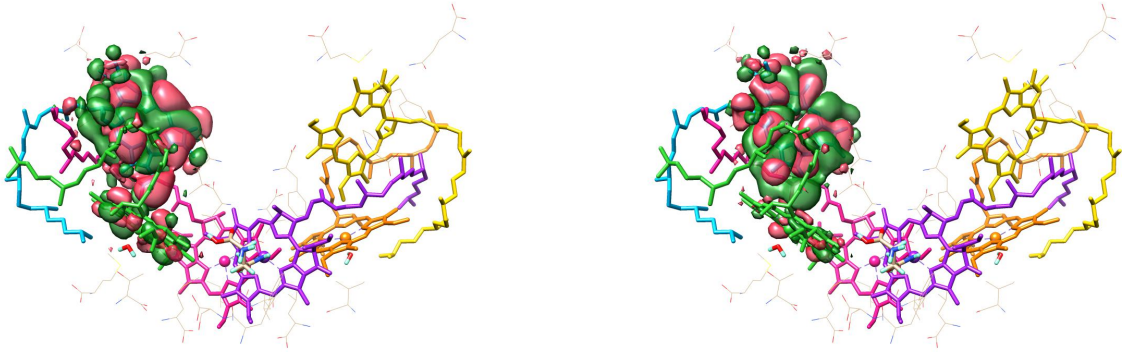
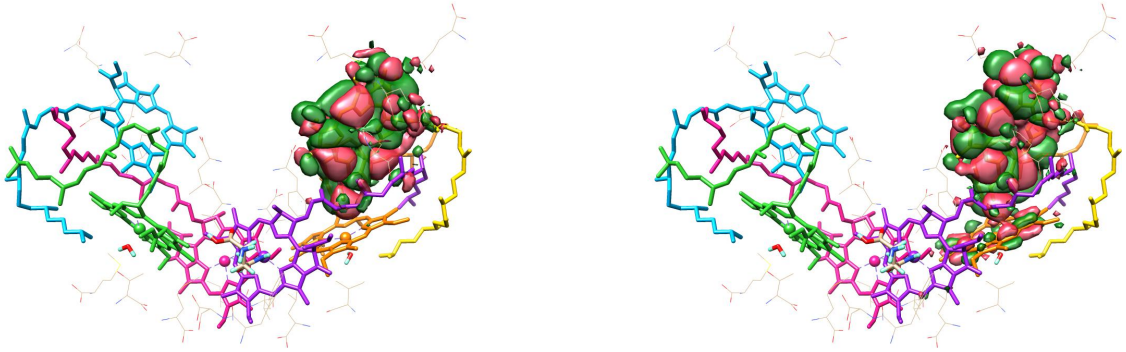


Figure A.44 : H197N with mutant water (ωB97X-D/6-31G**) excited states 12-22, (bar chart, left y axis) % of state contributed to by each cofactor (occupied orbital occupancy analysis with MultiWfn from Mulliken method) and (black diamonds, right y axis) oscillator strength of each state. Cofactors coloured as in all Figures in this thesis. TOP – occupied orbitals, BOTTOM – virtual orbitals.

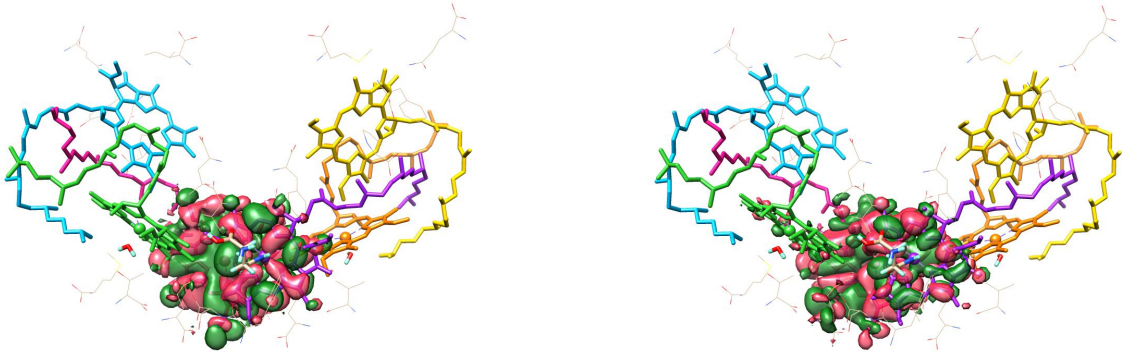
Up active (Chl D1 to Phe D1): 2307 → 2312
State 1: 65.18%
State 2: 3.72%



Down inactive (Phe D2 to Chl D2): 2310 → 2314
State 1: 3.17%
State 2: 57.50%



P D2 to P D1: 2311 → 2317
State 3: 69.01%
State 4: 3.45%



Down inactive (Phe D2 to Chl D2): 2305 → 2313
State 4: 28.64%
State 5: 27.20%
State 6: 17.59%

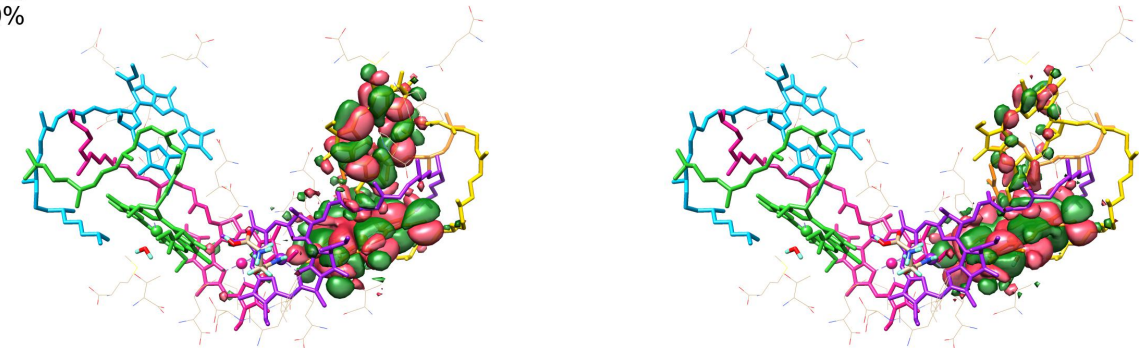
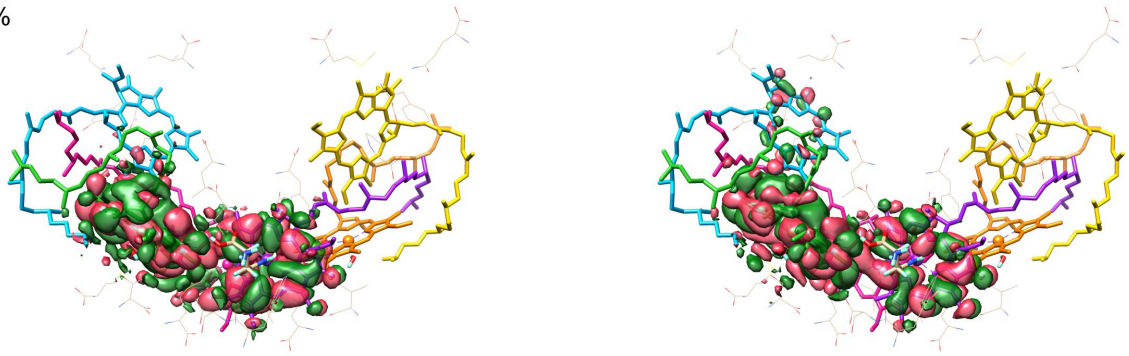
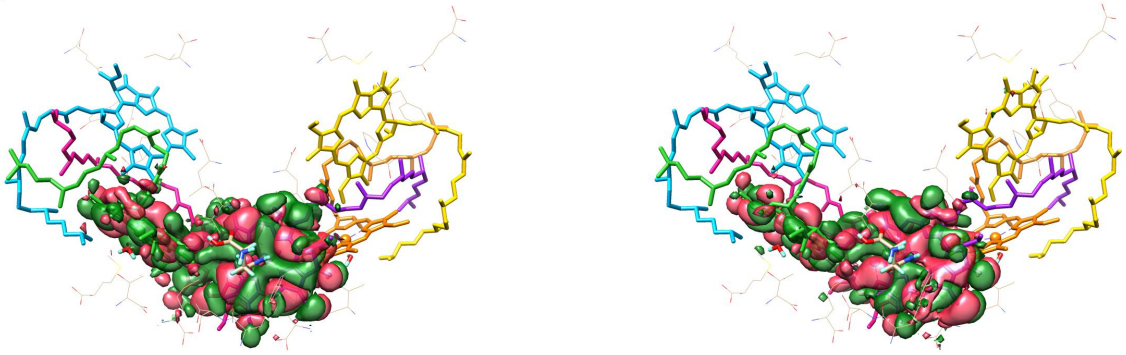


Figure A.45 : MO diagrams exemplifying all transition classes for H197N ωB97X-D/6-31G** including dominant transitions contributing to ES 1-6, LEFT COLUMN - Occupied MO, RIGHT COLUMN – Virtual MO (Page 1)

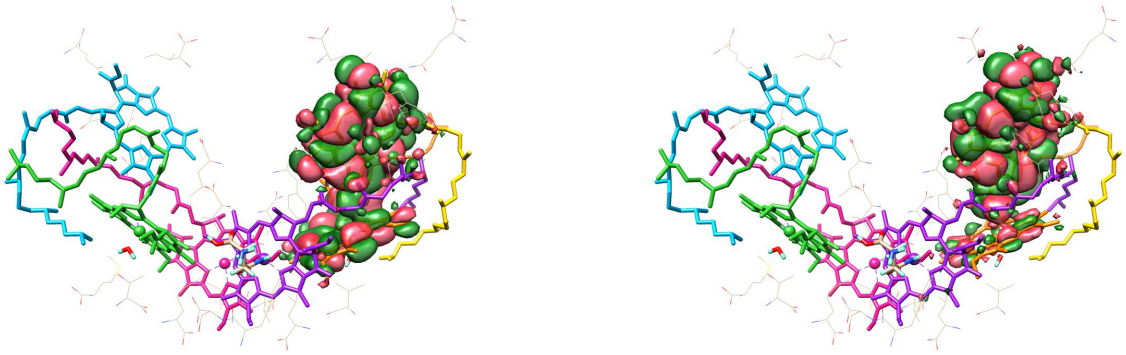
Up active (P D1 to Chl D1): 2309 → 2316
State 3: 5.95%
State 4: 11.73%
State 5: 38.76%
State 6: 8.77%



P D1 to P D2: 2308 → 2315
State 4: 14.83%
State 6: 36.23%



Up inactive (Chl D2 to Phe D2): 2303 → 2314
State 2: 15.83%



Down active (Chl D1 to P D2): 2304 → 2322
State 4: 2.45%
State 5: 6.65%

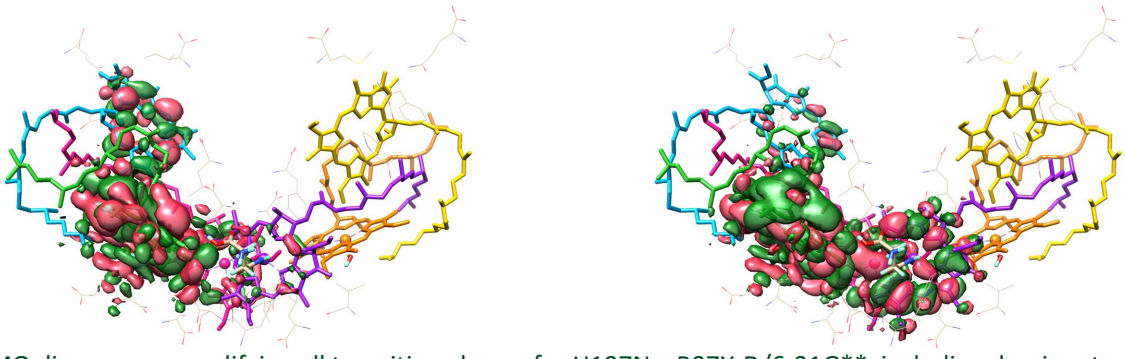


Figure A.45 : MO diagrams exemplifying all transition classes for H197N ωB97X-D/6-31G** including dominant transitions contributing to ES 1-6, LEFT COLUMN - Occupied MO, RIGHT COLUMN – Virtual MO (Page 1)

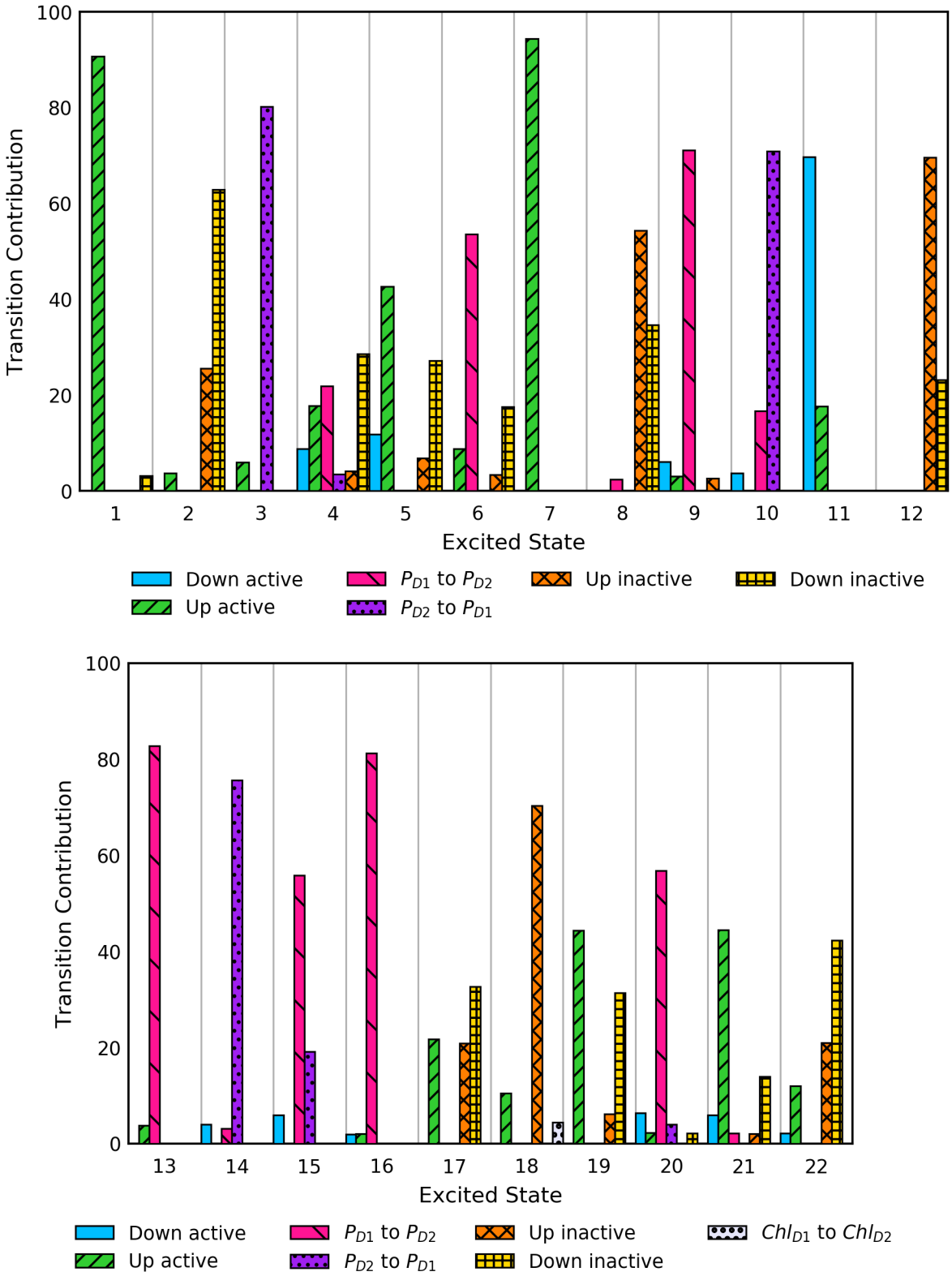


Figure A.46 : Contributions from each transition class for H197N (ωB97X-D/ 6-31G**), TOP : ES 1-12 (Qy and Qx regions), BOTTOM : ES 13-22 (Soret region)

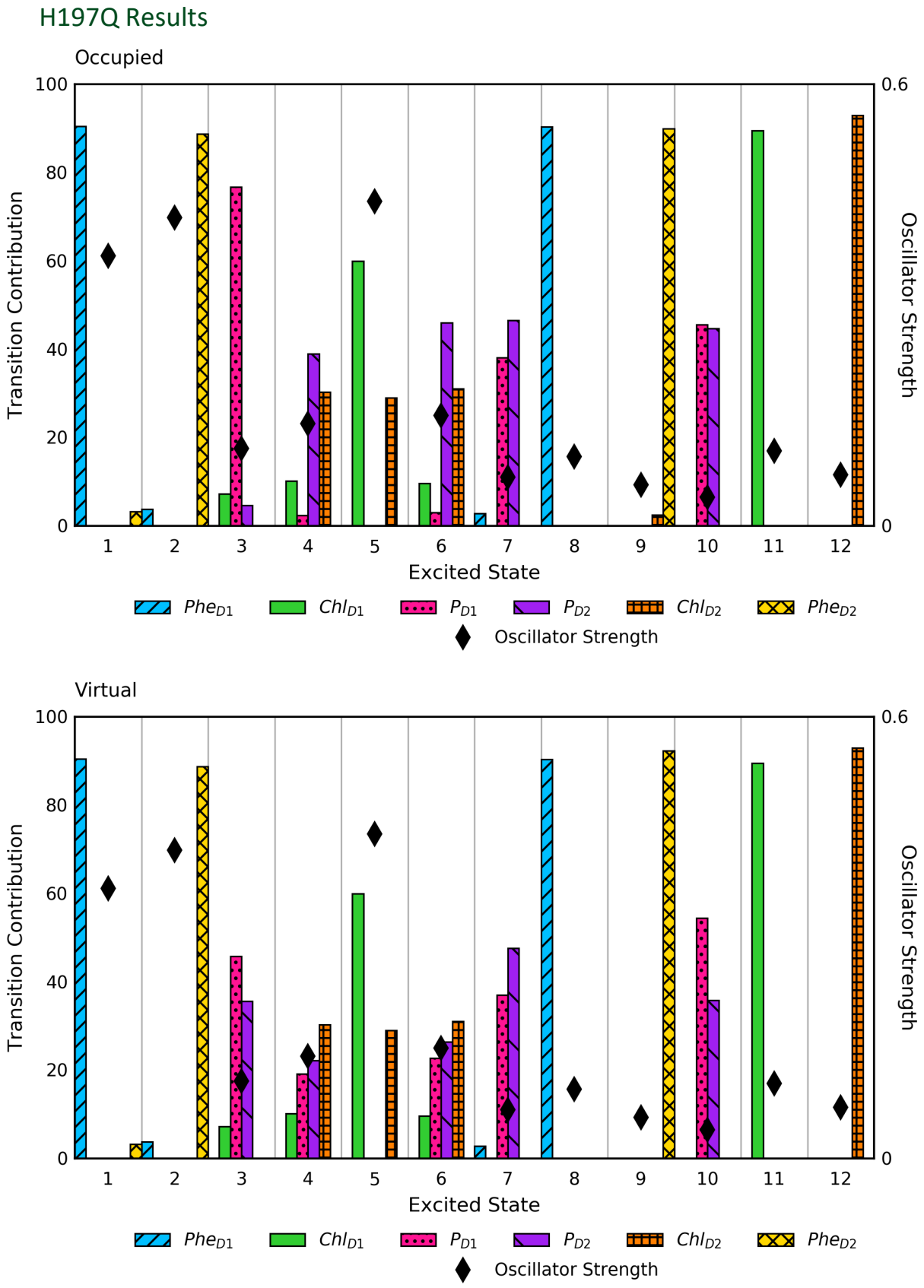


Figure A.47 : H197Q (ωB97X-D/6-31G**) excited states 1-12, (bar chart, left y axis) % of state contributed to by each cofactor (occupied orbital occupancy analysis with MultiWfn from Mulliken method) and (black diamonds, right y axis) oscillator strength of each state. Cofactors coloured as in all Figures in this thesis. TOP – occupied orbitals, BOTTOM – virtual orbitals.

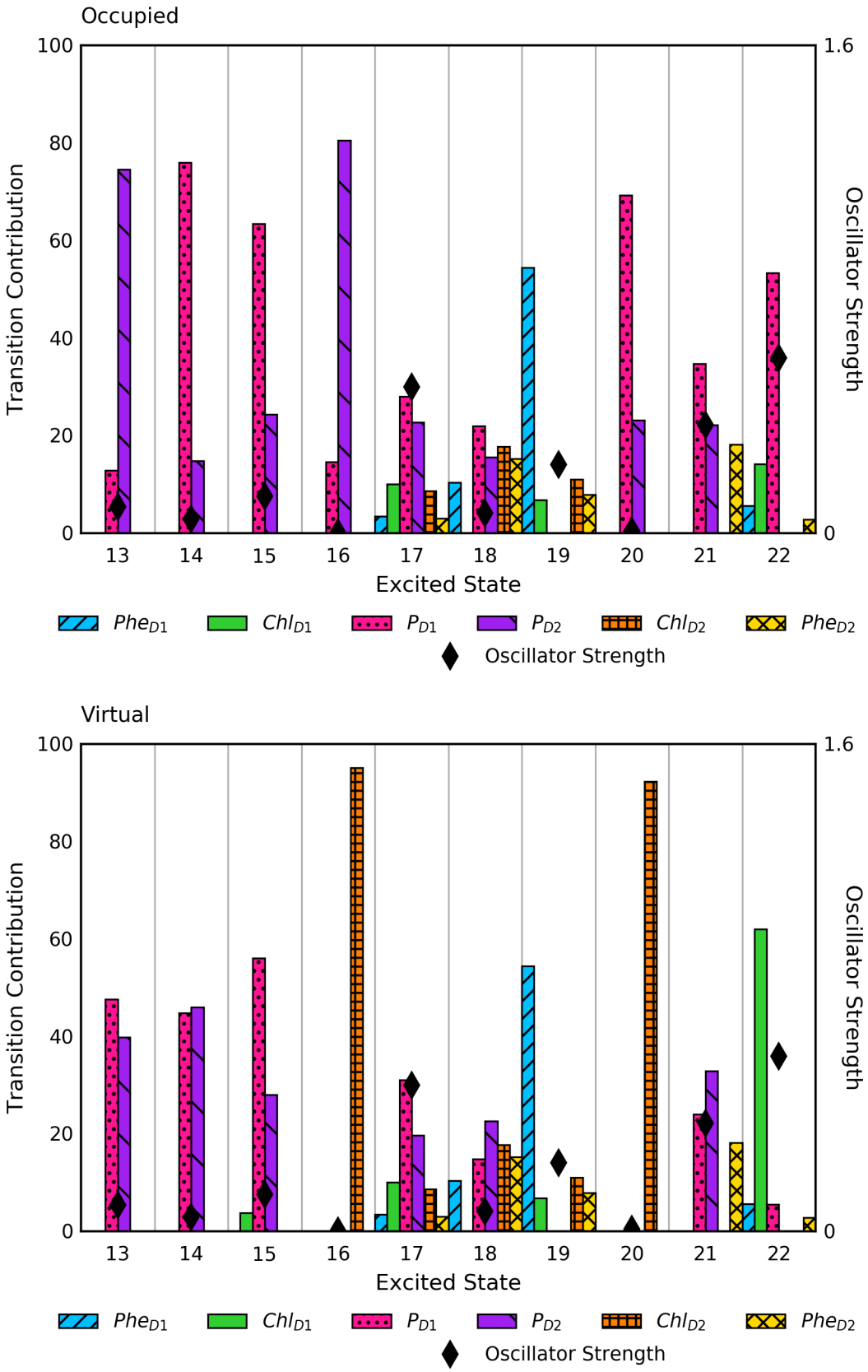
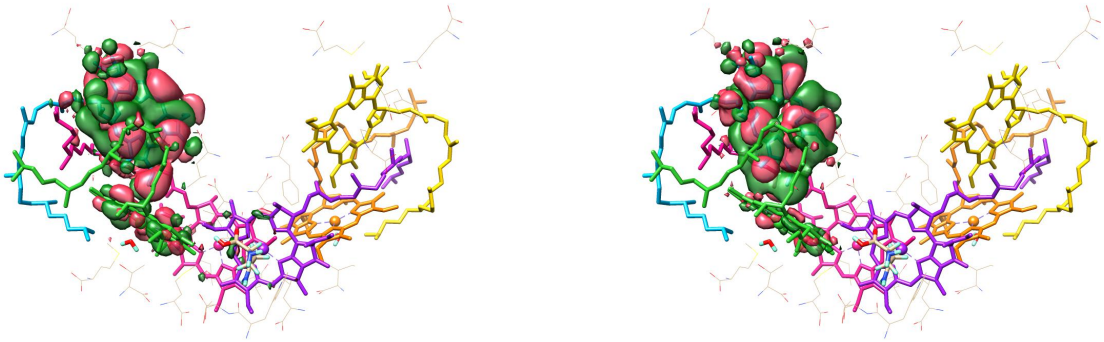
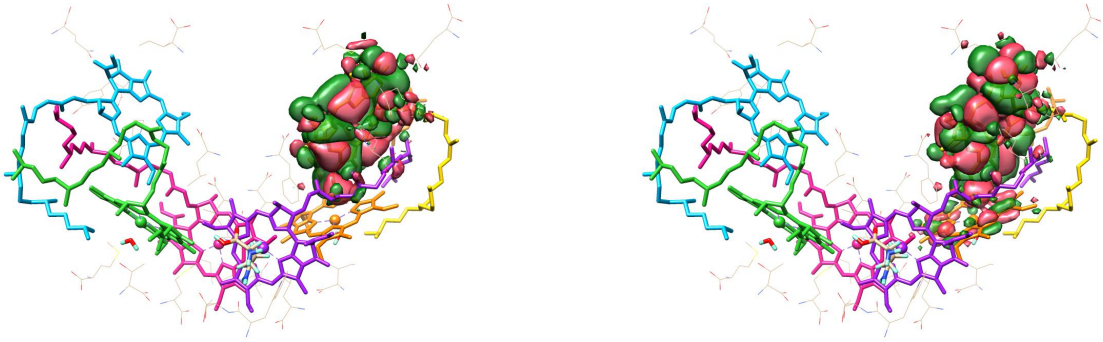


Figure A.48 : H197Q (ωB97X-D/6-31G**) excited states 13-22, (bar chart, left y axis) % of state contributed to by each cofactor (occupied orbital occupancy analysis with MultiWfn from Mulliken method) and (black diamonds, right y axis) oscillator strength of each state. Cofactors coloured as in all Figures in this thesis. TOP – occupied orbitals, BOTTOM – virtual orbitals.

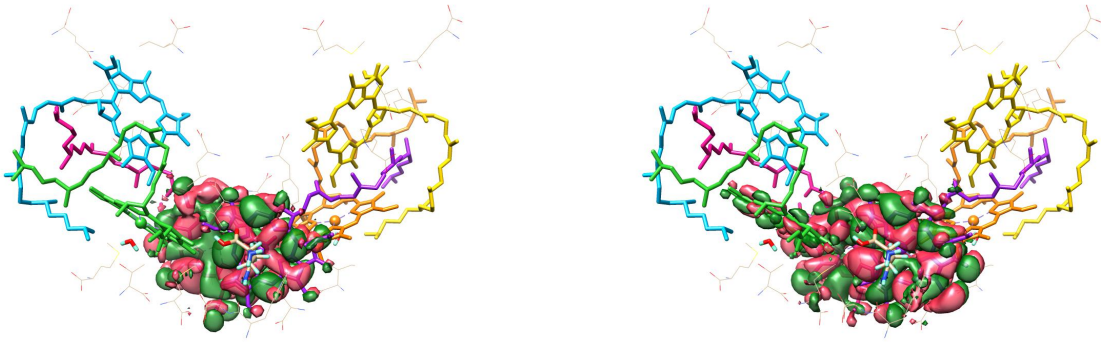
Up active (Chl D1 to Phe D1): 2306 → 2311
State 1: 65.02%
State 2: 3.77%



Down inactive (Phe D2 to Chl D2): 2308 → 2313
State 1: 3.23%
State 2: 57.59%



P D1 to P D2: 2310 → 2315
State 3: 35.14%
State 4: 2.31%



Down inactive (Phe D2 to Chl D2): 2304 → 2312
State 4: 26.45%
State 5: 23.06%
State 6: 24.31%

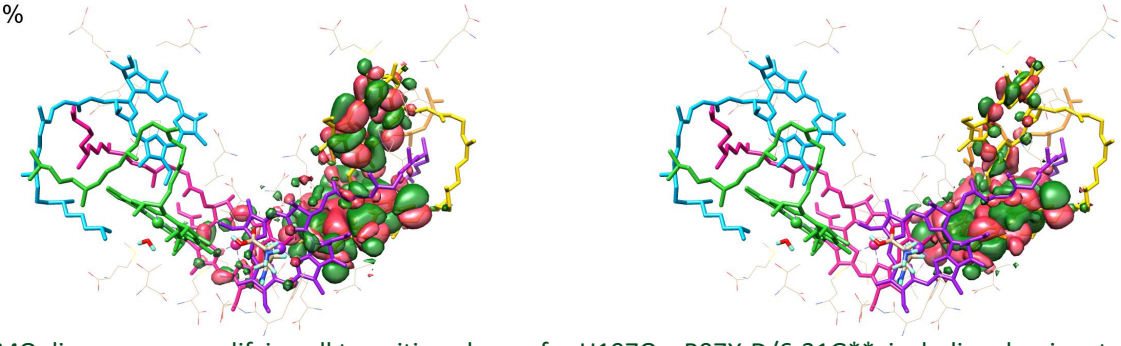
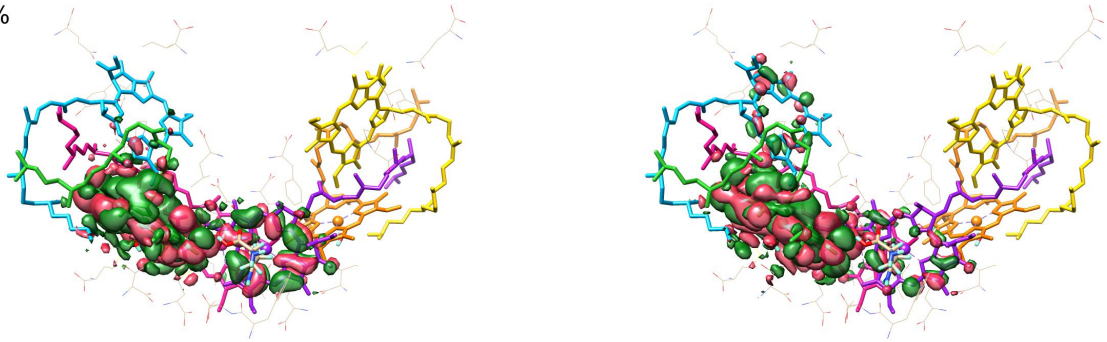
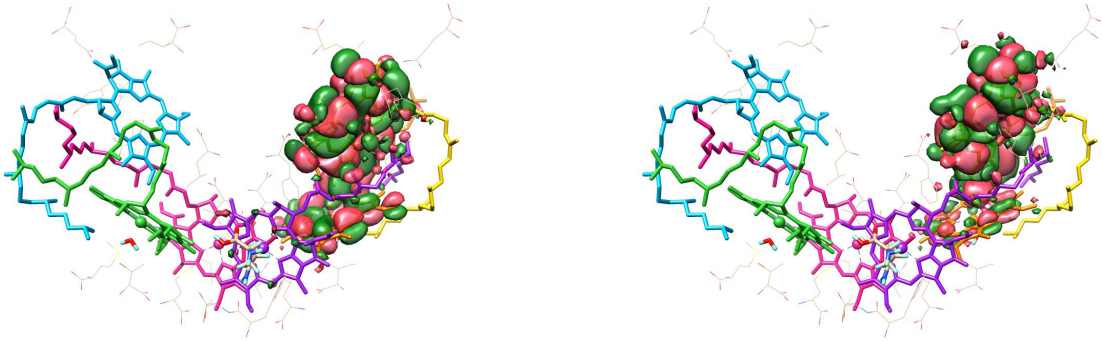


Figure A.49 : MO diagrams exemplifying all transition classes for H197Q ωB97X-D/6-31G** including dominant transitions contributing to ES 1-6, LEFT COLUMN - Occupied MO, RIGHT COLUMN – Virtual MO (PAGE 1).

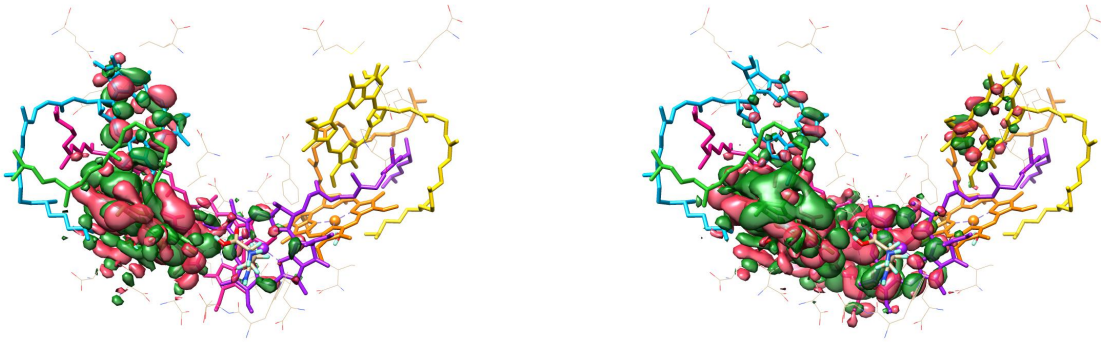
P D2 to P D1: 2307 → 2314
State 3: 7.23%
State 4: 10.16%
State 5: 49.26%
State 6: 9.58%



Up inactive (Chl D2 to Phe D2): 2302 → 2313
State 2: 15.92%



Down active (Chl D1 to P D1): 2301 → 2321
State 5: 7.01%



P D2 to P D1: 2309 → 2315
State 4: 16.76%
State 6: 19.96%

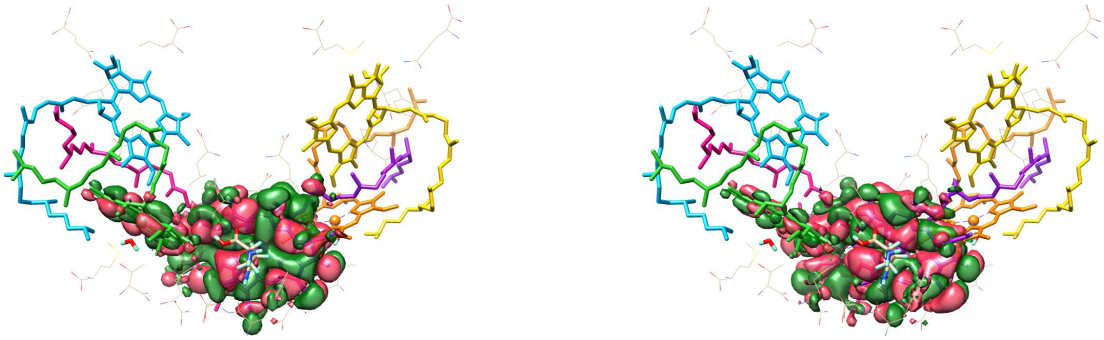


Figure A.49 : MO diagrams exemplifying all transition classes for H197Q ωB97X-D/6-31G** including dominant transitions contributing to ES 1-6, LEFT COLUMN - Occupied MO, RIGHT COLUMN – Virtual MO (PAGE 2).

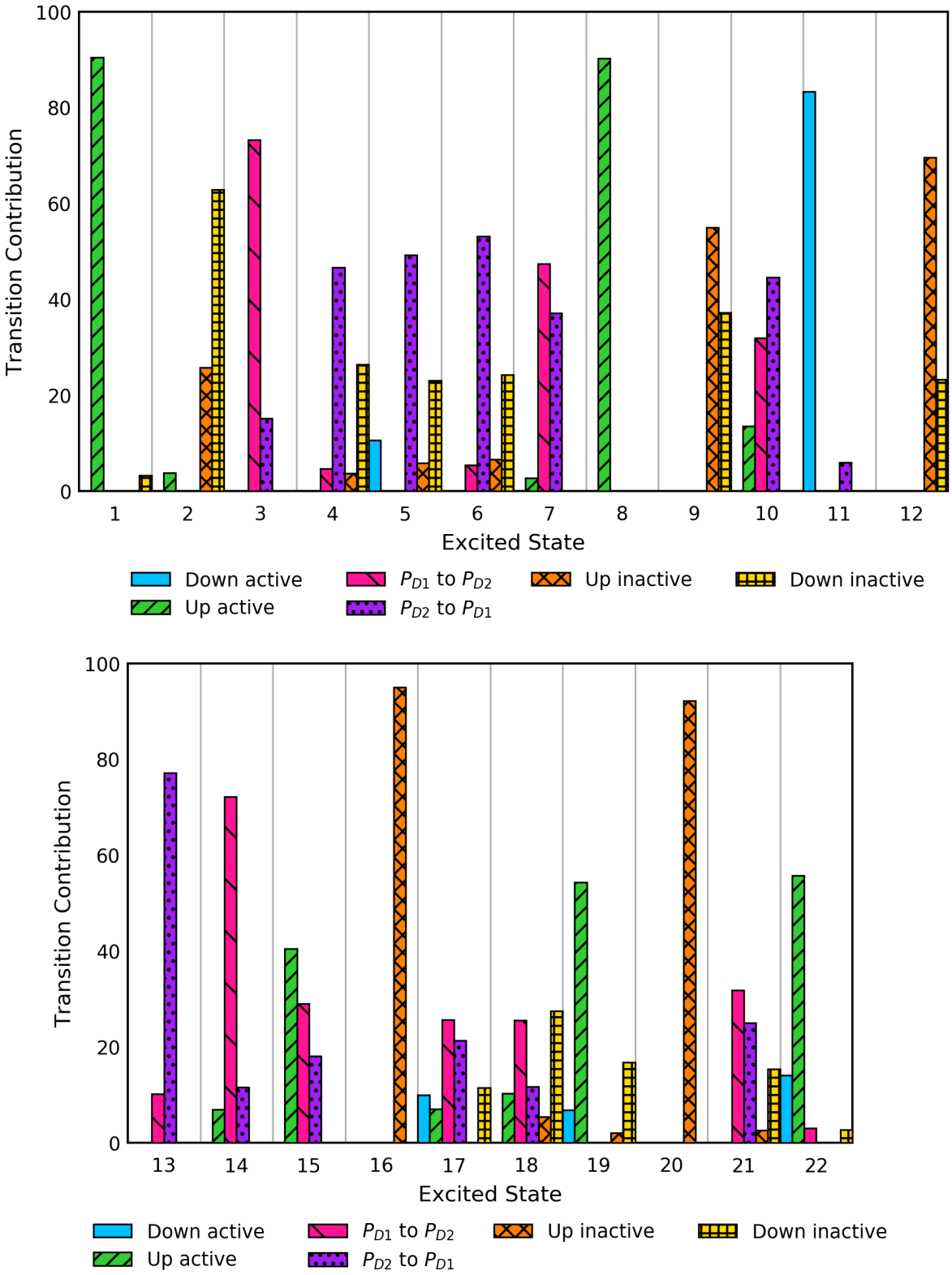


Figure A.50 : Contributions from each transition class for H197Q (ωB97X-D/ 6-31G**), TOP : ES 1-12 (Qy and Qx regions), BOTTOM : ES 13-22 (Soret region).

H198A Results

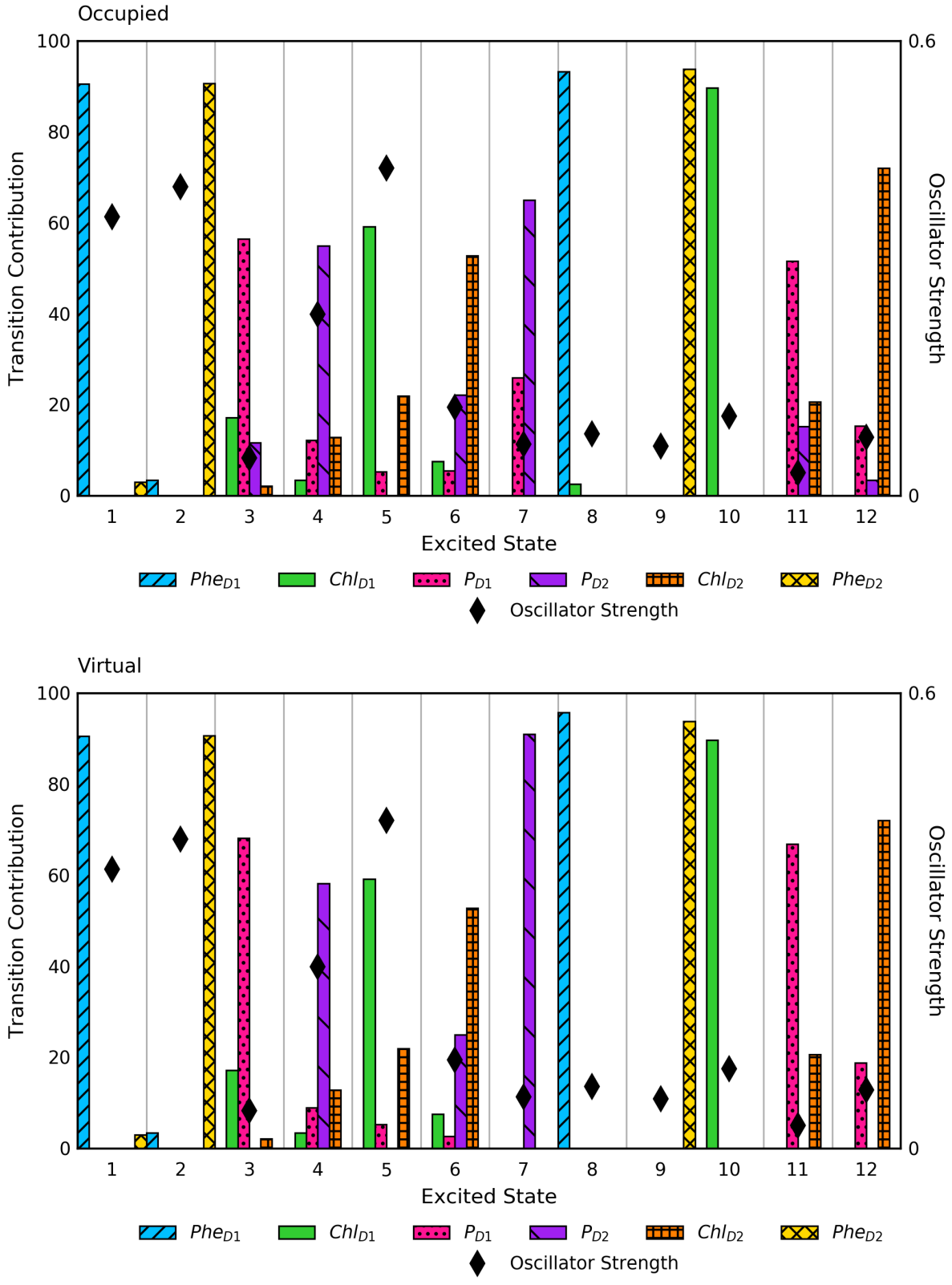


Figure A.51 : H198A with mutant water (ωB97X-D/6-31G**) excited states 1-12, (bar chart, left y axis) % of state contributed to by each cofactor (occupied orbital occupancy analysis with MultiWfn from Mulliken method) and (black diamonds, right y axis) oscillator strength of each state. Cofactors coloured as in all Figures in this thesis. TOP – occupied orbitals, BOTTOM – virtual orbitals.

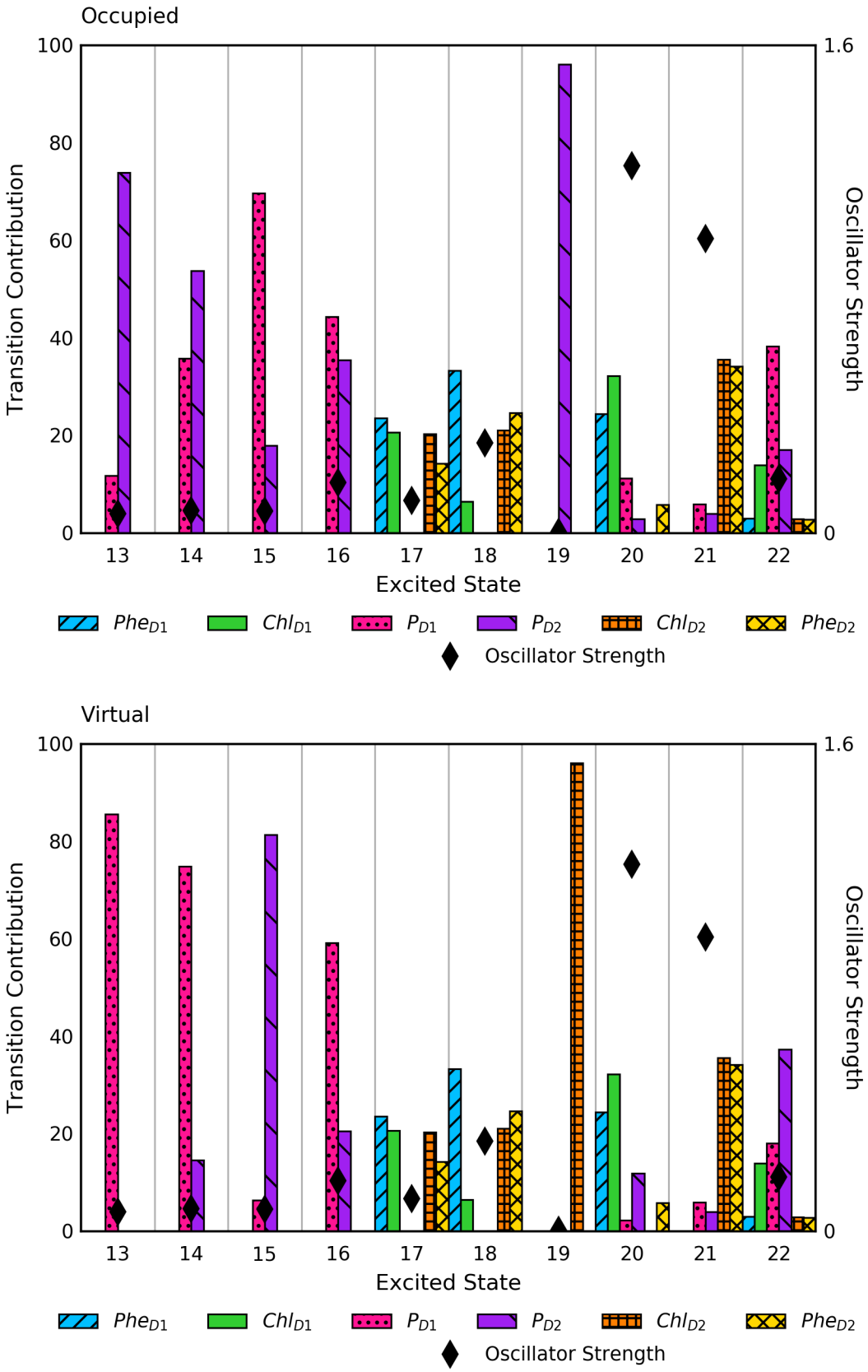
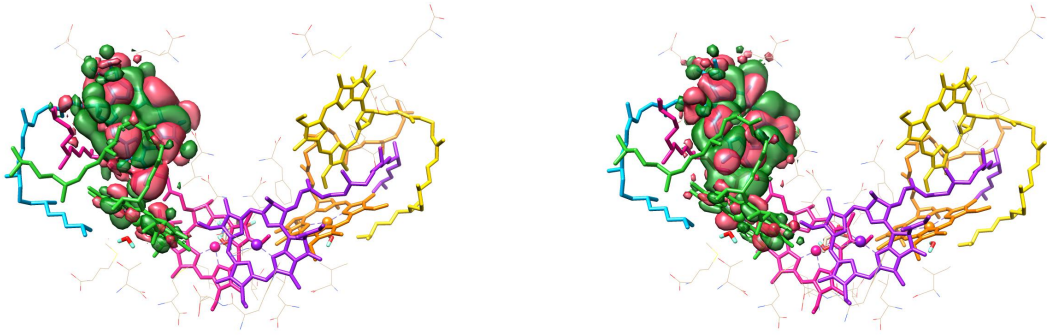
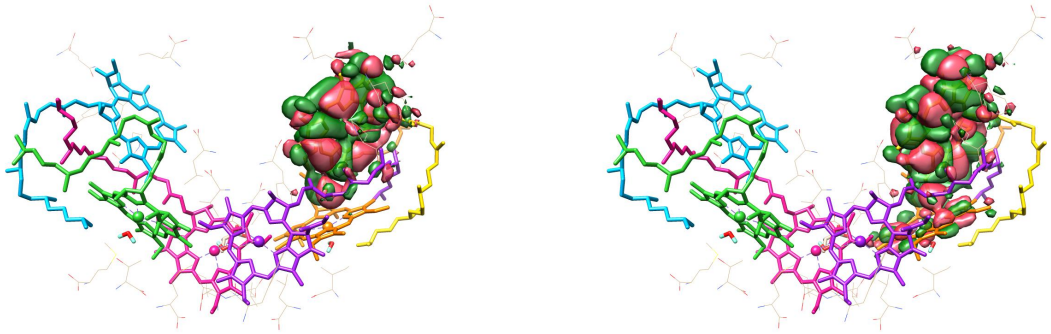


Figure A.52 : H198A with mutant water (ωB97X-D/6-31G**) excited states 13-22, (bar chart, left y axis) % of state contributed to by each cofactor (occupied orbital occupancy analysis with MultiWfn from Mulliken method) and (black diamonds, right y axis) oscillator strength of each state. Cofactors coloured as in all Figures in this thesis. TOP – occupied orbitals, BOTTOM – virtual orbitals.

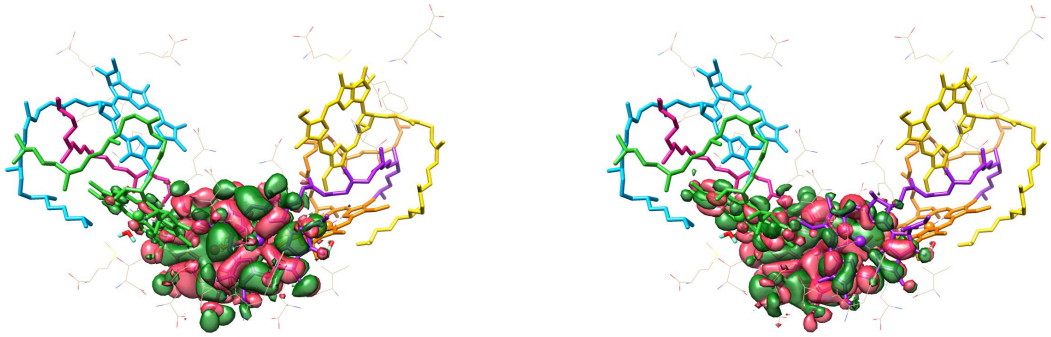
Local Phe D1 (Local): 2296 → 2301
State 1: 65.04%
State 2: 3.39%



Down inactive (Phe D2 to Chl D2): 2300 → 2305
State 1: 3.01%
State 2: 58.34%



P D2 to P D1: 2298 → 2304
State 3: 47.12%
State 4: 8.97%
State 5: 5.29%
State 6: 2.70%



P D1 to P D2: 2299 → 2306
State 4: 46.05%
State 6: 19.93%

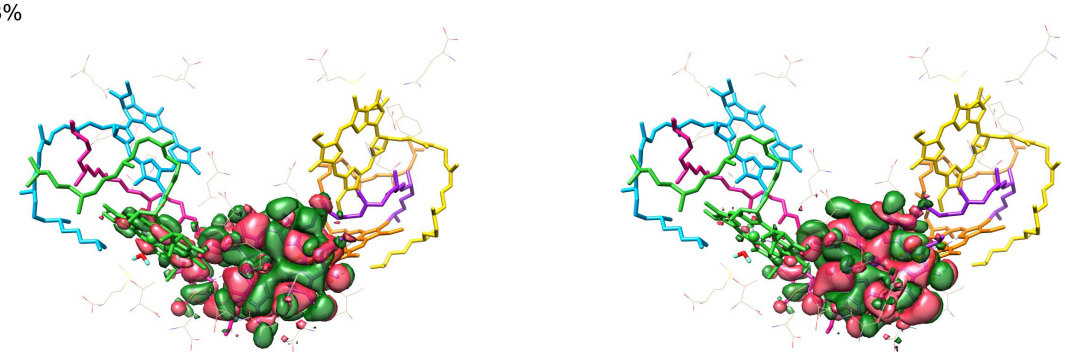
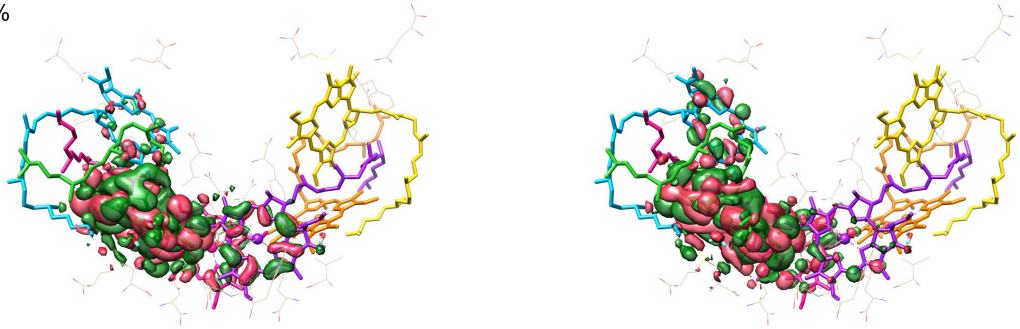
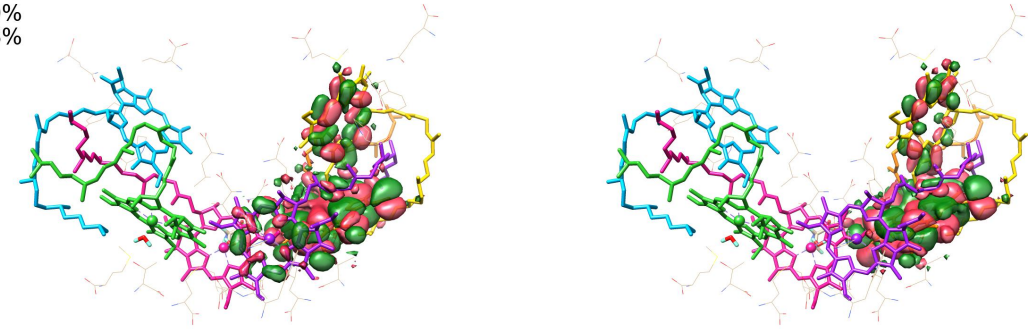


Figure A.53 : MO diagrams exemplifying all transition classes for H198A ωB97X-D/6-31G** including dominant transitions contributing to ES 1-6, LEFT COLUMN - Occupied MO, RIGHT COLUMN – Virtual MO (Page 1)

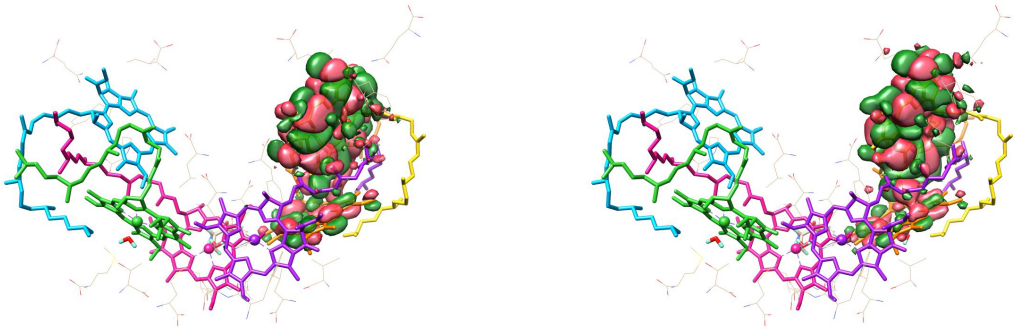
Down active (Chl D1 to P D1): 2297 → 2303
State 3: 17.11%
State 4: 3.40%
State 5: 48.18%
State 6: 7.55%



Down inactive (Phe D2 to Chl D2): 2295 → 2302
State 3: 2.15%
State 4: 12.87%
State 5: 19.00%
State 6: 42.08%



Up inactive (Chl D2 to Phe D2): 2293 → 2305
State 2: 16.55%



Up active (Chl D1 to Phe D1): 2290 → 2301
State 1: 11.72%

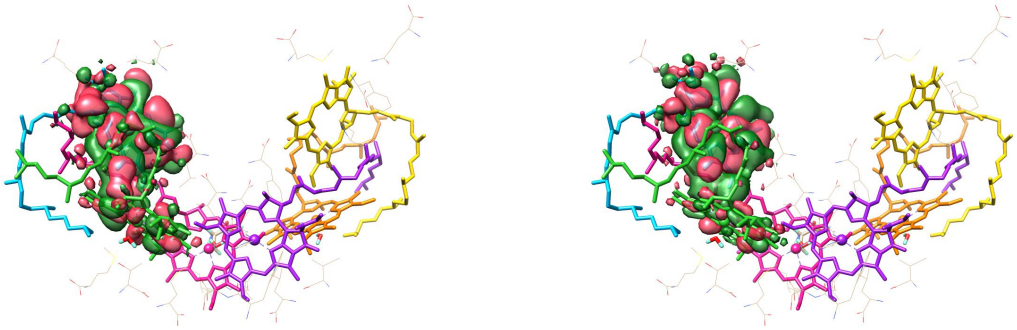


Figure A.53 : MO diagrams exemplifying all transition classes for H198A ωB97X-D/6-31G** including dominant transitions contributing to ES 1-6, LEFT COLUMN - Occupied MO, RIGHT COLUMN – Virtual MO (Page 2)

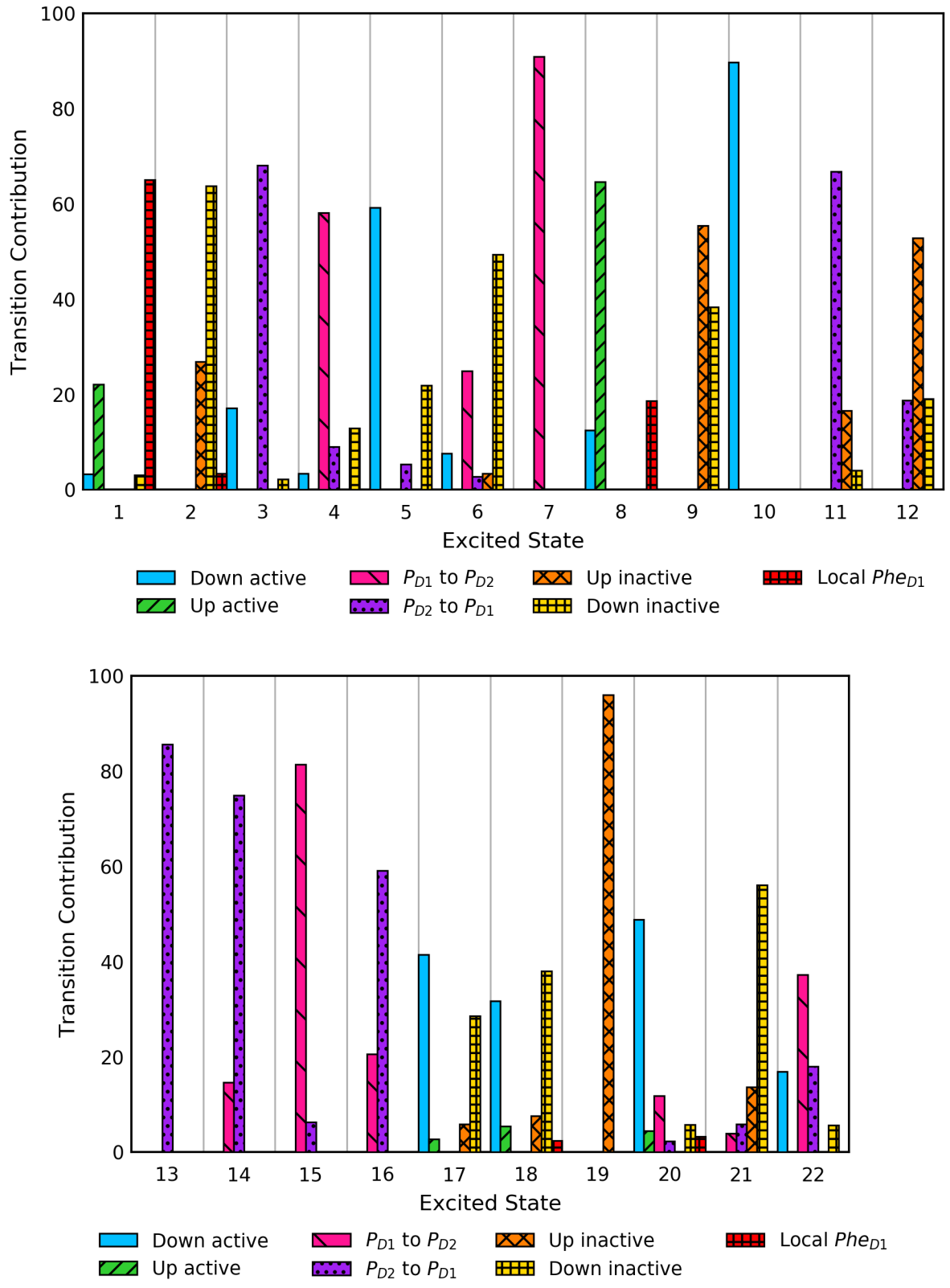


Figure A.54 : Contributions from each transition class for H198A (ωB97X-D/ 6-31G**), TOP : ES 1-12 (Qy and Qx regions), BOTTOM : ES 13-22 (Soret region)

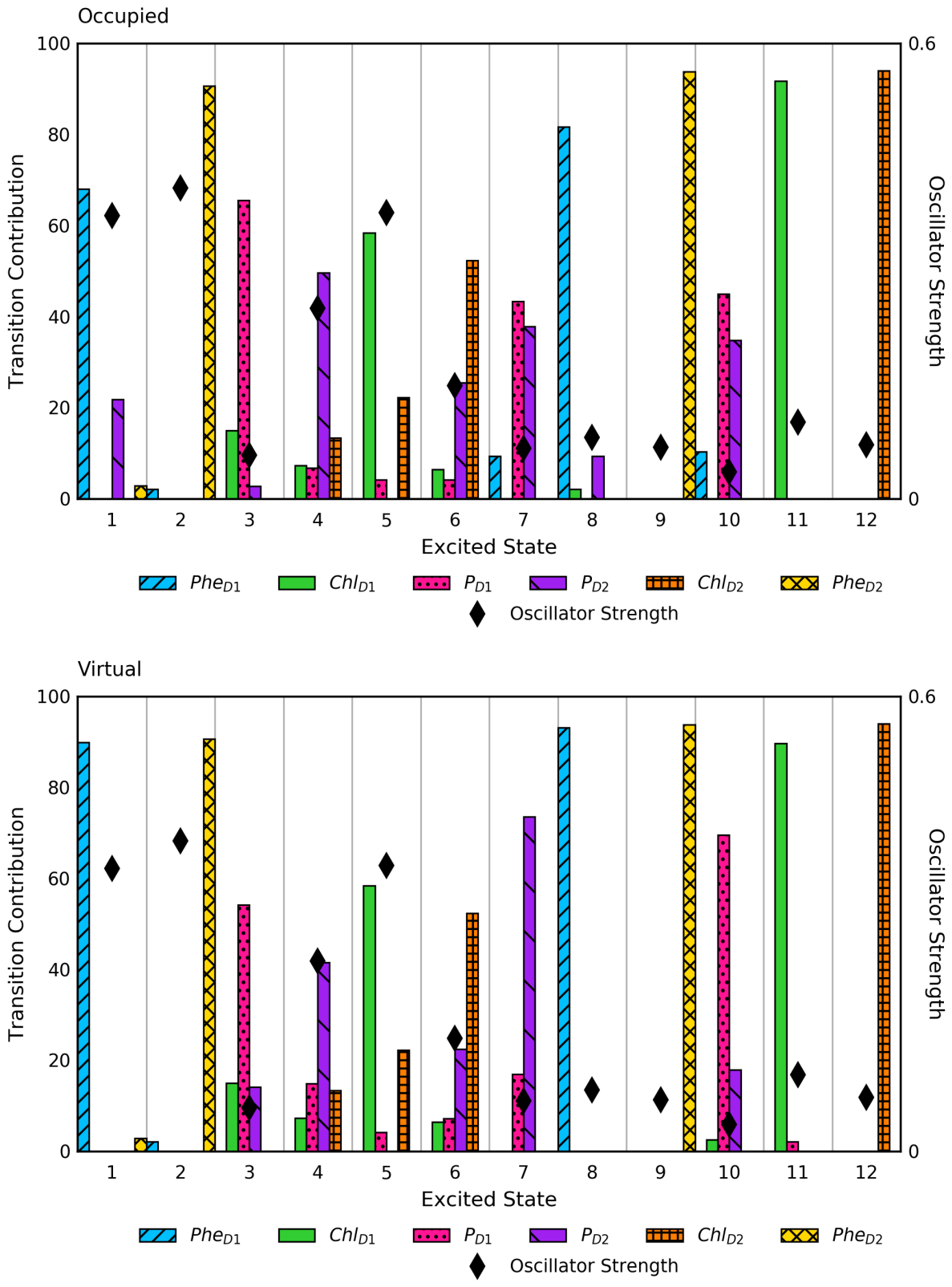


Figure A.55 : H198N with mutant water (ωB97X-D/6-31G**) excited states 1-12, (bar chart, left y axis) % of state contributed to by each cofactor (occupied orbital occupancy analysis with MultiWfn from Mulliken method) and (black diamonds, right y axis) oscillator strength of each state. Cofactors coloured as in all Figures in this thesis. TOP – occupied orbitals, BOTTOM – virtual orbitals.

H198N Results

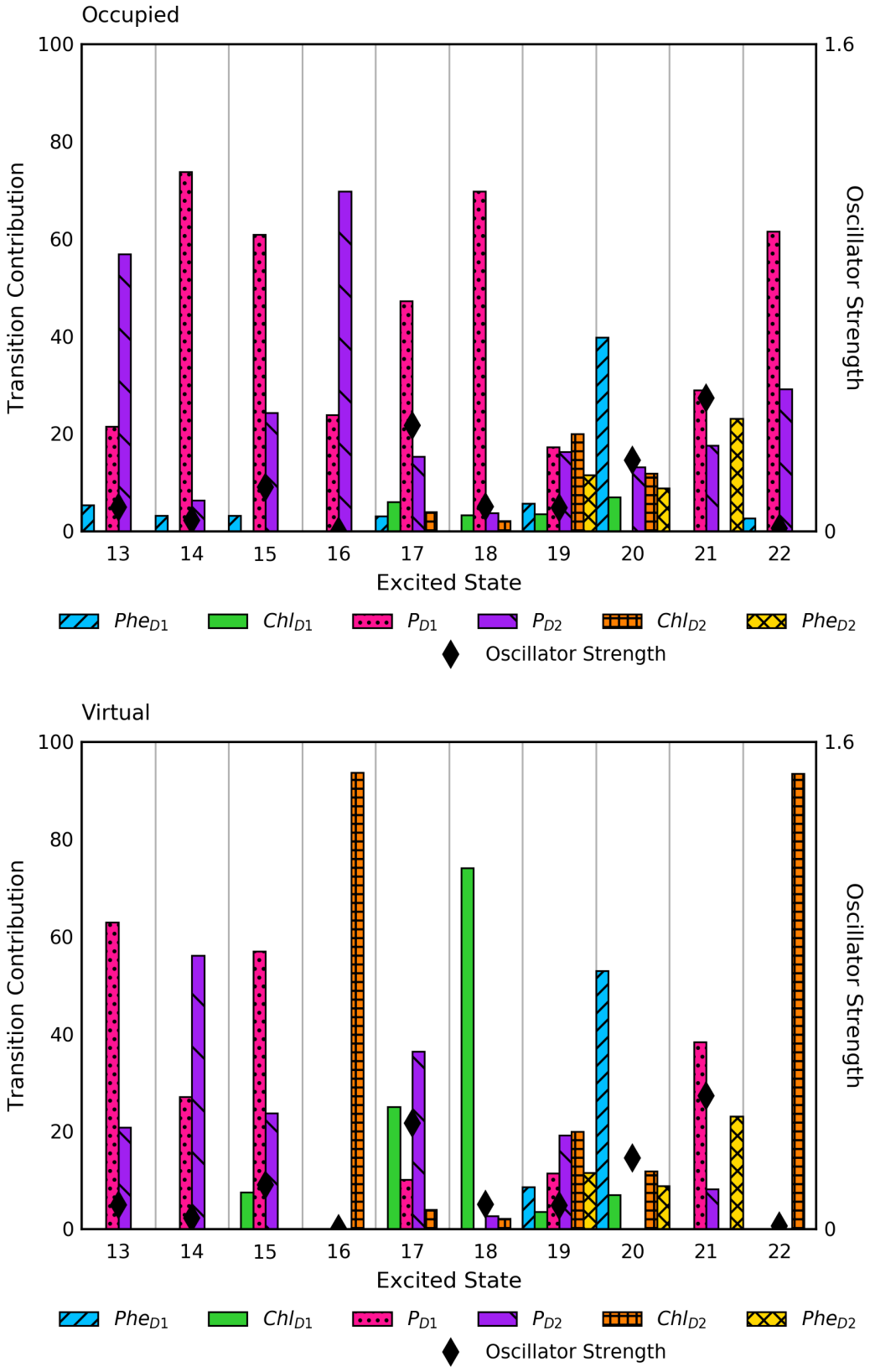
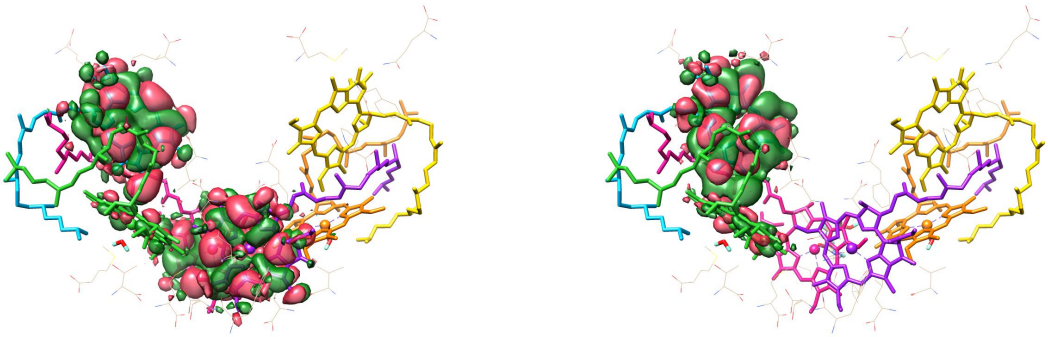
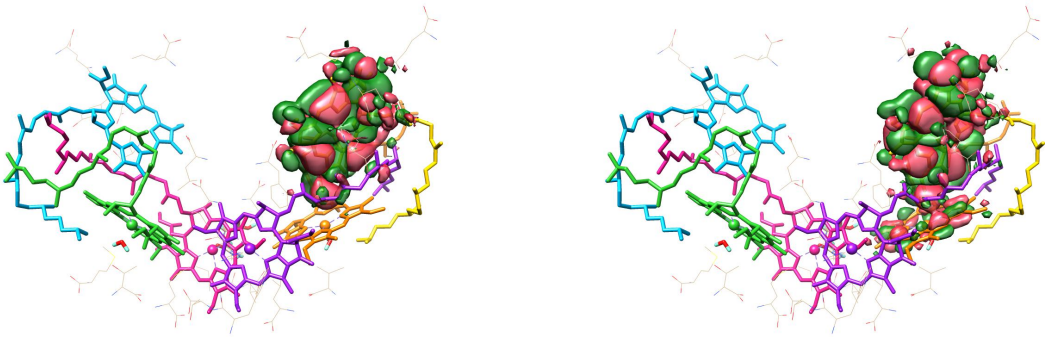


Figure A.56 : H198N with mutant water (ωB97X-D/6-31G**) excited states 13-22, (bar chart, left y axis) % of state contributed to by each cofactor (occupied orbital occupancy analysis with MultiWfn from Mulliken method) and (black diamonds, right y axis) oscillator strength of each state. Cofactors coloured as in all Figures in this thesis. TOP – occupied orbitals, BOTTOM – virtual orbitals.

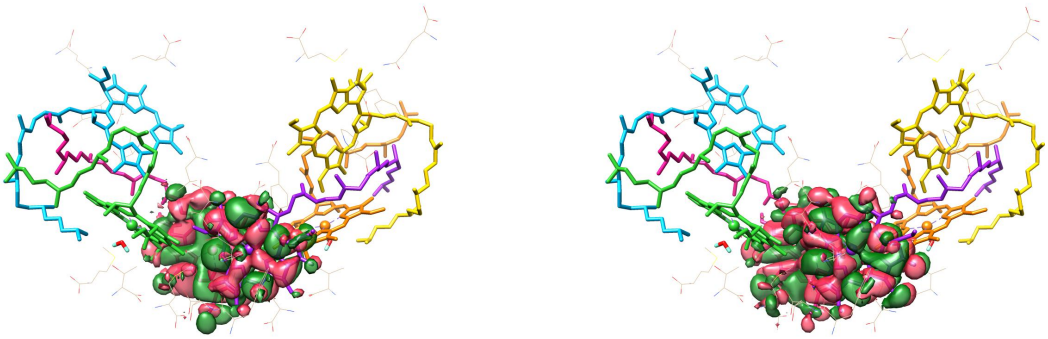
Up active (P D2 to Phe D1): 2306 → 2312
State 1: 43.51%
State 2: 2.17%



Down inactive (Phe D2 to Chl D2): 2309 → 2315
State 1: 2.89%
State 2: 58.88%



P D1 to P D2: 2311 → 2317
State 3: 45.93%
State 4: 6.73%
State 5: 4.14%
State 6: 2.05%



P D2 to P D1: 2310 → 2316
State 4: 36.18%
State 6: 18.36%

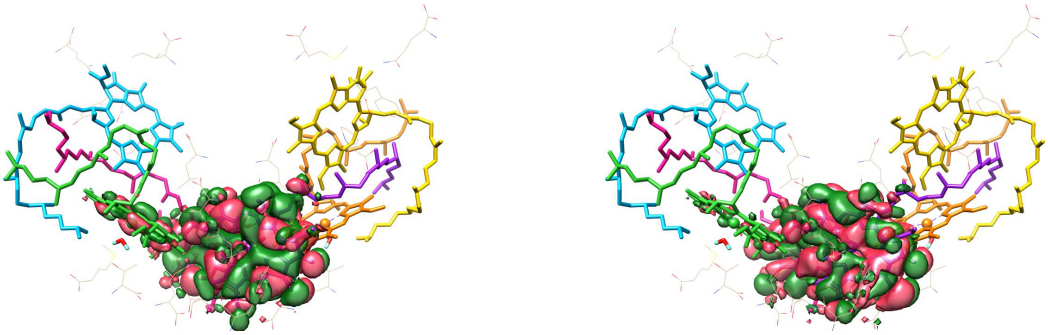
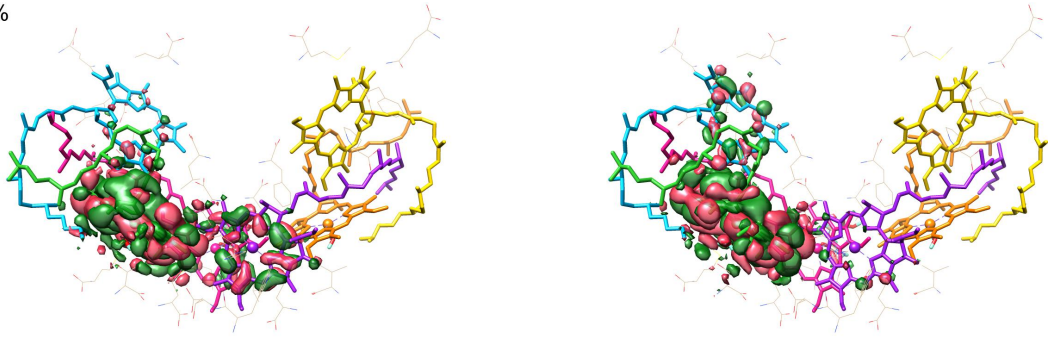
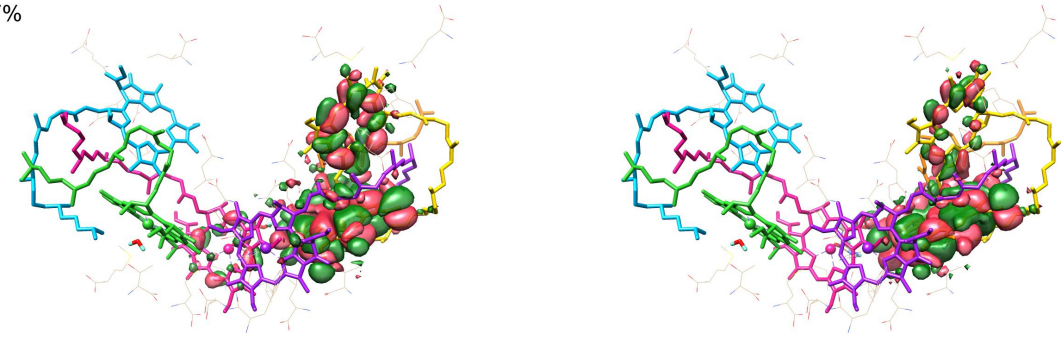


Figure A.57 : MO diagrams exemplifying all transition classes for H198N ωB97X-D/6-31G** including dominant transitions contributing to ES 1-6, LEFT COLUMN - Occupied MO, RIGHT COLUMN – Virtual MO (Page 1)

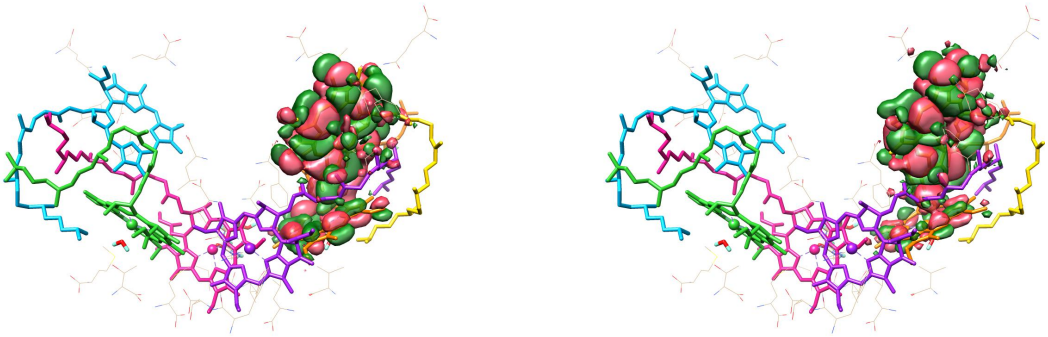
Up active (P D2 to Phe D1): 2308 → 2314
State 3: 14.99%
State 4: 7.27%
State 5: 48.50%
State 6: 6.39%



Down inactive (Phe D2 to Chl D2): 2305 → 2313
State 4: 13.41%
State 5: 19.28%
State 6: 41.67%



Up inactive (Chl D2 to Phe D2): 2303 → 2315
State 2: 16.13%



Down active (Chl D1 to P D1): 2302 → 2320
State 5: 6.51%

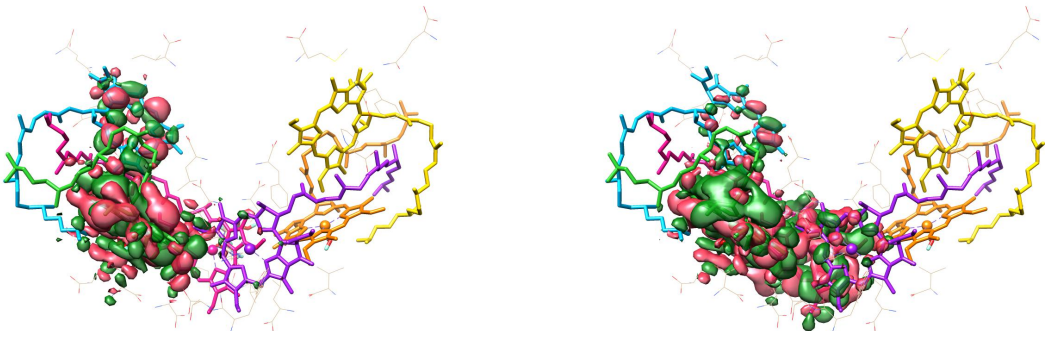


Figure A.57 : MO diagrams exemplifying all transition classes for H198N ωB97X-D/6-31G** including dominant transitions contributing to ES 1-6, LEFT COLUMN - Occupied MO, RIGHT COLUMN – Virtual MO (Page 2)

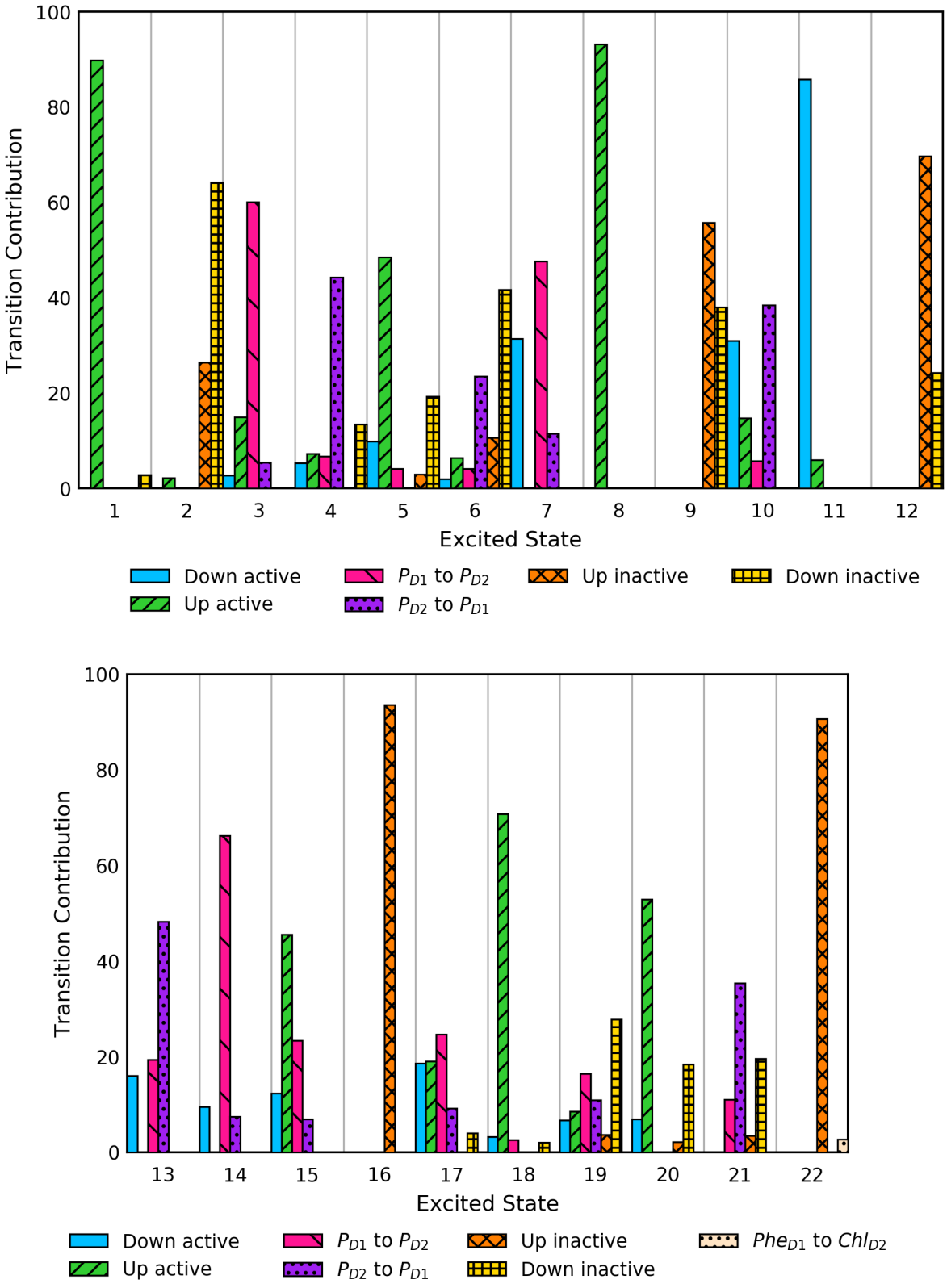


Figure A.58 : Contributions from each transition class for H198N (ωB97X-D/ 6-31G**), TOP : ES 1-12 (Qy and Qx regions), BOTTOM : ES 13-22 (Soret region)

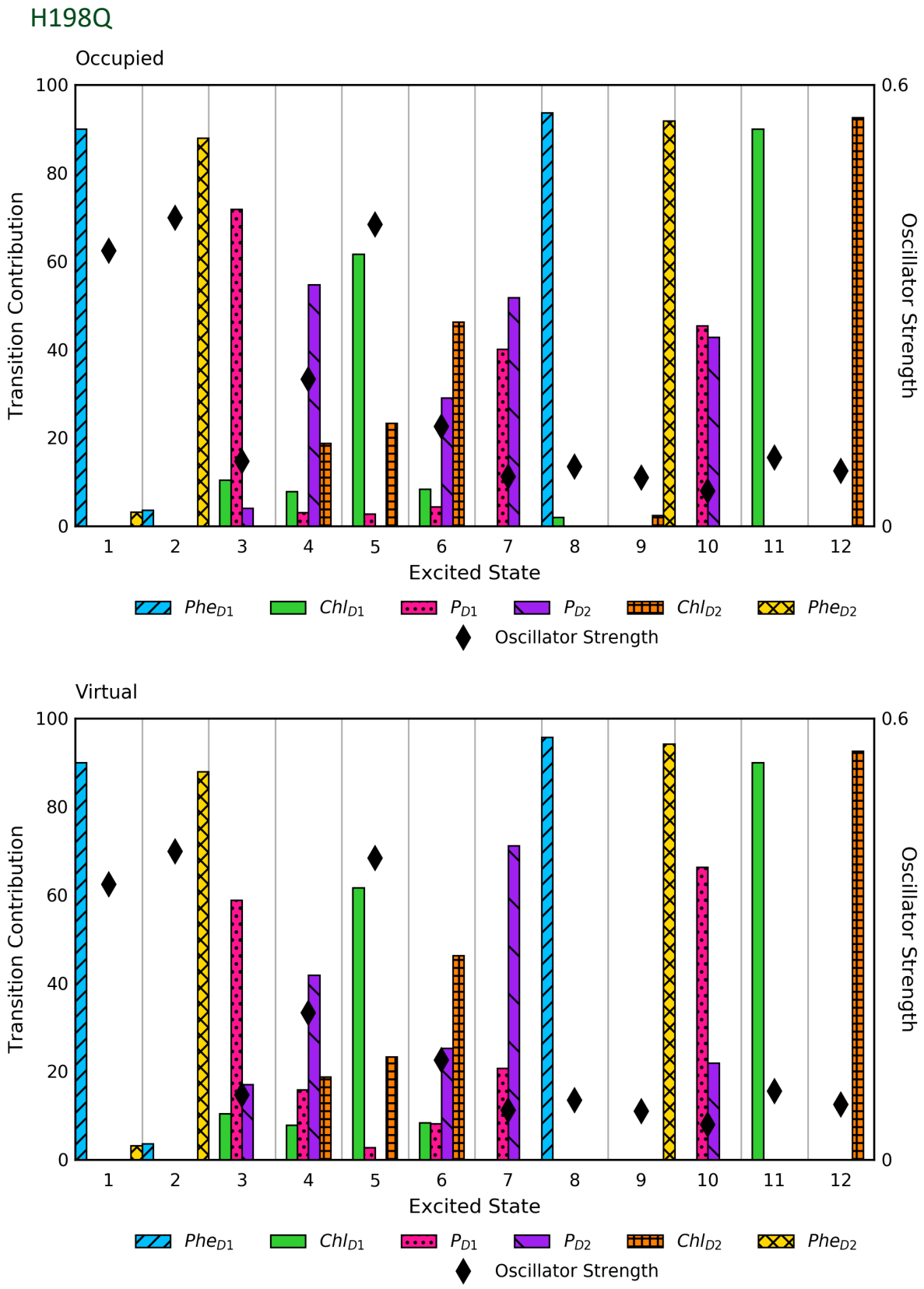


Figure A.59 : H198Q (ωB97X-D/6-31G**) excited states 1-12, (bar chart, left y axis) % of state contributed to by each cofactor (occupied orbital occupancy analysis with MultiWfn from Mulliken method) and (black diamonds, right y axis) oscillator strength of each state. Cofactors coloured as in all Figures in this thesis. TOP – occupied orbitals, BOTTOM – virtual orbitals.

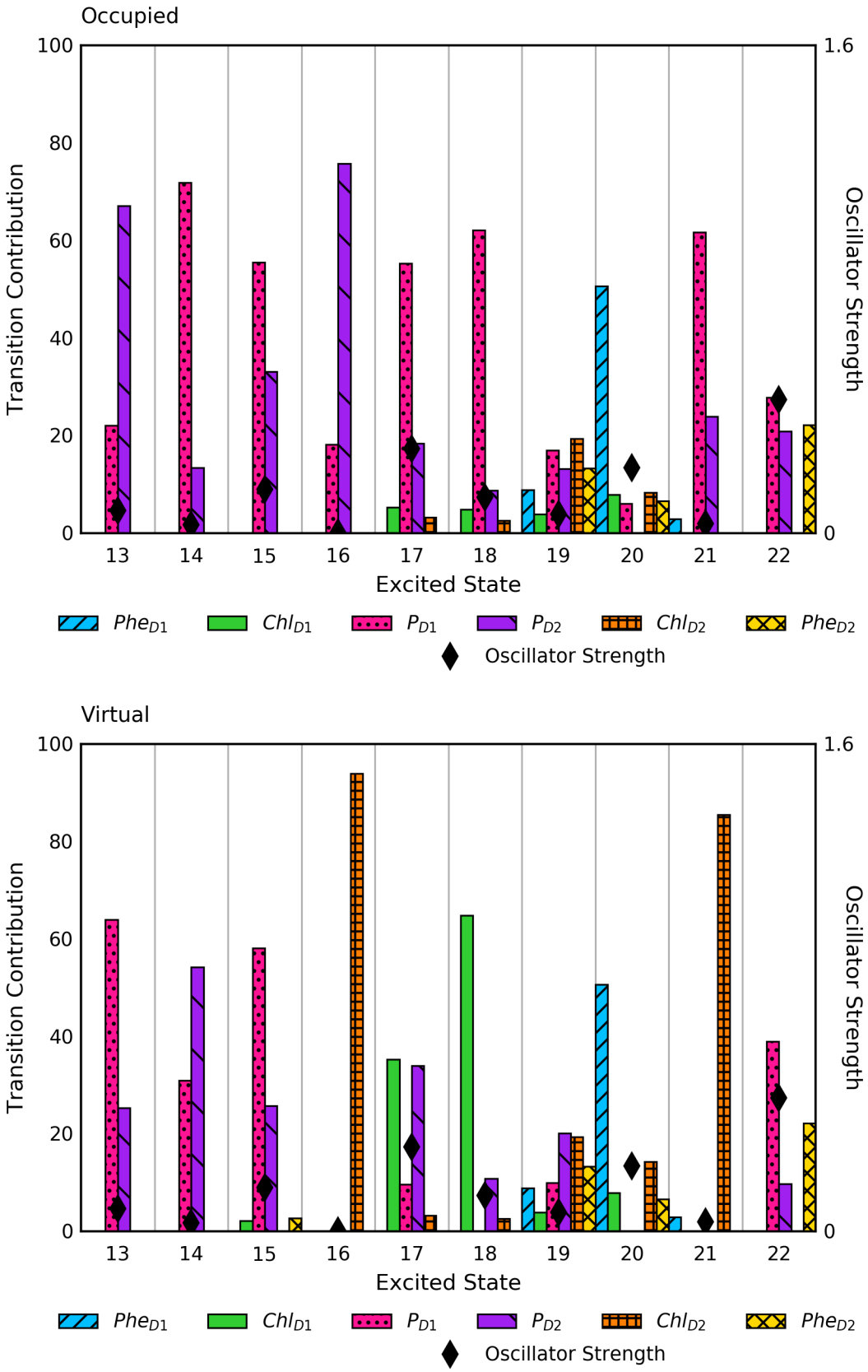
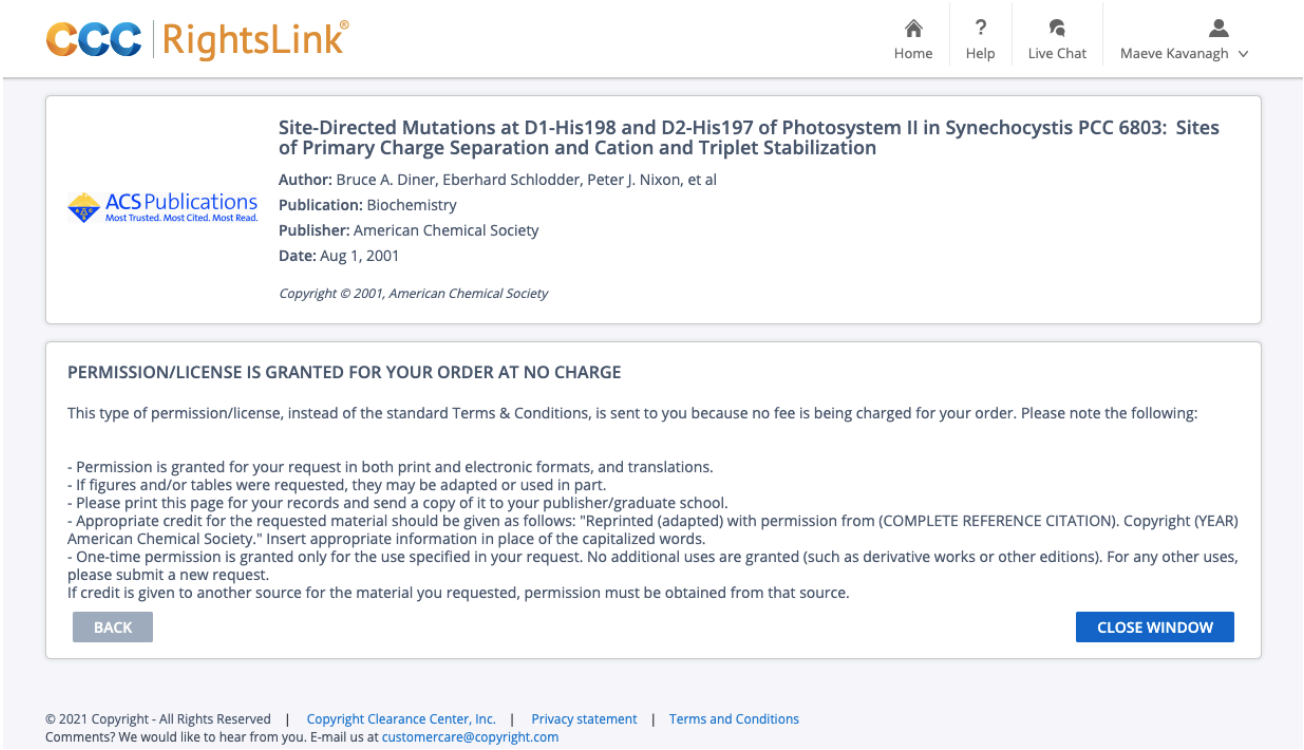


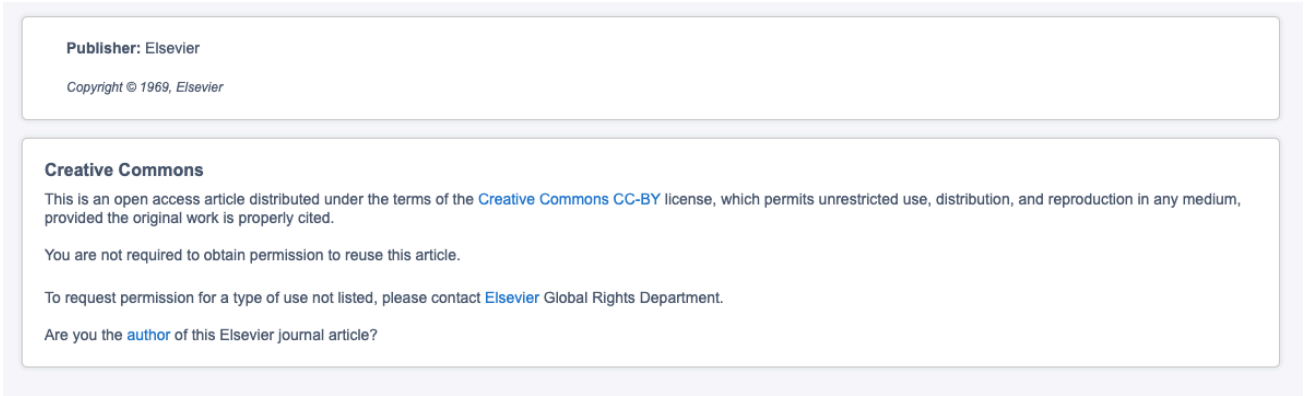
Figure A.60 : H198Q (ωB97X-D/6-31G**) excited states 13-22, (bar chart, left y axis) % of state contributed to by each cofactor (occupied orbital occupancy analysis with MultiWfn from Mulliken method) and (black diamonds, right y axis) oscillator strength of each state. Cofactors coloured as in all Figures in this thesis. TOP – occupied orbitals, BOTTOM – virtual orbitals.

Appendix Five – *Rights and Permissions*

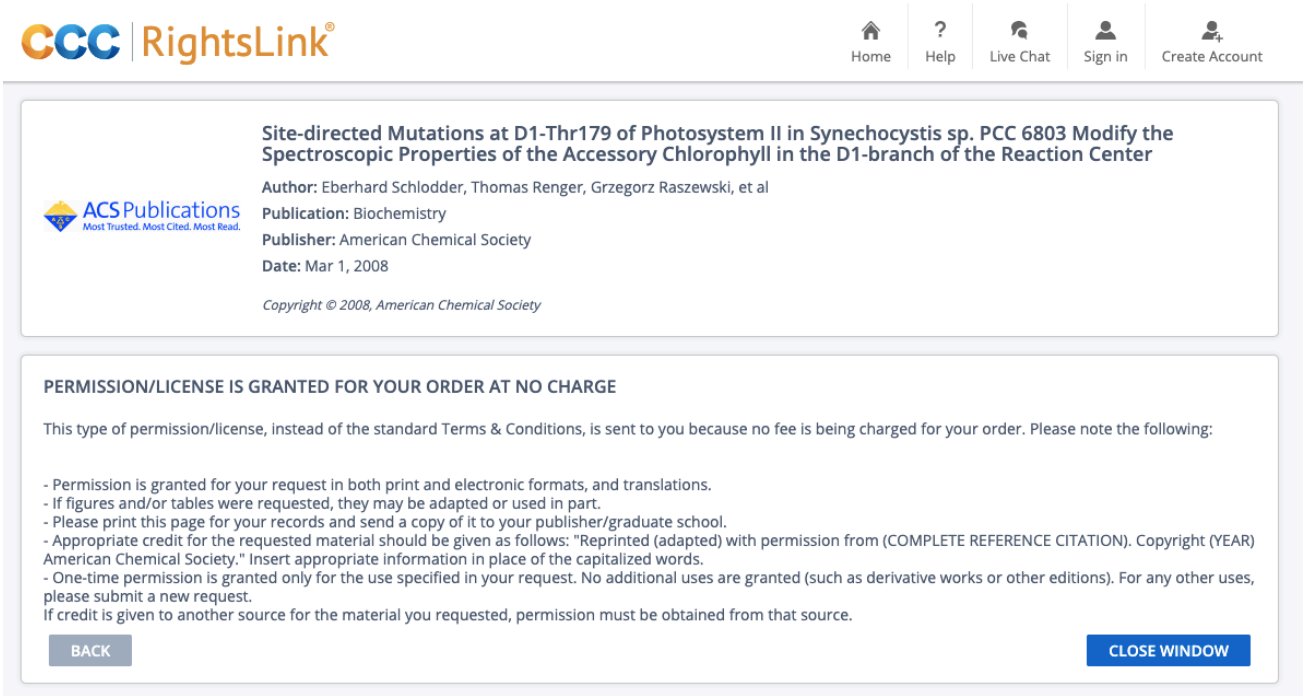
Permission for reuse of Figures 2.15 and 3.15:



Permission for reuse of Figure 4.3:



Permission for reuse of Figure 4.4:



Permission for reuse of Figure 1.25A is attached overleaf:

ELSEVIER LICENSE
TERMS AND CONDITIONS

Jun 17, 2021

This Agreement between Imperial College London -- Maeve Kavanagh ("You") and Elsevier ("Elsevier") consists of your license details and the terms and conditions provided by Elsevier and Copyright Clearance Center.

License Number	5073630890368
License date	May 21, 2021
Licensed Content Publisher	Elsevier
Licensed Content Publication	Biochimica et Biophysica Acta (BBA) - Bioenergetics
Licensed Content Title	Time-resolved spectroscopy at 10 K of the Photosystem II reaction center; deconvolution of the red absorption band
Licensed Content Author	Paul J.M. van Kan,Stephan C.M. Otte,Frank A.M. Kleinherenbrink,Maaike C. Nieveen,Thijs J. Aartsma,Hans J. van Gorkom
Licensed Content Date	Nov 5, 1990
Licensed Content Volume	1020
Licensed Content Issue	2
Licensed Content Pages	7
Start Page	146
End Page	152
Type of Use	reuse in a thesis/dissertation

Portion	figures/tables/illustrations
Number of figures/tables/illustrations	1
Format	both print and electronic
Are you the author of this Elsevier article?	No
Will you be translating?	No
Title	A TDDFT Investigation of Excited States of the Photosystem II Reaction Centre
Institution name	Imperial College London
Expected presentation date	Jun 2021
Portions	Figure 1A
Requestor Location	Imperial College London [redacted] London, London [redacted] United Kingdom Attn: Imperial College London
Publisher Tax ID	GB 494 6272 12
Total	0.00 USD
Terms and Conditions	

INTRODUCTION

1. The publisher for this copyrighted material is Elsevier. By clicking "accept" in connection with completing this licensing transaction, you agree that the following terms and conditions apply to this transaction (along with the Billing and Payment terms and conditions established by Copyright Clearance Center, Inc. ("CCC"), at the time that you opened your Rightslink account and that are available at any time at http://myaccount.copyright.com).

GENERAL TERMS

2. Elsevier hereby grants you permission to reproduce the aforementioned material subject to the terms and conditions indicated.

3. Acknowledgement: If any part of the material to be used (for example, figures) has appeared in our publication with credit or acknowledgement to another source, permission must also be sought from that source. If such permission is not obtained then that material may not be included in your publication/copies. Suitable acknowledgement to the source must be made, either as a footnote or in a reference list at the end of your publication, as follows:

"Reprinted from Publication title, Vol /edition number, Author(s), Title of article / title of chapter, Pages No., Copyright (Year), with permission from Elsevier [OR APPLICABLE SOCIETY COPYRIGHT OWNER]." Also Lancet special credit - "Reprinted from The Lancet, Vol. number, Author(s), Title of article, Pages No., Copyright (Year), with permission from Elsevier."

4. Reproduction of this material is confined to the purpose and/or media for which permission is hereby given.

5. Altering/Modifying Material: Not Permitted. However figures and illustrations may be altered/adapted minimally to serve your work. Any other abbreviations, additions, deletions and/or any other alterations shall be made only with prior written authorization of Elsevier Ltd. (Please contact Elsevier's permissions helpdesk here). No modifications can be made to any Lancet figures/tables and they must be reproduced in full.

6. If the permission fee for the requested use of our material is waived in this instance, please be advised that your future requests for Elsevier materials may attract a fee.

7. Reservation of Rights: Publisher reserves all rights not specifically granted in the combination of (i) the license details provided by you and accepted in the course of this licensing transaction, (ii) these terms and conditions and (iii) CCC's Billing and Payment terms and conditions.

8. License Contingent Upon Payment: While you may exercise the rights licensed immediately upon issuance of the license at the end of the licensing process for the transaction, provided that you have disclosed complete and accurate details of your proposed use, no license is finally effective unless and until full payment is received from you (either by publisher or by CCC) as provided in CCC's Billing and Payment terms and conditions. If full payment is not received on a timely basis, then any license preliminarily granted shall be deemed automatically revoked and shall be void as if never granted. Further, in the event that you breach any of these terms and conditions or any of CCC's Billing and Payment terms and conditions, the license is automatically revoked and shall be void as if never granted. Use of materials as described in a revoked license, as well as any use of the materials beyond the scope of an unrevoked license, may constitute copyright infringement and publisher reserves the right to take any and all action to protect its copyright in the materials.

9. Warranties: Publisher makes no representations or warranties with respect to the licensed material.

10. Indemnity: You hereby indemnify and agree to hold harmless publisher and CCC, and their respective officers, directors, employees and agents, from and against any and all claims arising out of your use of the licensed material other than as specifically authorized pursuant to this license.

11. No Transfer of License: This license is personal to you and may not be sublicensed, assigned, or transferred by you to any other person without publisher's written permission.

12. No Amendment Except in Writing: This license may not be amended except in a writing signed by both parties (or, in the case of publisher, by CCC on publisher's behalf).

13. Objection to Contrary Terms: Publisher hereby objects to any terms contained in any purchase order, acknowledgment, check endorsement or other writing prepared by you, which terms are inconsistent with these terms and conditions or CCC's Billing and Payment terms and conditions. These terms and conditions, together with CCC's Billing and Payment terms and conditions (which are incorporated herein), comprise the entire agreement between you and publisher (and CCC) concerning this licensing transaction. In the event of any conflict between your obligations established by these terms and conditions and those established by CCC's Billing and Payment terms and conditions, these terms and conditions shall control.

14. Revocation: Elsevier or Copyright Clearance Center may deny the permissions described in this License at their sole discretion, for any reason or no reason, with a full refund payable to you. Notice of such denial will be made using the contact information provided by you. Failure to receive such notice will not alter or invalidate the denial. In no event will Elsevier or Copyright Clearance Center be responsible or liable for any costs, expenses or damage incurred by you as a result of a denial of your permission request, other than a refund of the amount(s) paid by you to Elsevier and/or Copyright Clearance Center for denied permissions.

LIMITED LICENSE

The following terms and conditions apply only to specific license types:

15. **Translation**: This permission is granted for non-exclusive world **English** rights only unless your license was granted for translation rights. If you licensed translation rights you may only translate this content into the languages you requested. A professional translator must perform all translations and reproduce the content word for word preserving the integrity of the article.

16. **Posting licensed content on any Website**: The following terms and conditions apply as follows: Licensing material from an Elsevier journal: All content posted to the web site must maintain the copyright information line on the bottom of each image; A hyper-text must be included to the Homepage of the journal from which you are licensing at http://www.sciencedirect.com/science/journal/xxxxx or the Elsevier homepage for books at http://www.elsevier.com; Central Storage: This license does not include permission for a scanned version of the material to be stored in a central repository such as that provided by Heron/XanEdu.

Licensing material from an Elsevier book: A hyper-text link must be included to the Elsevier homepage at http://www.elsevier.com . All content posted to the web site must maintain the copyright information line on the bottom of each image.

Posting licensed content on Electronic reserve: In addition to the above the following clauses are applicable: The web site must be password-protected and made available only to bona fide students registered on a relevant course. This permission is granted for 1 year only. You may obtain a new license for future website posting.

17. **For journal authors:** the following clauses are applicable in addition to the above:

Preprints:

A preprint is an author's own write-up of research results and analysis, it has not been peer-reviewed, nor has it had any other value added to it by a publisher (such as formatting, copyright, technical enhancement etc.).

Authors can share their preprints anywhere at any time. Preprints should not be added to or enhanced in any way in order to appear more like, or to substitute for, the final versions of articles however authors can update their preprints on arXiv or RePEc with their Accepted Author Manuscript (see below).

If accepted for publication, we encourage authors to link from the preprint to their formal publication via its DOI. Millions of researchers have access to the formal publications on ScienceDirect, and so links will help users to find, access, cite and use the best available version. Please note that Cell Press, The Lancet and some society-owned have different preprint policies. Information on these policies is available on the journal homepage.

Accepted Author Manuscripts: An accepted author manuscript is the manuscript of an article that has been accepted for publication and which typically includes author-incorporated changes suggested during submission, peer review and editor-author communications.

Authors can share their accepted author manuscript:

- immediately
    - via their non-commercial person homepage or blog
    - by updating a preprint in arXiv or RePEc with the accepted manuscript
    - via their research institute or institutional repository for internal institutional uses or as part of an invitation-only research collaboration work-group
    - directly by providing copies to their students or to research collaborators for their personal use
    - for private scholarly sharing as part of an invitation-only work group on commercial sites with which Elsevier has an agreement
- After the embargo period
    - via non-commercial hosting platforms such as their institutional repository
    - via commercial sites with which Elsevier has an agreement

In all cases accepted manuscripts should:

- link to the formal publication via its DOI
- bear a CC-BY-NC-ND license - this is easy to do
- if aggregated with other manuscripts, for example in a repository or other site, be shared in alignment with our hosting policy not be added to or enhanced in any way to appear more like, or to substitute for, the published journal article.

Published journal article (JPA): A published journal article (PJA) is the definitive final record of published research that appears or will appear in the journal and embodies all value-adding publishing activities including peer review co-ordination, copy-editing, formatting, (if relevant) pagination and online enrichment.

Policies for sharing publishing journal articles differ for subscription and gold open access articles:

Subscription Articles: If you are an author, please share a link to your article rather than the full-text. Millions of researchers have access to the formal publications on ScienceDirect, and so links will help your users to find, access, cite, and use the best available version.

Theses and dissertations which contain embedded PJAs as part of the formal submission can be posted publicly by the awarding institution with DOI links back to the formal publications on ScienceDirect.

If you are affiliated with a library that subscribes to ScienceDirect you have additional private sharing rights for others' research accessed under that agreement. This includes use for classroom teaching and internal training at the institution (including use in course packs and courseware programs), and inclusion of the article for grant funding purposes.

Gold Open Access Articles: May be shared according to the author-selected end-user license and should contain a CrossMark logo, the end user license, and a DOI link to the formal publication on ScienceDirect.

Please refer to Elsevier's posting policy for further information.

18. **For book authors** the following clauses are applicable in addition to the above: Authors are permitted to place a brief summary of their work online only. You are not allowed to download and post the published electronic version of your chapter, nor may you scan the printed edition to create an electronic version. **Posting to a repository:** Authors are permitted to post a summary of their chapter only in their institution's repository.

19. **Thesis/Dissertation**: If your license is for use in a thesis/dissertation your thesis may be submitted to your institution in either print or electronic form. Should your thesis be published commercially, please reapply for permission. These requirements include permission for the Library and Archives of Canada to supply single copies, on demand, of the complete thesis and include permission for Proquest/UMI to supply single copies, on demand, of the complete thesis. Should your thesis be published commercially, please reapply for permission. Theses and dissertations which contain embedded PJAs as part of the formal submission can be posted publicly by the awarding institution with DOI links back to the formal publications on ScienceDirect.

Elsevier Open Access Terms and Conditions

You can publish open access with Elsevier in hundreds of open access journals or in nearly 2000 established subscription journals that support open access publishing. Permitted third party re-use of these open access articles is defined by the author's choice of Creative Commons user license. See our open access license policy for more information.

Terms & Conditions applicable to all Open Access articles published with Elsevier:

Any reuse of the article must not represent the author as endorsing the adaptation of the article nor should the article be modified in such a way as to damage the author's honour or reputation. If any changes have been made, such changes must be clearly indicated.

The author(s) must be appropriately credited and we ask that you include the end user license and a DOI link to the formal publication on ScienceDirect.

If any part of the material to be used (for example, figures) has appeared in our publication with credit or acknowledgement to another source it is the responsibility of the user to ensure their reuse complies with the terms and conditions determined by the rights holder.

Additional Terms & Conditions applicable to each Creative Commons user license:

CC BY: The CC-BY license allows users to copy, to create extracts, abstracts and new works from the Article, to alter and revise the Article and to make commercial use of the Article (including reuse and/or resale of the Article by commercial entities), provided the user gives appropriate credit (with a link to the formal publication through the relevant DOI), provides a link to the license, indicates if changes were made and the licensor is not represented as endorsing the use made of the work. The full details of the license are available at http://creativecommons.org/licenses/by/4.0.

CC BY NC SA: The CC BY-NC-SA license allows users to copy, to create extracts, abstracts and new works from the Article, to alter and revise the Article, provided this is not done for commercial purposes, and that the user gives appropriate credit (with a link to the formal publication through the relevant DOI), provides a link to the license, indicates if changes were made and the licensor is not represented as endorsing the use made of the

work. Further, any new works must be made available on the same conditions. The full details of the license are available at http://creativecommons.org/licenses/by-nc-sa/4.0.

CC BY NC ND: The CC BY-NC-ND license allows users to copy and distribute the Article, provided this is not done for commercial purposes and further does not permit distribution of the Article if it is changed or edited in any way, and provided the user gives appropriate credit (with a link to the formal publication through the relevant DOI), provides a link to the license, and that the licensor is not represented as endorsing the use made of the work. The full details of the license are available at http://creativecommons.org/licenses/by-nc-nd/4.0. Any commercial reuse of Open Access articles published with a CC BY NC SA or CC BY NC ND license requires permission from Elsevier and will be subject to a fee.

Commercial reuse includes:

- Associating advertising with the full text of the Article
- Charging fees for document delivery or access
- Article aggregation
- Systematic distribution via e-mail lists or share buttons

Posting or linking by commercial companies for use by customers of those companies.

20. **Other Conditions**:

v1.10

Questions? customercare@copyright.com or +1-855-239-3415 (toll free in the US) or +1-978-646-2777.

